

# Fault Zone Dynamic Processes

## Evolution of Fault Properties During Seismic Rupture



Marion Y. Thomas, Thomas M. Mitchell,  
and Harsha S. Bhat

*Editors*

---

**Geophysical Monograph Series**

# Geophysical Monograph Series

- 
- 175 **A Continental Plate Boundary: Tectonics at South Island, New Zealand** David Okaya, Tim Stem, and Fred Davey (Eds.)
- 176 **Exploring Venus as a Terrestrial Planet** Larry W. Esposito, Ellen R. Stofan, and Thomas E. Cravens (Eds.)
- 177 **Ocean Modeling in an Eddying Regime** Matthew Hecht and Hiroyasu Hasumi (Eds.)
- 178 **Magma to Microbe: Modeling Hydrothermal Processes at Oceanic Spreading Centers** Robert P. Lowell, Jeffrey S. Seewald, Anna Metaxas, and Michael R. Perfit (Eds.)
- 179 **Active Tectonics and Seismic Potential of Alaska** Jeffrey T. Freymueller, Peter J. Haeussler, Robert L. Wesson, and Göran Ekström (Eds.)
- 180 **Arctic Sea Ice Decline: Observations, Projections, Mechanisms, and Implications** Eric T. DeWeaver, Cecilia M. Bitz, and L.-Bruno Tremblay (Eds.)
- 181 **Midlatitude Ionospheric Dynamics and Disturbances** Paul M. Kintner, Jr., Anthea J. Coster, Tim Fuller-Rowell, Anthony J. Mannucci, Michael Mendillo, and Roderick Heelis (Eds.)
- 182 **The Stromboli Volcano: An Integrated Study of the 2002–2003 Eruption** Sonia Calvari, Salvatore Inguaggiato, Giuseppe Puglisi, Maurizio Ripepe, and Mauro Rosi (Eds.)
- 183 **Carbon Sequestration and Its Role in the Global Carbon Cycle** Brian J. McPherson and Eric T. Sundquist (Eds.)
- 184 **Carbon Cycling in Northern Peatlands** Andrew J. Baird, Lisa R. Belyea, Xavier Comas, A. S. Reeve, and Lee D. Slater (Eds.)
- 185 **Indian Ocean Biogeochemical Processes and Ecological Variability** Jerry D. Wiggert, Raleigh R. Hood, S. Wajih A. Naqvi, Kenneth H. Brink, and Sharon L. Smith (Eds.)
- 186 **Amazonia and Global Change** Michael Keller, Mercedes Bustamante, John Gash, and Pedro Silva Dias (Eds.)
- 187 **Surface Ocean–Lower Atmosphere Processes** Corinne Le Quère and Eric S. Saltzman (Eds.)
- 188 **Diversity of Hydrothermal Systems on Slow Spreading Ocean Ridges** Peter A. Rona, Colin W. Devey, Jérôme Dyment, and Bramley J. Murton (Eds.)
- 189 **Climate Dynamics: Why Does Climate Vary?** De-Zheng Sun and Frank Bryan (Eds.)
- 190 **The Stratosphere: Dynamics, Transport, and Chemistry** L. M. Polvani, A. H. Sobel, and D. W. Waugh (Eds.)
- 191 **Rainfall: State of the Science** Fırat Y. Testik and Mekonnen Gebremichael (Eds.)
- 192 **Antarctic Subglacial Aquatic Environments** Martin J. Siegert, Mahlon C. Kennicutt II, and Robert A. Bindschadler
- 193 **Abrupt Climate Change: Mechanisms, Patterns, and Impacts** Harunur Rashid, Leonid Polyak, and Ellen Mosley-Thompson (Eds.)
- 194 **Stream Restoration in Dynamic Fluvial Systems: Scientific Approaches, Analyses, and Tools** Andrew Simon, Sean J. Bennett, and Janine M. Castro (Eds.)
- 195 **Monitoring and Modeling the Deepwater Horizon Oil Spill: A Record-Breaking Enterprise** Yonggang Liu, Amy MacFadyen, Zhen-Gang Ji, and Robert H. Weisberg (Eds.)
- 196 **Extreme Events and Natural Hazards: The Complexity Perspective** A. Surjalal Sharma, Armin Bunde, Vijay P. Dimri, and Daniel N. Baker (Eds.)
- 197 **Auroral Phenomenology and Magnetospheric Processes: Earth and Other Planets** Andreas Keiling, Eric Donovan, Fran Bagenal, and Tomas Karlsson (Eds.)
- 198 **Climates, Landscapes, and Civilizations** Liviu Giosan, Dorian Q. Fuller, Kathleen Nicoll, Rowan K. Flad, and Peter D. Clift (Eds.)
- 199 **Dynamics of the Earth's Radiation Belts and Inner Magnetosphere** Danny Summers, Ian R. Mann, Daniel N. Baker, and Michael Schulz (Eds.)
- 200 **Lagrangian Modeling of the Atmosphere** John Lin (Ed.)
- 201 **Modeling the Ionosphere-Thermosphere** Jospeh D. Huba, Robert W. Schunk, and George V Khazanov (Eds.)
- 202 **The Mediterranean Sea: Temporal Variability and Spatial Patterns** Gian Luca Eusebi Borzelli, Miroslav Gacic, Piero Lionello, and Paola Malanotte-Rizzoli (Eds.)
- 203 **Future Earth - Advancing Civic Understanding of the Anthropocene** Diana Dalbotten, Gillian Roehrig, and Patrick Hamilton (Eds.)
- 204 **The Galápagos: A Natural Laboratory for the Earth Sciences** Karen S. Harpp, Eric Mittelstaedt, Noémi d'Ozouville, and David W. Graham (Eds.)
- 205 **Modeling Atmospheric and Oceanic Flows: Insights from Laboratory Experiments and Numerical Simulations** Thomas von Larcher and Paul D. Williams (Eds.)
- 206 **Remote Sensing of the Terrestrial Water Cycle** Venkat Lakshmi (Eds.)
- 207 **Magnetotails in the Solar System** Andreas Keiling, Caitriona Jackman, and Peter Delamere (Eds.)
- 208 **Hawaiian Volcanoes: From Source to Surface** Rebecca Carey, Valerie Cayol, Michael Poland, and Dominique Weis (Eds.)
- 209 **Sea Ice: Physics, Mechanics, and Remote Sensing** Mohammed Shokr and Nirmal Sinha (Eds.)
- 210 **Fluid Dynamics in Complex Fractured-Porous Systems** Boris Faybisenko, Sally M. Benson, and John E. Gale (Eds.)
- 211 **Subduction Dynamics: From Mantle Flow to Mega Disasters** Gabriele Morra, David A. Yuen, Scott King, Sang Mook Lee, and Seth Stein (Eds.)
- 212 **The Early Earth: Accretion and Differentiation** James Badro and Michael Walter (Eds.)
- 213 **Global Vegetation Dynamics: Concepts and Applications in the MC1 Model** Dominique Bachelet and David Turner (Eds.)
- 214 **Extreme Events: Observations, Modeling and Economics** Mario Chavez, Michael Ghil, and Jaime Urrutia-Fucugauchi (Eds.)
- 215 **Auroral Dynamics and Space Weather** Yongliang Zhang and Larry Paxton (Eds.)
- 216 **Low-Frequency Waves in Space Plasmas** Andreas Keiling, Dong-Hun Lee, and Valery Nakariakov (Eds.)
- 217 **Deep Earth: Physics and Chemistry of the Lower Mantle and Core** Hidenori Terasaki and Rebecca A. Fischer (Eds.)
- 218 **Integrated Imaging of the Earth: Theory and Applications** Max Moorkamp, Peter G. Lelievre, Niklas Linde, and Amir Khan (Eds.)
- 219 **Plate Boundaries and Natural Hazards** Joao Duarte and Wouter Schellart (Eds.)
- 220 **Ionospheric Space Weather: Longitude and Hemispheric Dependences and Lower Atmosphere Forcing** Timothy Fuller-Rowell, Endawoke Yizengaw, Patricia H. Doherty, and Sunanda Basu (Eds.)
- 221 **Terrestrial Water Cycle and Climate Change: Natural and Human-Induced Impacts** QiuHong Tang and Taikan Oki (Eds.)
- 222 **Magnetosphere-Ionosphere Coupling in the Solar System** Charles R. Chappell, Robert W. Schunk, Peter M. Banks, James L. Burch, and Richard M. Thorne (Eds.)
- 223 **Natural Hazard Uncertainty Assessment: Modeling and Decision Support** Karin Riley, Peter Webley, and Matthew Thompson (Eds.)
- 224 **Hydrodynamics of Time-Periodic Groundwater Flow: Diffusion Waves in Porous Media** Joe S. Depner and Todd C. Rasmussen (Eds.)
- 225 **Active Global Seismology** Ibrahim Cemen and Yuvel Yilmaz (Eds.)
- 226 **Climate Extremes: Patterns and Mechanisms** S.-Y. Simon Wang, Jin-Ho Yoon, Christopher C. Funk, and Robert R. Gillies (Eds.)

Geophysical Monograph 227

---

# Fault Zone Dynamic Processes

*Evolution of Fault Properties  
During Seismic Rupture*

Marion Y. Thomas  
Thomas M. Mitchell  
Harsha S. Bhat  
***Editors***

This Work is a co-publication between the American Geophysical Union and John Wiley and Sons, Inc.



WILEY

This Work is a co-publication between the American Geophysical Union and John Wiley & Sons, Inc.

This edition first published 2017 by John Wiley & Sons, Inc., 111 River Street, Hoboken, NJ 07030, USA and the American Geophysical Union, 2000 Florida Avenue, N.W., Washington, D.C. 20009

© 2017 the American Geophysical Union

All rights reserved. No part of this publication may be reproduced, stored in a retrieval system, or transmitted, in any form or by any means, electronic, mechanical, photocopying, recording, or otherwise, except as permitted by law. Advice on how to obtain permission to reuse material from this title is available at <http://www.wiley.com/go/permissions>.

**Published under the aegis of the AGU Publications Committee**

Brooks Hanson, Director of Publications

Robert van der Hilst, Chair, Publications Committee

For details about the American Geophysical Union visit us at [www.agu.org](http://www.agu.org).

**Wiley Global Headquarters**

111 River Street, Hoboken, NJ 07030, USA

For details of our global editorial offices, customer services, and more information about Wiley products visit us at [www.wiley.com](http://www.wiley.com).

**Limit of Liability/Disclaimer of Warranty**

While the publisher and authors have used their best efforts in preparing this work, they make no representations or warranties with respect to the accuracy or completeness of the contents of this work and specifically disclaim all warranties, including without limitation any implied warranties of merchantability or fitness for a particular purpose. No warranty may be created or extended by sales representatives, written sales materials, or promotional statements for this work. The fact that an organization, website, or product is referred to in this work as a citation and/or potential source of further information does not mean that the publisher and authors endorse the information or services the organization, website, or product may provide or recommendations it may make. This work is sold with the understanding that the publisher is not engaged in rendering professional services. The advice and strategies contained herein may not be suitable for your situation. You should consult with a specialist where appropriate. Neither the publisher nor authors shall be liable for any loss of profit or any other commercial damages, including but not limited to special, incidental, consequential, or other damages. Further, readers should be aware that websites listed in this work may have changed or disappeared between when this work was written and when it is read.

*Library of Congress Cataloging-in-Publication Data is available.*

ISBN: 978-1-119-15688-8

Cover image: Courtesy of Thomas M. Mitchell

Cover design by Wiley

Set in 10/12pt Times New Roman by SPi Global, Pondicherry, India

10 9 8 7 6 5 4 3 2 1

# CONTENTS

---

<b>Contributors.....</b>	vii
<b>Preface.....</b>	xi
<b>Part I: Structural Evidences of Coseismic Slip</b>	<b>1</b>
1 <b>Incipient Pulverization at Shallow Burial Depths Along the San Jacinto Fault, Southern California</b> <i>James J. Whearty, Thomas K. Rockwell, and Gary H. Girty.....</i>	3
2 <b>Seismic Rupture Parameters Deduced From a Pliocene-Pleistocene Fault Pseudotachylite in Taiwan</b> <i>Caitlyn S. Korren, Eric C. Ferre, En-Chao Yeh, Yu-Min Chou, and Hao-Tsu Chu.....</i>	21
3 <b>Fluid Inclusion Evidence of Coseismic Fluid Flow Induced by Dynamic Rupture</b> <i>Thomas M. Mitchell, Jose M. Cembrano, Kazuna Fujita, Kenichi Hoshino, Daniel R. Faulkner, Pamela Perez-Flores, Gloria Arancibia, Marieke Rempe, and Rodrigo Comila.....</i>	37
4 <b>Coseismic Damage Generation and Pulverization in Fault Zones: Insights From Dynamic Split-Hopkinson Pressure Bar Experiments</b> <i>Franciscus M. Aben, Mai-Linh Doan, Jean-Pierre Gratier, and François Renard.....</i>	47
5 <b>“Coseismic Foliations” in Gouge and Cataclasite: Experimental Observations and Consequences for Interpreting the Fault Rock Record</b> <i>Steven A. F. Smith, James R. Griffiths, Michele Fondriest, and Giulio Di Toro.....</i>	81
<b>Part II: Fault Properties During Dynamic Rupture</b>	<b>103</b>
6 <b>The Transition From Frictional Sliding to Shear Melting in Laboratory Stick-Slip Experiments</b> <i>David A. Lockner, Brian D. Kilgore, Nicholas M. Beeler, and Diane E. Moore .....</i>	105
7 <b>Powder Rolling as a Mechanism of Dynamic Fault Weakening</b> <i>Xiaofeng Chen, Andrew S. Elwood Madden, and Ze’ev Reches .....</i>	133
8 <b>Earthquake Source Properties From Instrumented Laboratory Stick-Slip</b> <i>Brian D. Kilgore, Art McGarr, Nicholas M. Beeler, and David A. Lockner.....</i>	151
9 <b>Dynamic Weakening and the Depth Dependence of Earthquake Faulting</b> <i>Nicolas Brantut and John D. Platt.....</i>	171
<b>Part III: Influence of Fault Properties on Coseismic Rupture</b>	<b>195</b>
10 <b>Scaling of Fault Roughness and Implications for Earthquake Mechanics</b> <i>François Renard and Thibault Candela .....</i>	197
11 <b>Fault Branching and Long-Term Earthquake Rupture Scenario for Strike-Slip Earthquakes</b> <i>Yann Klinger, Jin-Hyuck Choi, and Amaury Vallage .....</i>	217
12 <b>Influence of Fault Strength on Precursory Processes During Laboratory Earthquakes</b> <i>François. X. Passelègue, Soumaya Latour, Alexandre Schubnel, Stefan Nielsen, Harsha S. Bhat, and Raúl Madariaga .....</i>	229

<b>13 Upper Limit on Damage Zone Thickness Controlled by Seismogenic Depth</b> <i>Jean Paul Ampuero and Xiaolin Mao .....</i>	243
<b>14 Effect of Brittle Off-Fault Damage on Earthquake Rupture Dynamics</b> <i>Marion Y. Thomas, Harsha S. Bhat, and Yann Klinger .....</i>	255
<b>Index.....</b>	281

## CONTRIBUTORS

---

**Franciscus M. Aben**

Université Grenoble Alpes;  
CNRS, ISTerre  
Grenoble, France

**Jean Paul Ampuero**

Seismological Laboratory  
California Institute of Technology  
Pasadena, California, USA

**Gloria Arancibia**

Departamento de Ingeniería Estructural y Geotécnica  
Pontificia Universidad Católica de Chile  
Santiago, Chile

**Nicholas M. Beeler**

U.S. Geological Survey  
Menlo Park, California, USA;  
USGS Cascades Volcano Observatory  
Vancouver, Washington, USA

**Harsha S. Bhat**

Institut de Physique du Globe de Paris  
Université Sorbonne Paris Cité  
Université Paris Diderot, Paris, France;  
Laboratoire de Géologie  
Ecole Normale supérieure  
CNRS-UMR 8538, PSL Research University  
Paris, France

**Nicolas Brantut**

Rock and Ice Physics Laboratory and Seismological  
Laboratory  
Department of Earth Sciences  
University College London  
London, UK

**Thibault Candela**

Department of Earth and Planetary Sciences  
University of California–Santa Cruz  
Santa Cruz, California, USA;  
TNO, Geological Survey of the Netherlands  
Utrecht, Netherlands

**Jose M. Cembrano**

Departamento de Ingeniería Estructural y Geotécnica  
Pontificia Universidad Católica de Chile  
Santiago, Chile

**Xiaofeng Chen**

School of Geology and Geophysics  
University of Oklahoma  
Norman, Oklahoma, USA

**Jin-Hyuck Choi**

Institut de Physique du Globe de Paris  
Université Sorbonne Paris Cité  
Université Paris Diderot  
Paris, France

**Yu-Min Chou**

Department of Geosciences  
National Taiwan University  
Taipei, Taiwan, R.O.C.

**Hao-Tsu Chu**

Central Geological Survey  
Taipei, Taiwan, R.O.C.

**Giulio Di Toro**

School of Earth, Atmospheric  
and Environmental Sciences  
University of Manchester, Manchester, UK;  
Dipartimento di Geoscienze  
Università degli Studi di Padova, Italy;  
Istituto Nazionale di Geofisica e Vulcanologia  
Rome, Italy

**Mai-Linh Doan**

Université Grenoble Alpes;  
CNRS, ISTerre  
Grenoble, France

**Daniel R. Faulkner**

Department of Earth, Ocean,  
and Ecological Sciences  
University of Liverpool  
Liverpool, UK

**Eric C. Ferre**

Department of Geology  
Southern Illinois University  
Carbondale, Illinois, USA

**Michele Fontriest**

School of Earth, Atmospheric  
and Environmental Sciences  
University of Manchester  
Manchester, UK

**Kazuna Fujita**

Department of Earth and Planetary Systems Science  
Hiroshima University  
Hiroshima, Japan

**Gary H. Girty**

Department of Geological Sciences  
San Diego State University  
San Diego, California, USA

**Rodrigo Gomila**

Departamento de Ingeniería Estructural y Geotécnica  
Pontificia Universidad Católica de Chile  
Santiago, Chile

**Jean-Pierre Gratier**

Université Grenoble Alpes;  
CNRS, ISTerre  
Grenoble, France

**James R. Griffiths**

Department of Geology  
University of Otago  
Dunedin, New Zealand

**Kenichi Hoshino**

Department of Earth and Planetary Systems Science  
Hiroshima University  
Hiroshima, Japan

**Brian D. Kilgore**

U.S. Geological Survey  
Menlo Park, California, USA

**Yann Klinger**

Institut de Physique du Globe de Paris  
Université Sorbonne Paris Cité  
Université Paris Diderot  
Paris, France

**Caitlyn S. Korren**

Department of Geology  
Southern Illinois University  
Carbondale, Illinois, USA

**Soumaya Latour**

Laboratoire de Géologie, CNRS  
École Normale Supérieure  
Paris, France

**David A. Lockner**

U.S. Geological Survey  
Menlo Park, California, USA

**Raúl Madariaga**

Laboratoire de Géologie, CNRS  
École Normale Supérieure  
Paris, France

**Andrew S. Elwood Madden**

School of Geology and Geophysics  
University of Oklahoma  
Norman, Oklahoma, USA

**Thomas M. Mitchell**

Department of Earth Sciences  
University College London  
London, UK

**Xiaolin Mao**

Seismological Laboratory  
California Institute of Technology  
Pasadena, California, USA

**Art McGarr**

U.S. Geological Survey  
Menlo Park, California, USA

**Diane E. Moore**

U.S. Geological Survey  
Menlo Park, California, USA

**Stefan Nielsen**

Durham University  
Durham, UK

**François. X. Passelègue**

Laboratoire de Géologie, CNRS  
École Normale Supérieure  
Paris, France;  
University of Manchester  
Manchester, UK

**Pamela Perez-Flores**

Departamento de Ingeniería  
Estructural y Geotécnica  
Pontificia Universidad Católica de Chile  
Santiago, Chile

**John D. Platt**

Department of Terrestrial Magnetism  
Carnegie Institution for Science  
Washington, DC, USA

**Ze'ev Reches**

School of Geology and Geophysics  
University of Oklahoma  
Norman, Oklahoma, USA

**Marieke Rempe**

Institut für Geologie, Mineralogie, und Geophysik  
Ruhr-Universität Bochum  
Bochum, Germany

**François Renard**

Université Grenoble Alpes;  
CNRS, ISTerre  
Grenoble, France;  
PGP, Department of Geosciences  
University of Oslo  
Oslo, Norway

**Thomas K. Rockwell**

Department of Geological Sciences  
San Diego State University  
San Diego, California, USA

**Alexandre Schubnel**

Laboratoire de Géologie, CNRS  
École Normale Supérieure  
Paris, France

**Steven A. F. Smith**

Department of Geology  
University of Otago  
Dunedin, New Zealand

**Marion Y. Thomas**

Institut de Physique du Globe de Paris  
Université Sorbonne Paris Cité  
Université Paris Diderot, Paris, France;  
Department of Earth Sciences  
University of Oxford  
Oxford, UK

**Amaury Vallage**

Institut de Physique du Globe de Paris  
Université Sorbonne Paris Cité  
Université Paris Diderot, Paris, France

**James J. Whearty**

Department of Geological Sciences  
San Diego State University  
San Diego, California, USA

**En-Chao Yeh**

Department of Earth Sciences  
National Taiwan Normal University  
Wenshan District, Taipei, Taiwan, R.O.C.

## PREFACE

---

Why do earthquakes happen? Why do some faults slip aseismically, while others generate catastrophic ruptures, sometimes over thousands of kilometers of faults? This age-old issue has influenced and conditioned many societies for which earthquakes remain one of the most damaging and potentially the deadliest geohazard in densely populated areas. Because of the depth at which most seismic events nucleate, direct observations and measurements are impossible to make. Thus, a deterministic prediction of the timing, location, and magnitude of an earthquake seems unrealistic. However, since the plate tectonic revolution of the 1960s, significant progress has been made in understanding the physics of faulting. This, combined with short-term earthquakes statistics, is the key to develop better probabilistic forecasting models that are underpinned by physical constraints. Such models represent the most effective way to mitigate earthquake damage and human causalities.

Fault zones in the brittle crust are intricate structures with physical properties evolving over timescales ranging from a few seconds to millions of years and involving slip spanning several orders of magnitude, from millimeters to tens of kilometers. In particular, dynamic ruptures lead to change of on-fault and off-fault physiochemical properties and microstructure, which in turn affect nucleation processes, extent and timing of rupture, seismic wave radiation, and aseismic deformation. As a consequence, study of brittle faulting and earthquake processes is fundamentally multidisciplinary, involving field observations, geodetic and seismological measurements, laboratory experiments, numerical studies. Recently, a thorough effort has been made to bring together these different disciplines of earth sciences, in order to develop a better understanding of the dynamic processes occurring during earthquakes and the associated evolution of fault zones. Systematic micro- and macrostructural field studies [e.g., Faulkner *et al.*, 2006; Dor *et al.*, 2006; Mitchell and Faulkner, 2009; Savage and Brodsky, 2011], as well as seismic surveys [e.g., Li *et al.*, 2006; Cochran *et al.*, 2009; Froment *et al.*, 2014], have recently been performed on fault zones, a key component to understanding the energy balance of earthquakes [e.g., Rice, 2002; Kanamori, 2006]. Relating fault mechanics to fault zone structure, several authors have underlined the importance of combining field observations with geodetic and seismological measurements to understand

what controls the seismic and aseismic slip behavior [e.g., Biegel and Sammis, 2004; Thomas *et al.*, 2014; Audet and Burgmann, 2014]. Recent studies have successfully bridged the gap between rocks physics, laboratory experiments, and seismic observations of dynamic processes and fault zone evolution [e.g., Schubnel *et al.*, 2006; Brantut, 2015]. These multidisciplinary approaches, with a real feedback between field observations, laboratory experiments, and theoretical developments, allow the development of mechanically constrained numerical models of earthquake faulting that take into account the interplay between the dynamically evolving off-fault medium and the rupture propagation [e.g., Dunham *et al.*, 2011; Bhat *et al.*, 2012; Xu *et al.*, 2014]. If physically accurate, these numerical models are powerful tools to investigate dynamic rupture propagation, spontaneous dynamic off-fault deformation, and high-frequency ground motion, which are essential for seismic risk mitigation.

This desire to cross traditional disciplinary bounds and promote multidisciplinary studies provided the initial stimulus to organize the 2014 AGU Fall Meeting session, “Fault Zone Properties and Processes during Dynamic Rupture,” from which this monograph derives. Workshops on similar subjects were also sponsored by the International School of Geophysics in May 2013, titled “Properties and Processes of Crustal Fault Zones,” and by the Royal Society in May 2016, titled “Faulting, Friction and Weakening: From Slow to Fast Motion,” demonstrating that the community is now recognizing the importance of endorsing such an interdisciplinary approach. Papers in the present volume capture the current state of the art of this discipline by providing an overview of the existing knowledge on the physics of dynamic faulting. The contributions to the volume cover observational and experimental fault fabric and mechanics, the evolution of fault zone physical and chemical properties, dynamic rupture processes, and physically and observationally consistent numerical modeling of fault zones during seismic rupture.

Whearty *et al.* seek the upper limit of off-fault damage associated to dynamic rupture by studying the fault zone architecture of the San Jacinto Fault. Korren *et al.* conduct a field study in Taiwan and use pseudotachylite as a marker to determine seismic rupture parameters. Mitchell *et al.* display evidence of fluids channeled

through a network of microfractures associated with a passing earthquake rupture. Aben et al. perform high strain rate experiments and correlate them with field observations by analyzing several pulverized rock samples. Smith et al. study the microstructural evolution of calcite-dolomite gouges deformed experimentally during coseismic shearing and explore the consequences for interpreting the fault rock record. Lockner et al. analyze the condition for dynamic shear melting in laboratory stick-slip experiments. Chen et al. discuss the role of powder rolling as a mechanism of dynamic fault weakening earthquake rupture models. Kilgore et al., using laboratory experiments, develop methods to relate stick-slip to natural earthquakes and to determine earthquake source properties. Brantut and Platt investigate the efficiency of two major weakening mechanisms, flash heating and thermal pressurization, as a function of depth across a range of representative geological settings. Renard and Candela review the scaling properties of faults and earthquake slip roughness, compare with numerical models, and raise some implications for earthquake mechanics. Klinger et al., using paleoseismology and long-term morphology, explore the conditions for fault branching for strike-slip earthquakes. Passelègue et al. track the occurrence of precursory processes with increasing fault strength during laboratory earthquakes. Ampuero and Mao, using numerical simulation and fracture mechanics theory, show the geometrical control of the seismogenic depth on the damage zone thickness of mature faults. And finally, Thomas et al. present a numerical study that explores the nonlinear coupling between earthquake ruptures and the dynamically evolving off-fault medium.

We believe this is the first collection of manuscripts that takes a multidisciplinary approach to study the evolution of fault properties and processes at play during dynamic rupture, with particular emphasis on the effect of on-fault and off-fault thermal-hydrology-mechanics-chemical coupling on seismic ruptures. This monograph will therefore prove to be a valuable contribution for any Earth scientists, researchers, and students interested in earthquake processes and properties of fault zones.

*Marion Y. Thomas, Thomas M. Mitchell,  
and Harsha S. Bhat*

## ACKNOWLEDGMENTS

This volume has benefited from the work of a number of people. We would like to thank Mary Grace and Rituparna Bose for ably coordinating our editorial effort, the authors for their great contributions, and the reviewers for their constructive comments that improved the scientific quality of the volume.

## REFERENCES

- Audet, P., and R. Burgmann (2014), Possible control of subduction zone slow-earthquake periodicity by silica enrichment, *Nature*, 510(7505), 389–392.
- Bhat, H. S., A. J. Rosakis, and C. G. Sammis (2012), A micro-mechanics based constitutive model for brittle failure at high strain rates, *Journal of Applied Mechanics transactions of the Asme*, 79(3), 031016.
- Biegel, R. L., and C. G. Sammis (2004), Relating fault mechanics to fault zone structure, *Advances in Geophysics*, 47, 65–111.
- Brantut, N. (2015), Time-dependent recovery of microcrack damage and seismic wave speeds in deformed limestone, *J. Geophys. Res. Solid Earth*, 120(12), 8088–8109.
- Cochran, E. S., Y. G. Li, P. M. Shearer, S. Barbot, Y. Fialko, and J. E. Vidale (2009), Seismic and geodetic evidence for extensive, long-lived fault damage zones, *Geology*, 37(4), 315–318.
- Dor, O., T. K. Rockwell, and Y. Ben-Zion (2006), Geological observations of damage asymmetry in the structure of the San Jacinto, San Andreas and Punchbowl faults in Southern California: A possible indicator for preferred rupture propagation direction, *Pure and Applied Geophysics*, 163(2), 301–349, doi:10.1007/s00024-005-0023-9.
- Dunham, E. M., D. Belanger, L. Cong, and J. E. Kozdon (2011), Earthquake ruptures with strongly rate-weakening friction and off-fault plasticity. Part 2: Nonplanar faults, *Bulletin of the Seismological Society of America*, 101(5), 2308–2322.
- Faulkner, D. R., T. M. Mitchell, D. Healy, and M. J. Heap (2006), Slip on “weak” faults by the rotation of regional stress in the fracture damage zone, *Nature*, 444(7121), 922–925.
- Froment, B., J. J. McGuire, R. D. van der Hilst, P. Gouédard, E. C. Roland, H. Zhang, and J. A. Collins (2014), Imaging along-strike variations in mechanical properties of the Gofar transform fault, East Pacific Rise, *Journal of Geophysical Research: Solid Earth*, 119(9), 7175–7194.
- Kanamori, H. (2006), Lessons from the 2004 Sumatra-Andaman earthquake, *Philosophical Transactions: Mathematical, Physical and Engineering Sciences*, 364, 1927–1945.
- Li, Y.-G., P. Chen, E. S. Cochran, J. E. Vidale, and T. Burdette (2006), Seismic evidence for rock damage and healing on the San Andreas fault associated with the 2004m 6.0 Parkfield earthquake, *Bulletin of the Seismological Society of America*, 96(4B), S349–S363, doi:10.1785/0120050803.
- Mitchell, T. M., and D. R. Faulkner (2009), The nature and origin of off-fault damage surrounding strike-slip fault zones with a wide range of displacements: A field study from the Atacama fault system, Northern Chile, *Journal of Structural Geology*, 31(8), 802–816.
- Rice, J. R. (2002), New perspectives on crack and fault dynamics, pp. 1–24, *Mechanics for a New Millennium: Proceedings of the 20th International Congress of Theoretical and Applied Mechanics Chicago, Illinois, USA, 27 August–2 September 2000*, Springer Netherlands, Dordrecht.
- Savage, H. M., and E. E. Brodsky (2011), Collateral damage: Evolution with displacement of fracture distribution and secondary fault strands in fault damage zones, *Journal of Geophysical Research*, 116, B03405.

- Schubnel, A., P. M. Benson, B. D. Thompson, J. F. Hazzard, and R. P. Young (2006), Quantifying damage, saturation and anisotropy in cracked rocks by inverting elastic wave velocities, *Pure and Applied Geophysics*, 163(5-6), 947–973.
- Thomas, M. Y., J.-P. Avouac, J.-P. Gratier, and J.-C. Lee (2014), Lithological control on the deformation mechanism and the mode of fault slip on the Longitudinal Valley fault, Taiwan, *Tectonophysics*, 632, 48–63.
- Xu, S., Y. Ben-Zion, J.-P. Ampuero, and V. Lyakhovsky (2014), Dynamic ruptures on a frictional interface with off-fault brittle damage: Feedback mechanisms and effects on slip and near-fault motion, *Pure and Applied Geophysics*, 172(5), 1243–1267, doi: 10.1007/s00024-014-0923-7.

# **Part I**

# **Structural Evidences**

# **of Coseismic Slip**

# 1

## Incipient Pulverization at Shallow Burial Depths Along the San Jacinto Fault, Southern California

James J. Whearty, Thomas K. Rockwell, and Gary H. Girty

### ABSTRACT

We studied the fault zone architecture and searched for evidence of shallow damage production in weakly consolidated sandstones of the Bautista Formation along the Clark strand of the San Jacinto Fault in Rock House Canyon, western Salton Trough, California. Here, the fault juxtaposes tonalite on the northeast against strata of the Bautista Formation on the southwest. The fault core and associated damage zone is visible at two separate fault exposures that have experienced total burial depths of ~70 m and ~120 m, respectively. Physical damage in the sandstone “wall rock” of the lower exposure resembles incipient pulverization and exhibits a preferred crack orientation that is perpendicular to the fault, which in turn indicates the occurrence of significant in situ brittle deformation at this very shallow burial depth. The upper exposure at 70 m burial depth displays very little evidence of fragmentation of sand grains outside of the fault core; together, these observations suggest that the onset of pulverization occurs between about 70 and 120 m depth. Based on our observations and analysis of the data, we conclude that the observed physical damage at this shallow depth is likely the result of stresses produced during dynamic rupture.

### 1.1. INTRODUCTION

Physical damage within fault zones has been a growing topic of interest in recent years, especially within the San Andreas fault system in southern California [Wechsler *et al.*, 2011; Anderson, 2010; Rockwell *et al.*, 2009; Dor *et al.*, 2006a; Dor *et al.*, 2006b; Wilson *et al.*, 2005; Schulz and Evans, 1998; Evans and Chester, 1995; Rempe *et al.*, 2013]. Specifically, pulverization damage has been identified as an important result of mechanical processes stemming from dynamic stresses during earthquake ruptures [Morton *et al.*, 2012; Stillings, 2007; Schulz and Evans, 1998; Mitchell *et al.*, 2011], possibly as a result of supershear rupture [Doan and

Gary, 2009]. Pulverized texture is a special or unique type of brecciation, and is defined as intense subgrain fracturing of “wall rock” to the microns and tens of microns scale with little or no observable grain rotation [Wilson *et al.*, 2005; Dor *et al.*, 2006a; Rockwell *et al.*, 2009], with the implication being that pulverization is the result of in situ dynamic fracturing. In this chapter, we use the term *incipient pulverization* for subgrain fracturing, where the fractures exhibit only minor dilation and need not penetrate to the edge of the crystal.

While numerous studies have identified the occurrence of pulverization, the depth of initiation of this process has not yet been constrained. The exhumation depth on which the majority of the above studies have focused has been estimated at ~1–2 km or more [Anderson *et al.*, 2010; Evans and Chester, 1995], if a burial depth can be

Department of Geological Sciences, San Diego State University, San Diego, California, USA

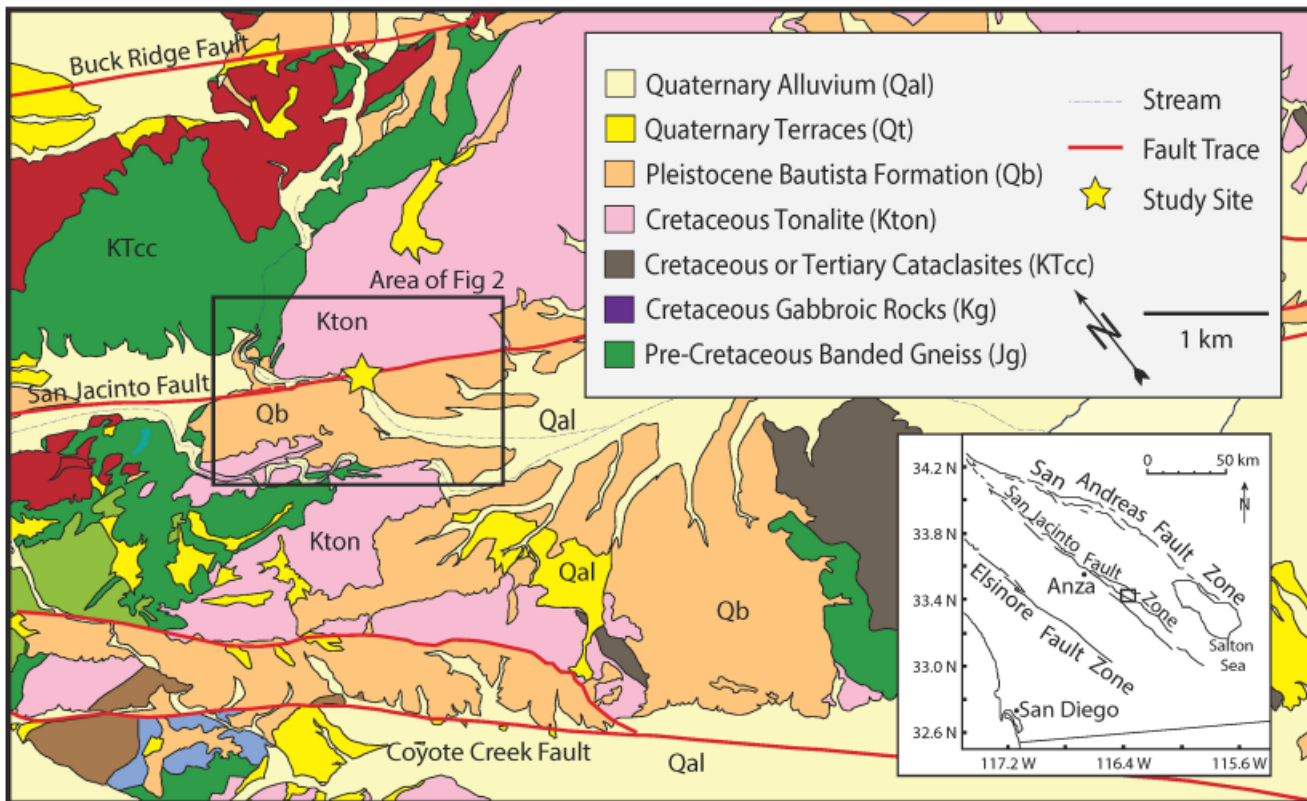


**Figure 1.1** Regional map with major active faults. Modified from Sharp [1967]. Inset: Major strike and slip systems with Southern California. Study site is within boxed area. See electronic version for color representation.

constrained at all [Dor *et al.*, 2009], and the deepest observations of pulverization have been attributed to depths as great as 6 km [Sagy and Korngreen, 2012]. The shallowest burial depth in which these processes have been identified is ~400 m in Horse Canyon along the San Jacinto Fault [Stillings, 2007; Morton *et al.*, 2012].

Our study focuses on two transects across well-exposed outcrops of weakly consolidated sandstone along the San Jacinto Fault (Figures 1.1 and 1.2), where we have reasonably accurate burial depth constraints of ~70 m and ~120 m, respectively (Figure 1.3). Strata of the Bautista Formation, the subject of this study, are Pleistocene in age [Sharp, 1967] and have never been buried by more than the top of the current fill surface in this area (Figure 1.3). As a result, any damage observed within the sandstone adjacent to the fault is interpreted as the result of seismic deformation at these shallow depths. The onset of pulverization and the development of a significant fault core along with a substantially greater amount of brittle deformation is observed at the lower transect. Comparison of the upper and lower fault exposures allows for a more accurate depth constraint on the initiation of these processes, and possibly the dynamics driving them.

## 1.2. GEOLOGIC SETTING

The study site is situated on the San Jacinto Fault in Rock House Canyon within Anza Borrego State Park (Figures 1.1, 1.2, and 1.3). Rock House Canyon lies ~17 km north of Borrego Springs and ~31 km southeast of Anza, California (Figure 1.1 inset), with Coyote Mountain to the south and Buck Ridge to the north. The fault crops out along a 120–130 m high canyon face (Figure 1.3) that due to stream capture in the early Holocene has been incised recently. At this outcrop, the San Jacinto Fault strikes N58W, and juxtaposes alluvial fan deposits of the Pleistocene Bautista Formation against Cretaceous tonalitic rocks [Frick, 1921; Sharp, 1967]. Tonalite underlies the Bautista Formation on the SW side of the fault at depth (Figure 1.1), so a bimaterial affect at seismogenic depth is unlikely.

With several fault strands that extend a total of ~250 km, the San Jacinto Fault is a major branch of the San Andreas Fault system. Initiation of slip along the San Jacinto Fault is inferred to have started in the early Quaternary [Janecke *et al.*, 2010; Rockwell *et al.*, 1990] with total right lateral displacement of 22–26 km [Sharp, 1967; Dorsey, 2002, 2006; Rockwell *et al.*, 2015]. In the

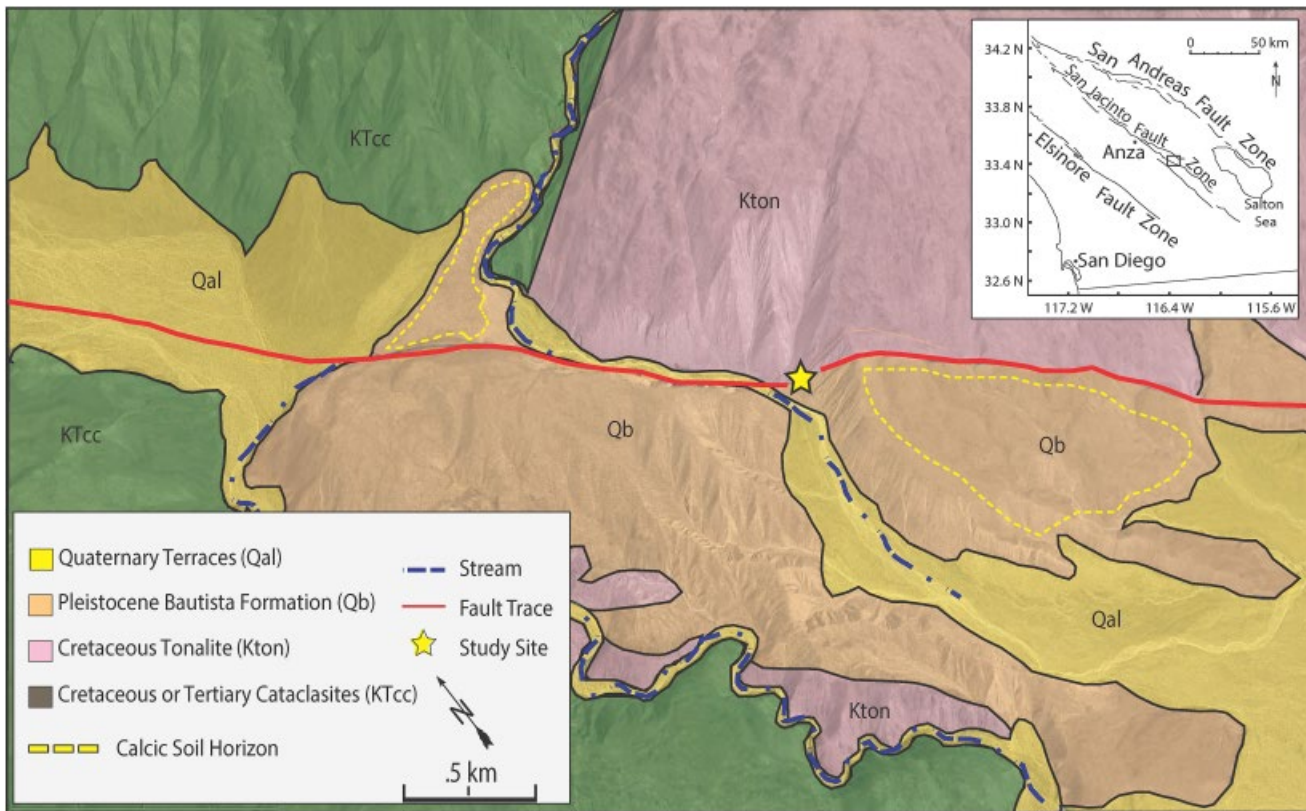


**Figure 1.2** Sample location within Rock House Canyon on the San Jacinto Fault. Geologic overlays interpreted from Sharp [1967]. Soil highlighted on the canyon rim is stage 1 to 2 calcic horizons and does not have an argillic horizon. Image from Google Earth. See electronic version for color representation.

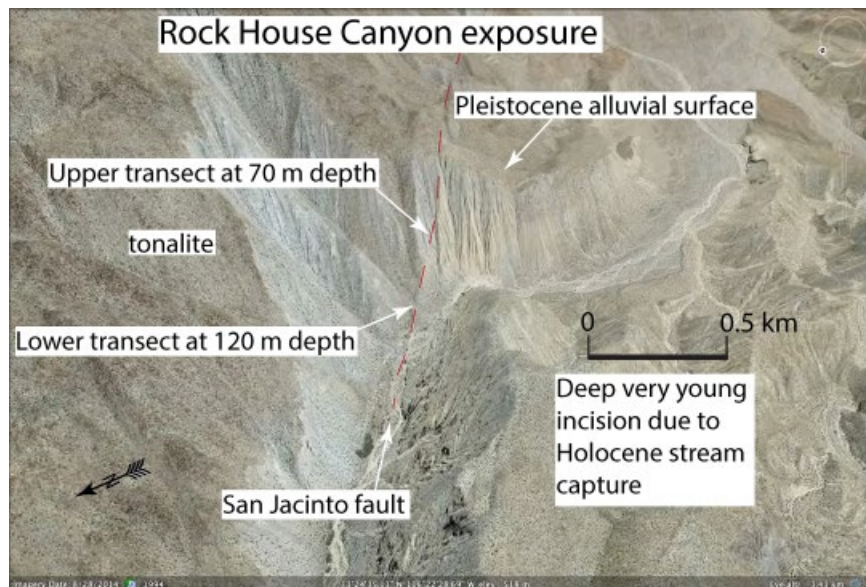


**Figure 1.3** Locations of both Upper and Lower transects are identified on the San Jacinto Fault. Burial depths of the transects are with respect to the Pleistocene alluvial surface. Figure is oriented to look southeast down the trend of the fault. Image from Google Earth. Scale bar is approximate because the picture is taken from an oblique angle.

vicinity of Anza, the San Jacinto Fault has experienced a constant slip rate of  $12.1 + 3.4 / -2.6 \text{ mm/yr}$  over the past several hundred thousand years [Blisniuk *et al.*, 2013]. At Rock House Canyon, the slip rate has been determined to be lower at  $9 \pm 2 \text{ mm/yr}$  [Blisniuk *et al.*, 2010], and the rate continues to decrease to the southeast towards the end of the surface trace of the Clark Fault. Similarly, slip in the most recent earthquake, which occurred in November 1800 [Rockwell *et al.*, 2015], reaches a maximum value near Anza of 3–4 m, and decreases to about 2.5 m at Rock House Canyon, with decreasing slip per event to the southeast [Salisbury *et al.*, 2012].

The field site is located along the Clark Fault, a strand of the San Jacinto Fault zone, extending ~120 km from near Hemet, California southeast to the Santa Rosa Mountains [Middleton, 2006]. The Clark strand is the longest, most continuous segment of the San Jacinto Fault [Sharp, 1967] with demonstrated capability of generating earthquakes in the low to mid M7 range [Salisbury *et al.*, 2012].

### 1.3. EXHUMATION DEPTH AND FAULT EXPOSURE AGE

We describe damage in both the Bautista Formation, which is the main focus of our study, along with the tonalitic wall rock on the northeast side of the Clark fault. These two units have significantly different inferred depths of exhumation, as the sandstone is Pleistocene in age and is exhumed only as deep as it was buried below the top of the locally preserved aggradation surface (Figure 1.3). In contrast, the tonalite is exhumed below a regional Tertiary erosion surface [Morton *et al.*, 2012; Rockwell, 2014], which is highly dissected in this area.

The Tertiary erosion surface, first recognized nearly a century ago [Sauer, 1929; Eckis, 1930], is locally capped by Eocene gravels [Abbott and Smith, 1978, 1989] and Miocene volcanic rocks [Abbott and Smith, 1978, 1989], and is regionally present at an elevation of about  $1300 \pm 100 \text{ m}$ . The elevations of the upper and lower exposures are ~590 m and ~540 m, respectively, suggesting that the tonalite has experienced between 0.6 and 0.9 km of exhumation in Rock House Canyon. In contrast, the sediments that compose the wall rock on the southeast side of the fault are weakly consolidated to unconsolidated gravelly silty sand interpreted to be locally derived alluvial fan deposits. They are mapped by Sharp [1967] as “Bautista beds,” but are herein considered to be part of the upper Bautista Formation. Our reasoning for this assignment follows from their unconsolidated nature, their local derivation, and the fact that they overlie a more consolidated section, which we assign to the lower Bautista Formation. In this area, the top surface of the alluvial fan deposits is preserved at an

elevation of about 660 m. Taking the elevation of the two exposures at 590 m and 540 m implies exhumation depths of about 70 m and 120 m for the upper and lower exposures, respectively (Figure 1.3). These exhumation depths are consistent with the poorly consolidated nature of the deposits in the two exposures and indicate that the Bautista Formation at this location has never been subjected to significant confining pressures.

The timing of exhumation is constrained by the early Holocene age of alluvial fan surfaces at Jack Ass Flats, located immediately to the northwest of Rock House Canyon about 1 km up-canyon from the exposures that we studied. The soil exposed in the canyon rim does not have an argillic horizon and is weakly developed, with a stage I to II calcic horizon (Figure 1.2). Although we do not describe the soil here in detail, comparison to the regional soil chronosequence of Bull [1991] suggests that these correlate to his Q3 alluvium, which Blisniuk *et al.* [2013] have dated as early to middle Holocene in age. The Rock House drainage used to flow through Jack Ass Flats but has now been captured by the drainage of lower Rock House Canyon, resulting in 75–85 m of rapid and youthful incision, as can be observed in Figure 1.3. The incision continues, as evidenced by the very steep canyon walls and multiple late Holocene terrace levels in the canyon bottom, some as high as 10 m above the active drainage. A late Holocene age for the continued incision of the canyon floor bottom is consistent with alluvial bars offset by about 20 m by the fault, which are situated about 10–15 m above the canyon bottom on a tributary drainage [Salisbury *et al.*, 2012]. Using the maximum slip rate measured in Rock House Canyon of 11 mm/yr, together with the 20 m offset, suggests that the lower fault core has been exposed for less than ~1800 years. From these observations, we infer that the two exposures of the fault core were buried until the recent stream capture, and that the observed damage may have been actively accruing up until exhumation in the Holocene.

### 1.4. WALL ROCK GEOLOGY

Neither transect yielded a completely undamaged sample of the Bautista Formation, although the outer sample from the upper transect, collected from about 1.2 m from the fault core, displays only very minor evidence of fracturing, part or all of which could be due to sediment transport. A comprehensive characterization of compositions typical of the Bautista Formation has not been published, but what is known is that regionally, sandstones within the unit are characteristically weakly consolidated, plutonoclastic, coarse arkosic wackes [Sharp, 1967]. For the two transects in our study, the pebbly to cobble-sized clasts are composed of tonalite and schist that appear to be locally derived from nearby canyons,

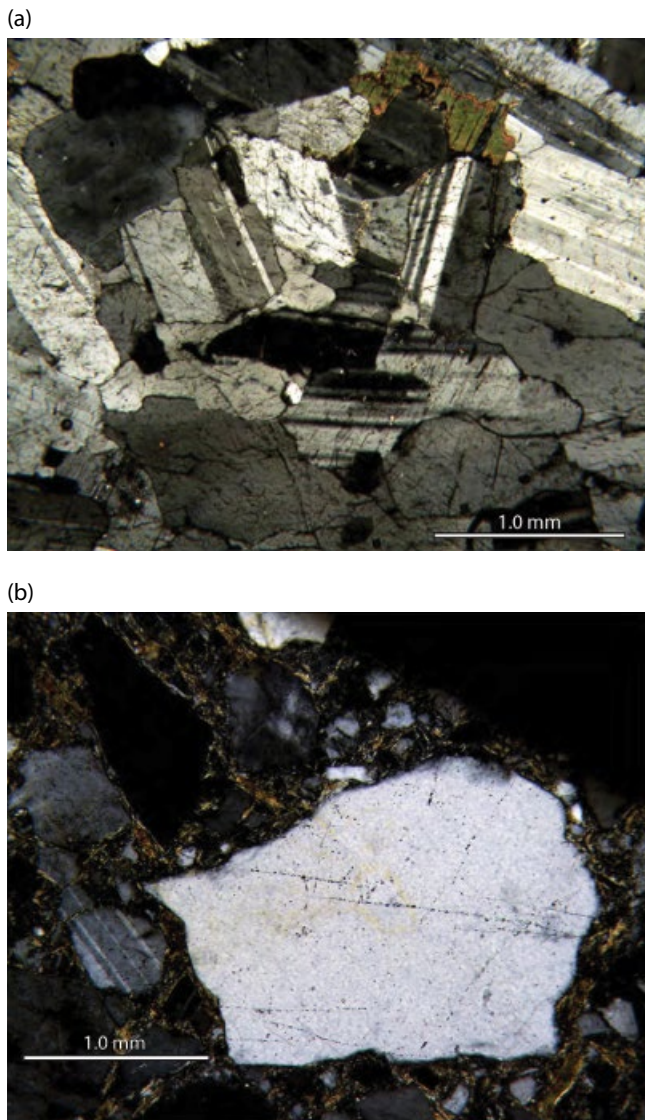


**Figure 1.4** Photomicrographs of unaltered protoliths. (a) Fabric of fresh tonalite taken 80 meters from lower transect damage zone. (b) Upper Bautista Formation taken from the upper transect.

and there is no significant difference between the clast assemblage in the upper and lower exposures. The upper exposure exhibits only very minor damage adjacent to the fault core, which does not look similar to damage seen at the lower exposure. The few cracks observed in quartz grains of the upper exposure appear randomly oriented and may have originated during transportation of the sediment. If so, then the few observed fractures are probably not the result of *in situ* damage processes. For this reason, we use this sample as representative of the undamaged Bautista Formation (Figure 1.4b), from which we compare the other samples for physical damage. The wall rock on the northeast side of the fault is

tonalite from the Clark Valley pluton [Sharp, 1967]. Neither exposure of the fault damage zone extended far enough into the pluton to expose unaltered tonalite, although the upper transect exposes fully pulverized tonalite for several meters out from the fault core. To assess the degree of damage of the tonalite on the northeast, we collected samples of fresh tonalite from about 80 m to the northeast of the fault near the lower transect. Point-count data provided in Whearty [2014] indicate that the unaltered tonalite is composed of 25% quartz, 61% plagioclase, 13% biotite, and trace amounts of chlorite, sphene, and hornblende (Figure 1.4a). In addition, tonalitic plutons of the area also have secondary minerals that include orthoclase, apatite, allanite, epidote, tourmaline, and opaque minerals [Sharp, 1967]. Large crystals within the samples studied by Whearty [2014] range in size from 0.7 to >4.0 mm. We take this as an example of the protolith of the damaged tonalite samples collected from the two transects discussed in this chapter (Figure 1.4a).

## 1.5. GENERAL DESCRIPTION OF EXPOSURES

### 1.5.1. Upper Transect

The upper transect (Figure 1.5) exposes a several-meter-wide section of highly damaged (pulverized) tonalite northeast of the main fault core, with colluvium covering the damaged rock farther to the northeast. A fossil northeastern fault core with a 2–4 cm thick gouge zone separates the pulverized tonalite from a 20–25 cm sliver of sediment derived from the lower Bautista Formation, which in turn is separated from wall rock composed of sediment characteristic of the upper Bautista Formation by the currently active fault trace (Figure 1.5). The pulverized tonalite that lies adjacent to the northeastern fault core is interspersed with a large amount of gouge-filled macroscopic fractures. The presence of gouge decreases to zero about 60 cm from the fossil fault core, and from there the tonalite displays a pulverized fabric [Dor *et al.*, 2006b] characterized by a salt and pepper appearance with a powdery texture [Wechsler *et al.*, 2011] for another ~150 cm before the exposure is covered by boulder-sized colluvium and talus.

The active fault core is eroded by a small drainage or rill and separates the sliver of lower Bautista from an exposure of the upper Bautista Formation. Sediment within the sliver is brown to dark green in color and is substantially more lithified than strata of the upper Bautista Formation making up the wall rock. At this location, the latter material is distinguished by a weakly consolidated matrix of silt and sand with pebble- to cobble-sized angular tonalite and schist fragments. Because the sliver of lower Bautista Formation does not resemble

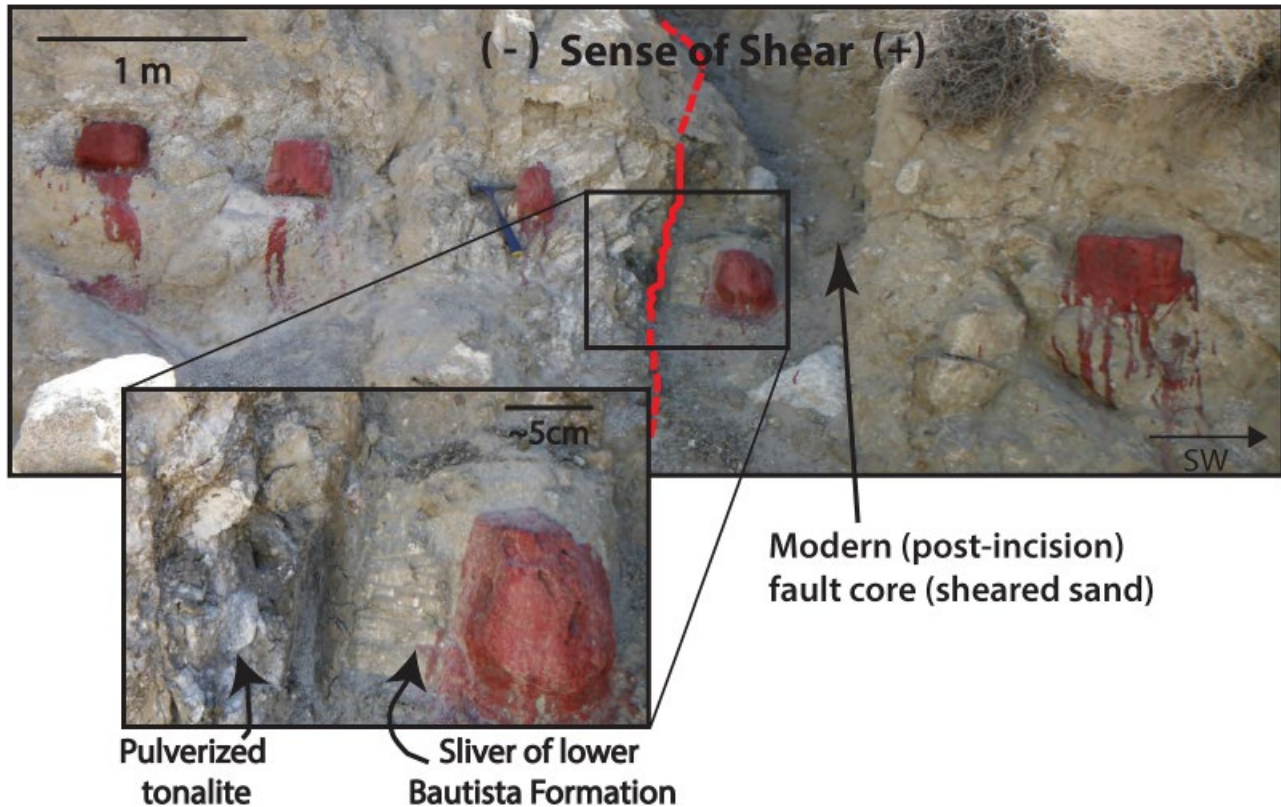


**Figure 1.5** Fault zone architecture observed at the upper location at Rock House Canyon. Specific sample locations are represented by the red patches, which are the actual samples in the field being prepared for removal by jacketing in epoxy. The transect incorporates three samples of pulverized tonalite taken northeast of a thin cataclasite layer, a sample from the sliver of lower Bautista Formation directly adjacent to the cataclasite, and a sample characterizing upper Bautista Formation approximately 1.2 m southwest of the cataclasite. See electronic version for color representation.

the wall rock at this location, we cannot use the latter as the undamaged protolith of lower Bautista from the upper transect.

### 1.5.2. Lower Transect

The fault zone architecture at the lower location (Figure 1.6) is characterized by multiple fault cores and damage zones. A fossil fault core, represented by a ~10 cm wide cataclasite zone, is responsible for the majority of the long-term total offset across the fault and also is likely responsible for most of the damage present at the outcrop. A ~30 cm wide sliver of tonalite is preserved on the northeast side of the fossil fault core, which in turn is separated from late Holocene alluvium by the modern, active trace of the fault. The active trace, above which the surface exhibits evidence of late Holocene rupture in the form of a narrow, linear trough, is a centimeter-wide zone of sheared alluvium adjacent to very coarse boulder-sized late Holocene alluvial fan deposits. Due to its young age and composition, there is no developed fault core

separating the tonalite sliver from the alluvium. That is, the active zone of shearing probably did not evolve until Rock House Canyon incised down to this level in the late Holocene.

The ~30 cm wide sliver of tonalite displays three zones that exhibit varying degrees of damage intensity, but it lacks the pulverized texture observed at the upper location (Figure 1.6). A 10 cm wide zone of angular tonalite fragments interspersed within 70%–80% gouge make up a transition zone (zone 1) adjacent to the cataclasite. In the next ~10 cm of the damage zone (zone 2) out from the fossil fault core, the percentage of matrix material, as well as the extent of fracturing of the tonalite, visibly decrease and the tonalite appears to be fresher and less altered. The outer 10 cm of the fractured tonalite sliver (zone 3) is much fresher in appearance than in zones 1 and 2 and exhibits widely spaced fractures as the principle example of damage. Locally, thin gouge seams may also be present, but these are uncommon. In addition to samples collected from zones 1, 2 and 3, we collected two rounded, cobble-sized fragments of tonalite from zone 3 for analysis.

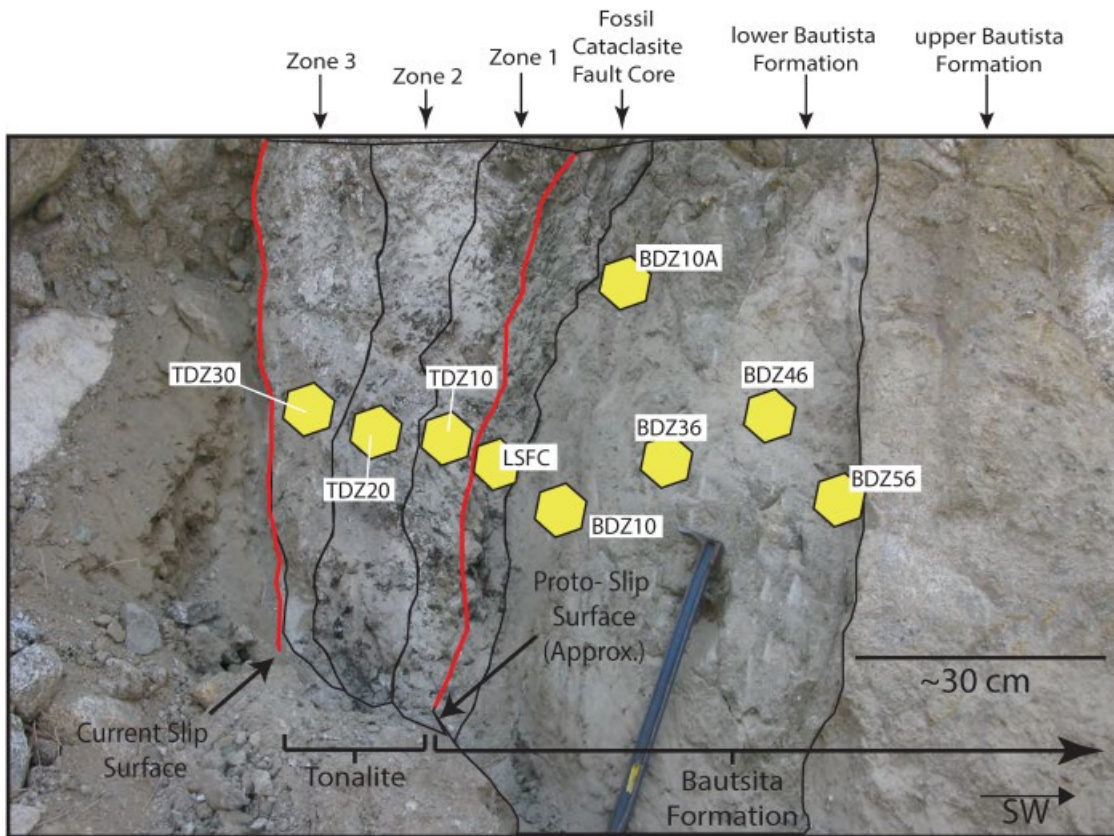


**Figure 1.6** Fault zone architecture of the lower transect displaying the presence of the fossil and current fault core. The tonalite sliver within the damage zone can be split into three zones with distinct alteration intensities. Weakly sheared sandstone is observed for ~55 cm before transition in upper Bautista Formation.

Immediately adjacent to the cataclasite on the southwest side is a sliver of damaged sandstone of the lower Bautista Formation that exhibits a weakly sheared clastic texture and fabric that is similar to the displaced sliver seen in the upper exposure. At this location, deposits of the lower Bautista Formation extend 55 cm from the fossil fault core to where a second fossil fault core marks an abrupt transition to strata representative of the upper Bautista Formation (Figure 1.6). The lower Bautista Formation is well consolidated and contains subangular tonalite and schist fragments up to 10 cm in size, set in a coarse-grained matrix. The upper Bautista Formation at this location contains large, angular rock fragments set within a poorly indurated coarse-grained silty sand matrix, similar to that observed in the upper transect.

Previous studies with observations of broad pulverized zones have been conducted on faults that experienced tens of kilometers of offset. The sediments of the Bautista Formation in this study, however, are only offset on the order of hundreds of meters, so the width of damage is expected to be less than that of previous studies. The width of damage seen at the lower transect is broader

than described, but the outcrop is eroded beyond about 4 m from the core. Regardless of this lateral extent of damage in the Bautista Formation, the relevant observation is that the damage is seen in unconsolidated sandstone at shallow confining stresses.

## 1.6. SAMPLING LOCATIONS

Within the two transects, samples were collected within each architectural zone. A fresh, unaltered tonalite fragment was collected ~80 m from the lower exposure with the purpose of establishing a baseline to compare with results from analyses on the damaged tonalite (Figure 1.4). The samples were encased in a jacket of epoxy (red coating of each sample, as seen in Figure 1.5) and marked so that the entire sample block was oriented. Relative to an orientation mark recorded in four samples from the lower exposure, thin sections were then cut from the sample blocks so that fracture orientations could be determined relative to the fault.

Twelve samples from the lower location were collected along a traverse at various distances from the fossil

fault core. Eight of the samples were collected from strata of the Bautista Formation, with distance from the fault core ranging from 10 to 396 cm (Figure 1.6). The remaining four samples were collected from the cataclasite fault core and the three zones within the tonalite sliver (14 cm, 20 cm, and 30 cm, respectively, from the cataclasite fault core). Analysis was also performed on the two fragments collected from the outer transition zone (zone 3) of the tonalite sliver.

In similar fashion, samples from the upper transect were collected from the architectural zones centered on the 3–5 cm thick gouge zone (Figure 1.5). Within the Bautista Formation, samples were collected at 23 cm and 126 cm from the fossil fault core, and for the pulverized tonalite, samples were collected at 50 cm, 114 cm, and 164 cm from the fossil fault core (represented by the red epoxy locations in Figure 1.5).

## 1.7. ANALYSIS METHODOLOGY

Petrographic analysis was based on oriented thin sections representative of each architectural zone. Point-count spacing was based on the diameter of the largest observed grain in a given thin section. Because this value was variable, the number of points counted was also variable. All thin sections were chemically stained to distinguish K-feldspar from plagioclase, and, in order to highlight pore space, vacuum impregnated with blue epoxy.

Brittle deformation was quantified using PaxIt! software. We used the standard line method for selecting grains: each quartz grain encountered along a line traverse that was >0.5 mm in diameter was analyzed, with each line traverse separated by 0.5 mm. Thus, 10 grains of this size is about the maximum number that would occur in each slide. The ratio of mineral area to total fracture length provided the fracture density, with an average of the 10 ratios representing the fracture density of the sample. PaxIt! also provides a tool to measure the angle of microcracks with respect to a vertical line within the four oriented thin sections. Comparing this angle (and subsequent orientation) allows us to determine the angle of the microcrack with respect to the fault plane.

Table 1.1 is first organized based on the diameter of a quartz grain, then quantifies thin-section brittle deformation based on a five-class grain scheme. The data shown are the percentage of quartz grains represented in each damage classification. The number of fractures on each quartz grain determines its classification:

- Class I (0 fractures)
- Class II (1–5 fractures)
- Class III (6–10 fractures)
- Class IV (11–15 fractures)
- Class V (>16 fractures)

## 1.8. UPPER TRANSECT OBSERVATIONS

### 1.8.1. Petrographic Analysis

Tonalite at this location is composed of 25%–31% quartz, 22%–46% plagioclase, and 21%–27% biotite with minor amounts of chlorite, feldspar, hornblende, and sphene. Trace amounts of secondary calcite is observed closer to the fault core. Grain sizes range from 0.005 to 1.2 mm in samples farthest from the fault core. The increase in pulverized texture with proximity to the fault core (Figure 1.7) is evident in a reduction in the average grain size to 0.005–0.6 mm only 50 cm from the fault core. Fresh biotite is locally replaced by chlorite, probably as a result of metasomatic reactions during cooling of the pluton, and is thus considered an inherited attribute. Altered biotite has a darker brown/red/orange hue. Uncommonly, black seams along the {001} cleavage plane are present. Such features may be composed of Fe and Mn oxyhydroxides or oxides. Undulatory quartz is a common feature observed in all samples and is also interpreted as inherited from the host rock. Intergranular alteration of plagioclase to clay is another common feature in the tonalitic samples from the upper transect.

Compositionally, samples from the upper and lower Bautista Formation present at the upper transect are similar, with 23%–25% quartz, 34%–36% plagioclase, 10%–19% biotite, and 10%–11% potassium feldspar with trace amounts of chlorite, white mica, sillimanite, and epidote. Throughout the specimens, tonalite and schist fragments ranging from 3 to 5 mm are present (Figure 1.5). Approximately 1 m from the active fault core, the Bautista Formation is composed of 75%–90% angular, coarse-grained quartz and plagioclase, ranging from ~0.05 to 2 mm in size. When part of a rock fragment, quartz and plagioclase can reach diameters of up to 4 cm. The percentage of matrix composed of light brown to brown silt-sized particles <0.005–0.01 mm in size reached 10%–25%. Polycrystalline and undulatory monocrystalline quartz grains are common features observed in all samples studied from the Bautista Formation. Quartz grains in the lower Bautista close to the fossil fault core of the upper exposure, which is between two fault splays, uncommonly display mode 1 cracks infilled with matrix and offset grain fragments.

### 1.8.2. Pulverization of Tonalite

Quartz and plagioclase within the tonalite are the predominant grains that display mode 1 cracks, volume expansion, and lack of grain rotation that is characteristic of pulverization damage (Figure 1.7). Samples still retain the primary appearance of the tonalite bedrock with distinct original grain boundaries, despite their

**Table 1.1** Quartz fracture summary.

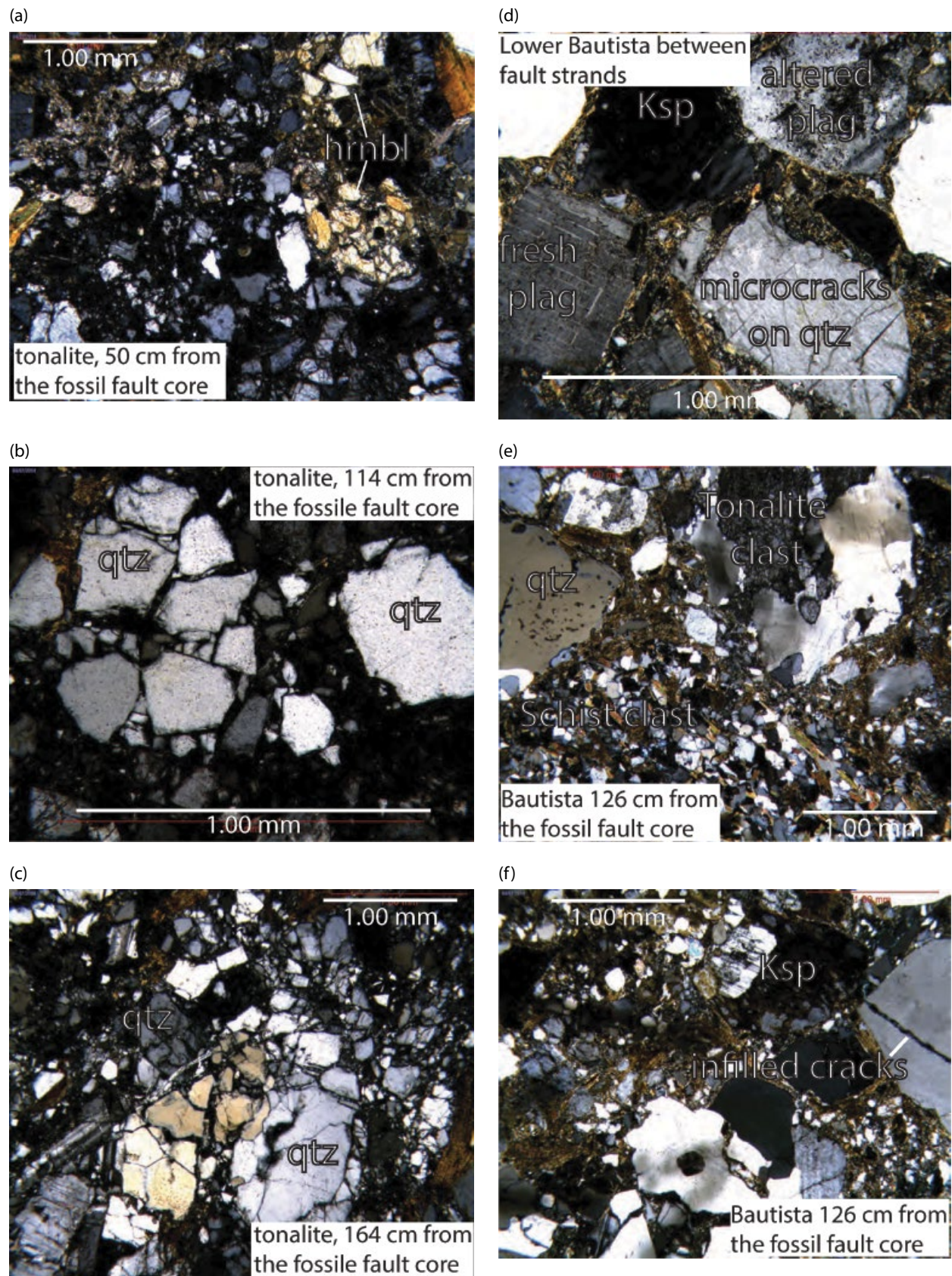


**Figure 1.7** Photomicrographs display common texture for pulverized tonalite (a, b, c) and Bautista Formation at the upper transect. The Bautista Formation (d, e, f) displays fresh sandstone appearance, with minimal matrix development and brittle damage. Tonalite pulverization observed with dilated quartz and plagioclase grains and lack of shear offset. Qtz=quartz, plag=plagioclase, hrnbl=hornblende, Ksp=K-spar.

highly fractured nature. Cracks range from <0.05 to 0.1 mm wide and display a jigsaw texture but lack significant clay or microbreccia infill. Furthermore, pulverized quartz fragments retain a common extinction angle, similar to those described by *Rockwell et al.* [2009] of pulverized granite along the San Andreas and Garlock faults. The intensity of pulverization appears to be related to distance from the fault core, with more intense shattering close to the fault.

### 1.8.3. Incipient Fracturing of Bautista

Compared to the pulverized tonalite, minimal brittle deformation is observed within quartz and plagioclase grains in sandstone samples from the upper Bautista Formation collected from the upper transect exposure. Mode 1 cracks that are present have a much smaller separation width (<0.01 mm), may be infilled with matrix material, and are fairly randomly oriented. Albeit very rare in occurrence within quartz grains, a second type of microcracks resembling incipient pulverization is visible in a very few grains. Such cracks are rarely through going, are limited to the near perimeter, and die out before propagating across the entire grain. However, as the origin of some fractures in the upper Bautista of the upper exposure are uncertain, we counted all fractures in our analysis regardless of origin, as tabulated in Table 1.1. Hence, the microcrack density reaches a maximum value of about 4.3 mm/mm<sup>2</sup> at 126 cm from the fossil fault core, but some of these cracks may have been formed during sediment transport. Nevertheless, the fracture density of the upper Bautista sandstone in the upper exposure is far less than that observed in the lower exposure and can therefore serve as a background level. In summary, of all quartz grains observed within specimens studied from the Bautista Formation from the upper transect, 79%–83% were categorized as Class I with no visible cracks apparent throughout the grain. The only brittle damage observed was in 14%–16% of the quartz grains categorized as Class II with 1–5 fractures, and many or most of these were randomly oriented and may not be due to in situ fracturing.

## 1.9. LOWER TRANSECT OBSERVATIONS

### 1.9.1. Petrographic Analysis

Architectural zones within the lower transect exhibit brittle deformation that is distinctly different from the upper exposure (Figure 1.8). Cataclasite from the fossil fault core contains rounded grains floating in >70% matrix (Figure 1.8b). A majority of fragments are quartz grains, which have undergone significant shear strain comminution, with grain sizes ranging from 0.01 to 0.5 mm.

Remnant crystals of plagioclase have a heavily altered, intergranular appearance.

Samples taken from both the upper and lower Bautista Formation are dominated by tonalitic and lesser amounts of metamorphic material. Samples within these zones have compositional ranges of 10%–40% quartz, 15%–27% plagioclase, and 8%–29% biotite with minor traces of chlorite, white mica, hornblende, and sphene (titanite). Unaltered clasts of tonalite and schist are present as well. Sandstone from the lower transect has a generally fresh appearance with angular mineral fragments that are 0.06 to >3.0 mm in diameter, and matrix percentages range from 10% to 15%. Increased comminution within specimens studied from the lower Bautista Formation is apparent with rounding of grains, overall grain size reduction (0.01–1.5 mm in diameter), and an increased percentage (50%–60%) of matrix, especially at close distances to the fossil fault core.

As shown in Figure 1.6, the lower exposure was divided into zones for easy discussion. Zones 1, 2, and 3 lie within the tonalite sliver; zone 1 contains mineral fragments that are subangular to angular and that range in size from 0.05 to 1.5 mm, with a majority of fragments less than 0.2 mm in size. In general, zone 1 is composed of 30%–40% quartz, 12%–16% plagioclase, and 5%–10% biotite, with smaller amounts of k-feldspar, sillimanite, chlorite, hornblende, and white mica.

Compositionally, zone 2 is similar to zone 1 but has not experienced as much mechanical deformation. Coarser grained crystals range from 0.7 to 1.5 mm in size and the percentage of matrix is not as high as in the neighboring zones. Observations made within zones 1 and 2 suggest that mixing of the sandstone and tonalite wall rocks contributed to the development of these zones prior to the consolidation of slip and development of the cataclasite fault core. Because white mica and sillimanite are found in the Bautista Formation from the schist-derived sand and clastics, and are not present in the Tonalite protolith, their occurrence in zones 1 and 2 on the northeast side of the fault provides the main basis for this inference of mixing.

Textures and fabrics seen in zone 3 more closely resemble that present in zone 1. Shear strain from the new location of the principal slip surface may have contributed to the smaller observed grain size, rounding of grains, and increased matrix percentage. Compositionally, the outer part of zone 3 is unique in that it is derived entirely from tonalite. Point-count results give compositional percentages of 20% quartz, 18% plagioclase, and 27% biotite with trace amounts of chlorite, calcite, and hornblende. All of the above minerals are embedded in a fine-grained (<0.005 mm) microbreccia matrix. Rock fragments displaying lesser degrees of brittle deformation are observed throughout the sample.

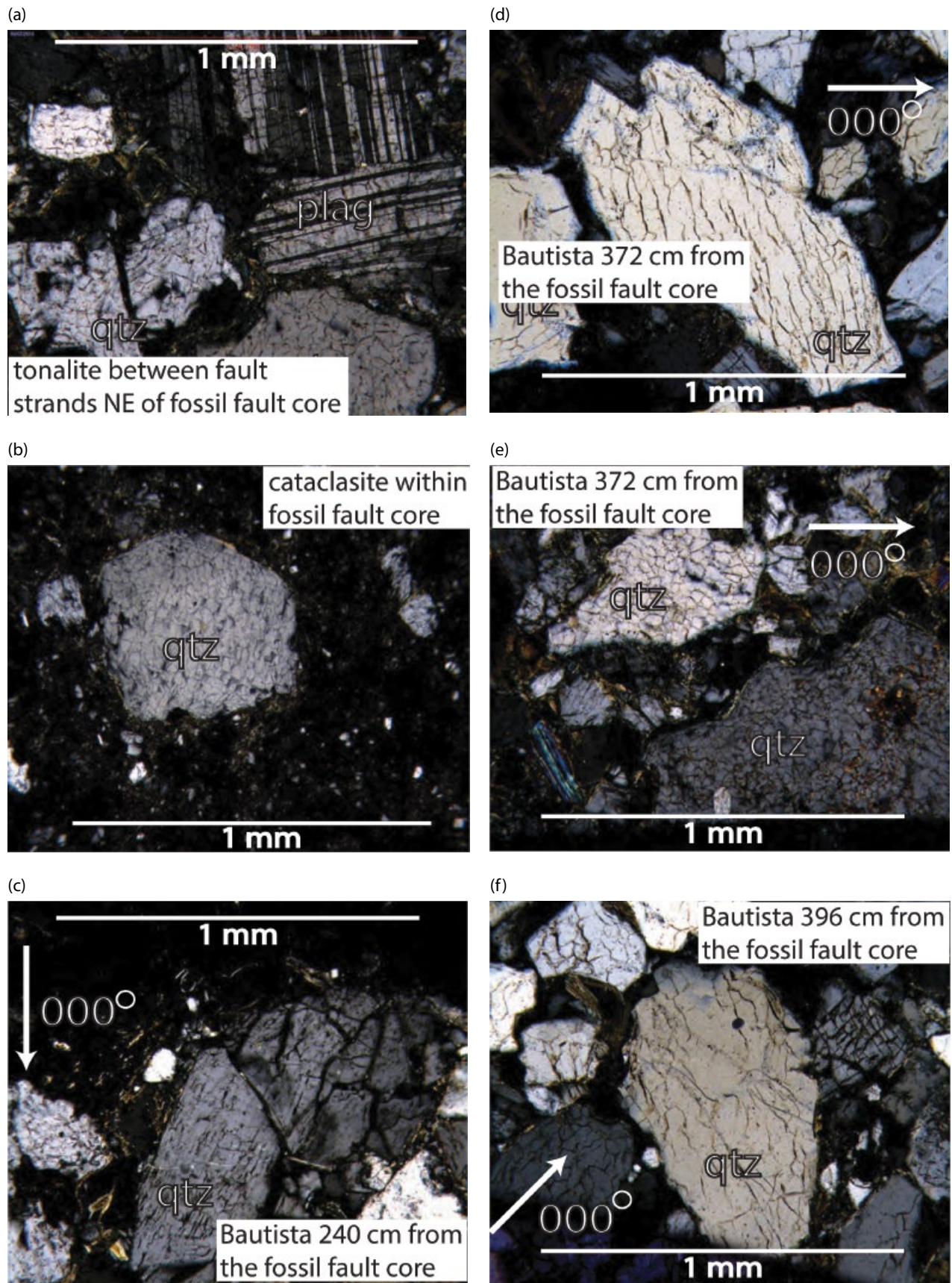


**Figure 1.8** Incipient pulverization is exhibited in the tonalite and the Bautista Formation in the lower transect. (a) displays the brittle damage within the Lower Tonalite. Shear strain comminution processes within the cataclasite (b) displaces fragments off of the fractured quartz grains. Cracks display a common orientation in Bautista Formation samples (c-f). qtz=quartz, plag=plagioclase.

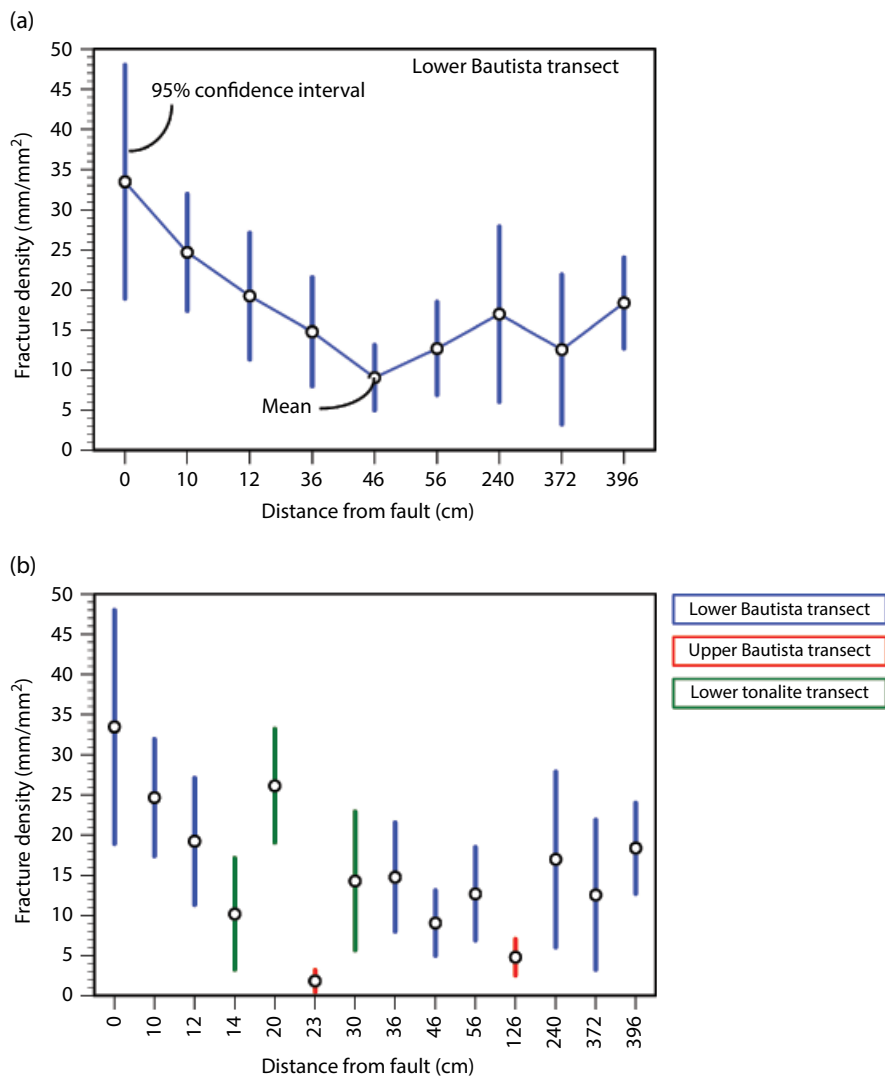


**Figure 1.9** Graphs plot the ratio of total microcrack length to grain area versus orthogonal distance to the fault along with 95% confidence interval bars. Graph in (a) displays a pattern of decreasing brittle deformation with distance to the fault at the lower transect within the Bautista Formation. Graph in (b) shows a higher density of brittle deformation within the tonalite and Bautista Formation and the lower transect compared to the upper transect, even at similar distances to the fault. See electronic version for color representation.

Two well-rounded, cobble-sized tonalite fragments that were incorporated into the outer part of zone 3 displayed an igneous texture similar to the protolith. Plagioclase, quartz, and biotite phenocrysts reach up to ~2 mm by ~3 mm in size, and matrix material is limited to <5%.

### 1.9.2. Incipient Pulverization in the Upper Bautista Sediments of the Lower Transect

Brittle deformation in sandstones of the upper Bautista Formation in the lower transect exhibit intense high-density micro-fracturing that we interpret as incipient pulverization. This fabric is ubiquitous throughout the fault exposure (Figure 1.8). The pulverization takes the form of microcracks that have propagated through selective

quartz and plagioclase grains. Unlike the microcracks observed in samples of the Bautista Formation from the upper transect, microcracks within the lower exposure have a much higher density within quartz and plagioclase crystals and a preferred orientation. Within plagioclase crystals, the microcracks tend to preferentially propagate along cleavage planes, but biotite cleavage planes do not show a propensity for this type of deformation.

The density of microcracks in quartz crystals that are >0.5 mm in diameter appears to be related to distance to the fault (Figure 1.9, Table 1.2). The highest fracture density measured was 33.5 mm/mm<sup>2</sup> in the cataclasite, which then drops to lower levels of around 12–18 mm/mm<sup>2</sup> within samples evaluated from the upper Bautista Formation. The microcracks have a measured length

**Table 1.2** Fracture density data.

	Lower Bautista Transect								Upper Bautista Transect		Lower Tonalite Transect			
	LSFC	BDZ10A	BDZ10	BDZ36	BDZ46	BDZ56	BDZ240	BDZ372	BDZ396	US201	US101	TDZ 10	TDZ20	TDZ30
<b>Distance to fault (cm)</b>	0.00	10.00	12.00	36.00	46.00	56.00	240.00	372.00	396.00	25.00	125.00	14.00	20.00	30.00
<b>Sample fracture densities (mm/mm<sup>2</sup>)</b>	49.15	38.56	14.95	9.98	13.73	7.10	47.53	15.60	13.53	6.54	5.96	6.93	24.22	9.08
	34.62	15.77	18.45	2.80	19.00	7.03	40.59	5.39	15.27	0.39	4.70	7.00	33.73	5.62
	25.59	23.85	30.75	4.40	13.27	4.86	14.12	45.71	12.45	2.71	3.11	5.29	38.22	8.67
	72.41	24.45	43.58	19.24	1.90	11.33	8.62	2.83	22.74	1.17	4.73	9.09	36.49	9.00
	30.64	5.43	13.43	21.44	1.43	15.13	20.31	5.96	28.08	1.37	6.32	5.37	8.58	5.00
	49.50	17.91	24.24	12.61	5.88	32.73	8.73	2.31	12.48	3.09	8.49	37.00	27.88	37.46
	38.23	38.00	17.38	4.87	4.50	12.76	15.00	7.35	5.97	0.32	10.58	12.10	17.42	4.58
	8.70	22.47	12.95	30.00	12.41	17.81	4.49	10.27	29.40	0.91	1.68	6.58	23.53	9.85
	21.08	29.17	8.81	16.26	9.25	9.43	3.38	21.36	17.30	1.39	1.32	4.50	16.46	33.42
	4.62	31.00	7.65	26.14	9.19	8.74	6.85	8.80	26.46	0.34	1.04	7.96	34.73	20.27
<b>Mean fracture density (mm/mm<sup>2</sup>)</b>	33.45	24.66	19.22	14.77	9.06	12.69	16.96	12.56	18.37	1.82	4.79	10.18	26.13	14.29
<b>95% confidence band</b>	14.53	7.28	7.87	6.76	4.06	5.78	10.92	9.32	5.63	1.36	2.26	6.92	7.06	8.60
<b>Mean Max</b>	33.45	24.66	19.22	14.77	9.06	12.69	16.96	12.56	18.37	1.82	4.79	10.18	26.13	14.29
<b>Min</b>	18.92	17.38	11.35	8.01	5.00	6.92	6.04	3.24	12.73	0.46	2.54	3.26	19.07	5.70

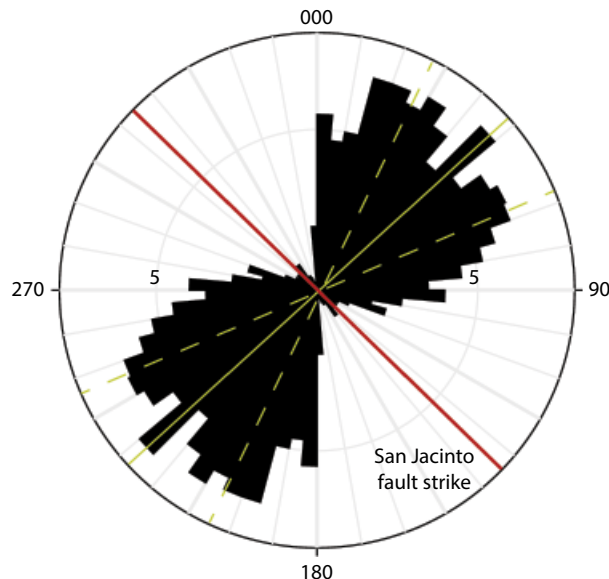


**Figure 1.10** Preferred orientation of ~1100 microcracks measured in four oriented samples from the Bautista Formation at the lower transect. The set of cracks have mean vectors of ~050° and ~230° and are nearly orthogonal to the strike of the fault at Rock House Canyon.

range of 0.01–0.35 mm with an average of 0.09 mm for samples analyzed from the upper and lower Bautista Formation. The set of fractures measured within specimens collected from both the upper and lower Bautista Formation have a distinctive northeast-southwest trend (Figure 1.10), which is nearly orthogonal to the strike of the fault. The uniformity of this observation suggests that the origin of the microcracks is related to in situ seismic deformation, or dynamic fracturing.

Unlike the tonalite in the upper exposure, extensive mode 1 cracking that is characteristic of pulverization is not observed throughout any part of the tonalite sliver at the lower exposure. Tonalite at this site exhibits microfracturing that is similar to that seen in the Bautista Formation, albeit at a lower density (Figure 1.9). In contrast to samples from the Bautista Formation, the highest measured crack density in the tonalite sliver (21 mm/mm<sup>2</sup>) is observed in zone 2, while zones 1 and 3 display similar, yet lower, densities of 9 mm/mm<sup>2</sup> and 11 mm/mm<sup>2</sup>, respectively (Figure 1.9). Maximum lengths of microcracks within quartz varied among the different zones, ranging from 0.24 to 0.45 mm.

In the lower transect, while fracture density is highest in the cataclasites, the proportion of cracks in quartz is highest in specimens from the upper Bautista Formation in the lower transect. Within these samples, 14.5%–23.1% of quartz grains >0.5 mm occurred within Class V (>16 cracks visible per grain) (Table 1.1). This percentage was

the highest measured of any other intensity class within the upper Bautista Formation. Intensity of damage decreases with the reduction of grain size, as shear strain offsets and displaces fragments from the initially cracked grain. Evidence of this is observed with the increase in the occurrence of Class II damage and the decrease in quartz grain size with proximity to the cataclasite. Similar observations are made in the tonalite sliver, as zone 2 has higher percentages of Class IV and V damaged grains in addition to having coarser grains. Class II (1–5 cracks) intensities are most prevalent in zones 1 and 3 as a result of their finer grain size. In contrast to the high percentages of Class I grains (0 cracks) at the upper transect, the percentage of this grain type within the upper Bautista Formation at the lower transect is <9% and never exceeds more than 24% within the entire lower transect.

## 1.10. DISCUSSION

### 1.10.1. Interpretations From Brittle Damage Observations

The observations of damage in the tonalite are consistent with previous studies [Dor *et al.*, 2006b; Rockwell *et al.*, 2009], with quartz and feldspar grains exhibiting intense fragmentation without grain rotation. As the maximum depth of exhumation for these rocks is less than 1 km, the results are similar to previous arguments that pulverization is a shallow phenomenon.

Comparisons of the textures observed in the upper and lower exposures of the upper Bautista Formation indicate that intense fracturing, which we interpret as incipient pulverization, may require some confining stress, as the unconsolidated sandstone in the upper exposure (70 m depth) exhibits very little damage, whereas similar sandstone in the lower exposure exhibits intense fracturing, albeit with only minor dilation. Within grains of similar diameter, intensities are substantially higher within the lower transect at comparable distances from the fault core (Table 1.2). Larger grain sizes (>0.5 mm) from the lower exposure fall predominately into Classes IV (11–16 cracks) and V (>16 cracks). Grains with comparable size from the upper transect are either undamaged (Class I) or fall into Class II (1–5 cracks), which only occurs in roughly 15% of counted grains, and many of these fractures may be inherited as they are more randomly oriented. These larger sized grains are the only ones that display brittle deformation in the upper exposure and only account for about 15% of the total quartz grains observed. Class I (0 cracks) grains in the lower transect occur at a significantly lower percentage, with a maximum of ~19% within the lower and 9% in the upper Bautista Formation. The low percentages of Class II grains and high percentages of Class I grains within the

upper exposure indicates that the conditions required for the initiation of these cracks is largely absent in the upper exposure, suggesting a depth of initiation of cracking and pulverization between 70 and 120 m.

If we assume that the damage present at Rock House Canyon represents the upper limits of confining pressure needed to produce incipient pulverization, which is typically seen at deeper exhumation depths [e.g., *Anderson*, 2010; *Morton et al.*, 2012; *Wechsler et al.*, 2011], we can estimate the confining stress needed for brecciation based on the equation

$$\sigma = \rho_{\text{bulk}} \times g \times h, \quad (1.1)$$

where  $\sigma$  is confining stress,  $\rho_{\text{bulk}}$  is bulk density of sandstone in Bautista Formation (~2 g/cc),  $g$  is acceleration due to gravity, and  $h$  is burial depth.

Confining stress ranges from ~1.4 MPa at the upper transect to ~2.4 MPa for the lower transect, from which we infer that the incipient pulverization is initiated within this confining stress interval. *Morton et al.* [2012], who previously documented the shallowest constraints of exhumation depth at ~400 m, observed pulverization in the form of complete shattering of grains and creation of separate fragments at a confining stress of ~10.8 MPa. These observations confirm that pulverization is a shallow dynamic rupture process.

The cracks exhibit a strong preference for fault-normal orientation (Figure 1.10), suggesting that compressive stress, or a cycling of compressive and tensile stresses, plays a strong role in their formation. This orientation is similar to observations from studies along the San Andreas Fault [*Dor et al.*, 2009; *Wilson et al.*, 2003], although they are generally perpendicular to the dominant crack orientations from *Rempe et al.* [2013]. Two obvious options for a cyclical stress state perpendicular to the fault are stresses due to a restraining or releasing bend, and dynamic stresses produced during rupture.

To test for the first option, we searched for evidence that the sediments in the Horse Canyon exposure may have passed through a bend or step. However, for ~15 km southeast from Rock House Canyon, the strike of the fault stays consistently between 300° and 310° with no evidence of folding or tilting of the Bautista Formation that would obscure the original orientation of these cracks. As the incipient cracking in the studied sandstone is on the southeast side of the fault, restraining bends to the northwest are not of consequence. As total fault slip in this area is on the order of 15 km [*Blisniuk et al.*, 2010], we infer that the damaged sandstone has never passed through a significant restraining step or bend. Consequently, we attribute the observed damage to dynamic rupture processes.

The mean crack orientation of 045° ± 5° indicates a near field stress state that is nearly fault-normal. *Dor et al.* [2009] also documented such a pattern in pulverized sandstone that was interpreted to have experienced a shallow burial depth along the San Andreas Fault. At 10 m from the fault core, the preferred fracture orientation was at a very high angle to the fault trace [*Dor et al.*, 2009]. Additionally, this pulverized texture decreased with distance from the fault core similar to the decrease in fracture density observed within the upper Bautista Formation in the lower transect. *Wilson et al.* [2003] also observed similar pulverization characteristics with a preferred microfracture set oriented perpendicular to the Punchbowl fault in southern California. This pattern of fracture orientation from these three studies suggests that fault normal compressive stress is a plausible cause for the production of incipient pulverized texture, especially in less consolidated sediments where the confining stress is low.

Alternatively, the brittle deformation observed in the lower transect displays several diagnostic characteristics that have been identified in previous studies and attributed to dynamic dilatational stresses. In other studies, deformed grains display mode 1 dilatational cracks that lack a sense of shear, have reduced grain size with minimal distortion to the primary rock structure [*Dor et al.*, 2009], and lack signs of chemical weathering [*Rockwell et al.*, 2009]. *Sibson* [1986] describes a similar dilatational deformation pattern as implosion breccias resulting from strike slip movement through a releasing bend. In our study, the cracking has not yet led to actual shattering and expansion of the crystal grains, probably because it is the incipient stage of pulverization or the confining stress is insufficient for complete pulverization. The tensile strength of quartz is typically in the several tens of MPa range, much greater than the confining stress at Rock House Canyon, which implies that if dilatational stresses are the cause or a contributing factor of the observed damage, then the dynamic stress during rupture would need to produce a significant negative stress. As the sediments are unconsolidated and not subjected to significant confining stress at this location, we consider deformation from purely dilatational stresses unlikely. Consequently, considering the preferred orientation of the cracks perpendicular to the fault and the shallow confining stress, we interpret the incipient pulverization observed in the weakly consolidated sandstone to result from dynamic compressive stress during earthquake ruptures, or a cycling of compressive and tensile stresses during dynamic rupture.

Another factor that may be tied to the burial depth and generation of crack damage is derived from experimental studies. Using a Split-Hopkinson Bar apparatus, several studies suggest that pulverization requires high strain rates [*Doan and Gary*, 2008, 2009], and that pulverization

may be inhibited at large depths due to excessive confining stress [Yuan *et al.*, 2011]. Shear wave velocities in unconsolidated sediments tend to be very low, which may limit strain rates. If so, then a minimum confining stress may be required for dynamic fracturing to occur, which is the observation from this study.

### 1.11. CONCLUSION

Weakly consolidated alluvial fan sediments of the Bautista Formation within Rock House Canyon display contrasting degrees of brittle deformation in samples recovered from two transects that have experienced burial depths of 70 and 120 m. Significantly higher levels of crack densities are observed in the sandy sediment of the lower transect with over 80% of quartz grains showing damage, while only a few quartz grains display cracking within the upper transect. The brittle deformation from the lower transect samples resembles incipient pulverization and is interpreted to be the result of cycling of compressive and tensile stresses generated during dynamic rupture, or in other words, dynamic fracturing. At this location, pulverization crack density is highest closest to the fault core, and in the coarser grains. Microcracks display a common preferred orientation that is roughly perpendicular to fault strike, a signature that has been observed in other studies of pulverization in rocks recovered from greater burial depths. The presence of the observed damage allows us to make accurate constraints on the upper limits of confining pressures needed to produce the pulverized texture during dynamic rupture, which appears to be between about 1.4 and 2.4 MPa.

### ACKNOWLEDGMENTS

We would like to thank Anza Borrego State Park for allowing us to explore and sample along the San Jacinto Fault within Rock House Canyon. Additional thanks to Joan Kimbrough, Jamie Purcell, Brian Rockwell, and Eric Haaker for assistance in the lab and field. This research was supported by NSF award EAR-0908515 and the Southern California Earthquake Center (Contribution number 6290). SCEC is funded by NSF Cooperative Agreement EAR-1033462 and USGS Cooperative Agreement G12AC20038.

### REFERENCES

- Abbott, P. L., and T. E. Smith (1978), Trace-element comparison of clasts in Eocene conglomerates, southwestern California and northwestern Mexico, *J. Geol.*, 86, 753–762.  
 Abbott, P. L., and T. E. Smith (1989), Sonora, Mexico, source for the Eocene Poway Conglomerate of southern California, *Geol.*, 17, 329–332.

- Anderson, K. (2010), Chemical and physical changes within the damage and pulverized zones of the Mojave segment of the San Andreas fault: Implications for the origin of pink potassium feldspar grains, Master's thesis, San Diego State Univ. Dept. of Geol. Sci.  
 Blisniuk, K., M. Oskin, A. Meriaux, T. Rockwell, R. C. Finkel, and F. J. Ryerson (2013), Stable, rapid rate of slip since inception of the San Jacinto fault, California, *Geophysical Research Letters*, 40, 4209–4213.  
 Blisniuk, K., T. K. Rockwell, L. A. Owen, M. Oskin, C. Lippincott, M. W. Caffee, and J. Dortch (2010), Late quaternary slip rate gradient defined using high-resolution topography and <sup>10</sup>Be dating of offset landforms on the southern San Jacinto fault zone, California, *J. Geophys. Res.*, 115, B08401.  
 Bull, W. (1991), *Geomorphic Responses to Climate Change*. The Blackburn Press, New Jersey.  
 Doan, M. L., and G. H. Gary (2008), Rocks pulverized near San Andreas fault: Insight from high strain rate experiments, *EOS Trans. AGU*, 89(53), Fall Meeting Suppl. Abstract S34B–06.  
 Doan, M. L., and G. H. Gary (2009), Rock pulverization at high strain rate near the San Andreas fault, *Nat. Geosci.*, 2, 709–712.  
 Dor, O., Y. Ben-Zion, T. K. Rockwell, and J. N. Brune (2006a), Pulverized rocks in the Mojave section of the San Andreas fault zone, *Earth Planet. Sci. Lett.*, 245, 642–654.  
 Dor, O., J. S. Chester, Y. Ben-Zion, J. N. Brune, and T. K. Rockwell (2009), Characterization of damage in sandstones along the Mojave Section of the San Andreas Fault: Implications for the shallow extent of damage generation, *Pure and Applied Geophysics*, 166, 1–27.  
 Dor, O., Rockwell, T. K., and Y. Ben-Zion (2006b), Geological observations of damage asymmetry in the structure of the San Jacinto, San Andreas, and Punchbowl faults in Southern California: A possible indicator for preferred rupture direction, *Pure and Applied Geophysics*, 163, 301–349.  
 Dorsey, R. J. (2002), Two-stage evolution of the San Jacinto fault zone: Crustal response to Pleistocene oblique collision along the San Andreas fault, *Eos Trans. AGU Fall Meeting Supplement*, 47, 933.  
 Dorsey, R. J. (2006), Quaternary landscape evolution in the San Jacinto fault zone, peninsular ranges in Southern California: Transient response to strike slip fault initiation, *Geomorphology*, 73, 16–32.  
 Eckis, R. (1930), The geology of the southern Part of the Indio quadrangle, California, Master's thesis, California Institute of Technology.  
 Evans, J. P., and F. M. Chester (1995), Fluid-rock interaction in faults of the San Andreas system: Inferences from San Gabriel fault rock geochemistry and microstructures, *J. Geophys. Res.*, 100, 13007–13020.  
 Frick, C. (1921), Extinct vertebrate faunas of the badlands of Bautista Creek and San Timoteo Canyon, Southern California, *University California Publications, Department Geological Sciences Bulletin*, 12, 277–424.  
 Janecke, S. U., R. J. Dorsey, D. Forand, A. N. Steely, S. M. Kirby, A. T. Lutz, B. A. Housen, B. Belgarde, V. E. Langenheim, and T. M. Rittenour, (2010), High geologic slip rates since Early Pleistocene initiation of the San Jacinto and

- San Felipe fault zones in the San Andreas fault system, Southern California, USA, *Geol. Soc. Am. Spec. Paper*, 475, 48 p.
- Middleton, T. J. (2006), Tectonic geomorphology of the southern Clark fault from Anza southeast to the San Felipe Hills: Implication of slip distribution for recent past earthquakes, Master's thesis, San Diego State University, 95 p.
- Mitchell, T. M., Y. Ben-Zion, and T. Shimamoto (2011), Pulverized fault rocks and damage asymmetry along the Arima-Takatsuki Tectonic Line, Japan, *Earth Planet. Sci. Lett.*, 308(3–4), 284–297.
- Morton, M., G. H. Girty, and T. K. Rockwell (2012), Fault zone architecture of the San Jacinto fault zone in Horse Canyon, southern California: A model for focused post-seismic fluid flow and heat transfer in the shallow crust, *Earth and Planetary Science Letters*, 329–330, 71–83.
- Rempe, M., T. M. Mitchell, J. Renner, S. Nippes, Y. Ben-Zion, and T. K. Rockwell (2013), Damage and seismic velocity structure of pulverized rocks near the San Andreas Fault, *J. Geophys. Res. Solid Earth*, 118(6), 2813–2831.
- Rockwell, T. K., T. E. Dawson, J. Young-Ben Horton, and G. Seitz, (2015), A 21 event, 4,000-year history of surface ruptures in the Anza Seismic Gap, San Jacinto fault and implications for long-term earthquake production on a major plate boundary fault, *Pure and Applied Geophysics*, 172(5), 1143–1165.
- Rockwell, T. K., C. Loughman, and P. Merifield (1990), Late Quaternary rate of slip along the San Jacinto fault zone near Anza, Southern California, *J. Geophys. Res.*, 95, 8593–8605.
- Rockwell, T. K., M. Sisk, G. H. Girty, O. Dor, N. Wechsler, and Y. Ben-Zion (2009), Chemical and physical characteristics of pulverized Tejon Lookout granite adjacent to the San Andreas and Garlock faults: Implications for earthquake physics, *Pure Appl. Geophys.* 166, 1725–1746.
- Sagy, A., and D. Korngreen (2012), Dynamic branched fractures in pulverized rocks from a deep borehole, *Geology*, 1–4, doi:10.1130/G33194.1.
- Salisbury, J. B., T. K. Rockwell, T. J. Middleton, and K. W. Hudnut (2012), LiDAR and field observations of slip distribution for the most recent surface ruptures along the central San Jacinto fault, *Bulletin of the Seismological Society of America*, 102, 598–619.
- Sauer, C. (1929), Land forms in the peninsular ranges of California as developed about Warner's Hot Springs and Mesa Grande, *U. Calif. Pub. Geog.*, 3, 199–290.
- Schulz, S. E., and J. P. Evans (1998), Spatial variability in microscopic deformation and composition of the Punchbowl fault, southern California: Implications for mechanisms, fluid rock interaction, and fault morphology, *Tectonophysics*, 295, 223–244.
- Sharp, R. V. (1967), San Jacinto fault zone in the Peninsular Ranges of Southern California, *Geological Society of America Bulletin*, 78, 705–730.
- Sibson, R. H. (1986), Brecciation processes in fault zones: Inferences from earthquake rupturing, *Pure and Applied Geophysics*, 124(1–2), 159–175.
- Stillings, M. P. (2007), Structural, textural, and geochemical analyses of fault damage zones: Clark strand, San Jacinto fault zone, southern California, A thesis presented to the faculty of San Diego State University.
- Wechsler, N., E. E. Allen, T. K. Rockwell, G. H. Girty, J. S. Chester, and Y. Ben-Zion (2011), Characterization of pulverized granitoids in a shallow core along the San Andreas Fault, Little Rock, CA, *Geophys. J. Int.*, 186, 401–417, doi: 10.1111/j.1365-246X.2011.05059.x.
- Wilson, B., T. Dewers, Z. Reches, and J. Brune (2005), Particle size and energetics of gouge from earthquake rupture zones, *Nature*, 434(7034), 749–752.
- Wilson, J.E., J.S. Chester, and F.M. Chester (2003), Microfracture analysis of fault growth and wear processes, *Punchbowl fault, San Andreas system, California, Journal of Structural Geology*, 25, 1855–1873.
- Whearty, J. J., (2014), Incipient pulverization at shallow depths along the San Jacinto fault, Southern California, Masters thesis, San Diego State University.
- Yuan, F., V. Prakash, and T. Tullis (2011), Origin of pulverized rocks during earthquake fault rupture, *J. Geophys. Res.*, 116, B06309, doi:10.1029/2010JB007721.

## 2

# Seismic Rupture Parameters Deduced From a Pliocene-Pleistocene Fault Pseudotachylyte in Taiwan

Caitlyn S. Korren<sup>1</sup>, Eric C. Ferre<sup>1</sup>, En-Chao Yeh<sup>2</sup>, Yu-Min Chou<sup>3</sup>, and Hao-Tsu Chu<sup>4</sup>

## ABSTRACT

Taiwan, a seismically active zone, has historically experienced many devastating earthquakes such as the 1999 Mw 7.6 Chi-Chi event. Understanding seismic risk in this highly populated region requires harnessing all paleoseismological indicators in the recent tectonic evolution of the island. Fault pseudotachylytes, widely regarded as earthquake fossils, provide a wealth of information on dynamic processes during seismic rupture. A new pseudotachylyte locality, discovered in Eastern Taiwan along the Hoping River in the Tananao metamorphic complex, provides an exceptional opportunity to constrain a Pliocene-Pleistocene (<4.1–3.0 Ma) seismic rupture. With a net displacement of 220 mm, seismic slip produced veins of frictional melt corresponding to a  $M_w 6.4 \pm 0.4$  earthquake. This measured displacement is compared to that inferred from vein thickness. Detailed microstructural observations reveal that only portions of the veins display criteria consistent with a melt origin, the rest being ultracataclasites. Outcrop-scale observations show that seismic slip took place along a dip-slip direction with a normal kinematic, consistent with the exhumation of the metamorphic complex. Our approach resolved all seismic rupture parameters for an ancient earthquake from a single pseudotachylyte vein. Finally, this study suggests that eastern Taiwan Pliocene-Pleistocene tectonics might have been an exhumation-related extension.

## 2.1. INTRODUCTION

Taiwan is a region of high seismicity and high population density [Dadson *et al.*, 2003]. The 1999 Mw 7.6 Chi-Chi earthquake, which claimed 2,415 lives and cost≈US\$10 billion, was a harsh reminder that seismic

risk is very high. This earthquake along the Chelungpu fault motivated the Taiwan Chelungpu Drilling Project (TCDP) aimed at recovering information and rocks from the fault zone. The TCDP uncovered the first fault pseudotachylytes in Taiwan [Otsuki *et al.*, 2009; Kuo *et al.*, 2014]. While interest in fault pseudotachylytes grew following this discovery, research has been hampered by abundant vegetation and the relative paucity of outcrops in Taiwan.

Fault pseudotachylytes have long been considered an unambiguous indicator of deformation at seismic slip rates [e.g., Sibson, 1977; Di Toro *et al.*, 2005; Wibberley and Shimamoto, 2005; Andersen and Austrheim, 2006; Di Toro *et al.*, 2006]. These rocks form through conversion

<sup>1</sup>Department of Geology, Southern Illinois University Carbondale, Illinois, USA

<sup>2</sup>Department of Earth Sciences, National Taiwan Normal University, Wenshan District, Taipei, Taiwan, R.O.C.

<sup>3</sup>Department of Geosciences, National Taiwan University, Taipei, Taiwan, R.O.C.

<sup>4</sup>Central Geological Survey, Taipei, Taiwan, R.O.C.

of mechanical work into frictional heat along the main slip plane, eventually leading to frictional melting due to fast slip rate and low thermal conductivity of rocks [Sibson, 1975; Maddock, 1983; Magloughlin, 1989]. In contrast, cataclasites and ultracataclasites form by comminution in the absence of melting.

*Chu et al.* [2012] discovered a new fault pseudotachylite locality along the Hoping River in Eastern Taiwan. These pseudotachylites cut through the mylonitic foliation of the Tananao gneisses dated by  $^{40}\text{Ar}$ - $^{39}\text{Ar}$  around 4.1–3.0 Ma [Wang et al., 1998] and must, therefore, be younger [*Chu et al.*, 2012]. This pseudotachylite constitutes a precious milestone of Taiwan's Pliocene-Pleistocene seismotectonics. Here we report new structural, microstructural, and paleoseismological observations on this pseudotachylite. Our contribution focuses on establishing the melt origin of the vein, the seismic event kinematics, the deformation history, and finally, on quantifying seismic displacement. Ultimately, our analysis provides all seismic focal parameters for a single Pliocene-Pleistocene earthquake.

## 2.2. GEOLOGIC SETTING

The main island of Taiwan formed by arc-continent collision along the boundary between the Philippine Sea Plate to the East and the Eurasian Plate to the West, with a convergence rate of  $\sim 82\text{ mm/yr}$  in a  $\sim \text{N}118^\circ\text{E}$  direction [Seno, 1977; Suppe, 1984; Yu et al., 1997; Malavieille et al., 2002; Huang et al., 2006] (Figure 2.1). This complex plate boundary comprises two subduction zones of opposite polarities. To the southwest, the oceanic crust of the South China Sea subducts along the Manilla Trench under the <6.5 Ma Luzon Volcanic Arc [e.g., Lin et al., 2003]. To the northeast, the arc-continent collision is relayed by subduction of the Philippine Sea Plate underneath the Eurasian plate along the Ryukyu Trench.

From East to West, Taiwan consists of a series of NNE-SSW oriented terranes (Figure 2.1). The Coastal Range consists of a Neogene andesitic island arc with volcanoclastics and turbidites intruded by Luzon volcanics [Ho, 1986; Sibuet and Hsu, 1997]. The Longitudinal Valley, regarded as a suture zone, consists of a collapsed forearc basin subsiding at  $10\text{ mm/yr}$  and bearing a major fault system striking  $020^\circ\text{E}$  with East dips around  $55^\circ$  [Yu and Liu, 1989; Willemin and Knipfer, 1994; Angelier et al., 1997]. The Inner Taiwan Mountain Belt bears two main metamorphic belts: the Central Range green schist belt to the east and the Central Range slate belt to the west. The eastern part of the Central Range includes the Tananao metamorphic complex that includes two metamorphic belts, the Tailuko belt with predominately amphibolite gneisses and the Yuli belt with predominantly

mafic-ultramafic compositions [Yen, 1963; Chu et al., 2012]. Other tectonostratigraphic units to the west include the Yilan Plain, the Hueshan Range, the Western Foothills, and the Western Taiwan Coastal Plain, which is the present foreland basin.

Active tectonic convergence between plates in Taiwan causes intense seismicity, marked for example, by the 1935  $M_w$  7.1 Hsinchu-Taichung earthquake [Bor-Shouh and Yeong, 1992], the 1951  $M_w$  7.0 east Rift Valley series of earthquakes [Shyu et al., 2007], and the 1999  $M_w$  7.6 Chi-Chi earthquake [Kao and Chen, 2000]. The Central Range region, which started to rise above sea level 5 Ma ago [Liu et al., 2000; Dadson et al., 2003; Beyssac et al., 2007], currently experiences high and increasing erosion rates of  $\sim 3\text{--}6\text{ mm/yr}$  [Dadson et al., 2003]. The rapid exhumation of the Tananao metamorphic complex results in mylonitization of the granitic protolith and formation of pseudotachylite veins (Figures 2.2, 2.3, and 2.4) in the Hoping River near a major lithological discontinuity between mylonitic gneisses and marbles [*Chu et al.*, 2012].

## 2.3. ANALYTICAL METHODS

### 2.3.1. Field Observations

Fieldwork along the Hoping River allowed measurement of structural elements such as mylonitic foliation, veins, fractures, mylonitic lineations, and striations. Kinematic observations regarding sense of displacement were systematically made in the XZ plane of finite strain. An integrative  $\sim 15\text{ m}$ -long transect across the main pseudotachylite veins was performed using a strand line for orientation. Digital photography and mosaics of images were collected to assist with structural analysis and quantification of structural elements. Samples were oriented using a structural compass. Twenty-two mylonitic foliations, nine mylonitic lineations, and twenty-one pseudotachylite generation planes were measured. The aspect ratio of six injection veins were measured (Table 2.1). The terminology used to describe pseudotachylite vein geometry is from Ferré et al. [2015].

### 2.3.2. Petrography

Polished thin sections of rocks  $\sim 30\text{ }\mu\text{m}$  thick were prepared by High Mesa Petrographics. Additional thin-sections from the original *Chu et al.* [2012] study were also examined. Digital photomicrographs were taken using an optical petrographic microscope to assist with mineral phase identification. Scanning electron microscopy (SEM) was performed at Southern Illinois University using a FEI Quanta FEG450 instrument at magnifications up to 2000x, while additional work was performed

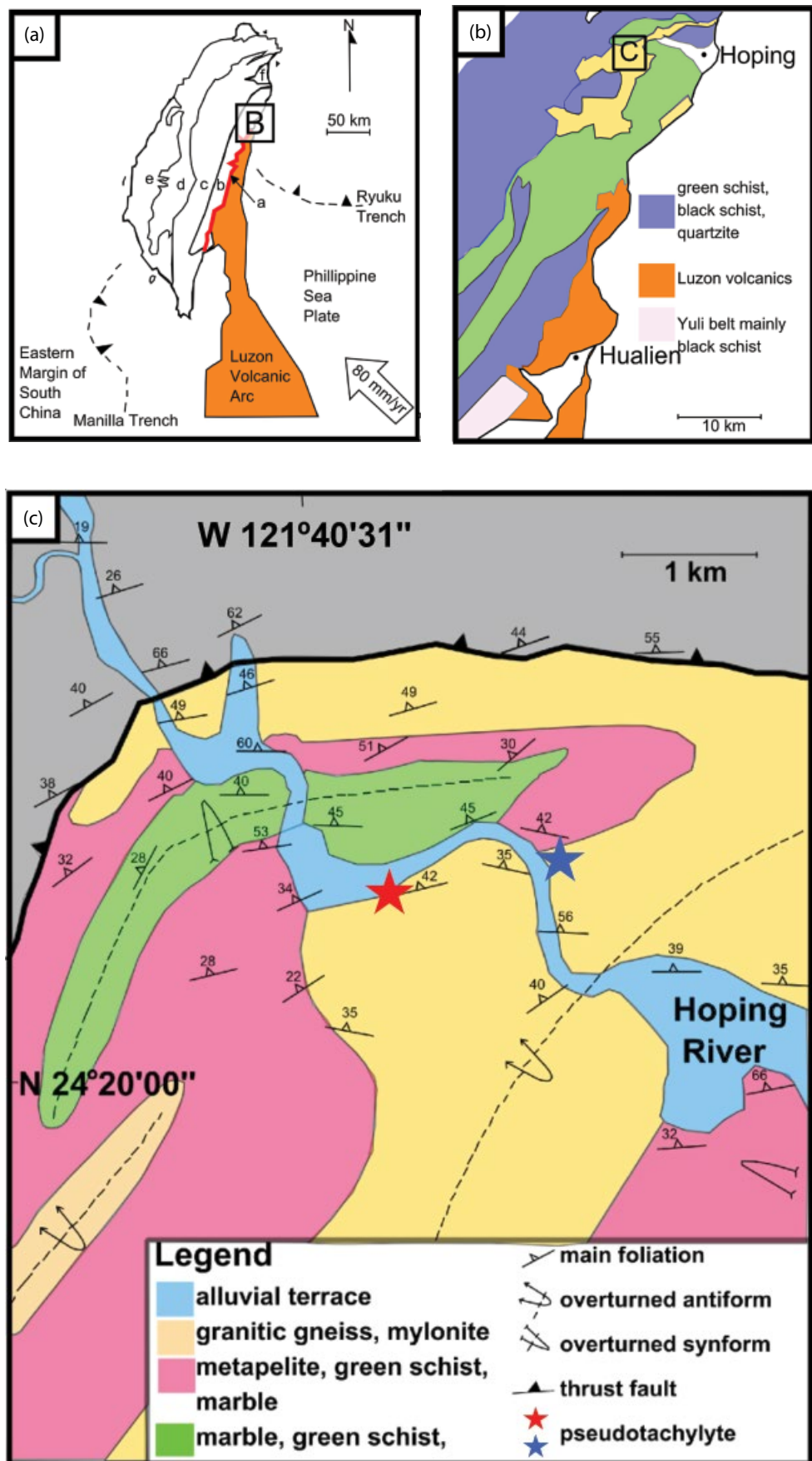


**Figure 2.1** (a) Main tectonostratigraphic units of Taiwan including the Coastal range associated with Luzon volcanic arc: (a) Longitudinal Valley fault, (b) Inner Taiwan Mountain Belt (Eastern Central range), (c) Hueshan range, (d) Western Foothills, (e) Western Taiwan Coastal Plain, and (f) Yilan Plain. (b) Hoping River area main units. (c) Hoping River detailed map [modified after Chu et al., 2012]. See electronic version for color representation.

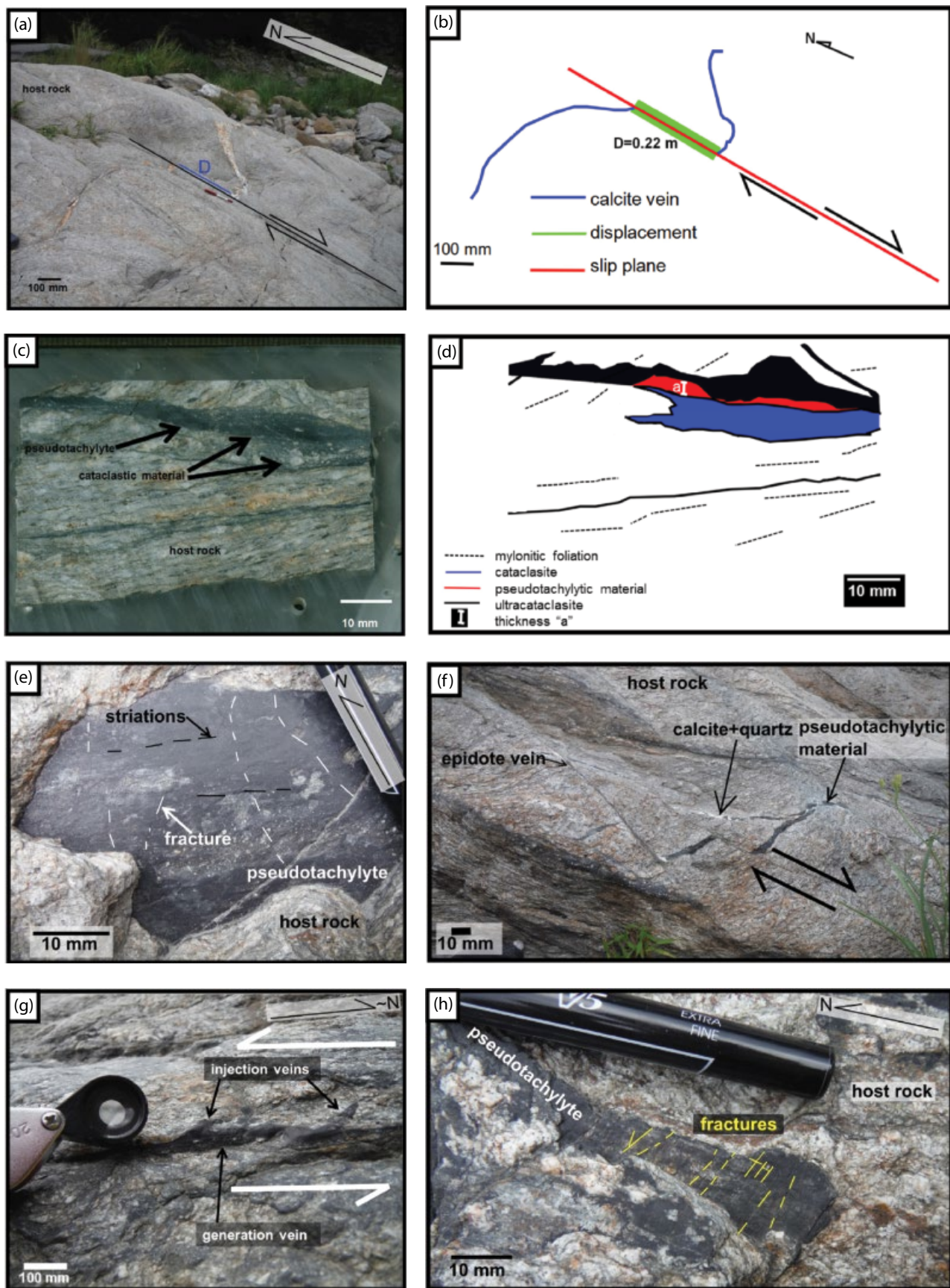


**Figure 2.2** (a) 220 mm displacement and slip direction; (b) schematic of (a); (c) composite cataclasite and pseudotachylite; (d) schematic of (c); (e) striations show slip direction; (f) field relations between calcite, pseudotachylite, and epidote veins, epidote shows slip direction; (g) asymmetric pseudotachylite veins indicate sense of slip; (h) fractures within the plane of the pseudotachylite. See electronic version for color representation.

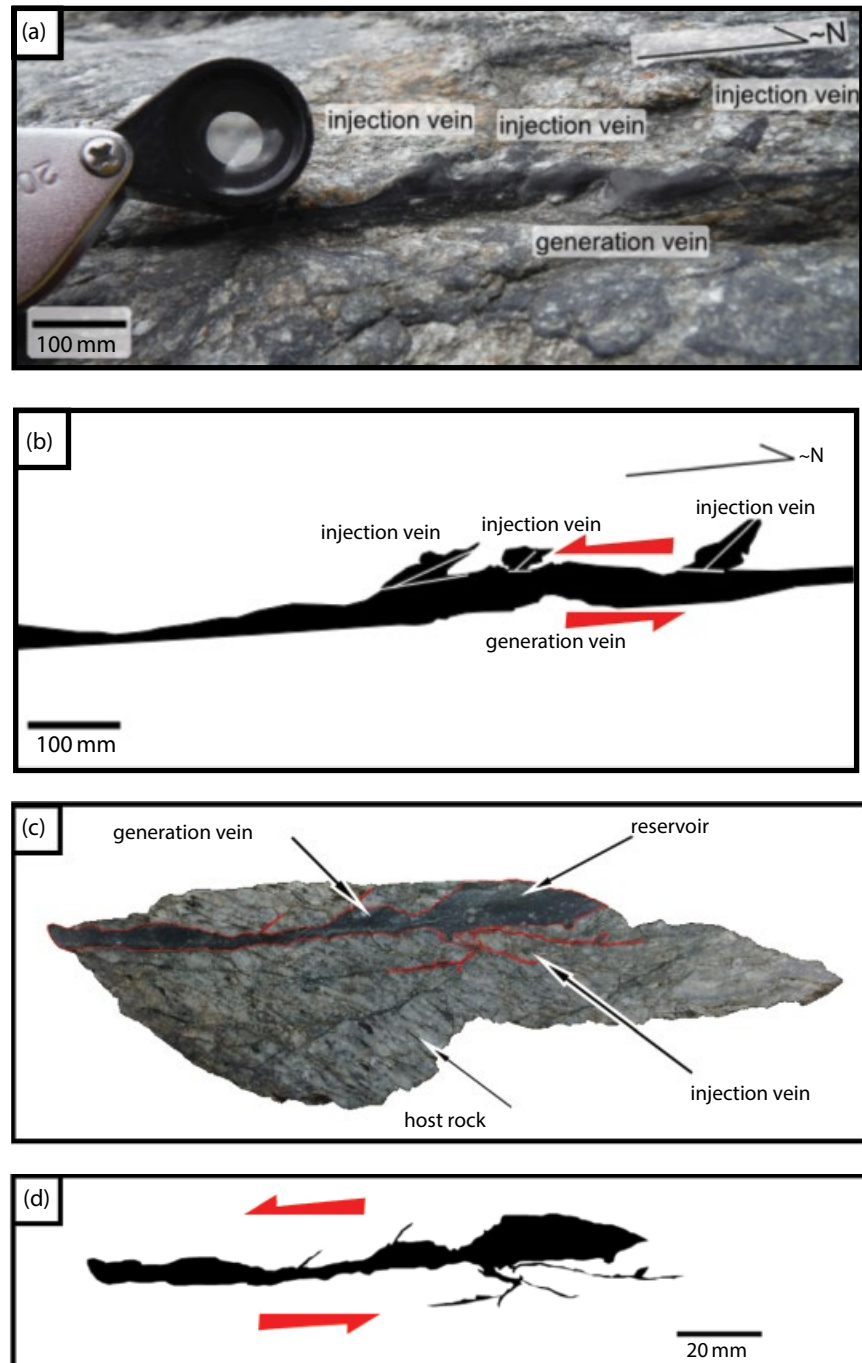


**Figure 2.3** Determination of slip sense in sections perpendicular to pseudotachylite veins and parallel to striae at the pseudotachylite/host rock interface. (a) and (b) Asymmetric injection veins interpreted to have formed in the  $\sigma_1/\sigma_2$  plane. The inferred sense of seismic slip is left lateral. (c) and (d) Same as (a) and (b), further along the same pseudotachylite vein.

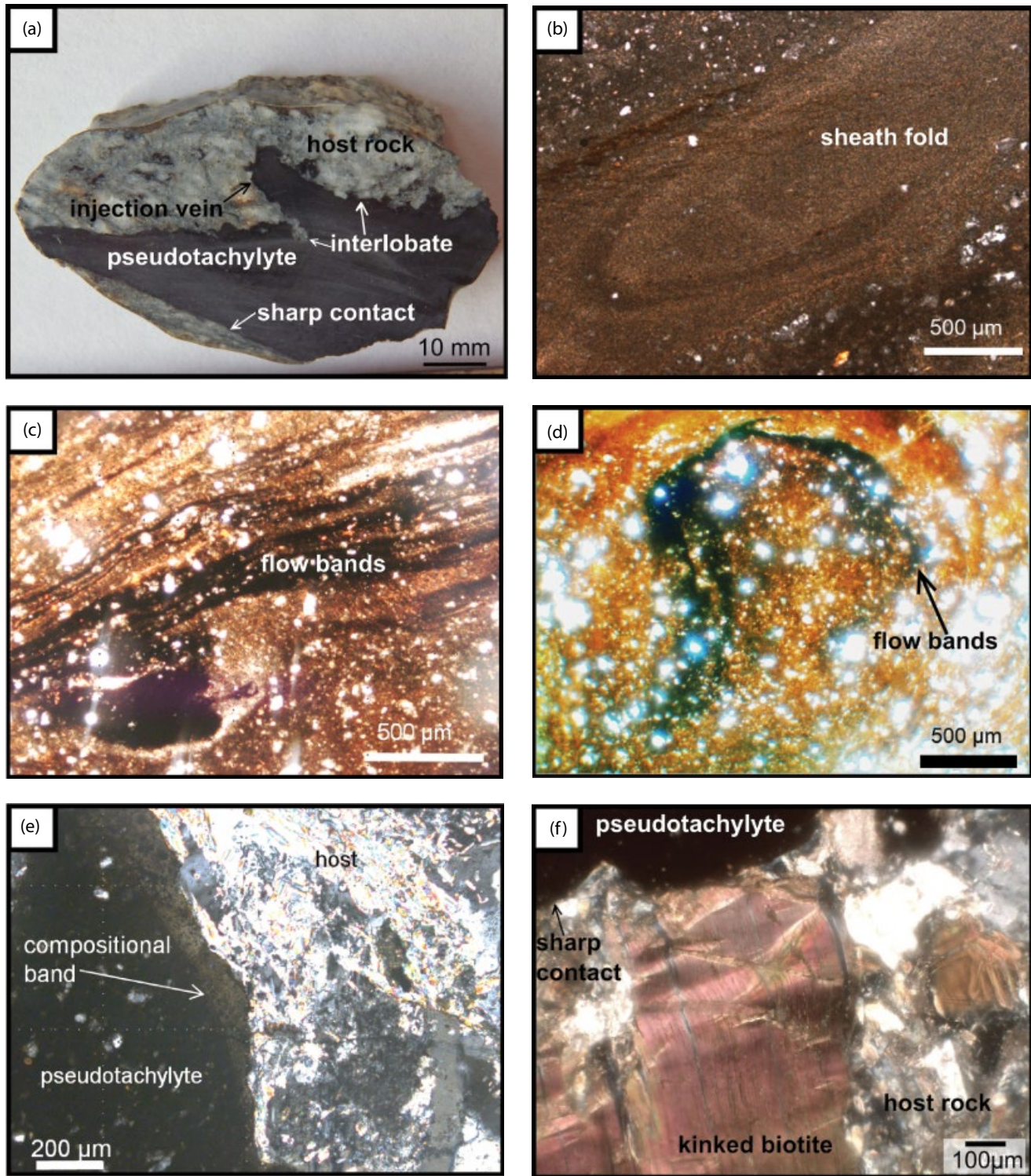


**Figure 2.4** (a) Pseudotachylyte forms interlobate and sharp contacts with host rock. (b) Sheath fold under cross-polarized light (CPL). (c) and (d). Flow banding and flow streaking in pseudotachylyte under CPL. (e) Sharp contact between host and pseudotachylyte and a compositional band in between under CPL. (f) Pseudotachylyte sharp contact with surrounding host rock portraying kinked hornblende, CPL.

**Table 2.1** Dimensions, aspect ratios, and melt overpressure in pseudotachylyte injection veins.

Vein #	Height (mm)	Width (mm)	Aspect Ratio	$\Delta$ pressure (GPa)
1	41	32	1.28	130
2	58	117	0.50	32
3	22	77	0.29	48
4	97	95	1.02	39
5	25	31	0.81	120
6	50	88	0.57	42
average	49	73	0.74	69
stdev	27	35	0.37	44

on a FEI Quanta 200F SEM for magnifications up to 8000x. The electron beam was set at 10 keV. Energy dispersive spectroscopy was used to determine the chemical composition of mineral phases.

## 2.4. RESULTS

In the following, *pseudotachylyte* refers to materials formed by frictional melting [Shand, 1916].

### 2.4.1. Field Data

The host rock to pseudotachylyte veins along the Hoping River is a granitic gneiss (in yellow in Figure 2.1c) consisting mainly of alkali feldspar, quartz, plagioclase, phengite, biotite, muscovite, epidote, sericite, and zircon. Secondary calcite fills interstitial spaces in the gneiss and originates from fluids percolating through the nearby marbles (in green in Figure 2.1c). The gneiss shows a strong mylonitic foliation at  $\approx 273^\circ$ ,  $43^\circ$  W (Figures 2.2, 2.5a, and 2.5d) and a mineral stretching lineation at  $\approx 279^\circ$ ,  $14^\circ$  W (Figure 2.5e).

Cataclasite and ultracataclasite veins, as well as cataclastic zones, occur throughout the main outcrop (red star on Figure 2.1c; coordinates: N24° 20'14.1", E121° 40'37.4"). Cataclasites contain angular clasts,  $<0.5$  mm in length, and range from grey to greenish in color with thickness  $<20$  mm. Within the cataclasite veins, darker and finer grained layers occur, particularly along the contact with the host rock. Small zeolite-rich veins tend to branch off of the cataclasite veins. The gneiss immediately around cataclasite veins shows centimeter-wide damage zones characterized by a high fracture density. A few cataclasite-ultracataclasite veins form injection veins into the host rock. En-echelon shear bands cut through the cataclastic veins.

The macroscopic distinction between ultracataclasites and pseudotachylytes requires detailed observations. The percentage of clasts tends to be lower in pseudotachylytes while the roundness of clasts seems lower in ultracataclasites.

At the hand specimen scale, the pseudotachylyte veins tend to occur subparallel to the mylonitic foliation (Figure 2.2c), whereas at the outcrop scale they are clearly discordant (Figure 2.5a). The mean orientation of 21 pseudotachylyte generation veins is  $168^\circ$ ,  $31^\circ$  W (Figure 2.5c).

The most extensive pseudotachylyte vein of the Hoping River locality is approximately 10 m long with a  $025^\circ$ ,  $35^\circ$  W generation plane. This vein shows striations along the contact between the vein and the host rock (Figure 2.2e). The striations consist of very small, relatively sharp, extremely straight and parallel ridges consistently elongated in the  $292^\circ$ ,  $35^\circ$  direction. Because these striations are consistent in orientation and parallel to the net slip direction determined from offset markers such as calcite veins, they constitute a new structural element indicative of seismic slip direction. These striations are distinct from the slickensides previously reported by Chu *et al.* [2012] because slickensides form asymmetric steps perpendicular to the slip direction. The vein carrying these striations provides opportunities to analyze the earthquake focal mechanism. The interface between the pseudotachylyte vein and the host rock also carries small tension fractures perpendicular to the host rock–pseudotachylyte contact and perpendicular to the seismic slip direction (Figure 2.2h). These fractures terminate at other intrapseudotachylyte fractures or at the contact between the pseudotachylyte and the host rock. The mode of formation of these fractures will be discussed in a later section. Injection veins exhibit sharp, lobate contacts with the host rock and form preferentially on one side of the pseudotachylyte (Figure 2.2g). Some injection veins display a perpendicular orientation with respect to the generation vein, but in general they display a consistent obliquity (Figure 2.3) that can be used as a shear sense indicator based on similar observations by Sibson [1975], Di Toro *et al.* [2005], and Griffith *et al.* [2009]. The injection vein height ranges from 25 to 97 mm while the thickness ranges from 31 to 117 mm. The aspect ratio of these veins ranges from 0.29 to 1.28 with an average at 0.74 (Table 2.1), a parameter that can be used to estimate the difference in pressure within the vein [Rowe *et al.*, 2012]. Injection veins typically contain fewer clasts than generation veins.

The structural relationships between deformation features at the Hoping River locality reveal a complex history. The pseudotachylyte generation veins cut through the mylonitic foliation, through most epidote and calcite veins (Figure 2.2). The displacement of markers such as calcite veins along the most extensive pseudotachylyte vein is consistently 220 mm in at least six different locations along strike. In places, centimeter-scale kink folds postdate the pseudotachylyte veins. The multiple pseudotachylyte veins observed at the Hoping River locality tend to be broadly parallel to each other (Figure 2.5c) and do not cut through each other.

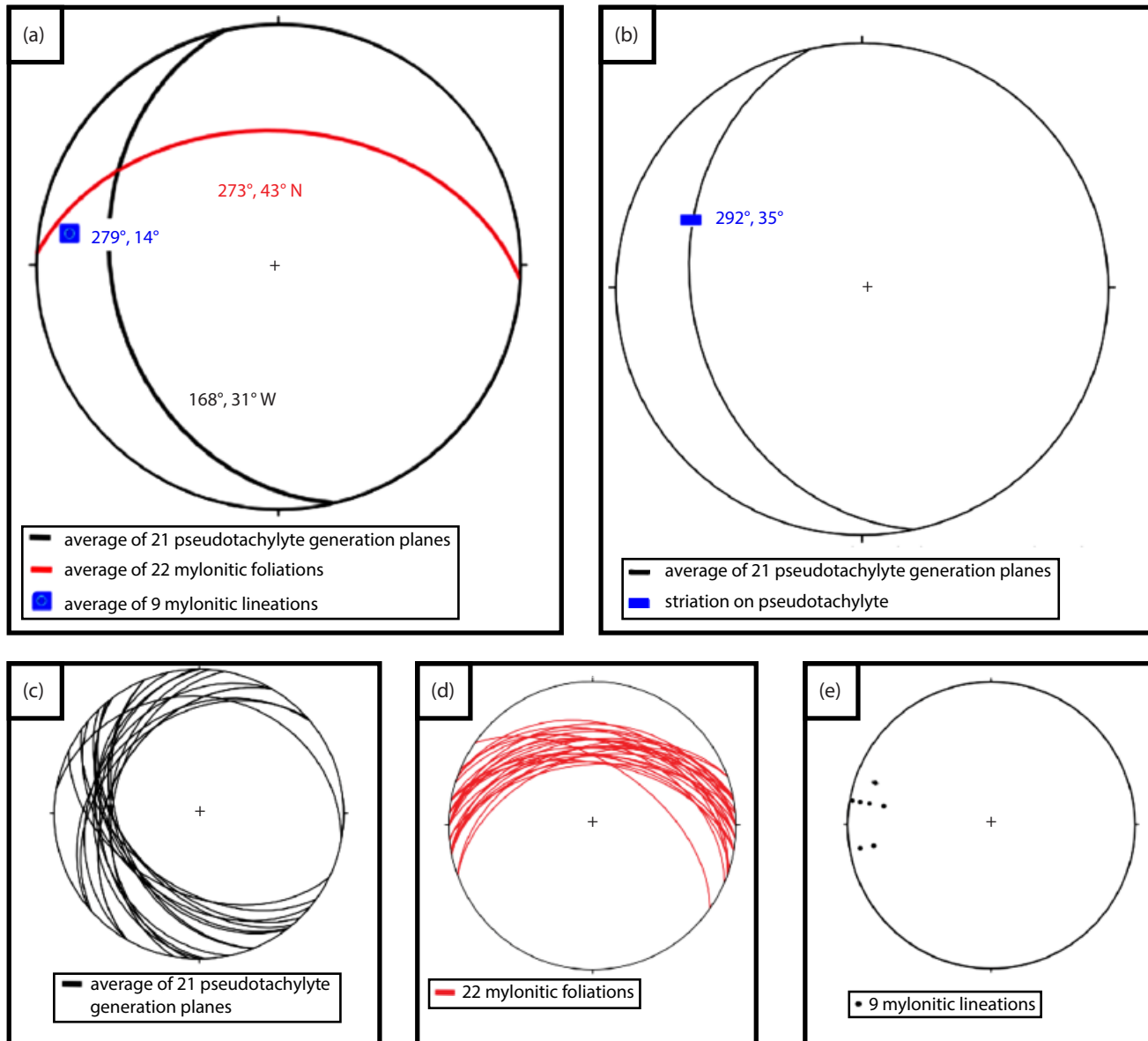


**Figure 2.5** (a) Stereonet of average field measurements from the Hoping River locality (all plots in lower hemisphere equal area). (b) Mean pseudotachylyte generation plane orientation. (c) Pseudotachylyte generation plane orientations. (d) Orientations of mylonitic foliations. (e) Mylonitic lineation.

Another ultracataclasite-pseudotachylyte locality (blue star on Figure 2.1c) occurs approximately 1 km east of the main locality described above. The attitude of most structural elements displays the same broad orientation.

#### 2.4.2. Petrographic Data

The host gneiss, cataclasites, ultracataclasites, and pseudotachylytes show a similar mineral assemblage, although the relative proportion of minerals varies between rock types [Chu *et al.*, 2012].

In cataclasites and ultracataclasites, quartz and feldspar clasts are less rounded than in pseudotachylytes. Quartz clasts are more rounded than feldspar clasts. In places, elongated and rotated clasts define a cataclastic flow alignment attesting of granular flow. Micaceous minerals and calcite are more abundant in the cataclasite and ultracataclasite than in the pseudotachylyte. A rim of fine-grained micas and clays surrounds some grains. Secondary epidote occurs on clasts and fill thin fractures. While most cataclasites display no fabric along their margin with host rock, where they do,

fabric strength increases away from the contact. Both feldspar and calcite clasts display undulose extinction. Feldspar clasts also exhibit polysynthetic twins, kinks, and microfaults, whereas calcite clasts exhibit thick, tabular, broken mechanical twins.

The pseudotachylytes contain clasts of quartz, alkali feldspar, epidote, and plagioclase with polysynthetic twins, zircon, minor calcite, micaceous phases, and clay material. A micaceous matrix, rather than an amorphous matrix, characterizes most of the pseudotachylyte. Tension fractures originating from the host rock–pseudotachylyte contact are less than  $10\text{ }\mu\text{m}$  in thickness. In detail, the contact between the pseudotachylyte and its host tends to be sharp and lobate (Figure 2.4a). Large biotite clasts along the contact between the pseudotachylyte and the host rock are fuzzy and contain holes. A light brown band of amorphous material characterizes part of the host rock–pseudotachylyte contact (Figure 2.4e). The host rock directly adjacent to the pseudotachylyte contains kinked biotite crystals indicative of high differential stress. The pseudotachylyte locally displays a sheath fold (Figure 2.4b). Multicolored compositional bands parallel to the vein margin appear optically isotropic and brown (Figures 2.4b and 2.4c). Clasts in the pseudotachylyte vary in size from tens of microns to two millimeters and are more rounded than their counterparts in the cataclasite. Clast size generally increases toward the pseudotachylyte–host rock contact. Some ultracataclasites host angular pseudotachylyte clasts.

#### 2.4.3. Scanning Electron Microscopy (SEM)

The most conclusive evidence for a melt origin in fault pseudotachylytes is generally provided by SEM because this method provides clear images without optical scattering. The material identified as cataclasite or ultracataclasite is completely free of microcrystallites and vesicles. In general, the boundary between cataclasite-ultracataclasite and host rock is gradational over a few tens to hundreds of millimeters. The size of angular clasts, from a few microns to millimeters, increases from the center of cataclasite-ultracataclasite veins toward the margin. In places, elongate clasts form an oblique fabric with respect to the vein margin. A few structures, characterized by a central clast surrounded by smaller clasts, are observed. Intragranular fractures are common in feldspar grains.

The pseudotachylyte–host rock contact is very sharp over a few microns (Figure 2.6c). Widely dispersed microcrystallites on the order of  $0.5\text{ }\mu\text{m}$  to  $10\text{ }\mu\text{m}$  show a radial growth pattern and preferred orientation (Figures 2.6a, b, d, e). Microcrystallites size increases from the pseudotachylyte margin toward the vein center, suggesting a possible quenching effect. Ankerite forms framboidal grains of 2 to  $5\text{ }\mu\text{m}$  in diameter.

## 2.5. INTERPRETATION OF FIELD AND PETROGRAPHIC RESULTS

New field and petrographic observations constrain the deformation history of the Hoping River granitic gneiss as part of the Tananao metamorphic complex. Mylonitic deformation in the Hoping River has been dated around 4.1–3.0 Ma using Ar-Ar on biotite from a gneiss located 1.5 km ESE from the pseudotachylyte locality [Wang *et al.*, 1998]. Intragranular feldspar microfractures and deformation bands indicate temperatures ca. 300–400 °C [e.g., Passchier and Trouw, 1996]. Thick, tabular calcite twin lamellae indicate temperatures greater than 300 °C [Ferrill *et al.*, 2004]. Undulose extinction in  $250\text{ }\mu\text{m}$  diameter quartz grains and kinked plagioclase twins are consistent with mylonitization at temperatures around 300 °C [e.g., Fitz Gerald and Stünitz, 1983].

As mylonitic deformation was still going on due to fast exhumation of the Central Range, strain became extremely localized near a prominent lithological discontinuity between the marbles and the granitic gneiss. Strain partitioning culminated in seismic slip accompanied by frictional melting. The following criteria help distinguish ultracataclasite from pseudotachylyte: pseudotachylytes tend to be darker and finer grained than ultracataclasites; clasts are fewer, smaller, and more rounded in pseudotachylytes than in ultracataclasites. The subparallel intertwining of ultracataclasite and pseudotachylyte layers in the same vein strongly suggests that both formed during the same seismic event. In places, pseudotachylyte angular clasts are embedded in ultracataclasite. In order for a pseudotachylyte fragment to have angular shapes the frictional melt had to have cooled down while high strain rate deformation continued. This observation shows that high-strain rate cataclasis, possibly caused by aftershocks, persisted moments after melt quenching. The subparallel and non-cross-cutting geometry of pseudotachylyte veins suggests that each vein formed due to a single seismic slip event. A similar pattern of subparallel pseudotachylytes formed in a mylonitic gneiss has been documented in the Italian Alps [Zechmeister *et al.*, 2007].

Internal flow structures within the pseudotachylyte veins attest of viscous laminar flow. The sheath fold indicates a melt flow direction parallel to the seismic slip direction (Figure 2.4b; Lin, 2008) Flow streaking lines point to viscosity gradient or flow velocity gradient within the pseudotachylyte vein (Figure 2.4c; Lin, 2008). Thermal corrosion of feldspar due to frictional heating is attested by the lobate, embayed outline of these grains. However, the lack of thermal corrosion microstructures in quartz, a mineral with melting temperature  $\approx 1700\text{ }^{\circ}\text{C}$ , supports relatively modest melting temperatures in the 600 to 1200 °C range. The presence of microcrystallites, established through SEM (Figure 2.6), provides the first

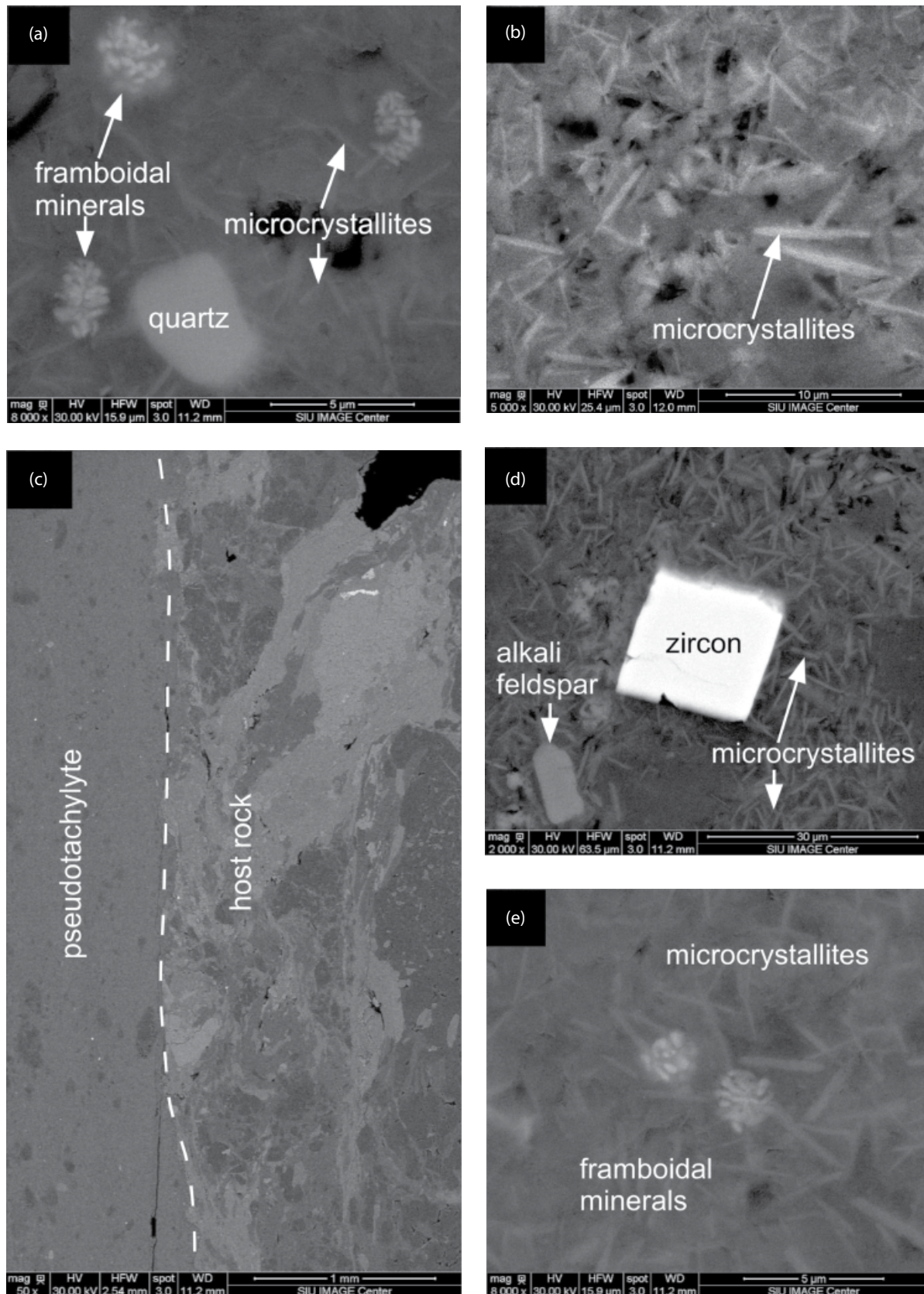


**Figure 2.6** (a) Frambooidal minerals, microcrystallites, and quartz in pseudotachylyte, backscattered electron microscopy (BSE). (b) Hoping River pseudotachylyte with randomly oriented microcrystallites, BSE. (c) Contact between Hoping River pseudotachylyte and metagranite host rock, SE. (d) Frambooidal minerals, microcrystallites, and alkali feldspar with rounded grain boundaries, BSE. (e) Accretionary grains around the indicated clast, higher z number than microcrystallites and less lathlike, BSE.

irrefutable evidence of the melt origin of these pseudotachylytes. At least a portion of the pseudotachylyte micaceous matrix may have formed through glass palagonitisation due to fluid alteration. This alteration obscures microstructural observations with an optical microscope.

The general absence of fault gouge and fault breccia at the Hoping River locality indicates that cataclasis took place at depths greater than 4 km [Sibson, 1977; 1986]. At the regional scale, the Tananao metamorphic complex is characterized by postmylonitic microfolding and kink folding. This small-scale folding, along with en-echelon deformation bands, clearly overprints pseudotachylyte veins along the Hoping River. This shows that regional deformation persisted after the seismic events responsible for the formation of pseudotachylyte.

The last increment of brittle deformation recorded at the Hoping River locality (red star; Figure 2.1c) is represented by chlorite-epidote-zeolite cataclastic shear fractures. This mineral assemblage attests of fluid alteration at temperatures <225 °C [Chu et al., 2012].

## 2.6. DISCUSSION

### 2.6.1. Estimates of Coseismic Melt Overpressure

In agreement with Sibson [1977] and Cowan [1999], we consider that the formation of a frictional melt requires seismic slip velocities due to the constraints imposed by heat transfer in rocks. The seismic velocities attained during formation of pseudotachylytes are required to generate the overpressure needed to open injection veins [Rowe et al., 2012].  $\Delta P$  quantifies the coseismic pressurization required to open a crack [Rubin, 1995; Rowe et al., 2012].

$$\Delta P = (\mu / (1-v)) \cdot (w_o / 2l), \quad (2.1)$$

where  $\mu$  is shear modulus,  $v$  is Poisson's ratio,  $w_o$  is maximum width, and  $l$  is height of injection veins.

Equation (2.1) relates the maximum width of an injection vein to the fluid overpressure ( $\Delta P$ ) in an opening mode fracture (mode I) of fixed length, embedded in an infinite, 2D linear elastic medium. The injected viscoelastic fluid exerts force perpendicular to the crack length. This equation assumes that pseudotachylytes represent 2D, linear, infinite bodies that underwent uniform stress loading. The equation in current form only accounts for normal stresses and does not account for excess fluid in the surrounding host rock. The maximum width ( $w_o$ ) and height ( $l$ ) of six injection veins provides the variables to calculate change in net pressure ( $\Delta P$ ). The Poisson ratio (0.21) and shear modulus ( $6.08 \times 10^8$  Pa) were experimentally measured from the Hoping River metagranite. The elastic stiffness of rocks, however, would likely change during seismic slip and would be lower in

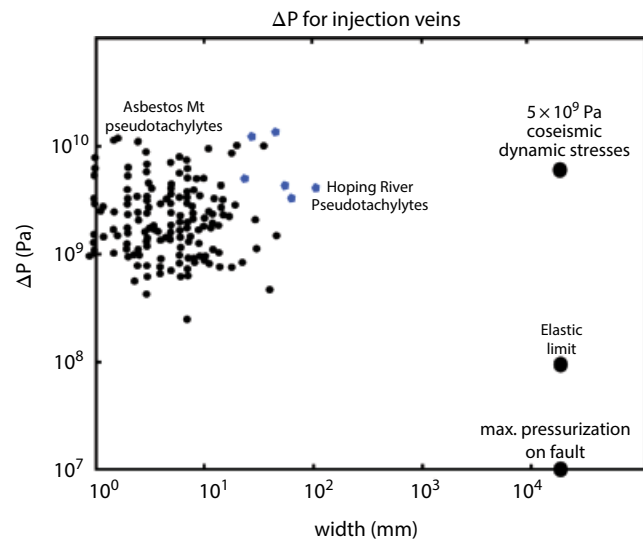


**Figure 2.7** Relationship between change in pressure and width of the Hoping River pseudotachylyte injection veins compared to the Asbestos Mountain, California, pseudotachylyte injection veins [after Rowe et al., 2012; Reches and Dewers, 2005].

catastically deformed host rock than in the undeformed one, as observed elsewhere by Griffith et al. [2012]. The overpressures deduced from these calculations (Figure 2.7) are typical of values accepted for coseismic dynamic stresses [Rowe et al., 2012; Reches and Dewers, 2005]. These very large overpressures further demonstrate that the Hoping River pseudotachylytes formed through slip at seismic velocities.

### 2.6.2. Determination of Seismic Displacement

The thickness of fault pseudotachylyte veins tends to show a broad proportionality with the magnitude and energy of the earthquake during which it formed [Sibson, 1975].

$$D = 436.a^2, \quad (2.2)$$

where  $D$  is displacement (in centimeters) and  $a$  is pseudotachylyte generation vein thickness (in centimeters).

This empirical equation yields realistic albeit approximate results [Di Toro et al., 2005; Zechmeister et al., 2007]. In our use of the equation, we assume that the pseudotachylyte generation vein formed as result of a single seismic slip event. The seismic displacement values obtained for the Hoping River pseudotachylytes using thicknesses of 1 to 2 mm range from 44 to 174 mm. These values appear to underestimate displacement compared to the value of 220 mm determined directly from offset markers. This difference can be explained by the fact that some frictional melt that had left the generation vein was emplaced in injection veins. Alternatively, melt productivity during seismic slip greatly depends on the host rock

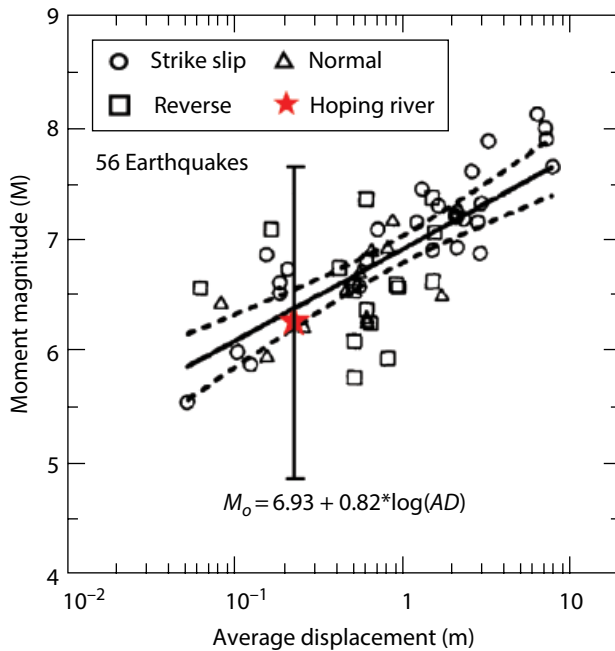


**Figure 2.8** Graph showing the magnitude of earthquake that the Hoping River pseudotachylite represents according to equation [after Wells and Coppersmith, 1994].

composition [e.g., Büttner *et al.*, 2013] and may have been lower at Hoping River compared to the Outer Hebrides, where the *Sibson* [1975] empirical equation is from.

### 2.6.3. Calculations of Seismic Moment Magnitude

Moment magnitude ( $M_w$ ) relates to the energy released by an earthquake (Figure 2.8). Here we use the empirical relationship between  $M_w$  and average displacement ( $AD$ ) measured along the slip plane [Wells and Coppersmith, 1994]:

$$M_w = 6.9 + (0.82 * \log(AD)). \quad (2.3)$$

The  $AD$  used for this relation refers to surface displacement as opposed to total or net displacement. This equation results from a regression and least squares analysis of 56 earthquakes of various fault types, including strike slip, reverse, and normal. Equation (2.3) yields a correlation coefficient  $r = 0.75$  to  $0.78$  (with a standard deviation of 0.4). The moment magnitude calculated using equation (2.3) for the Hoping River pseudotachylites, using the 220 mm measured displacement, is  $M_w 6.4 \pm 0.4$ .

### 2.6.4. Sense of Seismic Slip and Tectonic Significance

The direction of slip ( $292^\circ$ ,  $35^\circ$ ) was determined by two independent approaches. First, the net slip direction is determined in 3D from the displacement of calcite veins

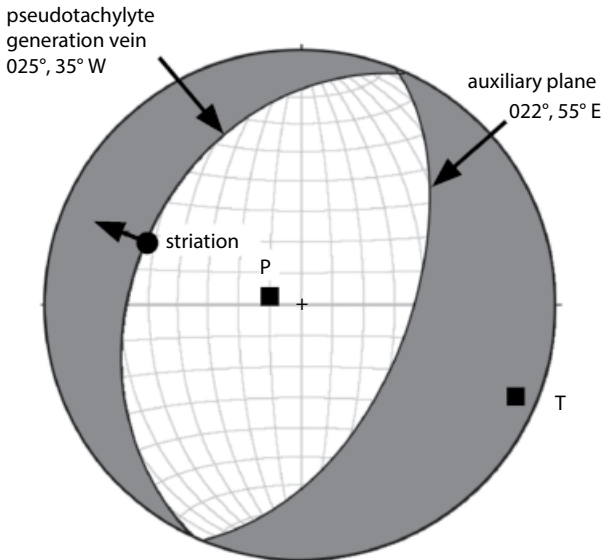


**Figure 2.9** Focal mechanism of pseudotachylite generation vein, normal dip slip.

by the main pseudotachylite generation vein. Second, the direction of seismic slip ( $292^\circ$ ,  $35^\circ$ ) is assessed from the striations present at the sharp contact between the pseudotachylite generation vein and the host rock. The two values are in perfect agreement. The sense of slip along the main pseudotachylite vein was determined first by observing the sense of displacement of offset markers (Figure 2.2a and 2.2b). Second, we interpreted the asymmetric injection veins observed to branch off the main generation vein as indicating the orientation of the principal stresses  $\sigma_1$  and  $\sigma_2$ . Both approaches indicate a normal sense of displacement along the main pseudotachylite generation vein. The coseismic sense of slip appears to be consistent with that indicated by the shear bands that postdate the pseudotachylite veins. The seismic event recorded by the main generation vein of pseudotachylite in the Hoping River corresponds to normal extensional motion along the slip plane (Figure 2.9).

While most tectonic models for Taiwan involve rapid exhumation of the Central Range since the Pliocene [Li, 1976], as a counterpart to subduction along the Coastal Range, no significant seismic activity has been documented yet with this exhumation. With present exhumation rates of 3.0–6.0 mm/yr [Dadson *et al.*, 2003], the Central Range of Taiwan remains a prime area for seismic activity. Recent seismicity (1995–2015) in the Tananao metamorphic complex area shows the dominance of reverse faulting mechanisms (Figure 2.10). The Hoping River pseudotachylite marks a significant seismic extensional event ( $M_w$  6.4) and provides, perhaps, an important clue regarding the Pliocene to present exhumation of the Tananao metamorphic complex.

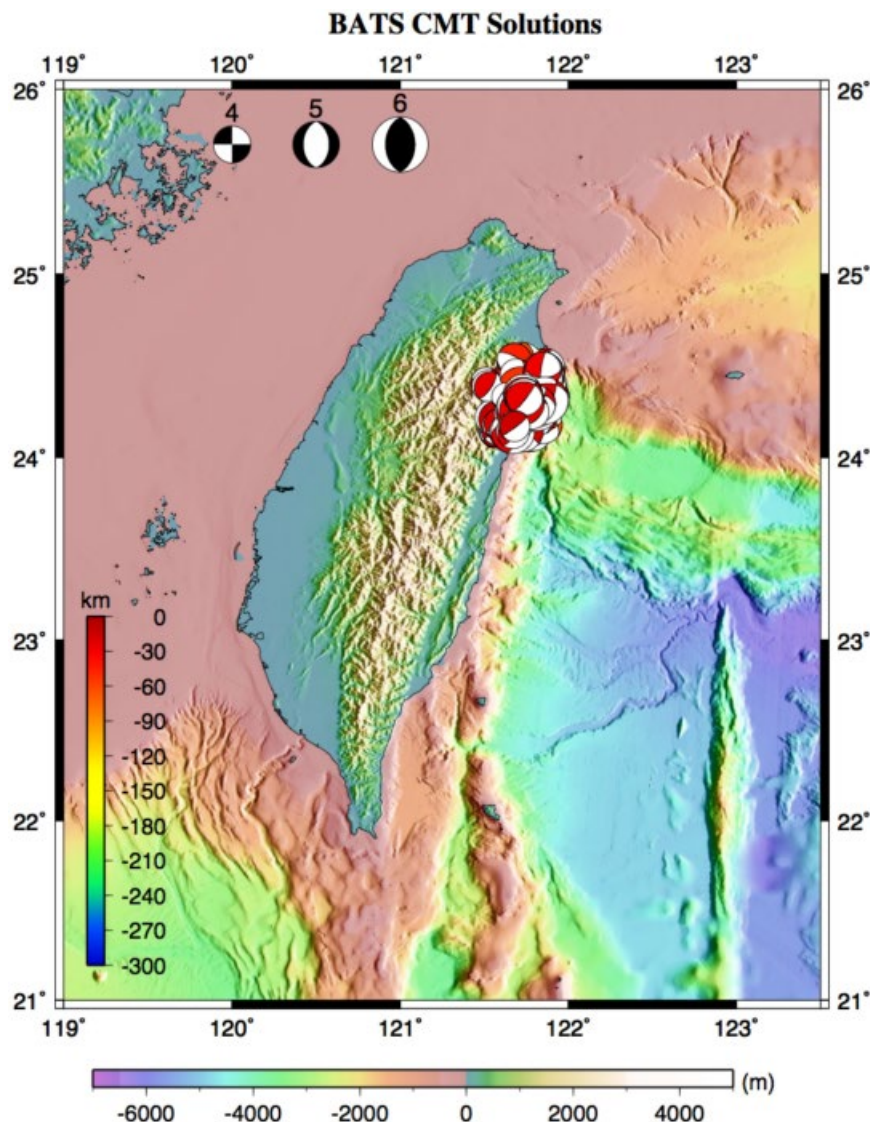


**Figure 2.10** Map of 1995–present earthquakes showing the dominance of reverse focal mechanisms in the vicinity of the Hoping River [Institute of Earth Sciences, Academia Sinica, Taiwan, 1996]. See electronic version for color representation.

More precise dating of this pseudotachylyte and others, in conjunction with studies of erosion rate, may explain more about the interaction between tectonics and erosion as well as the exhumation processes in an accretionary wedge.

## 2.7. CONCLUSION

Seismic deformation in the Tananao metamorphic complex resulted in the development of fault pseudotachylites. The age of this seismic deformation is currently poorly constrained but clearly postdates the 4.1–3.0 Ma mylonitic foliation. The Hoping River pseudotachylites provide a unique opportunity to investigate the seismic deformation and associated kinematics in the broader

context of Taiwan Pliocene-Pleistocene tectonics. The main Hoping River pseudotachylyte records previously documented normal seismic motion with a displacement estimated to 220 mm ( $M_w 6.4 \pm 0.4$ ) and a focus at depths estimated to  $\geq 4$  km with temperatures around 300–250 °C. While most tectonic models for Taiwan involve exhumation of the Central Range as a counterpart to subduction along the Coastal Range, no significant seismic activity has been documented yet with this exhumation. Yet rapid acceleration of exhumation of the Central Range of Taiwan started in the Pliocene. With present exhumation rates of 3.0–6.0 mm/yr, the Central Range of Taiwan remains a prime area for seismic activity. The Hoping River pseudotachylyte provides, perhaps, an important clue regarding the Pliocene to present exhumation of the

Tananao metamorphic complex. More precise dating of this pseudotachylite and others, in conjunction with studies of erosion rate, may provide important clues regarding the interaction between seismotectonics and erosion in an accretionary margin setting.

## ACKNOWLEDGMENTS

Caitlyn Korren acknowledges the fellowship from the National Science Foundation East Asia Pacific Summer Institute (Award #1415015) and the Ministry of Science and Technology of Taiwan, through which this study was funded. The logistical support provided by National Taiwan Normal University and the graduate group of En-Chao Yeh was also crucial in the successful completion of this project. Eric Ferré acknowledges support from the National Taiwan Normal University International Visiting Scholars Program and is also grateful to Charly Aubourg for introducing him to his Taiwanese colleagues. The constructive comments made by an editor (Marion Thomas) and two reviewers (Jian-Cheng Lee and W. Ashley Griffith) significantly helped us strengthening this work.

## REFERENCES

- Andersen, T. B., and H. Austrheim (2006), Fossil earthquakes recorded by pseudotachylites in mantle peridotite from the Alpine subduction complex of Corsica, *Earth and Planetary Science Letters*, 242, 58–72.
- Angelier, J., H. T. Chu, and J. C. Lee (1997), Shear concentration in a collision zone: Kinematics of the Chihshang Fault as revealed by outcrop-scale quantification of active faulting, Longitudinal Valley, eastern Taiwan, *Tectonophysics*, 274(1–3), 117–143.
- Beyssac, O., M. Simoes, J. P. Avouac, K. A. Farley, Y.-G. Chen, Y.-C. Chan, and B. Goffé (2007), Late Cenozoic metamorphic evolution and exhumation of Taiwan C8 - TC6001, *Tectonics*, 26(6).
- Bor-Shouh, H., and Y. Yeong Tein (1992), Source geometry and slip distribution of the April 21, 1935 Hsinchu-Taichung, Taiwan earthquake, *Tectonophysics*, 210(1–2), 77–90.
- Büttner, S. H., S. Sherlock, L. Fryer, J. Lodge, T. Diale, R. Kazondunge, and P. Macey (2013), Controls of host rock mineralogy and  $H_2O$  content on the nature of pseudotachylite melts: Evidence from pan-African faulting in the foreland of the Gariep belt, South Africa, *Tectonophysics*, 608, 552–575.
- Chu, H.-T., S.-L. Hwang, P. Shen, and T.-F. Yui (2012), Pseudotachylite in the Tananao Metamorphic Complex, Taiwan: Occurrence and dynamic phase changes of fossil earthquakes, *Tectonophysics*, 581, 62–75.
- Cowan, D. (1999), Do faults preserve a record of seismic slip? A field geologist's opinion, *Journal of Structural Geology*, 21, 995–1001.
- Dadson, S., N. Hovius, H. Chen, W. D. Dade, M. L. Hsieh, S. D. Willett, J. C. Hu, M. J. Horng, M. C. Chen, C. P. Stark, D. Lague, and J. C. Lin (2003), Links between erosion, runoff variability and seismicity in the Taiwan orogen, *Nature*, 426, 648–651.
- Di Toro, G., T. Hirose, S. Nielsen, G. Pennacchioni, and T. Shimamoto (2006), Natural and experimental evidence of melt lubrication of faults during earthquakes, *Science*, 311(5761), 647–649, doi:10.1126/science.1121012.
- Di Toro, G., S. Nielsen, and G. Pennacchioni (2005), Earthquake rupture dynamics frozen in exhumed ancient faults, *Nature*, 436, 1009–1012.
- Ferré, E. C., J. W. Geissman, A. Chauvet, A. Vauchez, and M. S. Zechmeister (2015), Focal mechanism of prehistoric earthquakes deduced from pseudotachylite fabric, *Geology*, doi:10.1130/G36587.1.
- Ferrill, D. A., A. P. Morris, M. A. Evans, M. Burkhard, R. H. Groshong Jr, and C. M. Onasch (2004), Calcite twin morphology: A low-temperature deformation geothermometer, *Journal of Structural Geology*, 26(8), 1521–1529.
- Fitz Gerald, J. D., and H. Stünitz (1993), Deformation of granitoids at low metamorphic grade. I: Reactions and grain size reduction, *Tectonophysics*, 221, 269–297.
- Griffith, W. A., A. J. Rosakis, D. D. Pollard, and C.-W. Ko (2009), Dynamic rupture experiments elucidate tensile crack development during propagating earthquake ruptures, *Geology*, 37, 795–798, doi: 10.1130/G30064A.1.
- Griffith, W.A., T. M. Mitchell, J. Renner, and G. Di Toro (2012), Coseismic damage and softening of fault rocks at seismic depths, *Earth and Planetary Science Letters*, 353–354, 219–230.
- Ho, C. S. (1986), A synthesis of the geologic evolution of Taiwan, *Tectonophysics*, 125(1–3), 1–16.
- Huang, C. Y., P. B. Yuan, and S. J. Tsao (2006), Temporal and spatial records of active arc-continent collision in Taiwan: A synthesis. *Geol. Soc. Am. Bull.*, 118, 274–288.
- Institute of Earth Sciences, Academia Sinica, Taiwan (1996), *Broadband Array in Taiwan for Seismology*. Institute of Earth Sciences, Academia Sinica, Taiwan. Other/Seismic Network. doi:10.7914/SN/TW.
- Kao, H., and W.-P. Chen (2000), The Chi-Chi earthquake sequence: Active, out-of-sequence thrust faulting in Taiwan, *Science*, 288(5475), 2346–2349.
- Kuo, L.-W., H.-C. Hsiao, S.-R. Song, H.-S. Sheu, and J. Suppe (2014), Coseismic thickness of principal slip zone from the Taiwan Chelungpu Fault Drilling Project-A (TCDP-A) and correlated fracture energy, *Tectonophysics*, 619–620, 29–35.
- Li, Y.-H. (1976), Denudation of Taiwan Island since the Pliocene epoch, *Geology*, 4(2), 105–107.
- Lin, A. (2008), *Fossil Earthquakes: The Formation and Preservation of Pseudotachylites*, Springer, New York.
- Lin, A. T., A. B. Watts, and S. P. Hesselbo (2003), Cenozoic stratigraphy and subsidence history of the South China Sea margin in the Taiwan region, *Basin Research*, 15(4), 453–478.
- Liu, T. K., Y. G. Chen, W. S. Chen, and S. H. Jiang (2000), Rates of cooling and denudation of the Early Penglai Orogeny, Taiwan, as assessed by fission-track constraints, *Tectonophysics*, 320(1), 69–82.

- Maddock, R. H. (1983), Melt origin of pseudotachylites demonstrated by textures, *Geology*, 11, 105–108.
- Magloughlin, J. F. (1989), The nature and significance of pseudotachylite from the Nason terrane, North Cascade Mountains, Washington, *Journal of Structural Geology*, 11, 907–917.
- Malavieille, J., S. E. Lallemand, S. Dominguez, A. Deschamps, C. Y. Lu, C. S. Liu, P. Schnuerle, J. Angelier, J. Y. Collot, B. Deffontaines, M. Fournier, S. K. Hsu, J. P. Le Formal, S. Y. Liu, J. C. Sibuet, N. Thareau, and F. Wang (2002), Arc-continent collision in Taiwan: New marine observations and tectonic evolution. *Geological Society of America Special Paper* 358: *Geology and Geophysics of an Arc-Continent Collision, Taiwan*, 358, 187–211.
- Otsuki, K., T. Hirono, M. Omori, M. Sakaguchi, W. Tanigawa, W. Lin, W. Soh, and S. S. Rong (2009), Analyses of pseudotachylite from Hole-B of Taiwan Chelungpu Fault Drilling Project (TCDP): Their implications for seismic slip behaviors during the 1999 Chi-Chi earthquake, *Tectonophysics*, 469(1–4), 13–24.
- Passchier, C. W., and R. A. J. Trouw (1996), *Microtectonics*, 1st ed., 289 pp., Springer-Verlag, Berlin.
- Reches, Z. E., and T. A. Dewers (2005), Gouge formation by dynamic pulverization during earthquake rupture, *Earth and Planetary Science Letters*, 235(1–2), 361–374.
- Rowe, C. D., J. D. Kirkpatrick, and E. E. Brodsky (2012), Fault rock injections record paleo-earthquakes, *Earth and Planetary Science Letters*, 335–336, 154–166.
- Rubin, A. M. (1995), Getting granite dikes out of the source region, *Journal of Geophysical Research*, 100, 5911–5929.
- Seno, T. (1977), The instantaneous rotation vector of the Philippine sea plate relative to the Eurasian plate, *Tectonophysics*, 42(2), 209–226.
- Shand, S. J. (1916), The pseudotachylite of Parijs (Orange Free State) and its relation to “trap shotten” and flinty crush-rock, *Quarterly Journal of the Geological Society of London*, 72, 198.
- Shyu, J. B. H., L.-H. Chung, Y.-G. Chen, J.-C. Lee, and K. Sieh (2007), Re-evaluation of the surface ruptures of the November 1951 earthquake series in eastern Taiwan, and its neotectonic implications, *Journal of Asian Earth Sciences*, 31(3), 317–331.
- Sibson, R. H. (1975), Generation of pseudotachylite by ancient seismic faulting, *Geophysical Journal of the Royal Astronomical Society*, 43, 775–794.
- Sibson, R. H. (1977), Fault rocks and fault mechanisms, *Journal of the Geological Society*, 133(3), 191–213.
- Sibson, R. H. (1986), Earthquakes and rock deformation in crustal fault zones, *Annual Review of Earth and Planetary Sciences*, 14(1), 149–175.
- Sibuet, J.-C., and S.-K. Hsu (1997), Geodynamics of the Taiwan arc-arc collision, *Tectonophysics*, 274(1–3), 221–251.
- Suppe, J. (1984), Kinematics of arc-continent collision, flipping of subduction, and back-arc spreading near Taiwan, *Geological Society of China Memoir*, 6, 21–33.
- Wang, P. L., L. H. Lin, and C. H. Lo (1998),  $^{40}\text{Ar}/^{39}\text{Ar}$  dating of mylonitization in the Tananao schist, eastern Taiwan, *Journal of the Geological Society of China*, 41, 159–183.
- Wells, D. L., and K. J. Coppersmith (1994), New empirical relationships among magnitude, rupture length, rupture width, rupture area, and surface displacement, *Bulletin of the Seismological Society of America*, 84(4), 974–1002.
- Wibberley, C. A. J., and T. Shimamoto (2005), Earthquake slip weakening and asperities explained by thermal pressurization, *Nature*, 436, 689–692.
- Willemann, J. H., and P. L. K. Knuepfer (1994), Kinematics of arc-continent collision in the eastern Central Range of Taiwan inferred from geomorphic analysis, *Journal of Geophysical Research: Solid Earth*, 99(B10), 20267–20280.
- Yen, T. P. (1963), The metamorphic belts within the Tananao Schist terrain of Taiwan, *Proceedings of the Geological Society of China*, 6, 72–74.
- Yu, S.-B., H.-Y. Chen, and L.-C. Kuo (1997), Velocity field of GPS stations in the Taiwan area, *Tectonophysics*, 274(1–3), 41–59.
- Yu, S. B., and C. C. Liu (1989), Fault creep on the central segment of the Longitudinal Valley fault, eastern Taiwan, *Proceedings of the Geological Society of China*, 32, 209–231.
- Zechmeister, M. S., E. C. Ferré, M. A. Cosca, and J. W. Geissman (2007), Slow and fast deformation in the Dora Maira Massif, Italian Alps: Pseudotachylites and inferences on exhumation history, *Journal of Structural Geology*, 29(7), 1114–1130.

# 3

## Fluid Inclusion Evidence of Coseismic Fluid Flow Induced by Dynamic Rupture

Thomas M. Mitchell<sup>1</sup>, Jose M. Cembrano<sup>2</sup>, Kazuna Fujita<sup>3</sup>, Kenichi Hoshino<sup>3</sup>, Daniel R. Faulkner<sup>4</sup>, Pamela Perez-Flores<sup>2</sup>, Gloria Arancibia<sup>2</sup>, Marieke Rempe<sup>5</sup>, and Rodrigo Gomila<sup>2</sup>

### ABSTRACT

Seismogenic fault fracturing can create considerable fracture permeability in and around fault zones initiating large fluxes of fluid, particularly at fault terminations and dilatational jogs. In this work we show that fluids can also be channeled and potentially mixed through a network of interconnected high-angle microfractures generated by transient stress perturbations associated with a passing earthquake rupture. By using the orientation, chemical composition, and salinity in ca. 200 fluid inclusions trapped in healed microfractures across the damage zone of a crustal-scale fault, we show that high-angle healed microfractures close to the damage zone/fault core boundary host high CO<sub>2</sub> contents and a wide range of salinities. The width of this zone is ~35 m. The high-angle microfractures are interpreted as having formed from the passage of earthquake ruptures as they are consistent with the inferred stress field from dynamic rupture models. We infer that the rapid creation of the fracture network leads to phase separation and fluid mixing, resulting in the highly variable fluid chemistry. The results suggest pore-fluid flow fluctuations are not only restricted to geometrical irregularities along faults, but also to regions of the damage zone close to a passing earthquake.

### 3.1. INTRODUCTION

The close interplay between the earthquake cycle and fluid migration in fault zones is well known [Cox, 2002; Faulkner and Armitage, 2013; Nur and Booker, 1972; Sibson, 1987]. During a slip event on one master fault, preexisting and/or newly created fractures perpendicular to the instantaneous extension direction will be sites of a

sudden, significant decrease in fluid pressure. The coseismic fracture network can then act in two ways. It may simply drive fluids into the extension fractures, lasting until internal fluid pressures reestablish equilibrium with the environmental hydrostatic pressures typical of upper crustal levels (such as the suction pump mechanism or dilatancy-diffusion effects [Nur and Booker, 1972]). Alternatively, if the coseismic fracture damage breached a low-permeability seal around an overpressured reservoir, it may promote large coseismic flux of previously trapped high-pressure fluids (the “fault valving” process, Sibson [1990]). Subsequent redistribution of pore pressure as a direct result of fluid flow can reduce fault strength and trigger earthquakes [Miller et al., 2004; Nur and Booker, 1972]. Under certain conditions, these mechanisms can result in the precipitation of hydrothermal minerals triggered by processes such as boiling, mixing with cold meteoric waters, and/or hydration reactions [Coombs, 1993; Sibson, 1987; Weatherley and Henley, 2013]. Such dynamically induced fluid flow is thought to

<sup>1</sup>Department of Earth Sciences, University College London, London, UK

<sup>2</sup>Departamento de Ingeniería Estructural y Geotécnica, Pontificia Universidad Católica de Chile, Santiago, Chile

<sup>3</sup>Department of Earth and Planetary Systems Science, Hiroshima University, Hiroshima, Japan

<sup>4</sup>Department of Earth, Ocean, and Ecological Sciences, University of Liverpool, Liverpool, UK

<sup>5</sup>Institut für Geologie, Mineralogie, und Geophysik, Ruhr-Universität Bochum, Bochum, Germany

be localized primarily in macroscopic-scale dilatational jogs and arrays of wing cracks where effective tensional stresses are expected [e.g., *Connolly and Cosgrove, 1999*].

More recently, several studies have shown that off-fault tensile stress fields can be generated surrounding dynamically propagating earthquake ruptures [*Rice et al., 2005*]. In such cases, these asymmetric stress fields can generate high-angle micro- to macroscopic extension fractures in the adjacent damage zone occurring preferentially on one side of the rupture [*Di Toro et al., 2005; Griffith et al., 2009*]. Such fractures have been shown to be fluid pathways for melt associated with frictional heating from earthquakes [*Di Toro et al., 2005; Griffith et al., 2012*] leading to the formation of pseudotachylite injection veins. However, no evidence to date has been presented of other fluids taking advantage of such dynamically created permeability.

In this study, salinity and gas measurements are presented on more than 200 fluid inclusions from oriented healed microfractures represented entirely by fluid inclusion planes (FIPs) in the damage zone of the Caleta Coloso fault, northern Chile. The variations in salinity, gas phase, and FIP orientation as a function of distance from the fault are examined. Using the salinity and nature of the gas phase as a proxy for fluid origin, an attempt is made to constrain the nature and timing of fluid flow in the seismic cycle and provide insights into the link between dynamic fracturing, hydrothermal fluid flow, and the extent of the coseismic fracture damage zone.

### **3.2. CALETA COLOSO FAULT, ATACAMA FAULT SYSTEM**

The Caleta Coloso fault is part of the Mesozoic Atacama fault system (AFS), which is situated in the continental margin of the South American plate, beneath which oceanic lithosphere has been subducted since early Palaeozoic time [*Brown et al., 1993; Mpodozis and Ramos, 1990*], and is an important structure within the forearc of the central Andes [*Cembrano et al., 2005; Scheuber and Gonzalez, 1999*]. The AFS is an arc-parallel strike-slip structure that accommodates some of the oblique convergence between the Nazca and South American plates (Figure 3.1a), extending for ca. 1000 km between Iquique (21°S) and La Serena (30°S) [*Brown et al., 1993; Cembrano et al., 2005; Scheuber and Gonzalez, 1999*] within the Cordillera de la Costa of the Central Andes. The large-scale geometry of the AFS was formed during the late Jurassic and early Cretaceous where brittle structures in excess of 60 km in length were formed by sinistral strike-slip movement. Some of the NS-striking master faults and subsidiary NW-striking splay faults are organized into strike-slip duplexes that occur at various scales from regional to local [*Cembrano et al., 2005*].

The Caleta Coloso fault is a crustal-scale strike-slip fault with a minimum sinistral slip of 5 km that has been largely passively exhumed from 5 to 10 km depth [*Cembrano et al., 2005*]. It is a substructure of the Caleta Coloso duplex (Figure 3.1b) and crosscuts the Cerro Cristales pluton [*González, 1990, 1996, 1999; Uribe and Niemeyer, 1984*], which consists of isotropic tonalites, granodiorites, and quartz-feldspathic diorites that are classified from the variable amounts of plagioclase, quartz, orthoclase, biotite, and amphibole. The Mesozoic magmatic arc of the north Chilean Coastal Cordillera was active before and during the early stages of the Caleta Coloso fault development [e.g., *Cembrano et al., 2005*]. The latest evidence of magmatic arc activity is represented by 139 to 124 Ma mafic dykes, whereas the cataclastic deformation at Caleta Coloso fault has been dated from 124 Ma onward [*Olivares et al., 2010*]. The structure of the Caleta Coloso fault is defined by a wide zone of “multiple” fault cores (Figure 3.1c,d) with an average thickness of ~400 m and a surrounding damage zone up to 150 m wide [*Faulkner et al., 2008; Mitchell and Faulkner, 2009*]. *Mitchell and Faulkner* [2009] previously reported the variation of fracture density and orientation of secondary fluid inclusions aligned as FIPs as a function of distance from the fault core in the granodiorite damage zone (Figure 3.2), indicating a damage zone half-width of approximately 150 m. They suggested that a high-angle set close to the fault may be related to earthquake rupture, consistent with theoretical predictions of off-fault rupture damage extending around 30–40 m from the plane of a propagating mode II rupture [*Rice et al., 2005*].

### **3.3. METHODOLOGY**

Doubly polished thin sections for fluid inclusion studies were made from orientated samples taken from distances of 20, 40, and 140 m from the fault core/damage zone boundary (Figure 3.2), approximately at the same sampling locations studied in *Mitchell and Faulkner* [2009]. Thin sections were cut perpendicular to the fault plane and parallel to the slip direction, as in *Mitchell and Faulkner* [2009], which provides the maximum visibility for fault-related microfractures [*Vermilye and Scholz, 1998*]. Orientations of microfracture traces were measured in these sections in order to confirm independently the observed FIP orientations from *Mitchell and Faulkner* [2009] that were acquired using a universal stage. Raman spectroscopic analyses were used to estimate the fluid-inclusion salinity and gas species (Figure 3.3), rather than the more conventional technique of microthermometric measurements of ice melting temperatures, because the fluid inclusions are too small to measure the melting temperature. Calibrations for the Raman spectral data can be found in the supplementary data.

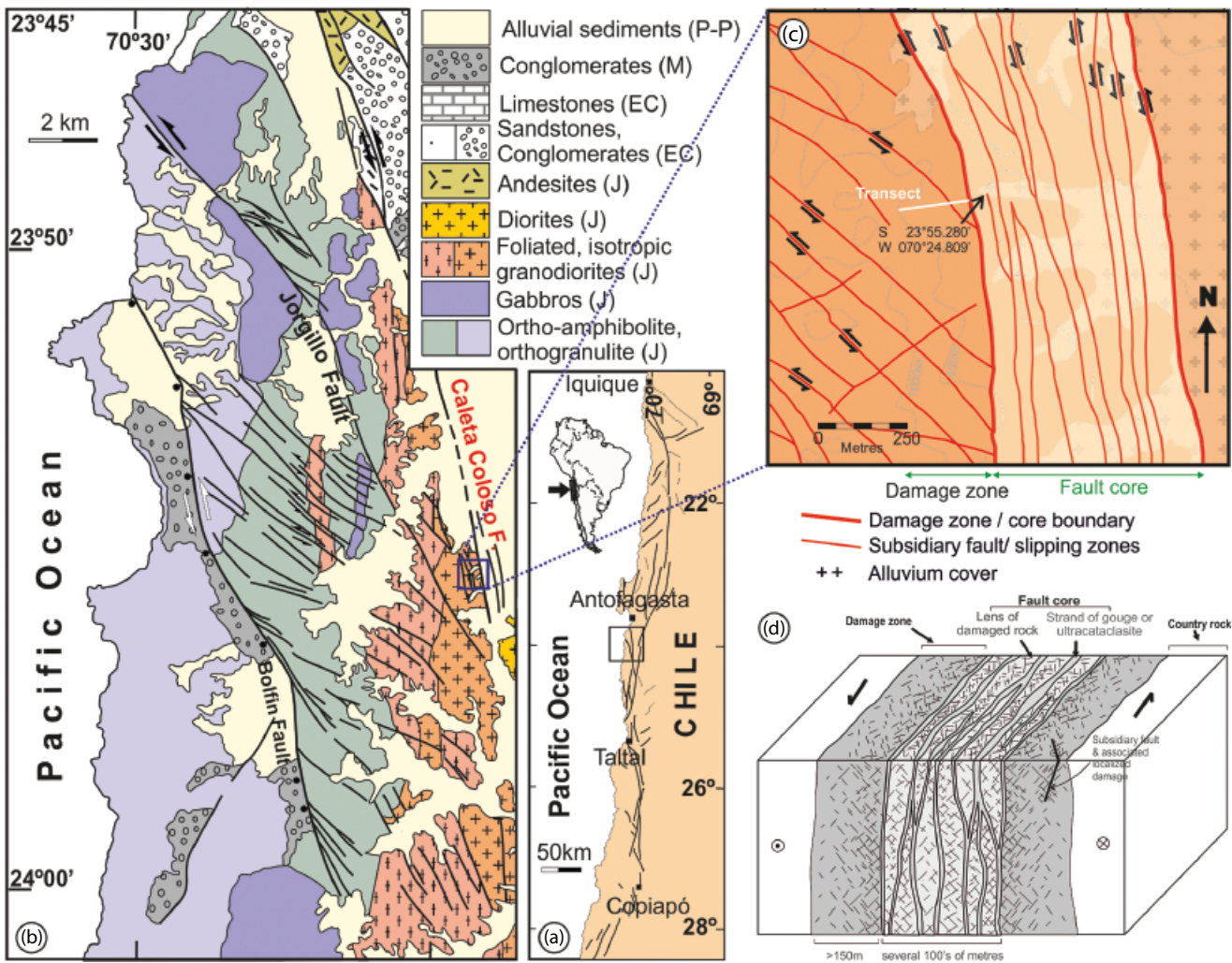


**Figure 3.1** Regional geological map (with inset) showing broad scale features of the Atacama fault system. (a) Atacama fault system (AFS) in the Coastal Cordillera of northern Chile, location of the Caleta Coloso fault in red. (b) Geology, geometry, and kinematics of the sinistral strike-slip Coloso duplex. J = Jurassic; EC = Early Cretaceous; M = Miocene; P-P = Plio-Pleistocene. Maps are simplified from Brown *et al.* [1993], Cembrano *et al.* [2005], and Scheuber and Gonzalez [1999]. (c) Geological map of Caleta Coloso fault, showing the location of the fracture density transect shown in Figure 3.2. (d) Typical strike-slip fault zone structures in a quartzofeldspathic country rock [after Faulkner *et al.*, 2003] multiple fault core, with associated damage zone.

### 3.4. RESULTS

The variation in microfracture trace orientation as a function of distance from the fault (Figure 3.4b) shows good agreement with that of *Mitchell and Faulkner* [2009], with a unique high-angle set closest to the fault. At 40m, the predominant set of fractures may have formed under dextral conditions, which will likely be related to local subsidiary splay faults that are found to crosscut the central damage zone of the Caleta Coloso fault [*Mitchell and Faulkner*, 2009]. Salinities from the sample farthest from the fault core (140m) are comparatively high and range from 6.8 to 23.9 wt.%  $\text{NaCl}_{\text{eq}}$

(Figure 3.4c), with no gas component and more randomly orientated microfractures. At 40m, there is a marked shift to intermediate to low salinities, with most fluid inclusions having salinities between 3 and 6 wt.%  $\text{NaCl}_{\text{eq}}$ , hosted in FIPs with an oblique orientation to the main fault and no gas component. Salinities of FIPs in the samples that are closest to the fault range from 0 to 18 wt.%  $\text{NaCl}_{\text{eq}}$ , with the lowest salinities being present exclusively in the high-angle FIPs. In addition,  $\text{CO}_2$  is only found in vapor phases of high-angle FIPs located at less than 20m from the fault core.

Microstructural examination of the high-angle FIPs shows that some are actually made of a series of healed

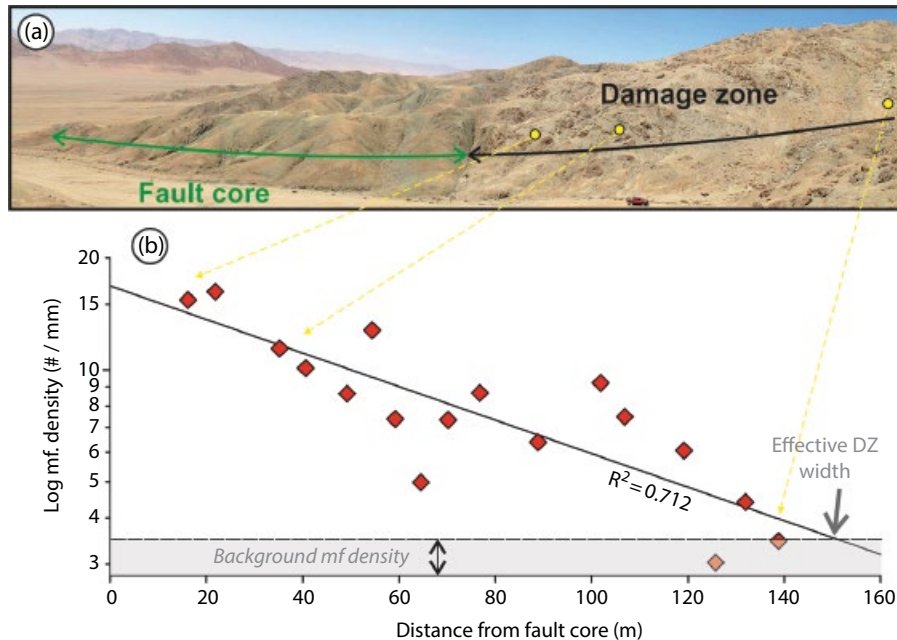


**Figure 3.2** (a) View looking south along the strike of the Caleta Coloso fault, showing sample locations. (b) Micro Fracture density as a function of distance from the fault core, modified from *Mitchell and Faulkner [2012]*.

*en echelon* microfractures organized into a single FIP (Figure 3.5). This geometry may indicate that some of the high-angle FIPs are extensional shear fractures in which, apart from slip-orthogonal extension, underwent a dextral strike-slip component of displacement. Alternatively, this geometry may represent the fringe of a propagating high-angle microfracture resulting in mixed-mode behavior at a crack termination. It is interesting to note that a similar observation by *Wilkinson and Johnston [1996]* was interpreted as due to catastrophic fluid-pressure drop subsequent to the linking of an array of *en-echelon* microfractures by oblique tensile veins.

### 3.5. DISCUSSION

Comparatively high salinities found at greater distances from the fault core could be representative of mostly magmatic/hydrothermally derived fluids, typical of the last stages of a waning magmatic arc. Here, high-salinity aqueous fluids and volatiles are exsolved from hydrous silicate melts during the ascent and crystallization of plutons [e.g., *Hedenquist and Lowenstern, 1994*]. High-salinity fluids might alternatively result from originally low-salinity fluids that have been involved in hydration reactions that progressively leave fluids enriched in salts. This is consistent with the granitic rocks having undergone greenschist facies retrograde alteration as represented by the widespread presence of epidote and chlorite, especially in the fault core [*Arancibia et al.,*

2015; *Cembrano et al., 2005*]. The high-angle FIPs, which are only present close to the core-damage zone boundary, host both the lowest salinity fluid inclusions and a wide range of overall salinities, which in turn is consistent with the processes above. More importantly, the only CO<sub>2</sub> vapor-rich content within the damage zone occurs closest to the fault core. Because low salinity may be an indicator of surficial/meteoric fluid influx [e.g., *Kriete et al., 2004*; *O'Hara and Haak, 1992*], we interpret this as the penetration of meteoric fluids from the surface to depth. Meteoric waters have been shown to penetrate as deep as 10 km through connected fracture systems [e.g., *Kerrick and Fyfe, 1981*; *Sharp et al., 2005*].

Figure 3.6a shows the expected orientation of microfractures for various models of off-fault damage generation in strike-slip faults: Andersonian fault growth, fault tip growth propagation (mode II and III), fault wear on rough faults, and earthquake rupture damage [see *Mitchell and Faulkner, 2009*; *Wilson et al., 2003*]. Such models can explain the large range in orientations of fractures and microfractures around faults, such as is seen in our FIP orientation data. *Di Toro et al. [2005]* related high-angle fractures around seismogenic faults to the transient tension field generated during propagating mode II fractures (in-plane shear), by computing the dynamic stress pattern associated with a rupture propagating close to the Rayleigh wave velocity ( $V_r$ ). Figure 3.6b shows a diagram of the typical stress field surrounding a propagating subshear rupture ( $0.6 V_r$ ), where transient

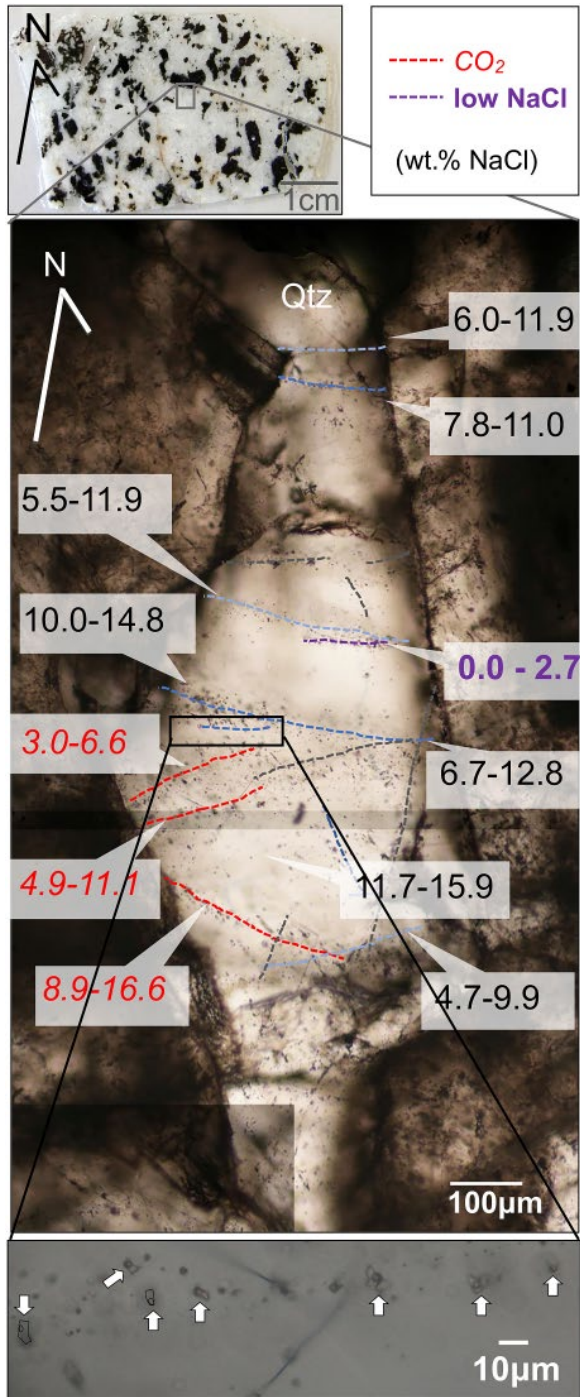


**Figure 3.3** Example of planes of secondary fluid inclusions in quartz within an oriented thin section at 20 m from the Caleta Coloso fault. FIPs have been highlighted with traces colored to show different sets of varying NaCl content. Numbers indicate the wt.% NaCl content and where  $\text{CO}_2$  was present. Red colored font indicates the salinities of the inclusions containing  $\text{CO}_2$ . Bottom image shows a scanning electronic microscope image of a fluid inclusion plane example. See electronic version for color representation.

tension and compression fields surrounding the rupture tip are shown (modified from *Di Toro et al.*, 2005). Such near-orthogonal fractures tend to form only at velocities approaching  $V_r$  [*Di Toro et al.*, 2005], where the maximum tension planes are oriented nearly orthogonal to the fault plane. Because the strength of rocks in tension is significantly less than that in compression, most fractures will develop on the side of the fault under tension [e.g., *Andrews*, 2005].

The observation of low-salinity fluid and  $\text{CO}_2$  vapor-rich content found exclusively together in high-angle microfractures closest to the fault is interpreted to be due to these microfractures being generated by effective tensile stress fields surrounding propagating ruptures. Formation of opening-mode fractures would locally reduce pore-fluid pressure, potentially triggering phase separation and  $\text{CO}_2$  degassing and trapping lower pressure fluid inclusions containing  $\text{CO}_2$ . Associated low salinities in the same FIPs may have resulted from rapid meteoric fluid inflow from shallow levels due to increased dynamic off-fault permeability [e.g., *Caine et al.*, 1996; *Gudmundsson et al.*, 2001; *Mitchell and Faulkner*, 2012]. This process, in turn, would result in the trapping of fluids as fluid inclusions as the fractures heal, lowering the permeability and preventing further significant fluid flow [e.g., *Brantley et al.*, 1990]. Many mineralized fault zones contain evidence of phase separation associated with coseismic dilation [e.g., *Weatherley and Henley*, 2013; *Wilkinson and Johnston*, 1996, and references therein]. Previous explanations for coseismic dilation and subsequent drops in fluid pressure in fault zone studies have been associated with the opening of dilatational jogs, and volume increase has been associated with formation of on-fault damage products and slip around geometric asperities [e.g., *Connolly and Cosgrove*, 1999]. We believe that this is the first study to demonstrate the influence of dynamic fractures in lateral damage zones on permeability development in fault zones.

The healing rate for a microfracture to form an FIP is strongly controlled by temperature, pressure, and fluid chemistry [*Smith and Evans*, 1984], and various studies have shown that microcracks in quartz can heal at rates ranging from hours to months [*Brantley et al.*, 1990; *Moore et al.*, 1994; *Morrow et al.*, 2001; *Smith and Evans*, 1984; *Tenthorey and Fitz Gerald*, 2006] under a range of hydrothermal conditions. At pressures of 200 MPa ( $\sim 8 \text{ km}$ ) and temperatures of 400°C, quartz microfractures can heal to fluid inclusions over several days. At 200°C, microfractures will take several months to heal, although this is still relatively fast in terms of earthquake recurrence intervals. If the meteoric fluid is undersaturated in silica, the healing process can accelerate [*Smith and Evans*, 1984]. Hence, with a geothermal gradient of

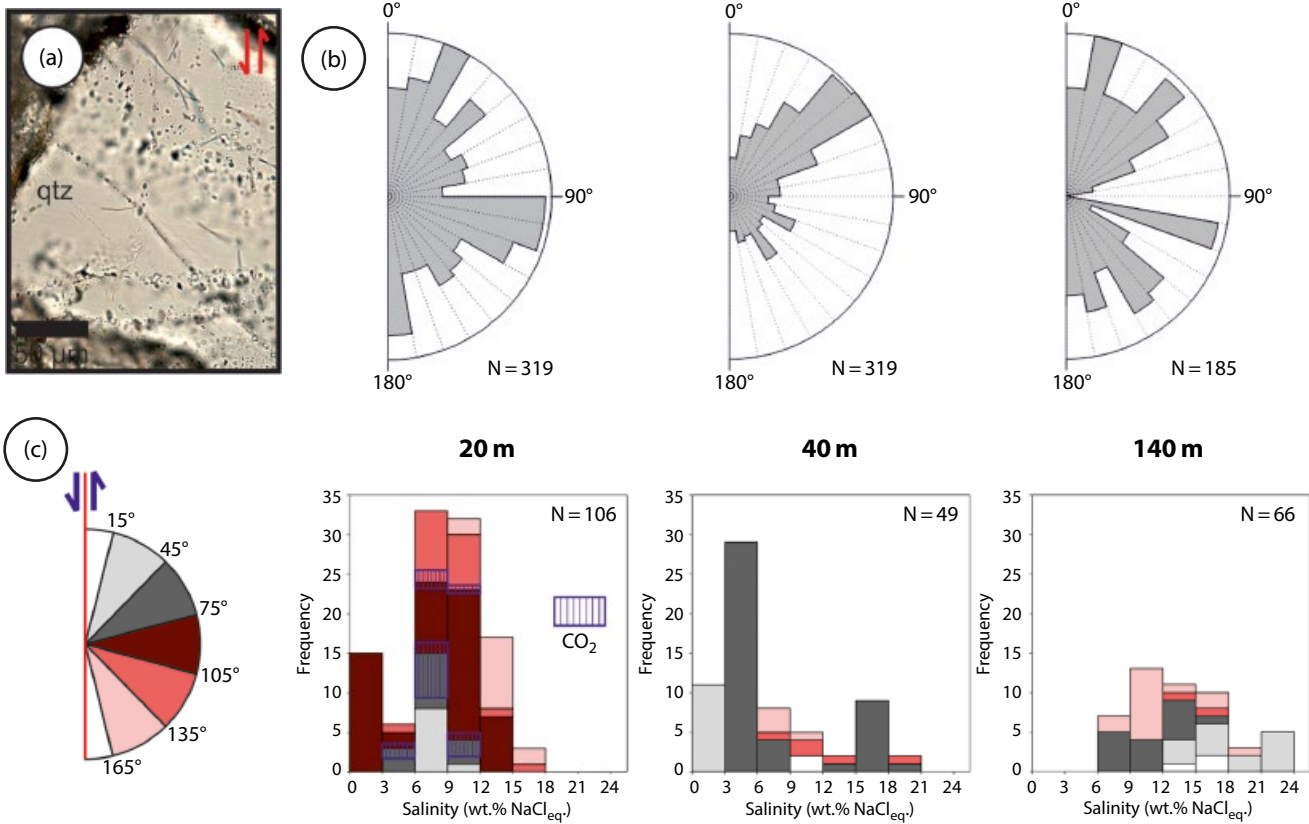


**Figure 3.4** (a) Example of typical fluid inclusion planes analyzed for salinity and gas phase content in quartz (qtz). (b) Rose diagrams showing FIP strike orientations relative to the Caleta Coloso fault observed in the damage zone as a function of distance from the fault core. (c) Histograms of salinities of fluid inclusions in the damage zone as a function of distance from the fault, which are color coded to show orientation relative to the Caleta Coloso main fault. Dashed boxes indicate the frequency of fractures in the highlighted orientation that contain CO<sub>2</sub>.

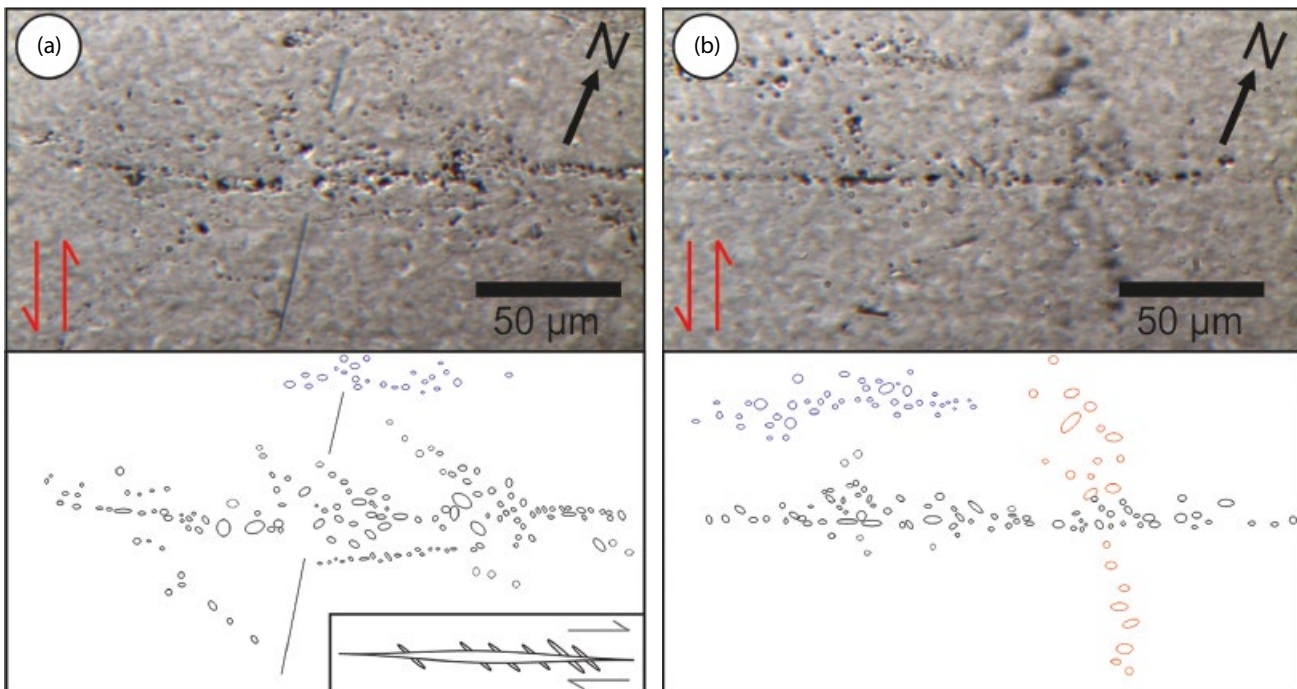


**Figure 3.5** (a) Example of a subvertical high-angle FIP crosscutting and postdating an open fracture, where the FIP shows a series of *en echelon* microfractures organized into a single FIP. Plane of image is horizontal. Inset shows schematic *en echelon* extension fractures linked into one hybrid FIP. (b) High-angle FIP crosscutting and overprinting a fault subparallel FIP [e.g., Scheuber and Gonzalez, 1999].

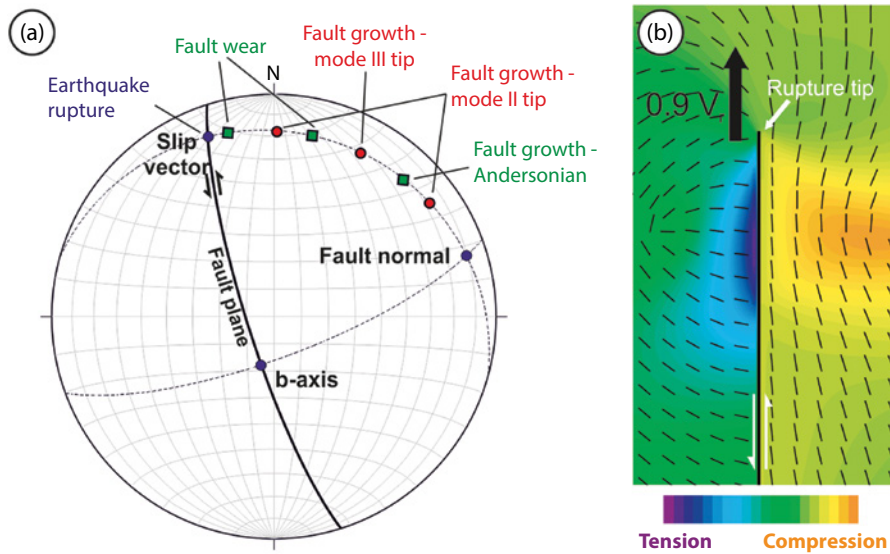


**Figure 3.6** (a) Equal area stereographic projection showing the expected orientation of microfractures of various fault damage models [Mitchell and Faulkner, 2009; Wilson et al., 2003]. Great circles with shear sense indicators represent fault plane orientation of the Caleta Coloso fault and filled circles show the orientation of the fault b-axis, normal and slip direction. (b) Stress field during rupture propagation in the vicinity of a crack tip, modified from Di Toro et al. [2005]. Maximum tension planes are orientated nearly orthogonal to the fault plane.

50–100°C per km [Henry and Pollack, 1988], FIPs may have formed on relatively short timescales. As the presence of fluids is required for any form of microfracture healing [Smith and Evans, 1984], newly generated mode I fractures could remain open while fluids are redistributed by the suction pump mechanism, only to begin healing when fluid saturates the crack [e.g., Sibson, 1987].

Ngo et al. [2012] show that microfractures are readily formed at angles of 70–80° to a rupture plane at rupture velocities between 0.7 and 0.9 of the Rayleigh wave velocity ( $V_r$ ), particularly at shallow depths. Microfractures will form at a slightly higher angle to the main fault than for a more deeply buried rock for a rupture traveling at the same velocity [e.g., Wald et al., 1996]. The range of fracture orientation can therefore be explained by multiple earthquake ruptures traveling at a range of velocities at different depths, during ongoing deformation and exhumation.

### 3.6. CONCLUSION

In summary, we have shown field evidence for fracture damage associated with passage of an earthquake rupture tip on a crustal-scale fault. The coseismic fracturing at these depths has produced a relatively narrow zone (30–40 m) of high-angle mode I fractures that have enhanced permeability and facilitated the flow of fluids parallel to the fault. We suggest that high-angle healed

microfractures (FIPs) closest to the fault are generated by effective tensile stress fields surrounding propagating ruptures, evidenced by trapped low-salinity fluid and CO<sub>2</sub> vapor-rich content. Coseismic reductions in pore-fluid pressure due to the formation of the high-angle opening-mode fractures potentially trigger phase separation and form lower fluid inclusions containing CO<sub>2</sub> as microfractures heal. Low salinity fluids also present may have been due to the rapid meteoric fluid inflow from shallow levels due to increased dynamic off-fault permeability, resulting in a wide range of salinities close to the fault.

### ACKNOWLEDGMENTS

Professor H. Hidaka of Hiroshima University is gratefully acknowledged for his kind support during Raman spectroscopic analyses. TMM acknowledges NERC grant NE/M004716/1 and DRF NERC grant NE/J024449/1. We thank Stephen Cox and Andrea Billi for their constructive reviews of the manuscript.

### REFERENCES

- Andrews, D. J. (2005), Rupture dynamics with energy loss outside the slip zone, *Journal of Geophysical Research-Solid Earth*, 110(B1).
- Brantley, S. L., B. Evans, S. H. Hickman, and D. A. Crerar (1990), Healing of microcracks in quartz: Implications for fluid-flow, *Geology*, 18(2), 136–139.

- Brown, M., F. Diaz, and J. Grocott (1993), Displacement History of the Atacama Fault System 25°00'S-27°00'S, Northern Chile, *Geological Society of America Bulletin*, 105(9), 1165–1174.
- Caine, J. S., J. P. Evans, and C. B. Forster (1996), Fault zone architecture and permeability structure, *Geology*, 24(11), 1025–1028.
- Cembrano, J., G. Gonzalez, G. Arancibia, I. Ahumada, V. Olivares, and V. Herrera (2005), Fault zone development and strain partitioning in an extensional strike-slip duplex: A case study from the Mesozoic Atacama fault system, Northern Chile, *Tectonophysics*, 400(1-4), 105–125.
- Connolly, P., and J. Cosgrove (1999), Prediction of static and dynamic fluid pathways within and around dilatational jogs, *Geological Society, London, Special Publications*, 155(1), 105–121. doi:10.1144/gsl.sp.1999.155.01.09
- Coombes, D. S. (1993), Dehydration veins in diagenetic and very-low-grade metamorphic rocks: Features of the crustal seismogenic zone and their significance to mineral facies, *Journal of Metamorphic Geology*, 11(3), 389–399. doi:10.1111/j.1525-1314.1993.tb00156.x
- Cox, S. F. (2002), Fluid flow in mid- to deep crustal shear systems: Experimental constraints, observations on exhumed high fluid flux shear systems, and implications for seismogenic processes, *Earth Planets and Space*, 54(11), 1121–1125.
- Faulkner, D. R., and P. J. Armitage (2013), The effect of tectonic environment on permeability development around faults and in the brittle crust, *Earth and Planetary Science Letters*, 375(0), 71–77. doi:http://dx.doi.org/10.1016/j.epsl.2013.05.006
- Faulkner, D. R., A. C. Lewis, and E. H. Rutter (2003), On the internal structure and mechanics of large strike-slip fault zones: field observations of the Carboneras fault in southeastern Spain, *Tectonophysics*, 367(3-4), 235–251.
- Faulkner, D. R., T. M. Mitchell, E. H. Rutter, and J. Cembrano (Eds.) (2008), *On the structure and mechanical properties of large strike-slip faults* (Vol. 299), Geological Society, London, Special Publications.
- González, G. (1990), Patrones estructurales, modelo de ascenso emplazamiento y deformación del Plutón Cerro Cristales, Cordillera de la Costa al Sur de Antofagasta, Chile. *Memoria para optar al título de Geólogo (inédita)*, Universidad Católica del Norte, Antofagasta, 124.
- González, G. (1996), Evolución Tectónica de la Cordillera de la Costa de Antofagasta (Chile): Con especial referencia a las deformaciones sinmagnéticas del Jurásico-Cretásico Inferior. *Berliner Geowissenschaftliche Abhandlungen (A)*, Band 181, 111 pp.
- González, G. (1999), Mecanismo y profundidad de emplazamiento del Plutón Cerro Cristales, *Cordillera de la Costa, Antofagasta, Chile, Revista Geológica De Chile*, 26, 23.
- Griffith, W. A., A. Rosakis, D. D. Pollard, and C. W. Ko (2009), Dynamic rupture experiments elucidate tensile crack development during propagating earthquake ruptures, *Geology*, 37(9), 795–798. doi:10.1130/g30064a.1
- Griffith, W. A., T. M. Mitchell, J. Renner, and G. Di Toro (2012), Coseismic damage and softening of fault rocks at seismogenic depths, *Earth and Planetary Science Letters*, 353-354(0), 219–230. doi:10.1016/j.epsl.2012.08.013
- Gudmundsson, A., S. S. Berg, K. B. Lyslo, and E. Skurtveit (2001), Fracture networks and fluid transport in active fault zones, *Journal of Structural Geology*, 23(2-3), 343–353. doi:http://dx.doi.org/10.1016/S0191-8141(00)00100-0
- Hedenquist, J. W., and J. B. Lowenstern (1994), The role of magmas in the formation of hydrothermal ore deposits. *Nature*, 370(6490), 519–527.
- Henry, S. G., and H. N. Pollack (1988), Terrestrial heat flow above the Andean Subduction Zone in Bolivia and Peru, *Journal of Geophysical Research: Solid Earth*, 93(B12), 15153–15162. doi:10.1029/JB093iB12p15153
- Kerrick, R., and W. S. Fyfe (1981), The gold-carbonate association: Source of CO<sub>2</sub> and CO<sub>2</sub> fixation reactions in Archaean lode deposits, *Chemical Geology*, 33(1-4), 265–294. doi: http://dx.doi.org/10.1016/0009-2541(81)90104-2
- Kriete, C., A. Suckow, and B. Harazim (2004), Pleistocene meteoric pore water in dated marine sediment cores off Callao, Peru, *Estuarine, Coastal and Shelf Science*, 59(3), 499–510. doi:http://dx.doi.org/10.1016/j.ecss.2003.11.001
- Miller, S. A., C. Collettini, L. Chiaraluce, M. Cocco, M. Barchi, and B. J. P. Kaus (2004), Aftershocks driven by a high-pressure CO<sub>2</sub> source at depth, *Nature*, 427(6976), 724–727.
- Mitchell, T. M., and D. R. Faulkner (2009), The nature and origin of off-fault damage surrounding strike-slip fault zones with a wide range of displacements: A field study from the Atacama fault system, northern Chile, *Journal of Structural Geology*, 31(8), 802–816. doi:DOI 10.1016/j.jsg.2009.05.002
- Mitchell, T. M., and D. R. Faulkner (2012), Towards quantifying the matrix permeability of fault damage zones in low porosity rocks *Earth and Planetary Science Letters*, 339-340(0), 24–31. doi:10.1016/j.epsl.2012.05.014
- Moore, D. E., D. A. Lockner, and J. D. Byerlee (1994), Reduction of permeability in granite at elevated temperatures, *Science*, 265(5178), 1558–1561.
- Morrow, C. A., D. E. Moore, and D. A. Lockner (2001), Permeability reduction in granite under hydrothermal conditions, *Journal of Geophysical Research-Solid Earth*, 106(B12), 30551–30560.
- Mpodozis, C., and V. A. Ramos (1990), The Andes of Chile and Argentina: Circum-Pacific Council for Energy and Mineral resources, *Earth Science Series*, 11, 31.
- Ngo, D., Y. Huang, A. Rosakis, W. A. Griffith, and D. Pollard (2012), Off-fault tensile cracks: A link between geological fault observations, lab experiments, and dynamic rupture models, *Journal of Geophysical Research-Solid Earth*, 117. doi:10.1029/2011jb008577
- Nur, A., and J. R. Booker (1972), Aftershocks caused by pore fluid-flow, *Science*, 175(4024), 885–887.
- O'Hara, K., and A. Haak (1992), A fluid inclusion study of fluid pressure and salinity variations in the footwall of the rector branch thrust, North Carolina, U.S.A., *Journal of Structural Geology*, 14(5), 579–589. doi:http://dx.doi.org/10.1016/0191-8141(92)90158-S
- Olivares, V., J. Cembrano, G. Arancibia, N. Reyes, V. Herrera, and D. Faulkner (2010), Significado tectónico y migración de fluidos hidrotermales en una red de fallas y vetas de un Dúplex de rumbo: Un ejemplo del Sistema de Falla de Atacama, *Andean Geology*, 37, 473–497.

- Rice, J. R., C. G. Sammis, and R. Parsons (2005), Off-fault secondary failure induced by a dynamic slip pulse, *Bulletin of the Seismological Society of America*, 95(1), 109–134.
- Scheuber, E., and G. Gonzalez (1999), Tectonics of the Jurassic-Early Cretaceous magmatic arc of the north Chilean Coastal Cordillera (22 degrees-26 degrees S): A story of crustal deformation along a convergent plate boundary, *Tectonics*, 18(5), 895–910.
- Sharp, Z. D., H. Masson, and R. Lucchini (2005), Stable isotope geochemistry and formation mechanisms of quartz veins: Extreme paleoaltitudes of the Central Alps in the Neogene, *American Journal of Science*, 305(3), 187–219. doi:10.2475/ajs.305.3.187
- Sibson, R. H. (1987), Earthquake rupturing as a mineralizing agent in hydrothermal systems, *Geology*, 15(8), 701–704.
- Smith, D. L., and B. Evans (1984), Diffusional Crack Healing in Quartz. *Journal of Geophysical Research*, 89(Nb6), 4125–4135.
- Tenthorey, E., and J. D. Fitz Gerald (2006), Feedbacks between deformation, hydrothermal reaction and permeability evolution in the crust: Experimental insights, *Earth and Planetary Science Letters*, 247(1-2), 117–129.
- Di Toro, G., S. Nielsen, and G. Pennacchioni (2005), Earthquake rupture dynamics frozen in exhumed ancient faults, *Nature*, 436(7053), 1009–1012.
- Uribe, F., and H. Niemeyer (1984), Franjas miloníticas en la Cordillera de la Costa de Antofagasta (Cuadrángulo de Cerro Cristales, 24°00'-24°15'S) y la distribución del basamento precámbrico, *Revista Geologica De Chile*, 23, 4.
- Vermilye, J. M., and C. H. Scholz (1998), The process zone: A microstructural view of fault growth, *Journal of Geophysical Research-Solid Earth*, 103(B6), 12223–12237.
- Wald, D. J., T. H. Heaton, and K. W. Hudnut (1996), The slip history of the 1994 Northridge, California, earthquake determined from strong-motion, teleseismic, GPS, and leveling data, *Bulletin of the Seismological Society of America*, 86(1B), S49–S70.
- Weatherley, D. K., and R. W. Henley (2013), Flash vaporization during earthquakes evidenced by gold deposits, *Nature Geosci*, 6(4), 294–298. doi:<http://www.nature.com/ngeo/journal/v6/n4/abs/ngeo1759.html> - supplementary-information
- Wilkinson, J. J., and J. D. Johnston (1996), Pressure fluctuations, phase separation, and gold precipitation during seismic fracture propagation, *Geology*, 24(5), 395–398. doi:10.1130/0091-7613(1996)024<0395:pfpsag>2.3.co;2
- Wilson, J. E., J. S. Chester, and F. M. Chester (2003), Microfracture analysis of fault growth and wear processes, Punchbowl fault, San Andreas system, California, *Journal of Structural Geology*, 25(11), 1855–1873.

# 4

## Coseismic Damage Generation and Pulverization in Fault Zones: Insights From Dynamic Split-Hopkinson Pressure Bar Experiments

Franciscus M. Aben<sup>1,2</sup>, Mai-Linh Doan<sup>1,2</sup>, Jean-Pierre Gratier<sup>1,2</sup>, and François Renard<sup>1,2,3</sup>

### ABSTRACT

Coseismic damage in fault zones contributes to the short- and long-term behavior of a fault and provides a valuable indication of the parameters that control seismic ruptures. This review focuses on the most extreme type of off-fault coseismic damage: pulverized rock. Such pervasively fractured rock that does not show any evidence of shear strain is observed mainly along large strike-slip faults. Field observations on pulverized rock are briefly examined and would suggest that dynamic (high strain rate) deformation is responsible for its generation. Therefore, these potential paleo-seismic markers could give an indication of the constraints on rupture propagation conditions. Such constraints can be determined from dynamic loading experiments, typically performed on a Split-Hopkinson Pressure Bar apparatus. The principle of this apparatus is summarized and experimental studies on dynamic loading and pulverization are reviewed. For compressive dynamic loading, these studies reveal a strain rate threshold above which pulverization occurs. The nature of the pulverization threshold is discussed by means of several fracture mechanics models. The experimental pulverization conditions are correlated with field observations by analyzing and discussing several earthquake rupture models. An indisputable rupture mechanism could not be established owing to a gap in experimental knowledge, especially regarding tensile dynamic loading.

### 4.1. INTRODUCTION

Damage to rock formations surrounding faults can have a major influence on the mechanical behavior of the faults, whether they are seismogenic or aseismically creeping faults. Fracturing may increase, at least temporarily, the permeability of the damaged rock, leading to episodic fluid flow that modifies its rheological properties [Sibson, 1996; Miller, 2013]. Fracturing may contribute to the development of anisotropy around the fault zone [Crampin and Booth, 1985; Zhao et al., 2011] and may also activate chemical reactions facilitating stress-driven

mass transfer creep [Gratier et al., 2013b, 2014]. Subsequent sealing of the fractures may strengthen the rock, contributing to mechanical segregation in a fault zone and possibly leading to localized earthquakes [Li et al., 2003; Zhao et al., 2011; Gratier et al., 2013a]. Such a heterogeneity could in turn be a tuning parameter in fault slip and earthquake dynamics [Bürgmann et al., 1994; Zöller et al., 2005].

Conversely, the behavior of the fault itself influences the amount and type of damage occurring in the damage zone [Faulkner et al., 2011]. This damage may be caused by a variety of quasi-static and dynamic deformation processes [Mitchell and Faulkner, 2009]. The mutual interaction between fault and damage zone is not yet fully understood, especially the long-term effects, including gradual chemical changes of the fault core gouge that might change the behavior of the fault zone from seismic

<sup>1</sup>Université Grenoble Alpes, ISTerre, Grenoble, France

<sup>2</sup>CNRS, ISTerre, Grenoble, France

<sup>3</sup>PGP, Department of Geosciences, University of Oslo, Oslo, Norway

to aseismic permanent creep [Richard *et al.*, 2014]. Consequently, damage development processes in faults are a crucial factor in understanding the mechanics of faults.

Within the damage zone, coseismically damaged rock formations provide a means of constraining fault and earthquake mechanics given that they were formed by seismic events. Coseismically damaged rocks differ from other damage zone rocks inasmuch that they are dynamically loaded in tension or compression by stress waves surrounding a propagating rupture tip for a short duration. Due to dynamic loading, the kinetics of fracture propagation controls the damage process [Grady, 1998] and not just the local state of stress as is the case for quasi-static crack growth.

The most extreme coseismic end-member is thought to be pulverized rock, and therefore this rock has the highest potential both as a seismic marker and as a process that drastically modifies the mechanical properties of the fault zone. Pulverized rocks are *in situ* exploded rocks that have been subjected to pervasive fracturing up to the micrometer scale, without any accumulation of shear strain. The fracture damage is mechanical in nature, and this type of rock is almost exclusively present in the top few kilometers along major strike-slip faults. Such rock could potentially be indicative of one or several paleoseismic events. Moreover, these rocks might give constraints on the magnitude, loading conditions, and rupture direction. For the time being, such constraints remain open questions.

Since being acknowledged as a source of information for earthquake events by Brune [2001] and Dor *et al.* [2006b], research on these rocks is still in a preliminary phase. A strict definition including more than the qualitative description given above has not yet been established for this type of rock. Furthermore, the factors setting these rocks apart from their lesser coseismically damaged peers in terms of damage process have yet to be defined.

These questions can partly be answered by mapping the processes and conditions in which pulverized rocks can be formed. This also includes studying nonpulverized coseismically damaged rocks to constrain the entire range of fracture damage products that might be expected during a seismic event. To this end, laboratory experiments are crucial whereby samples are exposed to stress wave loading, similar to the high-frequency waves emitted during an earthquake. In contrast to many other physical and mechanical experiments on rocks, a time transformation from laboratory loading rates to natural loading rates is not necessary; rather, the challenge is to simulate the fast loading rates of a seismic rupture.

This review-style chapter starts with a summary of field observations on pulverized rock, including an

outline of the issues regarding the definition of a pulverized rock. The current state-of-the-art high loading rate experiments will then be presented, first in general form and second for pulverization in particular. Since these experimental studies are performed mostly on the Split-Hopkinson Pressure Bar apparatus, a short overview of this technique is given. More details are then given of current dynamic fracture models and theories in the high strain rate regime to explain the transition to pulverized rocks. Finally, current experimental knowledge and field observations are linked to earthquake rupture mechanical models, and their implications for fault zones containing pulverized rocks are discussed.

## 4.2. FIELD OBSERVATIONS OF PULVERIZED ROCK RELATED TO COSEISMIC DAMAGE

### 4.2.1. Observations, Definition, and Microstructures of Pulverized Rock

The first observations of pulverized rocks were at or near the surface along the San Andreas fault between San Bernardino and Tejon Pass on granites and gneisses [Brune, 2001; Dor *et al.*, 2006b]. Prior to this, these rocks might have been overlooked or labeled as gouges and cataclasites after the classic definition [Sibson, 1977; Wilson *et al.*, 2005]. However, the features setting them apart from these classic fault zone rocks are well summarized in the field definition given by Dor *et al.* [2006b]: A rock is classified as pulverized when the original textures are preserved (Figure 4.1a), very little or no shear is visible and all the crystals in a sample yield a powdery rock-flour texture when pressed in the hand. This damage is widespread on the outcrop scale. At the field scale, these rocks can be easily recognized due to their badland-type morphology [Dor *et al.*, 2006a, 2006b, 2008; Mitchell *et al.*, 2011] (Figure 4.1b) and faster erosion rate compared with the surrounding rocks.

On a smaller scale, pulverized igneous crystalline rocks (granite, granodiorite, gneiss) are characterized by a large number of fractures seemingly oriented randomly in 3D and without any clear hierarchical organization (Figure 4.1c, d). The fracture density is very high and, in general, the fractures penetrate all mineral phases, although some minerals may contain fewer fractures in places where the rock is less pulverized. Fracture patterns can be either random or follow cleavage planes, and micas can be kinked or contain fewer fractures than other mineral phases (Figure 4.1e). The dilatational mode I fractures show very little offset, and the fragments bounded by the fractures show little to no rotation, as evidenced by cross-polarized images in which original grains can be clearly identified from the myriad of fragments (Figure 4.1f, g). Since weathering might alter granitic

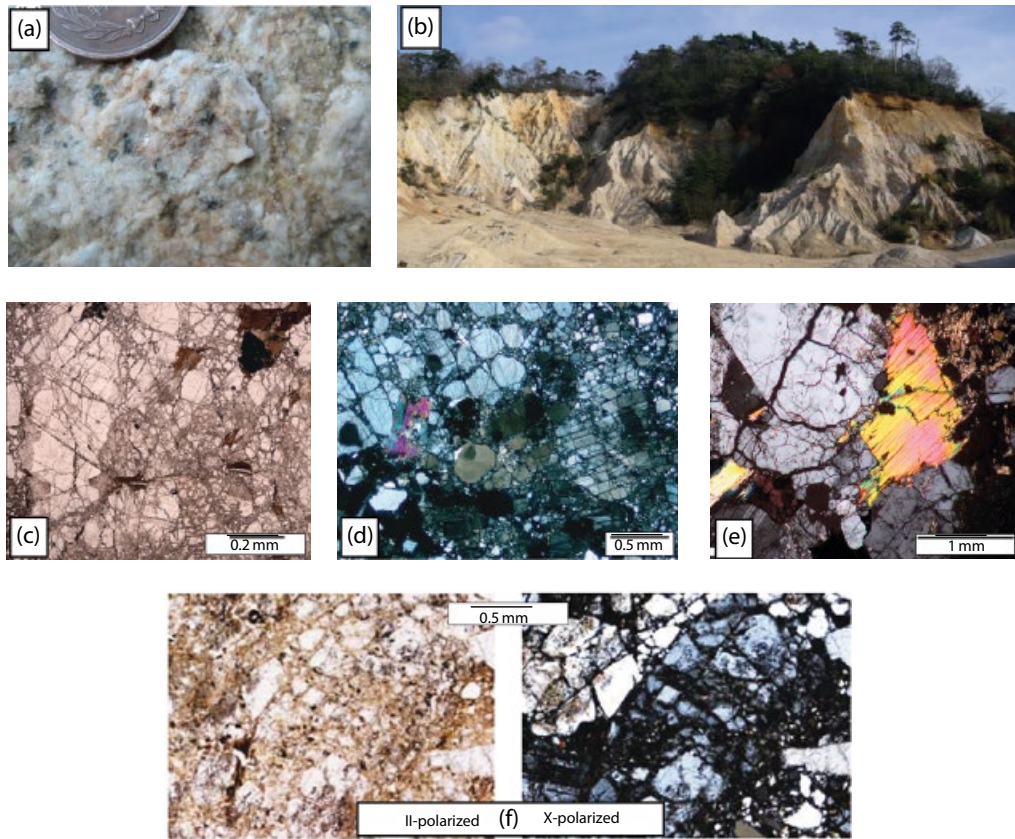


**Figure 4.1** (a) Image of a pulverized granite showing a clear pristine crystalline texture. (b) Typical badland erosion geomorphology related to pulverized rocks. (c)–(e) Photomicrographs of pulverized granitic rocks. Image (c) is taken with parallel polarizers, (d) and (e) with crossed polarizers. Image (e) contains a slightly buckled biotite grain. (f) Photomicrographs with parallel (left) and crossed (right) polarizers show that hardly any rotation or movement of fragments has occurred. Sources: (a), (b) Mitchell et al. [2011], (c) Rempe et al. [2013], (d) Wechsler et al. [2011], (e) Muto et al. [2015], and (f) Rockwell et al. [2009].

rocks toward a more fragile lithology, several authors have conducted mineralogical studies that have ruled out this mechanism [Rockwell et al., 2009; Mitchell et al., 2011; Wechsler et al., 2011] and they have proposed a mechanical origin instead. This, together with the microstructures, indicates a mechanical source for pulverization.

In some studies, geometric analyses have been conducted to characterize crystalline pulverized rocks in greater detail. Particle size distributions (PSD) were obtained on San Andreas pulverized rocks by Wilson et al. [2005], Rockwell et al. [2009], and Wechsler et al. [2011] using a specially calibrated laser particle size analyzer. The results indicated nonfractal PSD behavior toward larger grain sizes ( $>500\text{ }\mu\text{m}$ ). For smaller grain sizes ( $0.5\text{--}500\text{ }\mu\text{m}$ ), a  $D$ -value fractal exponent in the range 2.5–3.1 provided the best power law fit. Moreover, Wilson et al. [2005] constrained surface areas of up to  $80\text{ m}^2/\text{g}$ , although it is not clear whether this was actual gouge or pulverized rock. Muto et al. [2015] determined a

PSD from thin sections of pulverized rocks taken from the San Andreas fault and the Arima-Takatsuki Tectonic line (Japan). For both locations, fractal dimensions vary from 2.92 close to the fault core to 1.92 at some distance from the fault core, although the latter samples were not labeled as being pulverized. The  $D$ -values from Wechsler et al. [2011] and Muto et al. [2015] exceed the fractal dimensions of PSDs measured on experimental and field samples of gouges and cataclasites with a high shear strain component. These rocks give maximum  $D$ -values of  $\sim 2.5$  [e.g., Monzawa and Otsuki, 2003; Keulen et al., 2007; Stünitz et al., 2010]. Thus, PSDs of igneous crystalline pulverized rock are nonfractal at larger grain sizes, and at a finer fractal grain size range they have higher  $D$ -values compared to cataclasites and gouges, although this range of  $D$ -values is nonunique since the lower limits overlap with shear-related fault rocks.

All the “classic” characterizations of pulverized rock presented above were obtained from igneous crystalline

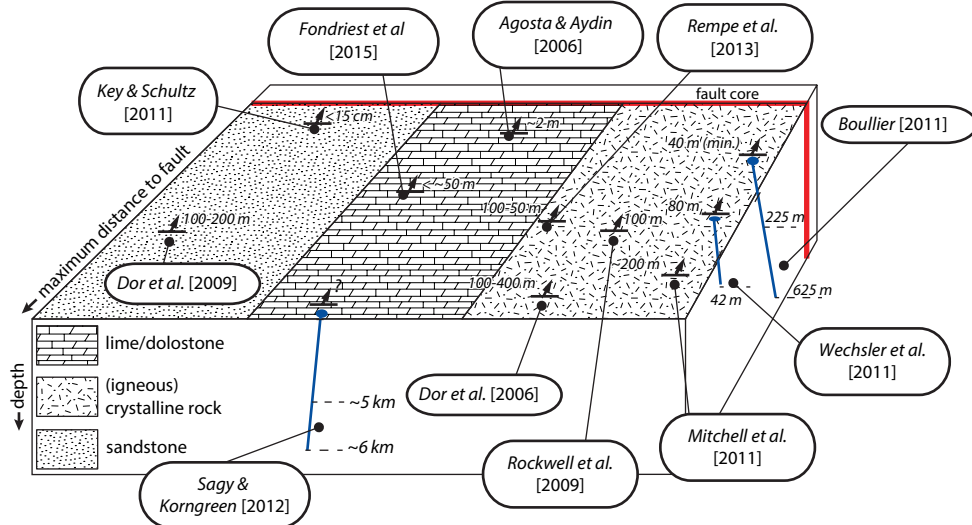


**Figure 4.2** Summary of studies on pulverized rocks in the field. The general lithology of the pulverized rock is indicated as well as the in situ location with respect to the fault, including in situ depth of observation (boreholes are indicated in blue). This depth must not be confused with the depth at which the pulverized rocks have been formed. See electronic version for color representation.

rock samples (Figure 4.2), taken mostly from along the San Andreas active fault zone and its nonactive strands [Wilson *et al.*, 2005; Dor *et al.*, 2006a, 2006b; Rockwell *et al.*, 2009; Wechsler *et al.*, 2011; Rempe *et al.*, 2013; Muto *et al.*, 2015]. Similar types of pulverized rock were also observed on the Arima-Takatsuki Tectonic Line [Mitchell *et al.*, 2011; Muto *et al.*, 2015] and the Nojima fault [Boullier, 2011] in Japan and along the North Anatolian fault in Turkey [Dor *et al.*, 2009] (Figure 4.2). Pulverized rocks have been identified in other lithologies as well. Pulverized limestone has been observed in inactive normal faults in Israel [Sagy and Korngreen, 2012] and in the Venere normal fault [Agosta and Aydin, 2006] in Italy. Pulverized dolostone is present in the Foiana fault [Fondriest *et al.*, 2015] in Italy (Figure 4.2). Pulverized sandstones are observed along the San Andreas fault [Dor *et al.*, 2006b, 2009] and near a small fault related to the Upheaval Dome impact event [Key and Schultz, 2011] (Figure 4.2). This last observation is unique because this fault was formed during a single meteor impact event.

A microstructural and geometric analysis was performed on pulverized sandstones from the San Andreas fault [Dor *et al.*, 2009]. The fracture damage is not homogeneously distributed over the quartz grains but is concentrated in several grains while others stay relatively intact (Figure 4.3a, b). The fractured grains show a Hertzian-like fracture pattern, indicating a compressional setting. Therefore, a grain-by-grain analysis rather than a bulk PSD was obtained, thus excluding any comparison with PSDs from igneous crystalline rock.

A trend of decreasing damage with increasing distance from the fault was observed. Key and Schultz [2011] obtained a PSD in pulverized sandstone with a  $D$ -value increasing from 0.77 for the original grain size to 1.55 for the pulverized rocks. This value is within the range measured for gouges [Keulen *et al.*, 2007; Stünitz *et al.*, 2010; Muto *et al.*, 2015] rather than for igneous pulverized rock ( $D > 1.92$ ).

Pulverized limestones and dolostones have not yet been subjected to geometrical analysis. Qualitatively, the fragments might be slightly larger than those of classic pulverized rocks [Fondriest *et al.*, 2015]. Also, thin section images reveal a hierarchy of fractures, and rather than random fracture orientations they show a shard-and-needle structure (Figure 4.3c). In contrast, limestone samples from a borehole in Israel do not show any fracture hierarchy but dynamic fracture branching instead [Sagy and Korngreen, 2012] (Figure 4.3d). Fragment sizes of  $\sim 20\text{ }\mu\text{m}$  were observed in samples from this borehole, well within the fragment size range of crystalline rocks.

This raises the following question: Are these “pulverized” sandstone, limestone, and dolostone formations similar to the classic pulverized igneous rock or is it simply that these studies have used different and potentially confusing definitions? According to the field definition of Dor *et al.* [2006b], the other lithologies are not strictly pulverized (e.g., no powdery flour texture for limestones, no pervasive fracture damage but more localized fractures for sandstone). On the microscale, geometrical differences exist between the lithologies, although current knowledge on the quantitative geometrical constraints in

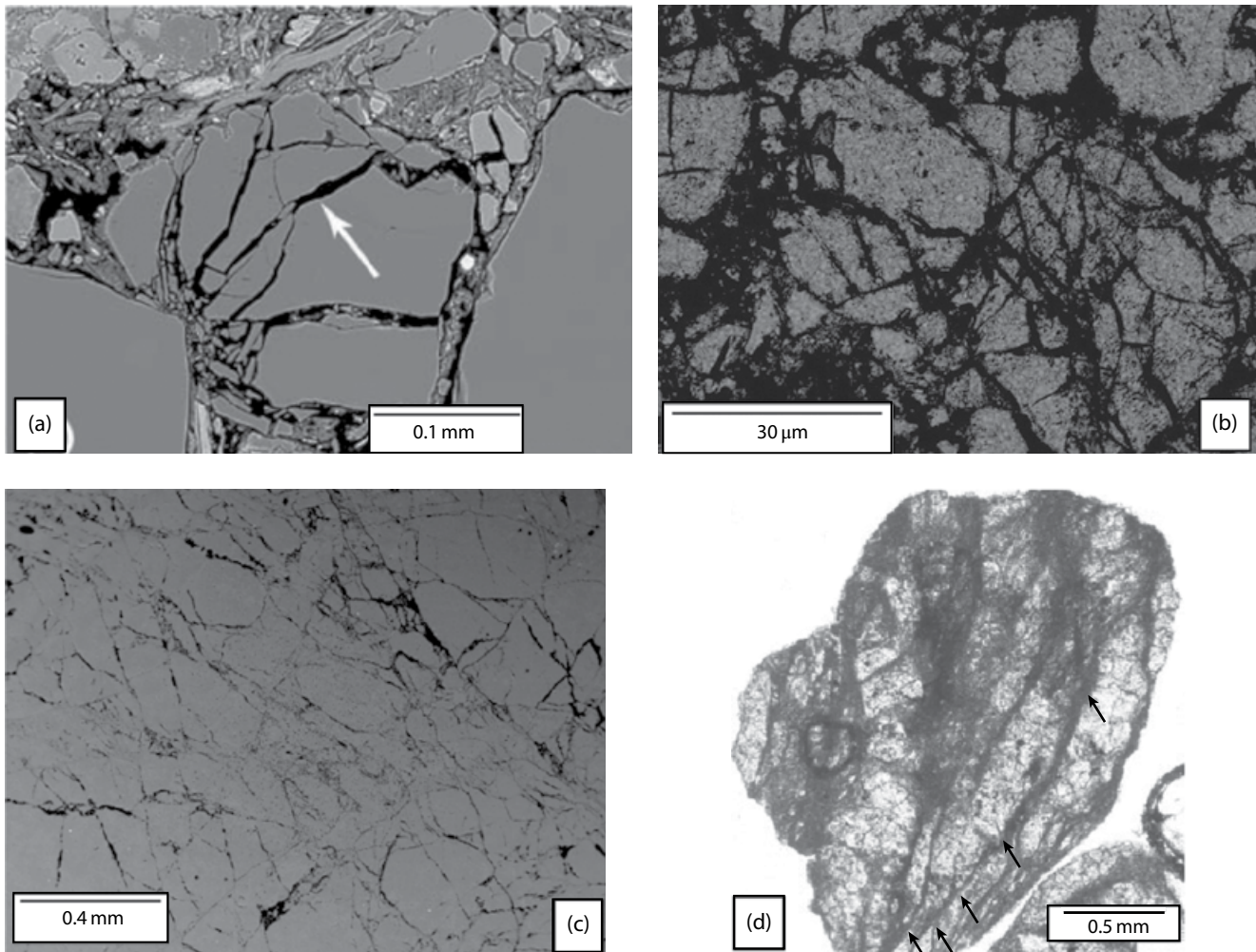


**Figure 4.3** (a), (b) Microphotographs of pulverized sandstones. (a) Shows Hertzian fractures in a quartz grain at the contact with another grain. Note that surrounding grains do not show any fracture damage. (b) Pulverized quartz grains with varying degrees of damage. (c) Photomicrograph of pulverized dolostone, showing hierarchical fractures and some needle- or shard-type fragments. (d) Photomicrograph of a pulverized limestone from a borehole in Israel showing very small-size dynamic branching (black arrows). Sources: (a) Dor *et al.* [2009], (b) Key and Schultz [2011], (c) Fondriest *et al.* [2015], (d) Sagy and Korngreen [2012].

limestones and dolostones remains sketchy. Nonetheless, the fact that classic pulverized rocks show a seemingly isotropic and random damage fabric, while limestones and dolostones show a more angular, hierarchical, and anisotropic fabric and sandstones a localized and heterogeneous fabric, would seem to indicate a different mechanical response to similar loading conditions or to different loading conditions and thus a different origin of formation.

However, shared features such as the general lack of shear strain, the pervasive homogeneous or heterogeneous fracture damage distribution, and dilatational nature of the fractures point toward a common source related to nearby faults. All these considerations might be further clarified by completed or future experiments so as to

monitor the whole formation process of pulverized rocks. Eventually, a clear definition for pulverized rock could then be proposed.

#### 4.2.2. Pulverized Rock at the Fault System Scale

Pulverized rocks are mainly observed in mature fault systems with a large amount of total slip. Most of these fault systems are strike-slip, and the maximum distance from the fault plane where pulverized rocks have been observed is of the order of hundreds of meters (Figures 4.2 and 4.4). For mature fault systems (offset >10 km), the size of the pulverized zone is of the same order of magnitude as the width of the total damage zone [taken from Faulkner *et al.*, 2011; Savage and Brodsky, 2011] (Figure 4.4).

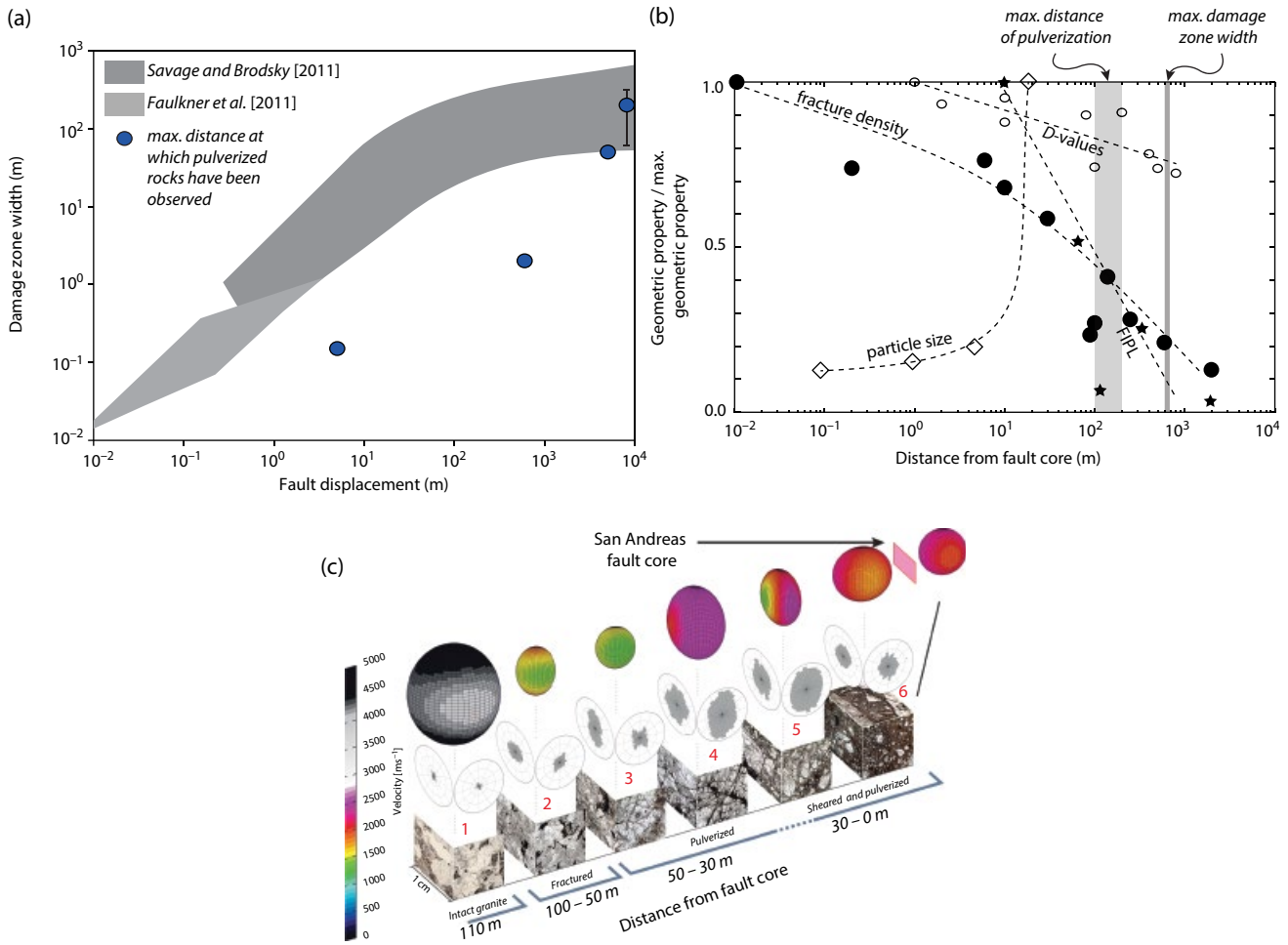


**Figure 4.4** (a) Total displacement along the fault versus the width of the damage zone based on the compilation of data by Savage and Brodsky [2011] and extended by Faulkner et al. [2011]. Blue circles indicate approximate maximum distance of pulverized rocks from the fault core from several field studies (see Figure 4.2). All displacements greater than  $10^4$  m are clustered at  $10^4$  m, and these observations vary between 50 and 400 m, indicated by the error bar. (b) Several geometrical properties (normalized by the maximum value) versus distance from the fault core. The particle size is from pulverized San Andreas fault granite [Rockwell et al., 2009], fracture density and D-values from the ATTL [Mitchell et al., 2011; Muto et al., 2015] and FIPL (Factor of Increase in Perimeter Length) measured on pulverized sandstone grains near the San Andreas fault [Dor et al., 2009]. (c) Summary of anisotropy within the damage zone of the San Andreas fault that includes pulverized rocks, obtained by Rempe et al. [2013]. Anisotropy is constrained by P-wave velocities (ellipsoids) and fracture orientations (rose diagrams). See electronic version for color representation.

The few observations of less-developed fault systems (offset <10 km) show that the maximum pulverization distance is several orders of magnitude less than the damage zone width. This might indicate that quasi-static or classic fault-related damage and dynamic damage or pulverization are not related to the same processes.

While the damage in damage zones may not be produced coseismically [Mitchell and Faulkner, 2009], pulverized rocks are thought to be created exclusively during earthquakes. Therefore, the magnitude of the seismic events, which, coupled with other factors, determines the dynamic loading conditions, can be taken into account

instead of total displacement. For mature faults, earthquake magnitudes may be high ( $M_w > 7$ ). For faults with less overall offset, the maximum earthquake magnitude is usually less than  $M_w = 7$ . Here, the maximum pulverization distance from the fault is smaller as well. For the Upheaval Dome Impact structure [Key and Schultz, 2011], the magnitude is unknown but probably much greater than for tectonic faults of similar size. However, the number of observations of pulverized rock is still limited and the global dataset should be extended to confirm the trends of maximum pulverization distance from the fault in relation to total offset or earthquake magnitude.

Three studies have reported in situ observations of pulverized rocks at depth (Figure 4.2): ~40 m depth [Wechsler *et al.*, 2011], 5–6 km depth [Sagy and Korngreen, 2012], and 225–625 m depth [A.-M. Boullier, pers. comm.]. For the last-mentioned author, constraints on laumontite-cement in the dilatant fractures show that the depth at the time of fracturing was between 3 and 8 km [A.-M. Boullier, pers. comm.]. Geological constraints on the depth of formation set from surface observations at the San Andreas fault indicate a maximum depth of about 4 km [Dor *et al.*, 2006b] and a minimum depth near the surface [Dor *et al.*, 2009]. Pulverized rocks are therefore a relative shallow crustal feature in the upper part of the seismogenic zone (<10 km depth).

Pulverized rocks are occasionally observed along bimaterial fault interfaces, where the pulverized rocks are distributed asymmetrically with a higher abundance on the stiffer side of the fault [Dor *et al.*, 2006a, 2006b, 2008; Mitchell *et al.*, 2011]. This does not exclude the presence of pulverized rock on the compliant side of the fault [Dor *et al.*, 2006b]. It is suggested that this asymmetric distribution of pulverized rocks is a strong argument in favor of a preferred rupture direction [Dor *et al.*, 2006a, 2008]. However, the response to dynamic loading of the lithology on the compliant side might be completely different to the response of the stiffer lithology, so that the presence of pulverized rocks might depend on lithology rather than on preferred rupture direction. Again, experimental work would help answer these issues. Other observations of pulverized rocks indicate no mechanical contrast across the fault, for instance, at the Nojima fault [Boullier, 2011 and pers. comm.].

Several studies have focused on the place of pulverized rocks within the damage zone and the transition from nonpulverized to pulverized rock. This is either achieved by geometrical constraints [Dor *et al.*, 2009; Rockwell *et al.*, 2009; Muto *et al.*, 2015], by measuring P-wave velocities [Rempe *et al.*, 2013], or by mapping fracture densities [Mitchell *et al.*, 2011; Rempe *et al.*, 2013]. In addition, permeability measurements have been performed [Morton *et al.*, 2012]. Regarding the fracture densities and geometric properties (Figure 4.4b), there is no clear or sudden transition from fractured rocks to pulverized rocks. Instead, within the sample resolution obtained, these properties evolve continuously from a background intensity outside the damage zone toward a peak intensity (high *D*-value or high fracture density) near the fault plane. Mean particle size measurement reveals a reverse trend: particles are larger the farther they are away from the fault. Close to the fault, pulverized rocks become more sheared and evolve toward cataclasite and gouge [Rempe *et al.*, 2013]. The fracture density decreases for these sheared cataclasites (Figure 4.4c).

Surprisingly, despite having the highest fracture density, pulverized rocks yield higher P-wave velocities than their less fractured peers located farther from the fault

core [Rempe *et al.*, 2013] (Figure 4.4c). Also, changes in permeability are less straightforward than expected: a nonlinear increase of several orders of magnitude with increasing fracture density is observed on samples taken at the surface of the San Andreas fault zone. However, for the last few meters of intensely pulverized rocks, the permeability drops dramatically despite even higher fracture densities [Morton *et al.*, 2012]. These observations are strong arguments in favor of treating pulverized rocks differently from fractured damage zone rocks.

A last but important note should be made on the general description of “a large number of fractures that are oriented seemingly randomly”: the fracture density count by Rempe *et al.* [2013] was performed on oriented samples so that fault-parallel and fault-perpendicular density could be established. This shows an anisotropic distribution of fractures with more fractures oriented fault-parallel than fault-perpendicular (Figure 4.4c). This is supported by the P-wave velocity measurements taken during the same study on similarly oriented samples: higher velocities are measured fault-parallel than fault-perpendicular, both in fractured and in pulverized samples. Thus, strictly speaking the classically pulverized rocks contain a nonisotropic damage distribution.

### 4.3. COSEISMIC OFF-FAULT DAMAGE BY ANALOGOUS LABORATORY EXPERIMENTS

The observations and analyses performed on the field samples described above only show the end product of coseismic loading in the case of pulverized rock and the end product of coseismic loading and fault sliding in the case of cataclastic rock. To constrain the mechanical conditions under which pulverized rocks can be created, laboratory tests are required. Such tests are based on the consideration that a sample loaded by an incoming stress wave, either in tension or compression, is analogous to the response of near-fault rocks to high-frequency waves during an earthquake.

To design such experiments, the approximate conditions and processes at which pulverized rocks are created first need to be considered. For this purpose, a short overview will first be given of the response of brittle material to a broad range of strain rates in order to illustrate the context of the problem at hand. The most suitable apparatus, the Split-Hopkinson Pressure Bar, for testing the origin of pulverized rocks will then be discussed.

#### 4.3.1. General Overview of the Strain Rate Sensitivity of Geomaterials

Geological materials have been fractured over a wide range of strain rates, from  $10^{-6}$  to  $10^6 \text{ s}^{-1}$ . From these experiments, a generalized conceptual failure model has been produced in which strain rate sensitivity has been

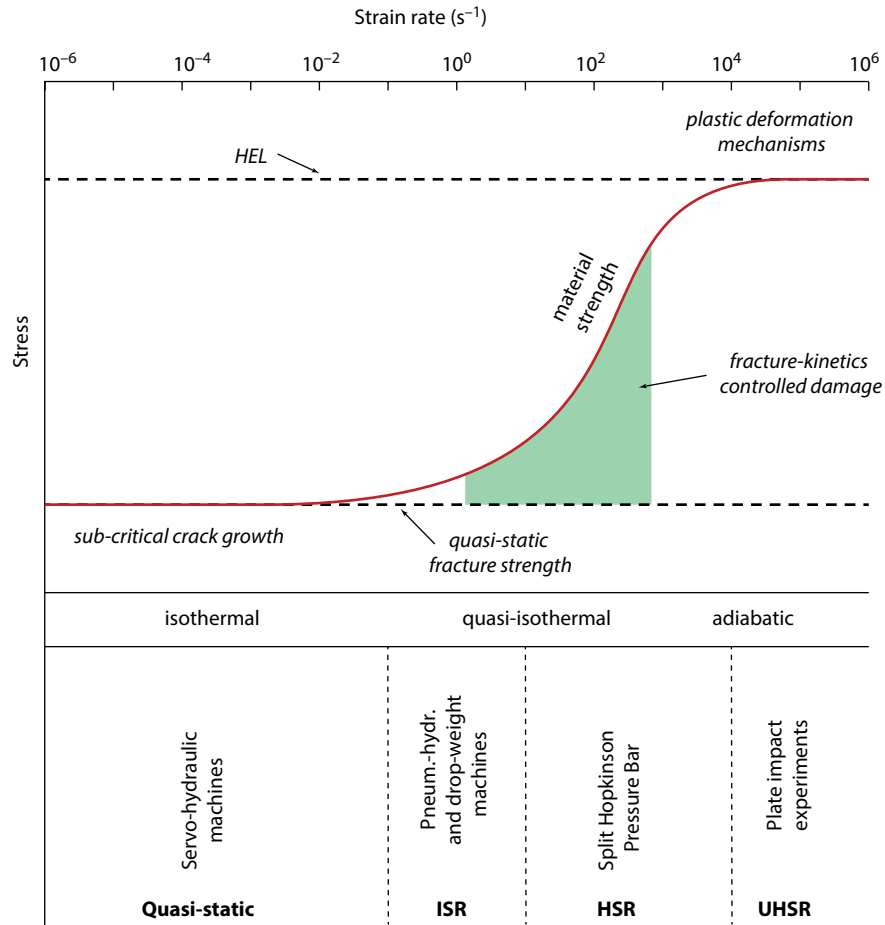


**Figure 4.5** Failure strength of materials for a broad range of strain rates. The strain rate values are broadly applicable to geological materials at or near the surface. Two different failure horizons are crucial: the quasi-static strength and the Hugoniot Elastic Limit. Four failure regimes are indicated: subcritical crack growth, quasi-static failure, fracture-kinetics controlled failure and shock-related plastic failure mechanisms. A suitable experimental loading apparatus is indicated for the various strain rates. The appropriate terms for the strain rate testing fields are ISR = intermediate strain rate, HSR = high strain rate, UHSR = ultra high strain rate. Adapted from Grady [1998] and Zhang and Zhao [2013a].

incorporated [Grady *et al.*, 1977; Grady, 1998]. Two failure surfaces are essential for the failure of rock materials (Figure 4.5): the quasi-static fracture limit and the Hugoniot Elastic Limit (HEL).

At the lowest strain rates ( $<10^{-6} \text{ s}^{-1}$ ), materials fail under isothermal conditions at relatively low stresses equal or less than the quasi-static fracture limit. Subcritical crack growth phenomena often play a major role in these conditions. At conventional laboratory strain rates ( $10^{-6}-10^{-1} \text{ s}^{-1}$ ), materials show little to no strain rate sensitivity and fail in a brittle manner at the quasi-static peak strength. The Griffith failure criterion (or models that have been developed from it) can predict the failure strength relatively accurately in terms of the activation and propagation of a critical flaw or a population of flaws (section 4.4.1).

At intermediate to high strain rates ( $10^{-1}-10^4 \text{ s}^{-1}$ ), the failure strength is strongly strain-rate dependent and the materials fail under quasi-isothermal conditions. This is due to inertia effects, which affect the fracture kinetics and allow transient loads or stress waves to exceed the quasi-static fracture limit (Figure 4.5). Due to this time-dependence of fracturing, several additional fractures have time to develop in addition to the weakest flaws, leading to a more diffuse fracture pattern. Models explaining fracturing within this fracture-kinetics controlled regime are discussed in section 4.4.

Once the inertial fracture delay has exceeded a certain threshold with respect to the loading rate (strain rates  $>10^4-10^5 \text{ s}^{-1}$ ), the material can go beyond the second failure surface: the HEL (Figure 4.5). Above this elastic limit, a range of alternative failure mechanisms are

activated, such as crystal plasticity and formation of micro-shear zones filled with nano-particles [Grady, 1998]. Moreover, the adiabatic conditions can result in local melting, leading to a drastic drop in the rock friction coefficient [Di Toro *et al.*, 2004]. Effectively, the HEL represents a high strain rate version of the brittle-ductile transition. The HEL is insensitive to changes in strain rate [Grady *et al.*, 1977; Grady, 1998].

Since the pulverized rocks observed in the field lack plastic deformation and partial melting, loading conditions close to and beyond the HEL are unlikely to cause pulverization. The pervasive fracture textures suggest that the pulverized rock forms in the fracture-kinetics-controlled strain-rate-strength domain (Figure 4.5). Experiments in this strain rate range involve the intermediate strain rate (ISR, strain rate  $10^{-1} - 10^1 \text{ s}^{-1}$ ) and high strain rate (HSR, strain rate  $10^1 - 10^4 \text{ s}^{-1}$ ) testing fields [Zhang and Zhao, 2013]. For ISR testing, pneumatic-hydraulic and drop-weight machines can be used; for HSR testing the most commonly used apparatus is the Split-Hopkinson Pressure Bar. This apparatus can be adjusted so that it includes the strain rate range of drop-weight machines, extending its range to lower strain rates of  $10^0 \text{ s}^{-1}$ . It has been used in all studies on pulverized rocks up to date.

### 4.3.2. Coseismic Damage by Compressional Loading Experiments

The Split-Hopkinson Pressure Bar (SHPB) apparatus (also known as Kolsky-bar) was developed in its current form by Kolsky [1949]. Given the relative novelty of this machine and its importance in all studies that have been performed up to date, the following section covers the basics of the apparatus. Specific attention is given to the manipulation of the imposed compressional stress wave. The current state of the art on dynamic loading experiments in relation to pulverized rocks is then summarized and discussed.

#### 4.3.2.1. Methodology of the Split-Hopkinson Pressure Bar Apparatus

**4.3.2.1.1. General Setup and Mechanical History by 1D-Wave Analysis** A typical SHPB setup includes an input bar and an output bar supported by low-friction ball bearings or Teflon-coated uprights (Figure 4.6a, b). The rock sample is placed between the two bars and can be held in place by a lubricant. A launch mechanism (gas gun, spring gun) accelerates a striker toward the input face of the input bar. The velocity of the striker depends on the launch mechanism: a spring gun produces lower velocities and is used to perform reproducible tests at lower strain rates ( $10^0 - 10^3 \text{ s}^{-1}$ ) than a gas gun ( $10^2 - 10^4 \text{ s}^{-1}$ ). At impact, a compressive planar stress wave is created that travels through the input bar (Figure 4.6a). Typically

the wave has a duration of less than 1 millisecond. This incident wave splits into a reflected wave and a transmitted wave at the input bar-sample interface (Figure 4.6a). The reflected wave travels back through the input bar, the transmitted wave travels through the sample and into the output bar (Figure 4.6a). Both transmitted and reflected waves then travel end-to-end in their respective bars.

In order to obtain the full stress-strain loading history, the propagation of the planar stress waves is recorded first. For this purpose, strain gauges are placed on the input and output bars (Figure 4.6a). The acquisition frequency of the gauges must be sufficiently high to ensure that the stress wave loading is monitored in acceptable detail (e.g., a frequency of 1–2 MHz). The strain gauges are placed on the bars at specific distances from their extremities so that the incident, reflected, and transmitted waves are recorded without overlap.

The raw data record is then preprocessed by identifying the first passage of the three waves (incident, reflected, and transmitted, Figure 4.6c). The first two waves are recorded on the input bar, where by definition the first signal is the incident wave and the remaining signals are the back-and-forth traveling reflected wave. The output bar contains exclusively the transmitted wave signal. Only the primary recordings of the reflected and transmitted waves are needed. The equation describing stress wave propagation along a thin bar is known as the Pochhammer-Chree equation [Graff, 1991], so that the three waves can be numerically projected backward (transmitted and reflected wave) and forward (incident wave) to the edges of the bars, and hence to the edges of the sample (Figure 4.6d).

The loading history is obtained by applying a 1D-wave analysis [Graff, 1991; Chen and Song, 2011]. The stress history is obtained by resolving the forces acting on the bar-sample interfaces for each wave (Figure 4.6e) (subscript *I*, *R* and *T* for incident, reflected and transmitted wave respectively). All symbols used in the formulas in this review are listed in Table 4.1. The force *F* is given by

$$F_{I/R/T} = -E_B A_B \times \varepsilon_{I/R/T}, \quad (4.1)$$

where  $E_B$  is the Young modulus of the bar material,  $A_B$  is the surface area of the bar extremities, and  $\varepsilon$  is the strain gauge data of the stress wave (the minus sign comes from the convention that the dilatational strain recorded by a strain gauge is positive). The stress ( $\sigma$ ) acting on the surfaces of the sample is computed as a simple force balance divided by the surface area of the sample ( $A_S$ ). For the sample output surface this is

$$\sigma_{out} = -\frac{F_T}{A_S} = -\frac{E_B A_B}{A_S} (\varepsilon_T). \quad (4.2)$$

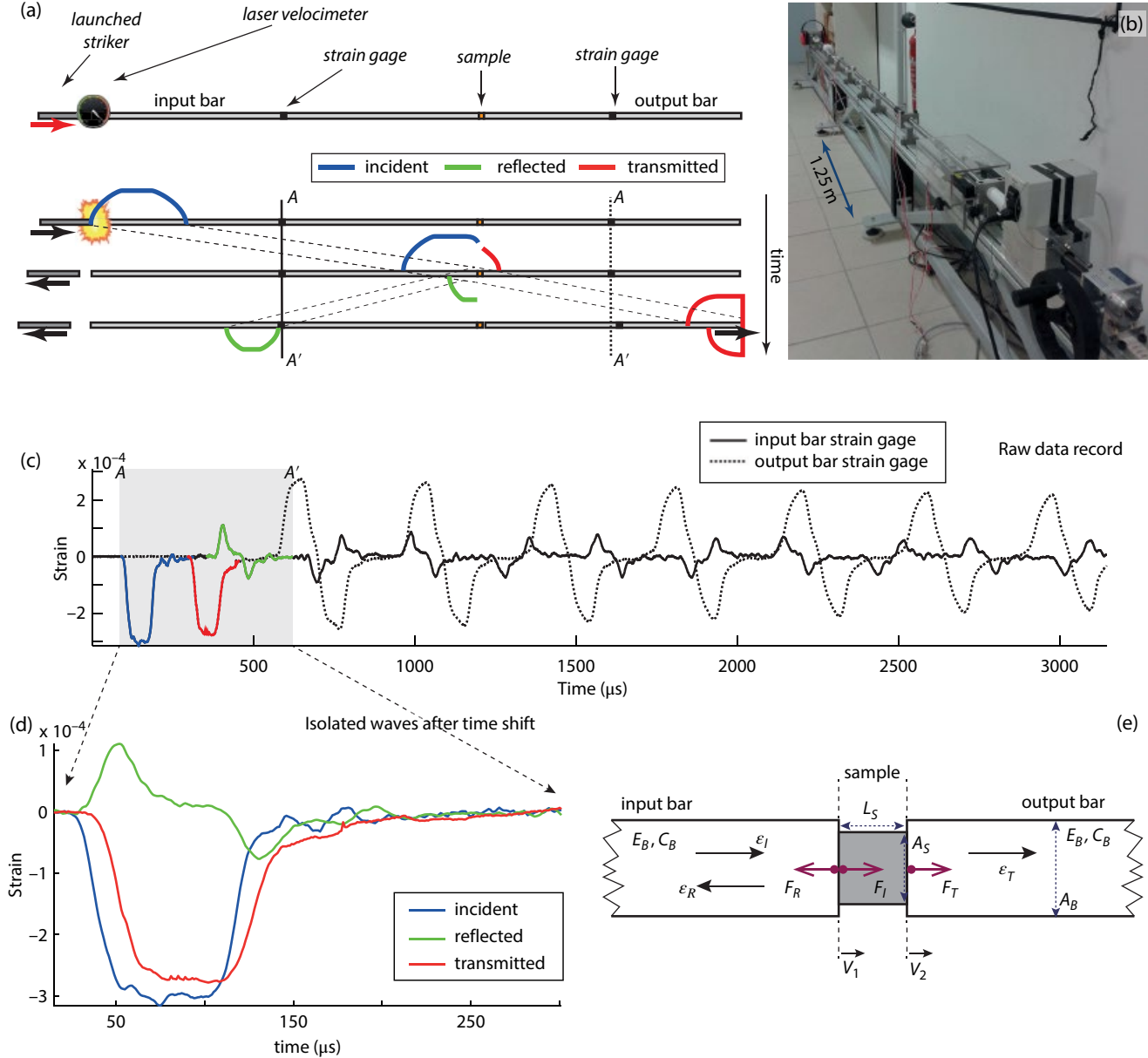


**Figure 4.6** (a) Sketch of a typical Split-Hopkinson Pressure Bar (SHPB), in this case a mini-SHPB with a spring gun as launching system. The velocimeter records the speed of the striker bar and triggers the data acquisition system. Strain gauges record the incident (blue), reflected (green), and transmitted (red) stress waves as they travel along the length of the bars, as indicated by the three time snapshots. A–A' indicates the time interval highlighted in gray in figure (c). (b) Photograph of a mini-SHPB apparatus at the ISTerre laboratory in Grenoble. (c) Raw data record of the input bar (black) and output bar (black dashed). The gray area corresponds to A–A' in figure (a) and encompasses the primary passing of the three stress waves, which are highlighted in color. The record shows no second loading because the transmitted and reflected waves do not show a sharp alteration in shape and intensity. (d) The incident, transmitted, and reflected waves after the time shift from the gauge locations to the bar interface. (e) Sketch of the sample and sample-bar interfaces with the bar properties and the direction of strain pulses, particle velocities, and forces. See text and equations (4.1)–(4.6). Figures (c) and (d) show a test during which a quartz-monzonite sample was deformed in the elastic regime. See electronic version for color representation.

And for the input surface:

$$\sigma_{in} = -\frac{F_I + F_R}{A_S} = -\frac{E_B A_B}{A_S} (\varepsilon_I + \varepsilon_R). \quad (4.3)$$

Note that the reflected wave has an opposite (tensional) strain and is thus effectively subtracted from the incident wave. Equations (4.2) and (4.3) are called the 1-wave analysis and 2-wave analysis, respectively. If the assumption of stress equilibrium along the length of the sample is satisfied, a 3-wave analysis yields the mean stress on the sample:

$$\sigma_{mean} = -\frac{F_I + F_R + F_T}{2A_S} = -\frac{E_B A_B}{2A_S} (\varepsilon_I + \varepsilon_R + \varepsilon_T). \quad (4.4)$$

However, in practice initial stress equilibrium issues render the 2-wave and 3-wave analyses less reliable. Use of the 1-wave analysis is recommended for testing brittle samples.

Strain and strain rate are computed from the relative difference in particle velocities of the input bar-sample interface ( $v_1$ ) and the output bar-sample interface ( $v_2$ ) (Figure 4.6e). These velocities are given by

$$v_1 = c_d^B (-\varepsilon_I + \varepsilon_R) \quad v_2 = -c_d^B \varepsilon_T, \quad (4.5)$$

where  $c_d^B$  is the P-wave velocity of the bar material. The relative difference in velocity divided by the sample length ( $L_s$ ) then gives the strain rate

$$\dot{\varepsilon} = \frac{v_1 - v_2}{L_s} = \frac{c_d^B}{L_s} (-\varepsilon_I + \varepsilon_R + \varepsilon_T). \quad (4.6)$$

A time integration of equation (4.6) gives the strain. For more details on 1D-stress analysis, see Graff [1991], Gama *et al.* [2004], and Chen and Song [2011].

#### 4.3.2.1.2. Assumptions and Pitfalls of 1D-Wave Analysis

To ensure a valid 1D-wave analysis for brittle samples, the following assumptions must be verified [Zhao and Gary, 1996; Gama *et al.*, 2004; Chen and Song, 2011; Zhang and Zhao, 2013]:

1. The stress wave propagation in the bar is 1D and longitudinal to the bar axis.
2. Stress is in equilibrium along the length of the sample during deformation.
3. Friction and radial inertia effects are kept minimal.
4. The sample is loaded once per test.

*1D longitudinal wave propagation:* Since the deformation history is obtained by 1D-wave analysis, this assumption is imperative. However, in an experimental setup there are always small alignment issues so that the bar interfaces are not perfectly perpendicular to the stress

wave propagation direction. Carefully aligning and calibrating the apparatus before an experiment reduces this error. Keeping the length/diameter ratio of the bars greater than 20 and input wave stresses below the elastic limit of the bar can further ensure 1D wave propagation.

The finite diameter of the bars causes dispersion of the stress waves in the bar by the appearance of multiple propagation modes [Graff, 1991]. This will affect especially the higher frequency components in the stress wave, which will travel more slowly than the lower frequency components. Thus, the stress wave measured at the strain gauge is different from the actual stress wave at the bar-sample interfaces. This dispersion can be described by the Pochhammer-Chree equations [Graff, 1991], and since in practice only the first propagation mode is activated, the stress wave dispersion can be modeled relatively easily. From this, the stress wave is corrected for the position at the sample-bar interfaces.

*Stress equilibrium along the length of the sample:* This assumption must be valid for the three-wave stress analysis to be applied. Also, a sample in stress disequilibrium might result in heterogeneous deformation: for instance, the input side of the sample might be fractured while the stress at the output side of the sample never exceeds the elastic limit. Given that at the onset of loading, a sample is always in stress disequilibrium for the duration of a “ring-up” period or equilibrium time [Nemat-Nasser *et al.*, 1991; Zhang and Zhao, 2013], it is crucial to know the stress level when equilibrium has been reached. Typical equilibrium times are at least four times the transit time [Ravichandran and Subhash, 1994] or  $\pi$  times the transit time [Davies and Hunter, 1963]. The transit time is the one-way P-wave travel time through the sample.

A simple model can be used to check whether a loading has been in stress equilibrium before nonelastic deformation has set in, based on linear elastic behavior and wave reflections [e.g., Ravichandran and Subhash, 1994]. In such models, the expected elastic behavior is then compared to the actual loading history, and the necessary adjustments can be made for further testing. The input data for such models are the bar material properties, sample length, and an estimate of the density and P-wave velocity of the tested material. Analysis of these models shows that the sample length, impedance mismatch between bar and specimen, and most importantly, the shape of the incident pulse in the early stages of loading, influence the equilibrium time. The manipulation of the incident pulse is discussed in detail in the next section.

*Friction and radial inertia effects:* A lubricant at the bar-sample interface can reduce friction at this interface. During dynamic loading, radial inertia gives rise to extra axial stress components and therefore results in radial confinement. This effect can be minimized by keeping the length/diameter ratio of the sample equal to or less than

one [Gama *et al.*, 2004; Chen and Song, 2011; Zhang and Zhao, 2013]. With increasing sample diameter, the radial and axial stress components increase [Forrestal *et al.*, 2007; Chen and Song, 2011]; thus, samples with a small diameter experience less inertia-related additional stress components.

*Single loading per test:* A second loading during a single test may be preferred in some cases but increases the difficulty in performing the 1D-wave analysis preprocessing due to wave overlapping. The occurrence of a second loading can be checked from the raw data record: the transmitted and reflected waves would record a sudden change in shape and amplitude in such a case. The risk of this happening can be reduced by installing a momentum trap [Zhang and Zhao, 2013] or reducing the length of the output bar so that it moves away from the sample before reloading from the input bar.

#### 4.3.2.1.3. Manipulation of the Incident Stress Wave

Loading conditions of a high strain rate test are defined by the stress magnitude, the loading duration, and the loading rate of the incident wave. A “standard” incident wave created by the impact of two similar bars is trapezium shaped. Here, we discuss how to manipulate this trapezium-shaped wave so that a reliable high strain rate test can be designed.

The magnitude of the incident wave determines the stress on the sample. The most straightforward way to adapt this is by changing the speed of the striker at impact (Figure 4.7a). A good approximation of the stress magnitude in an incident wave is given by the following equation for the impact of two similar bars [Graff, 1991]:

$$\sigma = \frac{\rho_B c_d^B}{2} v_B, \quad (4.7)$$

where  $v_B$  is the speed of the bar at impact and  $\rho_B$  is the density of the bar material. This shows that, besides the speed at impact, the striker and/or bar material also influences the magnitude of the incident wave (Figure 4.7c).

The duration of the incident wave depends on the P-wave velocity of the material and on the pulse length. The pulse length is given by twice the length of the striker [Graff, 1991]. Thus, by changing bar material or by increasing the striker length, the loading duration can be modified and controlled (Figure 4.7c). However, the finite length of the bars needs to be taken into account: when the loading duration is nearly equal to the distance between strain gauge and sample, the incident and reflected waves might overlap, making it impossible to clearly identify and isolate the different waves. Moreover, a longer loading duration might cause a switch from

dynamic loading to quasi-static loading once the stress pulse has reached a plateau of constant stress. It depends on the aim of the research if this is expedient.

It is crucial to control the loading rate on the sample to ensure that stress equilibrium is reached before nonelastic deformation occurs (see section 4.3.2.1.2). In addition, the dynamic mechanical properties of rocks are highly sensitive to loading rate or strain rate. As described above, the wave velocity (solely dependent on the P-wave velocity of the bar material) determines the loading duration. This means that a slower wave imposes a slower loading rate compared to a faster wave with equal magnitude and equal length. A change in magnitude also influences the loading rate. However, both variables significantly change the other loading conditions as well (loading duration and stress magnitude), which might be undesirable.

Therefore, the most powerful tool to manipulate the shape of the incident wave is the use of pulse shapers (Figure 4.7b). Pulse shapers are thin discs of a softer material. The impedance mismatch between the striker and the pulse shaper results in smoothing of the incident wave. Also, the thickness of the pulse shaper has to be taken into account: the thicker the pulse shaper, the more muffled the incident wave will become. The pulse shaper technique is highly suited to solving stress disequilibrium problems since it decreases the loading rate at the beginning of loading.

#### 4.3.2.2. Rock Pulverization in Compression by Split-Hopkinson Pressure Bar Experiments

Several studies on the dynamic compressional behavior of geological materials have been performed using the SHPB apparatus (Figure 4.8a, adapted from Zhang and Zhao, 2013). Many of these studies are from the (geo-)engineering or material science community and are not necessarily focused on coseismic damage and implications on fault behavior. Studies that do are scarce and are performed on crystalline granitic rock [Doan and Gary, 2009; Yuan *et al.*, 2011; Doan and D'Hour, 2012] or on Carrara marble [Doan and Billi, 2011] (Figure 4.8).

All crystalline geological materials show a single trend (Figure 4.8a): the dynamic peak strength of the sample increases with increasing strain rate. This confirms that the loadings are performed within the kinetics-controlled fracturing regime (Figure 4.5). The increase in strength of limestone and marble is stronger compared to granitic and basaltic rock at similar strain rate. However, it should be noted that the true uniaxial compressive strength is not known for each study; in this case, the data is normalized to the lowest dynamic strength value from that particular study.

Besides the increase in strength of rock material with higher strain rates, the (macroscopic) end-state also

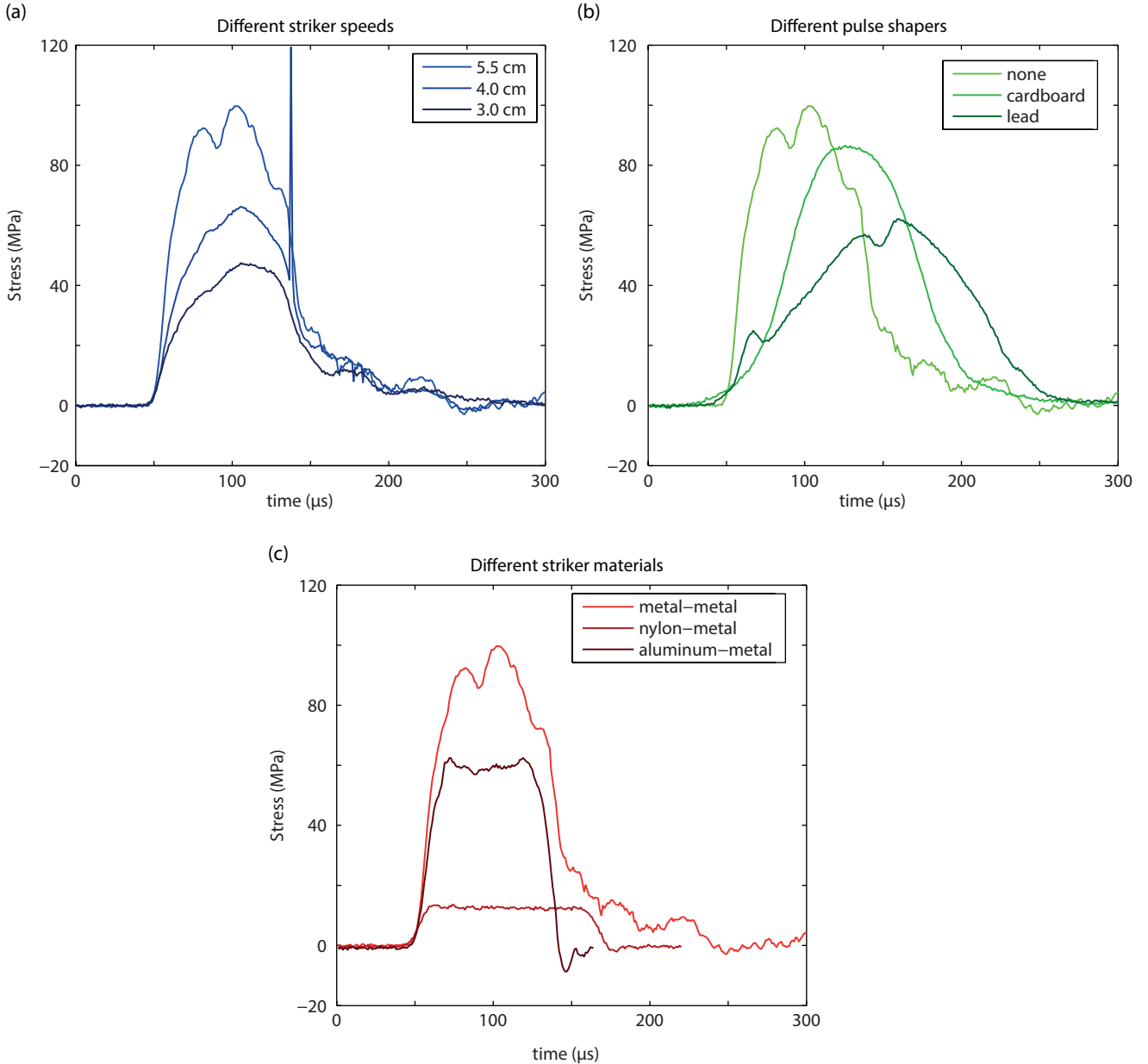


**Figure 4.7** Raw incident stress waves (no dispersion correction) produced by (a) steel-steel impact from a 20 cm striker with varying speeds (expressed as spring gun loading distance). (b) Stress waves produced by steel-steel impacts from a 20 cm striker, with addition of cardboard or lead pulse shapers. (c) Stress waves produced by the impact of a striker made from various materials (steel, aluminium, nylon) onto a steel bar.

changes. Failure end-states can be classified as intact, split (single or few fractures), and pervasively fractured/pulverized [Li *et al.*, 2005; Xia *et al.*, 2008; Doan and Gary, 2009]. Doan and Gary [2009] reported that the transition from split to pulverized is defined by a pulverization strain rate threshold between 100 and 150 s<sup>-1</sup> (Figure 4.8b). This was determined on San Andreas granites (the protoliths of the pulverized rocks observed by

Dor *et al.* [2006b]), which showed a large amount of initial fracture damage. Less damaged Tarn granites proved to have a pulverization strain rate threshold that was nearly twice as high ( $\sim 250 \text{ s}^{-1}$ ) [Doan and D'Hour, 2012] (Figure 4.8b). A similar strain rate was obtained on Westerly granite in unconfined condition [Yuan *et al.*, 2011]. Pulverization has been shown to occur at a higher strain rate when the samples experience confining

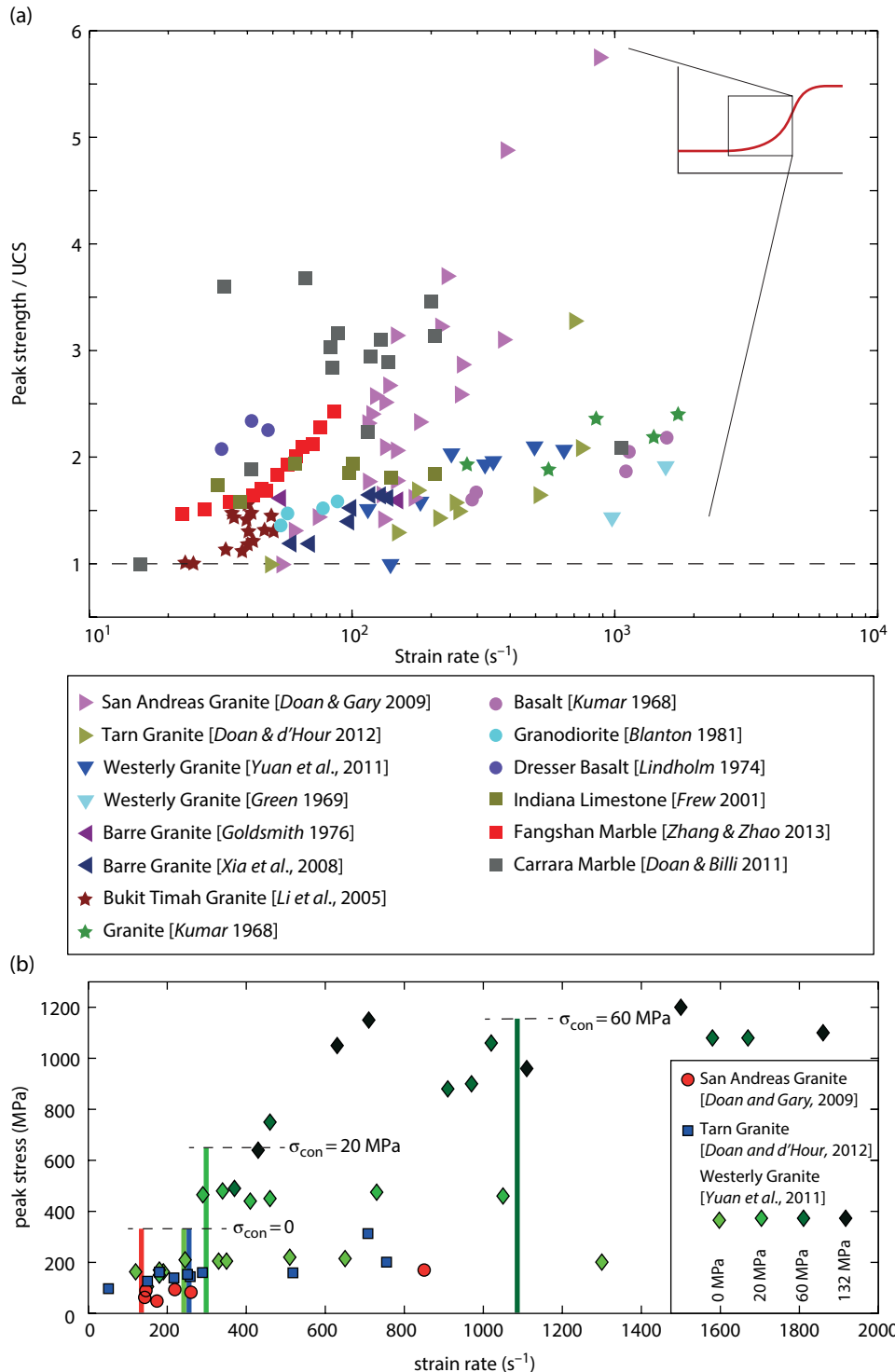


**Figure 4.8** (a) Compilation of dynamic compressive loading data obtained by SHPB experiments on geological materials [Green and Perkins, 1968; Kumar, 1968; Lindholm et al., 1974; Goldsmith et al., 1976; Blanton, 1981; Frew et al., 2001; Li et al., 2005; Xia et al., 2008; Doan and Gary, 2009; Doan and Billi, 2011; Yuan et al., 2011; Doan and D'Hour, 2012; Zhang and Zhao, 2013b]. The data fall within the kinetics-controlled fracturing regime (small inset top right). Figure modified from Zhang and Zhao [2013]. Note that the true UCS was not known for all data series; in this case, the strength has been normalized to the lowest dynamic strength. (b) Strain rate versus peak stress plot showing data of studies that specifically focus on pulverization in igneous crystalline rock. The colored vertical bars indicate the pulverization strain rate thresholds. The confining stress is indicated for the experiments by Yuan et al. [2011]. Note that the unconfined pulverization thresholds from the different studies cluster around  $200\text{ s}^{-1}$ , except for the initially damaged San Andreas granite samples.

pressure during loading [Yuan *et al.*, 2011] (Figure 4.8b). On the other hand, the pulverization strain rate threshold can be lowered by performing successive dynamic loadings with strain rates below the initial pulverization strain rate threshold, establishing a new pulverization threshold that is 50% lower, from  $180\text{ s}^{-1}$  to  $90\text{ s}^{-1}$  [Aben *et al.*, 2016].

However, three points regarding the pulverization of rocks in the studies mentioned above require some discussion. First, a qualitative method rather than quantitative measurements has been used to determine whether the sample is split or pulverized, although in practice the transition from a split sample (e.g., less than 10 fragments) to a pulverized sample is very clear, and difficulties in labeling them are rare.

Second, Yuan *et al.* [2011] imposed a confining pressure on the samples by using tight-fitting sleeves of different materials (Poly[methyl methacrylate], copper, brass). The authors assumed that the confining sleeves behaved as a perfect elastic material, and from this they derived the confining stress theoretically. Confining stresses as high as 132 MPa were reached. However, they did not measure the actual mechanical behavior of the sleeve (unlike Forquin *et al.* [2010]). Therefore, the true confining pressure during deformation is difficult to define and might deviate from their reported values. Nonetheless, the trend of an increasing pulverization strain rate threshold with increasing confining pressure is clear (Figure 4.8b).

Third, the strain rate histories during dynamic loading experiments are complex (Figure 4.9), since SHPB experiments are too fast to be servo-controlled. Moreover, when a sample is qualitatively pulverized, the strain rate history includes an extra strain rate peak after the initial strain rate peak [Xia *et al.*, 2008; Aben *et al.*, 2016] (Figure 4.9). Various authors have picked different representative strain rates from this history. For instance, strain rates have been obtained by taking the maximum strain rate, excluding the second strain rate peak [Doan and Gary, 2009; Doan and D'Hour, 2012], by averaging the strain rate [Yuan *et al.*, 2011] or by taking the strain rate value of the constant strain rate plateau [Xia *et al.*, 2008]. No supporting evidence has been given to show that these strain rates are representative of dynamic fracturing. Linear elastic fracture mechanics, adjusted to dynamic loading conditions [Bhat *et al.*, 2012], were applied to experimental data by Aben *et al.* [2016] to show that the strain rate plateau in between the two strain rate peaks coincides with the onset of dynamic fracturing. This is supported by high-speed camera data that were synchronized with the acquisition system of an SHPB apparatus (Figure 4.9), which shows that the formation of fractures concurs with the strain rate plateau or hinge point. Thus, although the different strain rate thresholds (Figure 4.8b) seem to be consistent and within the same range, precision can be increased in future

studies by picking similar representative strain rates according to a single convention.

A remarkable observation that distinguishes the experimentally pulverized rocks from the fragmented rocks is the strong reduction in the duration of the stress wave in the output bar (Figure 4.9a): from an initial duration of  $\sim 180\text{ }\mu\text{s}$  to  $\sim 90\text{ }\mu\text{s}$  in this example. Basically, the stress wave is “cut off” because the pulverized sample cannot transfer the stress anymore at atmospheric confinement. At higher confining pressures it is expected that the stress wave after pulverization will show a significant drop to a much lower stress amplitude. Such a reduction in the stress wave is not observed in the case of fragmented samples.

Microstructural analysis of postmortem crystalline samples shows very similar damage textures to field samples, with very little accommodated strain and pervasive fragmentation below grain size [Yuan *et al.*, 2011]. Grain size analyses performed on pulverized and fractured San Andreas and Tarn granite show that the mean particle size is greater than the values obtained on field samples [Doan and Gary, 2009]. This difference may be explained by the fact that the field samples have experienced several coseismic loadings and different stress states in between coseismic loadings.

The only other material tested for coseismic damage is Carrara marble [Doan and Billi, 2011]. Here again a transition from a fractured to a pulverized end-state has been observed qualitatively. The transition is not clearly indicative of a strain rate threshold: pulverization occurs from  $68\text{ s}^{-1}$ , but this strain rate overlaps with apparently intact and split samples. The threshold is in fact expressed much more clearly in terms of strain: above 1.3% residual strain, the samples are pulverized. Carrara marble therefore pulverizes at milder loading conditions than crystalline mineral aggregates. The microstructures obtained after the experiments on Carrara marble show some plastic deformation by twinning before fracturing. No detailed geometric quantification has been performed.

The transition from split to pulverized rocks is also visible in the amount of energy that is dissipated with an increase in axial strain [Doan and Billi, 2011; Aben *et al.*, 2016]. The apparently intact and fractured samples plot along a line with a relatively steep slope ( $103\text{ MJ/m}^3$  for Carrara marble). This slope decreases by more than 50% at higher strains, when samples have been classified as pulverized. This transition may reflect a change in dominant deformation mechanism. Hence, it may indicate the phase change from a crystalline material to a granular material: near the pulverization threshold the sample loses all cohesion and granular flow becomes the dominating mechanism for strain accommodation [e.g., Lyakhovsky and Ben-Zion, 2014]. When this process is inhibited immediately after this transition, the rock becomes cohesionless while the amount of accumulated shear strain is kept so that the original texture is preserved.

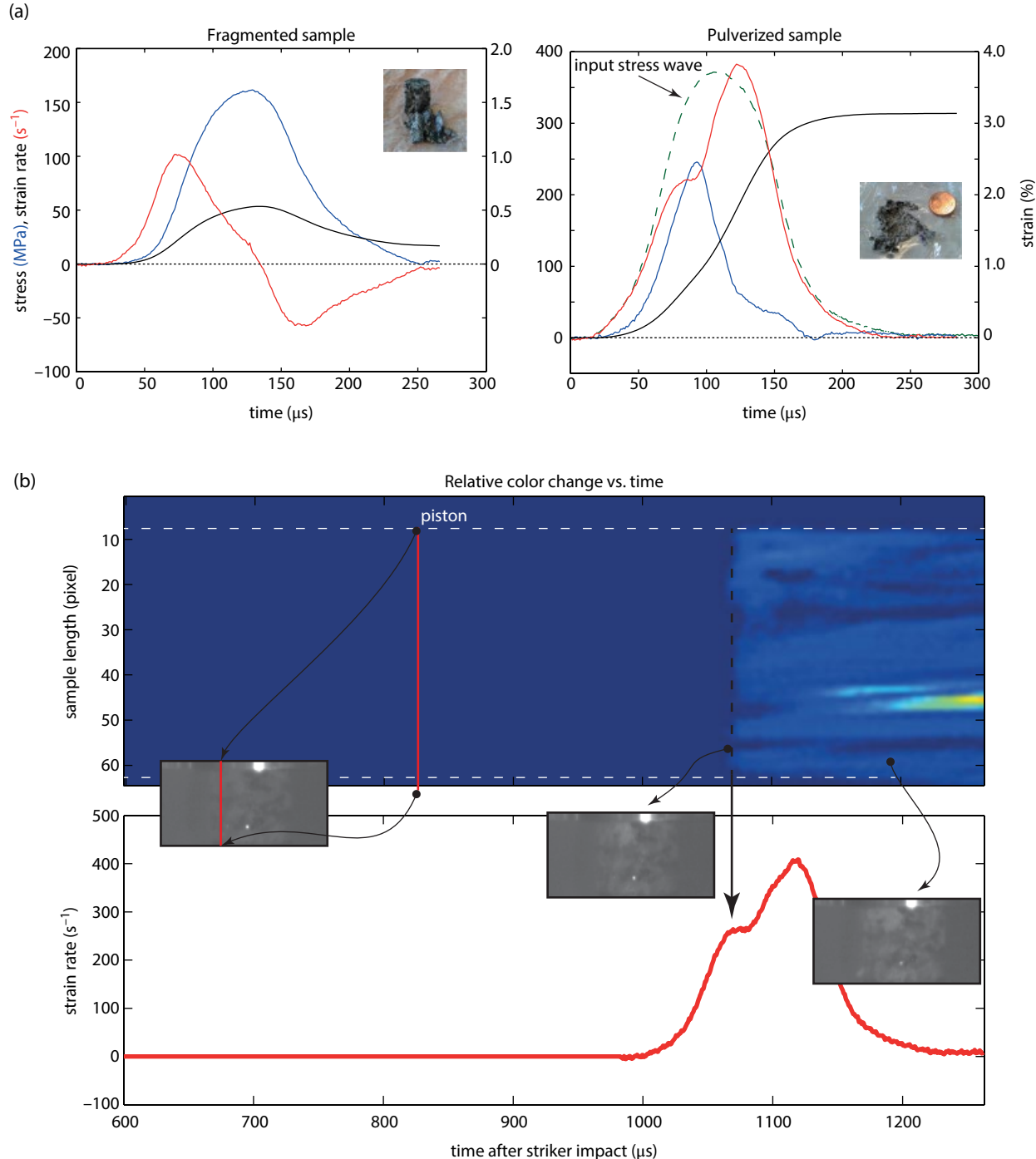


**Figure 4.9** (a) Mechanical data of a fragmented (left) and a pulverized (right) quartz-monzonite sample [from Aben et al., 2016]. The stress (blue), strain (black) and strain rate (red) parameters are plotted versus time. Note the distinctive difference in mechanical history, mostly expressed in the strain rate history, which includes a second strain rate peak in case of pulverization. The inset shows postmortem photographs of the samples. The input stress wave of the pulverized sample (green curve, vertically not to scale) highlights the reduction in period of the output stress wave (blue curve). (b) High-speed camera data (top) synchronized with the strain rate history (bottom) of a pulverized quartz-monzonite sample. The camera had an acquisition rate of 0.3 MHz, the mechanical data 1 MHz. Three camera stills from before, during, and after loading have been included. The top plot shows the relative color change along one column of pixels (indicated by the red line in the first still) with time. From this, it follows that fracturing initiates at the strain rate plateau (black arrow) between the initial peak and second strain rate peak. See electronic version for color representation.

Postloading petrophysical and geophysical properties were measured by *Aben et al.* [2016] on apparently intact and fragmented end-states. P-wave velocity measurements indicate a decrease in velocity in the axial direction as a function of dissipated energy. An even greater decrease is obtained for the radial directions, reflecting the development of an anisotropic damage structure in these samples. This is in accordance with measurements on field samples [*Rempe et al.*, 2013] (Figure 4.4c). The porosity measured on the same samples increases nonlinearly with increasing damage, suggesting some kind of percolation behavior for crack connectivity. Permeability measurements taken on dynamically fractured and pulverized samples show an initial increase in permeability with increasing amount of damage, followed by a sudden drop in permeability for jacketed pulverized samples [*Morton et al.*, 2012]. This observation matches permeability measurements on field samples. These two studies include not only pulverized samples but also dynamically fractured or split samples and suggest that a single high-magnitude earthquake [*Morton et al.*, 2012] or several successive earthquakes [*Aben et al.*, 2016] could create a damage zone structure as observed in the field. Section 4.5 discusses how the experiments are linked to fault mechanics and damage zone geometry.

#### 4.3.3. Dynamic Tensile Loading SHPB Experiments

To date, no publications on dynamic tensile loading and pulverization are available. However, dynamic tensile loading experiments have been performed on brittle (geo-)materials in the civil engineering community [*Zhang and Zhao*, 2013 and reference therein]. Within the strain rate range of interest, most experiments are performed on modified versions of the classical SHPB apparatus. Either direct or indirect tensile tests can be performed, following different adjustments of the SHPB [*Zhang and Zhao*, 2013; *Xia and Yao*, 2015]. In general, tensile testing produces less reliable results than compressive loading.

Direct tensile tests typically involve an anvil or a similar construction attached to the input bar so that a striker can be launched onto it from the opposite direction compared to standard compressive SHPB tests. The sample is fixed between the input and output bars, either by epoxy glue or a screw system. Often, the sample-bar connection involves a complex sample shape (e.g., dumbbell or bone-shaped). The attachment and sample shape can cause several additional complexities regarding the assumption of stress equilibrium and the 1D-wave analysis apart from standard considerations (section 4.3.2.1.2). Moreover, manipulation of the input wave by pulse shaping techniques becomes harder.

Several indirect tension tests have been designed for the SHPB: the Brazilian disc method, the three-point

bending technique, and spalling experiments [*Zhang and Zhao*, 2013; *Xia and Yao*, 2015]. The Brazilian disc method uses a disc of material wedged between the bars with the cylindrical surface in contact with the bar interfaces. The sample is consequently split between the contact points by a compressive stress wave loading. In the three-point bending technique, instead of a disc, a prism-shaped or semicircular sample is fixed so that the flat surface rests on two nipples attached to the output bar. For these methods, the loading and pulse shaping is similar to that of compressive tests. However, the three-point bending technique gives a flexural strength value rather than purely tensile strength. Also, stress equilibrium is hard to reach and verify due to the free surface area. The Brazilian disc and three-point bending methods are typically used for studying the initiation and propagation of single fractures. These single fracture methods are not very suitable since the concept of pulverized rocks requires the complexity and interaction of a large amount of fractures distributed in a volume.

The spalling test requires only a single bar on which a long slender sample is attached. A compressive stress wave travels through the bar and sample and then reflects at the free end of the sample. It then becomes a tensile stress wave that places the end of the sample under tension. For a reliable test, the amplitude of the stress wave must be lower than the compressive strength but higher than the tensional strength of the rock. This requirement, coupled with the need to monitor the stress wave dispersion in the long and often heterogeneous sample, is challenging.

Consequently, direct tensile dynamic experiments are the most interesting for generating pulverized rock. Results from such tests on geomaterials reveal that the tensional failure strength increases with strain rate [*Asprone et al.*, 2009; *Cadoni*, 2010; *Zhang and Zhou*, 2013]. The strength-strain rate curve starts rising between  $10^0$  and  $10^1 \text{ s}^{-1}$ , roughly one order of magnitude less than the compressional failure strength curve (Figure 4.8). Moreover, data from indirect tensile experiments show the curvature in the strength-strain rate data already between  $10^{-1}$  and  $10^0 \text{ s}^{-1}$  [*Zhang and Zhao*, 2013 and reference therein].

Postmortem samples from direct tensile dynamic tests typically show macroscopic failure along a single (mode I) fracture [*Asprone et al.*, 2009; *Cadoni*, 2010]. To our knowledge, there are no microscopic and microstructural analyses on postmortem samples available in the literature. Nonetheless, there are no reports of fragmented or pulverized end-states such as those observed on compressional dynamic loadings. It should be noted that direct tensile tests have been performed up to strain rates of  $\sim 100 \text{ s}^{-1}$ , which is below most pulverization thresholds that have been established for dynamic compressive loading.

Therefore, the question of whether the fracture-kinetics controlled regime for tensile loading results in less diffuse damage than the compressive fracture-kinetics regime, or whether pervasive tensile fracturing occurs at unexplored higher strain rates remains open to discussion and needs answering in the future.

Another possible experiment to generate pulverized rock, besides (uniaxial) compressive and tensile transient loading experiments, is hydro-fracturing due to a sudden drop in confining pressure. This would require the presence of a pressurized pore fluid pressure in the rock. During a transient drop in confining pressure, the difference between the pore fluid pressure and confining pressure can become equal or higher than the tensile strength of the rock so that the rock explodes due to the volumetric increase of the fluid. Note that the drop in confining pressure does not always result in a tensile state of confining pressure. Experiments that try to mimic this process involve rapid degassing of a gas-chamber with gas-saturated samples and are currently in a preliminary phase [Mitchell *et al.*, 2013].

#### 4.4. DYNAMIC BRITTLE DAMAGE MODELS

##### 4.4.1. Dynamic Versus Quasi-Static Damage: Strain Rate Effects on a Network of Microfractures

As discussed in section 3.1, coseismic damage is thought to be controlled by the kinetics of fracture network development. The high strain rate induced by the seismic waves will affect the collective behavior of the preexisting fractures present in the fault zone. Before discussing dynamic fracture damage, the processes controlling quasi-static fracturing will be reviewed and classical approaches for their modeling described.

For both static and dynamic loading, failure occurs through the following processes [Paterson and Wong, 2005, chap. 6]: (1) Nucleation of microfractures, which become activated, after which (2) the growth of microfractures is initiated. Initially, the fractures develop independently before they interact. (3) The interactions lead to stress shadowing and to the coalescence of microfractures to form a macroscopic fracture. Depending on the loading mode and the loading rate, each process has a different significance.

A tensile loading mode tends to initiate unstable mode I fractures that can propagate in the same direction without further increase in applied stress. The weakest flaw (e.g., pores, microcracks) in a sample will propagate and extend across the whole sample as soon as its stress intensity factor  $K$  exceeds a critical threshold value  $K_c$ , causing failure. This weakest flaw hypothesis, coupled with a power law distribution in flaw strength, gives the popular Weibull statistics of strength of a material [Weibull, 1939; Wong *et al.*, 2006].

A compressional loading mode leads to a different failure pattern where mode II cracks tend to deviate from their initial direction to become parallel to the principal stress direction. Any crack tilted relative to this direction will deviate from mode II to form a mode I wing crack whose progression is stable [Nemat-Nasser and Horii, 1982; Ashby and Sammis, 1990]. This means that propagation stops if no further stress is applied. For this reason, several microfractures are able to develop independently. Processes controlling fracture growth and coalescence will affect the final fracture pattern.

At high strain rates, several additional processes begin to interfere with the quasi-static processes described above.

1. An additional kinetic energy term cannot be neglected and must be taken into account for energy balance considerations [Grady, 1982].

2. The characteristic time for stress waves to propagate between fractures is not negligible compared to the characteristic time of propagation of a single fracture (Figure 4.10) [Denoual and Hild, 2000; Hild *et al.*, 2003].

3. Dynamic effects alter the way a single fracture propagates [Freund, 1990; Bhat *et al.*, 2012].

These additional processes will change the interaction between individual fractures, explaining the more intense fragmentation, and increase in strength that is observed for dynamic loading.

##### 4.4.2. Models Constraining the Decrease in Grain Size with Increasing Strain Rate

Dynamic fracture damage is characterized by fragmentation leading to an intense reduction in grain size, which can be explained by several theories. A first breakthrough came with the energy consideration of Grady [1982]. He showed that fragmentation releases kinetic energy in a sufficient quantity to sustain fracture energy production.

Indeed, the kinetic energy  $U_K = \int \frac{1}{2} \rho(\tau) v(\tau)^2 d\tau$  is dependent on the particle velocity  $v$  of each particle  $\tau$  constituting a volume  $V$  of mass density  $\rho$ . This velocity scales as the grain characteristic radius ( $R$ ) multiplied by strain rate  $\dot{\epsilon}$ , so that kinetic energy becomes  $U_K \propto R^5 \dot{\epsilon}^2$ . During fragmentation into  $N$  smaller spherical fragments of radii  $S = \frac{R}{\sqrt[3]{N}}$ , the kinetic energy decreases into

$$U_K = N U_{K,s} = \frac{1}{N^{2/3}} U_{K,R}. \quad \text{This released kinetic energy is converted into new surface energy. If all kinetic energy } (U_K = N U_{K,s} \propto N s^5 \dot{\epsilon}^2) \text{ is converted into surface energy } (U_s \propto N s^2), \text{ the characteristic fragment size } s \text{ would scale as } s \propto \dot{\epsilon}^{-2/3}. \text{ In a log-log diagram, giving characteristic fragment size versus strain rate, Grady's model would}$$

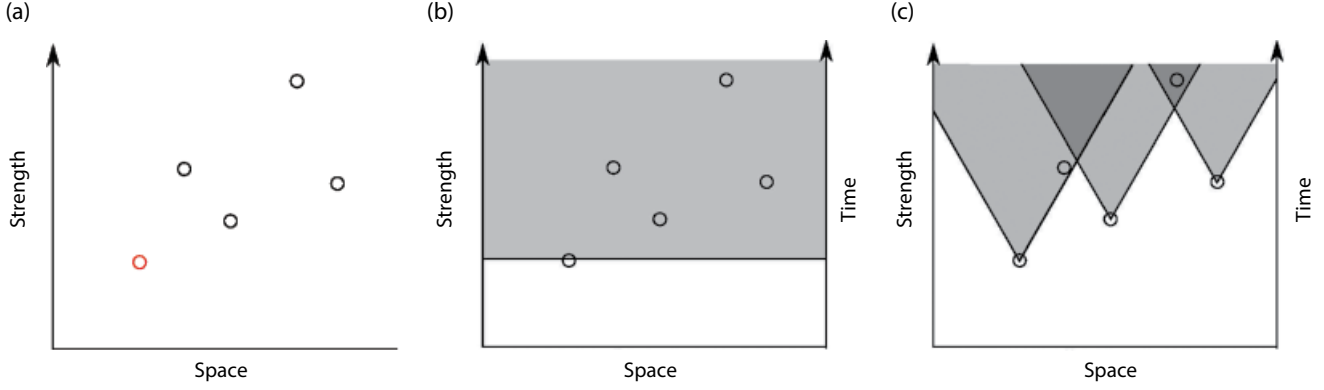


**Figure 4.10** 1D model for flaw propagation and interaction. (a) Preexisting flaws are scattered in space, with different strengths. As the stress increases, the weakest flaw fails. In case of a slow strain-loading rate (b), this flaw will propagate instantaneously compared to the strain rate. The sample will fail on this flaw only. (c) In case of fast loading, the stress relaxation waves will travel at finite speed. More flaws will be able to propagate, leading to a more fragmented final state. Sources: Hild et al. [2003], Doan and D'Hour [2012].

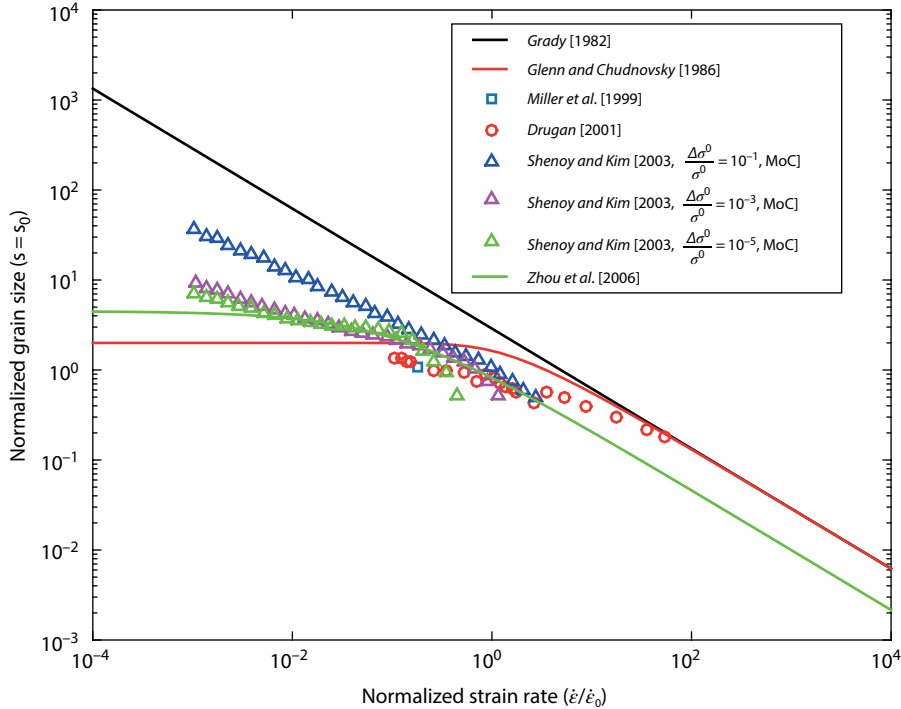


**Figure 4.11** Theoretical fragment size versus strain rate predicted by several authors for an expanding 1D bar undergoing dynamic fragmentation. Grady [1982] and Glenn and Chudnovsky [1986] derive average grain size for homogeneous media using the energy balance. Miller et al. [1999] use a finite element method, with a cohesive law. The model is recomputed using a semianalytical model based on the dynamic instability analysis by Drugan [2001]. Disorder effects are taken into account by Shenoy and Kim [2003], who assume flaws with variable strength  $\sigma_0$ . Their model is still semi-analytical with the method of characteristics (MoC) applied on cohesive elements. Multiple reflection waves are taken into account by Zhou et al. [2006], resulting in a smaller grain size. In all models, fragment size becomes considerably smaller when the strain rate is above a threshold strain rate  $\dot{\epsilon}_0$ .

correspond to a straight line (Figure 4.11). Such a release of kinetic energy has been considered to be the cause of the spectacular reduction in friction in catastrophic landslides [Davies et al., 2006] and is also assumed to operate in the formation of fault gouges [Davies et al., 2012].

Glenn and Chudnovsky [1986] refined this model by adding elastic energy in the energy balance. Contrary to kinetic energy, elastic energy is insensitive to strain rate and kinetic energy is negligible compared to elastic energy at low strain rate. Using the reformulation by Zhou et al. [2006],

the characteristic fragment size at low strain rate is shown to scale as

$$s_0 \propto \frac{EG_c}{\sigma_c^2}. \quad (4.8)$$

Fragment size increases with the critical energy release rate  $G_c$  and elastic moduli but decreases with the flaw nucleation threshold  $\sigma_c$  and remains independent of strain rate (Figure 4.11). Note that the parameter  $G_c$  bundles fracture energy per se and other plastic and frictional processes, and is often poorly known. As it estimates the energy required to create a new fracture area, it is sometimes abusively named fracture energy. It is related to the

critical intensity factor  $K_c$  through  $G_c = \alpha \frac{K_c^2}{E}$ , where  $\alpha$

depends on the loading condition (e.g., plane strain or plane stress). At high strain rate, kinetic energy dominates over elastic energy and Grady's law is restored (Figure 4.11). The transition between the two regimes takes place at the strain rate threshold:

$$\dot{\varepsilon}_0 = \frac{c_d \sigma_c^3}{E^2 G_c}. \quad (4.9)$$

The energy balance model is valid in case of equilibrium fragmentation, meaning that failure occurs as soon as a theoretical energy criterion is achieved [Grady, 2009]. However, it tends to overestimate grain size for nonequilibrium fragmentation, when there is a delay in failure [Miller *et al.*, 1999]. The reason for this is that during the additional time necessary for failure, new flaws can nucleate, propagate, and interact through stress waves.

These interactions between flaws become complex and numerical simulations are needed in order to model the change in fragment size with strain rate. The computations include cohesive elements between classical elastic elements. Cohesive elements are interface elements with edges that initially overlap. They can transmit forces  $F$  that depend on the displacement  $\delta$  of the edge of the cohesive elements (Figure 4.12). A cohesive law linking  $F$  to  $\delta$  is based on the physics of the individual failure process and must be established before performing the numerical simulations. Two such laws are commonly used: (1) Camacho and Ortiz [1996] introduced a linear weakening law that accounts for the finite propagation of individual fractures (Figure 4.12b). The area under the curve is related to the fracture energy  $G_c$ . (2) The law proposed by Miller *et al.* [1999] is (Figure 4.12c)

$$F = F_c \frac{\delta}{\delta_0} e^{-\frac{\delta}{\delta_0}}.$$

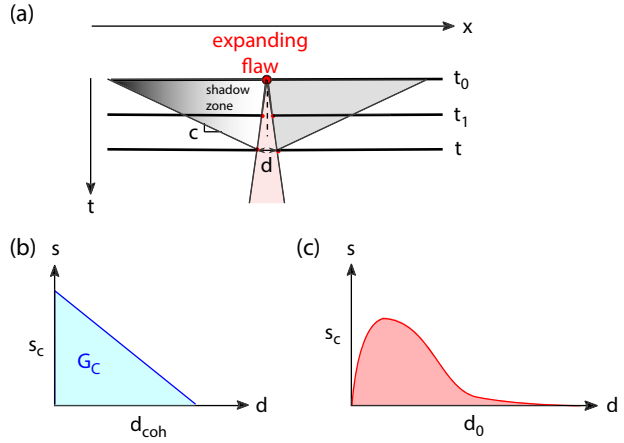


**Figure 4.12** Cohesive element model introduced in numerical fragmentation models to demonstrate progressive failure of flaws [Camacho and Ortiz, 1996]. (a) In the 1D configuration, cohesive elements are implemented as two node elements whose displacement  $\delta$  varies with time. During decohesion, healing waves are also released by the activated flaw. (b) With increasing displacement, flaws are less cohesive and sustain a smaller and smaller stress  $\sigma$ . The area under the curve is the fracture energy  $G_c$ . (c) Alternative cohesion model taking into account both activation and decohesion of the initial flaw.

When performing the numerical simulations, the problem regarding interactions between flaws is often reduced to the fragmentation of a dilating 1D bar. This is a geometry that is simple enough to focus on the effect of each individual process. Thanks to the increase in computational power of the last decades, it has now become possible to investigate a wide range of strain rates. Drugan [2001] first extended the model of Miller *et al.* [1999] by introducing a semianalytical model on a regular lattice of flaws. His simulations over three orders of strain rate magnitude confirmed the lower grain size compared to energy balance predictions, but they remained scattered (Figure 4.11). Using the simpler linear decay law of Camacho and Ortiz [1996], Zhou *et al.* [2006] were able to span eight orders of strain rate magnitude and found that their results would collapse on a single master law:

$$s = 4.5 \times \frac{s_0}{1 + 4.5 \times \left( \frac{\dot{\varepsilon}}{\dot{\varepsilon}_0} \right)^{2/3}} \quad (4.10)$$

where the characteristic grain size  $s_0$  and the transition strain rate  $\dot{\varepsilon}_0$  are the same as for Glenn and Chudnovsky [1986].

Stochastic effects have also been taken into account. Shenoy and Kim [2003] used the law by Miller *et al.* [1999] to estimate the effect of a heterogeneity  $\Delta\sigma_c$  at a flaw

nucleation threshold  $\sigma_c$ . They found that greater variability would induce greater grain size, because the weaker flaws will reduce the stress around them while they extend, effectively inhibiting further fragmentation by shadowing other potentially nucleating flaws with a higher strength (Figure 4.10). *Levy and Molinari* [2010] went further by testing several statistical strength distributions. They found that, after being normalized by an adequate interaction parameter, the characteristic fragment size distribution would collapse on the law of *Zhou et al.* [2006]. However, their model does not include any time delay in nucleation, so that their final grain size is smaller than that found by *Shenoy and Kim* [2003].

Figure 4.11 summarizes the results of the studies briefly discussed above. In spite of their increasing complexity, these numerical models tend to follow Grady's scaling law at higher strain rates. They also show that fragment size diminishes beyond a strain rate threshold, as suggested by the dynamic loading experiments. The applicability of the grain size studies is, however, limited by poor knowledge of the actual flaw distribution in strength and space. Moreover, partial opening of fractures leads to difficulties with converting the newly created fracture area into a corresponding grain size distribution. Discussing strain rate effect on material strength rather than grain size is an alternative to determining a critical strain rate threshold.

#### 4.4.3. Models Constraining the Increase in Strength with Increasing Strain Rate

The strength of a material can be modeled by reproducing the strain-stress curve, from which the peak stress acting on the sample during loading can be determined. A very simple example is the weakest link hypothesis, for which no fracture is activated (and the sample stays perfectly elastic) until the weakest flaw fails and instantaneously extends throughout the sample. In this extreme case of a brittle material, a fully analytical statistical strength law, the Weibull law [Weibull, 1939], can be derived, as long as the strength statistics of individual fractures are known (or equivalently, fracture length for Linear Elastic Fracture Mechanics).

Contrary to the discussion on fragment grain size, strength reflects the strain localization process that is initiated on the weakest flaws. Hence, if a uniform strength distribution is assumed for the sample flaws, this would greatly overestimate the sample strength. Discussion on sample strength is related to statistical approaches. The approach can stay fully stochastic so that the complexity of modern statistical physics (for example, percolation process, power laws in acoustic emissions, and phase transition modeling with increased correlation lengths [*Alava et al.*, 2006]) is maintained. However, this requires extensive numerical computational power.

A much easier approach is to assume that fractures remain at a moderate size all the time, so that at an intermediate scale (the mesoscopic scale) damage can be characterized by a local parameter. Usually, damage is described through a scalar parameter  $D$  that describes the diminution in elastic modulus:  $E = E(1 - D)$ . The parameter  $D$  lies between 0 (undamaged sample) and 1 (fully failed sample), so that an increasing amount of damage will induce strain softening and a diminution in strength. The same scheme can also be applied around an individual fracture to account for stress screening induced by the surrounding damage to implement self-consistent multiscale modeling of wing crack propagation [Paliwal and Ramesh, 2008; Bhat et al., 2012].

When multiple fractures develop, several questions arise: (1) How do the fracture statistics change in space and in length, and (2) how does this fracturing process affect the (macroscopic) stress-strain relationship?

*Hild* and coworkers [*Denoual and Hild*, 2000, 2002; *Hild et al.*, 2003; *Forquin and Hild*, 2010] tried to answer these questions by focusing on the change in activated fractures. They assumed a uniform distribution in space and a power law distribution in fracture strengths. The weakest flaws are activated first, but by the time they start to propagate through the sample, other cracks are activated (Figure 4.10). *Hild et al.* [2003] developed a statistical law that describes the number of fractures activated over time, which is controlled by the initial power law statistics in fracture length. The number of activated flaws saturates to a number that is lower than the number of initial flaws but is much higher than the single fracture that the Weibull model would have predicted for quasi-static loading. The number of activated fractures is converted into an effective damage parameter to acquire a full macroscopic stress-strain curve at constant stress rate  $\dot{\sigma}$ . From such an analytical solution it follows that peak strength scales as

$$\sigma_{c,dyn} \propto \left[ \frac{K_c^m}{\lambda_0} \right]^{\frac{1}{m+n}} \frac{n}{\dot{\sigma}^{m+n}}, \text{ where } K_c \text{ is the fracture toughness}$$

and  $\lambda_0$  is the initial density of the preexisting fracture. Strength increases with stress rate according to a power law that depends on the dimensionality of the problem ( $n=1$  for an expanding bar,  $n=3$  for an expanding sphere). Statistics in fracture length are included through the Weibull shape parameter  $m$  (smaller fractures are more preeminent at larger  $m$  values, yielding a smaller variability in sample strength). The scatter in sample strength at higher loading rate is reduced compared to quasi-static loading. The intersection between the quasi-static weakest link regime and the dynamic fragmentation regime defines a characteristic stress rate (Figure 4.13a) that scales as

$$\dot{\sigma}_c \propto \lambda_0^{-\frac{1}{m}} \Omega_0^{\frac{1}{n}} V^{-\frac{m+n}{mn}}. \quad (4.11)$$

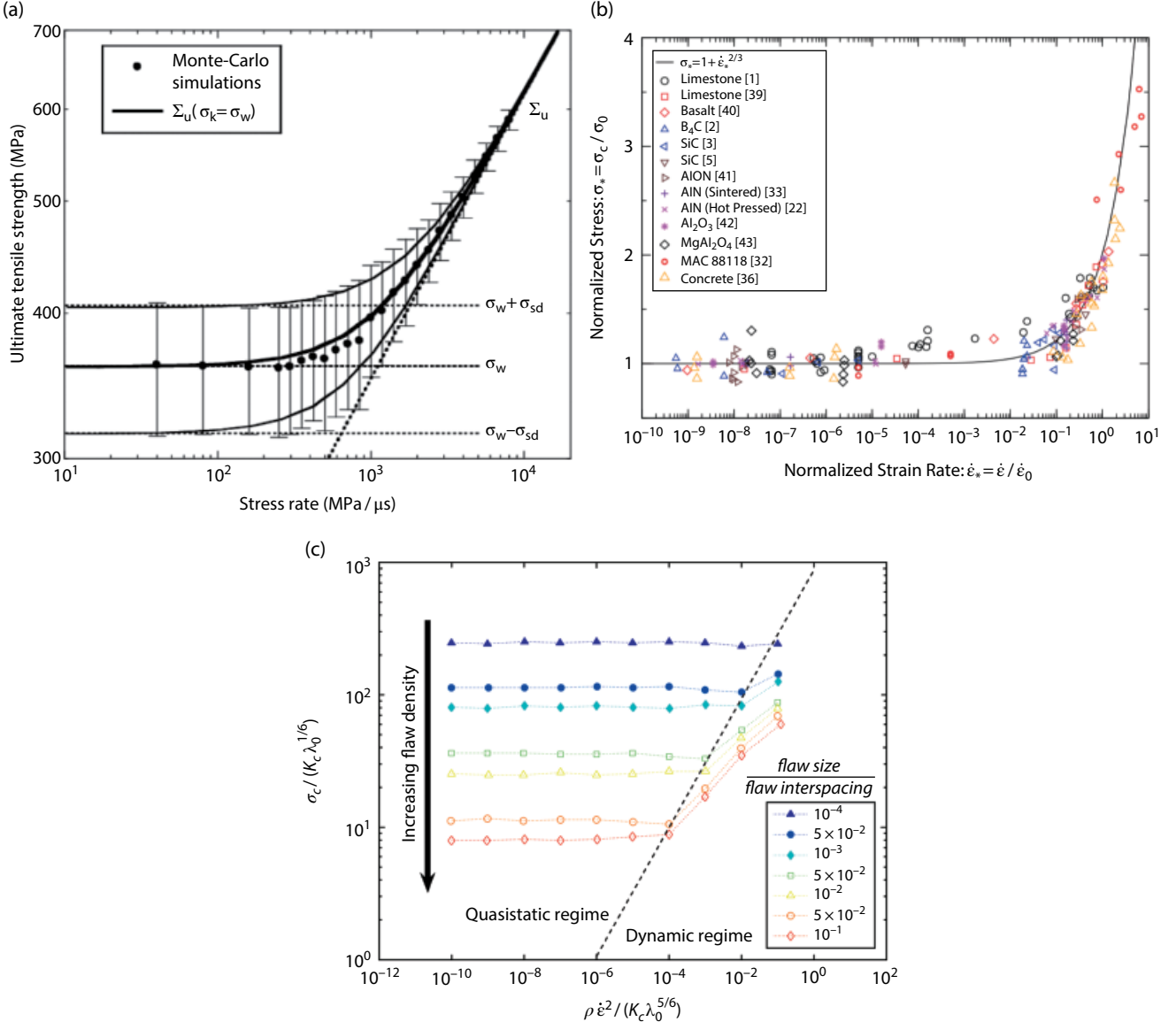


**Figure 4.13** Several models showing a sudden increase in strength with strain rate. Here, the focus is placed on three models that predict a dependence of the critical strain rate on the initial microstructural properties of the sample. (a) 1D model of expanding flaws [Hild *et al.*, 2003]. (b) Systematic study of the 2D model of Paliwal and Ramesh [2008]. Graph from Kimberley *et al.* [2013] (c) 3D study by Holland and McMeeking [2015] specifically focusing on the effect of flaw density.

The threshold is therefore strongly dependent on the initial microstructure of the material, since the initial size of the shadow zone  $\Omega_0$  and the initial fracture size increase the threshold and the flaw density  $\lambda_0$  decreases it. The threshold is also reduced for a larger volume  $V$  of the sample.

Since the analytical development of Hild *et al.* [2003], several micromechanical numerical models have been developed to describe high strain rate loading, especially in compression [Paliwal and Ramesh, 2008; Deshpande and Evans, 2008; Bhat *et al.*, 2012]. They assume that

flaws are wing cracks developing from the edges of pre-existing favorably oriented cracks [Ashby and Sammis, 1990]. Here, all flaws are assumed to have the same size so differences in activation stress are not taken into account. These models introduce elasto-dynamic effects affecting propagation of individual fractures. Mean field theory is used to model stress evolution at the sample scale [Paliwal and Ramesh, 2008; Deshpande and Evans, 2008], meaning that each flaw is surrounded by the same stress and can be screened by the accumulated damage to account for weakening. In this way, a peak stress can be

derived [Paliwal and Ramesh, 2008]. Deshpande and Evans [2008] developed this into a 3D model of wing crack development. The 2D model of Bhat *et al.* [2012] is more refined in its formulation of elasto-dynamic effects, with rigorous expressions of the dynamic stress intensity factor and taking into account the increase in dynamic fracture toughness with loading rate.

The model of Paliwal and Ramesh [2008] is popular in the mechanical engineering community since it is less computationally demanding than models that require full implementation of cohesive elements [e.g. Kraft *et al.*, 2008]. Hence, it has been used extensively to perform sensitivity studies [Graham-Brady, 2010; Kimberley *et al.*, 2013]. Kimberley *et al.* [2013] systematically explored the space parameter and found that all their results collapse on a normalized equation (Figure 4.13b):

$$\frac{\sigma}{\sigma_0} = 1 + \left( \frac{\dot{\varepsilon}}{\dot{\varepsilon}_0} \right)^{2/3}, \quad (4.12)$$

where the characteristic stress  $\sigma_0$  and the characteristic strain rate  $\dot{\varepsilon}_0$  depend on three material parameters ( $E$ ,  $K_c$  and  $c_d$ ) and two microstructural parameters describing the preexisting damage (average fracture size  $s$  and average flaw density  $\lambda_0$ ):

$$\sigma_0 \approx 2.4 \frac{K_c}{s \lambda_0^{1/4}} \quad (4.13)$$

$$\dot{\varepsilon}_0 \frac{\sigma_0 / E}{t_0} \approx 2.4 \frac{c_d K_c}{s E} \lambda_0^{1/4}. \quad (4.14)$$

Note that strain rate now increases with flaw density  $\lambda_0$ , contrary to the prediction of Hild *et al.* [2003]. This is due to the arbitrary choice of normalizing the critical strength  $\varepsilon_0 = \sigma_0 / E$  by the time  $t_0$ , a parameter that gives the time of stress wave propagating between two flaws. This parameter, which scales at  $\lambda_0^{-1/2}$ , could have been replaced by another scaling parameter. However, since the master law of equation (4.12) bundles several parameters together, including a small exponent (1/4) for flaw density (equation 4.13), the actual sensitivity to flaw density is difficult to assess, especially given the scatter in experimental data from Figure 4.13b.

Holland and McMeeking [2015] systematically studied the effect of the various parameters cited by Kimberley *et al.* [2013] (equations 4.13 and 4.14). Instead of the 2D model of Paliwal and Ramesh [2008], they used the 3D microstructural wing crack model [Deshpande and Evans, 2008]. They found that the effect of the initial flaw density is complex (Figure 4.13c) because the normalizing strain rate of the master curve effectively increases with strain rate (in their normalization, characteristic strain

rate scales as  $\lambda_0^{5/6}$ ), but the actual effect of the initial flaw density is that it reduces the strength of the sample and, more importantly, reduces the strain rate threshold at which the strength of the sample increases.

Elasto-dynamics embodies how stress waves affect fracture opening ahead of the fracture tip. The dynamic stress intensity factor diminishes with crack propagation speed [Freund, 1990; Bhat *et al.*, 2012], even when neglecting the transient loading of the fracture tip. In contrast, dynamic experiments on notched samples show that fracture initiation toughness increases with loading rate [Zhang and Zhao, 2013a], resulting in a higher strength of a material. Both of these effects are introduced in the model by Bhat *et al.* [2012]. They introduce an empirical law linking the dynamic initiation toughness  $K_c^d$  to the dynamic stress intensity factor  $\dot{K}$ :

$$\frac{K_c^d}{K_c} = 1 + \frac{\dot{K}}{K_c} \times 2 \times 10^{-5} [\text{s}], \quad (4.15)$$

where all quantities have been normalized to the static initiation toughness  $K_c$ . Also, when propagation commences, another empirical formulation describes the instant velocity of the crack tip and relates it to the dynamic stress intensity factor. Equation (4.15) introduces a dependence in strain rate from which Bhat *et al.* [2012] could model the increase in strength for a Dyonisus-Pentelicon marble at strain rates above  $10^2 \text{s}^{-1}$ . These results match the experimental results on this material. Despite the fact that the model lacks a thorough study of the effect of its individual parameters, it was easily extended to be applied to petrophysical issues, such as the sharp increase in permeability of pulverized rocks [Morton *et al.*, 2012; Perol and Bhat, 2013].

In this section, theoretical and numerical models all demonstrated that a strain rate threshold exists beyond which dynamic effects appear, leading to increasing strength and lower grain size, effectively inhibiting strain localization as previously observed in pulverized rocks. This threshold is partly controlled by the microstructural properties of the loaded solid. An intensively pre-damaged rock may be prone to further pulverization, which may affect the development of a very pulverized zone around an active fault [Doan and D'Hour, 2012].

## 4.5. DISCUSSION

### 4.5.1. Is Long-Distance Pulverization by Sub-Rayleigh Wave Speed Ruptures Possible?

Experimental results suggest that crystalline rocks can be pulverized near the surface (low confining pressure) when the strain rate during compressive loading

is  $\sim 200 \text{ s}^{-1}$  (Figure 4.8b). Rupture models can be used to verify if such loading conditions are realistic during an earthquake rupture event, especially at the relatively large distances from the fault at which pulverized rocks are observed (Figures 4.2 and 4.4a). The most basic rupture model is derived from Linear Elastic Fracture Mechanics and analyzes the asymptotic stress field around a moving crack tip [Freund, 1990]. Here, an earthquake rupture tip will be treated as a mode II crack. Relative to the large size of a crustal-scale fault, distances up to hundreds of meters can be assumed to fall within the crack tip zone.

The following solution is valid for rupture velocities below the Rayleigh wave speed velocity and has the following form for the singular stress field [Freund, 1990; equation 4.3.24]:

$$\sigma_{ij} = \frac{K_{II}(t)}{\sqrt{2\pi r}} \sum_{ij}^{\text{II}}(\theta, v), \quad (4.16)$$

where  $K_{II}$  is the elastic fracture intensity factor for a mode II fracture,  $r$  and  $\theta$  are polar coordinates relative to the fracture tip, and  $v$  is the fracture tip velocity. The variable  $\Sigma$  gives the angular variation of each stress component:

$$\begin{aligned} \sum_{11}^{\text{II}} &= -\frac{2\alpha_s}{D} \left\{ (1+2\alpha_d^2 - \alpha_s^2) \frac{\sin\left(\frac{1}{2}\theta_d\right)}{\sqrt{\gamma_d}} - (1+\alpha_s^2) \frac{\sin\left(\frac{1}{2}\theta_s\right)}{\sqrt{\gamma_s}} \right\} \\ \sum_{12}^{\text{II}} &= \frac{1}{D} \left\{ 4\alpha_d 2\alpha_s \frac{\cos\left(\frac{1}{2}\theta_d\right)}{\sqrt{\gamma_d}} - (1+\alpha_s^2) \frac{\cos\left(\frac{1}{2}\theta_s\right)}{\sqrt{\gamma_s}} \right\} \\ \sum_{22}^{\text{II}} &= \frac{2\alpha_s(1+\alpha_s^2)}{D} \left\{ \frac{\sin\left(\frac{1}{2}\theta_d\right)}{\sqrt{\gamma_d}} - \frac{\sin\left(\frac{1}{2}\theta_s\right)}{\sqrt{\gamma_s}} \right\}. \end{aligned} \quad (4.17)$$

$D$ ,  $\alpha_d$  and  $\alpha_s$  are material-dependent variables and  $\theta_{sld}$  and  $\gamma_{sld}$  depend on polar coordinates:

$$\begin{aligned} D &= 4\alpha_d\alpha_s - (1+\alpha_s^2)^2 \quad \alpha_{sld} = \sqrt{1 - \left(\frac{v}{c_{sld}}\right)^2} \\ \tan\theta_{sld} &= \alpha_{sld} \tan\theta \quad \gamma_{sld} = \sqrt{1 - \left(\frac{v \sin\theta}{c_{sld}}\right)^2}. \end{aligned} \quad (4.18)$$

Here,  $c_s$  and  $c_d$  are the S- and P-wave velocities, respectively. Note that  $D$ , called the Rayleigh function, vanishes

when the rupture tip velocity approaches the Rayleigh wave speed.

The energy-term in equation (4.16) is  $K_{II}$ , which can be related to the energy release rate  $G$ :

$$G = \frac{1-v^2}{E} A_{II}(v) K_{II}^2 \quad A_{II} = \frac{v^2 \alpha_s}{(1-v)c_s^2 D}, \quad (4.19)$$

where  $A_{II}$  is a function of the rupture tip speed,  $E$  is Young's modulus and  $v$  is Poisson's ratio. In turn, the energy release rate term can be adjusted to incorporate cohesive zone models so that the singularity of the stress field at the crack tip is eliminated [e.g., Ida, 1972; Poliakov et al., 2001; Rice et al., 2005]. Values of the energy release rate  $G$  (or substitute  $K_{II}$ -value) show considerable uncertainty because this parameter is difficult to define for earthquake ruptures and it changes with rupture velocity. In the literature,  $G$  values constrained for earthquakes range from  $1 \times 10^2$  to  $1 \times 10^8 \text{ J/m}^2$  [Kostrov and Das, 1988; Scholz, 2002 and references therein; Abercrombie and Rice, 2005].

From equations (4.16) and (4.17), it follows that the maximum stress and strain decay with  $r^{-0.5}$  and the strain rate decays with  $r^{-1.5}$  with increasing distance from the rupture tip (Figure 4.14a). Computations using the above equations show that comminution with extreme grain size reduction associated with gouge formation very close to the fault plane (mm scale) are likely to occur during a sub-Rayleigh wave speed rupture [Reches and Dewers, 2005]. But, 100 m from the fault core, a strain rate of  $\sim 0.2 \text{ s}^{-1}$  is insufficient to exceed the pulverization threshold [Doan and Gary, 2009]. Similar calculations fit the pulverization threshold of Carrara marble at 25 cm from the fault core [Doan and Billi, 2011]. For all these calculations, a  $K_{II}$  value of 30 MPa/m<sup>0.5</sup> was used.

Using a similar value for  $G$  as the studies above, a first-order approximation of the distance from the fault at which an intact igneous crystalline rock would be pulverized has been obtained. For this purpose, a pulverization strain rate threshold of  $200 \text{ s}^{-1}$  was taken. This yields a maximum pulverization distance of 6.2 and 26.2 cm for rupture velocities of respectively 0.8 and 0.91 times the shear wave speed (Figure 4.14b). Since the value used for  $G$  is in the lower range of values reported, an extreme value of  $10^8 \text{ J/m}^2$  has also been used. This led to a significant increase in maximum distance to 3.19 m (Figure 4.14b).

According to several geophysical and petrophysical properties, elastic properties in the damage zone are altered and, for example, the Young's modulus may decrease by 50% [Faulkner et al., 2006; Rempe et al., 2013]. This initial damage has a twofold effect: (1) The Linear Elastic Fracture Mechanics rupture model indicates strain rates are higher at greater distance from the

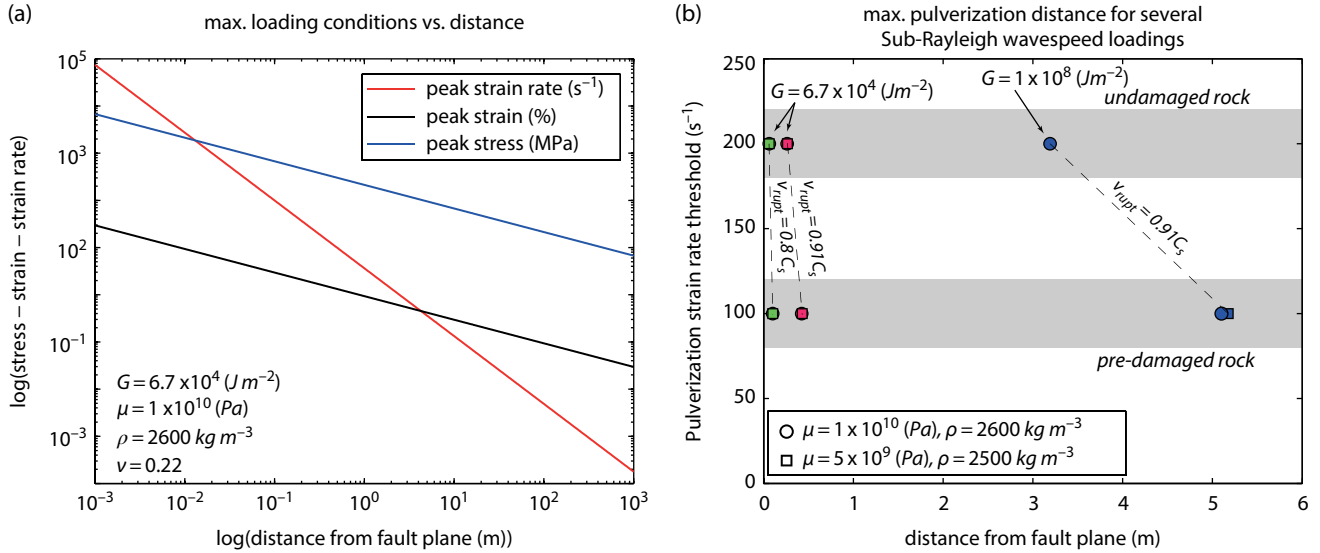


**Figure 4.14** (a) Variation in the maximum stress (blue), strain (black), and strain rate (red) with distance from the fault according to a linear elastic fracture mechanics approach. The parameters used for this model are given in the bottom left corner. (b) Maximum distance of the pulverization boundary from the fault plane versus the preset pulverization strain rate threshold for several different rupture conditions and damage zone rocks. A  $200 s^{-1}$  threshold for pristine rock and a  $100 s^{-1}$  for damaged rock have been used. Furthermore, initial (circle) or reduced (square) mechanical properties are used. Two extremes for the energy-release-rate are applied as indicated, as well as different rupture velocities. See electronic version for color representation.

fault [Doan and Billi, 2011], and (2) initially damaged rocks show a pulverization strain rate threshold reduced by up to  $\sim 50\%$  [Doan and D'Hour, 2012; Aben et al., 2016] (Figure 4.8b). Effect 1 causes, for the most extreme case ( $G = 10^8 \text{ J/m}^2$ ), an increase of at most several centimeters in the pulverization boundary (Figure 4.14b). Effect 2, tested by reducing the pulverization strain rate threshold by 50% to  $100 s^{-1}$ , causes an increase in distance of  $\sim 62\%$  for all rupture models (Figure 4.14b). In terms of absolute distance, this causes the pulverization boundary to migrate 5.18 m for the most extreme case.

Systematic loading by sub-Rayleigh ruptures without preferred rupture direction would result in a symmetric damage zone geometry (Figure 4.15a), where a band of pulverized rocks close to the fault is followed by dynamically fractured rock. The pulverization boundary is several orders of magnitude closer to the fault than the damage zone boundary. At depth, the coseismic damage zone thins significantly because confinement increases the pulverization threshold [Yuan et al., 2011]. It follows that strain rates induced by sub-Rayleigh wave speed ruptures are insufficient to exceed the pulverization threshold at distances from the fault where pulverized rocks have been observed (100 m or more). Nonetheless, near-fault pulverization during sub-Rayleigh wave speed ruptures is likely to occur and might be important for the formation of fault gouges [Reches and Dewers, 2005] and cataclasites.

#### 4.5.2. Alternative Conditions for Coseismic Pulverization

Several alternatives that might solve the dilemma outlined above are discussed here. Two general aspects can be taken into account: the rock response to dynamic compressive loading under different conditions (e.g., saturated) that might reduce the pulverization threshold, and rupture mechanisms other than sub-Rayleigh wave speed ruptures possibly causing transient loading conditions that are sufficient for pulverization at great distance from the fault plane. Because these alternatives represent ongoing research and will require further experimental development, they are briefly discussed below.

##### 4.5.2.1. Different Conditions During Loading: Pore Fluids

The established pulverization thresholds were determined under dry conditions, with and without confining pressure and with a variable amount of dynamically induced initial damage. However, the behavior of the pulverization threshold at other conditions has not yet been studied. One such condition that is likely to be found in nature is the presence of pore fluids. A high loading rate makes it hard for pore fluids to dissipate the stress, with the result that the rock is in an undrained state. According to the poroelastic theory, this would lead to a significant drop in effective failure strength. However, the pore fluid

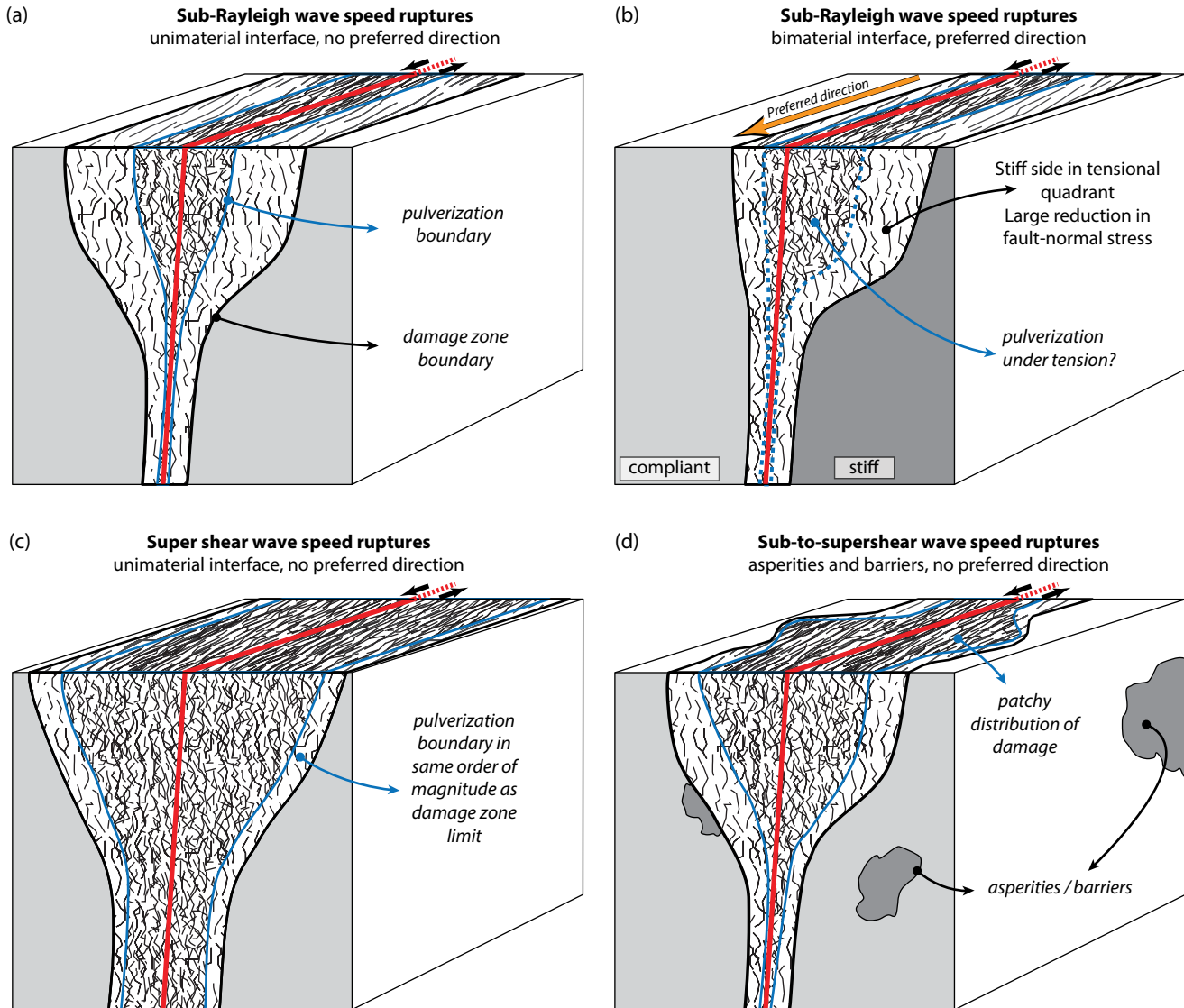


**Figure 4.15** Conceptual damage zone geometries for several different rupture types. The red line indicates the fault plane with sense of movement (black arrows). The pulverized interval is bordered by a blue line, the damage zone boundary by black. (a) Geometry for systematic bilateral sub-Rayleigh rupture. The zone of pulverized rocks has a small width and thins quickly with depth. (b) Geometry for unilateral sub-Rayleigh ruptures with a preferred direction. The damage would be concentrated in the tensional quadrant, including pulverized rocks. (c) Bilateral supershear rupture geometry with a much larger zone of pulverized rocks within the same order of magnitude as the damage zone boundary. Pulverized rocks can extend to much greater depths relative to sub-Rayleigh ruptures. (d) Asperity- and barrier-controlled damage zone geometry that shows a much more patchy distribution of damage along the fault due to dynamic rupture velocities from sub- to supershear. See electronic version for color representation.

effect on the pulverization strain rate threshold is still unknown and might be subject to future research.

#### 4.5.2.2. Sub-Rayleigh Wave Speed Loading Along a Bimaterial Interface

The loading conditions of a sub-Rayleigh rupture changes when the rupture occurs along a bimaterial

interface instead of a single material interface. The difference in elastic wave velocities between two sides of the fault leads to the development of a so-called Weertman-pulse or wrinkle-like rupture [Weertman, 1980; Andrews and Ben-Zion, 1997; Shi and Ben-zion, 2006]. This means that a dilatant “wrinkle” originates in the more compliant material that reduces or increases the fault-normal stress,

depending on whether the more compliant side is in the compressional or tensional quadrant of the rupture. Consequently, the fault-normal stress is reduced or increased on the stiffer side as well. Rupture models [Ben-Zion, 2001; Ben-Zion and Shi, 2005; Shi and Ben-Zion, 2006] show that a rupture in the direction of slip of the more compliant material is more stable and thus should be preferred. It therefore follows that the stiffer side of a fault should suffer more systematic extensional loading conditions.

Several authors relate the asymmetric distribution of pulverized rocks (that are more abundant on the stiffer side of the faults) to this systematic directional rupture property [Dor et al., 2006a, 2008; Mitchell et al., 2011] (Figure 4.15b). It follows that pulverized rocks must have formed during extensional loading. However, the limited data on tensile experiments do not reveal the same pervasive fracturing as that obtained under compressive dynamic loading. The contribution to the increase in strain rate is not yet fully understood, but the presence of Adams instabilities [Adams, 1995] during wrinkle-like ruptures can produce local short bursts in slip velocity [Shi and Ben-Zion, 2006]. This might result in local high strain rate peaks and subsequent pulverization.

On another note, the reduction in fault-normal stress related to wrinkle-like ruptures does fit the loading conditions that are necessary for hydrofracturing by a transient stress drop. However, wrinkle-like ruptures have a depth limit of  $\sim 3$  km [Ben-Zion and Shi, 2005] while pulverization by hydrofracturing needs sufficiently high fluid pressures that could be related to depth. Future research could focus on this promising mechanism.

#### 4.5.2.3. Supershear Wave Speed Loading

Several authors suggest that supershear velocity ruptures are capable of pulverization-inducing loading conditions [Doan and Gary, 2009; Yuan et al., 2011]. The stress field around a supersonic rupture tip that travels at constant velocity  $v$  ( $c_s < v < c_d$ ) has two nearly decoupled contributions: the P- and S-wave speed stress fields, with  $c_s$  the shear wave velocity and  $c_d$  the P-wave velocity of the material, respectively. Three velocity-regimes exist for supershear ruptures: unstable between  $c_s < v < \sqrt{2}c_s$ , the unique value  $v = \sqrt{2}c_s$ , and the stable regime  $\sqrt{2}c_s < v < c_d$ . At  $v = \sqrt{2}c_s$  the S-wave contribution to the rupture tip stress field disappears.

For the problem at hand, the most relevant modification to equation (4.16) to describe the P-wave contribution of the stress field is the replacement of the factor  $r^{-0.5}$  by  $r^{-q}$  where  $q$  varies between 0 and 0.5, depending on the rupture velocity [Freund, 1990; Dunham and Bhat, 2008; Mello et al., 2010]. This means that the P-wave contribution to the stress, strain, and strain-rate fields attenuates to a lesser extent with increasing distance from the rupture tip,

except for the unique case of  $v = \sqrt{2}c_s$ ,  $q = 0.5$ . Even more important, a Mach-cone forms at  $q \neq 0.5$  since the radiated S-waves are slower than the rupture tip itself. Therefore, the S-wave loading contribution does not attenuate with distance [Bernard and Baumont, 2005], at least not up to a certain length scale related to the maximum depth of the seismogenic zone [Dunham and Bhat, 2008; Ampuero, 2014]. For the Mach-cone, equation (4.16) will include the Heaviside step function, which implies a theoretical infinite loading rate when the Mach-cone travels through the damage zone rocks.

The loading conditions during a supershear rupture with  $v \neq \sqrt{2}c_s$  thus seem to be sufficient for pulverization at great distance from the fault. Even more, since the attenuation is nearly nonexistent, the pulverization boundary will be of the same order of magnitude as the damage zone boundary itself. This is also observed in the field (Figure 4.4a). Systematic bilateral ruptures would result in a symmetric damage zone with a large amount of pulverized rock (Figure 4.15c). Supershear ruptures have been observed on large faults with long straight sections only [Bouchon et al., 2001, 2010; Bouchon and Vallée, 2003; Dunham and Archuleta, 2004], which matches the observation of pulverized rocks at such faults. A supershear rupture is more likely to develop in the direction of slip of the stiffer material in case of a bimaterial fault surface [Weertman, 2002; Xia et al., 2005], resulting in an asymmetric damage distribution similar to that illustrated in Figure 4.15b, although it depends on whether more damage occurs in the tensile or compressive quadrant. However, the influence of asymmetric damage seems to eliminate this bimaterial effect [Bhat et al., 2010].

A major remark for supershear as a damaging mechanism is that shear wave loading induces the high strain rates far from the fault. The experiments described in this review only focus on P-wave loading, and to our knowledge, no studies have focused on pulverization by shear stress waves. Also, S-wave Mach cones have zero divergence; thus, no volumetric deformation is expected. This marks a current gap in knowledge.

#### 4.5.2.4. Heterogeneities Along the Rupture Interface

Heterogeneities along the fault plane, such as asperities and barriers, can cause acceleration of a sub-Rayleigh wave speed rupture toward supershear rupture speeds [Dunham et al., 2003; Dunham, 2007; Latour et al., 2013]. This mechanism requires less overall energy than the development of a stable supershear rupture. Such dynamic sub-to-super shear ruptures are likely to cause significant loading conditions far from the fault plane. However, pulverized rocks resulting from such ruptures would have a patchy distribution along the fault. These patches are geometrically related to the asperities or barriers (Figure 4.15d).

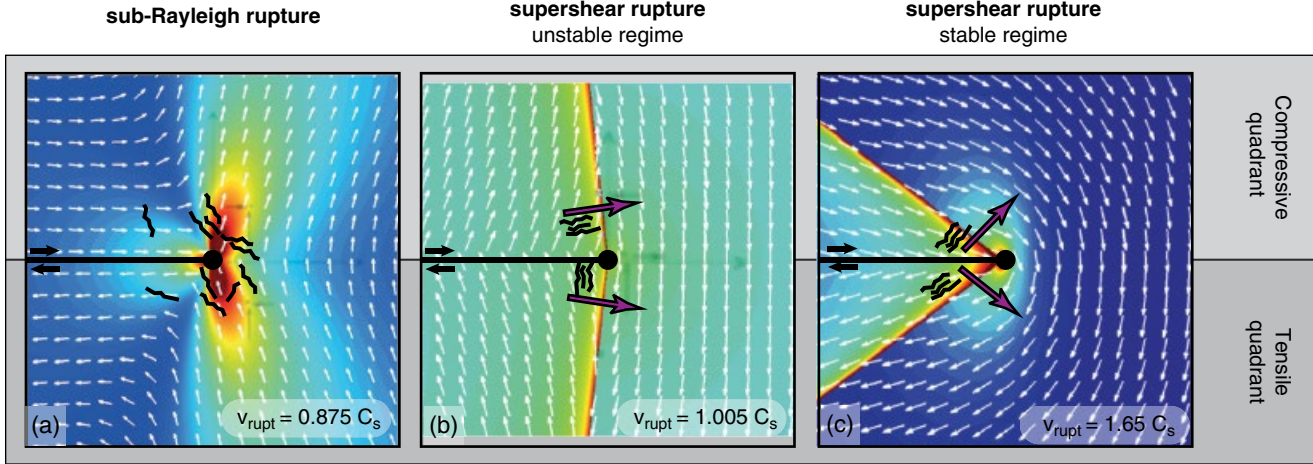


**Figure 4.16** Particle motion fields for different rupture velocities (bottom right corner) in a homogeneous elastic material [adjusted from Mello *et al.*, 2010]. The purple arrows show the direction of maximum compressive or tensile loading rate, which is the gradient of the particle velocity field. Illustrative fractures indicate the expected fracture orientation, based on the maximum loading rate direction. The compressive and tensile quadrants are indicated on the right side. (a) Sub-Rayleigh wave speed rupture. (b), (c) Two supershear ruptures with unstable (b) and stable (c) rupture velocity. See electronic version for color representation.

#### 4.5.3. Damage Anisotropy and Loading Conditions

Up to now, allowance has been made for maximum distance from the fault, depth, and asymmetric distribution of pulverized rock when analyzing the type of rupture necessary for pulverization. Another property now needs to be addressed: the damage anisotropy that has been observed in the field [Rempe *et al.*, 2013] as well as in laboratory experiments [Aben *et al.*, 2016]. If compressive SHPB experiments are projected to the setting of a fault zone to fit in with the anisotropy measured by Rempe *et al.* [2013], the transient compressive loading is parallel to the fault. Possibly, such anisotropy can be coupled to certain rupture modes. A qualitative illustration is given here of the approach that can be followed in analyzing fault rock anisotropy in combination with rupture models. Moreover, not all rupture mechanisms have been taken into consideration.

Although the upscaling of a 1D lab experiment to a complicated 3D radial stress field around a rupture tip is not straightforward, it is nonetheless worth discussing the direction of maximum extension or compression rate during some of the previously discussed rupture types in relation to damage anisotropy (Figure 4.16, adjusted from Mello *et al.* [2010]). Note that the direction of maximum stress is not necessarily the same as the direction of maximum loading rate. The effect of such decoupling (in the experiments both directions are similar) on damage anisotropy seems to be an open question. Besides, the maximum principal stress direction can vary from case

to case because the far-field stress needs to be taken into account. This is not the case for the loading rate: the tectonic loading rates are negligible with respect to coseismic transient loading rates. Figure 4.16 shows particle velocities, with the maximum gradient of the particle velocities being indicative of the direction of the maximum loading rate.

The direction of maximum loading rate rotates during a sub-Rayleigh wave speed rupture from fault (sub-)parallel toward (sub-)perpendicular (up to  $110^\circ$ ) when the stress field passes by a certain static point along the fault. The rotation thus occurs when stress is highest. This type of rupture is not therefore subject to unidirectional loading, making it hard to infer a clear anisotropy (Figure 4.16a). The S-wave Mach cones of unstable and stable supershear ruptures do have a unidirectional loading rate direction: an unstable supershear rupture has a maximum loading rate subparallel to the fault (Figure 4.16b). In the stable supershear regime the maximum loading rate is oriented at a higher angle to the fault (Figure 4.16c), although in both cases the angle changes with rupture speed. At  $v=\sqrt{2}C_s$  the S-wave contribution disappears and coseismic damage will be more or less similar to the Sub-Rayleigh wave case.

Regardless of the orientation, fracture damage anisotropy can be expected to develop by the unilateral directed loading rate during supershear rupture (Figure 4.16b, c). This mechanism has been used to explain the formation of large cracks parallel to the fault during the 2001 Kunlun earthquake [Bhat *et al.*, 2007].

#### 4.5.4. Other Implications for Fault Zones

Pulverization and coseismic damage are energy sinks that need to be taken into account for earthquake energy budgets. Seismic signals from pulverization-inducing earthquakes are different from the seismic signal predicted by an elastic model because pulverized rocks lose nearly all cohesion (Figure 4.9a). The stress amplitude of the wave is also significantly reduced. Such properties, observed in laboratory experiments, could provide a link to seismological observations of a major earthquake.

Pulverized rocks have different petrophysical and hydrological properties compared to nonpulverized damage zone rocks. Due to the contrast, post- and interseismic healing and sealing rates might differ spatially. For instance, *Richard et al.* [2014] showed that zones of microfracturing (i.e., pulverization) will heal faster than zones with only macroscopic fractures. This would result in a heterogeneous redistribution of strength in the damage zone during the interseismic phase. However, the reduced permeability of pulverized rocks may delay the transport of the precipitation product, or the increased surface area of pulverized rocks could increase the creep processes related to pressure solution. On a longer timescale this might result in differentiation of pulverized rocks from the rest of the damage zone in both mechanical and mineralogical terms. Possibly, such a differentiation becomes important for the formation of fault rocks that are prone to permanent creep.

### 4.6. PERSPECTIVES AND CONCLUSION

Pulverized rocks have mainly been observed in crystalline and cohesive granular rocks such as granitic rocks and limestones or dolostones, with the exception of sandstone. Also, pulverization is observed mostly near the surface along major strike-slip faults and is a shallow crustal feature (<10 km depth). The classic field definition of pulverization holds true only for igneous crystalline rocks and is ambiguous for limestones, dolostones, and sandstones. More experimental work is necessary to determine the nature of pulverization in these lithologies so that, with the help of dynamic fracture mechanics models, a more generalized definition can be developed.

Dynamic experiments in compression show that crystalline rocks can be pulverized under strain rates that fall well within the fracture kinetics controlled damage field. Pulverization in igneous crystalline rocks is revealed as a sharp threshold in strain rate. Whether other lithologies hold such a similar behavior remains to be investigated. Experimental studies show that the pulverization threshold decreases by initial damage or successive milder strain rate loadings but that it increases with confining pressure. The

change in pulverization threshold during other conditions, such as saturation, should be subject to future research.

An attempt has been made to link field observations with the experimentally determined loading conditions necessary for pulverization. For this purpose, a simple sub-Rayleigh wave speed rupture model has been used. This shows that this type of rupture is not capable of exceeding the pulverization threshold for rocks located far from the fault (of the order of 100 m), although it can pulverize near-fault rocks. A qualitative discussion regarding the loading conditions of other types of ruptures suggests that supershear ruptures would be capable of pulverization at these long distances from the fault, although shear stress wave loading by supershear Mach cones has not yet been studied in laboratory experiments, and the question of whether S-waves can pulverize rocks remains open to discussion for the time being.

The issue of damage asymmetry across the fault plane, which has been observed for several fault systems, has not yet been solved. Either supershear ruptures or wrinkle-like ruptures could develop a unilateral propagation preference, or the lithology on the opposite side of the fault reacts differently to dynamic loading conditions. A better understanding of the rock response to dynamic tensile loading must also be developed, since these loading conditions contribute 50% of an earthquake rupture. Another pulverization mechanism, hydrofracturing by a transient stress drop, might be a promising alternative to compressive dynamic loading.

This review has outlined the link between field observations and experimental work regarding pulverized rocks. The potential constraints that these experiments can give on the rupture mechanics of large faults is of great significance, and therefore experimental research on pulverized rocks and coseismic damage will be of ongoing interest to the fault mechanics community. Finally, the specific stress waves observed in laboratory pulverization experiments are different from those where rocks are fractured only. This difference, seen in the laboratory, could also be looked for on seismograms of natural earthquakes and therefore extend our understanding of strain dissipation during major earthquakes.

### ACKNOWLEDGMENTS

The authors would like to thank Anne-Marie Boullier for her helpful comments on the field section and her expertise on the Nojima fault in particular. The authors also thank Renaud Toussaint for the high speed camera acquisition. FMA was funded by the European Union's Seventh Framework Programme for research, technological development, and demonstration under grant agreement no. 316889 (ITN FlowTrans).

**Table 4.1** List of symbols.

$A$	Surface area
$A_B, A_S$	(bar, sample)
$c_d$	P wave velocity (velocity of dilatational stress wave)
$c_s$	S wave velocity (velocity of shear stress wave)
$D$	Fractal dimension (section 1)
$D$	Damage parameter (section 4)
$D$	Rayleigh function (section 5)
$\delta$	Displacement of cohesive elements (section 4)
$E$	Young's modulus
$\varepsilon$	Strain
$\dot{\varepsilon}$	Strain rate
$\dot{\varepsilon}_0$	Characteristic strain rate (= threshold in strain rate for pulverization)
$F$	Force
$F_I, F_R, F_T$	(incident, reflected, transmitted)
$G$	Energy release rate
$G_c$	Critical energy release rate
$K$	Stress intensity factor at a crack tip
$K_{II}$	Stress intensity factor at a mode II crack tip
$K'$	Stress intensity factor rate (= time derivative of $K$ )
$K_C$	Fracture toughness (= critical stress intensity factor)
$K^d$	Dynamic fracture toughness (= critical stress intensity factor)
$L$	Length of the sample
$\lambda_0$	Initial density of flaws in the solid
$m$	Shape parameter of Weibull function
$n$	Dimension of the model
$N$	Number of fragments
$\nu$	Poisson's ratio
$\theta$	Angle to the rupture plane (used in polar coordinates)
$r$	Distance from rupture tip (used in polar coordinates)
$R$	Grain size characteristic radius
$\rho$	Mass density
$\sigma$	Size of individual fragments after fragmentation (=radius for spherical fragments)
$\sigma_0$	Characteristic fragment size
$\sigma$	Stress
$\sigma_c$	Critical stress for activation of an individual flaw
$\Sigma$	Angular stress variation at the crack tip
$\tau$	Particle (in the sense on continuum mechanics)
$v$	Particle velocity (section 3 and 4)/Rupture velocity (section 5)
$U_K$	Kinetic energy
$V$	Volume of the sample
$\Omega_0$	Minimal size of the shadow zone around each propagating flaw

- Abercrombie, R. E., and J. R. Rice (2005), Can observations of earthquake scaling constrain slip weakening?, *Geophys. J. Int.*, 162(2), 406–424, doi:10.1111/j.1365-246X.2005.02579.x.
- Adams, G. G. (1995), Self-excited oscillations of two elastic half-spaces sliding with a constant coefficient of friction, *J. Appl. Mech.*, 62(4), 867–872, doi:10.1115/1.2896013.
- Agosta, F., and A. Aydin (2006), Architecture and deformation mechanism of a basin-bounding normal fault in Mesozoic platform carbonates, central Italy, *J. Struct. Geol.*, 28(8), 1445–1467, doi:10.1016/j.jsg.2006.04.006.
- Alava, M. J., P. K. V. V. Nukala, and S. Zapperi (2006), Statistical models of fracture, *Adv. Phys.*, 55(3-4), 349–476, doi:10.1080/00018730300741518.
- Ampuero, J.-P. (2014), Physical limits on damaged fault zone thickness: The role of seismogenic depth, in *AGU Fall Meeting 2014*, San Francisco.
- Andrews, D. J., and Y. Ben-Zion (1997), Wrinkle-like slip pulse on a fault between different materials, *J. Geophys. Res.*, 102(B1), 553–571, doi:doi:10.1029/96JB02856.
- Ashby, M. F., and C. G. Sammis (1990), The damage mechanics of brittle solids in compression, *Pure Appl. Geophys.*, 133(3), 489–521.
- Asprone, D., E. Cadoni, A. Prota, and G. Manfredi (2009), Dynamic behavior of a Mediterranean natural stone under tensile loading, *Int. J. Rock Mech. Min. Sci.*, 46(3), 514–520, doi:10.1016/j.ijrmms.2008.09.010.
- Ben-Zion, Y. (2001), Dynamic ruptures in recent models of earthquake faults, *J. Mech. Phys. Solids*, 49(9), 2209–2244, doi:10.1016/S0022-5096(01)00036-9.
- Ben-Zion, Y., and Z. Shi (2005), Dynamic rupture on a material interface with spontaneous generation of plastic strain in the bulk, *Earth Planet. Sci. Lett.*, 236(1-2), 486–496, doi:10.1016/j.epsl.2005.03.025.
- Bernard, P., and D. Baumont (2005), Shear Mach wave characterization for kinematic fault rupture models with constant supershear rupture velocity, *Geophys. J. Int.*, 162(2), 431–447, doi:10.1111/j.1365-246X.2005.02611.x.
- Bhat, H. S., R. L. Biegel, A. J. Rosakis, and C. G. Sammis (2010), The effect of asymmetric damage on dynamic shear rupture propagation II: With mismatch in bulk elasticity, *Tectonophysics*, 493(3-4), 263–271, doi:10.1016/j.tecto.2010.03.020.
- Bhat, H. S., R. Dmowska, G. C. P. King, Y. Klinger, and J. R. Rice (2007), Off-fault damage patterns due to supershear ruptures with application to the 2001 Mw 8.1 Kokoxili (Kunlun) Tibet earthquake, *J. Geophys. Res.*, 112(B6), B06301, doi:10.1029/2006JB004425.
- Bhat, H. S., A. J. Rosakis, and C. G. Sammis (2012), A micro-mechanics based constitutive model for brittle failure at high strain rates, *J. Appl. Mech.*, 79, 031016.1–031016.12, doi:10.1115/1.4005897.
- Bouchon, M., M.-P. Bouin, K. Hayrullah, M. Nafi Toksoz, M. Dietrich, and A. J. Rosakis (2001), How fast is rupture during an earthquake? New insights from the 1999 Turkey earthquakes, *Geophys. Res. Lett.*, 28(14), 2723–2726.
- Bouchon, M., H. Karabulut, M.-P. Bouin, J. Schmittbuhl, M. Vallée, R. Archuleta, S. Das, F. Renard, and D. Marsan (2010), Faulting characteristics of supershear earthquakes, *Tectonophysics*, 493(3-4), 244–253, doi:10.1016/j.tecto.2010.06.011.

## REFERENCES

- Aben, F. M., M.-L. Doan, T. M. Mitchell, R. Toussaint, T. Reuschlé, M. Fondriest, J.-P. Gratier, and F. Renard (2016), Dynamic fracturing by successive coseismic loadings leads to pulverization in active fault zones, *J. Geophys. Res. Solid Earth*, 121, 1–23, doi:10.1002/2015JB012542.

- Bouchon, M., and M. Vallée (2003), Observation of long supershear rupture during the magnitude 8.1 Kunlunshan earthquake, *Science*, 301(5634), 824–6, doi:10.1126/science.1086832.
- Boullier, A.-M. (2011), Fault-zone geology: Lessons from drilling through the Nojima and Chelungpu faults, *Geol. Soc. London, Spec. Publ.*, 359(1), 17–37, doi:10.1144/SP359.2.
- Brune, J. N. (2001), Fault-normal dynamic unloading and loading: An explanation for “non-gouge” rock powder and lack of fault-parallel shear bands along the San Andreas fault, in *AGU Fall Meeting 2001*, San Francisco.
- Bürgmann, R., D. D. Pollard, and S. J. Martel (1994), Slip distributions on faults: effects of stress gradients, inelastic deformation, heterogeneous host-rock stiffness, and fault interaction, *J. Struct. Geol.*, 16(12), 1675–1690, doi:10.1016/0191-8141(94)90134-1.
- Cadoni, E. (2010), Dynamic characterization of orthogneiss rock subjected to intermediate and high strain rates in tension, *Rock Mech. Rock Eng.*, 43(6), 667–676, doi:10.1007/s00603-010-0101-x.
- Camacho, G. T., and M. Ortiz (1996), Computational modelling of impact damage in brittle materials, *Int. J. Solids Struct.*, 33(20–22), 2899–2938, doi:10.1016/0020-7683(95)00255-3.
- Chen, W., and B. Song (2011), *Split Hopkinson (Kolsky) Bar Design, Testing and Applications*, 1st ed., Springer, New York.
- Crampin, S., and D. Booth (1985), Shear-wave polarizations near the North Anatolian Fault - II. Interpretation in terms of crack-induced anisotropy, *Geophys. J. R. Astron. Soc.*, 83, 75–92, doi:10.1111/j.1365-246X.1985.tb05157.x.
- Davies, E. D. H., and S. C. Hunter (1963), The dynamic compression testing of solids by the method of the Split Hopkinson Pressure Bar, *J. Mech. Phys. Solids*, 11, 115–179.
- Davies, T. R. H., M. J. McSaveney, and R. D. Beetham (2006), Rapid block glides : Slide-surface fragmentation in New Zealand’s Waikaremoana landslide, *Q. J. Eng. Geol. Hydrogeol.*, 39, 115–129.
- Davies, T. R. H., M. J. McSaveney, and C. J. Boulton (2012), Elastic strain energy release from fragmenting grains: Effects on fault rupture, *J. Struct. Geol.*, 38, 265–277, doi:10.1016/j.jsg.2011.11.004.
- Denoual, C., and F. Hild (2000), A damage model for the dynamic fragmentation of brittle solids, *Comput. Methods Appl. Mech. Eng.*, 183(3–4), 247–258, doi:10.1016/S0045-7825(99)00221-2.
- Denoual, C., and F. Hild (2002), Dynamic fragmentation of brittle solids: A multi-scale model, *Eur. J. Mech.*, 21, 105–120.
- Deshpande, V. S., and A. G. Evans (2008), Inelastic deformation and energy dissipation in ceramics: A mechanism-based constitutive model, *J. Mech. Phys. Solids*, 56(10), 3077–3100, doi:10.1016/j.jmps.2008.05.002.
- Doan, M.-L., and A. Billi (2011), High strain rate damage of Carrara marble, *Geophys. Res. Lett.*, 38(19), doi:10.1029/2011GL049169.
- Doan, M.-L., and V. D’Hour (2012), Effect of initial damage on rock pulverization along faults, *J. Struct. Geol.*, 45, 113–124, doi:10.1016/j.jsg.2012.05.006.
- Doan, M.-L., and G. Gary (2009), Rock pulverization at high strain rate near the San Andreas fault, *Nat. Geosci.*, 2(10), 709–712, doi:10.1038/ngeo640.
- Dor, O., Y. Ben-Zion, T. K. Rockwell, and J. N. Brune (2006b), Pulverized rocks in the Mojave section of the San Andreas Fault Zone, *Earth Planet. Sci. Lett.*, 245(3–4), 642–654, doi:10.1016/j.epsl.2006.03.034.
- Dor, O., J. S. Chester, Y. Ben-Zion, J. N. Brune, and T. K. Rockwell (2009), Characterization of damage in sandstones along the Mojave section of the San Andreas fault: Implications for the shallow extent of damage generation, *Appl. Geophys.*, 166, 1747–1773, doi:10.1007/s00024-009-0516-z.
- Dor, O., T. K. Rockwell, and Y. Ben-Zion (2006a), Geological observations of damage asymmetry in the structure of the San Jacinto, San Andreas and Punchbowl faults in Southern California: A possible indicator for preferred rupture propagation direction, *Pure Appl. Geophys.*, 163, 301–349, doi:10.1007/s00024-005-0023-9.
- Dor, O., C. Yıldırım, T. K. Rockwell, Y. Ben-Zion, Ö. Emre, M. Sisk, and T. Y. Duman (2008), Geological and geomorphologic asymmetry across the rupture zones of the 1943 and 1944 earthquakes on the North Anatolian fault: Possible signals for preferred earthquake propagation direction, *Geophys. J. Int.*, 173(2), 483–504, doi:10.1111/j.1365-246X.2008.03709.x.
- Drugan, W. J. (2001), Dynamic fragmentation of brittle materials: Analytical mechanics-based models, *J. Mech. Phys. Solids*, 49(6), 1181–1208.
- Dunham, E. M. (2007), Conditions governing the occurrence of supershear ruptures under slip-weakening friction, *J. Geophys. Res. Solid Earth*, 112(7), 1–24, doi:10.1029/2006JB004717.
- Dunham, E. M., and R. J. Archuleta (2004), Evidence for a supershear transient during the 2002 Denali fault earthquake, *Bull. Seismol. Soc. Am.*, 94(6B), 256–268, doi:10.1785/0120040616.
- Dunham, E. M., and H. S. Bhat (2008), Attenuation of radiated ground motion and stresses from three-dimensional supershear ruptures, *J. Geophys. Res.*, 113(B8), B08319, doi:10.1029/2007JB005182.
- Dunham, E. M., P. Favreau, and J. M. Carlson (2003), A supershear transition mechanism for cracks, *Science*, 299(5612), 1557–1559, doi:10.1126/science.1080650.
- Faulkner, D. R., T. M. Mitchell, D. Healy, and M. J. Heap (2006), Slip on “weak” faults by the rotation of regional stress in the fracture damage zone., *Nature*, 444(7121), 922–5, doi:10.1038/nature05353.
- Faulkner, D. R., T. M. Mitchell, E. Jensen, and J. Cembrano (2011), Scaling of fault damage zones with displacement and the implications for fault growth processes, *J. Geophys. Res.*, 116(B5), B05403, doi:10.1029/2010JB007788.
- Fondriest, M., S. Aretusini, G. Di Toro, and S. A. Smith (2015), Fracturing and rock pulverization along an exhumed seismogenic fault zone in dolostones: The Foiana fault zone (Southern Alps, Italy), *Tectonophysics*, doi:10.1016/j.tecto.2015.04.015. [online] Available from: <http://linkinghub.elsevier.com/retrieve/pii/S0040195115002401>.
- Forquin, P., and F. Hild (2010), A probabilistic damage model of the dynamic fragmentation process in brittle materials, *Adv. Appl. Mech.*, 44, 1–72.
- Forrestal, M. J., T. W. Wright, and W. Chen (2007), The effect of radial inertia on brittle samples during the split Hopkinson pressure bar test, *Int. J. Impact Eng.*, 34(3), 405–411, doi:10.1016/j.ijimpeng.2005.12.001.

- Freund, L. B. (1990), *Dynamic Fracture Mechanics*, Cambridge University Press, Cambridge.
- Gama, B. A., S. L. Lopatnikov, and J. W. Gillespie (2004), Hopkinson bar experimental technique: A critical review, *Appl. Mech. Rev.*, 57(4), 223, doi:10.1115/1.1704626.
- Glenn, L. A., and A. Chudnovsky (1986), Strain-energy effects on dynamics fragmentation, *J. Applied Physics*, 59(4), 1379–1380.
- Grady, D. E. (1982), Local inertial effects in dynamic fragmentation, *J. Appl. Phys.*, 53(1), 322–425.
- Grady, D. E. (1998), Shock-wave compression of brittle solids, *Mech. Mater.*, 29(3-4), 181–203, doi:10.1016/S0167-6636(98)00015-5.
- Grady, D. E. (2009), *Analysis of shock and high-rate data for ceramics: Equation of state properties and fragmentation in the ballistic environment* [technical report].
- Grady, D. E., R. E. Hollenbach, K. W. Schuler, and J. F. Callender (1977), Strain rate dependence in dolomite inferred from impact and static compression studies, *J. Geophys. Res.*, 82(8), 1325, doi:10.1029/JB082i008p01325.
- Graff, K. F. (1991), *Wave Motion in Elastic Solids*, Dover, New York.
- Graham-Brady, L. (2010), Statistical characterization of meso-scale uniaxial compressive strength in brittle materials with randomly occurring flaws, *Int. J. Solids Struct.*, 47(18-19), 2398–2413, doi:10.1016/j.ijsolstr.2010.04.034.
- Gratier, J.-P., F. Thouvenot, L. Jenatton, A. Tourette, M.-L. Doan, and F. Renard (2013a), Geological control of the partitioning between seismic and aseismic sliding behaviours in active faults: Evidence from the Western Alps, France, *Tectonophysics*, 600, 226–242, doi:10.1016/j.tecto.2013.02.013.
- Gratier, J.-P., D. K. Dysthe, and F. Renard (2013b), The role of pressure solution creep in the ductility of the Earth, *Adv. Geophys.*, 54, 47–179, doi:10.1016/B978-0-12-380940-7.00002-0.
- Gratier, J.-P., F. Renard, and B. Vial (2014), Postseismic pressure solution creep: Evidence and time-dependent change from dynamic indenting experiments, *J. Geophys. Res. Solid Earth*, 119, 2764–2779, doi:10.1002/2013JB010768. Received.
- Hild, F., P. Forquin, and A. R. Cordeiro da Silva (2003), Single and multiple fragmentation of brittle geomaterials, *Rev. française génie ..., 7(7-8)*, 973–1002. [online] Available from: <http://www.tandfonline.com/doi/abs/10.1080/12795119.2003.9692529> (Accessed 17 January 2014)
- Holland, C. C., and R. M. McMeeking (2015), The influence of mechanical and microstructural properties on the rate-dependent fracture strength of ceramics in uniaxial compression, *Int. J. Impact Eng.*, 81, 34–49, doi:10.1016/j.ijimpeng.2015.02.007.
- Ida, Y. (1972), Cohesive force across the tip of a longitudinal-shear crack and Griffith's specific surface energy, *J. Geophys. Res.*, 77(20), 3796, doi:10.1029/JB077i020p03796.
- Keulen, N., R. Heilbronner, H. Stünitz, A.-M. Boullier, and H. Ito (2007), Grain size distributions of fault rocks: A comparison between experimentally and naturally deformed granitoids, *J. Struct. Geol.*, 29(8), 1282–1300, doi:10.1016/j.jsg.2007.04.003.
- Key, W. R. O., and R. A. Schultz (2011), Fault formation in porous sedimentary rocks at high strain rates: First results from the Upheaval Dome impact structure, Utah, USA, *Geol. Soc. Am. Bull.*, 123(5-6), 1161–1170, doi:10.1130/B30087.1.
- Kimberley, J., K. T. Ramesh, and N. P. Daphalapurkar (2013), A scaling law for the dynamic strength of brittle solids, *Acta Mater.*, 61(9), 3509–3521, doi:10.1016/j.actamat.2013.02.045.
- Kolsky, H. (1949), An investigation of the mechanical properties of materials at very high rates of loading, *Proc. Phys. Soc. Sect. B*, 62(11), 676, doi:doi:10.1088/0370-1301/62/11/302.
- Kostrov, B. V., and S. Das (1988), *Principles of Earthquake Source Mechanics*, Cambridge University Press, London.
- Kraft, R. H., J.-F. Molinari, K. T. Ramesh, and D. H. Warner (2008), Computational micromechanics of dynamic compressive loading of a brittle polycrystalline material using a distribution of grain boundary properties, *J. Mech. Phys. Solids*, 56(8), 2618–2641, doi:10.1016/j.jmps.2008.03.009.
- Latour, S., C. Voisin, F. Renard, E. Larose, S. Catheline, and M. Campillo (2013), Effect of fault heterogeneity on rupture dynamics: An experimental approach using ultrafast ultrasonic imaging, *J. Geophys. Res. Solid Earth*, 118(11), 5888–5902, doi:10.1002/2013JB010231.
- Levy, S., and J. F. Molinari (2010), Dynamic fragmentation of ceramics, signature of defects and scaling of fragment sizes, *J. Mech. Phys. Solids*, 58(1), 12–26, doi:10.1016/j.jmps.2009.09.002.
- Li, X. B., T. S. Lok, and J. Zhao (2005), Dynamic characteristics of granite subjected to intermediate loading rate, *Rock Mech. Rock Eng.*, 38(1), 21–39, doi:10.1007/s00603-004-0030-7.
- Li, Y. G., J. E. Vidale, S. M. Day, D. D. Oglesby, and E. Cochran (2003), Postseismic fault healing on the rupture zone of the 1999 M 7.1 Hector Mine, California, earthquake, *Bull. Seismol. Soc. Am.*, 93(2), 854–869, doi:10.1785/0120020131.
- Lyakhovsky, V., and Y. Ben-Zion (2014), A continuum damage-breakage faulting model and solid-granular transitions, *Pure Appl. Geophys.*, doi:10.1007/s00024-014-0845-4.
- Mello, M., H. S. Bhat, A. J. Rosakis, and H. Kanamori (2010), Identifying the unique ground motion signatures of supershear earthquakes: Theory and experiments, *Tectonophysics*, 493(3-4), 297–326, doi:10.1016/j.tecto.2010.07.003.
- Miller, O., L. B. Freund, and A. Needleman (1999), Modeling and simulation of dynamic fragmentation in brittle materials, *Int. J. Fract.*, 96, 101–125, doi:10.1023/A:1018666317448.
- Miller, S. A. (2013), The role of fluids in tectonic and earthquake processes, *Advances in Geophysics*, 54, 1–46.
- Mitchell, T. M., Y. Ben-Zion, and T. Shimamoto (2011), Pulverized fault rocks and damage asymmetry along the Arima-Takatsuki Tectonic Line, Japan, *Earth Planet. Sci. Lett.*, 308(3-4), 284–297, doi:10.1016/j.epsl.2011.04.023.
- Mitchell, T. M., A. Billi, S. A. Miller, D. Goldsby, C. H. Scholz, J. K. Gran, and J. Simons (2013), Dynamic pulverization by rapid decompression, in *AGU Fall Meeting 2013*, San Francisco.
- Mitchell, T. M., and D. R. Faulkner (2009), The nature and origin of off-fault damage surrounding strike-slip fault zones with a wide range of displacements: A field study from the

- Atacama fault system, northern Chile, *J. Struct. Geol.*, 31(8), 802–816, doi:10.1016/j.jsg.2009.05.002.
- Monzawa, N., and K. Otsuki (2003), Comminution and fluidization of granular fault materials: Implications for fault slip behavior, *Tectonophysics*, 367(1-2), 127–143, doi:10.1016/S0040-1951(03)00133-1.
- Morton, N., T. M. Mitchell, M.-L. Doan, G. Girty, T. K. Rockwell, and J. Renner (2012), Ultra-high permeability induced by seismic shockwaves near the San Jacinto fault, in *AGU Fall Meeting 2012*, San Francisco.
- Muto, J., T. Nakatani, O. Nishikawa, and H. Nagahama (2015), Fractal particle size distribution of pulverized fault rocks as a function of distance from the fault core, *Geophys. Res. Lett.*, 1–9, doi:10.1002/2015GL064026.
- Nemat-Nasser, S., and H. Horii (1982), Compression-induced nonplanar crack extension with application to splitting, exfoliation, and rockburst, *J. Geophys. Res.*, 87(B8), 6805–6821, doi:10.1029/JB087iB08p06805.
- Nemat-Nasser, S., J. B. Isaacs, and J. E. Starrett (1991), Hopkinson techniques for dynamic recovery experiments, *Proc. R. Soc. London, Ser. A*, 435(1894), 371–391.
- Paliwal, B., and K. T. Ramesh (2008), An interacting micro-crack damage model for failure of brittle materials under compression, *J. Mech. Phys. Solids*, 56(3), 896–923, doi:10.1016/j.jmps.2007.06.012.
- Paterson, M. S., and T.-F. Wong (2005), *Experimental rock deformation: The brittle field*, Springer Verlag.
- Perol, T., and H. S. Bhat (2013), Micromechanics based permeability evolution in brittle materials at high strain rates, *American Geophysical Union 2013*.
- Poliakov, A. N. B., R. Dmowska, and J. R. Rice (2001), Dynamic shear rupture interactions with fault bends and off-axis secondary faulting, *J. Geophys. Res.*, 107(B11), 1–48, doi:10.1029/2001JB000572.
- Ravichandran, G., and G. Subhash (1994), Critical appraisal of limiting strain rates for compression testing of ceramics in a split Hopkinson pressure bar, *J. Am. Ceram. Soc.*, 77(1), 263–267.
- Reches, Z., and T. A. Dewers (2005), Gouge formation by dynamic pulverization during earthquake rupture, *Earth Planet. Sci. Lett.*, 235(1-2), 361–374, doi:10.1016/j.epsl.2005.04.009.
- Rempe, M., T. M. Mitchell, J. Renner, S. Nippes, Y. Ben-Zion, and T. K. Rockwell (2013), Damage and seismic velocity structure of pulverized rocks near the San Andreas Fault, *J. Geophys. Res. Solid Earth*, 118(6), 2813–2831, doi:10.1002/jgrb.50184.
- Rice, J. R., C. G. Sammis, and R. Parsons (2005), Off-fault secondary failure induced by a dynamic slip pulse, *Bull. Seismol. Soc. Am.*, 95(1), 109–134, doi:10.1785/0120030166.
- Richard, J., M.-L. Doan, J.-P. Gratier, and F. Renard (2014), Microstructures induced in porous limestone by dynamic loading, and fracture healing: An experimental approach, *Pure Appl. Geophys.*, doi:10.1007/s00024-014-0958-9. [online] Available from: <http://link.springer.com/10.1007/s00024-014-0958-9>.
- Rockwell, T. K., M. Sisk, G. Girty, O. Dor, N. Wechsler, and Y. Ben-Zion (2009), Chemical and physical characteristics of pulverized tejon lookout granite adjacent to the San Andreas and garlock faults: Implications for earthquake physics, *Pure Appl. Geophys.*, 166(10-11), 1725–1746, doi:10.1007/s00024-009-0514-1.
- Rosakis, A. J., and G. Ravichandran (2000), Dynamic failure mechanics, *Int. J. Solids Struct.*, 37(1-2), 331–348, doi:10.1016/S0020-7683(99)00097-9.
- Sagy, A., and D. Korngreen (2012), Dynamic branched fractures in pulverized rocks from a deep borehole, *Geology*, 40(9), 799–802, doi:10.1130/G33194.1.
- Savage, H. M., and E. E. Brodsky (2011), Collateral damage: Evolution with displacement of fracture distribution and secondary fault strands in fault damage zones, *J. Geophys. Res. Solid Earth*, 116(3), doi:10.1029/2010JB007665.
- Scholz, C. H. (2002), *The Mechanics of Earthquakes and Faulting*, 2nd ed., Cambridge University Press, Cambridge.
- Shenoy, V. B., and K.-S. Kim (2003), Disorder effects in dynamic fragmentation of brittle materials, *J. Mech. Phys. Solids*, 51(11-12), 2023–2035, doi:10.1016/j.jmps.2003.09.010.
- Shi, Z., and Y. Ben-zion (2006), Dynamic rupture on a bimaterial interface governed by slip-weakening friction, *Geophys. J. Int.*, 165(2), 469–484, doi:10.1111/j.1365-246X.2006.02853.x.
- Sibson, R. H. (1977), Fault rocks and fault mechanisms, *J. Geol. Soc. London*, 133(3), 191–213, doi:10.1144/gsjgs.133.3.0191.
- Sibson, R. H. (1996), Structural permeability of fluid-driven fault-fracture meshes, *J. Struct. Geol.*, 18(8), 1031–1042, doi:10.1016/0191-8141(96)00032-6.
- Stünitz, H., N. Keulen, T. Hirose, and R. Heilbronner (2010), Grain size distribution and microstructures of experimentally sheared granitoid gouge at coseismic slip rates: Criteria to distinguish seismic and aseismic faults? *J. Struct. Geol.*, 32(1), 59–69, doi:10.1016/j.jsg.2009.08.002.
- Di Toro, G., D. L. Goldsby, and T. E. Tullis (2004), Friction falls towards zero in quartz rock as slip velocity approaches seismic rates., *Nature*, 427(6973), 436–439, doi:10.1038/nature02249.
- Wechsler, N., E. E. Allen, T. K. Rockwell, G. Girty, J. S. Chester, and Y. Ben-Zion (2011), Characterization of pulverized granitoids in a shallow core along the San Andreas fault, Littlerock, CA, *Geophys. J. Int.*, 186(2), 401–417, doi:10.1111/j.1365-246X.2011.05059.x.
- Weertman, J. (1980), Unstable slippage across a fault that separates elastic media of different elastic constants, *J. Geophys. Res.*, 85(B3), 1455–1461, doi:doi:10.1029/JB085iB03p01455.
- Weertman, J. (2002), Subsonic type earthquake dislocation moving at approximately  $\sqrt{2}x$  shear wave velocity on interface between half spaces of slightly different elastic constants, *Geophys. Res. Lett.*, 29(10), 10–13.
- Weibull, W. (1939), A statistical theory of the strength of materials, *Ingenjörsvetenskapsakademiens Handl.*, 151, 1–4.
- Wilson, B., T. Dewers, Z. Reches, and J. N. Brune (2005), Particle size and energetics of gouge from earthquake rupture zones, *Geophys. Res. Lett.*, 32, 749–752, doi:10.1029/2003GL019277.
- Wong, T., R. H. C. Wong, K. T. Chau, and C. A. Tang (2006), Microcrack statistics, Weibull distribution and micromechanical modeling of compressive failure in rock, *Mech. Mater.*, 38(7), 664–681, doi:10.1016/j.mechmat.2005.12.002.

- Xia, K., M. H. B. Nasseri, B. Mohanty, F. Lu, R. Chen, and S. N. Luo (2008), Effects of microstructures on dynamic compression of Barre granite, *Int. J. Rock Mech. Min. Sci.*, 45, 879–887, doi:10.1016/j.ijrmms.2007.09.013.
- Xia, K., A. J. Rosakis, H. Kanamori, and J. R. Rice (2005), Laboratory earthquakes along inhomogeneous faults: Directionality and supershear, *Science*, 308(5722), 681–684, doi:10.1126/science.1108193.
- Xia, K., and W. Yao (2015), Dynamic rock tests using split Hopkinson (Kolsky) bar system: A review, *J. Rock Mech. Geotech. Eng.*, 7(1), 27–59, doi:10.1016/j.jrmge.2014.07.008.
- Yuan, F., V. Prakash, and T. Tullis (2011), Origin of pulverized rocks during earthquake fault rupture, *J. Geophys. Res.*, 116(B6), B06309, doi:10.1029/2010JB007721.
- Zhang, Q. B., and J. Zhao (2013), A review of dynamic experimental techniques and mechanical behaviour of rock materials, *Rock Mech. Rock Eng.*, doi:10.1007/s00603-013-0463-y.
- Zhao, D., Z. Huang, N. Umino, A. Hasegawa, and H. Kanamori (2011), Structural heterogeneity in the megathrust zone and mechanism of the 2011 Tohoku-Oki earthquake (Mw 9.0), *Geophys. Res. Lett.*, 38(17), 5–9, doi:10.1029/2011GL048408.
- Zhou, F., J.-F. Molinari, and K. T. Ramesh (2006), Characteristic fragment size distributions in dynamic fragmentation, *Appl. Phys. Lett.*, 88(26), 261918, doi:10.1063/1.2216892.
- Zhao, H., and G. Gary (1996), On the use of SHPB techniques to determine the dynamic behavior of materials in the range of small strains, *Int. J. Solids Struct.*, 33(23), 3363–3375.
- Zöller, G., M. Holschneider, and Y. Ben-Zion (2005), The role of heterogeneities as a tuning parameter of earthquake dynamics, *Pure Appl. Geophys.*, 162(6-7), 1027–1049, doi:10.1007/s00024-004-2660-9.

# 5

## "Coseismic Foliations" in Gouge and Cataclasite: Experimental Observations and Consequences for Interpreting the Fault Rock Record

Steven A. F. Smith<sup>1</sup>, James R. Griffiths<sup>1</sup>, Michele Fondriest<sup>2</sup>, and Giulio Di Toro<sup>2,3,4</sup>

### ABSTRACT

Foliated gouges and cataclasites are commonly interpreted as the product of distributed (aseismic) fault creep. However, foliated fault rocks are often associated with localized slip surfaces, the latter indicating potentially unstable (seismic) behavior. One possibility is that such fault zones preserve the effects of both seismic slip and slower aseismic creep. An alternative possibility explored here is that some foliated fault rocks and localized slip surfaces develop contemporaneously during seismic slip. We studied the microstructural evolution of calcite-dolomite gouges deformed experimentally at slip velocities  $<1.13\text{ m s}^{-1}$  and for total displacements of 0.03–1 m, in the range expected for the average coseismic slip during earthquakes of Mw 3–7. As strain progressively localized in the gouge layers at the onset of high-velocity shearing, an initial mixed assemblage of calcite and dolomite grains evolved quickly to an organized, foliated fabric. The foliation was defined mainly by compositional layering and grain size variations that formed by cataclasis and shearing of individual foliation domains. The most significant microstructural changes in the bulk gouge occurred before and during dynamic weakening ( $<0.08\text{ m displacement}$ ). Strain was localized to a bounding slip surface by the end of dynamic weakening, and thus microstructural evolution in the bulk gouge ceased. Our experiments suggest that certain types of foliated gouge and cataclasite can form by distributed brittle "flow" as strain localizes to a bounding slip surface during coseismic shearing.

### 5.1. INTRODUCTION

Foliated gouges and cataclasites are among the most common products of mid- to upper-crustal faulting [Engelder, 1974; Chester *et al.*, 1985]. In active and

exhumed fault zones, the structure of foliated gouges and cataclasites is commonly used to determine the shear sense and kinematics of faulting, as well as the strain distribution in deformed fault rocks [e.g., Rutter *et al.*, 1986; Chester and Logan, 1987; Tanaka, 1992; Cowan and Brandon, 1994; Cladouhos, 1999; Lin, 2001; Cowan *et al.*, 2003; Collettini and Holdsworth, 2004; Hayman *et al.*, 2004]. Interpreting the significance and possible mechanical behavior of fault rocks in the geological record requires a complete understanding of the nature and evolution of fault rock foliations.

In natural gouges and cataclasites, foliation can be defined by a wide range of fabric elements and

<sup>1</sup>Department of Geology, University of Otago, Dunedin, New Zealand

<sup>2</sup>School of Earth, Atmospheric and Environmental Sciences, University of Manchester, Manchester, UK

<sup>3</sup>Dipartimento di Geoscienze, Università degli Studi di Padova, Italy

<sup>4</sup>Istituto Nazionale di Geofisica e Vulcanologia, Rome, Italy

microstructures that reflect competition between brittle, plastic, and fluid-mediated deformation processes [Snoke *et al.*, 1998]. Microstructures that commonly contribute to foliations include compositional layering; particle size variations; preferred alignment of grains, grain boundaries, and fractures; and the orientation and connectivity of shear surfaces and dissolution surfaces. Foliations are commonly found in conjunction with discrete slip surfaces that indicate relatively localized deformation.

Where natural foliated gouges and cataclasites contain networks and overgrowths of phyllosilicate minerals, a convincing argument has been made that the phyllosilicate-rich foliations are formed by a combination of frictional sliding and dissolution-precipitation reactions, perhaps during aseismic fault creep [e.g., Wintsch *et al.*, 1995; Imber *et al.*, 1997; Manatschal, 1999; Stewart *et al.*, 2000; White, 2001; Wintsch and Yi, 2002; Gueydan *et al.*, 2003; Collettini and Holdsworth, 2004; Holdsworth, 2004; Jefferies *et al.*, 2006; Moore and Rymer, 2007; Collettini *et al.*, 2009; Holdsworth *et al.*, 2011; Wallis *et al.*, 2013; Wallis *et al.*, 2015]. Bos *et al.* [2000] and Niemeijer and Spiers [2006] provided experimental data in support of this interpretation by demonstrating that well-defined fault rock foliations can form by efficient dissolution-precipitation reactions accompanying granular flow and frictional sliding at low slip velocities ( $<1 \mu\text{m s}^{-1}$ ).

In other types of foliated fault rock, but particularly those in which cataclastic deformation is expected to dominate, Cowan [1999] argued that there is no compelling field or experimental evidence to rule out the possibility that foliations may form by distributed brittle “flow” during seismic slip. This alternative idea for the genesis of some foliated fault rocks has received little attention, despite the important consequences it has for interpreting the fault rock record. Experimental studies involving high-velocity ( $V > 0.01 \text{ m s}^{-1}$ ) shearing of gouge layers allow for the investigation of microstructure evolution under conditions approaching the seismic range [Niemeijer *et al.*, 2012]. In several recent studies, high-velocity shearing was associated with the development of a foliated or banded microstructure in gouge layers, interpreted to reflect rotation of platy minerals during shear [e.g., Kitajima *et al.*, 2010] or particle welding driven by frictional heating [e.g., Sawai *et al.*, 2012; Togo and Shimamoto, 2012; Yao *et al.*, 2013].

As part of a wider study into the mechanical behavior of mixed (multiphase) gouges, we performed a series of experiments on calcite-dolomite gouges at seismic slip rates ( $V_{\max} < 1.13 \text{ m/s}$ ). Calcite and dolomite are dominant minerals in many seismically active regions worldwide, where earthquake ruptures nucleate within and propagate

through thick sequences of carbonates (e.g., Italy, 2009 Mw 6.3 L’Aquila earthquake; Greece, 1995 Ms 6.6 Western Macedonia earthquake). The ability to apply moderately high normal stresses (17.3 MPa) to the experimental gouge layers and precisely control the total displacements allowed us to investigate gouge microstructure and grain size evolution in the range of displacements (0.03–1 m; Table 5.1) expected for earthquakes of approximately magnitude Mw 3–7 [Stirling *et al.*, 2013]. The overall aim of the experiments was to explore the idea put forward by Cowan [1999] that some types of foliated gouge and cataclasite could form at seismic slip rates.

## 5.2. METHODS

### 5.2.1. Starting Materials and Gouge Sample Preparation

Gouges were prepared from mixtures of 50 wt% calcite and 50 wt% dolomite. The calcite component was derived by crushing Carrara marble, composed of >98 wt% calcite with <2 wt% dolomite and muscovite (from X-ray powder diffraction analysis). Original metamorphic grains in the Carrara marble are large, equant grains 150–400  $\mu\text{m}$  in size. The dolomite component was derived by crushing sedimentary dolostones of the Mendola Formation of northeast Italy, a mid-Triassic unit 250–300 m thick [Fondriest *et al.*, 2015]. The Mendola Formation contains a matrix of micritic dolomite grains up to 10  $\mu\text{m}$  in size as well as elongate (approximately bedding-parallel) fenestrae that are filled with rhombohedral dolomite crystals up to 300  $\mu\text{m}$  long [Fondriest *et al.*, 2015].

Fragments of Carrara marble and Mendola Formation were crushed using a pestle and mortar, and the resulting material was passed through a 250- $\mu\text{m}$  sieve. All material that passed through the sieve was retained for the experimental gouge mixes. The calcite and dolomite components were weighed and mixed by slow tumbling for up to 1 hour to ensure a homogenous distribution of phases. X-ray powder diffraction analysis performed on the mixed gouges indicated a composition of 44.7 wt% calcite and 55.3 wt% dolomite ( $\pm 2$ –3 wt%) with no detectable accessory phases.

### 5.2.2. Experimental Procedures

Experiments were performed with SHIVA (Slow- to High-Velocity rotary-shear friction Apparatus) at the INGV, Rome [Di Toro *et al.*, 2010; Niemeijer *et al.*, 2011] using a sample holder for incohesive materials with rotary and stationary parts (Figure 5.1a) [Smith *et al.*, 2013]. The rotary base plate and the stationary base disc have a crosshatch pattern of surface roughness where they are

**Table 5.1** Summary of experiments performed on mixed calcite-dolomite gouges (50 wt%/50 wt%) with increasing displacements. See text for explanation of grain size measurements and units 1–3.

Exp.	Normal Stress (MPa)	<sup>a</sup> Max. Slip Vel. ( $\text{m s}^{-1}$ )	Displacement (m)	<sup>b</sup> Bulk shear strain, $\gamma$	Mean grain size calcite ( $d_{\text{equ}}/\mu\text{m}$ )	Mean grain size dolomite ( $d_{\text{equ}}/\mu\text{m}$ )	Max. grain size calcite ( $d_{\text{equ}}/\mu\text{m}$ )	Max. grain size dolomite ( $d_{\text{equ}}/\mu\text{m}$ )	Max. grain size calcite (%)	Max. grain size dolomite (%)	Unit 1 (%)	Unit 2 (%)	Unit 3 (%)
s800	17.3	—	—	—	6.4, 5.9 <sup>c</sup>	5.6	107.3, 45.88 <sup>c</sup>	55.4	—	—	—	—	—
s796	17.3	0.4	0.03	15	2.9	5.5	48.2	33.5	95.1	4.9	0.0	—	—
s801	17.3	0.56	0.05	25	3.7	5.3	21.9	24.9	73.6	26.2	0.2	—	—
s797	17.3	0.76	0.08	40	2.1	3.8	13.8	22.8	67.9	32.0	0.1	—	—
s798	17.3	1.13	0.19	95	1.9	4.1	15.3	28.3	55.4	43.9	0.7	—	—
s799	17.3	1.13	0.39	195	2.9	4.5	21.2	20.4	44.8	49.0	6.2	—	—
s530	17.3	1.13	0.99	495	—	—	—	—	—	—	—	—	—

<sup>a</sup> Target slip velocity in all experiments was  $1.13 \text{ m s}^{-1}$ , but this velocity was not obtained in the three shortest displacement experiments (see Figure 5.3). All experiments had the same acceleration and deceleration of  $7 \text{ ms}^{-2}$ .

<sup>b</sup> Calculated as total displacement divided by measured final thickness of gouge layer.

<sup>c</sup> First number includes largest measured clast, second number excludes largest measured clast.

in contact with the gouge layer (Figure 5.1c; amplitude of surface roughness  $200 \mu\text{m}$ , wavelength  $400 \mu\text{m}$ ). Normal load on the gouge layer is applied by the axial loading column of SHIVA [Di Toro *et al.*, 2010]. Normal load on the inner and outer sliding rings is modulated by five outer springs and one inner spring (Figure 5.1a). Each experiment used 3 g of gouge, resulting in a ring-shaped gouge layer (Figure 5.1b; 55 mm/35 mm ext./int. diameter) with an initial (precompaction) thickness of c. 2 mm.

Experiments were performed under room-dry conditions (room humidity varied between 50% and 80%) at a constant normal stress of  $17.3 \text{ MPa}$  and target maximum slip velocity of  $1.13 \text{ m s}^{-1}$  (Table 5.1). Angular rotation (and total displacement) in each experiment was controlled using two digital optical encoders located on the rotary column [Di Toro *et al.*, 2010; Niemeijer *et al.*, 2011]. Horizontal displacements of the axial column were measured using a direct current differential transformer (50 mm range and  $\sim 50 \mu\text{m}$  resolution) and in some experiments a linear variable differential transformer (3 mm range and  $\sim 0.03 \mu\text{m}$  resolution). Experimental data (e.g., axial load, torque, axial displacements, angular rotation) were acquired at a frequency up to  $25 \text{ kHz}$ , and determination of total displacement, slip rate, and shear stress followed methods outlined in Di Toro *et al.* [2010].

### 5.2.3. Microstructural Analysis

Quantitatively comparing the microstructure of two-phase gouges deformed in separate high-velocity experiments requires confidence that the starting materials in

each experiment were nearly identical, and that the gouge sample assembly and experimental conditions remained the same. In our experience, minor variations to any of these factors can result in changes to the final microstructure. For this reason, quantitative microstructural analysis (e.g., shear strain, grain size) presented in this chapter focuses on six experiments (one compaction experiment and five shear experiments) performed consecutively (on the same day) using gouge material from the same batch and with an identical sample assembly (Table 5.1). The five shear experiments had displacements in the range of 0.03–0.39 m (Table 5.1). We supplement these with an additional experiment (s530) with 1 m of displacement (Table 5.1). Because experiment s530 was performed with a different batch of starting gouge and a slightly modified sample holder, we found that aspects of the microstructure of this experiment (e.g., mean grain sizes, unit thicknesses; described below) were not directly comparable to the other five shear experiments. However, we use s530 in a qualitative way to illustrate general characteristics of the gouge fabric at relatively large displacements.

Fragments of deformed gouge layers were impregnated under vacuum using low-viscosity epoxy. Polished petrographic sections cut perpendicular to the gouge layers and approximately parallel to the slip direction (Figure 5.1b) were prepared for microstructural observations using a transmitted-light microscope and a Zeiss Sigma VP field-emission scanning electron microscope (SEM; in the Otago Centre for Electron Microscopy, University of Otago) operating in backscattered mode (acquisition conditions: accelerating voltage  $15 \text{ kV}$ ,

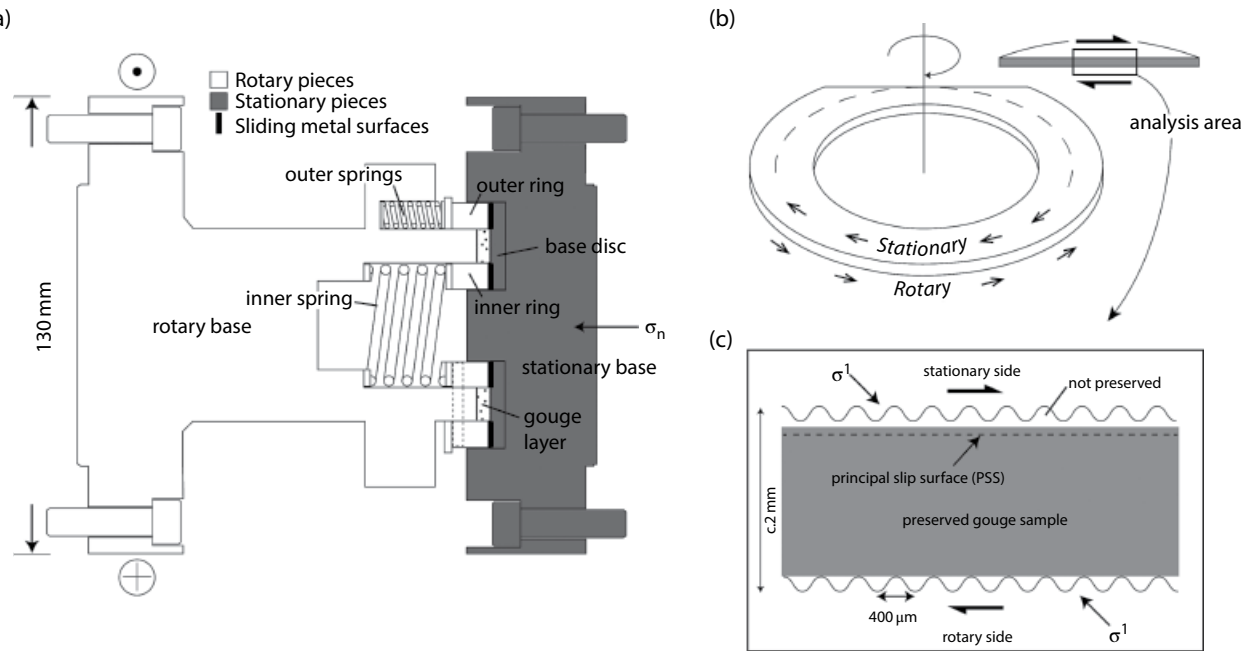


**Figure 5.1** Gouge sample holder and experimental setup. (a) Scale diagram of gouge holder with main parts labeled. (b) Geometry of the annular gouge layer. Thin sections were prepared perpendicular to gouge layer boundaries and approximately parallel to the sliding direction. The central part of each thin section (box labeled “analysis area”) was used for microstructural analysis. (c) Enlargement of the analysis area showing gouge layer boundaries. The gouge layer in each experiment was c. 2 mm thick prior to compaction. Where in contact with the gouge layer, the rotary and stationary pieces have surface roughness with wavelength of 400  $\mu\text{m}$  and amplitude of 200  $\mu\text{m}$ . The dashed line indicates the region where the principal slip surface (PSS) develops in the gouge layers. After the experiments, the gouge layers were quite cohesive and split close to the PSS. The grey area is typically preserved for microstructural analysis.

working distance 6–8.5 mm). Energy-dispersive X-ray spectroscopy (EDS) on the SEM was used to produce element maps showing the distribution of calcite (relatively enriched in calcium) and dolomite (relatively enriched in magnesium).

Microstructure and grain size in the starting materials and deformed samples were analyzed using quantitative image analysis techniques described in the sections that follow. To minimize potential errors associated with comparing the microstructure of different samples, petrographic sections were cut along the tangent to a circle lying between the inner and outer diameters of the ring-shaped gouge layer (dashed ring in Figure 5.1b). Quantitative microstructural analysis was performed on the central parts of the thin sections where the plane of the thin section is approximately parallel to the slip direction (Figures 5.1b, c).

Deformed gouge layers often split during sample preservation. A schematic indication of the gouge material that was typically preserved during sample recovery is shown in Figure 5.1c (grey area is preserved). The preserved area includes the bulk of the gouge layer, the localized principal

slip surface that forms during shearing, and also a thin sliver (up to 200  $\mu\text{m}$ ) of cohesive material on the stationary side of the principal slip surface.

## 5.3. RESULTS

### 5.3.1. Starting Gouge Microstructure

Figure 5.2a shows a SEM image of the calcite-dolomite starting gouge compacted to 17.3 MPa normal stress (the same normal stress used in the shear experiments). Calcite grains are mainly single-crystal grains, consistent with their derivation from large metamorphic grains in the Carrara marble. Dolomite grains are either single-crystal or polycrystalline (Figure 5.2b). The single-crystal dolomite grains are derived from the large rhombohedral dolomite crystals filling the fenestrae in the Mendola Formation. The polycrystalline grains are derived from the finer-grained micritic matrix of the Mendola Formation, which consists of regions with a granular (e.g., grain on left side in Figure 5.2b) or more crystalline (e.g., grain on right side in Figure 5.2b) texture. Calcite in

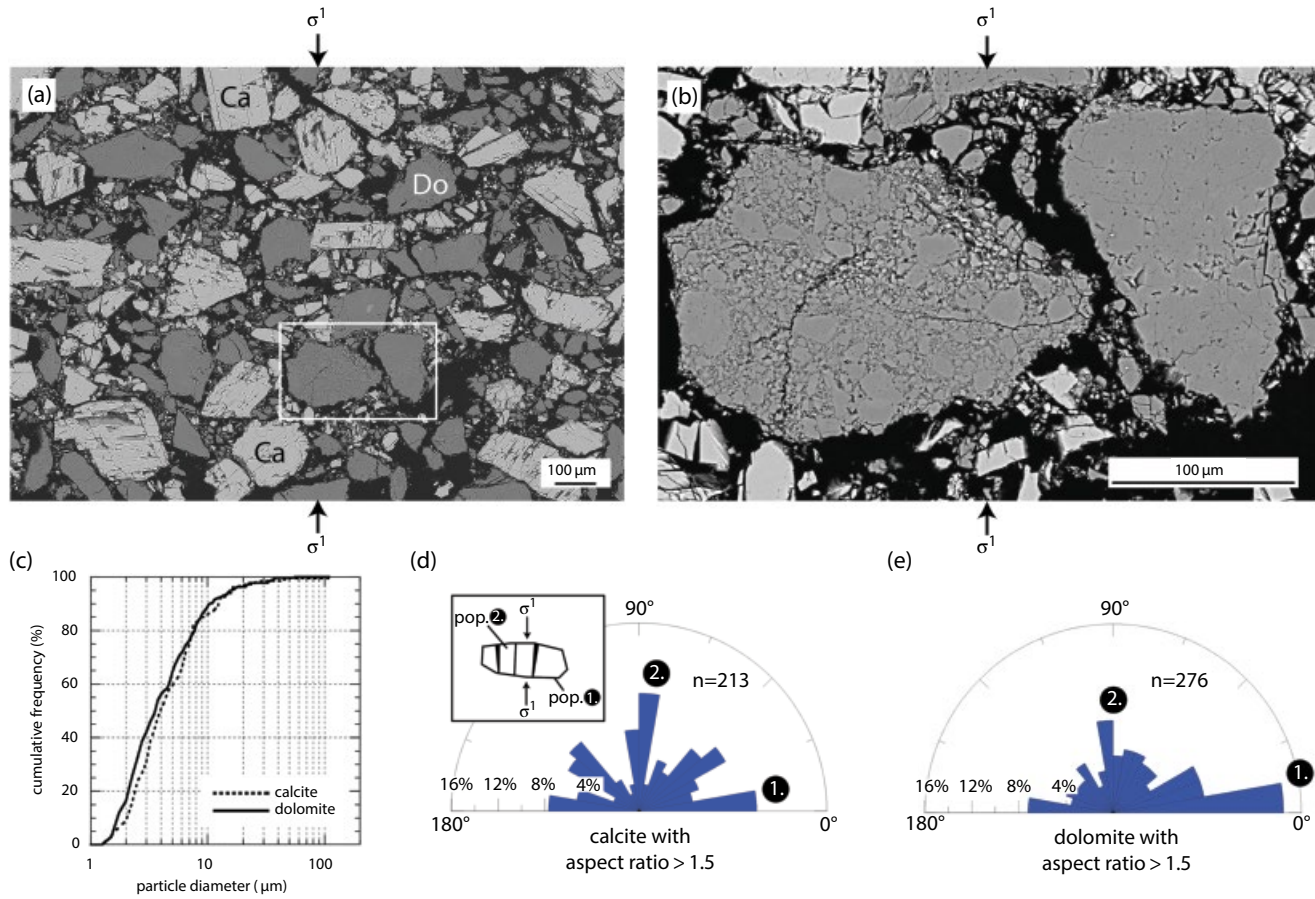


**Figure 5.2** Characterization of gouge starting materials. (a) Scanning electron microscope (SEM) image of mixed calcite-dolomite gouges compacted to 17.3 MPa normal stress. Ca = calcite; Do = dolomite. Thin section was prepared with the same orientation as for the shear experiments (Figure 5.1b, c). Arrows indicate orientation of compaction ( $\sigma^1$ ). Calcite and dolomite grains appear homogeneously mixed and are extensively fractured during compaction. (b) Enlargement of two dolomite grains shown in part a. The dolomite grain on the right is a polycrystalline grain consisting of tightly interlocking polygonal dolomite crystals, derived from the relatively coarse-grained dolomite veins or fenestrae-filling dolomite crystals in the starting rock (Mendola Formation). The dolomite grain on the left is an aggregate of subrounded grains bound together by a fine-grained ( $<5\mu\text{m}$ ) matrix. This type of polycrystalline dolomite grain is derived from the micritic matrix of the Mendola Formation. (c) Particle size distribution of gouge starting materials compacted to 17.3 MPa normal stress. Particle sizes were calculated from image analysis methods described in section 5.3.3.5. (d) Rose diagram summarizing the orientations of elongate (aspect ratio of best-fit ellipses  $>1.5$ ) calcite grains. The inset cartoon shows an interpretation of main populations 1 and 2. (e) Rose diagram summarizing the orientations of elongate (aspect ratio of best-fit ellipses  $>1.5$ ) dolomite grains.

the compacted starting material is twinned, although no twin preferred orientation was noted. Both calcite and dolomite grains are also heavily fractured (Figure 5.2a), particularly along twin and cleavage planes.

Image analysis (described in section 5.3.3.5) indicates that the grain size distributions of calcite and dolomite in the starting material are similar (Figure 5.2c), although calcite has a slightly larger mean grain size ( $6.37\mu\text{m}$ ) than dolomite ( $5.65\mu\text{m}$ ). Approximately 60% of calcite and dolomite grains in the starting material have aspect ratios (long axis of best-fit ellipse/short axis of best-fit ellipse;

see section 5.3.3.5) greater than 1.5. These elongate grains show a range of preferred orientations (Figure 5.2d, e). In both calcite and dolomite there is a population of grains (pop. 1 in Figure 5.2d, e) with long axes oriented subparallel to gouge layer boundaries (i.e., subperpendicular to the compaction direction,  $\sigma^1$ ). Grains of this population commonly fracture at high angles to their long axes during compaction (see inset Figure 5.2d), producing a second population of elongate grains (pop. 2 in Figure 5.2d, e) with long axes oriented subparallel to the compression direction. Calcite in the starting materials shows two

additional populations of elongate grains with long axes oriented obliquely to the compaction direction (Figure 5.2d).

### 5.3.2. Mechanical Data

The five shear experiments used for quantitative microstructural analysis were performed under identical conditions of normal stress (17.3 MPa) and slip velocity but with increasing displacements in the range of 0.03–0.39 m (Figure 5.3a). The target maximum slip velocity was  $1.13 \text{ m s}^{-1}$ . Acceleration and deceleration in each experiment were  $7 \text{ m s}^{-2}$ , meaning that only the two highest-displacement experiments reached the target slip velocity (Figure 5.3b).

An initial phase of transient strengthening occurred in the experiments before peak shear stress was reached after c. 0.02 m displacement (Figure 5.3a). Peak shear stress of c. 12 MPa corresponds to a friction coefficient ( $\mu = \text{shear stress}/\text{normal stress}$ ) of 0.7. Peak stress was followed by rapid dynamic weakening to reach (in the two experiments with the largest displacements) a much lower shear stress value of c. 4 MPa, corresponding to  $\mu$  of 0.25 (Figure 5.3a). The onset of dynamic weakening occurred at a slip velocity of c.  $0.5 \text{ m s}^{-1}$  (Figure 5.3b). The phase of rapid dynamic weakening was over by c. 0.08 m displacement (Figure 5.3a) as shear stress transitioned to “steady-state” values (only achieved in the experiment with 0.39 m displacement). During deceleration at the end of the experiments, shear stress recovered to c. 9.5 MPa (corresponding to  $\mu$  of 0.55; Figure 5.3a).

Experiments showed an initial phase of rapid axial shortening followed by more gradual shortening with increasing displacement (Figure 5.3a). Inspection of the sliding rings after disassembly of the sample holder suggests that no gouge loss occurred during most of the experiments, and thus axial shortening is interpreted to represent gouge compaction during shearing. The exception to this is the experiment with 0.05 m displacement that showed anomalous amounts of shortening at the onset of slip (Figure 5.3a). Minor gouge loss may have occurred during this experiment.

### 5.3.3. Deformed Gouge Microstructure

#### 5.3.3.1. Foliation Development and Microstructural Units

As observed in previous high-velocity gouge experiments on carbonates [De Paola *et al.*, 2011; Fondriest *et al.*, 2013; Smith *et al.*, 2013; Ree *et al.*, 2014; Bullock *et al.*, 2015; Smith *et al.*, 2015] and other rock types [e.g., Brantut *et al.*, 2008; Kitajima *et al.*, 2010; Oohashi *et al.*, 2011; Proctor *et al.*, 2014], shearing of the mixed calcite-dolomite gouge layers was associated with the progressive development of a

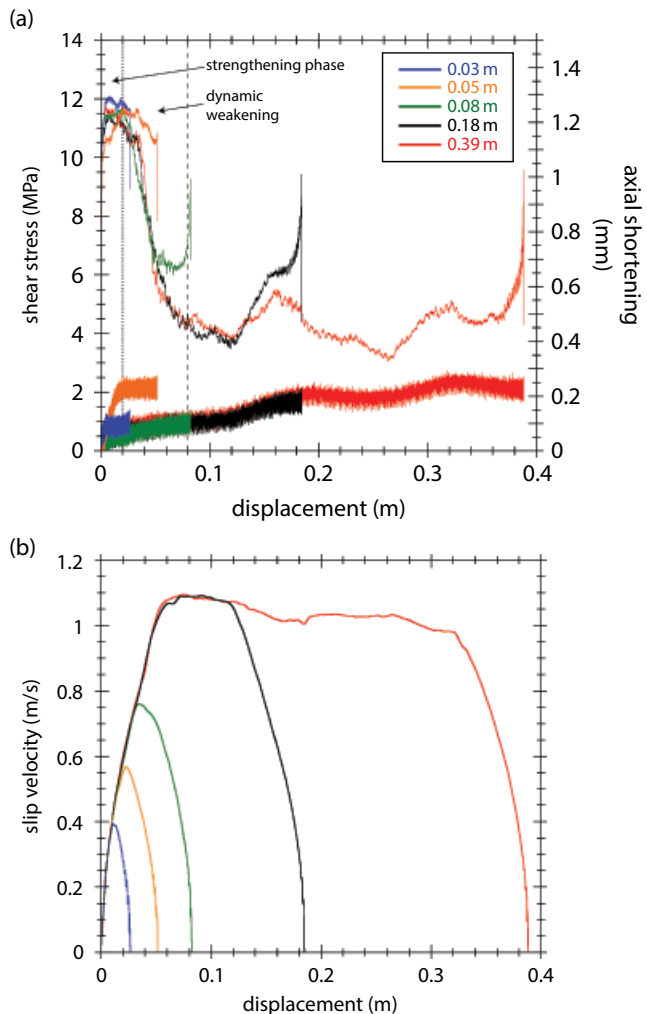


**Figure 5.3** Mechanical data. (a) Shear stress and axial shortening vs. displacement. All experiments showed an initial strengthening phase before peak stress (c. 12 MPa) was reached after c. 0.02 m of slip. Dynamic weakening occurred between c. 0.02 and 0.08 m. The two experiments with the largest displacements (0.18 m and 0.39 m) had a minimum shear stress value of approximately 4 MPa. Axial shortening followed a similar trend in all experiments, with total shortening of c. 0.2 mm after 0.39 m of slip. The experiment with 0.05 m displacement showed anomalously large amounts of shortening that probably reflects minor gouge loss. (b) Slip velocity vs. displacement for the same five experiments shown in part a. Acceleration and deceleration were  $7 \text{ m s}^{-2}$ . See electronic version for color representation.

discrete principal slip surface (PSS; Figure 5.4). In our experiments, the PSS formed at a distance of c. 200  $\mu\text{m}$  from the asperities on the stationary side of the gouge holder (see location of dashed line in Figure 5.1c).

In all deformed samples, the bulk gouge layer was dominated by a striking foliation (Figure 5.4), defined primarily by an organized banding of heavily fractured dolomite- and calcite-rich domains (Figure 5.4). In common

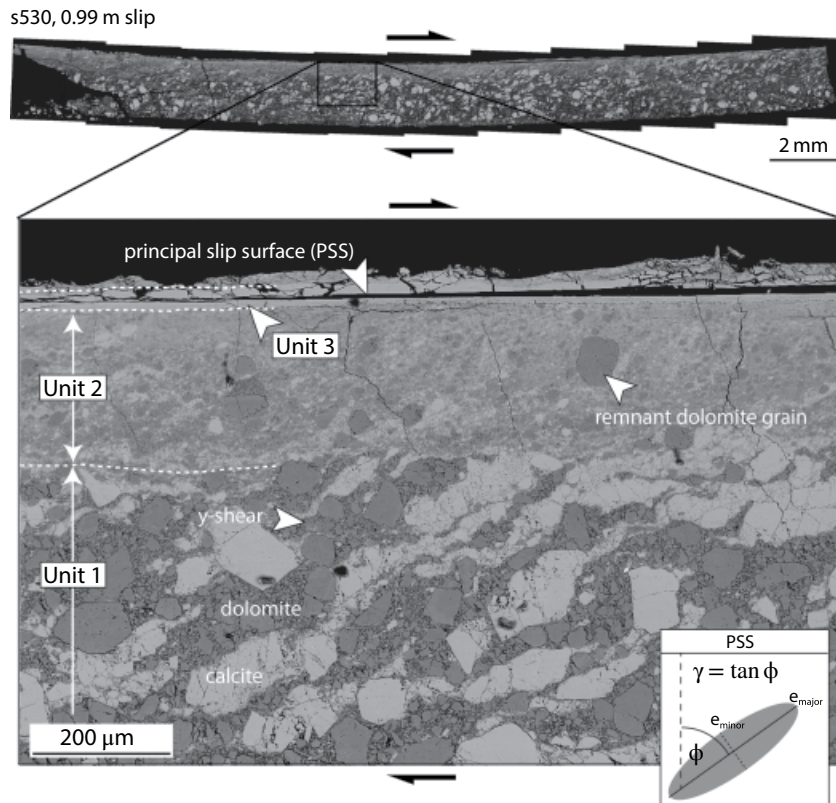


**Figure 5.4** SEM images of gouge layer s530 showing a striking foliation and the definition of three microstructural units. The foliation occurs across a range of scales and is mainly defined by compositional banding of heavily fractured domains of calcite and dolomite. In sample s530, at distances  $>300\text{ }\mu\text{m}$  from the principal slip surface (labeled as unit 1), the foliated gouge retains relatively coarse grain sizes comparable to the starting materials. Closer to the principal slip surface (labeled unit 2), the foliated gouge has a much finer grain size with the exception of a few remnant dolomite grains. A layer c.  $40\text{ }\mu\text{m}$  thick flanking the principal slip surface (labeled as unit 3) is very fine grained and has homogenous backscatter contrast. Inset shows the convention used to calculate and describe the orientations of the best-fit ellipses to each foliation domain (section 5.3.3.4).

with other high-velocity rotary shear experiments [e.g., *Kitajima et al.*, 2010], at least three distinct microstructural “units” were recognized on the basis of grain size variations, the degree of mixing between calcite and dolomite, and the general appearance of the foliation domains in optical and SEM images (Figure 5.4). The boundaries between the three microstructural units became sharper in samples with higher displacements (e.g., clear boundaries between units in s530 with 1 m displacement; Figure 5.4).

**5.3.3.1.1. Microstructural Unit 1** Unit 1 contains relatively large ( $10\text{--}150\text{ }\mu\text{m}$ ) intact grains of calcite and dolomite (similar in size to the starting materials, e.g., Figure 5.4). Most grains, however, are intensely fragmented and deformed into elongate domains of tightly packed and fine-grained ( $<10\text{ }\mu\text{m}$ ) aggregates of calcite and dolomite that define the foliation (Figure 5.5a, b). Overall, the foliation has an anastomosing style characterized by domains of fractured calcite and dolomite with

pinch-and-swell geometries (Figure 5.4). The foliation domains are generally inclined at approximately  $45^\circ$  to gouge layer boundaries (Figure 5.4; see quantitative analysis of foliations in section 5.3.3.4) but are sometimes deflected toward parallelism with gouge layer boundaries along Y-shears (Figure 5.4). Domains of fine-grained calcite and dolomite are up to  $200\text{ }\mu\text{m}$  long and  $100\text{ }\mu\text{m}$  wide, and derived in most cases from breakdown of single grains in the starting materials (Figure 5.5a). Large grains of calcite and dolomite have tails of fine-grained material (Figure 5.5c). The boundaries between calcite and dolomite domains are generally well defined and there is limited mixing between the two phases (Figure 5.5a). Interpenetration of small grains occurs across the boundaries between calcite and dolomite domains (Figure 5.5b). In areas where the calcite- or dolomite-rich domains become relatively thin, there is some mixing of small particles across phase boundaries (e.g., white arrows in Figure 5.5d point to small dolomite grains).

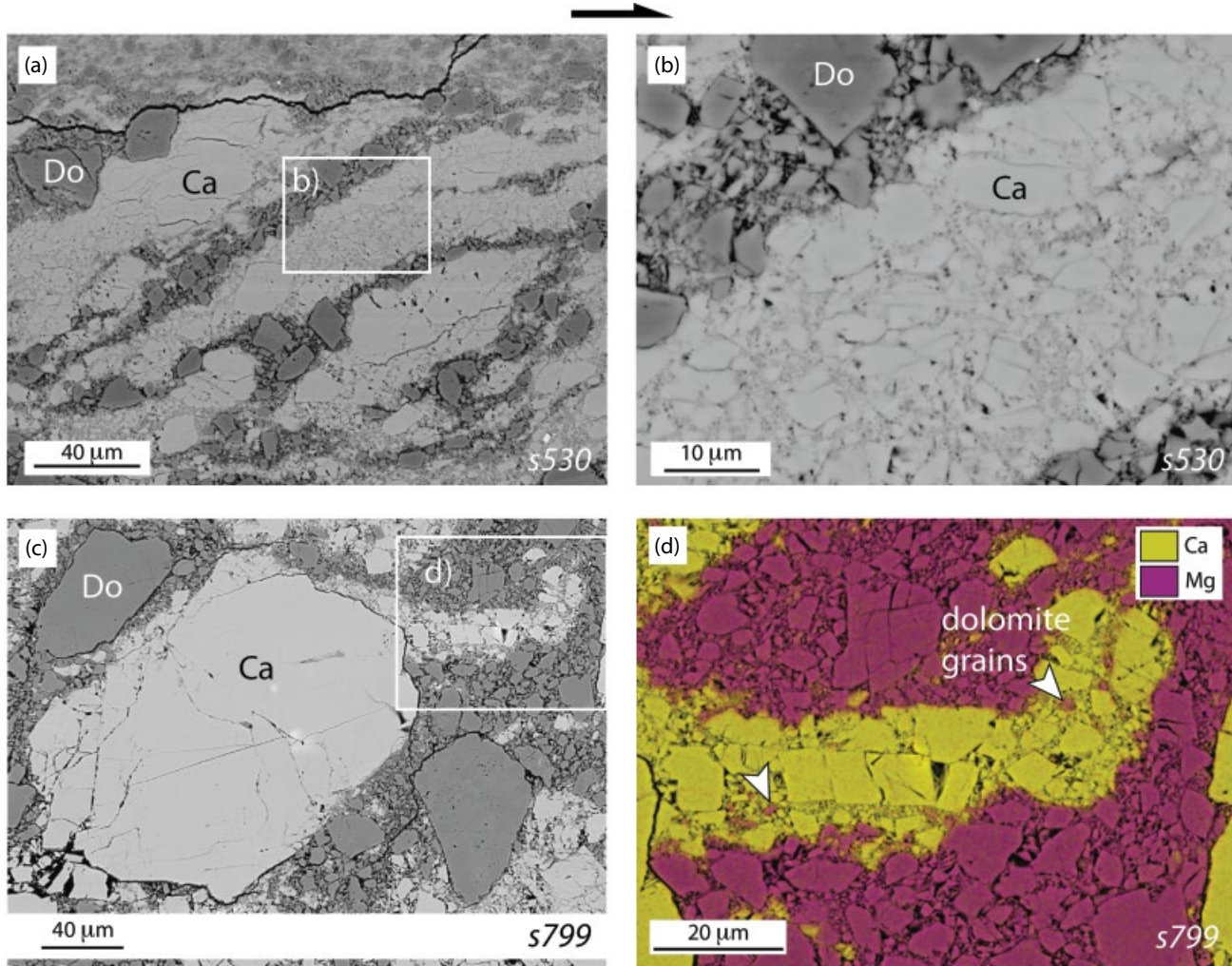


**Figure 5.5** Microstructural unit 1. Images a–c are SEM images and d is an energy-dispersive X-ray spectroscopy (EDS) map. (a) Relatively large and elongate domains of heavily fractured calcite and dolomite define the foliation in microstructural unit 1. Domains are clearly distinguished and there is little mixing between the two phases. (b) Detail of boundary between calcite and dolomite foliation domains. The boundary is irregular due to interpenetration of small calcite and dolomite grains. (c) Large calcite grain with tail of heavily fractured calcite extending into dolomite-rich matrix. (d) Detail of calcite tail showing small particles of dolomite (white arrows) mixed with calcite.

**5.3.3.1.2. Microstructural Unit 2** As in unit 1, the overall style of the foliation in unit 2 is anastomosing, and individual domains of dolomite and calcite have pinch-and-swell geometries (Figure 5.6a). Grain sizes in the matrix of unit 2 are generally  $<10\text{ }\mu\text{m}$  (Figure 5.6a), but remnant dolomite (and less frequent calcite) grains up to c.  $50\text{ }\mu\text{m}$  in size are dispersed throughout (Figures 5.4, 5.6a). The remnant grains often have tails of fine-grained material (e.g., large calcite in Figure 5.6a) and resemble mantled porphyroclasts in mylonites. Foliation domains are shorter and thinner than in unit 1 (Figure 5.6a, b). In general, individual grains of calcite and dolomite

$<10\text{ }\mu\text{m}$  in size have sharp, angular to subangular shapes and are cut by intragranular fractures (Figure 5.6b). Although foliation domains are generally well defined in unit 2 (Figure 5.6a), there are areas where significant mixing has occurred between the two phases, resulting in a fine-grained matrix with a relatively homogenous distribution of calcite and dolomite (Figure 5.6b).

**5.3.3.1.3. Microstructural Unit 3** Where present, unit 3 lies adjacent to the PSS and reaches a maximum thickness of c.  $50\text{ }\mu\text{m}$  (Figures 5.4, 5.7a). Calcite in unit 3 is present in two forms: (1) as elongate grains up to  $10\text{ }\mu\text{m}$

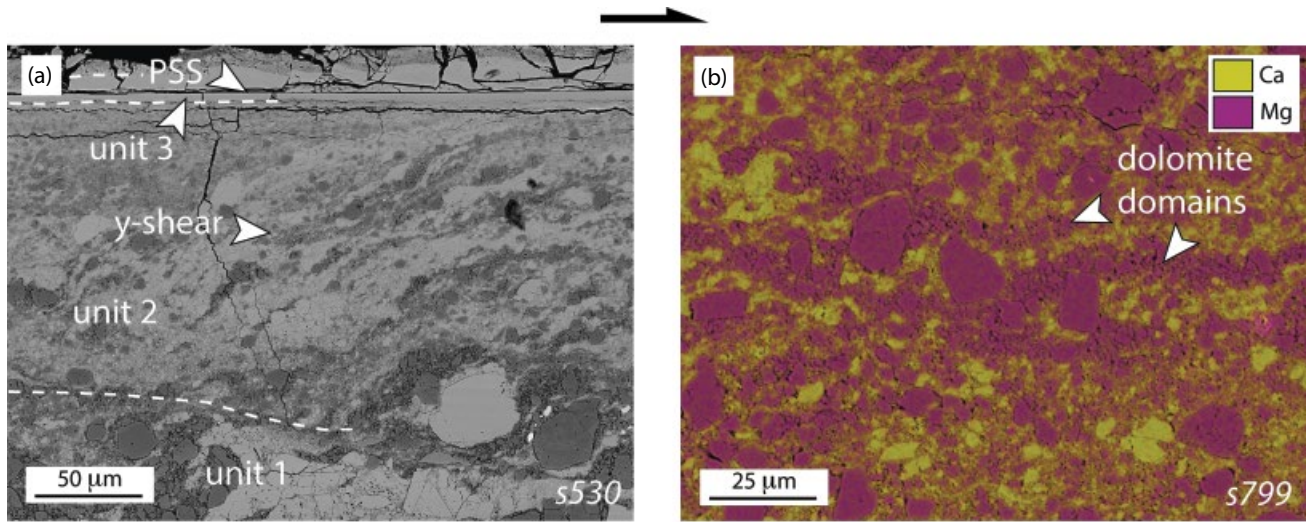


**Figure 5.6** Microstructural unit 2. (a) SEM image showing relatively thin (compared to unit 1 in Figure 5.5) and elongate domains of calcite and dolomite. Grain size is smaller than unit 1 except for larger remnant grains. Image also shows the PSS flanked by microstructural unit 3. (b) EDS map showing two elongate domains of fine-grained dolomite (white arrows) subparallel to the PSS (top edge of image). Surrounding these domains, the matrix has a more homogenous distribution of calcite and dolomite.

long that are generally oriented obliquely to the PSS, forming aggregates with a grain shape preferred orientation (Figure 5.7a) and indistinct grain boundaries; and (2) as extremely fine grained ( $<1\text{ }\mu\text{m}$ ) aggregates in which individual grains are not readily identifiable in SEM images (Figure 5.7b). These aggregates contain porous layers interbanded with domains that have little porosity and homogenous backscatter contrast (Figure 5.7b).

Dolomite grains up to c.  $20\text{ }\mu\text{m}$  in size have sharp grain boundaries and are cut by intragranular microfractures (Figure 5.7a). Some dolomite grains also contain alignments and clusters of small holes that are interpreted as degassing-related porosity (Figure 5.7b), reported in more detail from calcite-dolomite gouge experiments by *Mitchell et al.* [2015]. Large dolomite grains embedded in unit 2 are typically truncated where they encounter one of the margins of unit 3 (Figure 5.7c). Similar truncated dolomite grains were reported by *Fondriest et al.* [2013] (in 100 wt% dolomite gouges) to form experimentally at high slip velocities ( $V>0.1\text{ m/s}$ ) and in association with the development of highly reflective (mirror-like) principal slip surfaces.

EDS analysis shows that the extremely fine grained ( $<1\text{ }\mu\text{m}$ ) aggregates (e.g., Figure 5.7b) contain subtle layering defined by variations in the relative abundance of calcium and magnesium (Figure 5.7d). The grain size in such regions prohibited in-situ identification of mineral phases with the SEM. Powder X-ray diffraction

performed on material derived from unit 3 (in the experiments with 0.05 m and 0.39 m displacement) revealed up to 28 wt% magnesian-calcite and trace amounts of periclase [*Griffiths*, 2014]. Neither of these phases was identified by X-ray diffraction in the starting materials or in the bulk gouge layers, suggesting that they are restricted to unit 3.

### 5.3.3.2. Evolution of Microstructural Units with Displacement

Mosaics of optical and SEM images were used to trace the distribution of microstructural units 1–3 in the five deformed samples used for quantitative microstructural analysis (Figures 5.8, 5.9). Unit 1 is dominant up to c. 0.2 m displacement (Figures 5.8, 5.9). In the sample with 0.03 m displacement, unit 1 is crosscut by R1 Riedel shears (using the terminology of *Logan et al.* [1979]) oriented approximately  $15^\circ$  to gouge layer boundaries (Figure 5.8a). With increasing displacement the Riedel shears disappeared and unit 1 was progressively replaced by units 2 and 3 (Figures 5.8, 5.9). The most significant change in the relative proportions of units 1 and 2 occurred during dynamic weakening (Figure 5.9). Unit 3 is first recognized as a thin lens along and adjacent to the PSS in the sample with 0.05 m displacement (Figure 5.8b). With increasing displacement, unit 3 becomes slightly thicker and more continuous along the PSS (Figure 5.8c–e), although only the sample with 0.39 m displacement contains a significant layer of unit 3 (Figure 5.9).

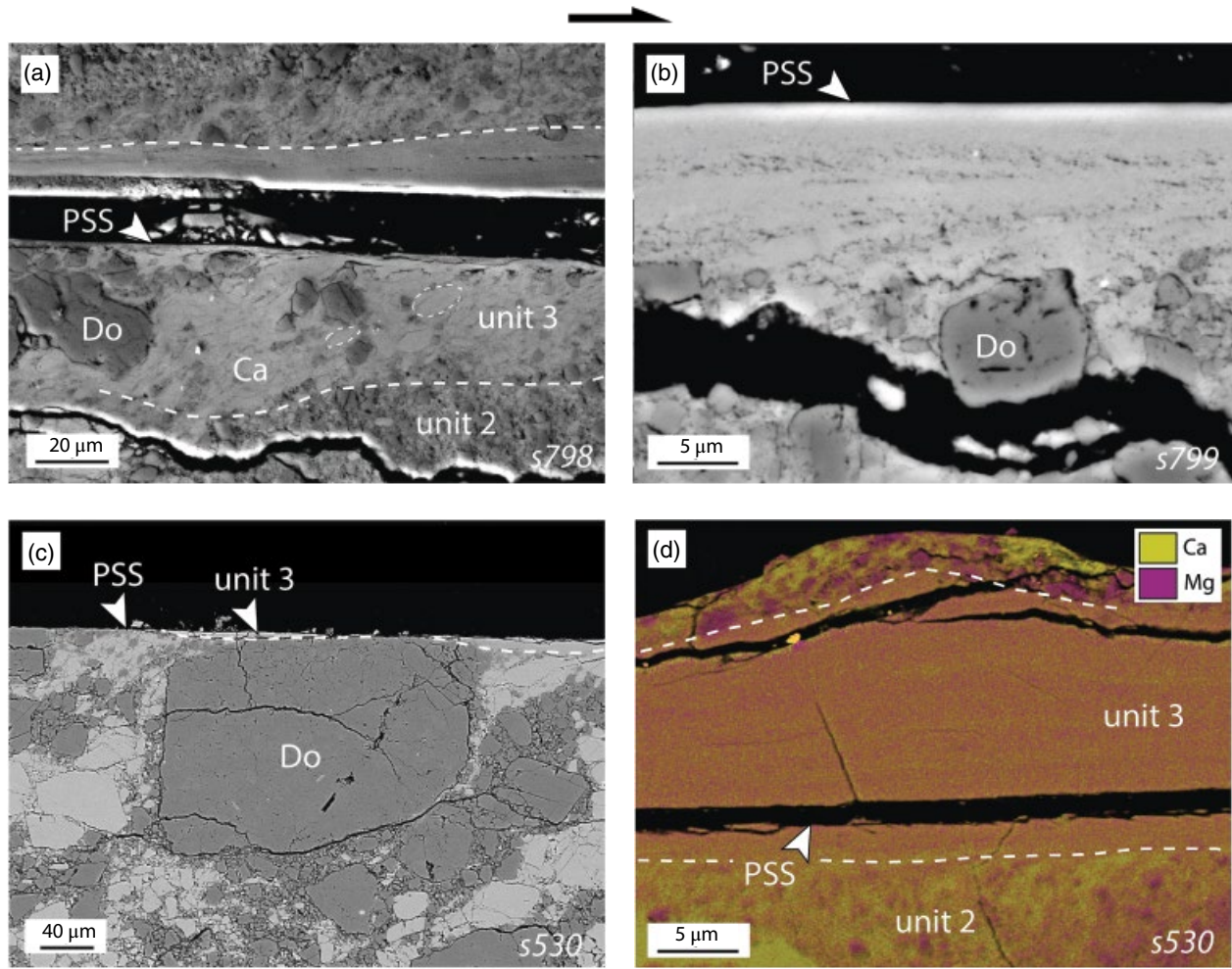


**Figure 5.7** Microstructural unit 3. Images a–c are SEM images and d is an EDS map. (a) Unit 3 is up to 50 μm thick and flanks the PSS. In this example, aggregates of small (c. 5 μm) and elongate calcite grains (two examples surrounded by dashed lines) define a grain shape preferred orientation oblique to the PSS. Relatively large grains of dolomite are embedded in the calcite aggregates. (b) Very fine-grained calcite with indistinct grain boundaries forms aggregates with homogenous backscatter contrast adjacent to the PSS. Layering is defined by alignments of holes (pore space) parallel to the PSS. Dolomite grains adjacent to the aggregates contain pore space interpreted as degassing-related porosity. (c) Large dolomite grains embedded in microstructural unit 2 are sharply truncated at the margins of unit 3. (d) Diffuse banding in unit 3 defined by variations in the relative content of calcium and magnesium. See electronic version for color representation.

### 5.3.3.3. Fracturing Mechanisms in Microstructural Units 1 and 2

Intragranular microfractures in calcite and dolomite indicate that grain size reduction in units 1 and 2 occurred primarily by brittle fracturing (Figures 5.5, 5.6). Brittle fracturing is also interpreted as the dominant deformation mechanism in remnant dolomite grains in unit 3 (Figure 5.7a). Four main fracturing mechanisms were recognized:

1. Impingement or “Hertzian” fracturing (Figure 5.10a) occurred when two grains of the same phase (calcite or

dolomite) and roughly the same size were brought into contact. Such fractures likely formed by tensile failure of grains when load was supported across grain bridges (or “force chains”) [e.g., *Mair and Hazzard, 2007; Sammis and Ben-Zion, 2008*]. This mechanism was particularly prevalent in dolomite grains (Figure 5.10a) but was also observed in calcite. Typically, the fractures associated with this mechanism radiate from a contact region between the two colliding grains, producing elongate grain fragments (or “beams”). The example in Figure 5.10a shows trails of calcite that originate at the

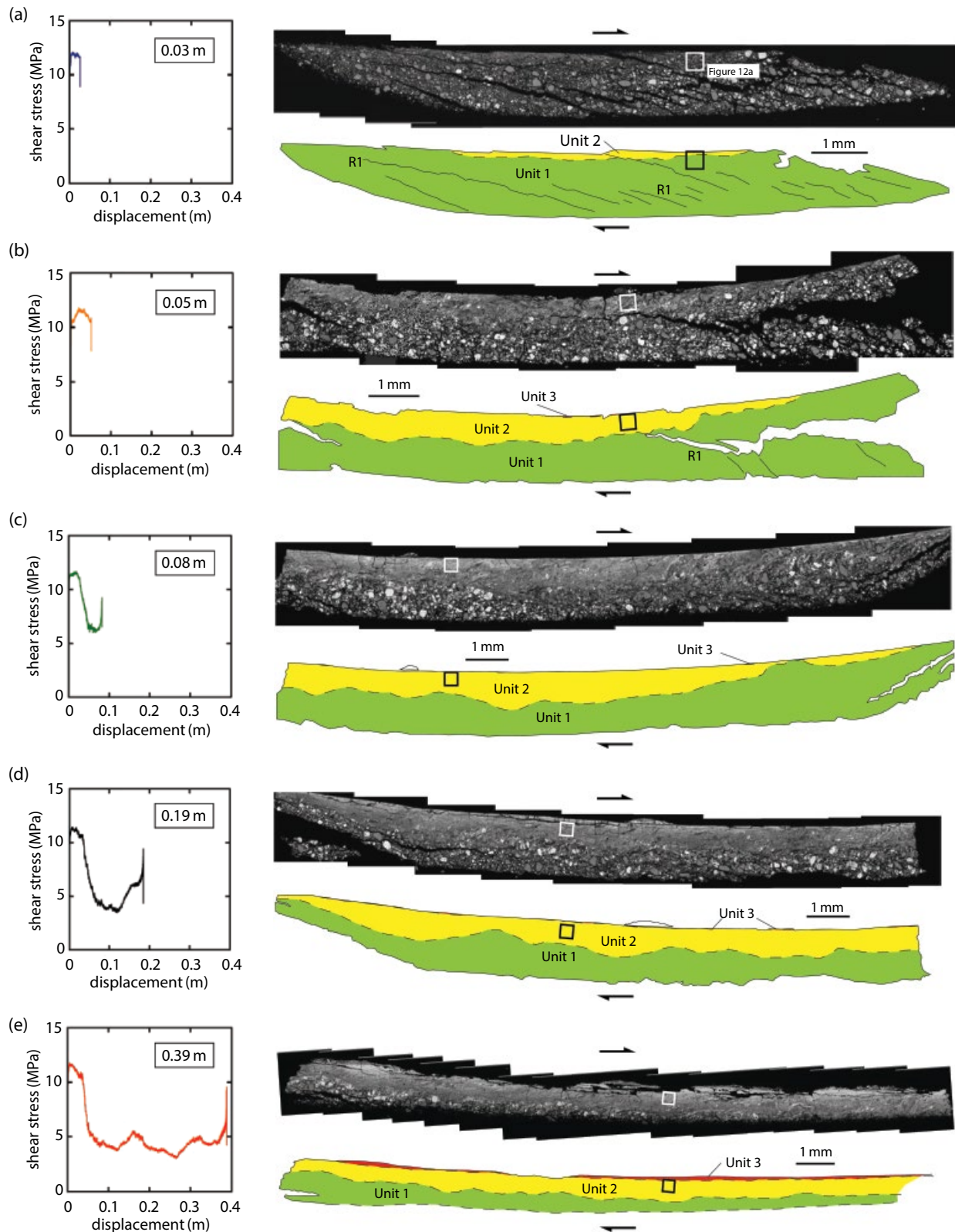


**Figure 5.8** Evolution of microstructural units 1–3 with increasing displacement. Each Figure part (a–e) shows a plot of shear stress vs. displacement (same data as shown in Figure 5.3a), and a SEM mosaic and corresponding line tracing of the distribution of units 1–3. Boxes on the SEM mosaics and line tracings show the locations of analysis areas in Figure 5.12a. (a) 0.03 m displacement, (b) 0.05 m displacement, (c) 0.08 m displacement, (d) 0.19 m displacement, (e) 0.39 m displacement.

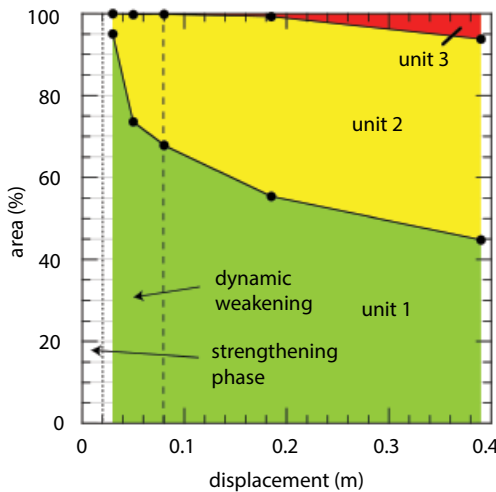


**Figure 5.9** Plot showing the area of sample occupied by microstructural units 1–3 vs. displacement. With increasing displacement, microstructural unit 2 becomes proportionally more important than unit 1. Unit 3 is recognizable after 0.05 m of slip (0.2% of sample area) but increases significantly only after 0.2 m of slip.

contact region between two large dolomite grains. This is interpreted as a calcite grain that was pulverized and expelled outward as the two dolomite grains moved closer together during shearing.

2. *Spalling and chipping* (Figure 5.10b) of angular fragments occurred along the outer margins of calcite and dolomite grains [Billi, 2009]. This produced grains with a central, relatively intact fragment (white dashed line, Figure 5.10b) and an outer mantle of finer-grained material defining an overall subrounded grain shape (black dashed line, Figure 5.10b).

3. *Breakdown of polycrystalline dolomite particles* (Figure 5.10c) by fracturing along grain boundaries produced aggregates of fine-grained gouge. The example in the center of Figure 5.10c is interpreted as a polycrystalline dolomite particle, most probably of the granular type described in section 5.3.1, that broke down into its constituent single grains during shearing.

4. *Fracturing of cleavage planes* (Figure 5.10d) in calcite (and more rarely in dolomite) occurred systematically in orientations at c. 45°–55° to gouge layer boundaries (angle measured clockwise in Figure 5.10d). Similar fracture orientations are observed also for the “Hertzian” fracturing mechanism (Figure 5.10a).

#### 5.3.3.4. Foliation Geometry and Shear Strain in Deformed Gouge Layers

In each deformed sample, SEM images (e.g., Figure 5.4) and EDS maps were used to outline individual domains of calcite and dolomite that collectively define the foliation (Figure 5.4). Outlines of calcite- and dolomite-rich

domains were imported into Image SXM software and used to calculate the best-fit ellipse for each domain (Figure 5.4, inset). The orientation of the major axis of the best-fit ellipse is represented by the angle,  $\phi$ , which was used as a proxy for shear strain,  $\gamma = \tan \phi$  (Figure 5.4, inset). This analysis was performed for many individual calcite- and dolomite-rich domains in microstructural units 1 and 2 to obtain measurements of the angles between each foliation domain and the PSS, and therefore proxy shear strain, across most of the thickness of each gouge layer (Figure 5.4). The assumption that the orientation of foliation domains is a reasonable proxy for shear strain is made on the basis that (i) domains of calcite and dolomite used in the analysis were derived from breakdown of single large grains in the gouge starting material, (ii) most grains in the starting material are roughly equidimensional and the starting material shows homogenous mixing between the two phases, and (iii) in terms of the values of strain and the overall strain distribution (Figure 5.11), our analysis gives comparable results to other high-velocity gouge experiments in which tabular strain markers were used to track the shear strain distribution [Rempe et al., 2014; Smith et al., 2015].

In the sample with 0.03 m displacement, foliation domains are inclined (angle  $\phi$ ) at approximately 45°–50° to gouge layer boundaries, corresponding to a shear strain of  $\gamma \sim 1.5$  across the measured thickness of the gouge layer (Figure 5.11a). In this sample, data were not collected from >600  $\mu\text{m}$  from the stationary side of the gouge layer, but the grain size preserved in that area is similar to the starting materials, and thus it is unlikely that  $\gamma$  was higher than c. 1.5. Due to fine grain size, data were also not collected from within c. 50  $\mu\text{m}$  of the stationary side of the gouge layer. However, the bulk shear strain in this gouge layer is 15 (Table 5.1), calculated as the total displacement (0.03 m) divided by the gouge layer thickness (2 mm). This indicates that most strain (>90%) in this sample is focused into a layer <50  $\mu\text{m}$  thick along the stationary side (Figure 5.11a). This layer corresponds to the incipient development of microstructural unit 2 (Figure 5.8a), which therefore represents a relatively high-strain “shear band” compared to microstructural unit 1.

After 0.05 m displacement, foliation domains closer than c. 200  $\mu\text{m}$  to the newly-formed PSS rotate progressively toward parallelism with the PSS, defining a zone with  $\gamma > 1.5$  (Figure 5.11b). At distances greater than c. 200  $\mu\text{m}$  from the PSS, foliation domains remain at c. 45°–50° to gouge layer boundaries (Figure 5.11b). The zone with  $\gamma > 1.5$  then becomes progressively wider (i.e., migrates away from the PSS) with increasing displacement (Figures 5.11b–e). This zone ( $\gamma > 1.5$ ) can be correlated with microstructural unit 2 (Figure 5.11), which becomes wider (Figure 5.8) and proportionally dominant (Figure 5.9) with increasing displacement. It is

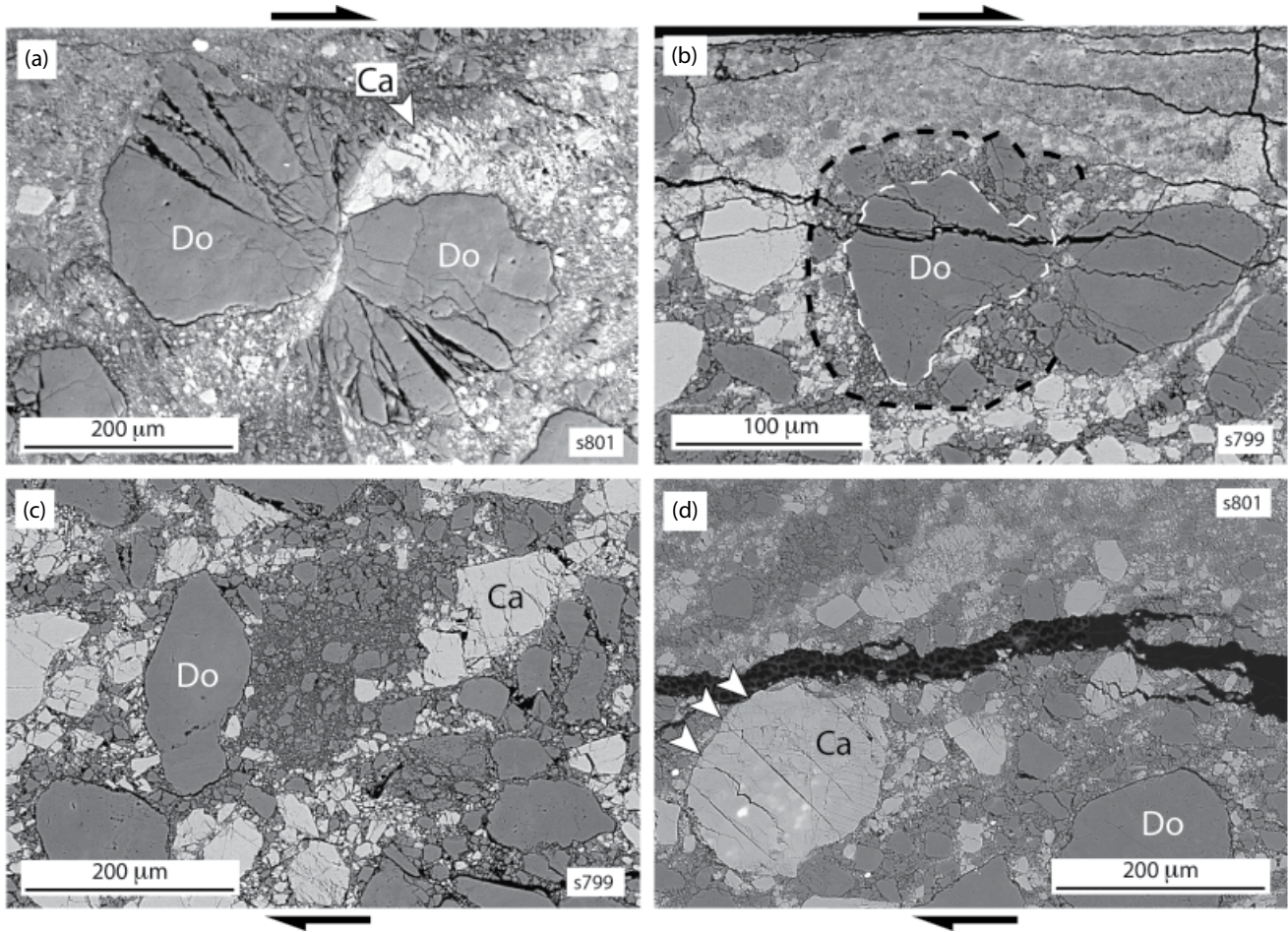


**Figure 5.10** SEM images illustrating the four main fracturing mechanisms identified in microstructural units 1 and 2. (a) Hertzian or impingement fracturing between two large dolomite grains in sample s801 (0.05 m slip). As they were brought into contact, the two large dolomite grains are interpreted to have “squeezed out” an intervening calcite grain that is preserved as tails of fine-grained material emanating from the contact region. (b) Spalling of fine-grained material from the outer margin of a large dolomite grain in sample s799 (0.39 m slip). White dashed lines surround central grain, black dashed lines surround outer mantle of fragmented material. (c) The aggregate of fine-grained dolomite in the center of the image is interpreted to derive from breakdown of a polycrystalline dolomite particle similar to that shown on the left of Figure 5.2b. Sample s799 (0.39 m slip). (d) Planar fractures (white arrows) in sample s801 (0.05 m slip) form along cleavage planes in calcite that are oriented at c. 45°–55° to gouge layer boundaries (angle measured clockwise).

evident that at higher displacements in unit 2, most notably at 0.19 m (Figure 5.11d) and 0.39 m (Figure 5.11e), there is much more scatter in the measured strain values, reflecting progressive mixing and disaggregation of grains comprising the foliation domains.

We stress that in each of these samples (Figure 5.11), the bulk  $\gamma$  values (Table 5.1) dictate that most displacement (strain) in the experiments must be accommodated within a high-strain layer that is not represented in our measurements of foliation angle/shear strain from microstructural units 1 and 2 (Figure 5.11). At relatively small displacements, the high-strain layer corresponds to the incipient microstructural unit 2 (Figure 5.11a), whereas

at larger displacements the high-strain layer corresponds to microstructural unit 3 and a discrete PSS embedded within unit 3 (Figures 5.11b–e).

#### 5.3.3.5. Grain Size Analysis

The size of calcite and dolomite grains was quantitatively evaluated from an area of  $300 \mu\text{m}^2$  in the starting materials and each deformed gouge sample (Figure 5.12a). The analysis areas for the deformed samples are shown in Figure 5.8. In the deformed samples, the analysis areas all have their upper edges along and parallel to the PSS (Figure 5.8). This was done to ensure that the analysis areas covered the regions of gouge that show a clear

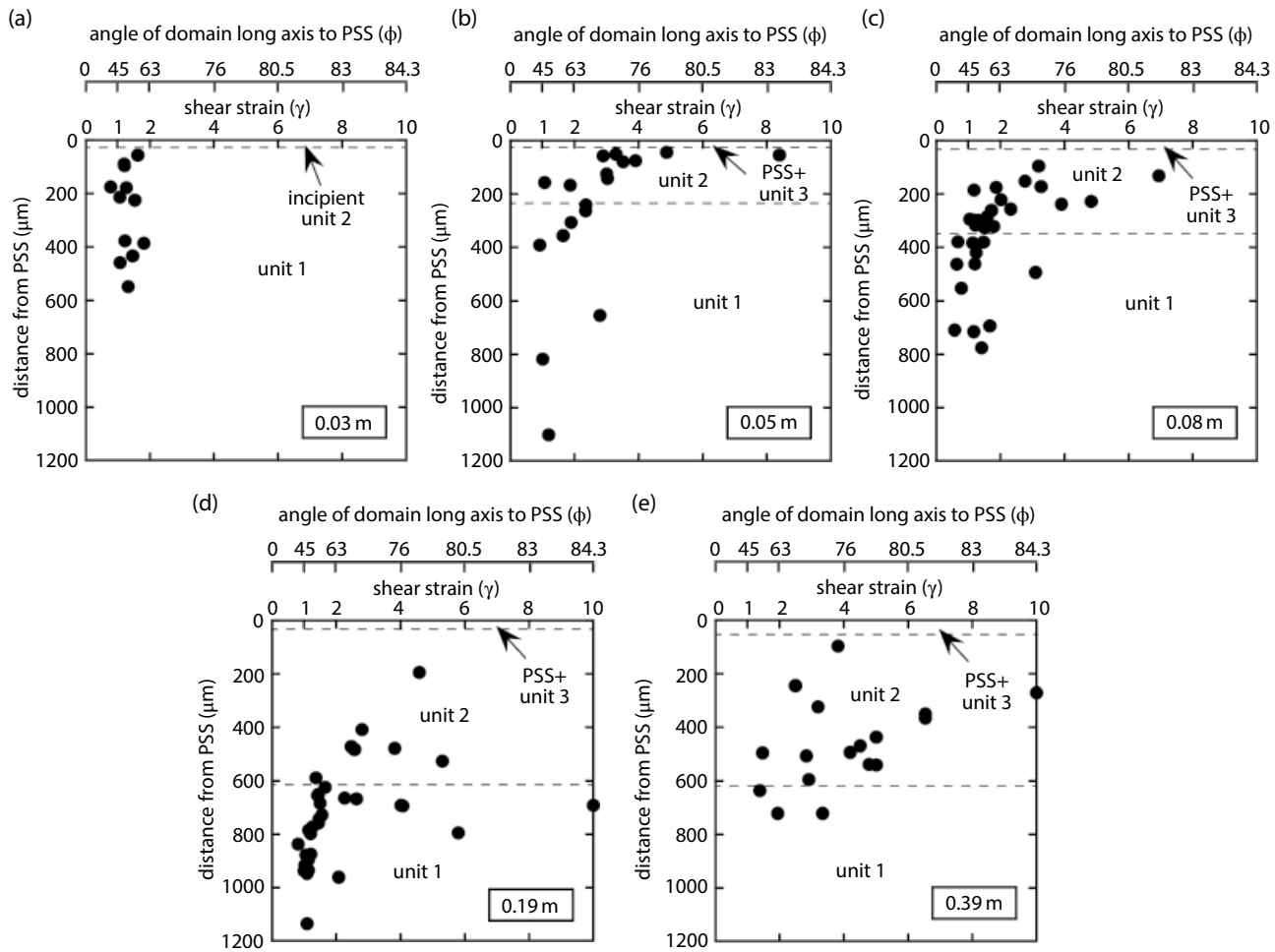


**Figure 5.11** Results of shear strain analysis. Plots show shear strain vs. distance from the PSS in samples with increasing displacement. Each data point is a measurement of shear strain calculated from the angle of one foliation domain (convention in Figure 5.4 inset). Dashed horizontal lines show the boundaries between microstructural units 1, 2, and 3. (a) 0.03 m displacement, (b) 0.05 m, (c) 0.08 m, (d) 0.19 m, (e) 0.39 m.

evolution of fabric and strain with displacement (i.e., the inception and evolution of microstructural unit 2; Figure 5.11).

An area of  $300\mu\text{m}^2$  was selected for each sample, and images (Figure 5.12a) were prepared showing grains of calcite and dolomite (and matrix) using the methods detailed in [Griffiths, 2014]. The minimum pixel dimension of grains that could be reliably identified and used for grain size analysis was set as  $25\text{ pixels}^2$ , corresponding to a grain diameter of approximately  $1.2\mu\text{m}$ . Grain size was measured in Image SXM and calculated as the diameter of an equivalent circle,  $d_{equ} = 2\sqrt{A/\pi}$ , where  $A$  is the measured area of the grain.

Results show that both the mean and maximum grain size in the analysis areas decreases significantly during the first  $0.08\text{ m}$  of displacement, coinciding with the strengthening and dynamic weakening phases observed in mechanical data (Figures 5.12a, b). Mean grain size

decreases to a greater extent in calcite than dolomite (Figure 5.12a). By the time that dynamic weakening has ended, grain size in the analysis areas has stabilized (Figures 5.12b, c). However, the mean grain size of calcite (and to a lesser extent dolomite) slightly increases again in the sample with  $0.39\text{ m}$  displacement (Figure 5.12a).

### 5.3.3.6. Clast Size Distribution Analysis

Two-dimensional clast size distributions (CSDs) were determined for calcite and dolomite in the starting materials and five deformed samples using the grain size data described in the preceding section (i.e., images shown in Figure 5.12a). For each sample, the cumulative number of clasts,  $N$ , larger than a given diameter,  $d_{equ}$ , was plotted in  $\log(N) - \log(d_{equ})$  diagrams (Figure 5.13). CSD curves following a good linear fit over a restricted dimensional range were described by a power-law relationship  $N \sim d_{equ}^{-D}$  ( $\log(N) \sim -D \log(d_{equ})$ ), where  $D$  is the fractal dimension.

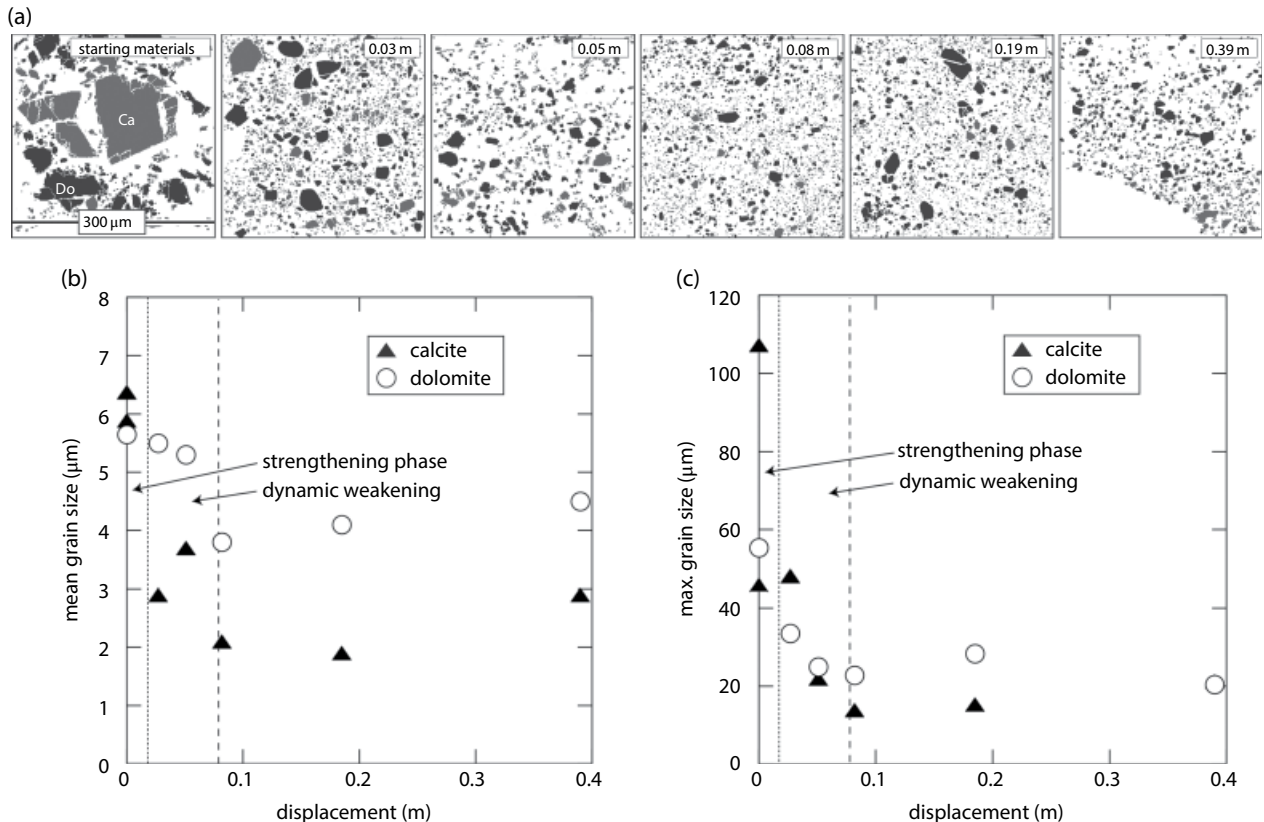


**Figure 5.12** Grain size analysis. (a) Grayscale images used to calculate grain size statistics in the starting materials and five deformed gouge samples. The location of each image is shown (for the deformed samples) in Figure 5.8. Images are  $300\text{ }\mu\text{m} \times 300\text{ }\mu\text{m}$ . Numbers at top of images are displacement values. (b) Mean grain size vs. displacement. For calcite in the starting materials (i.e., 0 m displacement) two values are given: the higher value includes the largest grain shown in Figure 5.12a, the lower value excludes the largest grain shown in Figure 5.12a. (c) Maximum grain size vs. displacement.

The “strength” of the power-law relationship over the analyzed fractal range is shown by the value of  $R^2$  (correlation coefficient), which is between 0.98 and 0.99 for the best-fit lines in the log-log distributions in all samples. We note that both the minimum and maximum grain sizes in the log-log distributions (Figure 5.13) are artificially constrained by, respectively, the lower cutoff in grain size that we imposed during image analysis and the maximum grain size used in the starting materials. As commonly observed in datasets of this type, there is a rollover effect at small grain sizes due to small particles being relatively difficult to detect and measure at a given scale of observation [Blenkinsop, 1991; Fagereng, 2011]. In our datasets, this rollover is observed at a characteristic grain size of  $<2\text{ }\mu\text{m}$  for calcite and c.  $3\text{--}4\text{ }\mu\text{m}$  for dolomite (start of rollover indicated by arrows in Figure 5.13). The rollover parts of the CSD curves were left out when fitting a straight line to the log-log plots. Our results also cover a limited dimensional range (up to two orders of

magnitude). For these reasons, we use  $D$  only to quantify relative differences between our experimental samples and to reveal aspects of the grain size distributions that are not apparent by simply plotting mean and maximum grain sizes (Figure 5.12).

The CSDs of calcite and dolomite in the starting materials (Figure 5.13a) cover a clast size range of  $1.5\text{--}60\text{ }\mu\text{m}$  and are characterized by two segments with distinctly different  $D$  values: a shallower segment at relatively small grain sizes ( $<8\text{ }\mu\text{m}$ ) with  $D$  values of 0.9 (calcite) to 1 (dolomite), and a steeper segment at larger grain sizes ( $>8\text{ }\mu\text{m}$ ) with  $D$  values of 1.75 (calcite) to 1.8 (dolomite). The  $D$  values for deformed samples are adequately fit by power-law distributions over most of the analyzed range of grain sizes. The  $D$  values of both calcite and dolomite increase substantially in the first  $0.08\text{ m}$  of slip, from  $D < 1.8$  in the starting materials to  $D \approx 3$  by the end of dynamic weakening (Figure 5.14). With increasing displacement above  $0.08\text{ m}$ , the  $D$  values remain roughly constant (Figure 5.14).

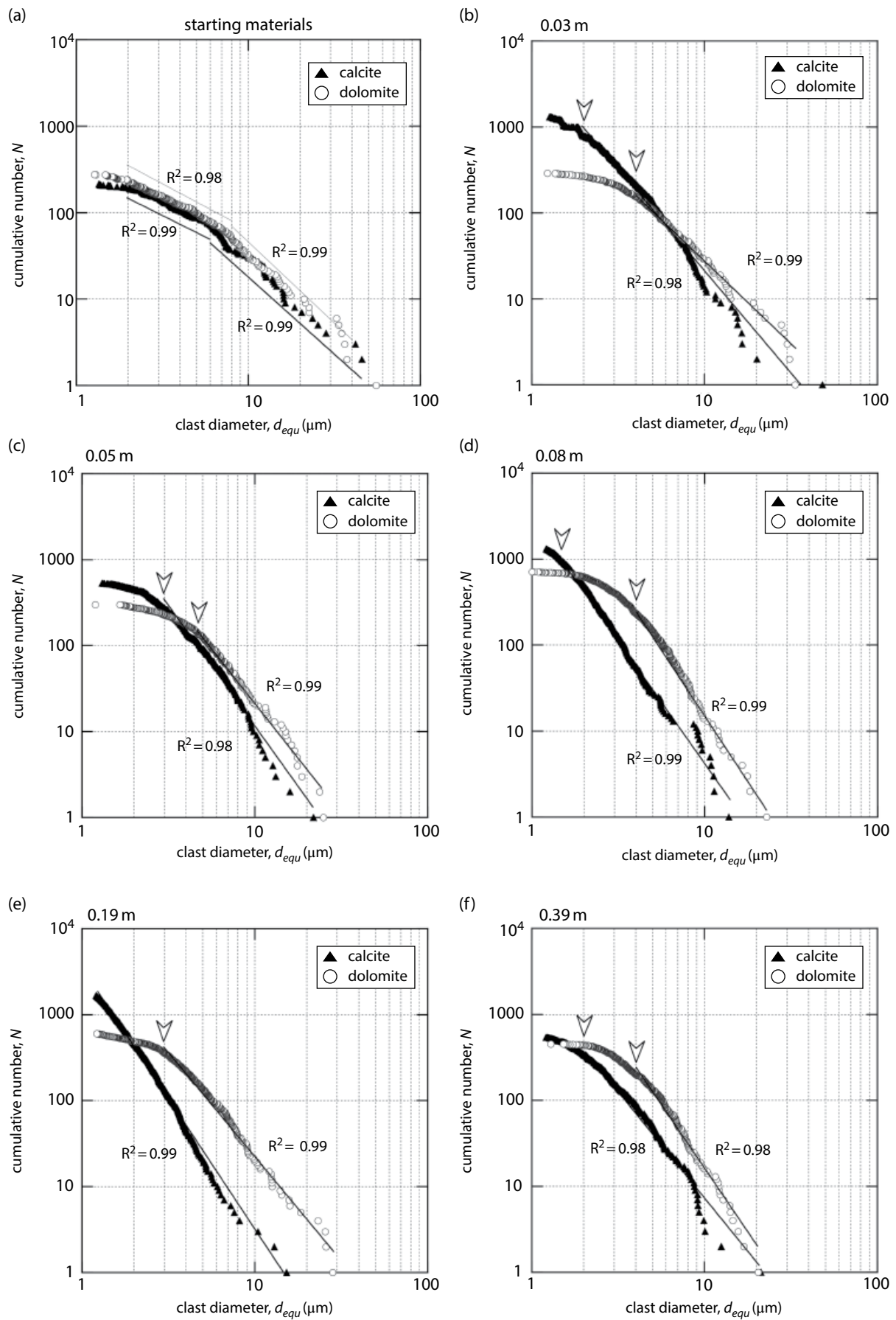


**Figure 5.13** Plots of log grain size ( $d_{eq}$ ) vs. cumulative number ( $N$ ). See text for details of method. Arrows indicate the smallest grain size used to calculate the 2-dimensional “fractal” dimension,  $D$ , from linear best-fit lines. (a) Starting materials. (b–f) Samples with increasing displacements between 0.03 m and 0.39 m.

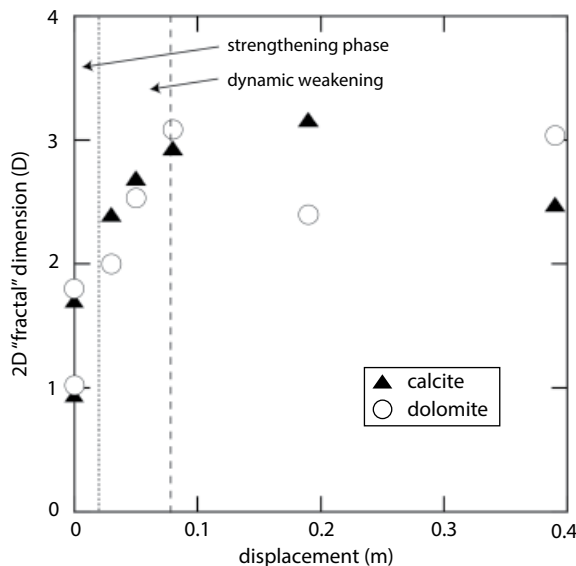


**Figure 5.14** Plot showing the evolution of the 2-dimensional “fractal” dimension,  $D$ , with increasing displacement. For the starting materials, two  $D$  values are given corresponding to the shallower and steeper segments of the CSD curves observed on the log-log plot in Figure 5.13a.

## 5.4. DISCUSSION

### 5.4.1. Fabric Development and Grain Size Reduction at High Slip Velocities

Our experiments indicate that at high slip velocities ( $V > 0.01 \text{ m s}^{-1}$ ) and for displacements representative of earthquakes of approximately  $M_w$  3–7, well-defined foliations can form in calcite-dolomite gouges from an initial mixed distribution of phases. Microstructural data document a progressive evolution of fabric and grain size that strongly correlates with gouge mechanical behavior. The most significant changes in microstructure, fabric geometry, and grain size in our experiments occurred before and during dynamic weakening. Once shear stress reached “steady state,” after approximately 0.08 m in these experiments, fabric and grain size in the bulk gouge layers essentially stabilized and did not experience further changes. In the following paragraphs, we build on previous work [e.g., Kitajima *et al.*, 2010; Yao *et al.*, 2013; Bullock *et al.*, 2015; De Paola *et al.*, 2015; Smith *et al.*, 2015] and interpret our results in the context of shear localization and the development of a PSS in the gouge layers (Figure 5.15).

During the initial gouge strengthening phase, strain was homogenously distributed ( $\gamma \sim 1.5$ ) across the bulk of the gouge layer and R1 Riedel shears were active (Figure 5.15a). A striking foliation developed (to form our microstructural unit 1) that we interpret to result from a combination of processes: grain size reduction occurred primarily by breakdown of polycrystalline grains and

fracturing of large grains in the starting materials. Where discrete intragranular fractures occur, they show a strong preferred orientation subparallel to the instantaneous shortening direction ( $\sigma_1$ ) during simple shear (Figure 5.15a). Such fractures likely form by tensile failure of grains because load is supported across grain bridges (or “force chains”) that develop in the gouge layers subparallel to the  $\sigma_1$  direction [e.g., Mair and Hazzard, 2007; Sammis and Ben-Zion, 2008]. Microstructures suggest that many grains (but particularly calcite grains) fractured when they rotated into an orientation such that a set of cleavage planes was subparallel to  $\sigma_1$  (Figure 5.15a). Fracturing throughout the gouge layer during initially distributed shearing produced fine-grained aggregates that were soft and readily deformable. The orientation of foliation domains at c.  $45^\circ$ – $50^\circ$  to gouge layer boundaries suggests that aggregates were compressed subparallel to  $\sigma_1$  and elongated subperpendicular to  $\sigma_1$  (Figure 5.15a). Together with the effects of distributed strain, this formed a foliation defined by elongate domains of crushed calcite and dolomite (Figure 5.15a). The overall low strain in microstructural unit 1 ( $\gamma \sim 1.5$ ) meant that there was minimal mixing between calcite and dolomite. By the end of the initial strengthening phase, strain had started to localize close to one margin of the gouge layer (Figure 5.15a; incipient microstructural unit 2).

During the dynamic weakening phase, lenses of microstructural unit 3 and a through-going PSS were established, accommodating most subsequent displacement at high strain rates (Figure 5.15b). Despite this progressive localization process during dynamic weakening, the gouge adjacent to the PSS also continued to deform (Figure 5.15b). This is indicated in our experiments by widening of microstructural unit 2 and rapid grain size reduction in unit 2 observed during dynamic weakening (Figure 5.15b). Grain size reduction caused an increase in the  $D$  values of the grain size distributions (Figure 5.14). However, the evolution of mean grain sizes (Figure 5.12b) and the common occurrence of relatively large remnant dolomite grains in units 2 and 3 indicate that dolomite was more resistant overall to grain size reduction.

The formation and evolution of microstructural unit 3 during dynamic weakening is interpreted to result from recrystallization and decomposition of fine-grained calcite and dolomite along and adjacent to the PSS (Figure 5.15c), driven by the frictional heat produced as a consequence of localized slip at high strain rates. Indistinct calcite grain boundaries (even at high magnifications in the SEM) and the grain-shape preferred orientation observed in some calcite aggregates in unit 3 (Figure 5.7a) suggest calcite recrystallization and grain welding. This is consistent with the detection in unit 3 of magnesian-calcite and periclase, probably formed by decomposition of dolomite at temperatures exceeding c.  $550^\circ\text{C}$

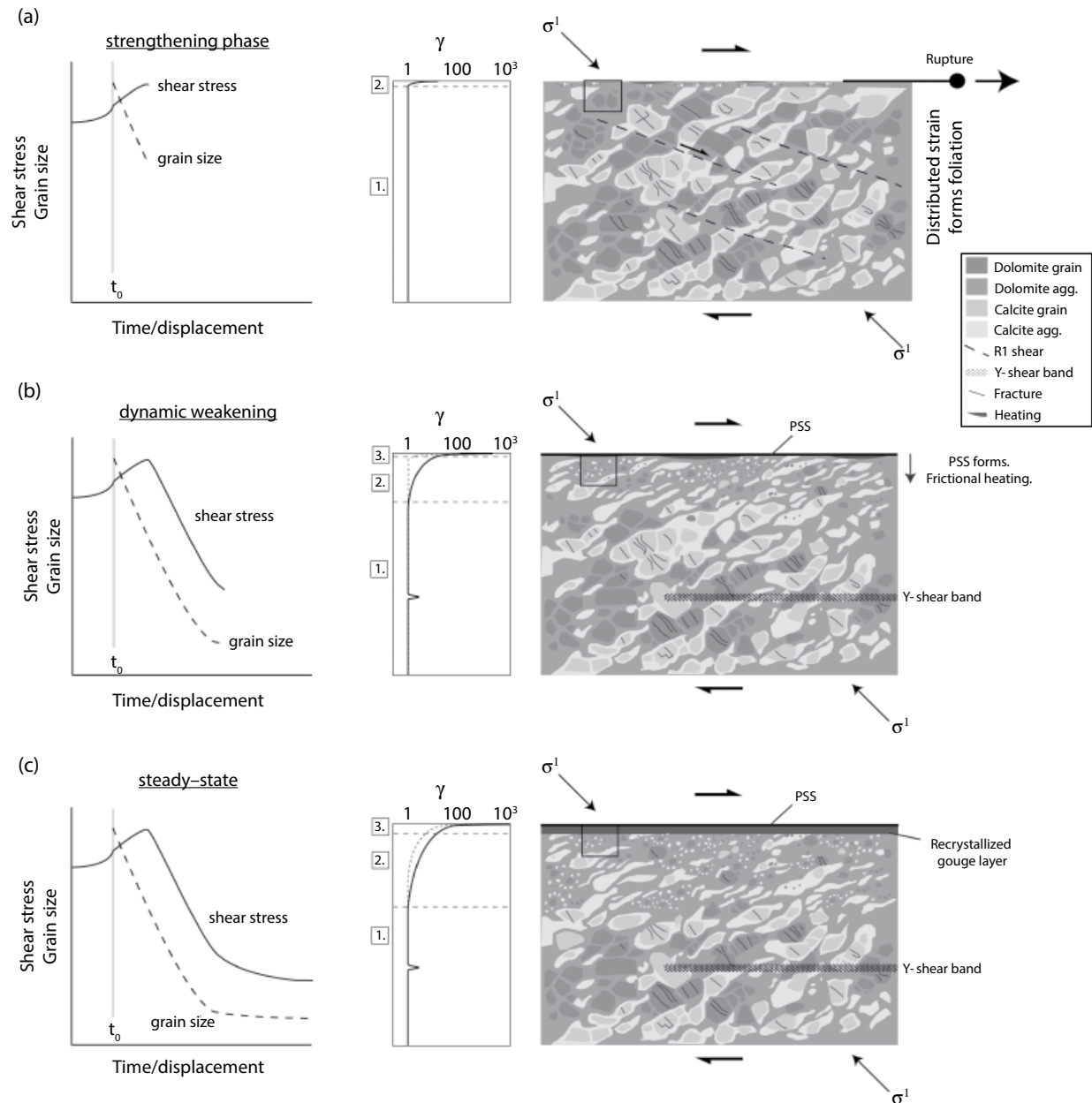


**Figure 5.15** Schematic synthesis of mechanical behavior and fabric evolution observed in mixed calcite-dolomite gouge experiments. Numbers in boxes refer to the microstructural units described in this chapter. (a) The initial stages of coseismic shearing are distributed across the gouge layer. R1 Riedel shears are active. Foliation develops by a combination of pervasive grain fracturing and rotation of individual foliation domains at relatively low strains. This accompanies strengthening observed in the mechanical data. By the end of the strengthening phase, strain has started to localize in a narrow band (microstructural unit 2) that will ultimately develop into a discrete PSS surrounded by microstructural unit 3. (b) Dynamic weakening accompanies progressive formation of a discrete PSS associated with lenses of unit 3. The PSS (and possibly unit 3) accommodates most subsequent displacement, but the gouge adjacent to the PSS also continues to deform, resulting in widening of microstructural unit 2. Y-shears form in the bulk gouge. (c) The PSS (and possibly unit 3) continues to accommodate most displacement once “steady-state” shear stress is attained. Frictional heating along the PSS causes decomposition of the carbonates and forms a semicontinuous layer of recrystallized gouge (microstructural unit 3) that becomes slightly thicker with increasing displacement. No significant changes to grain size or gouge fabric take place in units 1 and 2 once steady state is achieved.

[Samtani *et al.*, 2002; De Paola *et al.*, 2011; Fondriest *et al.*, 2013]. Our interpretation of unit 3 is also based on previous high-velocity experimental work documenting the formation of recrystallized "mylonitic" layers due to frictional heating along a discrete slip surface [Kim *et al.*, 2010; Brantut *et al.*, 2011; Smith *et al.*, 2013; Ree *et al.*, 2014; De Paola *et al.*, 2015; Green *et al.*, 2015]. It is noteworthy that the grain size of recrystallized calcite in microstructural unit 3 (<1 μm in the aggregates; Figure 5.7b) is much smaller than in experiments performed with pure (100 wt%) calcite gouge under similar conditions [Smith *et al.*, 2013; 1–10 μm with ribbon grains up to 50 μm]. We suggest that this is because dolomite inhibits recrystallization and postexperiment grain growth in calcite by effectively "pinning" calcite grain boundaries [Herwegh and Kunze, 2002; Delle Piane *et al.*, 2009].

After "steady-state" shear stress was attained in the experiments (Figure 5.15c), the PSS (and possibly microstructural unit 3) continued to accommodate most ongoing displacement at high strain rates, although unit 2 widened slightly, indicating that the bulk gouge also continues to deform (Figure 5.15c). Microstructural unit 3 increased in thickness to form a semicontinuous layer of recrystallized gouge as a result of continued frictional heating (and decomposition) along the PSS [Smith *et al.*, 2013].

We emphasize that although the strain rate along the PSS, and potentially within microstructural unit 3, must have been extremely high, the strain rates in the adjacent layers (microstructural units 1 and 2) throughout the experiments were much lower. Strain accommodated in microstructural unit 2 only increased from c. 1.5 to c. 8–10 during dynamic weakening (Figure 5.11). Nevertheless, this modest increase in strain was enough to cause substantial mixing of calcite and dolomite grains, as well as thinning and disaggregation of the foliation domains (Figure 5.15b). In microstructural unit 1, deformation essentially ceased once peak stress was reached and strain had localized to units 2–3 and the PSS (Figure 5.15b, c). Summarizing, progressive fabric, and grain size evolution in the bulk gouge layers occurred by cataclastic "flow" at relatively low strains and strain rates, in parallel with deformation occurring at high strain rates along the bounding PSS.

#### 5.4.2. A Coseismic Origin for Some Foliated Gouges and Cataclasites?

In the cores of natural faults exhumed from depths of c. 5–15 km, foliations present in gouge and cataclasite are commonly defined by interconnected networks and overgrowths of aligned phyllosilicate phases [e.g., Imber *et al.*, 1997; Manatschal, 1999; Stewart *et al.*, 2000; White, 2001; Wintsch and Yi, 2002; Gueydan *et al.*, 2003; Collettini and Holdsworth, 2004; Jefferies *et al.*, 2006; Collettini *et al.*, 2009; Wallis *et al.*, 2013]. In this type of foliated gouge

and cataclasite, there is abundant microstructural and geochemical evidence for the operation of frictional sliding accompanied by fluid-assisted deformation processes and dissolution-precipitation reactions. In such cases, a convincing argument has been made that the phyllosilicate-rich foliations were generated during aseismic fault creep, perhaps at low stresses leading to long-term fault zone weakening [Rutter *et al.*, 2001; Holdsworth, 2004; Moore and Rymer, 2007]. Experiments on clay-bearing gouge layers at low slip velocities indicate that mechanical rotation of clay particles can also form well-defined foliations [Rutter *et al.*, 1986; Logan *et al.*, 1992; Haines *et al.*, 2013]. Bos *et al.* [2000] and Niemeijer and Spiers [2006] showed that foliations defined by aligned and interconnected phyllosilicate seams developed in brine-saturated gouge experiments at low strain rates by granular flow accompanied by efficient dissolution-precipitation. In the same experiments, an increase in strain rate led to disruption of the foliation and formation of a random-fabric gouge [Niemeijer and Spiers, 2006].

In many other cases, foliations in natural gouge and cataclasite reflect the combined influences of compositional layering, grain size variations, preferred alignment of clasts and fractures, or an organized arrangement of shear surfaces [e.g., Chester and Logan, 1987; Chester and Chester, 1998; Fabbri *et al.*, 2000; Lin, 2001; White, 2001; Cowan *et al.*, 2003]. These types of foliated gouge and cataclasite are particularly common in brittle fault zones exhumed from depths of less than about 10 km, where grain size reduction by cataclasis is expected to become a dominant deformation mechanism [Sibson, 1977]. Although an "aseismic" interpretation is often adopted for the origin of such foliated cataclasites, our experimental gouges deformed at seismic slip velocities ( $V < 1.13 \text{ m s}^{-1}$ ) contain striking foliations defined primarily by compositional layering and grain size variations. This suggests that some natural examples of foliated gouge and cataclasite with similar microstructure may be better interpreted as the product of distributed brittle "flow" during coseismic slip, particularly if the foliations are found in conjunction with a bounding slip surface.

In our gouge experiments, the most striking foliations were established in the gouge layers at relatively low strain ( $\gamma < 1.5$ ), as deformation was progressively localized before and during the dynamic weakening process. In natural fault zones, few constraints are currently available on the initial thickness (or grain size distribution) of the coseismic shear zone that starts to deform after passage of the rupture front [Beeler *et al.*, 2008]. Based on field and borehole observations in active and exhumed faults, it is not unreasonable to think that the initial stages of coseismic shearing in large fault zones may be accommodated in gouge or breccia horizons exceeding tens of centimeters or more in thickness [Sibson, 2003, Sagi and Brodsky, 2009]. If this is true, initially distributed shearing

in such horizons may be sufficient to form “coseismic foliations” that occupy relatively thick fault rock layers, even if strain quickly localizes to a narrow band or slip surface.

## 5.5. CONCLUSIONS

High-velocity ( $V < 1.13 \text{ m/s}$ ) shear experiments on mixed calcite-dolomite gouges were performed to investigate fabric and grain size evolution and to explore the possibility that some natural foliated fault rocks may have a coseismic origin. Results indicate that for displacements representative of earthquakes of approximately  $M_w$  3–7, foliations can develop quickly from an initial mixed assemblage of calcite and dolomite grains. The most significant changes in gouge microstructure, foliation geometry, and grain size take place before and during dynamic weakening, as initially distributed strain becomes localized to a discrete slip surface. Formation of the slip surface is complete by the end of dynamic weakening, after which foliation and grain size in the bulk gouge layer stabilize and do not experience significant further changes. Although an “aseismic” interpretation is often adopted for the origin of foliated gouge and cataclasite in brittle fault zones, our experiments suggest that foliations defined by compositional banding, grain size variations, and preferred particle or fracture alignments could form by distributed brittle flow as strain localizes during coseismic shearing.

## ACKNOWLEDGEMENTS

This work was supported by the Marsden Fund Council (project UOO1417 to Smith), administered by the Royal Society of New Zealand, ERC StG no. 205175 USEMS (to Di Toro) and ERC CoG no. 614705 NOFEAR (to Di Toro). Marco Brenna and Kat Lilly provided assistance with the SEM in the Otago Centre for Electron Microscopy (OCEM) at the University of Otago. Brent Pooley prepared excellent thin sections. Fabio de Felice and Elena Spagnuolo provided assistance with experiments at the INGV, Rome. Marianne Negrini helped with preparation of figures. Christie Rowe and Rachel Bullock providing constructive reviews that helped to clarify many aspects of the paper.

## REFERENCES

- Beeler, N. M., T. E. Tullis, and D. L. Goldsby (2008), Constitutive relationships and physical basis of fault strength due to flash heating, *Journal of Geophysical Research: Solid Earth*, 113(B1).
- Billi, A. (2009), Microtectonics of low-P low-T carbonate fault rocks, *Journal of Structural Geology* 32, 1392–1402.
- Blenkinsop, T. G. (1991), Cataclasis and processes of particle-size reduction, *Pure and Applied Geophysics*, 136(1), 59–86.
- Bos, B., C. J. Peach, and C. J. Spiers (2000), Frictional-viscous flow of simulated fault gouge caused by the combined effects of phyllosilicates and pressure solution, *Tectonophysics*, 327(3–4), 173–194.
- Brantut, N., R. Han, T. Shimamoto, N. Findling, and A. Schubnel (2011), Fast slip with inhibited temperature rise due to mineral dehydration: Evidence from experiments on gypsum, *Geology*, 39(1), 59–62.
- Brantut, N., A. Schubnel, J. N. Rouzaud, F. Brunet, and T. Shimamoto (2008), High-velocity frictional properties of a clay-bearing fault gouge and implications for earthquake mechanics, *Journal of Geophysical Research: Solid Earth*, 113.
- Bullock, R. J., N. De Paola, and R. E. Holdsworth (2015), An experimental investigation into the role of phyllosilicate content on earthquake propagation during seismic slip in carbonate faults, *Journal of Geophysical Research: Solid Earth*, 120(5), 3187–3207.
- Chester, F. M., and J. M. Logan (1987), Composite planar fabric of gouge from the Punchbowl fault, California, *Journal of Structural Geology*, 9, 621–634.
- Chester, F. M., and J. S. Chester (1998), Ultracataclasite structure and friction processes of the Punchbowl fault, San Andreas system, California, *Tectonophysics*, 295(1–2), 199–221.
- Chester, F. M., M. Friedman, and J. M. Logan (1985), Foliated cataclasites, *Tectonophysics*, 111(1–2), 139–146.
- Cladouhos, T. T. (1999), A kinematic model for deformation within brittle shear zones, *Journal of Structural Geology*, 21(4), 437–448.
- Collettini, C., and R. E. Holdsworth (2004), Fault zone weakening and character of slip along low-angle normal faults: Insights from the Zuccale fault, Elba, Italy, *Journal of the Geological Society*, 161, 1039–1051.
- Collettini, C., C. Viti, S. A. F. Smith, and R. E. Holdsworth (2009), Development of interconnected talc networks and weakening of continental low-angle normal faults, *Geology*, 37(6), 567–570.
- Cowan, D. S. (1999), Do faults preserve a record of seismic slip? A field geologist’s opinion, *Journal of Structural Geology*, 21(8–9), 995–1001.
- Cowan, D. S., and M. T. Brandon (1994), A symmetry-based method for kinematic analysis of large-slip brittle fault zones, *American Journal of Science*, 294(3), 257–306.
- Cowan, D. S., T. T. Cladouhos, and J. K. Morgan (2003), Structural geology and kinematic history of rocks formed along low-angle normal faults, Death Valley, California, *Geological Society of America Bulletin*, 115(10), 1230–1248.
- De Paola, N., T. Hirose, T. Mitchell, G. Di Toro, C. Viti, and T. Shimamoto (2011), Fault lubrication and earthquake propagation in thermally unstable rocks, *Geology*, 39(1), 35–38.
- De Paola, N., R. E. Holdsworth, C. Viti, C. Collettini, and R. J. Bullock (2015), Can grain size sensitive flow lubricate faults during the initial stages of earthquake propagation? *Earth and Planetary Science Letters*, 431, 48–58.
- Delle Piane, C., L. Burlini, and K. Kunze (2009), The influence of dolomite on the plastic flow of calcite rheological, microstructural and chemical evolution during large strain torsion experiments, *Tectonophysics*, 467(1–4), 145.

- Di Toro, G., A. Niemeijer, A. Tripoli, S. Nielsen, F. Di Felice, P. Scarlato, G. Spada, R. Alessandroni, G. Romeo, G. Di Stefano, S. Smith, E. Spagnuolo, and S. Mariano (2010), From field geology to earthquake simulation: a new state-of-the-art tool to investigate rock friction during the seismic cycle (SHIVA), *Rendiconti Lincei-Scienze Fisiche E Naturali*, 21, 95–114.
- Engelder, J. T. (1974), Cataclasis and the generation of fault gouge, *Geological Society of America Bulletin*, 85, 1515–1522.
- Fabbri, O., A. M. Lin, and H. Tokushige (2000), Coeval formation of cataclasite and pseudotachylite in a Miocene forearc granodiorite, southern Kyushu, Japan, *Journal of Structural Geology*, 22(8), 1015–1025.
- Fagereng, A. (2011), Frequency-size distribution of competent lenses in a block-in-matrix melange, Imposed length scales of brittle deformation? *Journal of Geophysical Research—Solid Earth*, 116.
- Fondriest, M., S. Aretusini, G. Di Toro, and S. A. F. Smith (2015), Fracturing and rock pulverization along an exhumed fault zone in dolostones: The Foiana Fault Zone (Southern Alps, Italy), *Tectonophysics*, 654, 56–74.
- Fondriest, M., S. A. F. Smith, T. Candela, S. Nielsen, K. Mair, and G. Di Toro (2013), Mirror-like faults and power dissipation during earthquakes, *Geology*, 41, 1175–1178.
- Green, H. W., F. Shi, K. Bozhilov, G. Xia, and Z. Reches (2015), Phase transformation and nanometric flow cause extreme weakening during fault slip, *Nature Geoscience*, 8(6), 484–491.
- Griffiths, J. R. (2014), *Using earthquake-like laboratory experiments to reveal ancient seismicity in the rock record*, Bachelor of Science (with Honors), University of Otago.
- Gueydan, F., Y. M. Leroy, L. Jolivet, and P. Agard (2003), Analysis of continental midcrustal strain localization induced by microfracturing and reaction-softening, *Journal of Geophysical Research: Solid Earth*, 108(B2), 2064, doi:10.1029/2001JB000611.
- Haines, S., B. Kaproth, C. Marone, D. Saffer, and B. A. van der Pluijm (2013), Shear zones in clay-rich fault gouge: A laboratory study of fabric development and evolution, *Journal of Structural Geology*, 51, 206–225.
- Hayman, N. W., B. A. Housen, T. T. Cladouhos, and K. Livi (2004), Magnetic and clast fabrics as measurements of grain-scale processes within the Death Valley shallow crustal detachment faults, *Journal of Geophysical Research: Solid Earth*, 109(B5), B05409, doi:05410.01029/02003JB02902.
- Herwegh, M., and K. Kunze (2002), The influence of nano-scale second-phase particles on deformation of fine grained calcite mylonites, *Journal of Structural Geology*, 24, 1463–1478.
- Holdsworth, R. E. (2004), Weak faults: Rotten cores, *Science*, 303(5655), 181–182.
- Holdsworth, R. E., E. W. E. van Diggelen, C. J. Spiers, J. H. P. de Bresser, R. J. Walker, and L. Bowen (2011), Fault rocks from the SAFOD core samples: Implications for weakening at shallow depths along the San Andreas Fault, California, *Journal of Structural Geology*, 33(2), 132–144.
- Imber, J., R. E. Holdsworth, C. A. Butler, and G. E. Lloyd (1997), Fault-zone weakening processes along the reactivated Outer Hebrides Fault Zone, Scotland, *Journal of the Geological Society*, 154, 105–109.
- Jefferies, S. P., R. E. Holdsworth, C. A. J. Wibberley, T. Shimamoto, C. J. Spiers, A. R. Niemeijer, and G. E. Lloyd (2006), The nature and importance of phyllonite development in crustal-scale fault cores: An example from the Median Tectonic Line, Japan, *Journal of Structural Geology*, 28(2), 220–235.
- Kim, J. W., J. H. Ree, R. Han, and T. Shimamoto (2010), Experimental evidence for the simultaneous formation of pseudotachylite and mylonite in the brittle regime, *Geology*, 38(12), 1143–1146.
- Kitajima, H., J. S. Chester, F. M. Chester, and T. Shimamoto (2010), High-speed friction of disaggregated ultracataclasite in rotary shear: Characterization of frictional heating, mechanical behavior, and microstructure evolution, *Journal of Geophysical Research: Solid Earth*, 115.
- Lin, A. M. (2001), S-C fabrics developed in cataclastic rocks from the Nojima fault zone, Japan and their implications for tectonic history, *Journal of Structural Geology*, 23(6–7), 1167–1178.
- Logan, J. M., C. A. Dengo, N. G. Higgs, and Z. Z. Wang (1992), Fabrics of experimental fault zones: Their development and relationship to mechanical behaviour, in *Fault Mechanics and Transport Properties of Rocks*, edited by B. Evans and T. F. Wong, Academic Press, London, 33–68.
- Logan, J. M., M. Friedman, N. Higgs, C. Dengo, and T. Shimamoto (1979), Experimental studies of simulated gouge and their application to studies of natural fault zones, *Proceedings of Conference VIII on Analysis of Actual Fault Zones in Bedrock*, U.S. Geological Survey Open-File Report 79–1239.
- Mair, K., and J. F. Hazzard (2007), Nature of stress accommodation in sheared granular material: Insights from 3D numerical modeling, *Earth and Planetary Science Letters*, 259(3–4), 469–485.
- Manatschal, G. (1999), Fluid- and reaction-assisted low-angle normal faulting: Evidence from rift-related brittle fault rocks in the Alps (Err Nappe, eastern Switzerland), *Journal of Structural Geology*, 21(7), 777–793.
- Mitchell, T. M., S. A. F. Smith, M. H. Anders, G. Di Toro, S. Nielsen, A. Cavallo, and A. D. Beard (2015), Catastrophic emplacement of giant landslides aided by thermal decomposition: Heart Mountain, Wyoming, *Earth and Planetary Science Letters*, 411, 199–207.
- Moore, D. E., and M. J. Rymer (2007), Talc-bearing serpentinite and the creeping section of the San Andreas fault, *Nature*, 448(7155), 795–797.
- Niemeijer, A., G. Di Toro, A. Griffith, A. Bistacchi, S. A. F. Smith, and S. Nielsen (2012), Inferring earthquake physics and chemistry using an integrated field and laboratory approach, *Journal of Structural Geology*, 39, 2–36.
- Niemeijer, A., G. Di Toro, S. Nielsen, and F. Di Felice (2011), Frictional melting of gabbro under extreme experimental conditions of normal stress, acceleration, and sliding velocity, *Journal of Geophysical Research: Solid Earth*, 116.
- Niemeijer, A. R., and C. J. Spiers (2006), Velocity dependence of strength and healing behaviour in simulated phyllosilicate-bearing fault gouge, *Tectonophysics*, 427(1–4), 231–253.
- Oohashi, K., T. Hirose, and T. Shimamoto (2011), Shear-induced graphitization of carbonaceous materials during

- seismic fault motion: Experiments and possible implications for fault mechanics, *Journal of Structural Geology*, 33(6), 1122–1134.
- Proctor, B., T. M. Mitchell, G. Hirth, D. Goldsby, F. Zorzi, and G. Di Toro (2014), Dynamic weakening of serpentinite gouges and bare-surfaces at seismic slip rates, *Journal of Geophysical Research: Solid Earth*, doi:10.1002/2014JB011057.
- Ree, J. H., J. I. Ando, R. Han, and T. Shimamoto (2014), Coseismic microstructures of experimental fault zones in Carrara marble, *Journal of Structural Geology*, 66, 75–83.
- Rempe, M., S. A. F. Smith, F. Ferri, T. M. Mitchell, and G. Di Toro (2014), Clast-cortex aggregates in experimental and natural calcite-bearing fault zones, *Journal of Structural Geology*, 68, 142–157.
- Rutter, E. H., R. E. Holdsworth, and R. J. Knipe (2001), The nature and tectonic significance of fault-zone weakening: An introduction, *Nature and Tectonic Significance of Fault Zone Weakening*, 186, 1–11.
- Rutter, E. H., R. H. Maddock, S. H. Hall, and S. H. White (1986), Comparative microstructures of natural and experimentally produced clay-bearing fault gouges, *Pure and Applied Geophysics*, 124, 3–30.
- Sagy, A., and E. Brodsky (2009), Geometric and rheological asperities in an exposed fault zone, *Journal of Geophysical Research*, 114, B02301, doi:02310.01029/02008JB005701.
- Sammis, C. G., and Y. Ben-Zion (2008), Mechanics of grain-size reduction in fault zones, *Journal of Geophysical Research: Solid Earth*, 113(B2), doi:10.1029/2006JB004892.
- Samhani, M., D. Dollimore, and K. S. Alexander (2002), Comparison of dolomite decomposition kinetics with related carbonates and the effect of procedural variables on its kinetic parameters, *Thermochimica Acta*, 392, 135–145.
- Sawai, M., T. Shimamoto, and T. Togo (2012), Reduction in BET surface area of Nojima fault gouge with seismic slip and its implication for the fracture energy of earthquakes, *Journal of Structural Geology*, 38, 117–138.
- Sibson, R. H. (1977), Fault rocks and fault mechanisms, *Journal of the Geological Society, London*, 133, 191–213.
- Sibson, R. H. (2003), Thickness of the seismic slip zone, *Bulletin of the Seismological Society of America*, 93(3), 1169–1178.
- Smith, S. A. F., G. Di Toro, S. Kim, J. H. Ree, S. Nielsen, A. Billi, and R. Spiess (2013), Co-seismic recrystallization during shallow earthquake slip, *Geology*, 41(1), 63–66.
- Smith, S. A. F., S. Nielsen, and G. Di Toro (2015), Strain localization and the onset of dynamic weakening in calcite fault gouge, *Earth and Planetary Science Letters*, 413, 25–36.
- Snoke, A. W., J. Tullis, and V. R. Todd (1998), *Fault-Related Rocks: A Photographic Atlas*, Princeton University Press.
- Stewart, M., R. E. Holdsworth, and R. A. Strachan (2000), Deformation processes and weakening mechanisms within the frictional-viscous transition zone of major crustal-scale faults: Insights from the Great Glen Fault Zone, Scotland, *Journal of Structural Geology*, 22(5), 543–560.
- Stirling, M., T. Goded, K. Berryman, and N. Litchfield (2013), Selection of earthquake scaling relationships for seismic-hazard analysis, *Bulletin of the Seismological Society of America*, 103(6), 2993–3011.
- Tanaka, H. (1992), Cataclastic lineations, *Journal of Structural Geology*, 14(10), 1239–1252.
- Togo, T. and T. Shimamoto (2012), Energy partition for grain crushing in quartz gouge during subseismic to seismic fault motion: An experimental study, *Journal of Structural Geology*, 38, 139–155.
- Wallis, D., G. E. Lloyd, R. J. Phillips, A. J. Parsons, and R. D. Walshaw (2015), Low effective fault strength due to frictional-viscous flow in phyllonites, Karakoram fault zone, NW India, *Journal of Structural Geology*, 77, 45–61.
- Wallis, D., R. J. Phillips, and G. E. Lloyd (2013), Fault weakening across the frictional-viscous transition zone, Karakoram fault zone, NW Himalaya, *Tectonics*, 32(5), 1227–1246.
- White, S. R. (2001), Textural and microstructural evidence for semi-brittle flow in natural fault rocks with varied mica contents, *International Journal of Earth Sciences*, 90(1), 14–27.
- Wintsch, R. P., R. Christoffersen, and A. K. Kronenberg (1995), Fluid-rock reaction weakening of fault zones, *Journal of Geophysical Research: Solid Earth*, 100(B7), 13021–13032.
- Wintsch, R. P., and K. Yi (2002), Dissolution and replacement creep: A significant deformation mechanism in mid-crustal rocks, *Journal of Structural Geology*, 24(6–7), 1179–1193.
- Yao, L., S. L. Ma, T. Shimamoto, and T. Togo (2013), Structures and high-velocity frictional properties of the Pingxi fault zone in the Longmenshan fault system, Sichuan, China, activated during the 2008 Wenchuan earthquake, *Tectonophysics*, 599, 135–156.

**Part II**

**Fault Properties During**

**Dynamic Rupture**

# 6

## The Transition From Frictional Sliding to Shear Melting in Laboratory Stick-Slip Experiments

David A. Lockner<sup>1</sup>, Brian D. Kilgore<sup>1</sup>, Nicholas M. Beeler<sup>1,2</sup>, and Diane E. Moore<sup>1</sup>

### ABSTRACT

Pseudotachylites are thought to be caused by fault surface melting due to frictional heating during earthquakes. We report on pseudotachylite formation in the laboratory during spontaneous stick-slip on dry, bare-surface granite faults in room temperature triaxial experiments. A continuous melt layer averaging 7 microns in thickness was formed on sawcut surfaces during stick-slip events at 400 MPa confining pressure. At this pressure, dynamic weakening during stick-slip caused total stress drops that ranged from 172 to 414 MPa shear stress (peak normal stress was 249 to 639 MPa) with 1.2 to 4.2 mm slip. In contrast, repeated stick-slip cycles at 50 MPa confining pressure produced fine-grained fault gouge but showed no evidence of melting. Event duration ranged from 0.07 ms for low stress events to 0.32 ms at high stress, and average slip velocity ranged from 0.3 to 20 m/s. Based on thermocouple measurements within 3 mm of the fault, maximum temperatures in some 400 MPa events exceeded 1500°C. By operating at normal stresses 10 to 50 times greater than those used in unconfined rotary machines, triaxial stick-slip experiments are able to develop high transient temperatures and create pseudotachylites, even with limited total slip.

### 6.1. INTRODUCTION

In recent years, a variety of high-speed rotary shear machines have been developed to measure frictional properties of natural and simulated fault materials at sustained slip speeds as high as ~10 m/s that are representative of coseismic slip speeds [Chang *et al.*, 2012; Di Toro *et al.*, 2004; Di Toro *et al.*, 2011; Han *et al.*, 2011; Han *et al.*, 2007; Hirose and Shimamoto, 2005; Nielsen *et al.*, 2008; Reches and Lockner, 2010; Spray, 2010]. The rapid slip that occurs on a fault during an earthquake can lead to significant frictional heating that under appropriate conditions may cause pressurization of pore water trapped in the fault zone (thermal pressurization) [Andrews, 2002; Noda *et al.*, 2009] and to devolatilization reactions

(dehydration and decarbonation) [Han *et al.*, 2007; Brantut *et al.*, 2008, 2016] that can limit fault heating and lead to dynamic fault weakening [Sulem and Famin, 2009; Brantut *et al.*, 2010; Noda *et al.*, 2009]. Ultimately, continued deformation of narrow principal slip surfaces can lead to melting and the formation of pseudotachylites [Sibson, 1975; Spray, 1987; 2010; Hirose and Shimamoto, 2005; Di Toro *et al.*, 2006, 2009, 2011; Jiang *et al.*, 2015; Proctor and Lockner, 2016]. The work expended per unit area of a fault surface,  $W$ , in time interval  $\Delta t$  is

$$W = \tau V \Delta t = \tau \delta = \mu \sigma_n \delta, \quad (6.1)$$

where  $\tau$  is shear stress,  $V$  is slip speed,  $\mu$  is coefficient of friction,  $\delta$  is fault slip, and  $\sigma_n$  is effective normal stress. For faults at midcrustal and subduction zone depths, we expect effective normal stress of 50 to 500 MPa or more. Then 1 m slip at, for example, an average shear stress of 100 MPa could raise the temperature of a 4 cm wide shear

<sup>1</sup>U.S. Geological Survey, Menlo Park, California, USA

<sup>2</sup>USGS Cascades Volcano Observatory, Vancouver, Washington, USA

zone by 1000°C. Given the significant energy release that occurs in large earthquakes, it may be surprising that pseudotachylites are not common features of active faults.

In experimental studies, most high-speed rotary laboratory apparatuses are unconfined and are limited to normal stresses of about 20 MPa. The great advantage of these machines is the ability to provide nearly unlimited slip. In this case, low normal stress is offset by extended slip duration so that temperature increases of hundreds of degrees can be achieved through frictional heating. While valuable insights into the evolution of frictional properties of rocks continue to be made with rotary machines, it is important to perform comparable experiments using different fault geometries, sample sizes and, in particular, normal stresses and confinement.

The triaxial test geometry refers to an axisymmetric configuration in which a jacketed cylindrical sample is placed in a chamber that is pressurized with a fluid. Then, deviatoric stress is applied to the sample by advancing a piston against the sample end (Figure 6.1a, b). This test geometry has been used for decades to study rock and fault zone properties at elevated pressures and temperatures appropriate to the mid- to lower-crustal conditions where most of the earthquake hazard resides. Dynamic stick-slip events that occur spontaneously in laboratory tests have been identified as the laboratory equivalent to natural earthquakes [Brace and Byerlee, 1966]. While elevated temperature and pressure are desirable characteristics of the triaxial geometry, a limitation is that fault displacement is generally restricted to less than 15 mm. Furthermore, slip on an inclined fault surface results in dynamic coupling of shear and normal stress. Nevertheless, the ability to conduct dynamic tests on rock at in situ conditions means that high-pressure stick-slip tests in the triaxial geometry can provide observations relevant to earthquake source mechanics. In early experiments [Teufel and Logan, 1978], frictional self-heating and surface melt in the triaxial geometry were proposed. However, questions regarding the stability of the thermal dyes used to infer peak temperature made interpretation of results unclear. Later, Lockner and Okubo [1983] reported heat production during stick-slip on a unique biaxial earthquake simulator, containing a 2 m long fault. Operating at normal stress below 5 MPa, surface temperature increase, based on nearby thermocouple readings, was only a few degrees and heat production accounted for over 90 percent of the energy release. More recently, Koizumi *et al.* [2004], Proctor and Lockner [2016], and Moore *et al.* [2016] have provided convincing observations of surface melt in triaxial granite stick-slip experiments above 150 MPa confining pressure. Passelègue [2014] has reported evidence of flash melting at asperities for experiments run at 50 to 100 MPa confining pressure.

Typical laboratory stick-slip events at low confining pressure report stress drops that are roughly 10% to 20% of peak stress in a biaxial apparatus [Lockner and Okubo, 1983] and a rotary machine [Beeler *et al.*, 2014]. Karner and Marone [2000] reported stress drops on a double direct shear apparatus that ranged from about 10% at high strain rates to about 50% at low strain rates. However, it has been noted that in the triaxial geometry, stress drops can be larger than those produced in the double direct shear geometry and can be correlated with confining pressure. For example, Summers and Byerlee [1977] report 70% stress drops for bare surface and crushed granite layers in granite sawcut experiments at a confining pressure of 630 MPa. In the direct shear and rotary shear geometries, shear and normal stresses are decoupled and dynamic shear stress drops occur at nearly constant normal stress. In the triaxial test configuration, shear and normal stress, as resolved on the fault surface, are coupled. Consequently, dynamic fault slip is accompanied by decreases in both shear and normal stress. The reduction in normal stress should result in a larger stress drop in this configuration, although this effect alone should increase the stress drop by a factor of only about 1.5 [McGarr and Fletcher, 2007]. We will show stress drops ranging from <10% at low confining pressure to 100% above 300 MPa. If we are to relate laboratory stick-slip to natural earthquakes in more than a superficial way, the mechanics that control rupture dynamics in the laboratory must be understood in detail.

In the present study we produce stick-slip events at confining pressures from 40 to 400 MPa (70 to 640 MPa normal stress). Fault surfaces show clear evidence for surface melting at high normal stress. In addition, we find systematic changes in rupture characteristics as a function of normal stress and total work. Thermocouples embedded in the rock within 3 mm of the fault surface record temperature transients that imply average surface heating from about 10°C to over 1500°C. Energy density during stick-slip ranges from 1 to 946 kJ m<sup>-2</sup>, and the short slip duration results in an estimated power density as large as 2000 kJ m<sup>-2</sup> s<sup>-1</sup>. The thin shear zone (<10 μm), short event duration, and large energy density result in the intense surface heating and melt production in these experiments. This combination of conditions will not commonly be found in natural earthquakes, but through proper scaling, the results reported here should provide insight into earthquake processes.

## 6.2. EXPERIMENTAL PROCEDURE

Room-dry cylindrical samples of Westerly granite with 25.4 mm diameter and 63.5 mm length were tested in a triaxial apparatus at constant confining pressures of 40 to 400 MPa. Samples contained simulated faults that

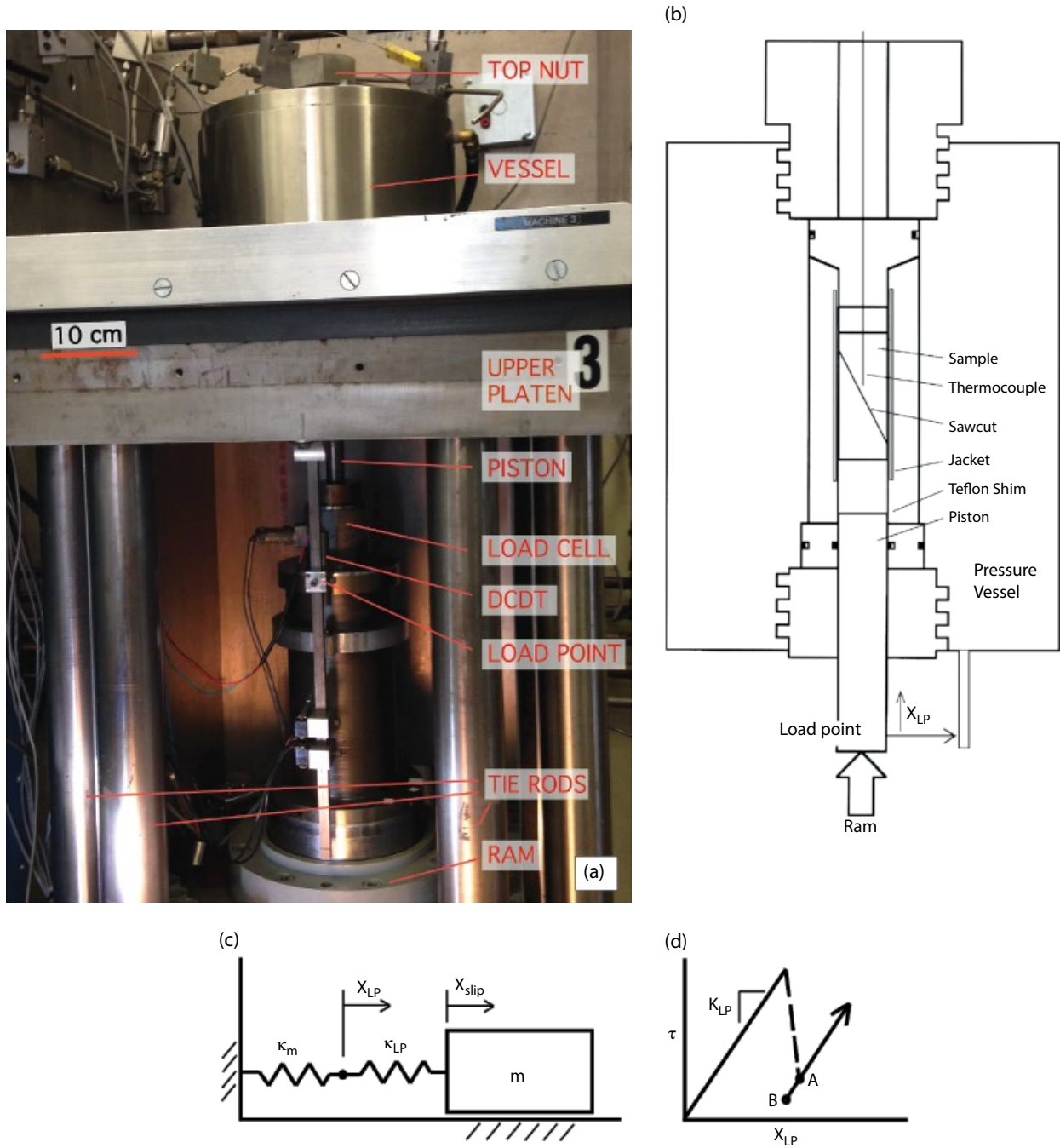


**Figure 6.1** (a) Triaxial loading frame used in experiments. Samples are placed in pressure vessel (top) and axial force is applied by hydraulic ram on bottom. (b) Schematic diagram of sample and pressure vessel. Axial load and displacement are measured outside of the pressure vessel. (c) Spring-slider approximation of sample and loading frame. Active servo control eliminates  $k_m$  from the system. However, stick-slip events are too fast for servo-control systems to respond and dynamic unloading stiffness is  $k_T = 1/(k_{LP}^{-1} + k_m^{-1})$ . (d) Representation of stick-slip event with stress plotted versus load point displacement. Solid lines have slope =  $k_{LP}$ . Stick-slip is represented by dashed line (and has slope =  $-k_m$ ). Following stick-slip, the system comes to rest at point A. Within 3 s, the servo-control system brings load point position back to the control value and reduces stress on the sample to point B. See electronic version for color representation.

were sawcuts inclined at an angle  $\beta=30^\circ$  to the sample axis (Figure 6.1b). Sawcuts were surface ground and hand lapped with #600 Al<sub>2</sub>O<sub>3</sub> abrasive (approximately 15 µm grain size) to provide uniform starting surfaces with 5 to 10 micron roughness. One half of each sample pair had a 1.5 mm diameter hole drilled to within 2 to 3 mm of the simulated fault surface. A 0.6 mm diameter bare K-type thermocouple was embedded at the bottom of each hole with Portland cement to measure heat generated during stick-slip. Thermocouples were small and unsheathed to minimize thermal mass and provide the fastest possible response time. Grout was used, rather than epoxy or other bonding agent, to closely approximate the thermal conductivity and heat capacity of the surrounding granite sample. Additional details of the thermal analysis are presented in section 6.3.8. Samples were placed between steel end caps and slipped into a 3.2 mm wall-thickness polyurethane tube to isolate them from the silicone oil confining fluid.

In each test, the sample was placed in the pressure vessel and confining pressure ( $P_c$ ) was applied. Then the piston was advanced under computer control using a fast-acting servo-control system. A 0.12 mm greased Teflon shim was placed between the piston and the steel end cap to allow lateral slip of the lower sample half that accommodates shearing on the inclined fault. Axial stress ( $\sigma_a$ ) was measured with an external load cell. Axial shortening ( $x_{LP}$ ) was also measured outside the pressure vessel at the base of the piston using a DCDT displacement sensor. Since the servo system controls the position of this point relative to the pressure vessel, this is referred to as the load point. Slip on the fault surface,  $\delta$ , is not measured directly. However, it can be computed with reasonable accuracy by accounting for elastic shortening of the sample column according to

$$\delta = \frac{x_{LP} - \frac{\tau}{k_{LP}}}{\cos\beta}, \quad (6.2)$$

where  $k_{LP}$  is stiffness of the sample column as determined at the load point (nominally 149 MPa/mm) and  $\tau$  is shear stress resolved on the sawcut. The test frame is designed to be stiff to minimize the elastic energy stored during loading. Consequently, the stiffness as measured at the load point is dominated by the stiffness of the granite sample and the steel piston. Because these elements are loaded in series, their compliances, defined as the inverse of stiffness, are additive. The granite sample is shorter but has a lower Young's modulus than the piston, so that the elastic shortening of the sample and piston contribute about equally to the load point displacement.

For the inclined fault geometry used in these experiments, shear ( $\tau$ ) and normal ( $\sigma_n$ ) stresses resolved on the sawcut are calculated from the measured stresses (axial and confining pressure) according to

$$\tau = \frac{1}{2}\sigma_\Delta \sin 2\beta \quad (6.3a)$$

$$\sigma_n = P_c + \frac{1}{2}\sigma_\Delta (1 - \cos 2\beta), \quad (6.3b)$$

where  $\sigma_\Delta = \sigma_a - P_c$  is differential stress. All tests are conducted at constant confining pressure, such that as axial stress increases, both shear and normal stress resolved on the sawcut increase, according to equation (6.3). Finally, as slip occurs on the sawcut, the area of overlap of the two sample halves decreases. This change in area is accounted for in the reported stresses, according to a standard procedure described in Tembe *et al.* [2010, appendix A2]. The true contact area decreases by roughly 3.5% for each millimeter of fault slip.

Data were collected at three different sampling rates. Axial stress, axial displacement, and confining pressure were sampled at 10 samples per second, averaged over 10 consecutive samples and recorded at 1 sample per second. The thermocouple and axial stress outputs were recorded at 100 samples per second (in addition to the 1 Hz axial stress recording). Finally, a laser doppler vibrometer was employed to measure piston velocity during stick-slip to infer slip duration. The vibrometer is a line-of-sight instrument that provides both velocity and distance of a reflective target at 10<sup>6</sup> samples per second. With this device we recorded motion of the piston or load cell near the load point (Figure 6.1). Confining pressure precision is ±0.1 MPa and accuracy is ±0.3 MPa. Axial and differential stresses have precision of ±0.1 MPa and accuracy of ±0.2 MPa or ±0.2%, whichever is greater. Load point position precision is ±0.2 µm and accuracy is ±0.5%.

## 6.3. RESULTS

### 6.3.1. General Observations

A total of 112 stick-slip events were recorded in 15 experiments at confining pressures between 40 and 400 MPa as listed in Table 6.1. Normal stress at the onset of stick-slip ranged from 69 to 639 MPa. One hertz data for two representative tests are plotted in Figure 6.2 as shear stress versus fault displacement. The 100 MPa confining pressure experiment contained 17 stick-slip events (diagonal-sloping stress drops) in 8 mm of fault slip. Dynamic stress drops ranged from about 1/3 to 2/3 of peak stress and average slip was about 0.5 mm. By comparison, the fault loaded at 400 MPa confining pressure was significantly stronger and produced two stick-slip events with total stress drops and average slip of about 2.6 mm.

**Table 6.1** Stick-slip event parameters.

$P_c$ (MPa)	$\delta$ (mm)	$\tau_p$ (MPa)	$\Delta\tau$ (MPa)	% $\Delta\tau/\tau_p$	$\sigma_{n,p}$ (MPa)	$W_T$ (kJ/m <sup>2</sup> )	$T^*$ (ms)	$\langle V \rangle$ (m/s)	$\theta_m$ (°C)	$Q$ (kJ/m <sup>2</sup> )	$\tau_f$ (MPa)
40	0.0965	54.7	10.9	20	71.6	3.53	0.109	0.9			
40	0.0940	51.0	9.8	19	69.5	3.50					
40	0.0246	50.0	2.2	4	69.0	0.972	0.083	0.3			
50	0.1843	69.1	21.9	32	90.0	9.74					
50	0.1864	70.3	24.2	34	90.6	8.60					
50	0.1823	69.3	22.7	33	90.0	8.91					
50	0.1767	68.1	22.8	33	89.2	7.91					
50	0.1815	72.0	20.9	29	91.7	10.3					
50	0.1892	68.6	24.1	35	89.7	8.58					
50	0.2227	76.3	28.2	37	94.1	11.8					
50	0.3343	76.2	43.3	57	94.2	14.8					
50	0.2108	73.8	24.0	32	92.7	11.9					
50	0.1921	75.5	24.1	32	93.8	10.4					
50	0.1958	75.5	25.2	33	93.8	10.0					
50	0.1757	66.3	20.7	31	88.4	8.91					
50	0.1652	64.3	19.9	31	87.2	8.04					
50	0.1667	64.6	19.7	31	87.5	8.20					
50	0.1651	67.4	21.5	32	89.1	7.35					
50	0.1593	63.4	18.8	30	86.7	7.64					
50	0.1633	63.7	19.5	31	86.9	7.84					
50	0.1721	68.5	22.0	32	89.5	7.73					
50	0.1725	68.6	22.4	33	89.7	7.69					
50	0.1725	68.3	22.5	33	89.5	7.60					
50	0.1669	68.7	21.4	31	89.9	7.72					
50	0.1685	65.1	19.9	31	87.7	8.38					
60	0.1871	78.5	22.8	29	105.5	9.47	0.107	1.7	114	4.33	23.2
60	0.2234	88.4	25.7	29	111.2	12.9	0.132	1.7	118	5.36	24.0
60	0.3700	84.9	44.1	52	108.8	17.7	0.109	3.4	200	8.51	23.0
100	0.3597	113.2	37.1	33	165.6	31.2	0.076	4.7	273	10.2	28.4
100	0.3600	130.5	40.2	31	175.5	34.5					
100	0.3846	113.5	50.2	44	165.7	28.2					
100	0.3795	116.5	38.2	33	167.3	34.2	0.076	5.0	328	12.5	33.0
100	0.3749	113.7	48.5	43	165.7	27.2					
100	0.3375	109.6	43.8	40	163.3	23.8					
100	0.3352	108.0	36.2	33	162.7	27.0	0.125	2.7	200	8.26	24.6
100	0.7756	127.8	89.1	70	174.0	60.2					
100	0.3528	112.5	42.6	38	165.0	29.1					
100	0.3424	123.1	40.1	33	171.1	33.6					
100	0.3382	116.7	34.3	29	167.7	31.4	0.120	2.8	272	13.8	40.8
100	0.3894	120.7	38.7	32	169.8	36.8	0.075	5.2	351	13.4	34.3
100	0.5588	107.5	69.0	64	162.3	36.6					
100	0.5377	106.5	65.3	61	161.8	34.7					
100	0.5280	107.4	67.5	63	162.3	33.3					
100	0.6574	115.9	77.6	67	167.0	46.6					
100	0.5896	108.2	64.1	59	162.7	40.9	0.173	3.4	321	18.1	30.6
100	0.5731	111.2	75.6	68	164.4	35.4					
100	0.4515	133.7	50.9	38	177.4	46.0					
100	0.3950	125.4	39.6	32	172.5	39.2	0.076	5.2	391	15.1	38.3
100	0.3931	117.7	40.0	34	168.0	35.5	0.131	3.0	277	14.7	37.5
100	0.5210	121.5	58.5	48	170.3	41.4					
100	0.5190	105.4	64.2	61	161.0	33.7					
100	0.5175	109.9	69.0	63	163.6	32.1					
100	0.3018	111.6	34.6	31	164.5	23.1					
100	0.3010	116.0	29.7	26	167.2	28.9	0.069	4.4	401	14.8	49.3

(Continued)

**Table 6.1** (Continued)

$P_c$ (MPa)	$\delta$ (mm)	$\tau_p$ (MPa)	$\Delta\tau$ (MPa)	% $\Delta\tau/\tau_p$	$\sigma_{n,p}$ (MPa)	$W_T$ (kJ/m <sup>2</sup> )	$T^*$ (ms)	$<V>$ (m/s)	$\theta_m$ (°C)	$Q$ (kJ/m <sup>2</sup> )	$\tau_f$ (MPa)
100	0.2955	110.9	34.4	31	164.1	22.3					
100	0.3080	103.1	33.2	32	159.4	23.5	0.122	2.5	170	8.02	26.0
100	0.3056	112.6	34.7	31	164.9	24.5					
100	0.3039	104.3	33.4	32	160.5	23.3	0.115	2.6	175	7.98	26.2
100	0.2542	121.3	28.0	23	169.8	24.1					
100	0.2112	110.5	30.5	28	163.9	14.9	0.102	2.1	203	8.72	41.3
100	0.1968	100.7	22.1	22	158.3	15.1					
100	0.2932	116.7	35.6	31	167.5	21.3	0.104	2.8	191	8.23	28.1
100	0.2908	111.6	33.9	30	164.5	23.3					
100	0.2827	110.9	34.0	31	164.1	21.3					
100	0.3177	110.0	42.5	39	163.9	21.8					
100	0.3174	108.5	42.5	39	162.8	21.8					
100	0.3174	108.3	42.5	39	162.8	22.0					
100	0.3248	105.6	35.0	33	161.3	25.5	0.099	3.3	196	8.00	24.6
100	0.3182	112.9	35.8	32	165.2	25.0					
100	0.3281	105.5	33.4	32	161.1	26.7	0.120	2.7	206	10.1	30.8
100	0.3297	109.0	35.3	32	163.1	27.4	0.072	4.6	283	10.4	31.6
100	0.3115	111.9	35.2	31	164.8	24.1					
100	0.3091	126.0	35.0	28	172.7	29.4					
100	0.3139	113.6	36.0	32	165.5	25.0					
100	0.3136	106.5	39.6	37	161.8	23.4					
100	0.3130	109.2	42.9	39	163.1	21.4					
150	1.2515	172.1	172.1	100	249.2	90.5			659	25.9	20.7
150	1.3129	174.0	174.0	100	250.5	99.5			691	45.2	34.5
200	1.0321	218.2	125.7	58	326.3	144					
200	0.9755	224.4	118.1	53	329.6	148					
200	0.9697	177.6	129.9	73	302.9	89.5					
200	1.3901	211.5	183.0	87	322.1	143					
200	1.1254	190.4	154.3	81	310.4	102					
200	1.0792	187.0	150.1	80	308.3	93.5					
200	0.9423	208.7	118.0	57	320.8	124					
200	0.5853	175.8	67.0	38	301.7	79.5					
200	0.1156	131.8	13.0	10	275.8	14.1					
200	0.4468	155.6	49.8	32	290.0	56.5					
200	0.8231	211.4	94.7	45	321.7	126					
200	0.5451	161.9	72.0	44	293.3	57.2					
200	0.8630	212.2	87.2	41	322.9	134	0.089	9.7	913	39.5	45.8
200	0.8430	210.2	85.3	41	321.7	133	0.089	9.5	748	32.2	38.2
300	2.2736	275.8	235.2	85	459.6	336	0.240	9.5			
300	2.3236	282.6	282.6	100	462.9	312	0.261	8.9			
300	2.4228	275.1	275.1	100	459.0	337	0.299	8.1			
300	3.0698	340.6	340.6	100	496.9	504	0.311	9.9	1332	108	35.1
300	2.9281	313.4	313.4	100	481.1	476	0.303	9.7	1511	118	40.3
300	2.6258	312.5	312.5	100	481.3	390	0.283	9.3	1221	97.4	37.1
300	0.9412	257.2	99.8	39	448.4	164	0.162	5.8	556	36.2	38.4
300	2.0611	272.5	220.9	81	457.7	314	0.131	15.7	1619	85.0	41.2
400	2.9281	340.5	340.5	100	596.1	499	0.221	13.2	1719	118	40.2
400	1.1001	292.2	113.7	39	569.4	229	0.122	9.0	766	41.2	37.5
400	3.0225	327.1	327.1	100	588.9	529	0.157	19.3	2134	121	39.9
400	3.6836	414.4	414.4	100	639.1	758	0.209	17.6			
400	4.2150	385.7	385.7	100	623.4	946					
400	2.7959	350.9	350.9	100	603.1	453					
400	2.3424	312.9	312.9	100	580.5	323					
400	2.3306	293.7	293.7	100	569.5	320					
400	1.9458	255.2	255.2	100	547.9	211					
400	1.2120	302.3	124.8	41	575.0	256	0.093	13.0	996	42.0	34.6
400	2.5692	319.8	319.8	100	584.4	386					
400	1.3360	294.8	125.1	42	570.1	290	0.093	14.4	1013	42.3	31.6

Note: Stresses have been corrected for true area of contact that decreases on the sawcut with continued slip. Displacement is the computed fault-parallel displacement after elastic shortening of the sample, as measured at the load point, has been removed.

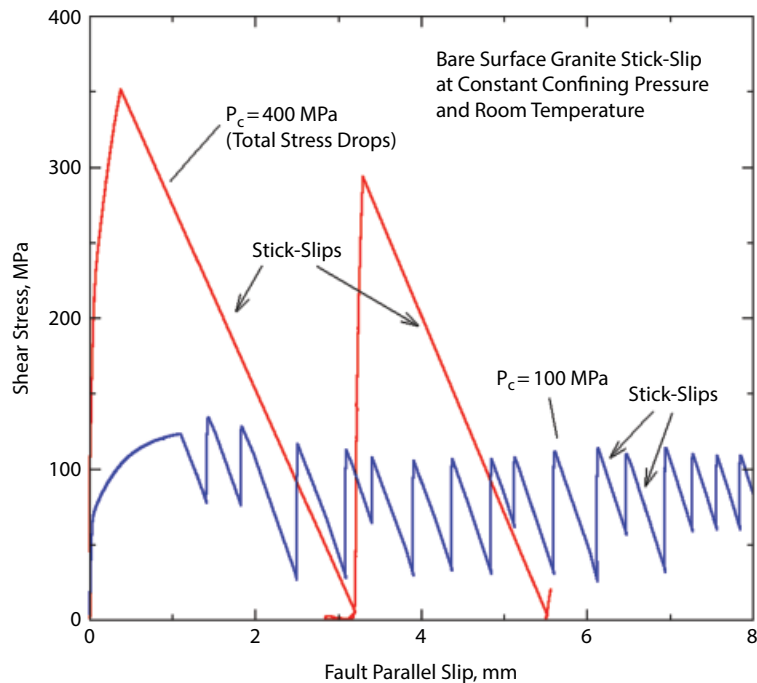


**Figure 6.2** Two representative experiments plotting stress versus fault slip at  $P_c=100\text{ MPa}$  (blue) and  $400\text{ MPa}$  (red). Seventeen stick-slip events (diagonal lines) are shown in the  $100\text{ MPa}$  test and two events are shown in the  $400\text{ MPa}$  test. Not only are displacements much larger at  $400\text{ MPa}$ , but the stress drops are complete. See electronic version for color representation.

Recorded data for a stick-slip event at  $400\text{ MPa}$  confining pressure are shown at three different time scales in Figure 6.3. This was a total stress drop event, with peak shear and normal stresses of  $327.1$  and  $588.9\text{ MPa}$ , respectively, and fault slip of  $3.023\text{ mm}$ . Figure 6.3a is a time plot of the  $100\text{ Hz}$  data for shear stress, load point displacement, and temperature change as measured  $2.4\text{ mm}$  from the sawcut surface. At this time scale the shear stress drop is abrupt. Since the load point displacement is a control parameter, in an ideal experiment it would show a linear increase with time that represents the  $2\mu\text{m/s}$  imposed loading rate. This appears as the accumulated  $100\mu\text{m}$  increase in load point position after  $50\text{ s}$ . The transient jump in displacement at the time of the stick-slip event is the result of the rapid unloading of the sample column at a rate that is too fast for the servo-control system to respond. The hydraulic servo-valve required  $2\text{ s}$  to move the ram back to the computer-prescribed position. The temperature record shows a peak of about  $6^\circ\text{C}$  two seconds after the stick-slip event. When compared to the theoretical solution for heat flow from a planar source (section 6.3.8), the computed fault surface temperature exceeded  $2000^\circ\text{C}$ . The abrupt  $3^\circ$  transient peak at the time of the stick-slip occurs too soon for a heat pulse to arrive from the fault surface and probably represents local heating of the thermocouple due to distortion of the borehole in response to the violent motion of the stick-slip.

While most of the remainder of the chapter will analyze the low-frequency data, modeling of the frictional heating of the fault surface depends critically on thickness of the sheared gouge layer and slip duration. Prior to each experiment, faults were ground flat and lapped to provide a uniform starting roughness of approximately  $10\mu\text{m}$ . This surface texture was designed so that after only a few tens of microns of slip, a uniform and repeatable layer of fine-grained gouge would be produced. Gouge thickness and melt features are discussed in section 3.7. However, determination of slip duration (rise time,  $T^*$ ) is problematic when the fault is inside a pressure vessel. As a proxy for a direct measurement of surface displacement, we have recorded velocity of the end of the piston near the load point. Slip of the fault surface will produce a stress wave that travels down the piston. While the overall motion of the piston outside of the pressure vessel will be complex due to multiple reflections in the sample column, we postulate that the initial pulse traveling down the piston provides the duration of the stick-slip event. We therefore measured the velocity of the piston near the load point using a laser vibrometer with a  $1\text{ MHz}$  sampling rate. A  $100\text{ ms}$  recording of velocity and displacement is plotted in Figure 6.3b. The first  $10\text{ ms}$  show a rapid oscillation of the piston followed by a longer period oscillation (approximately  $20\text{ ms}$  period) that probably represents ringing of the tie rods connecting the ram to the platen. The beginning of the vibrometer record

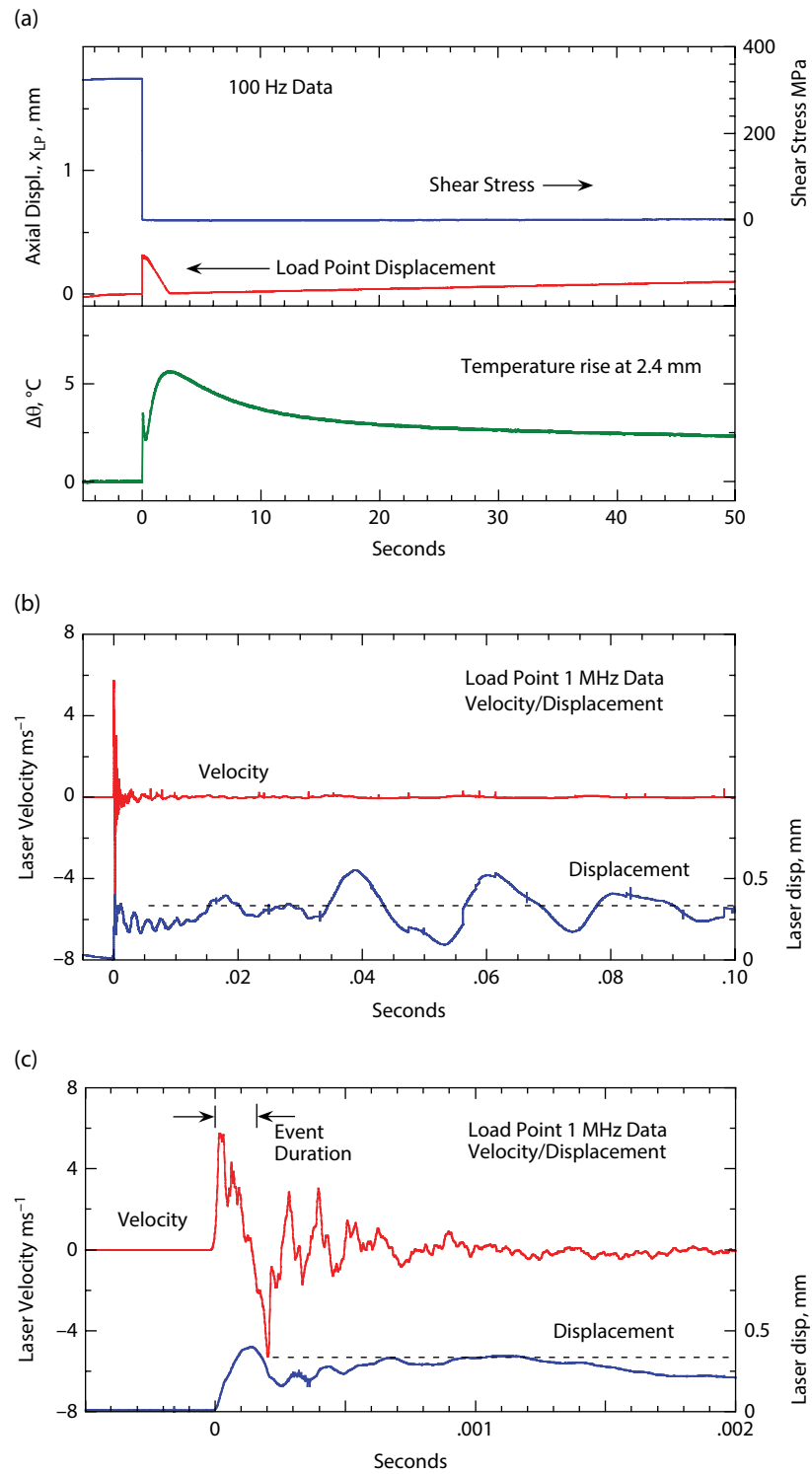


**Figure 6.3** A total stress drop stick-slip event is plotted at three different time scales. (a) On a 50 s time scale, the stress drop is abrupt. Displacement jumps ahead about 0.3 mm and requires 2 s for the servo system to regain control. The gradual increase in displacement is the prescribed computer-controlled loading rate. Temperature due to frictional heating is recorded 2.4 mm from the fault surface. A 6°C peak occurs 2 s after the stick-slip and implies a maximum fault temperature  $>1500^\circ\text{C}$ . (b) Velocity and displacement records (from the laser vibrometer recording) for vertical motion of the piston adjacent to the load point (outside of the pressure vessel). In this 100 ms plot, the stick-slip event duration is still not resolved. The 50 Hz vibration probably represents free oscillation of the tie rods excited by the stick-slip event. A constant offset of 0.3 mm occurs at the time of the event. (c) An expanded view showing 2 ms of the high-speed record. Displacement has reached 0.3 mm after 0.16 ms, which we interpret as the event duration. See electronic version for color representation.

is expanded to show the first 2 ms of the record following the stick-slip in Figure 6.3c. The dashed horizontal line represents the DC offset in the displacement record following the ring down of the free oscillations of the piston. Notice that the displacement first reaches this level between 0.1 and 0.2 ms. We use this interval as an indication of the stick-slip event duration  $T^*$ .

### 6.3.2. Elastic Unloading Response of Load Frame

Stick-slip instabilities are the result of an interaction of the fault surface, as it undergoes an abrupt loss of shear strength, with the loading frame that provides stored elastic energy [Johnson and Scholz, 1976; Shimamoto *et al.*, 1980; Kilgore *et al.*, 2017 (this volume)]. We begin by discussing some of the characteristics of the loading frame. The deformation machine is designed to be stiff so that it minimizes the storage of elastic energy and thereby reduces the likelihood of stick-slip instability. The general response of triaxial machines has been analyzed in detail, for example, in Shimamoto *et al.* [1980]. Since load-bearing members are made of hardened steel, the machine response to axial load is essentially elastic. In these experiments, stiffness is estimated from

$$k_{LP} = \Delta\tau / \Delta x_{LP}. \quad (6.4)$$

This quantity is specific to our test geometry and sample dimensions, relating shear stress to load point displacement. A more common definition of stiffness relates force,  $F$ , to displacement:  $\Delta F = \kappa \Delta x$ . Because the different components of the load frame are loaded in series (all support the same axial force), it is more convenient to work with compliance,  $c = 1/\kappa$ , because the compliances of the different elements are additive.

The load point is a convenient position to analyze the quasi-static response of the test machine. For a sample in quasi-static equilibrium, two forces are balanced at the load point: force exerted by the piston and force exerted by the ram (Figure 6.1). The load point position,  $x_{LP}$ , refers to the vertical position of the load point relative to the base of the pressure vessel and is one of the parameters measured in the experiment. The direct coupling of elements that exerts force at the load point is piston – sample – top nut – vessel. All elements can be considered elastic and the pressure vessel, given its physical dimensions, is orders of magnitude stiffer than the sample column. The most compliant element is generally the rock sample itself, followed by the steel piston between the sample and the ram. A change in load point position will result in a change in force exerted by the piston as  $\Delta F_{piston} = \Delta x_{LP}/c_{LP}$ , where  $c_{LP}$  is compliance of the sample column. The second force path providing counterforce

between the load point and the pressure vessel is through the machine frame: ram – bottom platen – tie rods – top platen – pressure vessel. These components are all stiff relative to the sample column. When the hydraulic servo-control valve operates, it essentially removes these elements from the system response and  $c_{LP}$  becomes the total machine compliance. Since the response time for the servo-valve is 20–50 msec, shorter duration events are too fast for a servo-controlled response and the natural load frame compliance dominates. In this case, compliances of the machine frame components can be lumped together into a single “machine” compliance  $c_m$ , and the change in counter force at the load point becomes  $\Delta F_{ram} = -x_{LP}/c_m$ .

Consider the case immediately before and after a stick-slip event, when the servo-control system has not yet responded. Before the stick-slip, the load point is at a position  $x_{LP0}$  and the sample and load frame are supporting axial force  $F_0$ . After stick-slip, the sample column is shortened by the axial component of the slip event  $x_{slip} = \delta \cos \beta$ , the axial force is reduced by  $\Delta F$ , and an increment of displacement  $\Delta x_{LP}$  has occurred at the load point. It is simple to show that the load point advances by

$$\Delta x_{LP} = -c_m \Delta F. \quad (6.5)$$

Thus, the rapid jump in load point position accompanying the stick-slip event as shown at time zero in Figure 6.3a provides a direct measure of the machine compliance  $c_m$ . Additionally, compliance of the loading column,  $c_{LP}$ , can be determined from the slope of the reloading curve following a stick-slip event when the fault surface is locked. Finally, we note that the axial component of fault slip,  $x_{slip}$ , can be related to the accompanying decrease in force by

$$x_{slip} = -c_T \Delta F, \quad (6.6)$$

where  $c_T = c_m + c_{LP}$ . The quantity  $x_{slip}$  can be used to compute the change in elastic energy consumed in the stick-slip event. Compliances and stiffnesses for the different system components have been determined as part of the experimental procedure, and values are listed in Table 6.2.

The mechanical response of the loading frame, as discussed in this section, is often represented by a single degree of freedom, lumped-mass, spring-slider model, where the servo-controlled response has a single spring element,  $k_{LP}$ , between the load point and the sample, as depicted in Figure 6.1c. The second spring element to the left of the load point,  $k_m$ , is eliminated from the system response as long as displacement is controlled by the servo system. However, for slip times shorter than the servo response time, displacement at the load point is no

**Table 6.2** Loading frame elastic parameters.

Symbol	Parameter	Value
$k_{LP}$	Load point stiffness	$149 \pm 2$ MPa/mm
$k_m$	Machine stiffness	$1270 \pm 60$ MPa/mm
$k_T$	Total stiffness	$133 \pm 3$ MPa/mm
$\kappa_{LP}$	Load point force stiffness	$174 \pm 2$ kN/mm
$\kappa_m$	Machine force stiffness	$1480 \pm 70$ kN/mm
$\kappa_T$	Total force stiffness	$156 \pm 5$ kN/mm
$c_{LP}$	Load point compliance	$(5.75 \pm 0.11) \times 10^{-9}$ m/N
$c_m$	Machine compliance	$(0.675 \pm 0.034) \times 10^{-9}$ m/N
$c_T$	Total compliance	$(6.43 \pm 0.19) \times 10^{-9}$ m/N

longer actively controlled and the response is more like the full double spring system depicted in Figure 6.1c. This simple model has been successful in representing laboratory stick-slip [Johnson and Scholz, 1976; Rice and Tse, 1986; Kilgore *et al.*, 2017 (this volume)]. For very rapid stick-slip, the lumped mass model may no longer be appropriate as distribution of mass in the sample, piston, and other elements becomes important and a fully dynamic solution is required. This situation is discussed further in the following sections.

### 6.3.3. Calculating Stress Drop and Total Slip

High-speed displacement, velocity, and stress data were recorded for only a limited number of stick-slip events. Consequently, we developed a method for determining stress drop and displacement from the slow 1 Hz data. Since the applied loading rate was slow, the stress and displacement at the onset of each stick-slip event are well determined in the 1 Hz data. Following each stick-slip, the fault surfaces come to rest and lock up with no indication of measurable afterslip. Thus, the reloading curve following stick-slip constrains the ending stress and displacement. The problem becomes determining ending stress and displacement as depicted by point A in Figure 6.1d from stress and displacement recorded one to two seconds later in the 1 Hz data. The rapid displacement reversal following the stick-slip event in Figure 6.3a represents the servo-control valve moving the ram backward at full speed and bringing the load point position back to the computer-prescribed position. The displacement rate of the ram and accompanying unloading rate of the sample column are determined from plots like Figure 6.3a. In addition, the displacement adjustment in the seconds following stick-slip is proportional to the stress change between points A and B in Figure 6.1d, according to equation (6.4). This is all that is needed to calculate the ending stress and displacement of the fault surface from the apparent stress and displacement as recorded at 1 Hz.

### 6.3.4. Observed Stress Drop and Slip

Data for the 112 recorded stick-slip events are listed in Table 6.1. Confining pressure ranged from 40 to 400 MPa and resulted in peak shear stress,  $\tau_p$ , spanning 50 to 414 MPa. Associated shear stress drops,  $\Delta\tau$ , ranged from 2.2 to 414 MPa. In all, 16 of the highest normal stress stick-slips underwent total stress drops. Peak stress is plotted as a function of peak normal stress for the full catalog of 112 events in Figure 6.4a. Following equations (6.3a) and (6.3b), experiments run at the same confining pressure form a locus of points on a line with slope =  $\sin 2\beta / (1 - \cos 2\beta) \approx 1.732$ . This results in the linear groupings of events in Figure 6.4. Peak stress, even for stick-slip events under nominally identical conditions, shows considerable variability, having a standard deviation of roughly 9% of the average value at each confining pressure. This variability, especially at higher pressure, may reflect differing degrees of welding of the slip surface following melting in previous slip events [Proctor and Lockner, 2016]. The same strength data are replotted as coefficient of friction  $\mu = \tau/\sigma_n$  in Figure 6.4b. Coefficient of friction at peak stress is often referred to as the static coefficient of friction. These friction values show a gradual decrease with increasing normal stress, consistent with Byerlee's law [Byerlee, 1978].

In Figure 6.5 we plot shear stress drop  $\Delta\tau$  as a function of  $\tau_p$ . Lines of constant percent stress drop are included for reference. There is an overall trend of increasing stress drop with increasing peak stress with a power law exponent of about 1.6. When events are sorted by peak stress, the lowest quartile has an average stress drop of 22 MPa while the upper quartile has an average stress drop of 229 MPa.

We next look at how stress drop varies with fault slip. In the simple spring-slider model, unloading rate is determined by the machine stiffness  $\kappa_T = 1/c_T$  where, as we discussed previously, the lumped compliance  $c_T = c_{LP} + c_m$ . In this case, stress drop should vary with fault slip according to equation (6.6). We test this prediction in Figure 6.6, which is a log-log plot of change in axial force versus  $\Delta x_{slip}$ . Load point stiffness  $\kappa_{LP}$  (=174 kN/mm) and total stiffness  $\kappa_T$  (=156 kN/mm) are plotted for reference. While data are bounded by  $\kappa_T$ , many data points fall as much as 20% below the stiffness curve, indicating more slip than expected. The total stress drop events are overdriven and come to rest with a gap between the piston and the sample column. If this gap opens while slip is still occurring on the fault, the assumption that the system is unloading elastically at a rate given by  $\kappa_T$  is no longer valid and excess slip can occur. By a similar argument, the loading frame tends to become stiffer with increasing confining pressure. So dynamic unloading may have an initial slope of  $-\kappa_T$  that then becomes smaller for the larger stress

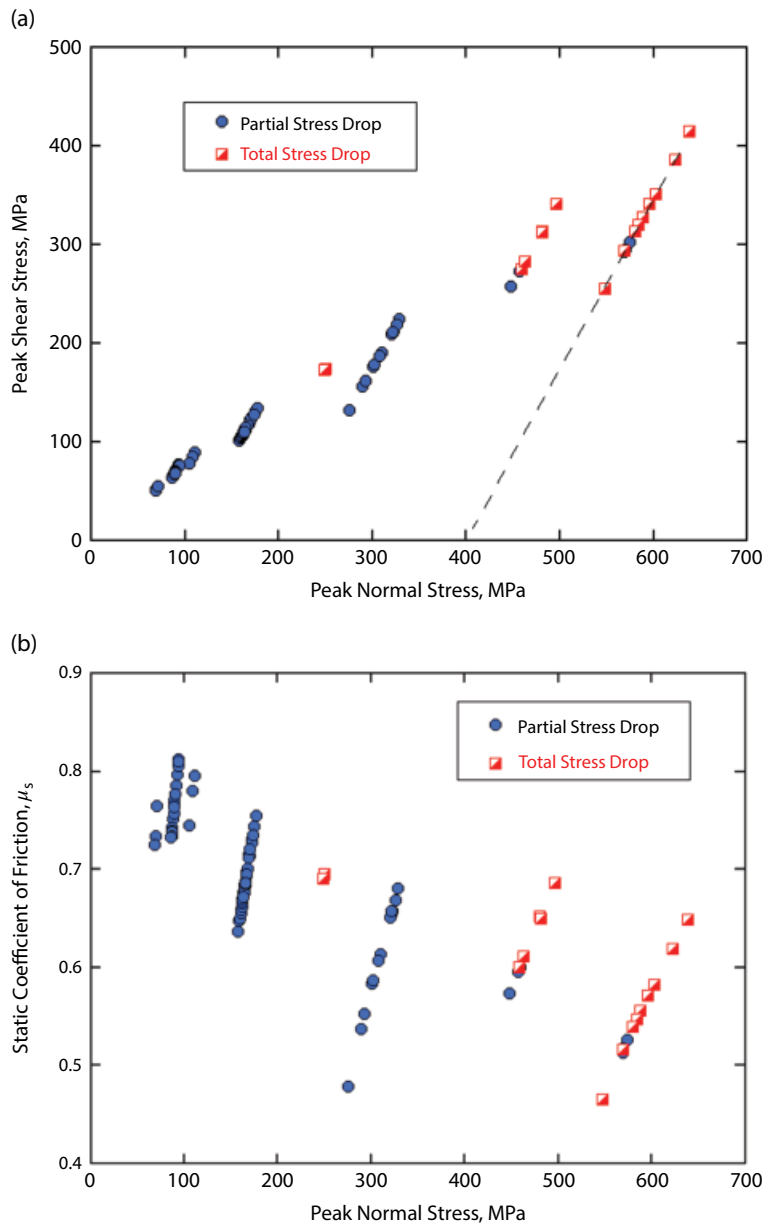


**Figure 6.4** (a) Peak shear stress plotted versus peak normal stress at the onset of stick-slip for all 112 events. At constant confining pressure, shear and normal stress increase along a loading path of fixed slope determined by the sawcut angle (equation [6.3]). The events that are farthest to the right, for example, were run at  $P_c = 400$  MPa. Nearly all of these were total stress drop events. While increased confining pressure tends to result in increased strength, there is notable variability in peak stress for tests run at each confining pressure and therefore under nominally identical conditions. The sequence of 100 MPa events plotted in Figure 6.2 demonstrates this variability. (b) The same events are plotted as peak (static) coefficient of friction. The decreasing trend in friction follows Byerlee's law. See electronic version for color representation.

drop events. These details are not well quantified and the variations in apparent stiffness shown in Figure 6.6 may be a measure of uncertainty in our stress drop and total energy calculations. In Figure 6.7, we plot predicted fault-parallel slip, based on stress drop and  $\kappa_T$ , as a

function of observed fault-parallel slip for total stress drop stick-slip events. Although four events came to rest at the expected slip, many events slid more than 0.5 mm beyond the point where the driving force that the piston imparted to the sample had dropped to zero.

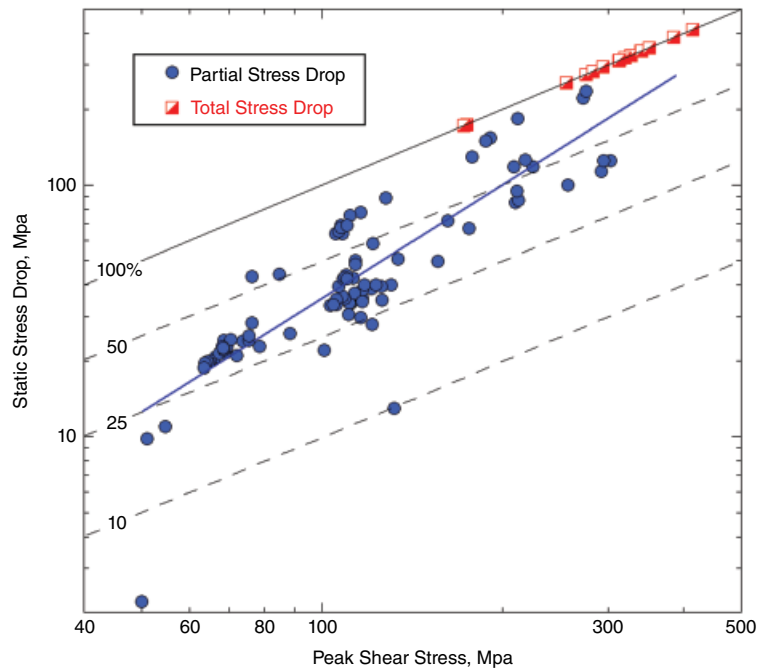


**Figure 6.5** Static shear stress drop is plotted versus peak shear stress. Total stress drop events are shown as red squares. Diagonal lines represent constant percent stress drop. There is a gradual increase in percent stress drop with increasing confining pressure. See electronic version for color representation.

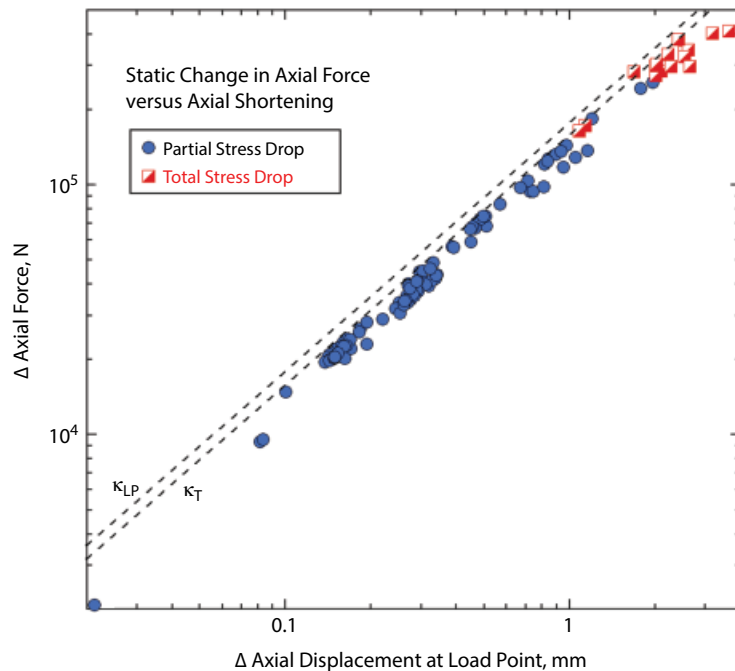


**Figure 6.6** Change in axial force plotted versus axial shortening due to slip on the sawcut. Since stick-slip happens faster than the servo-control response, unloading response should fall along the lower dashed line that represents the total system stiffness,  $\kappa_T$ . See electronic version for color representation.

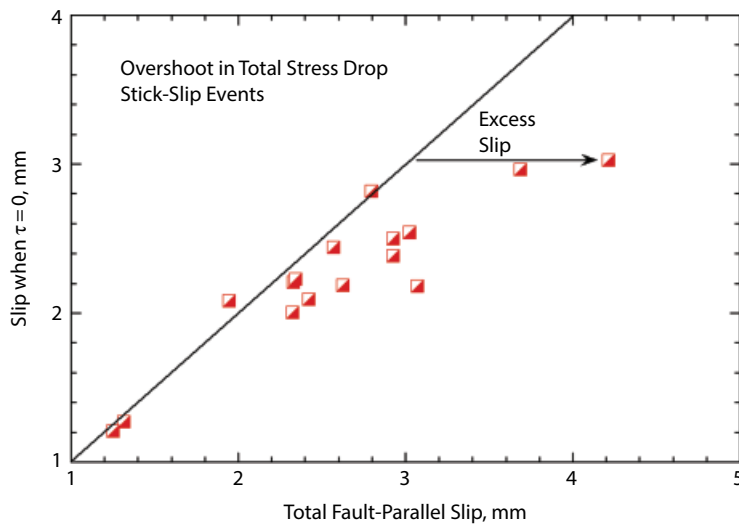


**Figure 6.7** Horizontal axis represents measured fault slip for total stress drop events. The vertical axis is computed fault slip when shear stress has dropped to zero ( $\Delta\tau = -k_T \Delta\delta$ ). Events that plot to the right of the diagonal line have continued to slide (presumably driven by stored kinetic energy) past the point where they are driven by the piston. See electronic version for color representation.

### 6.3.5. Total Energy Release

Stick-slip event durations are so short that the servo-control systems cannot respond until slip has ended. In this case, the sample and loading frame can be considered a closed system in which stored elastic energy is consumed without input of energy from the surroundings (i.e., no additional work done by hydraulic pumps or other control systems). If the frame unloads linearly with slip on the fault, the change in elastic energy of the load frame is

$$\Delta E_{el} = \frac{1}{2}(F_p + F_e)\Delta x_{slip}, \quad (6.7)$$

where  $F_p$  and  $F_e$  are axial force at the start and end of the stick-slip event.

There is a net displacement of the piston into the pressure vessel during the stick-slip events, resulting in  $\int PdV$  work as the confining fluid is compressed. Work in compressing the confining fluid varies with confining pressure and on average represents 37% of the total energy release. This work is part of the response of the loading system and not related to fault properties. Consequently, we subtract it from the elastic energy release (equation [6.7]) and report the resulting energy, normalized by the fault surface area, as total work  $W_T$ . This total work is plotted as a function of fault parallel slip in Figure 6.8. As expected,  $W_T$  increases with increasing slip. A power law fit to the partial stress drop events gives

$$W_T [\text{kJ m}^{-2}] = 121\delta^{1.44}, \quad (6.8)$$

with  $\delta$  measured in mm. The total stress drop events, on average, have 25% greater slip than would be predicted by the partial stress drop events.

### 6.3.6. Slip Duration and Velocity

Stick-slip event duration becomes important in modeling the temperature rise that occurs due to frictional heating of the fault surface. Event duration is difficult to measure directly on a fault surface inside the pressure vessel at high pressure. An internal load cell was constructed to obtain a near-field measure of stress drop, but unfortunately it malfunctioned. As explained in section 6.2, slip duration is inferred from motion of the piston outside the pressure vessel near the load point. Vertical velocity and displacement of the top surface of the load cell, adjacent to the load point, were sampled at 1 MHz in 37 experiments using a laser doppler vibrometer. The estimates of slip duration range from 0.07 to 0.32 ms and are plotted as a function of total slip in Figure 6.9. Lower energy/shorter slip events tend to cluster with event durations averaging  $T^* = 0.11$  ms and average slip  $\delta = 0.59$  mm. Average velocity of these events is therefore 5.4 m/s. Total stress drop events have longer durations averaging 0.27 ms and larger slip (average slip = 2.76 mm). Average velocity for total stress drop events is 10.2 m/s, about twice as fast as the smaller events. The largest average velocity of 19.3 m/s was recorded for a total stress drop event at 400 MPa confining pressure.

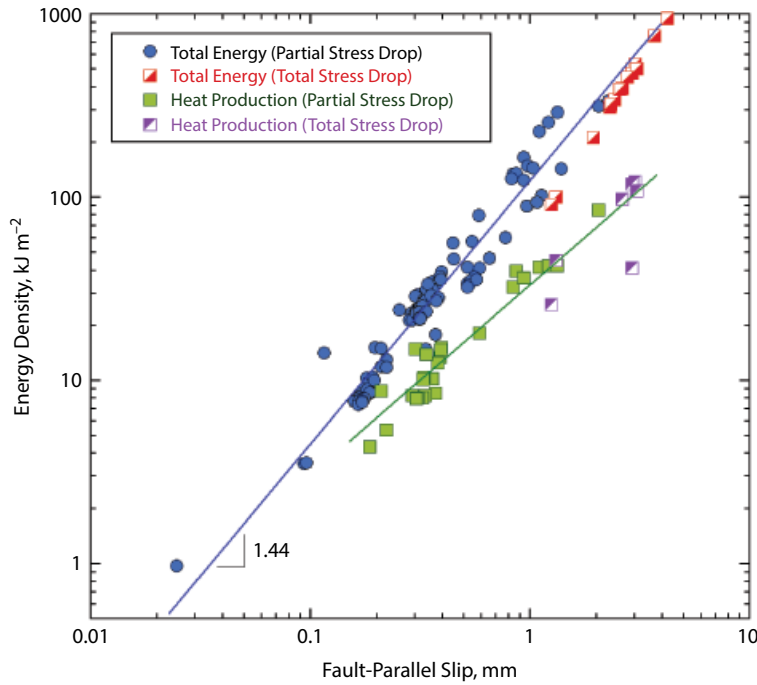


**Figure 6.8** Blue and red symbols are total energy release in stick-slip events calculated from total slip and average unloading stress. Green and purple squares are heat generated during stick-slip as inferred from 1D heat flow model and the temperature rise recorded by thermocouples 2 to 3 mm from the fault surface (see section 3.8). The proportion of energy that results in heating of the fault is less for high confining pressure events that produce surface melt. See electronic version for color representation.

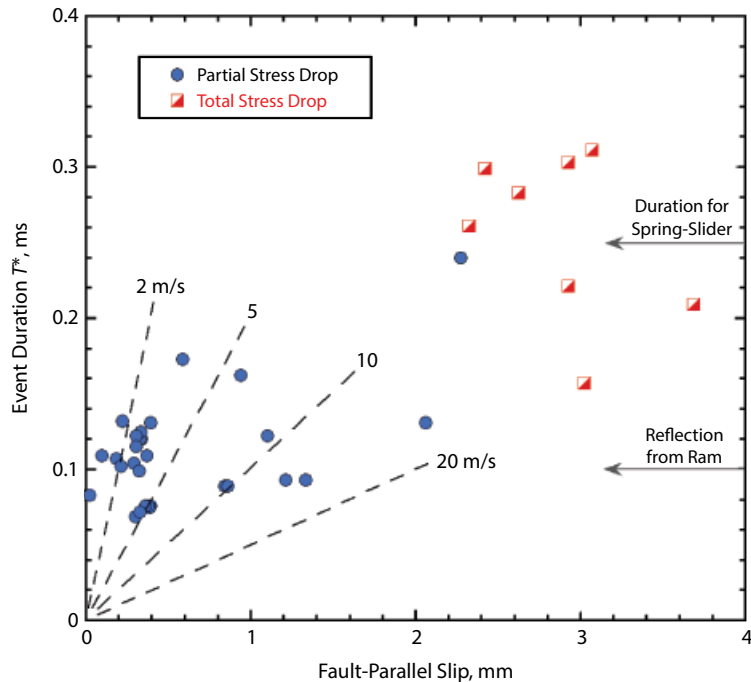


**Figure 6.9** Event duration plotted versus fault slip. Events tend to cluster into two groups. High-stress events that produce surface melt have more than twice the slip duration and five times the total slip of the low-stress stick-slips. Average slip speeds vary from about 1 m/s for the low stress events to as much as 20 m/s for some total stress drop events. Indicated on right is event duration predicted by lumped-mass spring-block model ( $T^* = 0.25$  ms). Also shown at 0.1 ms is predicted arrival at the fault of the wave traveling down the piston and reflected back from the load cell (see Figure 6.1A). See electronic version for color representation.

### 6.3.7. Characterization of the Fault and Surface Melting

Scanning electron microscope (SEM) images were made of selected samples by either separating the sample halves along the sawcut or by epoxying samples together and cutting parallel to the cylinder axis and perpendicular to the sawcut. Prior to each experiment, samples were prepared by surface grinding the sawcuts and then hand lapping with #600  $\text{Al}_2\text{O}_3$  abrasive to provide a uniform starting roughness of approximately 10  $\mu\text{m}$ . Secondary-electron (SE) SEM images (Figure 6.10) show the texture of the starting surfaces. Individual grains have been plucked from the sawcuts during grinding. Otherwise, surfaces are flat at long wavelengths with a scalloped

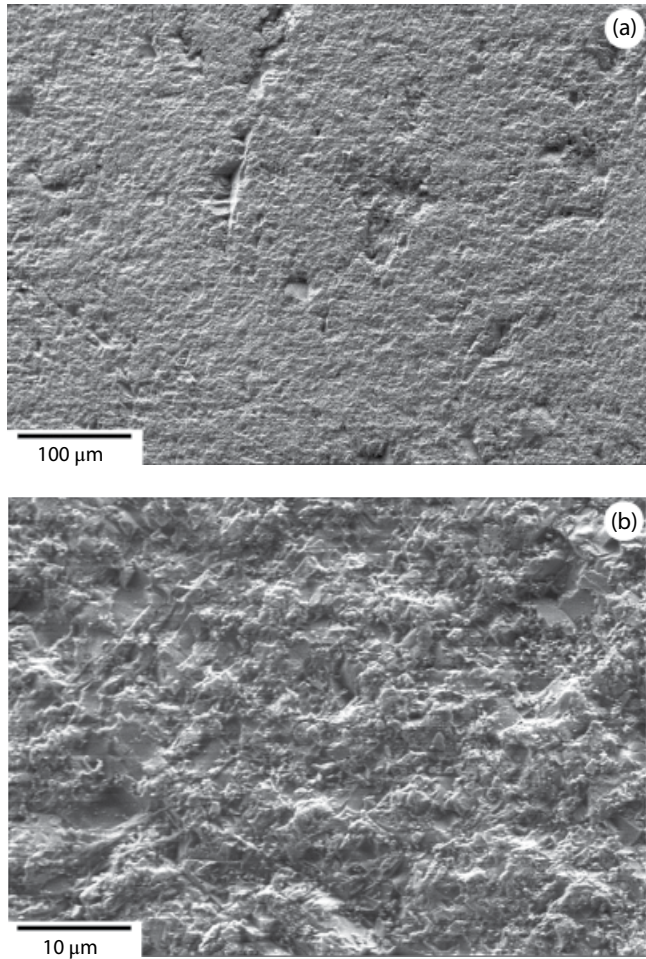


**Figure 6.10** Secondary-electron (SE) SEM images of initial roughness of granite surfaces after hand lapping with #600  $\text{Al}_2\text{O}_3$  grit. All samples were prepared in the same manner. (a) Low-magnification view, showing scattered deep pits produced by plucked grains. (b) Close-up image of a feldspar, whose surface topography is influenced by its two nearly perpendicular cleavages.

texture over distances <20  $\mu\text{m}$ . This initial fault roughness was chosen so that after only a few tens of microns of slip, a uniform layer of fine-grained gouge would be produced.

An example of the sliding surface after 8.8 mm slip and 22 stick-slip events at 50 MPa confining pressure is shown in Figure 6.11. These SE SEM images show that a fine-grained gouge has developed on the sawcut and slip was localized along slickensided Y or boundary shears. Polished thin-section, backscattered-electron (BSE) SEM images of a sample after 8.6 mm slip and 19 stick-slip events at 100 MPa confining pressure are shown in Figure 6.12. Sawcut surfaces separated slightly during removal from the pressure vessel and prior to injection of epoxy. Average gouge layer thickness in the thin section images was 7  $\mu\text{m}$  with a range of 2–16  $\mu\text{m}$ . This gouge layer thickness becomes important in estimating the temperature rise due to frictional heating in the stick-slip events. Figure 6.12b shows a dark band (between the white arrows) that could represent a slip surface equivalent to the slickensided shear in Figure 6.11. If this is the actual principal slip surface (PSS) and the rest of the gouge layer does not shear during stick-slip, sliding is occurring on a remarkably thin layer (<0.5  $\mu\text{m}$ ). We will use a range of PSS thickness between zero and 7  $\mu\text{m}$  in our thermal calculations to include the possible range of surface heating during stick-slip.

No evidence for surface melting was found in either the 50 or 100 MPa confining pressure SEM images. Instead, surfaces were separated by a thin layer of granular gouge formed by grinding and crushing of the approximately 10  $\mu\text{m}$  surface roughness (Figure 6.10) of the preroughened faults. Some grain fragments were as much as 10  $\mu\text{m}$  in size, reflecting the starting surface roughness. However, the majority of grains are submicron in size. In some cross-sectional images, coarser grains fill depressions in the sawcut surfaces that apparently represent voids left by grains plucked during surface grinding. These large sheltered grains appear in stark contrast to the fine grains that constitute the PSS due to comminution during shearing.

Fault surfaces of samples deformed at 400 MPa confining pressure have a remarkably different appearance from samples deformed at low pressure. When sample halves are separated, surfaces are usually bonded (welded) on the sawcut and separate irregularly within the weakened damage zone adjacent to the sawcut. SEM images from two samples are shown in Figure 6.13. Secondary-electron photos (Figure 6.13c, d) are taken from a sample that underwent 4.1 mm of combined slip in a partial stress-drop stick-slip followed by a total stress-drop stick-slip. These images are compared to backscattered-electron images (Figure 6.13a, b, e, f) of a second 400 MPa test sample that underwent a similar partial and then total

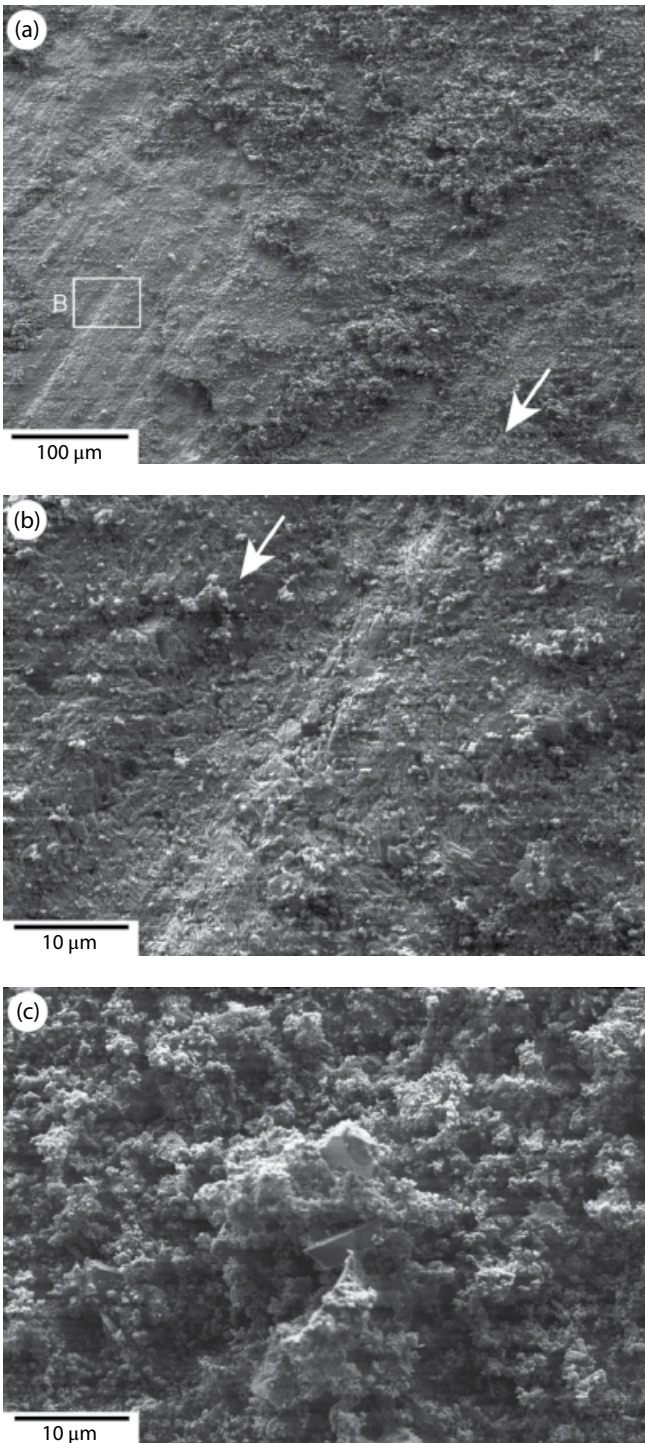


**Figure 6.11** SE images of one of the sawcuts after shearing at 50 MPa confining pressure. White arrows show the direction of motion of the granite block. (a) Slip is localized along slickensided subsidiary shear in a layer of fine-grained gouge developed between the sawcuts. The white box shows the location of (b). (b) and (c) are higher-magnification views of the rough-textured slickensided surface and the loose, granular gouge overlying it, respectively.

stress-drop stick-slip sequence with combined slip of 4.4 mm. As seen in cross-section (Figure 6.13a, b), groups of elongate voids span the lengths of phyllosilicate minerals adjoining the sawcuts. The delicate filaments that crisscross the openings (Figure 6.13b) may correspond to the glassy structures visible on the sawcut surfaces (Figure 6.13c, d). To be so well preserved, these structures must have formed at the end of the final, total stress drop stick-slip. The shears are considerably less porous where situated between quartz and feldspar minerals (Figure 6.13e, f); no large voids were seen, although some stretched vesicles are present (Figure 6.13f). In addition, fragmented crystals in the damage zone adjacent to the shears, for example, the clast-filled depression in Figure 6.13f, appear to be fused together by vesicular glass. Compositional layering across the thickness of the shears is common. The bright central band of the shear in Figure 6.13e (total thickness indicated by the black bar) and the bright streaks of the shear in Figure 6.13f are enriched in Fe, Ti, and Mg derived from biotite. Many additional photos of melt textures are presented in *Moore et al. [2016]*.

### 6.3.8. Frictional Heating of the Fault Surface

In this section we analyze temperature transients following stick-slip from thermocouples grouted in axial boreholes at a nominal distance of 2.5 mm from the sawcut surface. A representative thermocouple output, recorded at 100 Hz, is plotted in Figure 6.3a. A temperature transient with peak value of 6°C occurred approximately 2 s after the stick-slip event. As described in the following analysis, this represents heating of the fault surface of more than 1500°C. Usable temperature recordings were obtained from 34 stick-slip events. A convenient scaling quantity for 1D heat flow is the thermal half width  $a_0 = (4\alpha t)^{1/2}$ , where  $\alpha$  is thermal diffusivity. The thermal half width represents the approximate distance that a thermal pulse will propagate in time  $t$ . Consistent with *Lachenbruch [1980]*, we use granite diffusivity of  $\alpha = 1.2 \times 10^{-6} \text{ m}^2 \text{ s}^{-1}$  throughout our calculations. Then, for an inclined fault surface with semimajor radius of 12.7 mm, a 1D approximation for heat flow near the center of the fault can be used for nearly 30 s before 3D sample geometry becomes important. A thermocouple 2.5 mm from the fault should see a time delay of 0.5 to 1 s for heat conducting away from the slip surface. We use a 1D heat flow analysis, following *Cardwell et al. [1978]* and *Lachenbruch [1980]*, to fit the temperature histories following stick-slip for thermocouple distance and total heat production. Then, using our estimates of slip duration and gouge width, we back-calculate the maximum temperature on the fault. A similar procedure was used by *Lockner and Okubo [1983]* to model heat production on a large biaxial press.

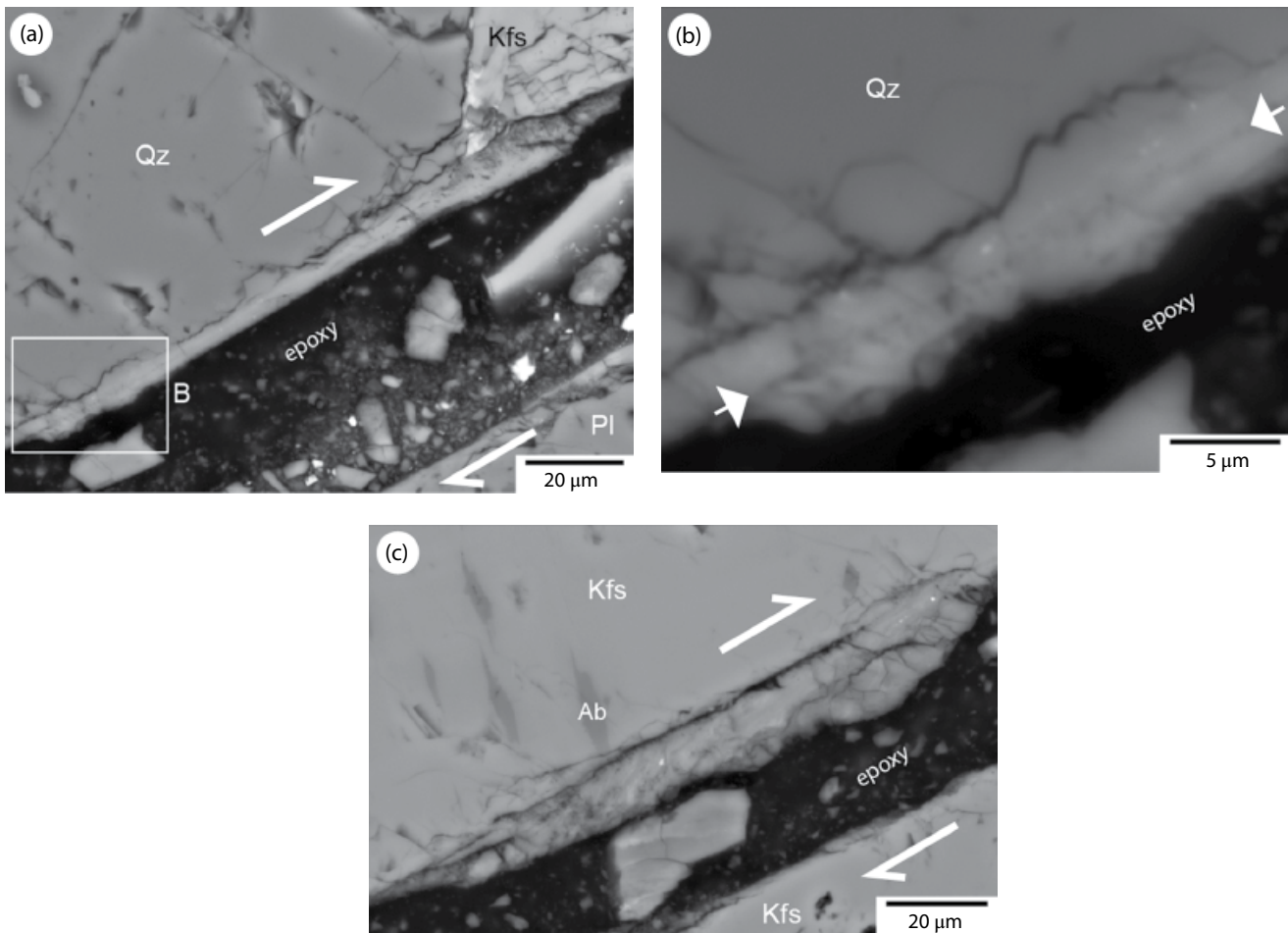


**Figure 6.12** Deformation textures developed along the sawcut after slick-slip at 100 MPa confining pressure. The sample was sectioned perpendicular to the sawcut and parallel to the cylinder axis; backscattered electron (BSE) SEM photos are oriented to show right-lateral shear (indicated by paired white half-arrows). (a) Lower- and (b) higher-magnification views of the gouge layer, which is finer grained, on average, than that formed at 50 MPa. The faint dark line down the center of the gouge layer (between the white arrows in B), may be a slip surface equivalent to the slickensided shear in Figure 6.11. The gouge appears to consist of “clasts” of denser (brighter) gouge in a more porous matrix. (c) Fragmentation of earlier-formed, dense gouge in one or more subsequent stick-slip events. Abbreviations: Ab, albite; Kfs, K-feldspar, Pl, plagioclase, Qz, quartz.

For simplicity, we assume that the PSS has thickness  $2a$  and is represented by the gouge zone thickness as observed in the SEM images. We further assume uniform strain rate within the gouge during a stick-slip event. Since there is some indication that the PSS for an individual stick-slip event may actually be ten times narrower than the gouge layer (see preceding section), assigning shearing to the entire gouge layer will provide a lower bound on the estimate of maximum temperature. We see no evidence for injection of the melt into the wall rock. Furthermore, we see no evidence for melting of wall rock or significant widening (by melting) of the PSS, and unlike high speed rotary experiments that are unconfined, gouge is not ejected from the fault zones in our confined tests. Consequently, the measured thickness of the PSS as

presented in images like Figures 6.12 and 6.13 provides an accurate upper bound on the width of the melt layer during stick-slip. For times following the stick-slip duration (denoted by  $T^*$ ), temperature rise at distance  $x$  from the fault axis is given by [Cardwell *et al.*, 1978]

$$\theta(x,t) = \theta_0 + \frac{Q}{4\rho c_p a T^*} \int_0^{T^*} \left\{ \text{erf} \left[ \frac{x+a}{(4\alpha[t-t_0])^{1/2}} \right] - \text{erf} \left[ \frac{x-a}{(4\alpha[t-t_0])^{1/2}} \right] \right\} dt_0 \quad t > T^*, \quad (6.9)$$

where the integral is evaluated numerically. Here,  $\theta$  is temperature,  $\rho$  is density,  $c_p$  is specific heat,  $a$  is shear zone

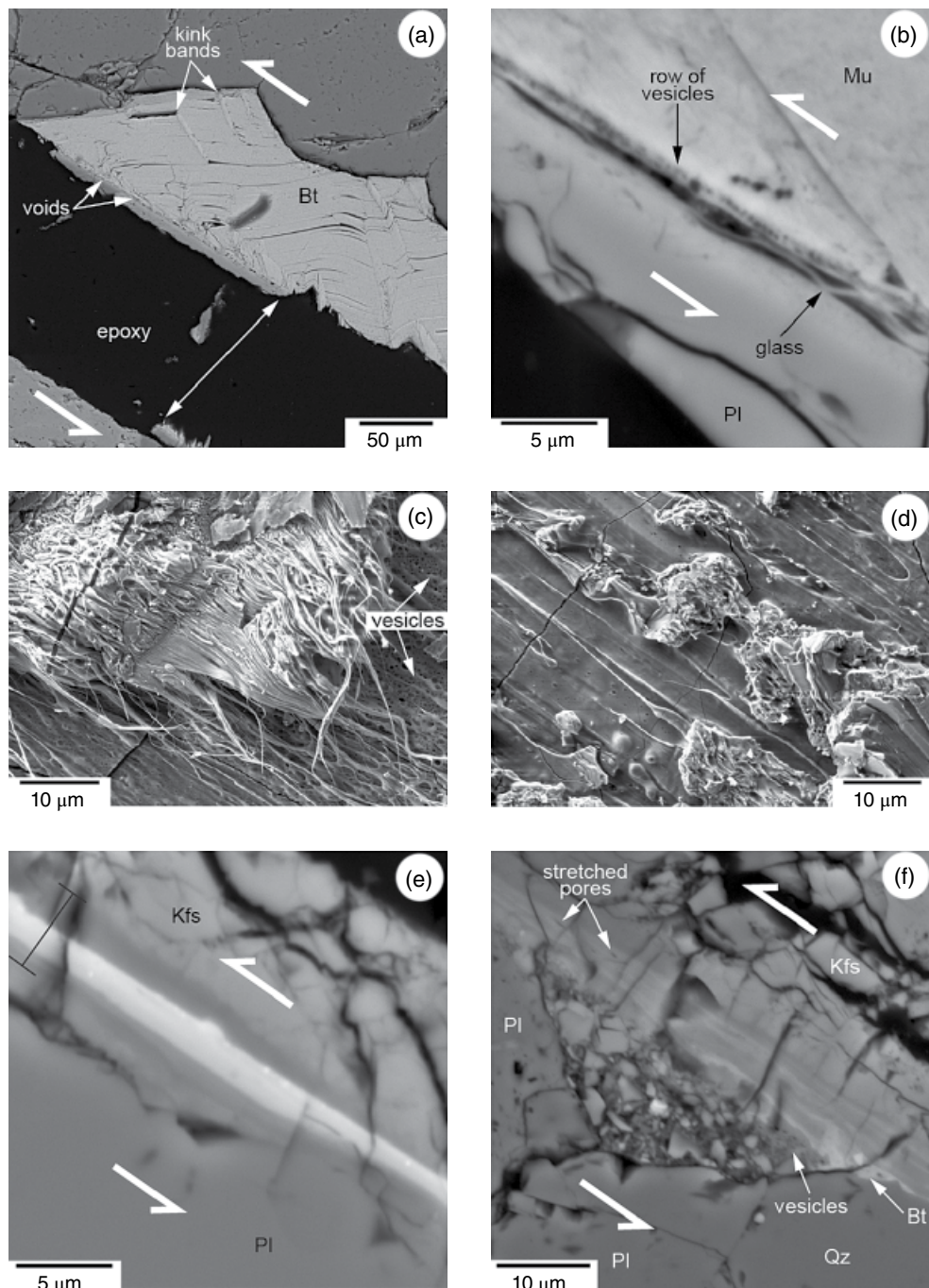


**Figure 6.13** Glass textures in SEM images from two samples deformed at 400 MPa confining pressure. (a) and (b) Textures developed adjacent to phyllosilicate minerals (BSE images). The driving blocks were welded together at the shear and typically separated along adjoining, weakened damage zones. The PSS at the base of the kinked and folded biotite (Bt) in (a) is marked by a row of elongate voids. In B, glassy filaments crisscross an elongate void between muscovite (Mu) and plagioclase (Pl). A row of vesicles ( $\leq 500$  nm diameter) marks the base of the muscovite. (c) and (d) Glassy textures in views looking down on the sawcut (SE images), including glassy filaments, glassy surface coatings, and rounded and stretched vesicles that indicate degassing. (e) and (f) Shears located between feldspar (Pl, Kfs) and quartz (Qz) crystals are devoid of large voids and commonly are compositionally layered (BSE images). The bright central zone in (e) is enriched in elements obtained from biotite (K, Fe, Ti, Mg); total shear thickness is indicated by the black bar. The shear in (f) contains a few stretched pores, and the matrix of the debris-filled pit sealed off by the shear appears to be vesicle-filled glass.

half width, and  $Q$  is total heat generated per unit cross-sectional area of the fault during stick-slip. If  $\tau_{av}$  is average shear stress on the fault during stick-slip, then  $Q \approx \tau_{av} \delta$ .  $Q$  includes the heat of melting PSS material rather than increasing temperature and would not be accounted for in the thermal modeling. This turns out to be a relatively small correction and is discussed below. In our calculations we use  $\rho = 2800 \text{ kg m}^{-3}$  and  $c_p = 840 \text{ J kg}^{-1} \text{ }^\circ\text{C}^{-1}$ . Equation (6.9) assumes uniform heat production within a zone of thickness  $2a$  and at constant rate over the time interval  $[0, T^*]$ . If melt is produced during stick-slip, dynamic shear resistance may vary significantly both with time and position on the fault surface. Still, given the limited data available, this 1D model is appropriate for placing basic constraints on fault heating and energy release. *Cardwell et al.* [1978] note that the maximum possible temperature rise occurs when  $a < \ll a_\theta$  and is given by

$$\theta_m - \theta_0 = \frac{Q}{\rho c_p (\pi \alpha T^*)^{1/2}}. \quad (6.10)$$

During and after stick-slip, the maximum temperature will be at the center of the PSS. Therefore, in the model, maximum temperature following stick-slip is given by

$$\theta_{x=0} = \theta_0 + \frac{Q}{2\rho c_p a T^*} \int_0^{T^*} \left\{ \operatorname{erf} \left[ \frac{a}{(4\alpha[t-t_0])^{1/2}} \right] \right\} dt_0 \quad t > T^*. \quad (6.11)$$

Estimates of slip duration from the laser vibrometer data range from 0.07 to 0.32 ms (see above). Thus, the thermal half width at the end of stick-slip events is estimated to be between 18 and 39  $\mu\text{m}$ . Average gouge half-width from the SEM images described in the preceding section was 3.5  $\mu\text{m}$ , although the dynamic PSS in individual stick-slip events might be significantly less than this. We conclude that for the fault geometry tested here,  $a/a_\theta = 0.09\text{--}0.2$  at time  $T^*$  and both event duration and fault width are important in limiting maximum temperature (equation [6.11]). Maximum PSS temperature is estimated by fitting equation (6.9) to the thermocouple recordings between 1 and 4 s (Figure 6.14).

Before presenting results, we consider the accuracy of the thermal modeling. Narrow PSS and short event duration mean that peak temperatures, measured just 2.5 mm from the fault, are less than 0.5% of the modeled peak temperatures on the fault surface. Thermocouples are grouted into a blind hole with an accuracy of about  $\pm 0.1 \text{ mm}$ . This produces an uncertainty in estimating peak temperature of  $\pm 5$  percent. Uncertainty in event

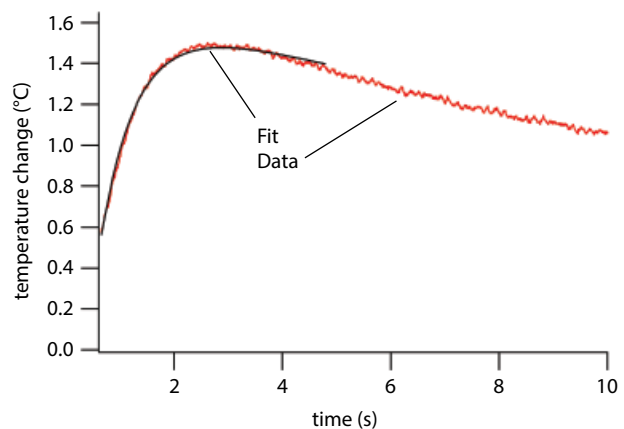


**Figure 6.14** Temperature record (red) for a thermocouple 2.6 mm from a 300 MPa stick-slip event and sampled at 100 Hz. 1D model fit (black) predicts a peak temperature rise on the fault of 506 °C and total heat production of 36.2 kJ m<sup>-2</sup>. See electronic version for color representation.

duration, the rate at which heat is produced at different times within a stick-slip, and buffering of temperature rise due to latent heat of fusion as gouge melts, will all contribute to errors in our calculation of peak temperature and total heat production. A sensitivity analysis of the model parameters indicates that a 10% error in  $T^*$  results in ~3.5% error in peak temperature. Assuming uniform heat production during a stick-slip gives a lower bound on peak temperature. Also, the error in peak temperature estimates varies nonlinearly with slip duration. If slip duration is only 20–40  $\mu\text{s}$  as suggested by *Koizumi et al.* [2004] or *Passelègue et al.* [2013], a 1200 °C calculated peak temperature rise based on our event durations would instead represent ~3000 °C rise and is probably unrealistic. If, on the other hand, slip duration was actually as long as 2 ms, the same 1200 °C estimate would be reduced to ~400 °C and would be inconsistent with observations of pervasive melt.

There is a direct trade-off between peak temperature and shear zone width. Consequently, we present results of peak temperature for a range in  $a$ . Since temperature is measured at a distance  $\sim 350a$ , and at time  $\sim 20,000 T^*$ , total heat production estimates are insensitive to errors in either  $a$  or  $T^*$ . Grain crushing (creating new surface area) and melting (through latent heat of fusion) will both consume energy that would otherwise go into increasing fault temperature. While these processes can be important in the overall energy budget, they should not have a large effect on our computed peak temperature estimates. The measured thermocouple reading only responds to the actual PSS temperature. If this temperature is limited by pervasive melting, then the calculated peak temperature will reflect this reduced temperature rise. This does mean that our estimate of total heat production will not include

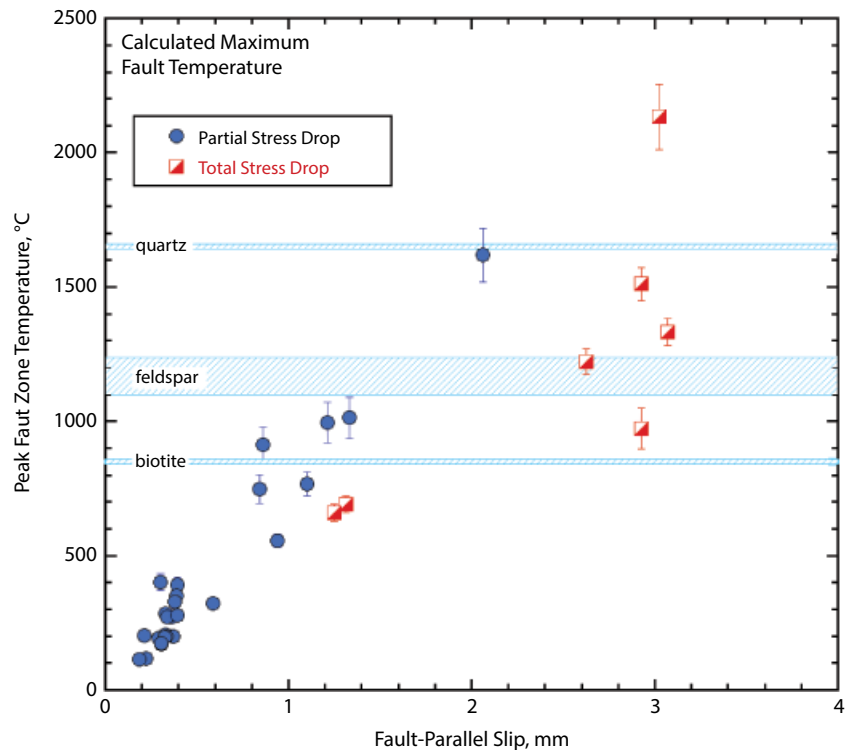


**Figure 6.15** Maximum calculated surface temperature at center of PSS is plotted versus slip. Temperatures are based on matching thermocouple transients and slip duration to a 1D heat conduction model. Upper limits of error bars assume the maximum theoretical heating for zero fault thickness. Lower limits assume an average PSS thickness of  $14\text{ }\mu\text{m}$  (twice the average observed PSS thickness). Total stress drop events generally have predicted maximum temperature above the melting temperature for feldspar. In some cases, maximum temperature may exceed quartz melting temperature. See electronic version for color representation.

heat of fusion due to melting or heat of vitrification that is released as the melt solidifies to form a glassy surface layer. These energy terms can be estimated by knowing the width of the melt layer, heat of fusion ( $\sim 64\text{ kJ/mol}$ ), and heat of vitrification ( $\sim 52\text{ kJ/mol}$ ) [Tenner *et al.*, 2007]. We estimate uncertainty in peak temperature for the larger events of about  $\pm 100^\circ\text{C}$ . At intermediate confining pressures, where partial melt is developed, surface heating may be heterogeneous [Brown and Fialko, 2012], so local peak temperature may be higher than the average surface temperature computed here. Flash heating is also likely to lead to localized melting at asperity contacts well before pervasive surface melt formation occurs [Rice, 2006; Beeler *et al.*, 2008]. Accuracy in estimating total heat production will depend on thermocouple location and heterogeneity of surface heating but not on details of fault thickness or slip duration. We estimate an accuracy in total heat production of approximately  $\pm 10\%$ .

Results of the temperature calculations are plotted as a function of total slip in Figure 6.15. The lower bound of error bars is determined by assuming uniform deformation of a  $14\text{ }\mu\text{m}$  wide slip surface. Thermal weakening and other processes may reduce the PSS to submicron thick-

ness. Therefore, as an upper bound for the error bars, we use the limiting temperature for a shear zone with zero thickness (equation [6.10]). Maximum calculated gouge temperature increases with slip and confining pressure. The largest calculated PSS temperature is in excess of  $2000^\circ\text{C}$  and is obtained for a total stress drop event at  $400\text{ MPa}$  confining pressure. The largest partial stress drop temperature is for a  $300\text{ MPa}$  stick-slip event with  $2.06\text{ mm}$  slip and  $81\%$  stress drop.

The same model fitting procedure that provides maximum PSS temperature also provides an estimate of total heat production on the fault surface. Total heat production is compared to total work in Figure 6.8. Both quantities increase with increasing confining pressure, but the fraction of energy release that is converted to fault heating is less for the most energetic events. As already mentioned, the heat production plotted in Figure 6.8 does not include heat required to melt the fault gouge. Melting the nonquartz fraction of a  $7\text{ }\mu\text{m}$  gouge layer requires roughly  $3\text{ kJ m}^{-2}$  or only a few percent of the typical heat production listed in Table 6.1. This is equivalent to the heat needed for about a  $50^\circ\text{C}$  peak temperature rise of the same fault zone.

#### 6.4. DISCUSSION

There have been a number of studies of the mechanics of laboratory stick-slip as well as measurements of associated frictional heating. *Johnson and Scholz* [1976] demonstrated that the lumped-mass spring-slider model provided a good representation of stick-slip events in a biaxial press with  $\sigma_n = 10\text{--}20 \text{ MPa}$  and  $T^* \sim 1 \text{ ms}$ . *Kilgore et al.* [2017] have expanded on that study by varying machine stiffness. They show that the spring-slider model also provides a good fit to stick-slip events on a double-direct-shear apparatus at  $\sigma_n = 2 \text{ MPa}$  and  $T^*$  of 0.3 to 1.1 ms. *Okubo and Dieterich* [1984] reported slip durations of a few ms for stick-slip on a large 2 meter fault using a direct measurement of fault velocity. *Shimamoto et al.* [1980], using a triaxial apparatus, reported slip duration of  $\sim 3 \text{ ms}$  in tests on sandstone at 30 to 100 MPa confining pressure. In their experiments, stick-slip required movement of a relatively massive pressure vessel that may explain the longer event durations. Their preferred model was a two degree of freedom spring-slider. Much shorter slip durations of 0.01–0.03 ms have been suggested in recent triaxial experiments [*Passelegue et al.*, 2013; *Koizumi et al.*, 2004]. In contrast to the *Kilgore et al.* [2017] and other studies cited above, the *Passelegue et al.* [2013] and *Koizumi et al.*, [2004] studies did not measure the time dependence of fault slip directly. Rather, the short event durations were based on indirect observations and were associated with propagation of the rupture front through the sample. These times will be significantly shorter than the slip duration and have been identified in biaxial experiments [*Johnson and Scholz*, 1976; *McLaskey and Kilgore*, 2013; *McLaskey et al.*, 2014, *Passelegue et al.*, 2013].

Unlike *Shimamoto's* [1980] design, in our experimental geometry, the upper sample half is mounted adjacent to the massive pressure vessel. Consequently, most axial and lateral motion involves movement of the lower sample half and piston. Analysis of our test geometry (section 6.3.2) has shown that the sample and piston are the most compliant elements in our loading system. The stress drop from a stick-slip event will propagate down the piston, reaching the load cell and ram after approximately 0.05 ms. At this point, the hydraulic ram will begin to move. Given the large mass of the ram, after 0.3 ms (the largest estimated event duration), even for the largest stick-slip events with total slip of  $\sim 3 \text{ mm}$ , the ram will have advanced less than 0.06 mm. Thus, the stick-slip events in this loading configuration are driven by elastic unloading of the sample and piston.

When the stress drop traveling down the 0.23 m-long piston encounters the more massive load cell and ram, the contrast in acoustic impedance will cause a reflected wave to travel back up the piston and arrive at the fault

approximately 0.1 ms after the start of the stick-slip. This agrees with the average slip duration of the smaller stick-slip events (Figure 6.9). This reflected pulse may control the event duration for the partial stress drop events. Measurements of stress and fluid pressure transients during stick-slip on a nearly identical machine [*Weeks*, 1980, chapter 4] showed similar results. In a series of 10 events on wet granite at 98 MPa effective confining pressure, Weeks found a bimodal distribution of shear stress drops clustering at approximately 38 and 63 MPa. Using a piezoelectric transducer between the piston and sample, he noted a single pronounced rapid stress drop for the smaller stick-slip events. However, the larger events all produced two distinct stress pulses separated by 0.1 ms. His interpretation was that the larger stick-slips were actually double events. Given the time delay between pulses, it is possible that a reflected pulse, traveling up the piston, may trigger additional slip and extend the total event duration in our experiments. The spring-slider model can also be applied as an approximation to the dynamics in these events. In this case, we use the mass of the piston and lower sample half and the dynamic unloading stiffness ( $\kappa_T = 156 \times 10^6 \text{ N m}^{-1}$ ). Event duration for undamped motion is [*Johnson and Scholz*, 1976; *Rice and Tse*, 1986; *Kilgore et al.*, 2017]

$$T^* = \pi \sqrt{\frac{m}{\kappa_T}} \quad (6.12)$$

and results in  $T^* = 0.25 \text{ ms}$ . This model assumes constant dynamic friction and a lumped mass driven by a separate spring. In the present case, however, the piston and sample are the spring, so a better model would have mass distributed uniformly along the spring. A dynamic model that takes into account the true geometry of the sample and loading frame may be needed for accurate characterization of the rupture dynamics. This exercise is left for future study.

Comparison of the thermocouple measurements to the 1D conductive heat flow model shows that both maximum PSS temperature and total heat production during stick-slip increase with increasing confining pressure. Estimated maximum temperatures, based on the 1D thermal model, are plotted in Figure 6.15. The maximum calculated PSS temperature is in excess of 2000°C and is obtained for a total stress drop event at 400 MPa confining pressure. Events with slip in excess of 2 mm have calculated peak temperatures over 1100°C (onset of feldspar melt) and also show pervasive surface melt features in SEM. As the PSS temperature increases, mineralogical phase changes will have a profound effect on shear strength. Granite strength quickly degrades above about 650°C [*Wong*, 1982]. First, phyllosilicate minerals

(biotite, muscovite, chlorite) will break down and release water ( $\sim 850^\circ\text{C}$ ). In the SEM images, vesicles appear in the glassy substrate of the slip surface (Figure 6.13) and are associated with crystals of phyllosilicate minerals adjacent to the fault. This degassing within the low-permeability granite can lead to localized pore pressure buildup that would reduce the effective normal stress and therefore fault strength. The delicate glassy filaments shown in Figure 6.13c and d can only survive if they are in open chambers on the fault surface (seen in cross-section in Figure 6.13b). These are always associated with phyllosilicate grains and may be the result of opening of the fault by localized water vapor release that exceeds the normal stress (localized thermal pressurization). Similar effects have been discussed for decarbonation reactions in high-speed carbonate experiments [Han *et al.*, 2007; Brantut *et al.*, 2010]. Melting temperatures for feldspars are between 1100 and 1250°C and will be reduced for the fine (submicron) particles within the gouge layer. Chemical analysis of the quenched melt using the energy dispersive system indicates that they have composition of feldspars  $\pm$  biotite and may also include quartz. There is some indication in the 400 MPa experiments that quartz grains are becoming rounded or showing other signs of melting ( $T_{\text{melt}} \sim 1650^\circ\text{C}$ ). Further study will be required to fully determine what is happening to quartz in these experiments. Since feldspar is the main constituent of the granite gouge, once its melting temperature is exceeded, a continuous layer of melt can form on the slip surface and drastically reduce shear resistance. Continuous glassy layers are observed in the 200 MPa runs (mixed with unmelted gouge particles) and have computed surface temperatures consistent with melting of feldspar. Once a continuous melt layer forms on the slip surface and reduces shear strength, additional heat production ( $=\tau\delta$ ) will be reduced. Enthalpy of fusion of the feldspar ( $\sim 64 \text{ kJ/mol}$ , [Tenner *et al.*, 2007]) will provide an additional energy sink. However, for a 7  $\mu\text{m}$  thick gouge layer, this becomes approximately  $3 \text{ kJ m}^{-2}$  and is less than 1% of the heat production during stick-slip.

Two additional features of the SEM images are noteworthy. First, there is no indication that melting is sufficiently aggressive to erode the walls of the sawcut. Second, we see no indication of injection of melt into fractures in the walls of the sawcut. Apparently, there is sufficient melt produced to coat the slip surface, but not enough excess melt to become mobile and migrate out of the gouge layer. We estimate that at the end of stick-slip, the thermal half width is 5 to 10 times greater than the gouge layer, yet even in the most energetic events, there is no evidence of melt outside the gouge. Kinetics may inhibit off-fault melt formation in the short time interval that the wall rock is above the melt temperature. Alternatively, reduction in viscosity as the melted PSS continues to heat may significantly reduce shear resistance and therefore

heat production as stick-slip continues. More sophisticated calculations than the constant heat production model used here may resolve this issue.

Constant speed rotary tests at lower normal stress show fault weakening [Chang *et al.*, 2012; Di Toro *et al.*, 2011; Han *et al.*, 2011] that requires displacements of 5 mm or often much more. Some weakening processes may be related to development of ultrafine gouge particles [Han *et al.*, 2011; Reches and Lockner, 2010] or dewatering of ultrafine particle surfaces [Sammis *et al.*, 2011]. These processes appear to require finite slip to occur and are unlikely to be controlling the onset of abrupt weakening that produces stick-slip in our experiments. However, once stick-slip has begun, they may contribute to continued weakening. High-speed measurements have been reported for local stress changes during passage of dynamic rupture events on a 2 m fault earthquake simulator [Lockner and Okubo, 1983; McLaskey and Kilgore, 2013; Okubo and Dieterich, 1984]. These experiments show a nearly constant dynamic frictional strength following the passage of the rupture front for stick-slip events involving about 100  $\mu\text{m}$  total slip at normal stresses of 1–5 MPa. The relatively low normal stress and total slip in those experiments resulted in fault surface heating of only a few degrees [Lockner and Okubo, 1983]. However, in our measurements, the systematic increase in stress drop with increasing normal stress would imply a steady decrease in dynamic friction. This drop in friction may be caused by the steady increase in surface temperature for higher normal stress and larger slip events. Reduction in static strength is much more modest than this, at least up to 600°C. Wong [1982] reported strength loss of about 30% in intact granite between room temperature and 600°C. Blanpied *et al.* [1995] reported increasing frictional strength in dry granite gouge to over 800°C and in wet gouge at 1  $\mu\text{m s}^{-1}$  slip rate to 400°C, at which point strength rapidly dropped with further temperature increase. While flash weakening at asperity contacts may be responsible for the progressive reduction of dynamic friction at higher normal stress [Beeler *et al.*, 2008; Rice, 2006], in principle, it should not be normal-stress dependent. Furthermore, it is difficult to demonstrate through direct observation, either during or after stick-slip, that asperity contacts have melted, although there is recent evidence for this [Passelègue, 2014]. In our experiments, the transition to continuous melt on the fault occurs at about 200 MPa confining pressure. For these conditions, we see a continuous coating of melt mixed with unmelted granular particles. The relative proportion of melt to stronger granular particles will change systematically with increasing temperature and may be responsible for the steady decrease in dynamic strength with increasing confining pressure. By 400 MPa confining pressure, discrete gouge particles are often completely converted to

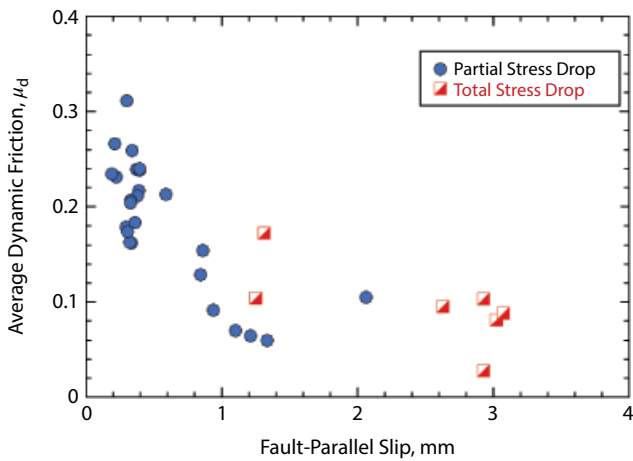


**Figure 6.16** Average dynamic friction is calculated from equations (6.9) and (6.13) using thermocouple data and the observed total fault slip. Dynamic friction of high stress events is only about one third of dynamic friction of low stress events and is probably the result of thermal weakening of the PSS. See electronic version for color representation.

melt along the PSS. Total stress drop events that represent the maximum dynamic weakening generally show the maximum computed surface temperatures.

Because energy expended to heat the fault surface is  $\int \tau_f d\delta$ , average dynamic friction can be approximated by

$$\hat{\mu}_d \approx \frac{Q}{\hat{\sigma}_n \delta}. \quad (6.13)$$

This neglects work expended in fracture energy and in melt production. However, as already discussed, these terms are probably small compared to the work used to heat the fault. We plot this estimate of average dynamic friction, which is based on the thermocouple data, in Figure 6.16. Average dynamic friction for events that slid <0.5 mm is 0.22. For events that slid >2 mm, average dynamic friction drops to 0.08. This decrease in friction implies a significant weakening due to heating of the PSS. Melt formation is a likely cause of this dynamic strength loss.

We use the 1D thermal model to estimate total heat production. For a thermocouple 2–3 mm from the fault, peak temperature occurs about 2 s after the stick-slip event so that details of the precise slip duration and PSS thickness become unimportant. Calculated heat production is plotted in Figure 6.8 as green and purple squares, representing partial and total stress drop events, respectively. In addition, total energy release is plotted in blue (normal stick-slip) and red (total stress drop events). Total energy is calculated from static axial force (before and after each stick-slip) and fault slip. Therefore, the estimates of total energy and heat production are obtained by completely independent measurements. Heat production accounts for about 50% of the energy release for the small stick-slip

events and drops to less than 20% of energy release for the total stress drop events. This is consistent with a systematic decrease in dynamic friction at high confining pressure due to surface melt and reduced shear resistance. As a result, the relative efficiency of generating surface heat is reduced and a greater proportion of energy release is radiated away from the fault. Work expended in crushing fault gouge particles and in melting the PSS is not included in the plotted heat production. Energy consumed in grain comminution is unknown but generally considered to be small in this bare surface fault geometry. Much of the initial grain comminution in the 7  $\mu\text{m}$  gouge layer occurs quasi-statically during creep on the sawcut before the first stick-slip event. Examples of this creep are shown in Figure 6.2 during strain hardening prior to the first stick-slip. Given the observed fault width, feldspar melt formation is roughly  $3 \text{ kJ m}^{-2}$  and within the measurement uncertainty plotted in Figure 6.8. An additional unknown factor is the influence of increasing viscosity of the silicone oil confining fluid with increasing confining pressure. Since the lower sample half shifts laterally during stick-slip, it forces movement of the oil in the pressure chamber. Viscous drag will increase at higher confining pressure and will consume additional energy. In future experiments we will assess the importance of viscous drag in the energy balance by replacing silicone oil with argon gas. For now, we do not know the importance of this effect in influencing stick-slip characteristics.

The thermal half width of a dynamic event will increase roughly as  $\sqrt{T^*}$ . This means that longer event duration can heat a wider zone and therefore limit the peak temperature, even if the PSS is narrow. For stick-slip events reported here, slip duration is less than 1 ms and  $\alpha_0 = 20$  to 50  $\mu\text{m}$ . For an earthquake with slip duration of 1 to 10 s, the thermal half width can increase to 2–7 mm, and reduce the peak temperature to 1% of the peak temperature produced in our experiments. Thus, shear stress, gouge width, slip speed, and slip duration all contribute to the maximum temperature attained during an earthquake, as discussed by Cardwell *et al.* [1978] and Lachenbruch [1980].

The general stick-slip behavior and how it varies with confining pressure can be illustrated with a single-degree-of-freedom spring-slider model. We carried out simulations that are intended to show general trends in behavior rather than a precise match to the observed measurements. The model we use has constant static friction ( $\mu_s = 0.7$ ) and temperature-dependent dynamic friction, with  $\mu_d$  decreasing linearly between 700°C and 1200°C to approximate the effects of increasing partial melt:

$$\begin{aligned} \mu_d &= 0.60 & \theta < 700^\circ\text{C} \\ \mu_d &= 1.37 - 0.0011\theta & 700^\circ\text{C} \leq \theta \leq 1200^\circ\text{C} \\ && (\text{linear decrease in } \mu_d) \end{aligned} \quad (6.14)$$

$$\mu_d = 0.05 \quad \theta > 1200^\circ\text{C}.$$

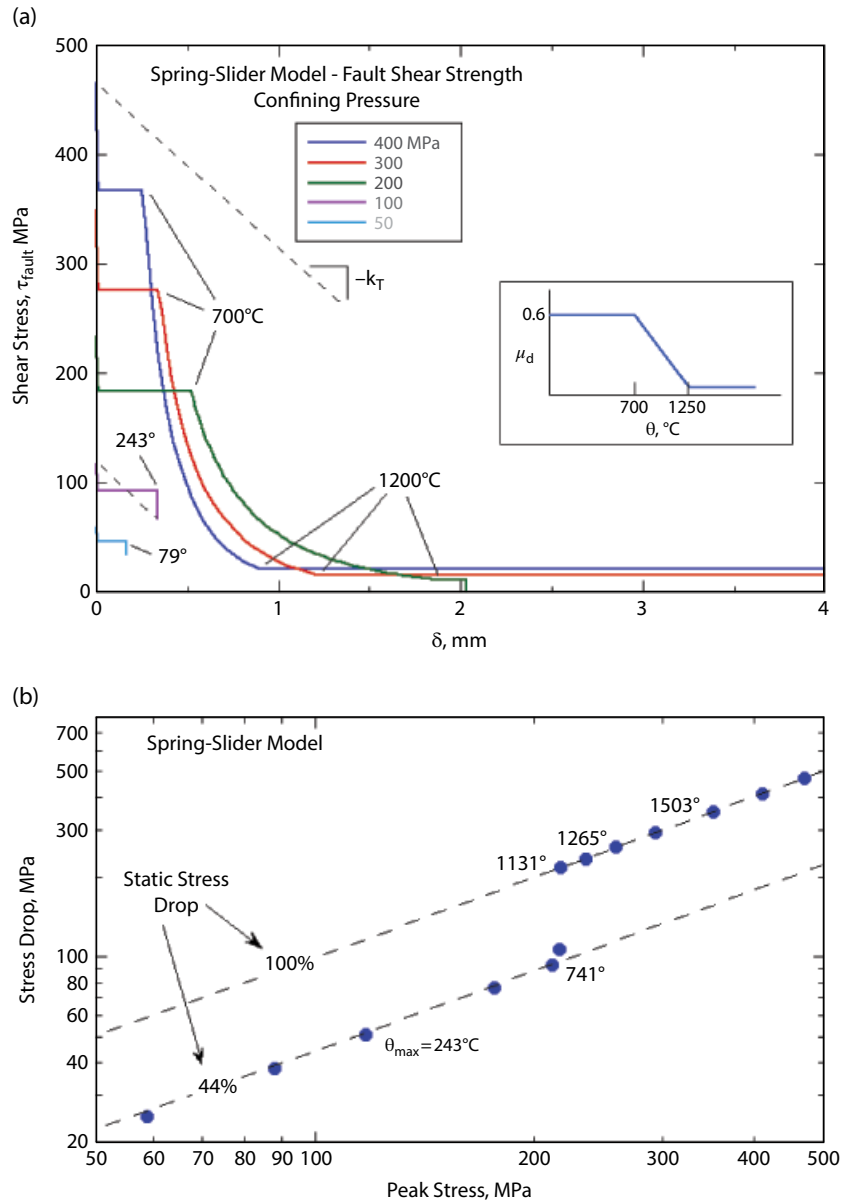


**Figure 6.17** (a) Spring-slider model for stick-slip events using temperature-dependent dynamic friction (see insert). At low confining pressure (50 and 100 MPa) the fault does not reach thermal weakening temperature. As confining pressure increases, the onset of thermal weakening occurs at progressively shorter displacement. (b) Stress drop plotted versus peak stress. Maximum fault temperature is shown for selected runs. At low confining pressure, the constant ratio of  $\mu_d/\mu_s$  results in a constant 44% stress drop for the simple spring-slider model. However, the onset of thermal weakening produces a large, delayed stress drop that results in total stress drop stick-slip events. The transition to total stress drop events in the experimental data (Figure 6.5) is more gradual and may represent a more complex temperature and velocity-dependent fault rheology or may indicate that a distributed mass dynamic model is needed to describe the system response. See electronic version for color representation.

This simple model has no radiated energy loss so that some small high-temperature dynamic friction must be included to bring the fault to rest. As with actual experiments, simulations are run at constant confining pressure that, in combination with the prescribed friction, determines  $\tau_f$  and  $\sigma_n$  according to equation (6.3). An unloading

machine stiffness of  $k_T = 150 \text{ MPa/mm}$  is assumed and a single value of mass  $m$  is chosen to give slip duration in all simulations of 0.1–0.3 ms. The initial conditions in each simulation have the fault at rest and  $\tau_f$  and  $\sigma_n$  prescribed by  $\mu_s$  and  $P_c$ . Then, fault strength is spontaneously dropped to  $\mu_d$ . In each time step, acceleration,

velocity, and displacement are calculated and an increment of frictional heating is added to the fault temperature according to  $\Delta\theta = 0.54\theta_{\max}$ , where  $\theta_{\max}$  is the thin fault limiting temperature (equation [6.10]). The factor of 0.54 is consistent with the reduced temperature rise for a finite-width fault that is smaller than the thermal width [Cardwell *et al.*, 1978]. While this is only an approximate representation of the 1D diffusion equation, it is sufficient for our purposes. The new fault temperature is used to adjust  $\mu_d$  for the next time step.

Simulations between 50 and 400 MPa confining pressure are shown in Figure 6.17a. In all cases, the initial sliding resistance is constant ( $\mu_d = 0.6$ ) as the fault heats. At 100 MPa, the fault temperature is 243°C by the end of the stick-slip, and after sliding at constant shear stress  $\tau_f$  drops to match the applied machine load represented by the dashed line. At  $P_c = 200$  MPa, fault temperature has risen to 700°C at 0.53 mm and fault weakening continues until the surface temperature reaches 1200°C at 1.89 mm slip. This is a total stress drop event and shear stress drops to zero when sliding stops at 2.03 mm. Due to the higher stress in the 300 and 400 MPa simulations, weakening begins at progressively shorter slip. Both of these are also total stress drop events. Static stress drops for a suite of runs that include these simulations, plotted in Figure 6.17b. For the simplified friction model used in these calculations, the lower temperature runs have a constant stress drop of 44%. Then, with the onset of surface melting, static stress drop abruptly jumps to 100%. Some additional complexity in fault rheology is needed to reproduce the more gradual increase in stress drop that is observed in the experimental data (Figure 6.5).

A characteristic feature of the spring-slider model is that for constant dynamic friction, the event duration is independent of stress drop and is controlled by mass and stiffness (equation [6.12]). However, in the simulations plotted in Figure 6.17, there is a double stress drop. First, shear resistance is reduced to the low temperature value of  $\mu_d = 0.6$  and then, fault heating provides a second later stress drop. The delay in the onset of the second stress drop results in extending the total time of the stick-slip event beyond the duration predicted by equation (6.12). This effect may contribute to the systematic lengthening of  $T^*$  for the larger stick-slip events shown in Figure 6.9. In addition, the fixed slip duration in the spring-slider model will only be valid for partial stress drops in which the driving force decreases linearly with displacement. For a total stress drop event, this is no longer the case and once the driving stress drops to zero, the moving block can continue to slide much farther with no additional restoring force trying to bring it to rest. This is likely to be an additional contributing factor in the large displacements observed in some of the total stress drop events.

The pseudotachylite formation reported here would represent an unusual case for naturally occurring earthquakes. Rupture is short, intense, and on a thin, smooth, dry fault surface. The total stress drop associated with surface melting in our experiments is not common for earthquakes, although a small number of large stress drop earthquakes have been reported. Kilgore *et al.* [2017] point out that the limited sample size in most laboratory experiments leads to breakout of the rupture to a free surface so that loading frame stiffness controls rupture duration rather than back-propagation of stopping phases for natural earthquakes. There are exceptions to this situation in the laboratory. Lockner *et al.* [1982] were able to arrest stick-slip in a large biaxial press by destressing the ends of the fault before rupture. Also, acoustic emissions are naturally occurring dynamic instabilities that can be contained on fault surfaces and that, although they are small, are indistinguishable in other aspects from natural earthquakes [McLaskey and Kilgore, 2013; McLaskey and Lockner, 2014]. Still, total stress drops during stick-slip may be related to the limited sample size and boundary conditions in laboratory tests as compared to earthquakes.

While normal stresses in these experiments are consistent with earthquakes that occur at mid crustal or subduction zone conditions, slip during large earthquakes is substantially greater than the 1 to 3 mm obtained here. Larger slip implies that wider PSS could be heated to melting conditions than the 10-micron-scale slip surfaces generated here. Since crustal and megathrust faults are generally wet, the heating and vaporizing of fluids, with the possibility of reduced effective normal stress, could limit frictional heating and prevent melt formation. This may be a common occurrence in natural earthquakes. Now that we have placed constraints on heating of dry laboratory fault surfaces at elevated normal stress, future work will involve stick-slip on wet faults and the conditions needed to develop fluid pressurization [e.g., Proctor and Lockner, 2016]. Even though dynamic laboratory events are rapid, the convenience of producing high stress and controlled pore pressure, both at room and elevated temperature, make triaxial stick-slip experiments appealing for investigating dynamic rupture processes.

## 6.5. CONCLUSIONS

A total of 112 stick-slip events were generated on bare surface granite sawcut samples spanning a decade range of confining pressure and normal stress. Strength, stress drop, slip, duration, average slip speed, surface temperature, and heat production all increased with increasing confining pressure. Average dynamic friction systematically decreased with confining pressure and resulted in total stress drops for most events above  $P_c = 200$  MPa.

SEM observations showed that extensive surface melt formed in experiments above about  $P_c = 200$  MPa. At the highest confining pressure, slip surfaces contained open chambers with delicate glassy filaments and degassing vents adjacent to phyllosilicate minerals. Some of the open voids were a few microns in height and had lateral extent in excess of 50  $\mu\text{m}$ . Average gouge layer thickness was 7  $\mu\text{m}$ , but the active slip surface during stick-slip may have been much narrower than that. Event duration was estimated to range from about 0.1 to 0.3 ms, resulting in a thermal half width at the end of stick-slip of 22 to 38  $\mu\text{m}$ . Details of the timing of strength loss due to melt formation and temperature-dependent viscosity will have important implications for the timing of heat production and the efficiency of seismic radiation. These considerations are beyond the scope of the present study but will be important in applying laboratory results to natural earthquakes. While a lumped-mass spring-slider model may provide an adequate representation of the stick-slip dynamics, the physical dimensions of the sample and loading frame suggest that a more elaborate distributed mass model may be necessary to understand the detailed slip response. When more precise near-field measurements of stress and displacement are obtained, this issue will be addressed in greater detail. The experiments reported here provide a unique way of measuring coseismic fault properties at in situ stresses. One advantage of the triaxial apparatus is that elevated ambient temperature and pore pressure can be added in a relatively routine manner to allow for more accurate replication of natural conditions that exist at depth on seismogenic faults.

## ACKNOWLEDGMENTS

We thank S. Cox, A. McGarr, G. McLaskey, and A. Schubnel for thoughtful comments that greatly improved the manuscript. Any use of trade, firm, or product names is for descriptive purposes only and does not imply endorsement by the U.S. Government. We also acknowledge J. Weeks for his innovative high-speed measurements of stick-slip processes that remained unsurpassed for over 30 years.

## REFERENCES

- Andrews, D. J. (2002), A fault constitutive relation accounting for thermal pressurization of pore fluid, *J. Geophys. Res.*, 107, doi:2310.1029/2002JB001942.
- Beeler, N. M., T. E. Tullis, and D. L. Goldsby (2008), Constitutive relationships and physical basis of fault strength due to flash heating, *J. Geophys. Res.*, 113(B01401), doi:10.1029/2007JB004988.
- Beeler, N. M., T. Tullis, J. Junger, B. Kilgore, and D. Goldsby (2014), Laboratory constraints on models of earthquake recurrence, *J. Geophys. Res.*, 119, 8770–8791, doi:10.1002/2014JB011184.
- Blanpied, M. L., D. A. Lockner, and J. D. Byerlee (1995), Frictional slip of granite at hydrothermal conditions, *J. Geophys. Res.*, 100(B7), 13,045–13,064.
- Brace, W. F., and J. D. Byerlee (1966), Stick-slip as a mechanism for earthquakes, *Science*, 153, 990–992.
- Brantut, N., F. X. Passelègue, D. Deldicque, J. Rouzaud, and A. Schubnel (2016), Dynamic weakening and amorphization in serpentinite during laboratory earthquakes, *Geology*, 44(8), 607–610, doi:10.1130/G37932.1.
- Brantut, N., A. Schubnel, J. Corvisier, and J. Sarout (2010), Thermochemical pressurization of faults during coseismic slip, *J. Geophys. Res.*, 115(B5).
- Brantut, N., A. Schubnel, J. Rouzaud, F. Brunet, and T. Shimamoto (2008), High-velocity frictional properties of a clay-bearing fault gouge and implications for earthquake mechanics, *J. Geophys. Res.*, 113(B10).
- Brown, K., and Y. Fialko (2012), ‘Melt welt’ mechanism of extreme weakening of gabbro at seismic slip rates, *Nature*, 488, 638–641, doi:10.1038/nature11370.
- Byerlee, J. D. (1978), Friction of rocks, *Pure Appl. Geophys.*, 116, 615–626.
- Cardwell, R. K., D. S. Chinn, G. F. Moore, and D. L. Turcotte (1978), Frictional heating on a fault zone with finite thickness, *Geophys. J. R. Astr. Soc.*, 52, 525–530.
- Chang, J. C., D. A. Lockner, and Z. Reches (2012), Rapid acceleration leads to rapid weakening in earthquake-like laboratory experiments, *Science*, 338, 101–105, doi:10.1126/science.1221195.
- Di Toro, G., D. Goldsby, and T. E. Tullis (2004), Friction falls towards zero in quartz rock as slip velocity approaches seismic rates, *Nature*, 427, 436–439.
- Di Toro, G., R. Han, T. Hirose, N. De Pao, S. Nielsen, K. Mizoguchi, F. Ferri, M. Cocco, and T. Shimamoto (2011), Fault lubrication during earthquakes, *Nature*, 471, 494–499, doi:doi:10.1038/nature09838.
- Di Toro, G., T. Hirose, S. Nielsen, G. Pennacchioni, and T. Shimamoto (2006), Natural and experimental evidence of melt lubrication of faults during earthquakes, *Science*, 311.
- Di Toro, G., G. Pennacchioni, and S. Nielsen (2009), Pseudotachylites and earthquake source mechanics, in *Fault-Zone Properties and Earthquake Rupture Dynamics*, edited by E. Fukuyama, pp. 87–133.
- Han, R., T. Hirose, T. Shimamoto, Y. Lee, and J. Ando (2011), Granular nanoparticles lubricate faults during seismic slip, *Geology*, 39(6), 599–602, doi:0.1130/G31842.1.
- Han, R., T. Shimamoto, T. Hirose, J.-H. Ree, and J. Ando (2007), Ultralow friction of carbonate faults caused by thermal decomposition, *Science*, 316, 878–881, doi:10.1126/science.1139763.
- Hirose, T., and T. Shimamoto (2005), Growth of molten zone as a mechanism of slip weakening of simulated faults in gabbro during frictional melting, *J. Geophys. Res.*, 110.
- Jiang, H., C.-T. Lee, J. Morgan, and C. Ross (2015), Geochemistry and thermodynamics of an earthquake: A case study of pseudotachylites within mylonitic granitoid, *Earth and Planetary Sci. Lett.*, 430, 235–248, doi:<http://dx.doi.org/10.1016/j.epsl.2015.08.027>.
- Johnson, T. L., and C. H. Scholz (1976), Dynamic properties of stick-slip friction of rock, *J. Geophys. Res.*, 81, 881–888.

- Karner, S. L., and C. Marone (2000), Effects of loading rate and normal stress on stress drop and stick-slip recurrence interval, in *Geocomplexity and the Physics of Earthquakes*, Geophys. Monogr. Ser., vol. 120, edited by J. B. Rundle *et al.*, pp. 187–198, AGU, Washington, D. C.
- Kilgore, B. D., A. McGarr, N. M. Beeler, and D. A. Lockner (2017), Earthquake source properties from instrumented laboratory stick-slip, in *AGU Monographs, Fault Zone Dynamic Processes: Evolution of Fault Properties During Seismic Rupture*, edited by M. Y. Thomas, T. Mitchell, and H. S. Bhat (this volume).
- Koizumi, Y., K. Otsuki, A. Takeuchi, and H. Nagahama (2004), Frictional melting can terminate seismic slips: Experimental results of stick-slips, *Geophys. Res. Lett.*, 31(L21605), doi:10.1029/2004GL020642.
- Lachenbruch, A. H. (1980), Frictional heating, fluid pressure, and the resistance to fault motion, *J. Geophys. Res.*, 85(B11), 6097–6112.
- Lockner, D. A., and P. G. Okubo (1983), Measurements of frictional heating in granite, *J. Geophys. Res.*, 88, 4313–4320.
- Lockner, D. A., P. G. Okubo, and J. H. Dieterich (1982), Containment of stick-slip failures on a simulated fault by pore fluid injection, *Geophys. Res. Lett.*, 9, 801–804.
- McGarr, A., and J. Fletcher (2007), Near-fault peak ground velocity from earthquake and laboratory data, *Bul. Seism. Soc. Amer.*, 97(5), 1502–1510, doi:10.1785/0120060268.
- McLaskey, G. C., and B. Kilgore (2013), Foreshocks during the nucleation of stick-slip instability, *J. Geophys. Res.*, 118, 1–16, doi:10.1002/jgrb.50232.
- McLaskey, G. C., B. D. Kilgore, D. A. Lockner, and N. M. Beeler (2014), Laboratory generated M -6 earthquakes, *Pure App. Geophys.*, 171(10), 2601–2615, doi:10.1007/s00024-013-0772-9.
- McLaskey, G. C., and D. A. Lockner (2014), Preslip and cascade processes initiate laboratory stick-slip, *J. Geophys. Res.*, 119(8), 6323–6336, doi:10.1002/2014JB011220.
- Moore, D. E., D. A. Lockner, N. M. Beeler, and B. D. Kilgore (2016), Gallery of melt textures developed in Westerly Granite during high-pressure triaxial friction experiments, *U.S. Geological Survey Open File Report*, 2016-1059, 75 p., doi:<http://dx.doi.org/10.3133/ofr20161059>.
- Nielsen, S., G. Di Toro, T. Hirose, and T. Shimamoto (2008), Frictional melt and seismic slip, *J. Geophys. Res.*, 113.
- Noda, H., E. Dunham, and J. R. Rice (2009), Earthquake ruptures with thermal weakening and the operation of major faults at low overall stress levels, *J. Geophys. Res.*, 114, doi:10.1029/2008JB006143, 2009.
- Okubo, P. G., and J. H. Dieterich (1984), Effects of physical fault properties on frictional instabilities produced on simulated faults, *J. Geophys. Res.*, 89, 5815–5827, doi:10.1029/JB089iB07p05817.
- Passelègue, F. X. (2014), *Experimental study of the seismic rupture*, PhD thesis, Ecole Normale Supérieure de Paris, available at <ftp://ftp.geologie.ens.fr/incoming/tempo/passelegue/PhDFXP.pdf>, 193 p.
- Passelègue, F. X., A. Schubnel, S. Nielsen, H. S. Bhat, and R. Madariag (2013), From sub-Rayleigh to supershear ruptures during stick-slip experiments on crustal rocks, *Science*, 340, 1208–1211, doi:10.1126/science.1235637.
- Proctor, B., and D. A. Lockner (2016), Pseudotachylite increases the post-slip strength of faults, *Geology*, 44, 1003–1006.
- Reches, Z., and D. A. Lockner (2010), Fault weakening and earthquake instability by powder lubrication, *Nature*, 467, 452–455, doi:10.1038/nature09348.
- Rice, J. R. (2006), Heating and weakening of faults during earthquake slip, *J. Geophys. Res.*, 111, doi:10.1029/2005JB004006.
- Rice, J. R., and S. T. Tse (1986), Dynamic motion of a single degree of freedom system following a rate and state dependent friction law, *J. Geophys. Res.*, 91, 521–530.
- Sammis, C., D. A. Lockner, and Z. Reches (2011), The role of adsorbed water on the friction of a layer of submicron particles, *Pure App. Geophys.*, 168(12), 2325–2334, doi:10.1007/s00024-011-0324-0.
- Shimamoto, T., J. Handin, and J. Logan (1980), Specimen-apparatus interaction during stick-slip in a triaxial compression machine: A decoupled two-degree-of-freedom model, *Tectonophysics*, 67, 175–205.
- Sibson, R. (1975), Generation of pseudotachylite by ancient seismic faulting, *Geophys. J. R. Astron. Soc.*, 43, 775–794.
- Spray, J. G. (1987), Artificial generation of pseudotachylite using friction welding apparatus: Simulation of melting on a fault plane, *J. Struct. Geol.*, 9, 49–60.
- Spray, J. G. (2010), Frictional melting processes in planetary materials: From hypervelocity impact to earthquakes, *Annu. Rev. Earth Planet. Sci.*, 38, 221–254, doi:10.1146/annurev.earth.031208.100045.
- Sulem, J., and V. Famin (2009), Thermal decomposition of carbonates in fault zones: Slip-weakening and temperature-limiting effects, *J. Geophys. Res.*, 114(B3).
- Summers, R., and J. Byerlee (1977), Summary of results of frictional sliding studies, at confining pressures up to 6.98 kb, in selected rock materials, *U.S. Geological Survey, Open File Report* 77-142, 129 p.
- Tembe, S., D. A. Lockner, and T.-f. Wong (2010), Effect of clay content and mineralogy on frictional sliding behavior of simulated gouges: Binary and ternary mixtures of quartz, illite and montmorillonite, *J. Geophys. Res.*, 115(B03416), doi:10.1029/2009JB006383.
- Tenner, T. J., R. A. Lange, and R. T. Downs (2007), The albite fusion curve re-examined: New experiments and the high-pressure density and compressibility of high albite and NaAlSi<sub>3</sub>O<sub>8</sub> liquid, *American Mineralogist*, 92, 1573–1585, doi:10.2138/am.2007.2464.
- Teufel, L. W., and J. M. Logan (1978), Effect of displacement rate on the real area of contact and temperatures generated during frictional sliding of Tennessee sandstone, *Pure Appl. Geophys.*, 116, 840–872.
- Weeks, J. D. (1980), Some aspects of frictional sliding at high normal stress, PhD Thesis, Stanford University, Stanford, California, 171 p.
- Wong, T.-f. (1982), Effects of temperature and pressure on failure and post-failure behavior of Westerly granite, *Mechanics of Materials*, 1, 3–17.

# 7

## Powder Rolling as a Mechanism of Dynamic Fault Weakening

Xiaofeng Chen, Andrew S. Elwood Madden, and Ze'ev Reches

### ABSTRACT

For millennia, human-made machinery incorporated rolls and wheels to reduce frictional resistance, yet similar elements are practically absent in natural systems. We found in rock shear experiments that tiny, cylindrical rolls composed of nanoparticulate gouge spontaneously develop along experimental faults and lead to drastic dynamic weakening. The experiments were conducted on granite samples with a rotary apparatus at slip velocity range of 0.001–1 m/s and normal stress up to 14.4 MPa. At moderate slip velocities of <0.1 m/s, the fault slip localized along flakes of highly smooth surfaces that frequently displayed a multitude of cylindrical rolls. Roll diameters are  $\sim 1 \mu\text{m}$ , their length range is 2–20  $\mu\text{m}$ , and they are made of tightly-packed ultrafine (20–50 nm) powder grains. These rolls are systematically oriented normal to the slip direction. The presence of rolls correlates well with reduction of the macroscopic friction. We propose that development of powder rolls on fault principal slip zone surfaces leads to a transition from sliding-dominated slip to rolling-dominated slip, thus serving as an effective mechanism of fault weakening.

### 7.1. INTRODUCTION

Dynamic fault weakening is critical for fault stability and seismic behavior, and thus experimental efforts have been devoted to understanding this issue at a wide range of conditions, from seismic slip velocity of a few m/s, down to very low velocity of submicron per second [Dieterich, 1979; Di Toro *et al.*, 2011; Reches and Lockner, 2010]. Commonly, rock frictional strength is determined through macroscopic measurements on samples with slip surface area of a few  $\text{cm}^2$  to 1  $\text{m}^2$  [Lockner and Okubo, 1983], and these measurements led to useful friction laws. However, the macroscopic data cannot provide direct, physical evidence of the weakening mechanisms that are

usually defined by micron-scale processes and can be revealed through microscopic analyses. We present here high-resolution analysis of experimental fault surfaces that revealed micron scale powder rolls that developed spontaneously, converted the rock fault into natural roller-bearing, and weakened the fault.

Several weakening mechanisms were proposed during the last few decades, and a few are supported by direct, physical observations. It was shown that time-dependent deformation of touching asperities controls the velocity-dependent and healing characteristics of planar faults slipped at very low velocity [Dieterich and Kilgore, 1994]. Dynamic weakening is clearly associated with rock melting of experimental gabbro faults that slipped at high velocity ( $V \geq 1 \text{ m/s}$ ) for long distances ( $>5 \text{ m}$ ) [Tsutsumi and Shimamoto, 1997]. Fault weakening was also attributed to flash heating at touching asperities [Rice, 2006] and lubrication by silica gel that

School of Geology and Geophysics, University of Oklahoma, Norman, Oklahoma, USA

forms along quartzitic faults during slip at moderate velocities (0.003–0.1 m/s) [Goldsby and Tullis, 2002; Di Toro *et al.*, 2004; Hayashi and Tsutsumi, 2010]. It was recently proposed that powder-lubrication within a fine-grain powder layer can lead to profound dynamic weakening [Reches and Lockner, 2010; Han *et al.*, 2010]. Powder lubrication is an appealing mechanism because fine-grain rock powder, known as gouge, is found along almost all faults of the brittle crust regardless of fault composition [Ben-Zion and Sammis, 2003]. Further, comminution into fine-grain gouge is the first process to occur experimentally along rocks of all compositions and at all slip-velocities [Boneh *et al.*, 2013]. It is further expected that as slip progresses, fine-grain powder with many submicron to nanoscale grains would react and transform by physical and chemical processes. The activation of these processes, for example, amorphization, dehydration, decomposition, melting, or sintering, depends on slip conditions (normal stress, velocity, temperature) and fault composition. For example, silica-gel lubrication occurs at moderate slip velocities of ~0.003–0.1 m/s only along siliceous rocks [Di Toro *et al.*, 2004; Hayashi and Tsutsumi, 2010], which could naturally occur during seismic events [Kirkpatrick *et al.*, 2013; Rowe and Griffith, 2015]. Fault smoothing to mirror-like surfaces made of nanograins occurs primarily along carbonate faults at seismic slip velocities (>0.05 m/s) [Chen *et al.*, 2013; Siman-Tov *et al.*, 2013; Fondriest *et al.*, 2013].

Our rock friction experiments revealed two central features: First, the fault-slip was localized within a thin zone of the gouge layer, in agreement with many field and experimental observations [Ben-Zion and Sammis, 2003; Di Toro *et al.*, 2004; Han *et al.*, 2010; Reches and Lockner, 2010; Chen *et al.*, 2013; Siman-Tov *et al.*, 2013]. Second, cylindrical, elongated rolls developed from the cohesive gouge grains, and their formation strongly correlated with the dynamic weakening of the experimental fault. Similar powder rolls were previously observed in friction experiments of silicon [Zanoria *et al.*, 1995a,b], quartz [Nakamura *et al.*, 2012], chert [Hayashi and Tsutsumi, 2010], ceramics [Boch *et al.*, 1989], and alumina [Dong *et al.*, 1991] with measurable friction reduction [Zanoria *et al.*, 1995a,b]. Our work shows that powder rolling can be an effective weakening mechanism of faults.

## 7.2. MATERIALS AND METHODS

### 7.2.1. Test Apparatus and Procedure

We used a rotary shear apparatus (ROGA) to study the rock friction [appendix; also see Reches and Lockner, 2010]. The apparatus can apply up to 35 MPa of normal

stress, slip velocities of 0.0003 to 1 m/s, and infinite slip distances. Measurements of normal load, shear load, slip velocity, displacement, temperature, and dilation are continuously monitored with sampling rate of 50–1000 Hz.

The experimental fault was made of two cylindrical blocks: a stationary one with a raised ring (63.2 mm and 82.3 mm as inner and outer diameters), and a rotating one that is flat-topped (101.6 mm diameter and 50.8 mm height). The blocks were pressed against each other along the raised ring. The sliding surfaces were ground flat and roughened with 600-grit (16 µm) SiC powder. Two thermocouples were embedded at 3 mm away from the sliding surfaces. The experiments were conducted either with fresh, ground blocks or with an experimental fault that has already been sheared (Table 7.1).

We present results of three loading styles (Table 7.1) that were discussed in great detail by Liao *et al.* [2014]. In “constant-velocity,” the samples were loaded at classical constant velocity with short acceleration and deceleration stages (<1 s). In “ramp-velocity” runs, the acceleration and deceleration are equal in absolute magnitude but inverse in sign, the two stages are equal in duration (each half of the experiment), and there is no constant velocity stage. In “power-control” runs, the experimental fault was loaded under constant velocity power-density where power-density = slip velocity × shear stress [Boneh *et al.*, 2013]. The loading style is mentioned here only for documentation, and for noting that the presence of rolls (or lack of them) does not depend on the loading style. The mechanical effects are analyzed by Liao *et al.* [2014].

### 7.2.2. Experimental Fault Rock

The experiments presented here were conducted with samples of Radiant Red granite quarried at Fredricksburg, TX. It has a bulk density of 2614 kg/m<sup>3</sup> and a uniaxial strength of 146.5 MPa. The mineralogy determined by powder X-ray diffraction was composed of quartz (43.6%), albite (19.7%), microcline (22.8%), and biotite (13.9%) in weight percent.

### 7.2.3. Microanalysis Techniques

After a friction experiment, the experimental fault was opened and inspected. We commonly observed vitreous, cohesive, curved flakes on the fault surfaces that were collected for microanalysis. The flakes were sputtered with a metal (Au-Pt) layer about 15 nm thick, and then imaged with the scanning electron microscope (SEM); we used

**Table 7.1** Summary of experiments with the Radiant Red granite sample. Rolls quality is defined in the text and in Figure 7.4. Loading conditions are 1 for constant velocity, 2 for ramp velocity (velocity rise then drop), and 3 for constant power-density.

Exp. #	$\sigma_n$ (MPa)	Velocity (m/s)	Distance (m)	$\mu_i$	$\mu_f$	Flakes & Rolls	Rolls Quality	Loading Condition
2554	2.3	0.001	0.55	0.79	0.74	Yes	A	3
2600	2.3	0.014	3.79	0.7	0.3	Yes	B	3
2683	2.4	0.05	12.94	0.62	0.33	Yes	C	3
2704	6.5	0.017	0.14	0.6	0.46	Yes	B	3
2713	1.1	0.012	2.41	0.78	0.49	Yes	C	1
2714	1.1	0.024	2.4	0.75	0.42	Yes	C	1
2715	1.1	0.048	2.42	0.78	0.38	Yes	C	1
2716	1.1	0.047	4.82	0.72	0.34	Yes	A	1
2751	2.4	1.000 (max)	2.33	0.8	0.72	No		2
2752	2.4	0.267	2.85	0.85	0.68	No		1
2785	2.3	0.850 (max)	3.47	0.82	0.84	No		2
2806	3.8	0.036	4.34	0.6	0.34	Yes	A	1
2807	10.6	0.013	0.1	0.65	0.58	Yes	B	1
2810	10.6	0.024	1.95	0.64	0.48	Yes	A	1
2813	14.4	0.012	1.49	0.7	0.49	Yes	C	1
2832	2.6	0.048	3.63	0.54	0.35	Yes	B	1
3240	2.2	0.001	1.37	0.5	0.38	Yes	B-C	1
3241	2.1	0.004	1.32	0.53	0.34	Yes	B-C	1
3242	2.2	0.012	1.33	0.53	0.38	Yes	A	1
3243	2.2	0.036	1.38	0.52	0.34	Yes	A-B	1
3244	2.1	0.116	1.64	0.56	0.49	No		1
3245	2.1	0.325	1.79	0.5	0.58	No		1
3248	5.8	0.012	1.34	0.6	0.43	Yes	B-C	1
3249	5.6	0.036	1.39	0.72	0.63	Yes	D	1
3250	5.6	0.012	3.95	0.65	0.4	Yes*		1
3251	5.6	0.004	1.25	0.53	0.38	Yes	B-C	1
3252	5.5	0.137	1.69	0.75	0.63	No		1
3253	5.5	0.006	3.79	0.7	0.31	Yes	C	1
3255	1.3	0.001	1.42	0.54	0.58	No		1
3256	1.2	0.004	1.27	0.61	0.59	No		1
3257	1.2	0.035	2.69	0.65	0.29	Yes	C	1
3258	1.2	0.111	2.96	0.55	0.5	No		1
3259	1.2	0.036	5.43	0.51	0.16	Yes	A-B	1
3260	1.2	0.012	6.01	0.51	0.24	Yes*		1

\* Runs 3250 and 3260 generated tiny powder flakes that are too small for sampling.

the Zeiss NEON 40 EsB high-resolution field emission SEM at the University of Oklahoma. The highest resolution revealed the Au-Pt conductive coating layer grains, which are typically smaller than 20 nm. We used atomic force microscopy (AFM, Pacific Nanotechnology Nano R2) to determine the surface topography of the flakes at the submicron scale.

Caution should be made to keep the integrity of the flakes and preserve the slip surface. To preserve the

powder rolls, mechanical shaking and air-blown should be minimized during collecting and transportation of the flakes. The general guideline to detect rolls in SEM inspection is to look for patches of smooth slip surfaces at low magnification first, and then concentrate on looking for rolls features such as parallel alignments of roll-like gouge aggregates, pavement of destroyed rolls, and residual of depression footprints.

### 7.3. EXPERIMENTAL RESULTS

#### 7.3.1. Macroscopic Friction Evolution

We performed 34 runs (Table 7.1) on samples of Radiant Red granite, with total slip of 0.1–12.94 m, normal stress of 1.1–14.4 MPa, and slip velocity of 0.001–1 m/s. The friction coefficient and slip velocity of typical velocity-controlled and power-controlled experiments are shown in Figure 7.1. In most experiments of low to moderate slip-velocity (0.001–0.1 m/s), the peak friction coefficient of  $\mu_p = 0.5$ –0.8 dropped to steady state values of  $\mu_{ss} = 0.2$ –0.4 after slip distance of 0.5–2 m (Table 7.1, Figure 7.1a, b). Experiments of high slip-velocity ( $V > 0.1$  m/s) did not display clear slip weakening and even displayed gentle frictional strengthening (Table 7.1). The experimental observations reveal that the macroscopic friction varies with both slip velocity and normal stress, as discussed later. These observations, including the slip-rate dependency, are consistent with previous macroscopic frictional behavior measurements of silicate rocks

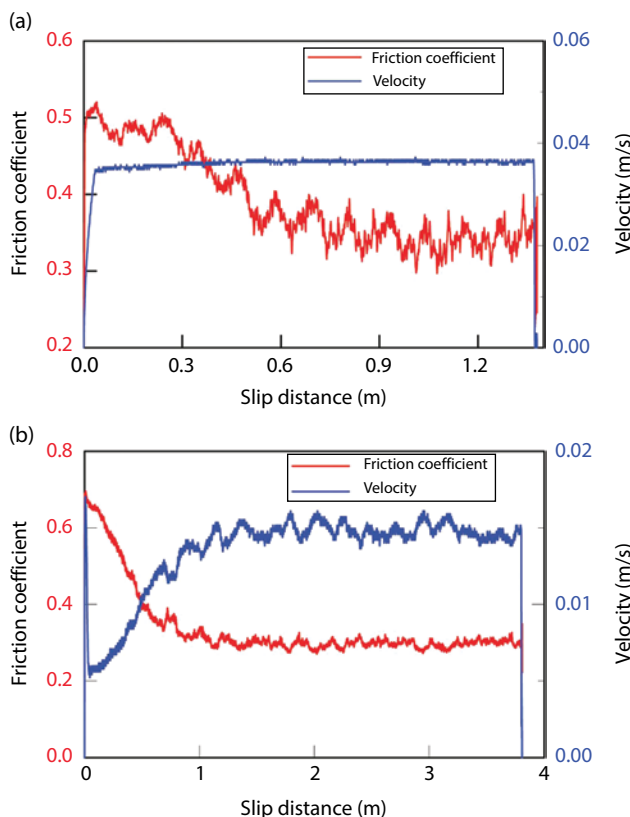


**Figure 7.1** Experimental friction evolution with slip distance in rotary shear experiments with Radiant Red granite. (a) Constant-velocity experiment at 0.036 m/s (run 3243). (b) Power-controlled experiment in which the power-density (= shear stress  $\times$  slip velocity) was maintained constant by the feedback control (run 2600).

under similar conditions [Kuwano and Hatano, 2011; Reches and Lockner, 2010; Liao and Reches, 2013].

The comminution of the solid granite blocks typically leads to destruction of micas [Reches and Lockner, 2010]. The Red Radiant granite behaves similarly, and the mineralogical composition of the gouge powder by X-ray diffraction showed total disappearance of the biotite, with drop from 13.9% in the original rock (above) to 0.1% in the gouge. We also noted increase of relative abundance of quartz (increase from 43.6% to 49.1%), and albite (increase from 19.7% to 32.9%), in contrast to microcline decrease (down from 22.8% to 17.9%). These changes in the relative abundance reflect the relative resistance of the granite minerals to mechanical wear.

#### 7.3.2. Microstructure

##### 7.3.2.1. Smooth Surfaces

The microstructural analysis was conducted on the cohesive flakes (Figure 7.2a, b) that were collected at various stages of slip (Table 7.1). The flakes formed within the freshly formed gouge powder of the experimental fault after displacement of tens of cm or more. Flakes were found in both experiments that started with fresh, ground fault surfaces, and with a fault surface cover with gouge of previous runs. These flakes were observed in both velocity-controlled and power-controlled loading (Table 7.1). Flakes were found on both blocks of the experimental fault, while sometimes they were preferentially bound onto one block. The flakes revealed distinct microstructural features in SEM and AFM analyses; these features are described below.

At the scale of light microscopy, the flakes are cohesive, a few hundred microns thick, and covered with clear slip-parallel striations (Figure 7.2a, b). Internally, the flakes are made of a layered 3D structure of agglomerated powder grains, which are less than one micron in size, with a few angular, larger grains embedded in the porous matrix (Figure 7.2c). The flakes have two distinctly different zones. The rough, porous, coarse zone (Figure 7.2b, d) was attached to the solid, rough surface of the host rock. The other zone formed a smooth and shiny surface (Figure 7.2a, b, e) that faced similar smooth surfaces on the matching side of the fault.

At the SEM scale, the shiny surface is a 0.1–0.5  $\mu\text{m}$  thick layer composed of a well-compacted, dense mosaic of ultra-fine grains that are 20–50 nm in size (Figure 7.2c). This dense mosaic (Figure 7.3b, c, e) was likely formed by local adhesion or sintering of the ultra-fine grains. This dense surface is commonly covered with submicron platelets stacking on top of the shiny surface (Figure 7.3a, b, f), micron-sized wear debris, and agglomerated nanograins that form slip-parallel rows (Figures 7.2e, 7.4a). As these smooth surfaces face each other on the opposite

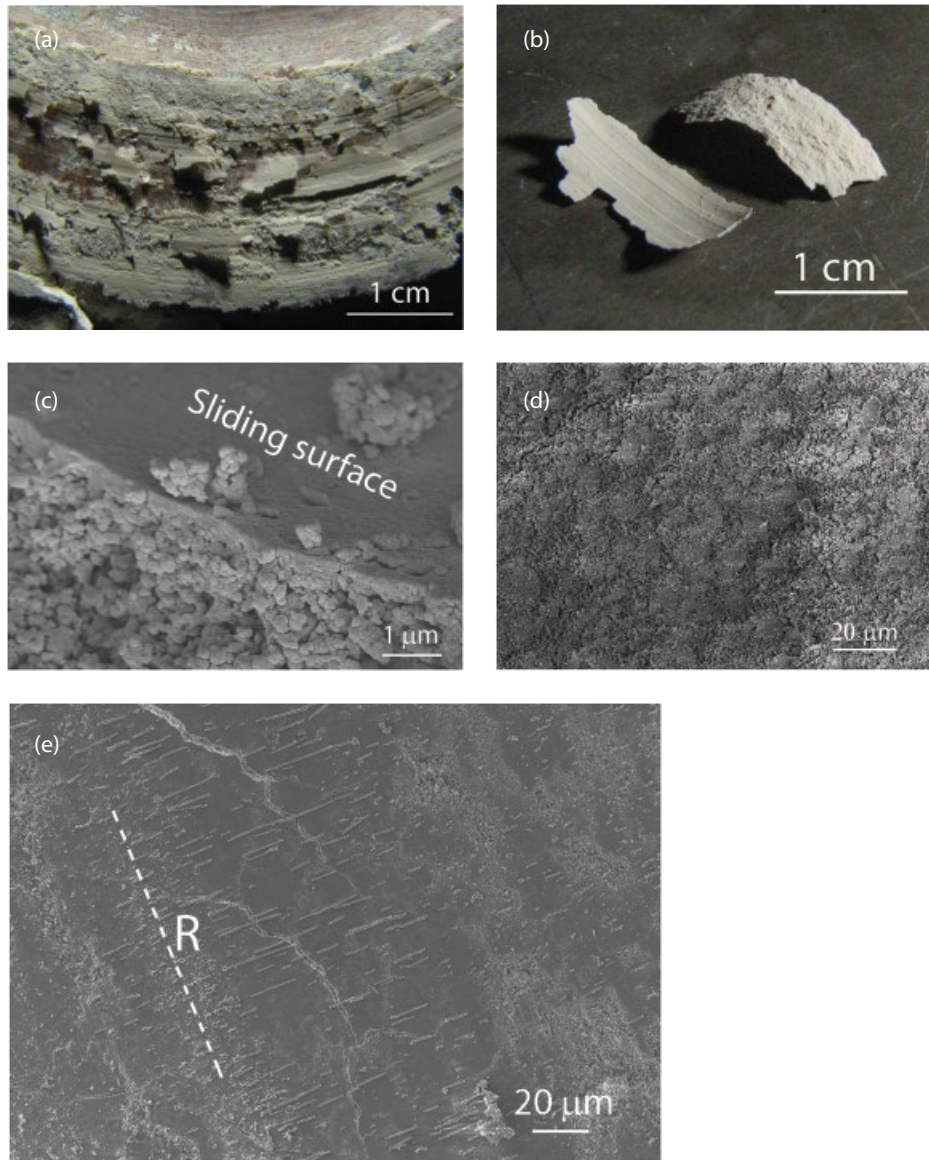


**Figure 7.2** The cohesive, shiny, powder flakes that formed on experimental faults during slip. (a) Fault surface showing several pieces of flakes formed on the slip surface (run 3253). (b) The curvy flakes; note the smoothness and slip striations on the flake top surface (left), and the coarse bottom surface (right) (run 3251). (c) SEM view of a flake cross-section showing internal 3D structure, with the substrate loosely compacted with relatively coarse grains, and the top smooth surface ~0.3  $\mu\text{m}$  thick (sliding surface) with dense compacted finer grains (run 2716). (d) SEM view of the bottom side of a powder flake that was attached to the host rock block showing rough surface made of loose agglomerated coarse grains (run 2683). (e) General view of the powder flake surface showing patches of smooth areas with uniformly oriented powder rolls, and slip-parallel rows (marked *R*) of powder debris (run 2600).

sides of the fault, they are interpreted as zones of slip localization within a gouge layer of disorganized fine powder grains (Figure 7.2a). Similar smooth surfaces of localized slip were observed in many friction experiments of solid rocks and gouge layers and natural faults [Han *et al.*, 2010; Smith *et al.*, 2011; Chen *et al.*, 2013; Kirkpatrick *et al.*, 2013; Siman-Tov *et al.*, 2013; 2015]. We refer to the smooth, shiny surface as a principal slip zone (PSZ).

### 7.3.2.2. Powder Rolls

The most striking feature observed on the PSZs is the presence of “powder rolls” that are (1) made of aggregated nanoparticulate gouge powder grains, (2) cylindrical in shape, (3) trend normal to slip direction, and (4) develop only on isolated patches of smooth, clean surfaces of the PSZ (Figure 7.2e). Description and interpretation of these powder rolls are presented below.

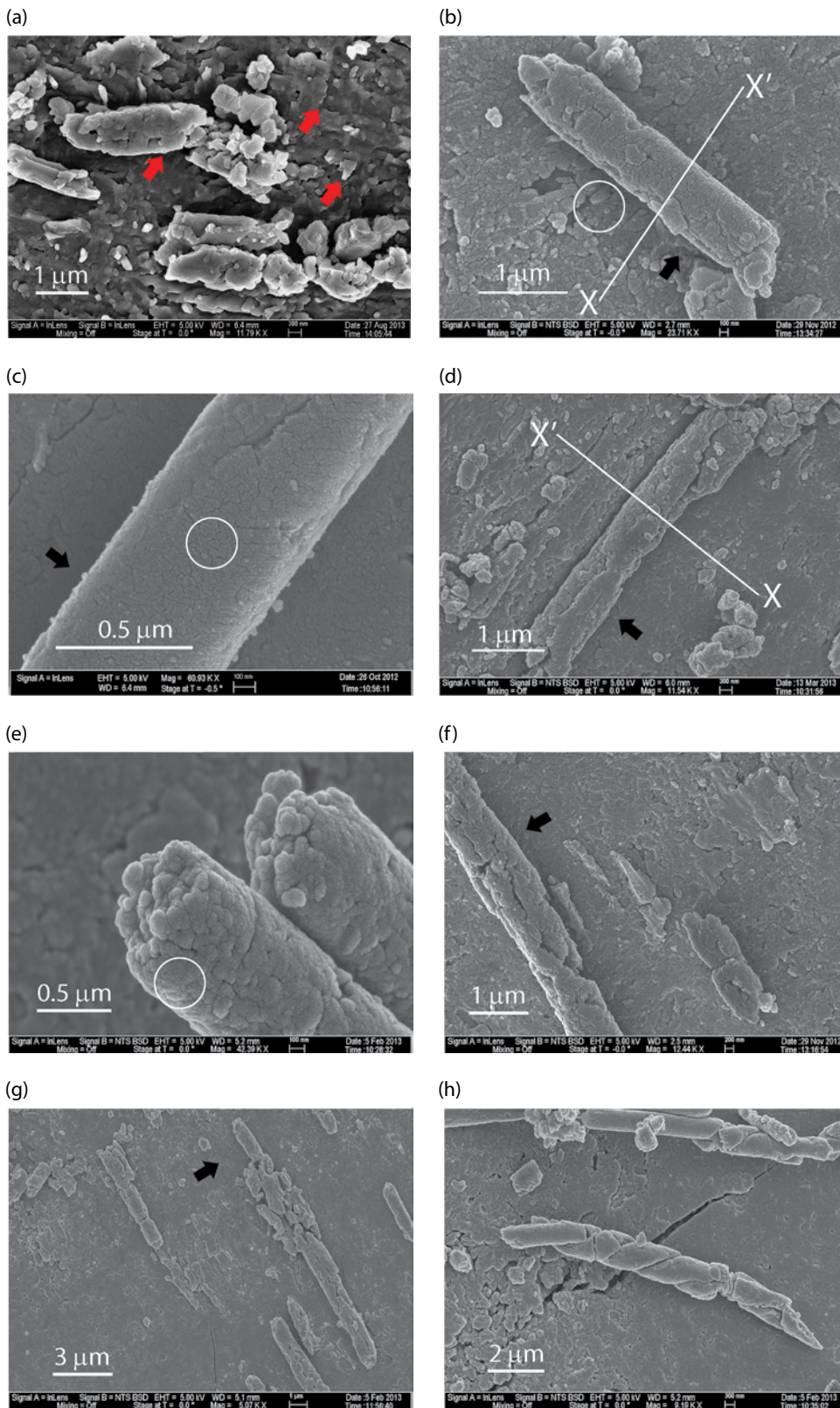


**Figure 7.3** Close-up views of powder rolls. In all images: small, black arrows indicate rolling direction; XX' are cross-sections with asymmetric deformation of the slip surface beneath the rolls shown schematically in I; small white circles indicate areas of “glued” grains that are suspected as result of sintering. (a) Rolls developed on smooth PSZ. Note submicron-size thin platelets wrapping up the rolls stacking on the PSZ surface (hollowed arrows) (run 2832). (b), (c), and (d) Deformation of the PSZ surfaces below rolls while rolls maintain round shape (run 2683, 2554, and 2807 for B, C, and D, respectively). Note the mosaic structures composing the rolls and PSZ. (e) Well-compacted rolls with solid interior. Note the interior is composed of grains of <100 nm (run 2716). (f) and (g) Broken rolls left traces on PSZ surface showing smearing of materials and axial fracturing. (h) Two rolls twisted against each other (run 2716).

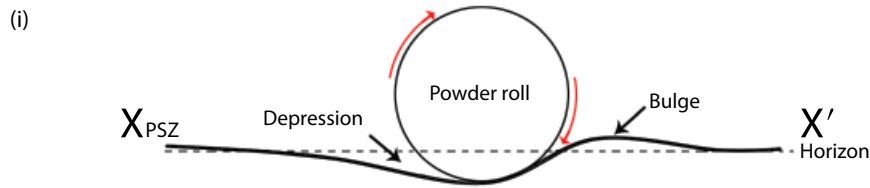


**Figure 7.3** (Continued) (i) Schematic cross-section drawing of the asymmetric deformation structure across scanlines of XX' in b and d. The gentle depression zone and bulge zone is recognized in b, c, and d.

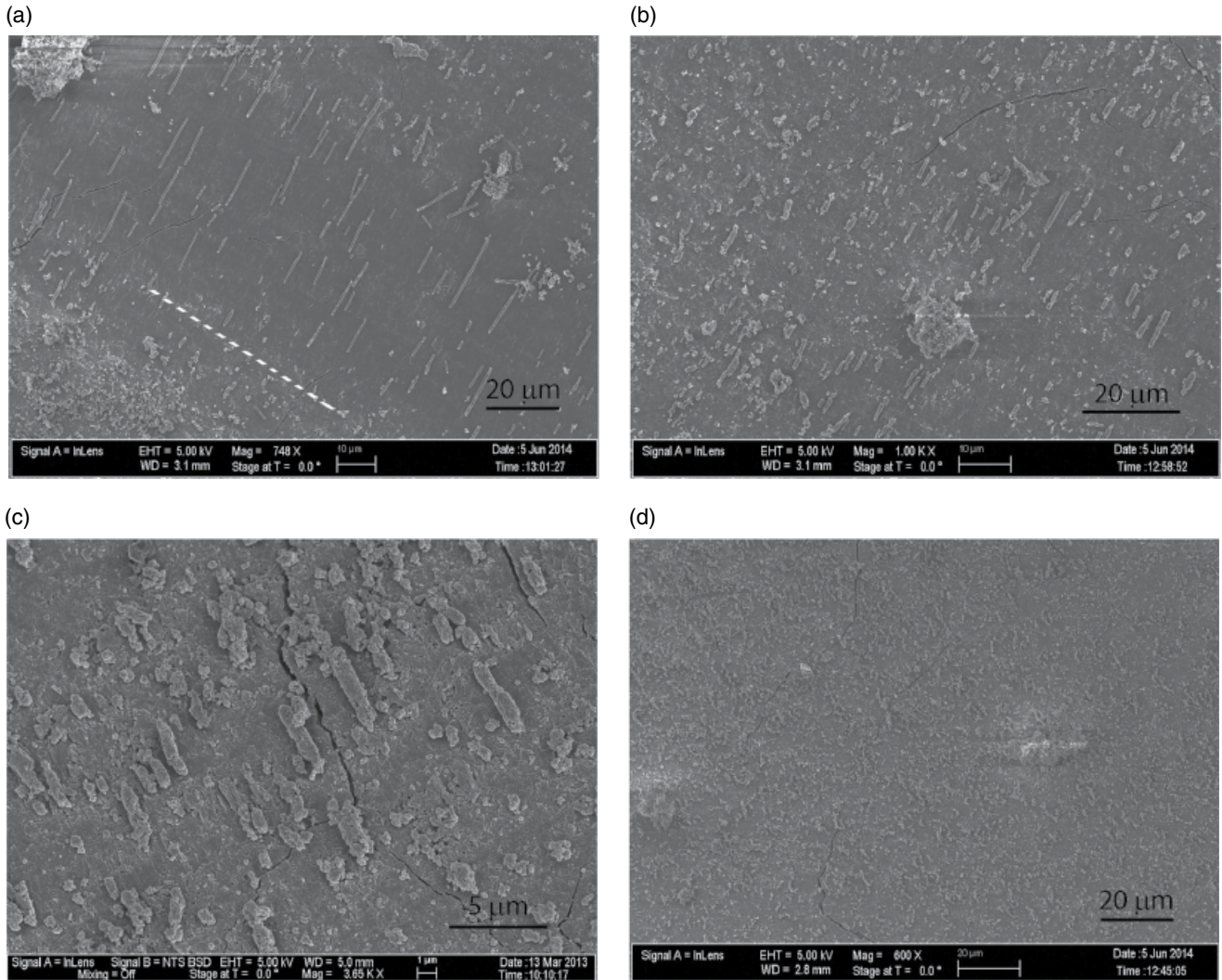


**Figure 7.4** General view of rolls showing the quality of powder rolls from best (quality rank A) to worst (quality rank D) as documented in Table 1. (a) Rolls with the best quality (A) after run 3243. (b) Rolls with quality rank B after run 3243. (c) Rolls with quality rank C after run 2813. (d) Rolls with the worst quality (D) after run 3249. White dashed line in A represents traces of wear debris parallel to slip direction.

The rolls are invariably made of agglomerated powder grains of particle size of 20 to 100 nm (Figure 7.3b, c, e). The best-formed rolls are long cylinders, with well-rounded, smooth outer surface formed by closely packed grains in a 3D structure with a few voids (Figure 7.3a, c). A roll with a solid center is usually well compacted and externally smooth (Figure 7.3b, c, h), whereas a less well-

developed roll contains more voids and deviates from the cylindrical shape (Figure 7.3d, f, g). Some rolls are poorly developed, with partial compaction and rough exterior (Figure 7.3a, d, f). The roll diameters have a narrow range of 0.5–1.75 μm (Figure 7.5a) with mean diameter of  $1.04 \pm 0.25$  μm; their lengths vary from 1 to 26 μm. Many rolls are partly destroyed by axial fractures (Figure 7.3f, g, c),

and broken rolls are smeared on the slip surfaces (Figure 7.3f, g). The appearance of both intact and fractured rolls suggests that they undergo a life cycle, which will be discussed later.

The quality of the powder rolls was evaluated in the SEM images based on the following qualitative criteria (Table 7.1): A. Well-developed rolls of idealized cylindrical shape, distributed on well-developed, smooth PSZ, with systematic orientation normal to slip direction (Figure 7.4a). B. Rolls that are nearly ideal, cylindrical shape; distributed on well-developed, smooth PSZ; but with occurrence of scattered particles in roll areas. Rolls are orientated parallel to each other, with local deviations. Appearance of a few broken rolls and a few truncated, short rolls is common (Figure 7.4b). C. Rolls deviate from cylindrical shape, with many broken and

smeared rolls; truncated, short rolls; and many scattered particles (Figure 7.4c). D. Well-established PSZ surfaces with many particles, rolls are loosely compacted and close to grain-aggregates (Figure 7.4d). The quality of rolls on a single flake may vary from high-quality rolls to low-quality rolls (Figure 7.4a, b).

Close-up view of the contacts between the powder rolls and the PSZ surface reveals that the rolls deform the host PSZ by forming a depression in which one side is gently inclined (cross-section in Figure 7.3i and inward arrow in Figure 7.3b, d, f), whereas the other side bulges abruptly out of the depression (outward arrow in Figure 7.3b, d, f). This deformation occurs while the rolls remain cylindrical.

Finally, a central observation is that the long axes of the rolls are systematically oriented normal to the striations (parallel to slip direction) (Figures 7.2e, 7.4a–c, 7.5b). The

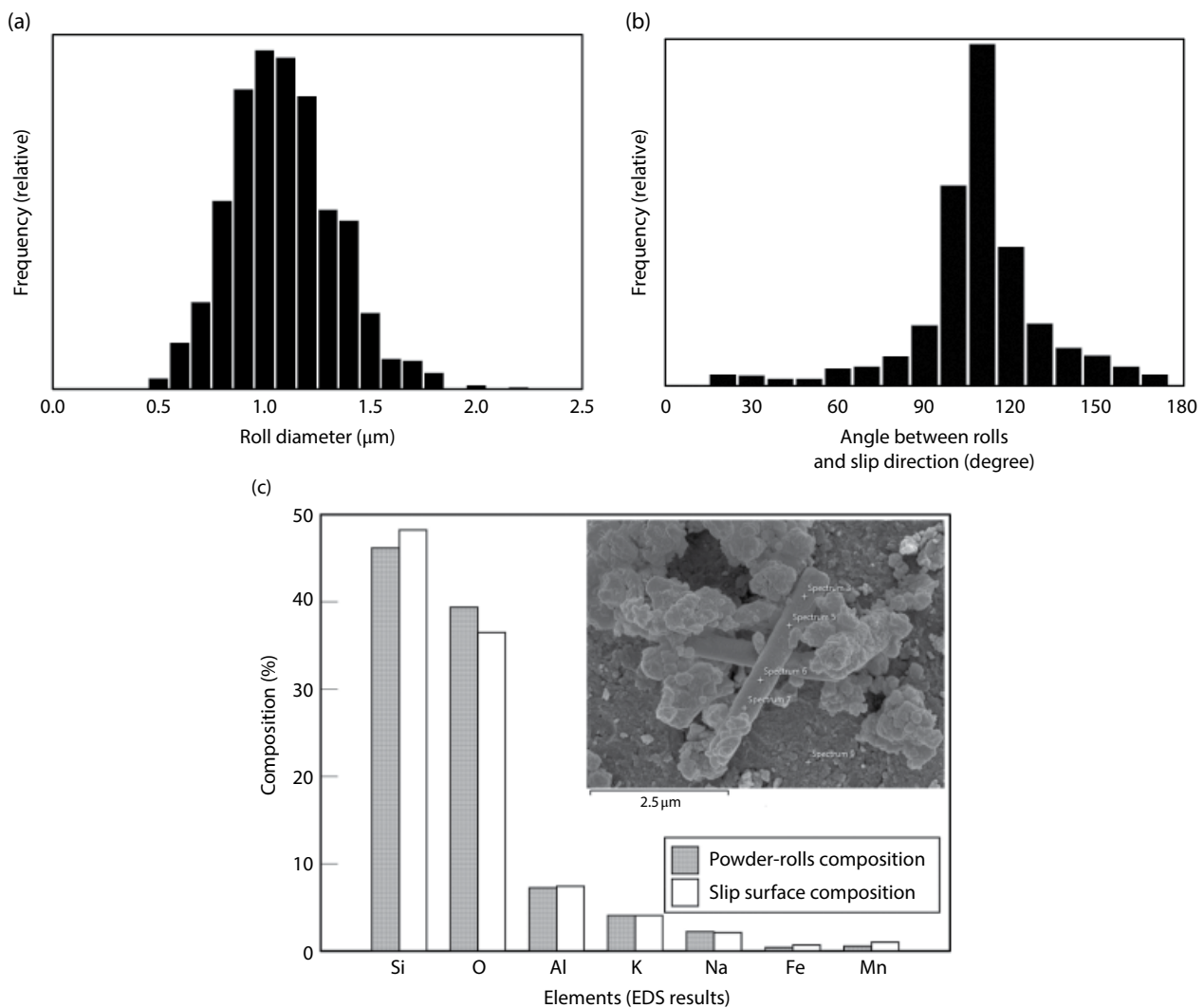


**Figure 7.5** (a) Frequency distribution of rolls diameter measured on 14 SEM images of 1183 rolls with average diameter of  $1.04 \pm 0.25 \mu\text{m}$ . (b) Rolls' orientation with respect to slip direction showing an average of  $95^\circ \pm 26^\circ$  from slip. (c) EDS analysis of the powder rolls showing similar elemental composition (in wt%) between powder rolls and slip surface. Inset is the SEM image of the analyzed area.

mean orientation of the measured 1183 rolls in 12 experiments is  $95^\circ \pm 26^\circ$ . We found that the rolls have the same composition as the PSZ (Figure 7.5c), which indicates that both were derived from the same ultra-fine gouge powder without partitioning.

## 7.4. ANALYSIS

### 7.4.1. Formation of Powder Rolls

The present study focuses on the developments of powder rolls and their effect on fault strength. The section below outlines the conditions that are essential for powder roll formation based on the present observations (above) and results of recent analyses of fault processes along natural faults and high-velocity shear experiments.

#### 7.4.1.1. Gouge Powder, Thermal Processes, and Localization within Fault Zones

Powder rolls developed within the gouge layer of the granite fault due to the combined effect of three conditions: presence of ultra-fine particles, intense heating, and slip localization. Many studies of gouge powder in experimental and natural faults revealed the dominance of ultra-fine grains that are a few tens of nanometer in size [Olgaard and Brace, 1983; Chester et al., 2005; Wilson et al., 2005; Reches and Lockner, 2010; Chen et al., 2013; Chou et al., 2014; Siman-Tov et al., 2015; Green et al., 2015]. It is generally known that the chemical and physical behavior of nano-materials differ from bulk solid behavior due to large surface area and grain packing [Navrotsky, 2001; Hochella et al., 2008]. For example, the mechanical interactions between ultra-fine grains are dominated by interparticle forces (electrostatic, van der Waals, hydrogen/capillary) that become increasingly significant as particle sizes are reduced. The interparticle forces operate over length scales of Ångstroms to nanometers (van der Waals/hydrogen), tens to hundreds of nanometers (electrostatic), or up to microns (capillary), and thus are greatest for the nanoscale grains.

Further, when ultra-fine grains are subjected to high-velocity shear, they are likely to be heated above the mean temperature of the fault zone. For example, flash heating modeling indicate that small, touching asperities are intensely heated that could lead to weakening or even melting [Rice, 2006]. Dolomite grains, tens of nanometer in size, were decomposed and sintered into a cohesive layer while the mean temperature was below the decomposition temperature [Green et al., 2015]. SEM/TEM analyses of dozens of shear experiments across lithologic types have demonstrated that fault gouge is composed of aggregates of nano- to microscale particles [Chester et al., 2005; Wilson et al., 2005; Green et al., 2015]. The grain-aggregation is driven by the interparticle forces and

are enhanced by the frictional heating of the smaller grains [Green et al., 2015; Siman-Tov et al., 2015]. These combined processes facilitate intense agglomeration and the formation of new structural entities like the smooth principal slip surfaces [Kirkpatrick et al., 2013]; mirror surfaces [Siman-Tov et al., 2013, 2015]; cohesive, smooth flakes [Chen et al., 2013]; and powder rolls as described below.

#### 7.4.1.2. Formation and Life Cycle of Powder Rolls

The powder rolls in the present experiments are strikingly similar in diameter, length, and orientation to debris rolls found in shear experiments of ceramics, silicon, quartz, chert, and alumina [Boch et al., 1989; Dong et al., 1991; Zanoria et al., 1995a,b; Hayashi and Tsutsumi, 2010; Nakamura et al., 2012]. These similarities suggest a general mechanism of roll formation and destruction [Zanoria et al., 1995a] (Figure 7.6). During initial slip, the experimental fault surfaces wear to generate a fine-grain gouge layer [Reches and Lockner, 2010; Boneh et al., 2013] that separates the solid rock blocks (Figure 7.6a). The slip is initially accommodated within the entire gouge layer but quickly localizes along discrete thin PSZs. The frictional heating and further grain-size reduction within the PSZs lead to grain compaction, agglomeration, local sintering enhanced by quartz amorphization [Nakamura et al., 2012; Kirkpatrick et al., 2013], and absorption of atmospheric water [Hayashi and Tsutsumi, 2010]. These processes lead to the formation of cohesive gouge flakes with smooth, continuous top PSZ surfaces (Figures 7.2c, 7.6b). Debris of gouge powder grains and delaminated fragments of the PSZ layer overlie the PSZ surfaces (Figure 7.6c). Locally, this debris agglomerates into powder rolls by the shear-induced torque between the opposing slipping surfaces of the PSZs (Figure 7.6d). The rolling of the powder rolls further enhances the compaction of both the powder rolls themselves and the PSZ and also help clean up the PSZ surface by incorporating encountered particles (Figure 7.3b). As this process is shear driven, it generates powder rolls with axes normal to slip direction (Figure 7.5b). As rolls encounter rough areas or areas with more wear debris, the rolls are vulnerable to damage by collapse and fracturing (Figures 7.3e–g, 7.4c). The debris of the failed rolls are re-agglomerated into new rolls and smooth surfaces until a dynamic balance of steady state between formation and destruction is reached. Fault slip along the smooth patches of PSZ was facilitated by rolling of the powder rolls, and the weakening along these spots lowers the overall friction.

The development of the PSZ along faults is critical for roll formation as powder rolls were observed only on cohesive gouge flakes (Table 7.1). Smooth, clean PSZs form more quickly in the pin-on-disc friction experiments,

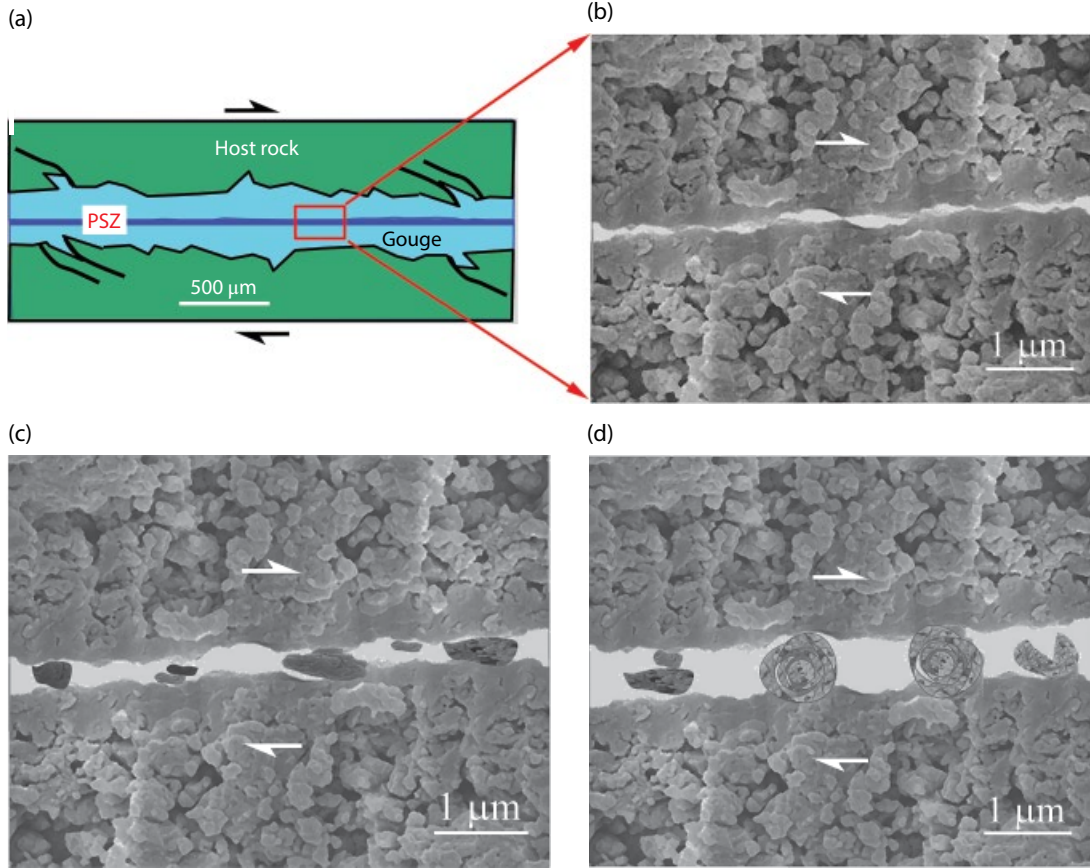


**Figure 7.6** Proposed mechanism of the life cycle of powder rolls (see text). (a) Schematic drawing of fault zone structure. Slip localization within a narrow zone (PSZ), a few microns thick, inside the gouge layer. (b) Formation of PSZ as a layer of compacted ultra-fine grains resting on a porous matrix of coarser grains (Figure 7.2c). (c) Debris of grains, agglomerated grains, and delaminated PSZ between the two smooth PSZ surfaces. (d) Rolling of the debris (left) into powder rolls (center), and eventual destruction (right side). Shear direction marked by half arrows. The PSZ cross-sections are actual SEM images.

and this is probably the reason for observing high-quality powder rolls in these experiments [Zanoria *et al.*, 1995a,b; Nakamura *et al.*, 2012].

#### 7.4.2. Frictional Strength and Powder Rolling

##### 7.4.2.1. Macroscopic Friction Evolution

We found that the existence of powder rolls is systematically associated with reduction of the macroscopic friction coefficient. This reduction is first observed by comparing the peak friction coefficient,  $\mu_p$ , and the steady-state friction coefficient,  $\mu_{ss}$ , for all experiments (Figure 7.7a). The figure reveals consistent friction reduction in experiments with powder rolls (solid dots), and no (or minor) friction reduction in experiments without powder rolls (open dots). Second, the steady-state friction coefficient normalized against the peak value,  $\mu_{ss}/\mu_p$ , shows a systematic decrease with slip distance in experiments with rolls (solid dots in Figure 7.7b). The data

points of runs with rolls fit exponential slip-weakening predicted by Mizoguchi *et al.* [2007] (Figure 7.7b), as shown in the following curve in Figure 7.7b,

$$\frac{\mu_{ss}}{\mu_p} = 0.43 + 0.57 \exp\left(\frac{\ln(b) \cdot D}{D_c}\right), \quad (7.1)$$

where  $\mu_{ss}$  is the steady-state friction coefficient,  $\mu_p$  is the peak friction coefficient,  $D$  is slip distance, and  $D_c$  is the distance over which  $\mu_{ss}/\mu_p$  reduces to the fraction  $b$  of the total weakening. The best-fit exponential curve to the data in Figure 7.7b is for  $b = 0.1$ , and  $D_c = 4.3$  m. The trend for rolls is in reasonable agreement with the observations of Zanoria *et al.* [1995a, b] for silica samples sheared at controlled humidity and temperature (diamonds in Figure 7.7b). This slip-weakening trend in our experiments fits well the classical slip-weakening curves observed here (Figure 7.1) and elsewhere [Di Toro *et al.*, 2011].

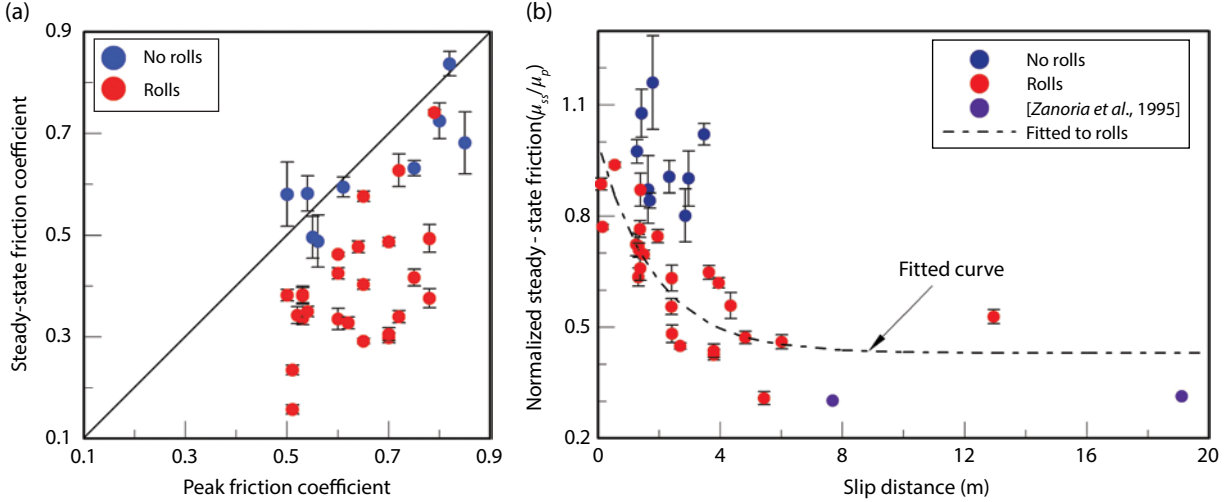


**Figure 7.7** Correlation between rolls and friction reduction. (a) The steady-state friction coefficient,  $\mu_{ss}$ , as a function of peak friction coefficient,  $\mu_p$ , for all experiments. Note that runs with rolls (solid dots) are plotted below the friction equality line indicating friction reduction, whereas runs without rolls (open dots) are distributed around the equality line indicating minor weakening or strengthening. (b) Normalized steady-state friction coefficient,  $\mu_{ss}/\mu_p$ , as function of slip distance. Runs with rolls (solid dots) showed systematic dependence of  $\mu_{ss}/\mu_p$  on slip distance (dashed curve and equation) that agrees with the observations of Zanoria et al. [1995a, b] (diamonds). Runs without rolls (open dots) show no systematic friction reduction for similar slip-distances.

Finally, we deduce that this systematic association between powder rolls presence and the weakening, which follows the predicted style of slip-weakening [Mizoguchi *et al.*, 2007], strongly support our view that the powder-rolling facilitates this dynamic weakening.

#### 7.4.2.2. Rolling Friction Mechanics

The powder rolls described above are distributed on smooth PSZs (Figures 7.2e, 7.3, 7.4), are oriented normal to the slip direction (Figures 7.2e, 7.4a–c, 7.5b) and form between two PSZs (Figure 7.6). We thus idealize the system of multiple, parallel powder rolls of equal diameter (Figure 7.5a) placed between two smooth PSZs by a roller-bearing. In this section, we use this roller-bearing model to evaluate powder-rolling mechanics.

Consider the rolling of a cylinder (or a sphere) on a flat surface (Figure 7.8a). This motion can be described by the transition between two idealized end members. *Sliding* occurs when the roll slides at velocity  $V$  with respect to the surface, but it does not spin, namely, its angular velocity vanishes,  $\omega = 0$ . In this case, the resistance to slip can be expressed as  $F_s = \mu_{slide} \cdot F_N$ , where  $F_s$  and  $F_N$  are the shear force and normal force acting on the roll, and  $\mu_{slide}$  is the sliding friction coefficient between the roll and the surface. *Rolling* occurs when the motion is fully accommodated by the roll's rotation along the surface, and in this case  $V = 2R\omega$ , where  $R$  is the roll's radius. Along parts of the contact between a roll and the surface, the shear stress is lower than the shear resistance (friction and/or adhesion), and thus these parts are “glued” to the

surface. The gluing makes it possible for the roll to rotate rather than slide. For example, the high friction between rubber tires of a car and the road facilitates the car's motion.

We now analyze the rolling friction of the powder rolls following the approach and results of *Eldredge and Tabor* [1955] and *Tabor* [1955]. They examined the system of a hard steel sphere that rolls between two flat, parallel blocks of softer metals (tin, lead, copper) (Figure 7.8a). In this model, the soft plates are plastically deformed as recognized by the grooved tracks, and the size of the deformed zone can be evaluated from the size of the grooves. In the experiments of *Eldredge and Tabor* [1955] and *Tabor* [1955], the shear force, normal force, and indentation depth into the softer surface were measured, allowing calculation of the shear stress,  $P_f$  and normal stress,  $P_m$ , that act on the soft plate indentation zone. They showed that  $P_f = P_m$ , as expected, because both these stresses reflect the plastic strength of the same plate. In their experiments, the authors found that the shear force is  $F_s = k F_N 1.5/D$ , where  $F_s$  and  $F_N$  are the shear and normal forces on a single sphere,  $D$  is the sphere's diameter, and  $k$  is a constant that depends on the soft metal properties.

We adopt this model of rolling friction to the cylindrical powder rolls in our experiments. Figure 7.8a displays a cross-section of a loaded powder roll that is sheared between two smooth PSZs. Roll diameter is  $D$  and length is  $L$ . We assumed that (A)  $P_f = P_m$  (following Eldredge and Tabor's observations); (B) the powder roll does not

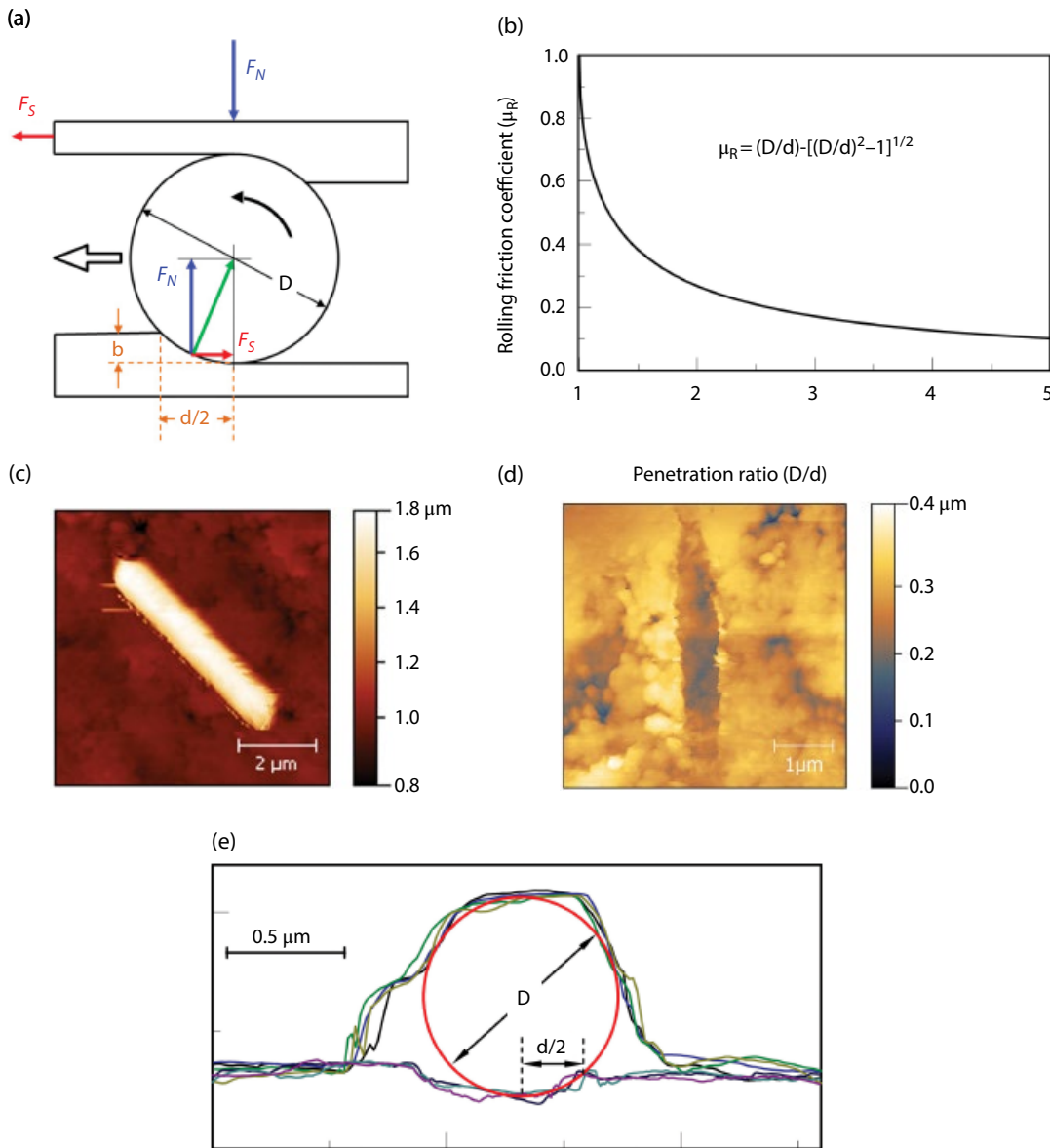


**Figure 7.8** Rolling friction of powder rolls (see text). (a) Idealized two-dimensional model, after Eldredge and Tabor [1955] and Tabor [1955], of a cylindrical roll of diameter  $D$  and length  $L$  sheared between two softer slip surfaces. The stressed roll penetrates the slip surface over penetration zone of width  $d/2$  and penetration depth  $b$ . (b) Rolling friction coefficient,  $\mu_R$ , as function of the penetration ratio,  $D/d$ ; inset:  $\mu_R$  as equation (7.4) in the text. (c) Atomic force microscopy (AFM) morphology of a single roll (bright zone trending NW–SE) resting on PSZ surface (run 2810); note the roll is  $\sim 1 \mu\text{m}$  higher than the substrate. (d) AFM morphology of the PSZ surface after the powder roll was pushed away with AFM tip; note N–S depression about 100 nm deep of the removed roll. (e) A series of seven profiles derived from across the AFM images of c and d normal to the roll. The four upper curves, taken in c, delineate both the PSZ and top of the roll. The three lower curves, taken in d, delineate the PSZ without the roll and reveal the shape and depth of the depression. A circle of  $D = 0.85 \mu\text{m}$  was visually fitted to be bound by the upper and lower profiles; this circle is the idealized roll that was removed. Note that the down-facing parts of the roll cannot be traced by the AFM tip, and thus the upper profiles cannot accurately delineate the sides of the roll. The roll penetrated the PSZ over a region of  $d/2 \sim 0.29 \mu\text{m}$ .

deform, based on our observations that most rolls are cylindrical (Figure 7.3); and (c) the smooth PSZ surface deforms (bulges and depressions in Figure 7.3b, d, f) by  $F_s$  and  $F_n$  loading.

The loading by the normal force  $F_n$  deforms the PSZ surface in a zone of width  $d/2$  and depth  $b$  (Figure 7.8a). The mean stress on the zone of  $d/2$  width is

$$P_m = F_n / \left( L \cdot \frac{d}{2} \right). \quad (7.2)$$

The shear force  $F_s$  acts parallel to the PSZ surface and on a zone of thickness  $b$ , and thus the mean stress on this zone is

$$P_F = F_s / (L \cdot b). \quad (7.3)$$

From the geometry of the deformation area, one can derive that

$$b = \frac{1}{2} \left( D - \sqrt{D^2 - d^2} \right). \quad (7.4)$$

By using assumption (A), equations (7.2) and (7.3), and substituting with equation (7.4), we get

$$\mu_R = \frac{F_s}{F_n} = \frac{2b}{d} = \frac{D}{d} - \sqrt{\frac{D^2}{d^2} - 1}. \quad (7.5)$$

The last equation provides the rolling friction coefficient as  $\mu_R$  due to the work associated with the plastic deformation. This equation is used to display the predicted rolling friction as function of the penetration factor  $D/d$  (Figure 7.8B).

#### 7.4.2.3. Model Application to Experimental Observations

The derivation above indicates that the rolling friction  $\mu_R$  is a function of the intensity of the penetration depth ratio  $D/d$  (Figure 7.8b). Small  $D/d$  ratio implies large penetration, which corresponds to a softer slip surface, and the inverse for large  $D/d$ . The model predicts a friction drop with increasing  $D/d$  (Figure 7.8b), for example,  $\mu_R < 0.3$  for  $D/d > 1.8$ . Microscale images showed that the powder rolls in the experiments were sheared between two smooth slip surfaces (PSZ), and that they could support the normal stress, at least temporarily, as evidenced by the observations of perfectly rounded rollers (Figure 7.3). This structure indicates that the rolls converted the experimental fault into a roller-bearing as proposed above, and switch the friction from sliding mode to rolling mode. It is important

to note that unlike steel rolls of industrial bearings where rolls persist over different shear conditions, the powder rolls undergo formation-and-destruction cycles throughout the shear (Figure 7.6).

To test the above model, we used the AFM to measure the geometric relations of a roll and PSZ. Two sets of surface topographic maps were measured: the first with the roll resting on the PSZ (Figure 7.8c), and the second after the roll was pushed away to reveal the topography of the PSZ depression (Figure 7.8d). Figure 7.8e displays elevation profiles normal to the roll as taken from the two maps. The two sets of profiles suggest that a roll of  $\sim 0.85 \mu\text{m}$  fits the profile (circle in Figure 7.8e), and the penetration zone is  $d/2 \sim 0.29 \mu\text{m}$ . These values yield  $\mu_R \sim 0.4$ , which is similar but lower than the 0.47 macroscopic friction coefficient in this experiment.

## 7.5. DISCUSSION

The discovery of powder rolls in the SEM/AFM analyses of our sheared granite faults was an unexpected, fascinating surprise. After characterizing the rolls, we focused on quantification of the relations between the micron-scale rolls and the macroscopic frictional strength, as described above. These relations, as well as the general presence of the powder-rolls, posed some important questions with regard to dynamic weakening by powder rolls and its general significance. Some of these questions are discussed in this section.

### 7.5.1. Faulting Conditions that Enhance Powder Rolls Formation

Powder rolls were not observed in all our experiments (Table 7.1). Part of this limited appearance stems from sampling difficulties; for example, many opportunities exist for losing powder rolls during sample collection and preparation, and locating the small, clean, smooth areas in the cohesive gouge flake top surfaces is not always an easy task. Beyond these technical difficulties, there are limiting mechanical factors displayed on a map of the normalized experimental steady-state friction coefficient,  $\mu_{ss}/\mu_p$ , as functions of the normal stress,  $\sigma_n$ , and slip velocity,  $V$  (Figure 7.9). The figure shows that powder rolls (solid circles) are present in runs of  $V < 0.07 \text{ m/s}$ , and that the lowest values of  $\mu_{ss}/\mu_p$  (as low as 0.3) are restricted to  $V = 0.003\text{--}0.06 \text{ m/s}$  and  $\sigma_n = 1\text{--}5 \text{ MPa}$ . Experiments without powder rolls and high friction (open circles) appear in runs at  $V > 0.1 \text{ m/s}$ , and at combined low velocity ( $V < 0.004 \text{ m/s}$ ) and low normal stress ( $\sigma_n < 2 \text{ MPa}$ ).

This distribution of powder rolls and associated friction values is compatible with previous experimental

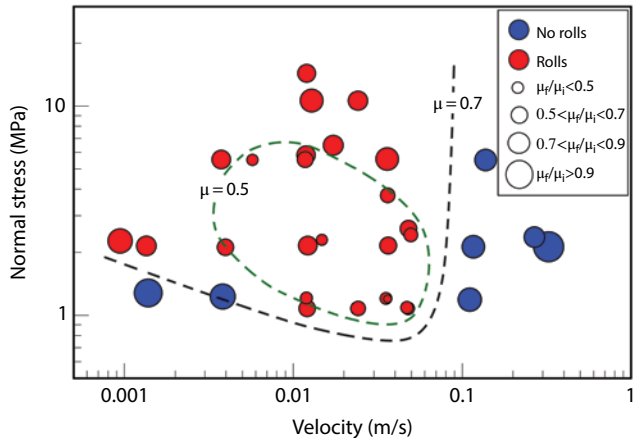


**Figure 7.9** A friction map (after Boneh *et al.* [2013]) displaying normalized steady-state friction coefficient,  $\mu_{ss}/\mu_p'$ , as a function of normal stress and slip velocity. Symbol size is proportional to the normalized friction. Note the strong correlation of low friction with the presence of rolls (solid dots).

studies of granite friction [Reches and Lockner, 2010; Kuwano and Hatano, 2011; Liao and Reches, 2013]. These studies showed that the steady-state friction of granitic rocks changes non-monotonically with slip velocity (Figure 1 in Reches and Lockner [2010]): High friction coefficient at  $V < 0.005$  m/s, minimum friction values ( $\mu_{ss} \sim 0.3$ ) at  $V = 0.01\text{--}0.05$  m/s, and strengthening to static friction values at  $V > 0.07$  m/s. Figure 7.9 reflects this trend. The strengthening at  $V > 0.07$  m/s was attributed to dehydration of the water coating of the fine-grain gouge powder during high-velocity heating [Sammis *et al.*, 2011].

More specifically, our analysis shows that powder roll formation requires development of PSZ surfaces of localized slip (Figures 7.2, 7.3, 7.4, 7.6, and appearance of rolls accompanied formation of cohesive gouge flakes in Table 7.1). The PSZ formation is enhanced by elevated fault temperature that depends on power-density (shear stress  $\times$  velocity) [Boneh *et al.*, 2013]. The velocity range of  $V = 0.01\text{--}0.05$  m/s generates favorable conditions of humidity and temperature that are necessary for PSZ and roll development [Zanoria *et al.*, 1995a]. At low velocity (low power-density), the fault temperature does not reach the range for PSZ formation or cannot maintain stable PSZ surfaces, and this results in covering the fault surface by incohesive gouge and associated high friction coefficient. At  $V > 0.07$  m/s, the slip conditions change. The elevated temperature due to high power-density led to dehydration, local melt, and intense chattering slip [Reches and Lockner, 2010]. The chattering vibrations destroy the powder-rolls and the PSZ, which then lead to fault strengthening at  $V > 0.07$  m/s as observed here and reported elsewhere [Reches and Lockner, 2010; Kuwano and Hatano, 2011; Liao and Reches, 2013].

## 7.5.2. Mechanisms of Dynamic Fault Weakening

### 7.5.2.1. Powder Rolling

Our observations of powder rolls, PSZ structure, roll orientations, and deformation structures are direct evidence for rolling during the friction experiments. We argue, based on previous observations of rolls in other contexts [Hayashi and Tsutsumi *et al.*, 2010; Zanoria *et al.*, 1995a, b; Nakamura *et al.*, 2002], that powder-rolling could be active as a general mechanism of powder lubrication (solid lubrication [Wornyoh *et al.*, 2007]). Further, our experiments show that powder rolling requires two ingredients: (1) the existence of ultra-fine powder, and (2) the localization of slip along discrete, smooth surfaces. These ingredients are common in faults in the upper crust. First, natural fault zones contain granular layers that are dominated by particles in the range of 20–100 nm. For example, the few cm thick ultracataclasite (cohesive, ultra-fine-grained rock) zone in the core of the North San Gabriel fault [Chester *et al.*, 2005], or the gouge zone of the exposed San Andreas fault in Tejon Pass area [Wilson *et al.*, 2005]. Second, slip localization is commonly observed in natural fault zones [Ben-Zion and Sammis, 2003; Katz *et al.*, 2003; Sibson, 2003; Chester *et al.*, 2005]. Thus, it is expected that powder-rolling would activate dynamic weakening of natural faults.

### 7.5.2.2. Other Weakening Mechanisms

The present analysis focuses on the physical evidence for powder rolling; however, the evidence does not exclude the possible operation of other mechanisms. The activity of alternative mechanisms, for example, thermal pressurization or flash heating, is typically demonstrated through comparison between macroscopic model predictions and macroscopic experimental data, but these models do not necessarily have recognizable physical evidence. For example, thermal pressurization, which theoretically is an effective mechanism of dynamic weakening [Andrews, 2002; Ujiie *et al.*, 2011], does not necessarily modify the fault structure, and thus does not generate distinct recognizable features. The flash heating model theoretically determines the heat and deformation of a few atomic layers at contacting asperities [Rice, 2006; Beeler *et al.*, 2008; Goldsby and Tullis, 2011]. These contacts are heated very fast (micro-sec) to easily flow or even melt, which should reduce the macroscopic friction. However, to the best of our knowledge, no study has found direct observations (crystallographic or structural) that is the product of flash heating. We thus conclude that other mechanisms, for example, thermal pressurization or flash heating, which inherently leave no physical traces, could have been active and contributing to the dynamic weakening in the present experiments.

We also noticed that the mechanical conditions of our experiments are similar to those reported previously for friction experiments on quartz-rich rocks [Goldsby and Tullis, 2002; Di Toro *et al.*, 2004; Hayashi and Tsutsumi *et al.*, 2010]. The common features for the previous experiments are velocity range of  $V = 0.003\text{--}0.1 \text{ m/s}$ , appearance of shiny, flaky gouge on fault surfaces, and the formation of silica gel. The silica gel formed thin, amorphized layers of fluid-like material, and the observed weakening was attributed to gel lubrication. In our experiments with granite sample, silica gel could form due to the presence of quartz. Indeed, minor amounts of silica gel could enhance powder rolling by establishment of cohesive gouge layer, facilitating rolls formation, and enhancing compacting and densification of rolls and PSZs. Our experiments did not display evidence of fluid-like flow structures on the slip surfaces, which in contrast were covered with solid grains and rolls that deformed the PSZs (Figures 7.3, 7.4). We thus envision that silica-gel could be active in PSZ and rolls formation with only minor contribution to the macroscopic weakening.

### 7.5.3. Why Are Powder Rolls Not Commonly Observed?

Powder rolls of similar diameter, length, and orientation were found in shear experiments of ceramics, silicon, quartz, chert, and alumina as discussed above [Boch *et al.*, 1989; Dong *et al.*, 1991; Zanoria *et al.*, 1995a,b; Hayashi and Tsutsumi, 2010; Nakamura *et al.*, 2012]. Yet, similar rolls are not commonly observed along experimental and natural faults. This apparent rare occurrence partly reflects the need for special care and sample treatment for finding the delicate powder rolls. For example, before our first rolls observation, we ran hundreds of friction experiments with the same rocks and at similar conditions with no rolls found [Reches and Lockner, 2010; Chang *et al.*, 2015; Chen *et al.*, 2013; Boneh *et al.*, 2013]. Once we developed the proper methods (section 7.2.2) for the SEM samples, rolls were found in most experiments (above, Table 7.1) and in several rock types. Thus, rolls may develop but may be overlooked due to sampling limitation.

Further, powder rolls do not form instantaneously and are destroyed by high-velocity chattering (above). In summary, the apparent lack of rolls reflects either lack of appropriate sampling procedures, insufficient power for growth, or too high power that leads to roll destruction.

## 7.6. SUMMARY

The present set of experiments performed with a rotary shear apparatus on Radiant Red granite demonstrated that powder rolling is an effective mechanism of powder

lubrication and contributes to the dynamic weakening at moderate velocity ranges up to a few cm/s and moderate normal stress ranges up to a few MPa. This conclusion is based on the following observations:

1. Macroscopic friction reduction correlates with the observation of cohesive flakes and microscopic powder rolls present on flake surfaces (Figures 7.7, 7.9).
2. A series of observations (Figures 7.2, 7.3, 7.6, 7.8) suggests that powder rolls were formed by rolling, and that they rolled instead of slid on the PSZ surfaces. The central observations are the spontaneous development of powder rolls and PSZ, which together form a “roller-bearing” micro-structure; the rolls orientations; and asymmetric depression on the PSZ.
3. Our model of rolling friction is generally compatible with the experimental results (Figure 7.8), yet the calculated friction coefficient is lower than the measure’s overall friction (equation 7.4).
4. It is proposed that powder rolling is a likely mechanism of solid lubrication.

## ACKNOWLEDGMENTS

We thank D. Lockner, J. Fineberg, and E. Aharonov for discussions. Thanks to two anonymous reviewers for insightful comments that led to significant improvement of the manuscript. This work was supported by NSF Geosciences awards 0732715 and 1045414 and NEHRP2011 award G11AP20008.

## APPENDIX

### Rotary Shear Apparatus

The experimental apparatus, called ROGA (Rotary Gouge Apparatus), was built and operated in the University of Oklahoma. It includes three main components: (1) loading system, (2) control and monitoring system, and (3) a closed cell to test gouge powder under confined conditions and elevated pore-pressure. ROGA’s frame is 1.8 m tall with two decks (Figures 7.10a–c) that are connected to each other by four internally enforced rectangle legs. The sample (Figure 7.10d) is loaded by a rotary train from below and by the normal stress from above. The power system includes

1. A 100 HP three-phase motor and controller that provides constant torque of up to 3000 Nm from 0 RPM to 3300 RPM. The motor velocity is monitored and controlled through an 8192 sector encoder.
2. A 225 kg flywheel to boost motor torque; it is engaged with a pneumatic clutch.
3. An electromagnetic large clutch that is capable of full engagement in 30 ms.
4. A hydraulic piston system with axial load up to 9500 N.

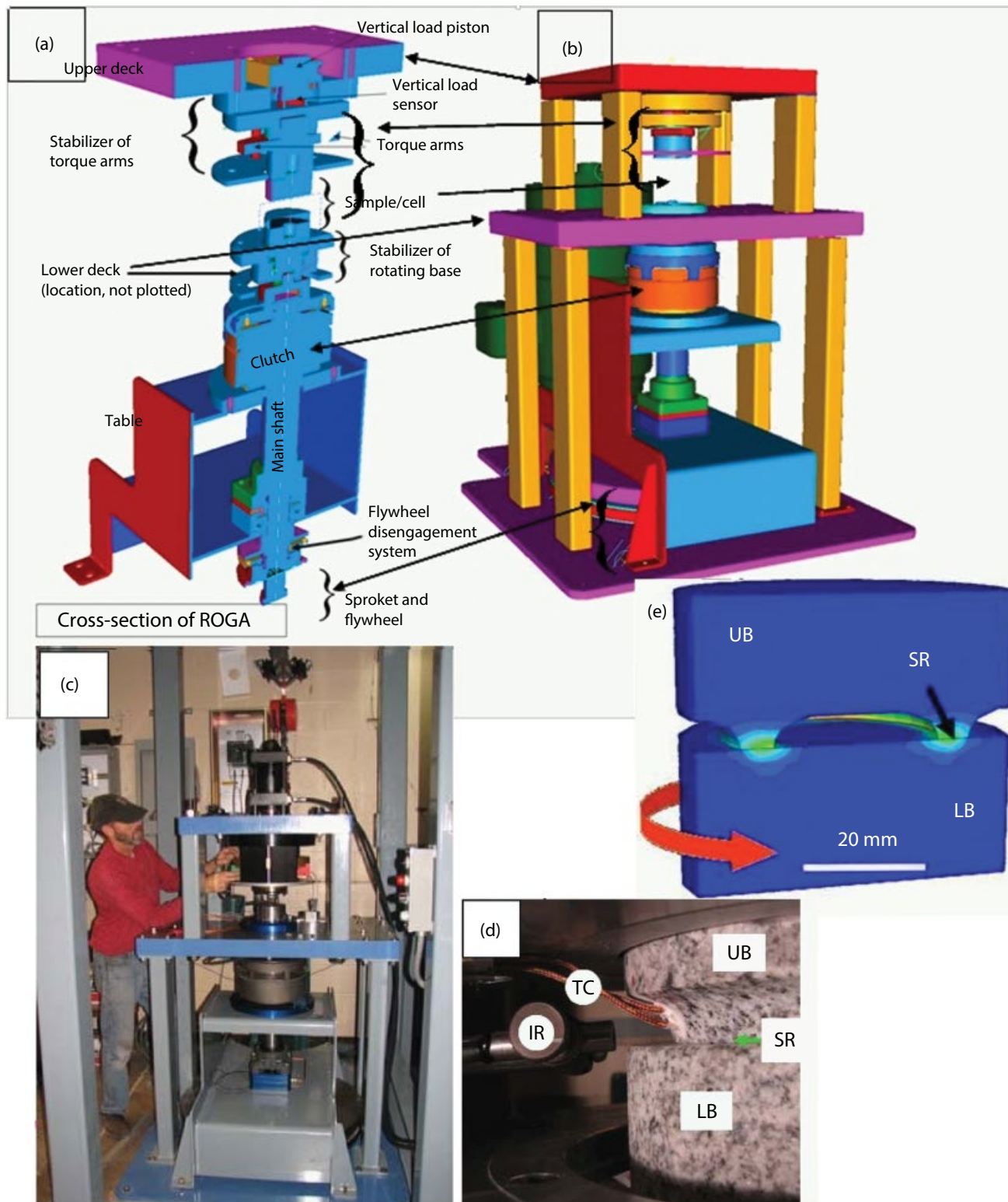


**Figure 7.10** The rotary shear apparatus. (a) Cross-section displaying power train. (b) 3D view of the assembled apparatus. (c) The apparatus with builder Joel Young. (d) Sample blocks assembled in the loading frame. LB = lower block; UB = upper block; SR = sliding ring; TC = thermocouple wires; IR = infrared sensor. (e) Sample design shown as vertical cut-through of two cylindrical blocks of solid granite rock. The colors indicate temperature distribution due to frictional heating calculated using a finite-element model.

The control and monitoring system is based on National Instruments components, and it includes an SCXI-1100 with modules 1124 (analog control), 1161 (relay control), 1520 (load cell/strain gage), and 1600 (data acquisition and multiplexer), as well as a USB-6210 (encoder measurements). We use LabView as the main control software. Digital sampling rate is up to 10 kHz. Load-cells for axial load and torque are made by Honeywell, gouge dilation/compaction is measured with four eddy-current sensors (about 1 micron accuracy), temperature measurement is with thermo-couples, and sample velocity is monitored by an encoder.

## REFERENCES

- Andrews, D. J. (2002), A fault constitutive relation accounting for thermal pressurization of pore fluid, *J. Geophys. Res.*, 107(B12), 2363, doi:10.1029/2002JB001942.
- Beeler, N. M., T. E. Tullis, and D. L. Goldsby (2008), Constitutive relationships and physical basis of fault strength due to flash heating, *J. Geophys. Res.: Solid Earth*, 113, B1.
- Ben-Zion, Y., and C. G. Sammis (2003), Characterization of fault zones, *Pure Appl. Geophys.*, 160, 677–715.
- Boch, P., F. Platon, G. Kapelski (1989), Tribological and interfacial phenomena in  $\text{Al}_2\text{O}_3/\text{SiC}$  and  $\text{SiC}/\text{SiC}$  couples at high temperature, *J. Eur. Ceram. Soc.*, 5, 223–228.
- Boneh, Y., A. Sagy, and Z. Reches (2013), Frictional strength and wear-rate of carbonate faults during high-velocity, steady-state sliding, *Earth Planet. Sci. Lett.*, 381, 127–137.
- Chen, X. (2015), Rock friction and dynamic faulting at the micro-to nano-scales, Doctoral dissertation, University of Oklahoma.
- Chen, X., A. S. Madden, B. R. Bickmore, Z. Reches (2013), Dynamic weakening by nanoscale smoothing during high velocity fault slip, *Geology*, 41, 739–742.
- Chester, J. S., F. M. Chester, A. K. Kronenberg (2005), Fracture surface energy of the Punchbowl fault, San Andreas system, *Nature*, 437, 133–136.
- Chou, Yu-Min, et al. (2014), Identification and tectonic implications of nano-particle quartz (<50nm) by synchrotron X-ray diffraction in the Chelungpu fault gouge, Taiwan, *Tectonophysics*, 619, 36–43.
- Di Toro, G., D. L. Goldsby, T. E. Tullis (2004), Friction falls towards zero in quartz rock as slip velocity approaches seismic rates, *Nature*, 427, 436–439.
- Di Toro, G., R. Han, T. Hirose, N. De Paola, S. Nielsen, K. Mizoguchi, F. Ferri, M. Cocco, and T. Shimamoto (2011), Fault lubrication during earthquakes, *Nature*, 471, 494–498.
- Dieterich, J. H. (1979), Modeling of rock friction: 1. Experimental results and constitutive equations, *J. Geophys. Res.*, 84, 2161–2168.
- Dieterich, J. H., and B.D. Kilgore (1994), Direct observation of frictional contacts: New insights for state-dependent properties, *Pure Appl. Geophys.*, 143, 283–302.
- Dong, X., J. Said, M. H. Stephen (1991), Tribological characteristics of  $\alpha$ -Alumina at elevated temperatures, *J. Am. Ceram. Soc.*, 74(5), 1036–1044.
- Eldredge, K. R., and D. Tabor (1955), The mechanism of rolling friction: I. The plastic range, *Proc. Royal Soc. A*, 229, 181–198.
- Fondriest, M., S. A. F. Smith, T. Candela, S. B. Nielsen, K. Mair, G. Di Toro, (2013), Mirror-like faults and power dissipation during earthquakes, *Geology*, 41, 1175–1178.
- Goldsby, D. L., and T. E. Tullis (2002), Low frictional strength of quartz rocks at subseismic slip rates, *Geophys. Res. Lett.*, 29, 25-1–25-4.
- Goldsby, D.L., and T. E. Tullis (2011), Flash heating leads to low frictional strength of crustal rocks at earthquake slip rates, *Science*, 334, 216–218.
- Green, H.W., F. Shi, K. Bozhilov, G. Xia, and Z. Reches (2015), Phase transformation and nanometric flow cause extreme weakening during faulting, *Nat. Geosci.*, 8, 484–489.
- Han, R., T. Hirose, and T. Shimamoto (2010), Strong velocity weakening and powder lubrication of simulated carbonate faults at seismic slip rates, *J. Geophys. Res.*, 115, B03412.
- Hayashi, N., and A. Tsutsumi (2010), Deformation textures and mechanical behavior of a hydrated amorphous silica formed along an experimentally produced fault in chert, *Geophys. Res. Lett.*, 37, L12305.
- Hochella, M. F., S. K. Lower, P. A. Maurice, R. L. Penn, N. Sahai, D. Ll Sparks, and B. S. Twining (2008), Nanominerals, mineral nanoparticles, and Earth systems, *Science*, 319 (5870), 1631–1635.
- Katz, O., Z. Reches, and G. Baer (2003), Faults and their associated host rock deformation: Part I. Structure of small faults in a quartz-syenite body, southern Israel, *J. Struct. Geol.*, 25, 1675–1689.
- Kirkpatrick, J. D., C. D. Rowe, J. C. White, and E. E. Brodsky (2013), Silica gel formation during fault slip: Evidence from the rock record, *Geology*, 41(9), 1015–1018.
- Kuwano, O., and T. Hatano (2011), Flashing weakening is limited by granular dynamics, *Geophys. Res. Lett.*, 38, L17305.
- Liao, Z., J. C. Chang, and Z. Reches (2014), Fault strength evolution during high velocity friction experiments with slip-pulse and constant-velocity loading, *Earth Planet. Sci. Lett.*, 406, 93–101.
- Liao, Z., and Z. Reches. (2013), Modeling dynamic-weakening and dynamic-strengthening of granite in high-velocity, in *Earthquake Research and Analysis: New Advances in Seismology*, S. D'Amico, ed., InTech, Available from www.intechopen.com/books.
- Lockner, D. A., and P. G. Okubo (1983), Measurements of frictional heating in granite, *J. Geophys. Res.*, 88, 4313–4320.
- Mizoguchi, K., T. Hirose, T. Shimamoto, and E. Fukuyama (2007), Reconstruction of seismic faulting by high-velocity friction experiments: An example of the 1995 Kobe earthquake, *Geophys. Res. Lett.*, 34, L01308.
- Nakamura, Y., J. Muto, H. Nagahama, I. Shimizu, T. Miura, and I. Arakawa (2012), Amorphization of quartz by friction: Implication to silica-gel lubrication of fault surfaces, *Geophys. Res. Lett.*, 39, L21303.
- Navrotsky, A. (2001). *Thermochemistry of nanomaterials*. Rev. Min. Geochem., 44(1), 73–103.
- Olgaard, D. L., and W. F. Brace (1983). The microstructure of gouge from a mining-induced seismic shear zone, *International Journal of Rock Mechanics and Mining Sciences & Geomechanics Abstracts*, 20(1), 11–19.

- Reches, Z., and D. A. Lockner (2010), Fault weakening and earthquake instability by powder lubrication, *Nature*, **467**, 452–455.
- Rice, J. R. (2006), Heating and weakening of faults during earthquake slip, *J. Geophys. Res.*, **111**, B05311.
- Rowe, C. D., and W. A. Griffith. (2015), Do faults preserve a record of seismic slip? A second opinion. *J Struct. Geol.*, **78**, 1–26.
- Sammis, C. G., D. A. Lockner, and Z. Reches (2011), The role of adsorbed water on the friction of a layer of submicron particles, *Pure Appl. Geophys.*, **168**, 2325–2334.
- Sibson, R. H. (2003), Thickness of the seismic slip zone, *Bull. Seismol. Soc. Am.*, **93**, 1169–1178.
- Siman-Tov, S., E. Aharonov, Y. Boneh, and Z. Reches (2015), Fault mirrors along carbonate faults: Formation and destruction during shear experiments, *Earth Planet. Sci. Lett.*, **430**, 367–376.
- Siman-Tov, S., E. Aharonov, A. Sagy, and S. Emmanuel (2013), Nanograins form carbonate fault mirrors, *Geology*, **41**, 703–706.
- Smith, S.A.F., A. Billi, G. Di Toro, and R. Spiess (2011), Principal slip zones in limestone: Microstructural characterization and implications for the seismic cycle (Tre Monti Fault, Central Apennines, Italy), *Pure Appl. Geophys.*, **168**, 2365–2393.
- Tabor, D. (1955), The mechanism of rolling friction. Part II: The elastic range, *Proc. Royal Soc. A*, **229**, 198–220.
- Tsutsumi, A., and T. Shimamoto (1997), High-velocity frictional properties of gabbro, *Geophys. Res. Lett.*, **24**, 699–702.
- Ujiie, K., A. Tsutsumi, and J. Kameda (2011). Reproduction of thermal pressurization and fluidization of clay-rich fault gouges by high-velocity friction experiments and implications for seismic slip in natural faults, *Geological Society, London, Special Publications*, **359**(1), 267–285.
- Wilson, B., T. Dewers, Z. Reches, and J. Brune (2005), Particle size and energetics of gouge from earthquake rupture zones, *Nature*, **434**, 749–752.
- Wornyoh, E.Y.A., V. K. Jasti, and C. F. Higgs III (2007), A review of dry particulate lubrication: Powder and granular materials, *J. Tribology*, **129**, 438–449.
- Zanoria, E. S., S. Danyluk, and M. J. McNallan (1995a), Formation of cylindrical sliding-wear debris on silicon in humid conditions and elevated temperatures, *Tribol. Trans.*, **38**, 721–727.
- Zanoria, E. S., S. Danyluk, and M. J. McNallan (1995b), Effects of length, diameter and population density of tribological rolls on friction between self-mated silicon, *Wear*, **181–183**, 784–789.

# 8

## Earthquake Source Properties From Instrumented Laboratory Stick-Slip

Brian D. Kilgore<sup>1</sup>, Art McGarr<sup>1</sup>, Nicholas M. Beeler<sup>1,2</sup>, and David A. Lockner<sup>1</sup>

### ABSTRACT

Stick-slip experiments were performed to determine the influence of the testing apparatus on source properties, develop methods to relate stick-slip to natural earthquakes and examine the hypothesis of McGarr [2012] that the product of stiffness,  $k$ , and slip duration,  $\Delta t$ , is scale-independent and the same order as for earthquakes. The experiments use the double-direct shear geometry, Sierra White granite at 2 MPa normal stress and a remote slip rate of 0.2  $\mu\text{m/sec}$ . To determine apparatus effects, disc springs were added to the loading column to vary  $k$ . Duration, slip, slip rate, and stress drop decrease with increasing  $k$ , consistent with a spring-block slider model. However, neither for the data nor model is  $k\Delta t$  constant; this results from varying stiffness at fixed scale.

In contrast, additional analysis of laboratory stick-slip studies from a range of standard testing apparatuses is consistent with McGarr's hypothesis.  $k\Delta t$  is scale-independent, similar to that of earthquakes, equivalent to the ratio of static stress drop to average slip velocity, and similar to the ratio of shear modulus to wavespeed of rock. These properties result from conducting experiments over a range of sample sizes, using rock samples with the same elastic properties as the Earth, and scale-independent design practices.

### 8.1. INTRODUCTION

In this chapter we determine how and under what circumstances laboratory stick-slip source properties can be compared to those of natural earthquakes. To make such a comparison requires (1) a mechanical understanding of laboratory scale earthquakes (2) an accounting for any contributions to source properties that are unique to the laboratory test, and (3) if source properties are scale dependent, a procedure to extrapolate laboratory source parameters to the Earth. To accomplish the first two goals we designed an experimental program of well-instrumented stick-slip. The experiments access a wider range of fault slip, slip rate, and duration than in prior studies by systematically varying the combined elastic properties

of the fault and testing machine. The approach provides a more detailed view of the mechanics of stick-slip, the nature of the contributions to source properties from the testing apparatus, and allows us the necessary physical understanding to accomplish the third goal of properly relating stick-slip source properties to earthquakes.

The control variable that affects slip, slip rate, and duration in the experiments is the elastic shear stiffness [Walsh, 1971], most often referred to simply as "stiffness" throughout this report. Stiffness is the amount that on-fault shear stress in the direction of slip changes per increment of slip, i.e., the slip derivative of the shear stress on the fault,  $k = d\tau/d\delta$ , where  $\tau$  is shear stress and  $\delta$  is the fault slip. The particular value of stiffness provides fundamental control on the properties of the slip portion of a stick-slip cycle, as we explain here with a simple example in which the fault follows a static-kinetic fault strength relation. In a stick-slip test [Brace and Byerlee, 1966], the fault is loaded at a constant velocity. The fault

<sup>1</sup>U.S. Geological Survey, Menlo Park, California, USA

<sup>2</sup>USGS Cascades Volcano Observatory, Vancouver, Washington, USA

remains stuck for some period of time during which the shear stress increases linearly with time, analogous to a natural earthquake recurrence interval. The rate of shear stress increase during this “stick” phase is the product of the loading velocity and the stiffness. Thus, the stiffness influences the length of the interseismic period, the recurrence time of stick-slip. When the shear stress eventually reaches the static strength, the fault fails, dropping strength to the kinetic level, allowing accelerating slip rate as the elastic strain stored in the rock and testing machine is released. During this “slip” phase, the stress drop is the product of the total slip and the stiffness. Equivalently, the unloading stiffness during the slip phase is the ratio of the static stress drop to total slip,  $\Delta\tau/\Delta\delta$ , and the stiffness influences the earthquake source properties of stick-slip.

In detail and depending on the particular design and dimensions of the testing machine and the rock samples, the stiffness can predominately reflect the elastic properties and dimensions of the rock samples, those of components of the testing machine, or some combination of both [Shimamoto *et al.*, 1980]. For example, for tests employing bare fault surfaces, loading is often provided by a servo-control system that is configured to load the fault at a constant slip rate, using a moving reference location on the loading column as the position feedback point for control. The position of the servo feedback point relative to the fault surface impacts the stiffness and therefore the stability of the control system. If a fault slip measurement is made directly across the fault, with the sensor mounts very near the fault, and if that measurement is used as the control measurement point, since the rock samples are relatively small and the elastic modulus of the rock sample is high, the loading stiffness is very high, directly reflecting the modulus of the sample material. If instead the fault slip control reference point is elsewhere on the loading column, then the resulting loading stiffness is lower and can reflect a combination of the properties of the machine and the sample material.

In the present study, as in most studies of stick-slip, the rock samples around the fault have high elastic modulus and small dimension, and are too stiff to allow the fault to slide unstably [Johnson and Scholz, 1976]. That is, stick-slip often is difficult to access in laboratory geometries (e.g., “triaxial” and “double direct shear”; see subsequent descriptions) unless the loading system adds compliance in addition to that of the rock samples, resulting in a stiffness that includes compliance from the machine. In particular, while our experiments are conducted under servo-control loading, they are designed to reliably produce stick-slip, in part by using highly polished surfaces with a short slip weakening distance [Dieterich, 1978], and also so that the loading and unloading stiffnesses are approximately identical. These desired

properties are achieved by selecting the value of stiffness that is determined, essentially entirely, by a compliant element placed in the loading column between the control point and the fault, and by placing the control point for loading far from the fault.

A few prior studies have explored the influence of stiffness on laboratory stick-slip and the implications for natural earthquakes. Notably, *Byerlee and Brace* [1968] investigated how rock type, confining pressure, strain rate, and stiffness affect stick-slip behavior in triaxial experiments. In these experiments the loading stiffness was varied between the design stiffness of the apparatus and a value an order of magnitude lower, by adding a compliant fluid column in-line with the hydraulic axial loading. Their experiments showed that the stress drop depends on rock type and confining pressure, but not on stiffness. They concluded that the amplitude of motion from natural earthquakes would increase with depth, vary as a function of rock type, but, consistent with natural scale-independent stress drop, would not vary with stiffness. In contrast, by considering possible scaling between the stick-slip and earthquakes, *Walsh* [1971] noted that the shear stiffness of large earthquakes, the ratio of shear modulus  $\mu$  to the fault dimension  $L$  is 4 to 5 orders of magnitude less than the laboratory stiffness, as measured by stress drop and total slip,  $\Delta\tau/\Delta\delta$ . As a consequence, *Walsh* [1971] cautioned that experiments at reduced stiffness are needed to determine how and whether stick-slip results can be scaled to natural earthquakes. Though no comprehensive experimental studies have been conducted to date, Walsh’s recommendation that differences in stiffness and in fault dimension must be taken into account in scaling laboratory slip to natural settings has been implemented in a number of applications of stick-slip to earthquakes [McGarr, 1994, 1999].

Similarly, fundamental differences between stick-slip and earthquakes may affect the scaling of laboratory measured event durations to that of an earthquake. Since natural rupture propagation speeds are fixed by the elastic properties of rock, earthquake duration is proportional to fault dimension. For example, assuming a crack-like rupture expanding at 85% of the shear wave speed  $\beta$ , and then arrest proceeding as back propagating shear waves, the rupture duration would be  $\Delta t \approx 1.1L/\beta$ . There is not always such a straightforward expectation for the duration of laboratory stick-slip. For example, in rupture propagation experiments, slip duration can be much longer than the fault length divided by the wavespeed [e.g., Beeler *et al.*, 2012]. This is because the ends of the fault are not confined; instead of the slip beginning to slow down when the rupture front reaches the unconfined end of the fault, the slip continues. And in this case, stick-slip duration is relatable to the resonance period of the testing machine [Johnson and Scholz, 1976],

which may not be controlled directly by the dimensions of the fault itself. Therefore, as with stiffness, there is an expected difference in duration between the lab and field because laboratory fault dimensions are not always explicitly tied to the elastic properties of the mechanical system. Since other earthquake source properties such as slip velocity and acceleration depend on the event duration, more generally, scaling of laboratory stick-slip to natural events requires an understanding of interactions between the on-fault source and the testing machine. Experimentally determining those interactions is a primary part of first of the three goals of this study, as described at the outset of this introduction.

Recent progress by *McGarr* [2012] relating stick-slip to earthquakes provides the most immediate motivation for the experiments and analysis of our study. *McGarr* [2012] uses data from rupture propagation experiments of *Lockner and Okubo* [1983] and *Johnson and Scholz* [1976] to advance two hypotheses: (1) while stick-slip stiffness and event duration might be individually expected to differ substantially from those of natural earthquakes of the same fault dimension, the products  $k\Delta t$  for earthquakes and for stick-slip are scale independent, and (2) the products  $k\Delta t$  for stick-slip and earthquakes are the same

order of magnitude. That the product is scale independent for earthquakes is expected from simple models of rupture propagation and arrest and is consistent with observed earthquake source properties, as follows. Combining the expected duration of the crack propagation and arrest model described above with *Walsh's* [1971] dimensional relation for stiffness leads to the product being approximately the ratio of elastic material properties, the shear modulus to the shear wave speed,

$$k\Delta t \approx 1.1 \frac{\mu}{\beta}. \quad (8.1a)$$

For shorthand, throughout the remainder of this chapter, we refer to this ratio of the modulus and wave speed as the impedance. Here taking the ratio to be on the order of 10 MPa s/m (e.g.,  $\mu=30$  GPa,  $\beta=3$  km/s), the product (8.1a) is around 11 MPa s/m, consistent with seismological data (Figure 8.1a). Stick-slip values of the product are similar (Table 8.1). *Johnson and Scholz* [1976] measured duration and stiffness directly in rupture propagation experiments on a 20 cm long fault and found  $k=12$  GPa/m,  $\Delta t=1$  ms, and the product to be approximately 12 MPa s/m. In experiments on a 2 meter fault,

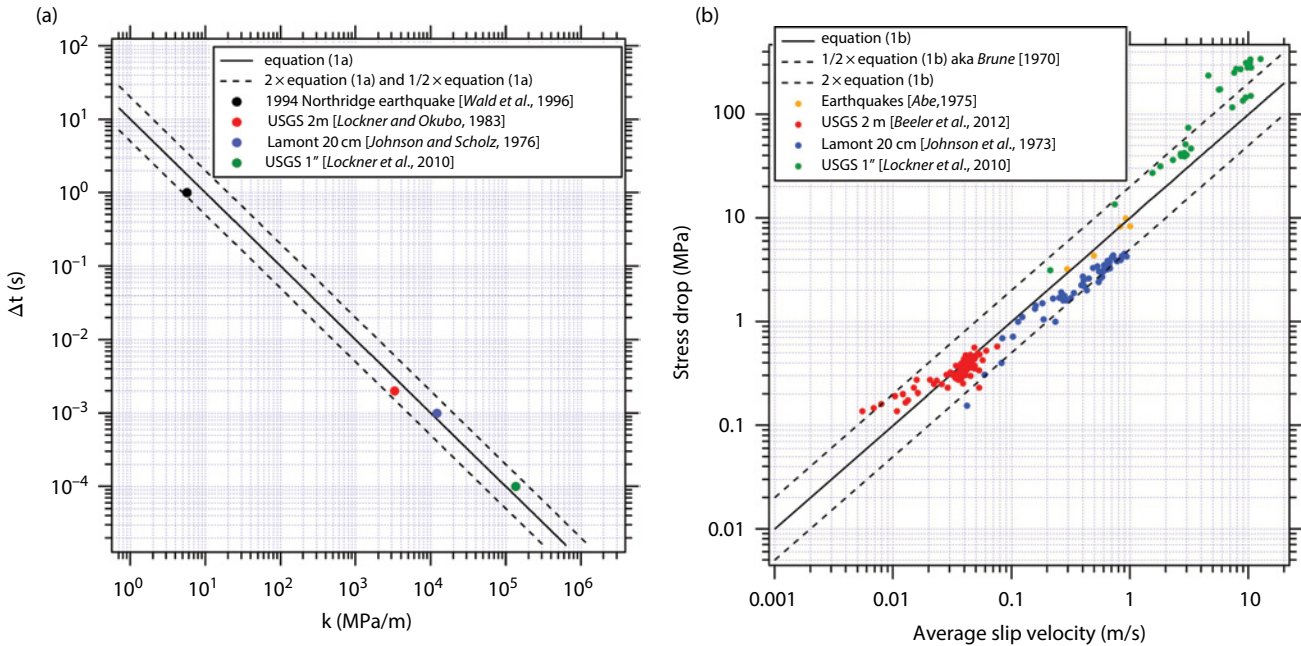


**Figure 8.1** Scale-independent laboratory and earthquake source properties. (a) Duration versus stiffness for stick-slip in three testing machines [*Johnson and Scholz*, 1976; *Lockner and Okubo*, 1983; *Lockner et al.*, 2017] and for a typical earthquake [*Wald et al.*, 1996]. The solid line is the scale-independent prediction, equation (8.1a) with the impedance  $\mu/\beta=10$  MPa s/m, and the two dashed lines are one half and two times equation (8.1a). (b) Static stress drop versus average slip velocity. Data for individual stick-slip events are shown for the three testing machines in part (a) [*Johnson et al.*, 1973; *Beeler et al.*, 2012; *Lockner et al.*, 2017] and from five Japanese earthquakes [*Abe*, 1975]. The solid and dashed lines are as in part (a). The lower dashed line is equivalently the prediction of the Brune model [Brune, 1970].

**Table 8.1** Testing machine properties.

Apparatus	$\Delta t$ (ms)	Stiffness (GPa/m)	$k\Delta t$ (MPa s/m)	Sample Mass (kg)	Fault Area ( $m^2$ )	Sample Dimension (m)	Estimated Sample $k\Delta t$ (MPa s/m)
Lamont 20 cm biaxial	1.2	10	12	1.46	0.006	0.18	30.5
USGS 2 m biaxial	2	3.3	6.6	2430	0.8	1.5	37.4
USGS 1 inch triaxial	0.1	135	13.5	0.087	0.001013	0.064	30.5
USGS DDS (this study)	0.5	27	13.5	0.432	0.005	0.08	27.3

Note: DDS=double direct shear configuration.

*Lockner and Okubo* [1983] found  $k = 3.3 \text{ GPa/m}$ ,  $\Delta t = 2 \text{ ms}$ , and the product is  $6.6 \text{ MPa s/m}$  (Figure 8.1a). More recently, *Lockner et al.* [2010, 2017 (this volume)] conducted room temperature stick-slip experiments on a 5 cm long granite fault at elevated confining pressure in a triaxial geometry and found  $k = 135 \text{ GPa/m}$ ,  $\Delta t = 0.1 \text{ ms}$ , and the product is  $13.5 \text{ MPa s/m}$ .

Furthermore, *Johnson and Scholz* [1976] note that the product can also be expressed using more standard earthquake source properties as

$$k\Delta t \approx \frac{\Delta\tau_s}{\hat{V}}, \quad (8.1b)$$

where  $\hat{V} (= \Delta\delta/\Delta t)$  is the spatially and temporally averaged slip velocity. Consistent with the crack model estimate (8.1a), for the 1968 Saitama, Japan, earthquake the ratio estimated from equation (8.1b) is  $11 \text{ MPa s/m}$  [*Abe*, 1975]. Similarly for other large earthquakes in Japan, the 1931 Saitama, 1943 Tottori, 1948 Fukui, 1963 Wasaka, and 1968 Saitama earthquakes are consistent with scale independence and a representative value of  $\sim 10 \text{ MPa s/m}$  [*Abe*, 1975] (solid line, Figure 8.1b). These data are superimposed as open diamonds on Figure 8.1b along with individual experiments from the Lamont [*Johnson et al.*, 1973], USGS 2 meter [*Beeler et al.*, 2012], and USGS triaxial [*Lockner et al.*, 2010, 2017] testing machines. The lab data are consistent with the earthquake data within reasonable uncertainties. The lower dashed line is a stress drop one half that of the solid line (equation [8.1b]), effectively a Brune model,  $\Delta\tau_s = \hat{V}\mu/(2\beta)$  with  $\mu/\beta = 10 \text{ MPa s/m}$  [*Brune*, 1970], whereas the upper dashed line is a stress drop twice as large as the solid line. There are deviations from these apparent bounds for the very lowest stress drops in *Beeler et al.* [2012] and largest stress drops of *Lockner et al.* [2010, 2017]; these deviations that are reasonably well understood are discussed in section 8.4.2.

While *Johnson and Scholz* [1976] point out that similar values of the product (8.1a) for earthquakes and for stick-

slip in the Lamont biaxial could be “a fortuitous result of the loading machine design,” the fact that the relationship holds in two other testing machines with fault lengths that vary by more than an order of magnitude suggests instead a robust and useful relationship for relating stick-slip experiments to earthquakes [*McGarr*, 2012]. In any event, the origin of this scale independence of stick-slip properties warrants further investigation and it is the primary motivation for the present study. In this chapter we report the results from stick-slip experiments conducted in a biaxial double direct shear configuration (DDS) [*Dieterich*, 1978]. Stick-slip is documented by directly measuring shear stress drop, fault slip, slip velocity, event duration, and the stiffness of various components of the loading system. The experiments are intended to determine the physical and machine-dependent controls on stick-slip source properties. The focus is on seismically observable quantities and how those values relate to their natural counterparts. The measurements are also used to develop a mechanical model of the experiments. With these new observations of stick-slip source properties and insights on interactions between the source fault and the testing machine, we determine the origin of and limits on the scale independence of stick-slip.

## 8.2. EXPERIMENTAL PROCEDURES

The experiments were conducted at ambient room temperature and humidity conditions using the DDS test apparatus (Figure 8.2a, b) [*Dieterich*, 1978; *Linker and Dieterich*, 1992; *Kilgore et al.*, 1993, *Kilgore et al.*, 2012] and samples manufactured from Sierra White granite from Raymond, California. The sample geometry is the standard for this apparatus: two smaller side blocks of granite with linear dimensions of  $5 \times 5 \times 2 \text{ cm}$  and one larger center block measuring  $8 \times 5 \times 4 \text{ cm}$ . The two sliding fault areas are each  $5 \times 5 \text{ cm}$ . A constant normal stress of  $2 \text{ MPa}$  is maintained by the horizontally aligned hydraulic ram where the output of a load cell is the servo feedback signal. The applied shear force is generated by

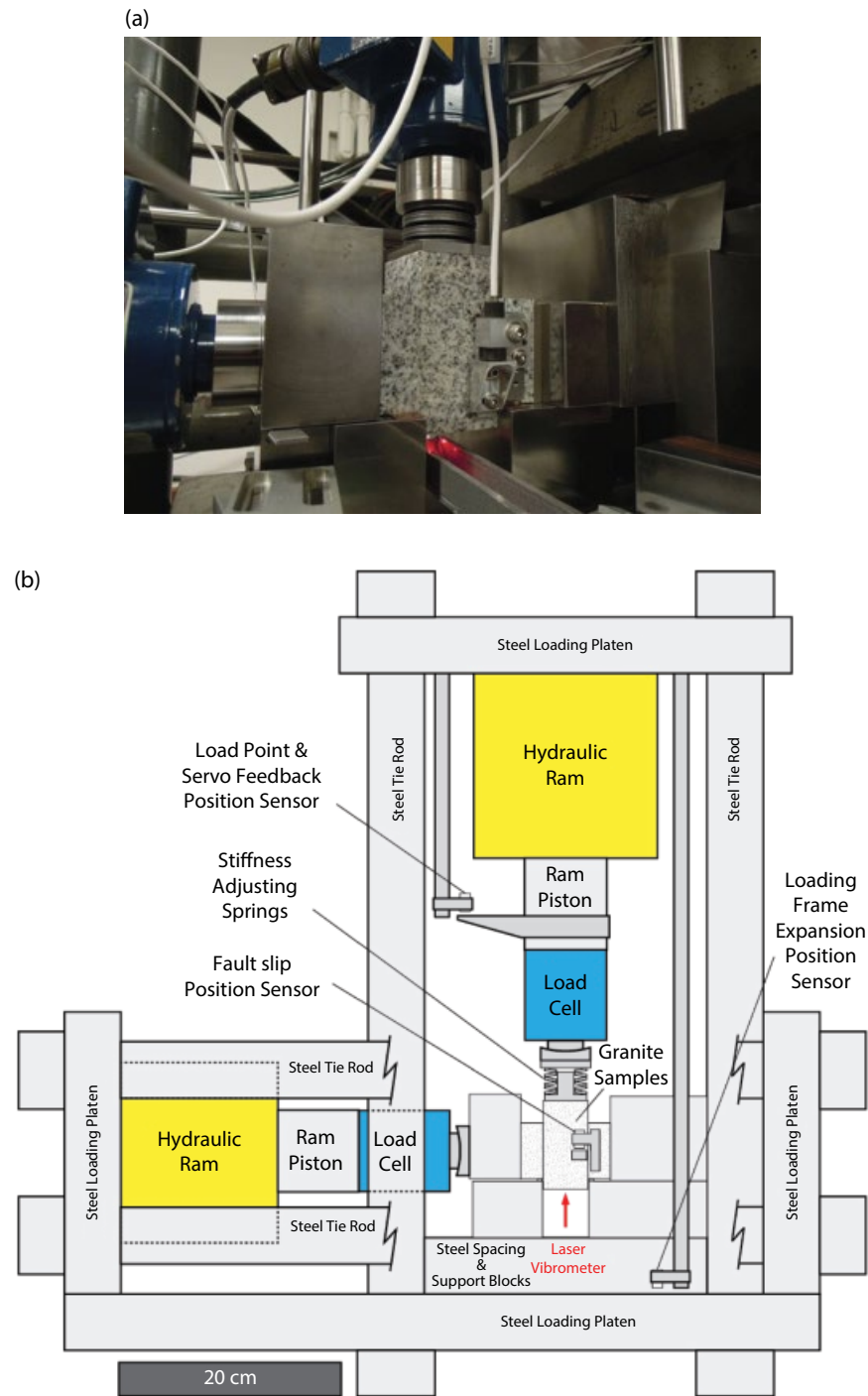


**Figure 8.2** Experimental geometry. (a) Photograph of the apparatus. The configuration from left to right is load cell for normal stress, steel spacer block, left stationary sample, center sample, right stationary sample, and steel spacer blocks. The configuration from top to bottom is load cell for shear stress, steel piston, springs, steel spacer, and center sample. The channel structure below the center sample block holds a 45° mirror which directs the laser vibrometer beam to the bottom surface of the sample. The fault displacement sensor in front has a white wire protruding from it. (b) Detailed scale drawing of the apparatus, including the measurement and control points of displacements used to determine the stiffness of the apparatus and fault slip.

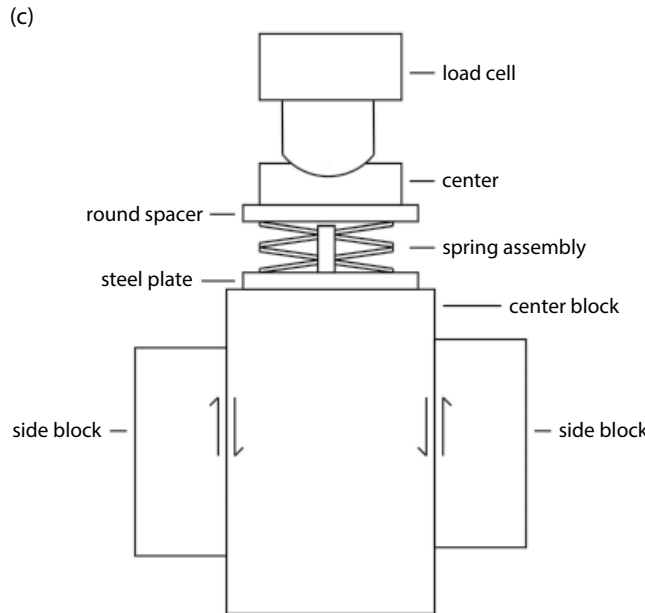


**Figure 8.2** (Continued) (c) Sketch of the details of the sample configuration (not to scale).

the vertically aligned hydraulic ram. The position of the shear force piston (located between the hydraulic ram and load cell) relative to the shear-loading frame is the servo feedback signal and the load point for these tests. In all tests, the shear-forcing piston is advanced at a constant rate of  $0.2\mu\text{m/sec}$ . Position feedback from the load point, rather than force feedback from the load cell, prevented the shear loading servo system from overcompensating after each stick-slip event and, depending on the stiffness, usually allowed the system to complete more than one stick-slip cycle without interruption until the position sensors moved beyond their range and needed to be reset. Examples of complete experiments are found in a Supplement that is available from the corresponding author. A computer control program provided the reference signals for both the normal stress and shear force servo systems.

The fault surfaces are prepared by first machine grinding those surfaces flat with a #100 grit abrasive wheel, then finished by hand lapping the sliding surfaces on dry #600 SiC wet-dry sand paper attached to a glass plate. The fault surfaces are resurfaced with new #600 SiC wet-dry sand paper after each run. The average roughness of the prepared fault surfaces was measured to be approximately  $\text{Ra} \leq 0.5$  microns, using a Qualitest TR200 portable surface roughness tester. The flatness and smoothness of the fresh fault surfaces is qualitatively demonstrated by the adhesion between two fault surfaces when those surfaces are pressed together by hand with a twisting motion. The fault surfaces adhere to each other, though with less strength than the bonding observed when machinist's gauge blocks are "wringed" together. After each run, no sliding surface damage or accumulated fault gouge was readily apparent, though a finger swipe revealed the presence of fine fault gouge.

The principal measurements in these tests are shear and normal stress applied to the simulated fault surfaces, fault shear and normal displacement, motion of the shear-loading piston relative to the loading frame, and fault slip rate. To properly document the rapid and transient stick-slip motions in these tests, all the sensors and signal conditioning used in these experiments to document those motions were either selected, or designed and built in the lab, to produce signals with a linear response to  $50\text{ kHz}$  or better. The canister load cells measuring the shear and normal stresses applied to the faults are the only exception; they have a resonant frequency of  $4\text{ kHz}$  and a linear response below that. All sensor signals were recorded continuously at 500,000 samples per second, averaged on the fly, and data were saved to disk at the rate of 1,000 samples per second. During rapid slip events, all signals were recorded for approximately 0.5 seconds using a pre-trigger/post-trigger transient waveform recorder, saving data to disk at the rate of a million samples per second.

Fault-parallel slip and fault-normal displacement are measured with small eddy-current position sensors mounted within a few millimeters of one of the sliding faults. The proximity of these position sensors to the fault motion minimizes the sensitivity of those measurements to the elastic deformation of the surrounding test apparatus and the granite samples. The motion of the shear and normal stress loading pistons relative to the loading frame, as well as the deformation of the loading frame, were measured using similar position sensors. The velocity of the center sliding sample block during stick-slip was measured directly using a single-point laser vibrometer that is mounted on a tripod with feet that rest

upon small vibration isolation pads on the concrete floor of the laboratory. The floor provides a stable and stationary reference for the velocity measurement. The laser is directed at a 45° mirror that is held by an extending arm attached to the vibrometer itself. The mirror directs the laser to the bottom of the center block, where it reflects back to the mirror and the vibrometer.

The primary goal of these experiments is to determine the dependence of earthquake source properties on the characteristics of the testing machine. This was accomplished by inserting small disc springs between the shear force load cell and the center sample block (Figure 8.2c), which allowed the stiffness of the shear-loading column of the test apparatus to be reduced incrementally. The disc springs were selected with ratings that exceeded the forces applied during the tests, no springs showed any signs of permanent deformation during the tests, and it is assumed that the springs performed within their fully elastic limits. The number and orientation of the disk springs permitted the stiffness of the shear force column to be adjusted over an order of magnitude. The disc springs are not individually calibrated devices, although each has a manufacturer's intended spring constant of about 14 N/ $\mu$ m. Friction between stacked springs and between the springs and their mounting device was not accounted for during these tests. Accordingly, shear loading and unloading stiffness was determined empirically in all tests. The loading stiffness was determined from fitting the linear portion of the stress versus load point displacement records during loading (see examples in the Supplement available from the corresponding author). Unloading stiffness was determined using the ratio of the static stress drop to the total event slip, as inferred from the high-speed records (see below).

### 8.3. RESULTS

Experiments were conducted at eight different values of shear loading stiffness, here and throughout defined as the increment change in shear stress per meter of advancement of the shear load piston. Stiffness was varied between approximately 0.92 and 23.3 GPa/m, and between 6 and 16 stick-slip events were recorded for each stiffness. The summary values of number of events, slip, slip velocity, static stress drop, stiffness, and their measurement uncertainties are listed in Table 8.2. Figure 8.3 shows two representative examples of the scaled data from slip events at the highest (Figure 8.3a) and lowest (Figure 8.3b) stiffnesses. The horizontal axis is time and both events are shown at the same total scale (0.0017 s). The vertical stress axis is the same for both events while the velocity and slip have different scales for each event. At high stiffness (Figure 8.3a) stress drop, slip and slip velocity are relatively small. Event duration is also much shorter than at low stiffness.

In detail, the velocity record at high stiffness is complex, showing three local maxima. These may be related to slip on the two parallel faults in the DDS geometry not being exactly coincident in time. However, at low stiffness, ignoring the small-amplitude high-frequency oscillation (Figure 8.3b), the velocity-time history is so simple as to be well represented by a sine function, similar to the study by *Johnson and Scholz* [1976]. There are complications in the stress measurements. For both events shown, and as is typical throughout this suite of experiments, the normal stress is not exactly constant over the slip event. Apparently, vibrations produced by rapid slip have shorter periods than the response time of the fault normal servo-control system. These vibrations are larger and have longer periods for the larger stress drop at low stiffness, but we do not find that these normal stress artifacts affect any of the conclusions of this study. At low stiffness where the slip speeds are the largest, the shear stress record shows a systematic oscillation with a period around 0.00016 seconds (Figure 8.3b). This is of the order of the resonance frequency of the load cell (4 kHz) and is likely to be related to the instrument rather than the fault behavior. Although this is not ideal, for all events at all stiffness we use the initial and final values of the load cell measured stress to determine stress drop, in other words, the static stress drop, and so we believe that the oscillations do not affect any of the conclusions of this study.

As seen in Figure 8.3b, for the stick-slip generated by the least stiff shear loading column, the shear stress dropped more or less gradually to a new static level. For the stick-slip generated by the most stiff shear loading column (Figure 8.3a), the shear stress drop displays an apparent rapid stress overshoot, followed by recovery to a new static stress level. The duration of the rapid shear stress drop in the events with the stiffest shear loading column unfortunately coincides with the resonant period of the load cell, and since the stress recovery following the overshoot occurs after slip has stopped, it is unclear whether the overshoot is real or instrument resonance. Improved measuring stress techniques are planned for future work to resolve this issue. While the static stress drop is used to estimate the unloading stiffness, this apparent overshoot is a relatively small fraction of the static stress drop, and the uncertainty associated with the apparent overshoot also does not effect the overall conclusions of this study. That is because this is a study of scaling; the eventual scaling relations presented below are power law, and even first-order measurement errors do not have a significant impact (see Figure 8.5 and associated discussion).

For most stick-slip events (see Figure 8.3), the onset of slip was characterized by an emergent signal from the fault slip sensor. The emerging slip signal is likely caused by a combination of accelerating fault creep and a small

**Table 8.2** Stick-slip of granite at 2 MPa normal stress, 0.2  $\mu\text{m}/\text{s}$  loading rate, and variable stiffness.

N	$\Delta t_{\text{obs}}$ ( $\mu\text{s}$ )	$\Delta\delta$ ( $\mu\text{m}$ )	V (m/s)	$V_{\text{peak}}$ (mm/s)	$\Delta\tau_s$ (MPa)	$k_{\text{load}}$ (MPa/m)	$k_{\text{unload}}$ (MPa/m)	Spring Assembly Mass (kg)	Total Mass (kg)	Loading $k\Delta t$ (MPas/m)	Unloading $k\Delta t$ (MPas/m)
6	$1095.7 \pm 21.1$	$816.4 \pm 157$	0.7451	$1064.4 \pm 185.9$	$0.744 \pm 0.101$	$977.5 \pm 147.1$	$922.3 \pm 85.2$	0.1412	0.6472	1.071	1.011
11	$759.3 \pm 32.2$	$293.8 \pm 29.5$	0.3869	$628.9 \pm 35.2$	$0.5031 \pm 0.0348$	$1570.9 \pm 105.6$	$1719.1 \pm 83.1$	0.0954	0.6008	1.193	1.305
15	$908.3 \pm 7.3$	$192.1 \pm 18.5$	0.2115	$345.6 \pm 31$	$0.5108 \pm 0.0398$	$2473.2 \pm 76.9$	$2664.7 \pm 77.4$	0.0478	0.5532	2.246	2.420
11	$560.6 \pm 34.6$	$47.1 \pm 11.6$	0.08402	$131.5 \pm 25.8$	$0.209 \pm 0.055$	$4522.5 \pm 341.9$	$4428.3 \pm 394$	0.0305	0.5359	2.535	2.483
16	$329.1 \pm 8.2$	$18 \pm 0.7$	0.05469	$106.4 \pm 1.8$	$0.264 \pm 0.019$	$15319 \pm 622.5$	$14673 \pm 624$	0.0478	0.5532	5.042	4.829
11	$359.2 \pm 14.1$	$51.6 \pm 2.4$	0.1437	$215.7 \pm 10$	$0.514 \pm 0.038$	$9267.7 \pm 416$	$9267.7 \pm 416$	0.0689	0.5743	3.329	3.329
16	$257.3 \pm 5$	$12.9 \pm 0.2$	0.05014	$89.6 \pm 2.3$	$0.277 \pm 0.018$	$20876 \pm 153$	$21538 \pm 1594$	0.0911	0.5965	5.372	5.542
15	$281.7 \pm 8.8$	$10.7 \pm 0.4$	0.03798	$78 \pm 3.2$	$0.25 \pm 0.004$	$20323 \pm 207.1$	$23308 \pm 893$	0.133	0.6384	5.725	6.566

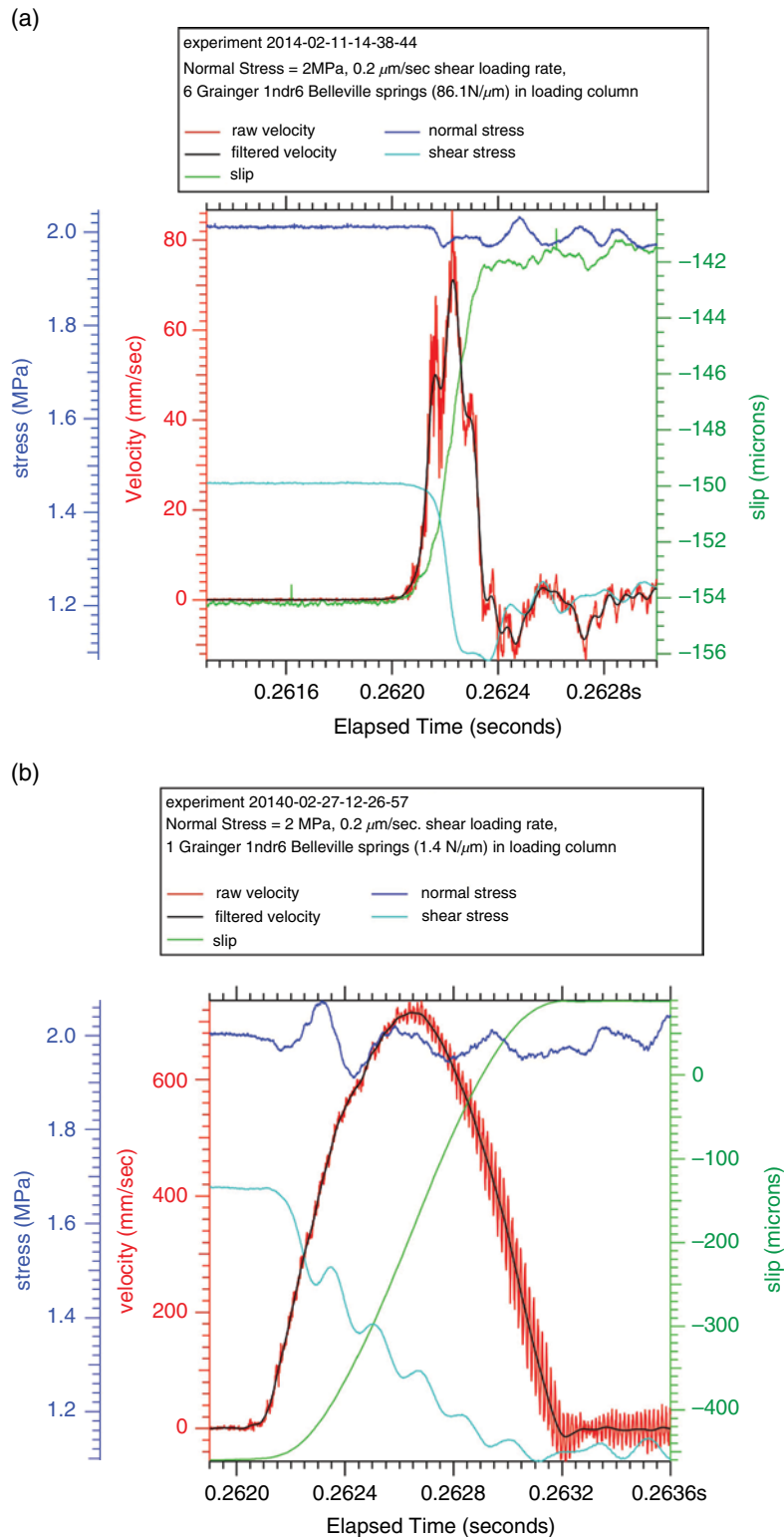


**Figure 8.3** Stress, slip, and slip velocity during slip events at high and low stiffness. (a) Data at unloading stiffness of 23 GPa/meter. (b) Data at unloading stiffness of 0.9 GPa/meter.

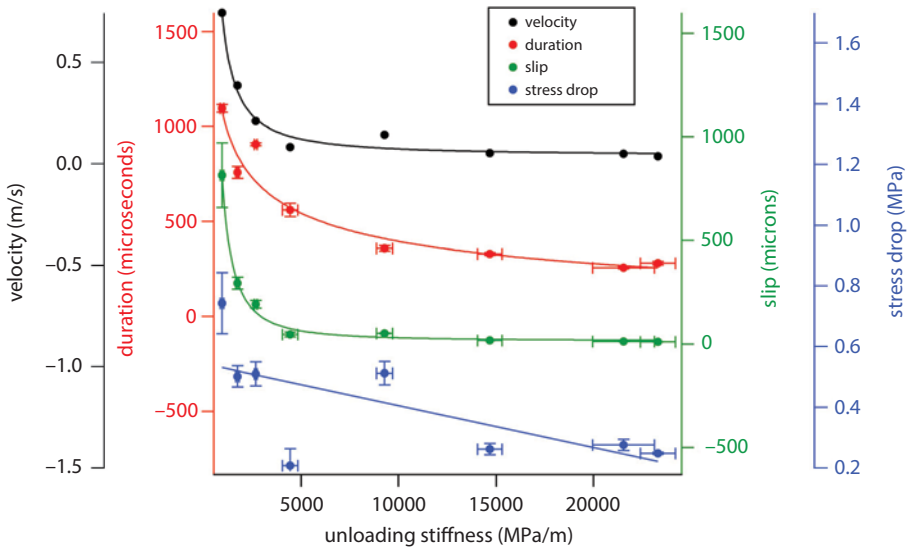


**Figure 8.4** Duration, average slip velocity, slip, and stress drop with unloading stiffness. Error bars indicate  $\pm$  one standard deviation. Data are listed in Table 8.1.

component of elastic shear deformation of the sample between the mounting points of the fault slip sensor on each side of the fault. In contrast, the slip velocity of the center sliding block, measured by the laser vibrometer, revealed a more abrupt onset of fault motion. We use the abrupt acceleration of fault slip from the velocity records to determine the start of fault slip and the subsequent zero crossing of the velocity record to determine the end of fault slip. Those same start and end picks were also used to determine event duration.

The average velocity is the ratio of total slip to duration while the peak velocity was measured directly by the laser vibrometer. A simple integration of the observed slip velocity (not shown) produces a slip record that closely matches the observed slip record, demonstrating the validity and self-consistency of the separate velocity and slip measurements. The unloading stiffness is the ratio of the static stress drop to the total slip while the loading stiffness was determined by measuring the stress change on the loading column per increment of loading displacement over much of the shear loading portion of each stick-slip cycle. The loading and unloading stiffnesses are similar, as expected (Table 8.2). The results for all events at each stiffness were averaged, and the resulting values and associated standard deviations of the measurements are tabulated in Table 8.2. The average values of slip, duration, slip velocity, and stress drop with unloading stiffness are also shown in Figure 8.4.

Decreasing stiffness by a factor of 25 increases slip event and slip velocity. Slip increases monotonically by 74 times from 11 to 816 microns, and average slip rate increases by 19 times from 0.04 to 0.74 m/s, also following a well-constrained trend. It is worth noting that these

systematic changes in slip rate differ from earthquake scaling; as typically reported, slip rate is independent of rupture dimension, i.e., stiffness. A decrease in duration is similarly well defined, but the variation is much weaker than for slip and velocity, changing by 3.9 times from 1.1 to 0.28 ms. In contrast to total slip, average slip velocity, and duration, there is no systematic dependence of static stress drop on stiffness. There is a net decrease from 0.74 to 0.25 MPa, but this is a factor of only 3. The weak relationship is perhaps complicated by the tests at unloading stiffness of  $\sim 9.3$  GPa/m that show a high stress drop relative to the trend from the other tests. However, we have no reason to exclude this result and conclude that these preliminary tests show no clear dependence of stress drop on stiffness.

These above-described relations between stiffness, slip, duration, slip velocity, and stress shown in Figure 8.4 are the new experimental observations of possible stick-slip scaling from this study. A summary of the dependences of slip, duration, and slip velocity on the imposed changes in stiffness are indicated by the curves superimposed on Figure 8.4; these are fits to the data with a power law that captures the relationships. Thus, the qualitative interpretation is that all of these quantities depend nonlinearly on stiffness. In contrast, the dependence of stress drop on changes in stiffness is unclear. The linear relation fit to the stress drop data shown in Figure 8.4 (open diamonds) is a poor representation, even given the uncertainty of the measurements. That is, the dependence of stress drop on machine stiffness is not resolved by this dataset. The variability seen between data at different stiffnesses may reflect actual variations of the physical properties of the fault surface.

## 8.4. INTERPRETATION AND SCALING RELATIONS FROM STICK-SLIP

The systematic relationships between stiffness, duration, stress drop, and slip rate in this dataset do not follow the expected scaling of earthquakes seen in previous stick-slip studies as compiled in Figure 8.1 and as suggested by *McGarr* [2012]. In the following section, we develop explanations for the scaling relationships depicted in Figure 8.5. Analysis relating laboratory stick-slip to natural earthquakes is found in the subsequent section (8.4.2) below.

### 8.4.1. Slider Block Model

The systematic relationships in this dataset closely follow expectations from modeling the fault and testing machine as a slider-block [*Johnson and Scholz*, 1976; *Rice and Tse*, 1986]. Accordingly, the duration of a slip event,  $\Delta t$ , is half the resonance period of the machine,  $T$ , and is inversely proportional to the square root of the system stiffness. In the case of undamped motion the relation is

$$\Delta t = \pi \sqrt{\frac{m}{Ak}}, \quad (8.2a)$$

where  $m$  is mass and  $A$  is fault area [*Johnson and Scholz*, 1976; *Rice and Tse*, 1986]. In the test configuration (Figure 8.2b), the compliant disc springs are below the end of the shear loading piston and immediately above the center fault block. The rest of the testing machine above the springs, including the piston, load cell, platen, and frame is much stiffer and can be treated as stationary. The two side fault blocks are stationary, so the “fault” consists only of the center block and the spring assembly, consisting of the springs and a center post and screw. The mass of the spring assembly varies between tests at different stiffnesses, while the center block has a mass of  $\sim 0.432\text{ kg}$ , resulting in variations in fault mass of up to 21% (Table 8.2). Measured duration from the experiments is shown as the black dots on the log log plot of duration versus stiffness in Figure 8.5a. Predicted duration from equation (8.2a) based on the known mass, the area of both faults in the DDS geometry, and unloading stiffness is shown by the open diamonds. A fit to those predictions with equation (8.2a) is shown as a dashed line. The prediction, based on a model with no free parameters, matches the observations to within the data uncertainties. Two other fits to the observations are also shown. The first empirically uses the form of equation (8.2a) where duration varies inversely with the square root of stiffness, treating the constants such as mass, fault area as a single free parameter (black dashed line). The second is the power law fit first shown in Figure 8.4 (in Figure 8.5a, it is the

black solid line). The slope of the power law fit is  $-0.46$ , very close to the expected  $-0.5$  from equation (8.2a). From this analysis we conclude that the weak systematic dependence of duration on stiffness (Figure 8.4) likely is independent of the frictional properties of the fault (stress drop) and is imposed by the nature of the testing machine-fault interaction.

Although the predicted and observed durations agree to within the data uncertainty, the respective fits with equation (8.2a) (dashed lines) are slightly offset. An apparent offset of this sense, while not resolved in these experiments, is expected due to radiation losses or fracture energy not accounted for in equation (8.2a). The appendix develops an approach for estimating apparent stress, radiated energy and overshoot, based on this offset. Nonetheless, because of the offset we use the empirical data fit (solid line, Figure 8.5a) to illustrate other predictions from the slider block model that are consistent with the systematic variation of slip velocity and slip with stiffness, as follows. For slip velocity, the average velocity is  $\hat{V} = \Delta\delta/\Delta\tau$ . As the stiffness is  $k = \Delta\tau_s/\Delta\delta$ , the expected relation between velocity and stiffness for undamped motion is

$$\hat{V} = \frac{\Delta\tau_s}{\pi} \sqrt{\frac{A}{mk}}. \quad (8.2b)$$

In this case the relationship involves the fault properties via the stress drop, as well as a dependence on stiffness from the testing machine. In any event the prediction (8.2b) (Figure 8.5b, dashed line) matches the observations and differs little from a fit of a power law to the data (black line). Note here that the prediction in Figure 8.5b is not a fit to the data with the power law exponent fixed at 1. Rather, it is the prediction of the spring slider relation (8.2b) using the coefficient  $10^{-1.43}$  from the fit of that equation to the duration and stiffness data shown in Figure 8.5a (dashed line). The expected total slip resulting from undamped motion is

$$\Delta\delta = \pi \hat{V} \sqrt{\frac{m}{Ak}}. \quad (8.2c)$$

Again, the prediction from the model (dashed line, Figure 8.5c) is consistent with the observations and is nearly identical to an unconstrained power law fit to the data.

### 8.4.2. Relationships Between Stick-Slip and Earthquake Source Properties

Since scaling of duration with stiffness in these experiments follows a slider-block model, the experiments do not conform to *McGarr’s* [2012] hypothesis (Figure 8.6a) and cannot be directly scaled to natural earthquakes.

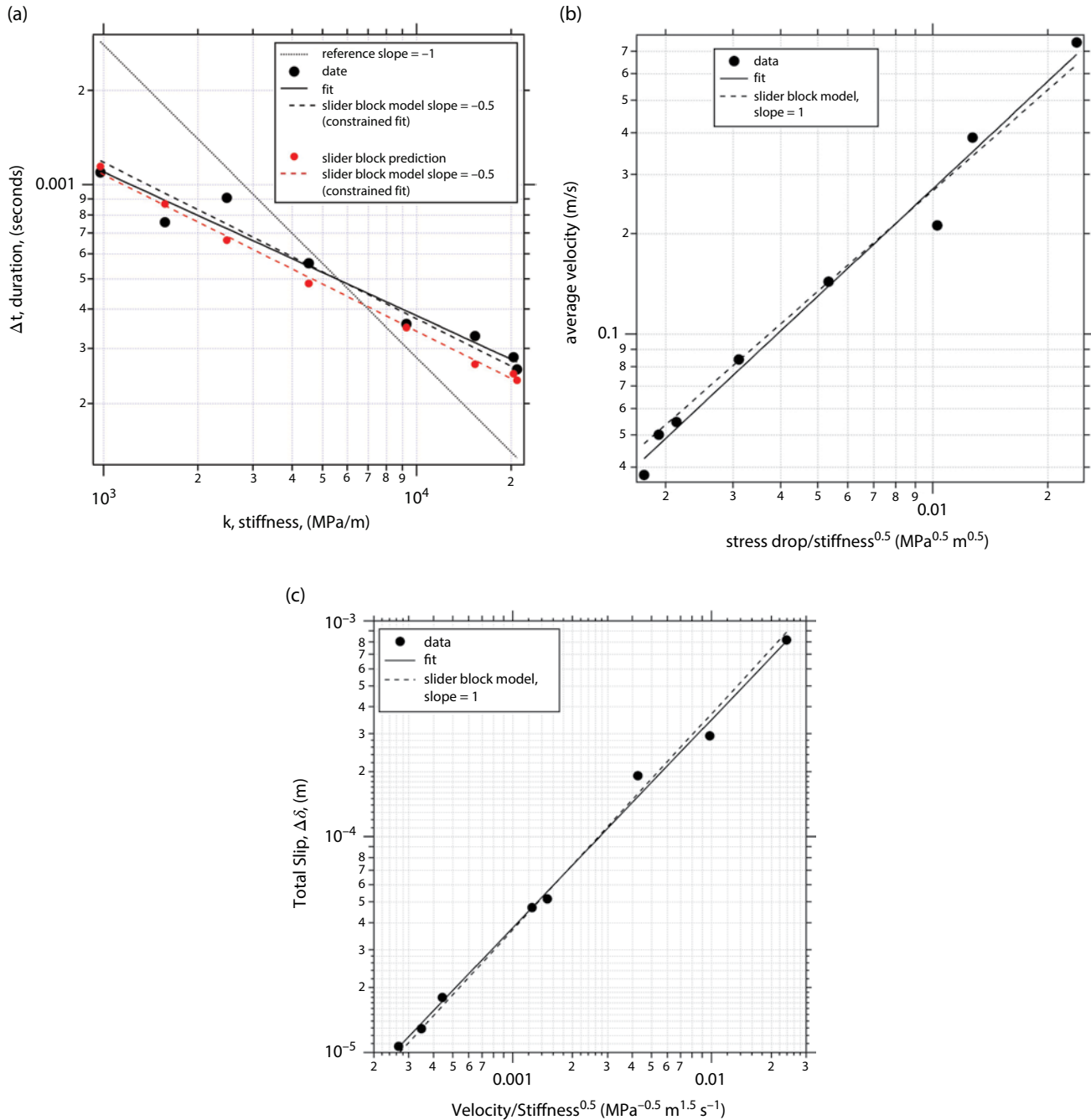


**Figure 8.5** Comparisons between data and predictions from a slider block model. (a) Duration versus stiffness. Open diamonds are the predictions of equation (8.2a) for duration from the known fault mass, stiffness, and area (Table 8.2). The dashed line is a constrained fit to these predictions with  $n = -1$ . Black dots are the observed durations. The black solid line is a fit of these data to a power law  $y = Cx^n$ , where  $C = 10^{-1.58}$ ,  $n = -0.46$ . The black dashed line is a constrained fit with  $n = -0.5$ , resulting in  $C = 10^{-1.43}$ . The dotted line is a reference line for an inverse proportionality between duration and stiffness, a constrained fit to the data with  $n = -1$ . (b) Average sliding velocity versus stress drop/(stiffness<sup>0.5</sup>). The solid line is a fit resulting in  $n = 1.07$ . The dashed line is a prediction from the power law relation equation (8.2b) using the appropriate coefficient from the fit shown in (a) ( $10^{1.43}$ ). (c) Total slip versus average velocity/sqrt(stiffness). The solid line is a fit resulting in  $n = 0.96$ . The dashed line is a prediction from the power law relation equation (8.2c) using the coefficient from the fit shown in (a).

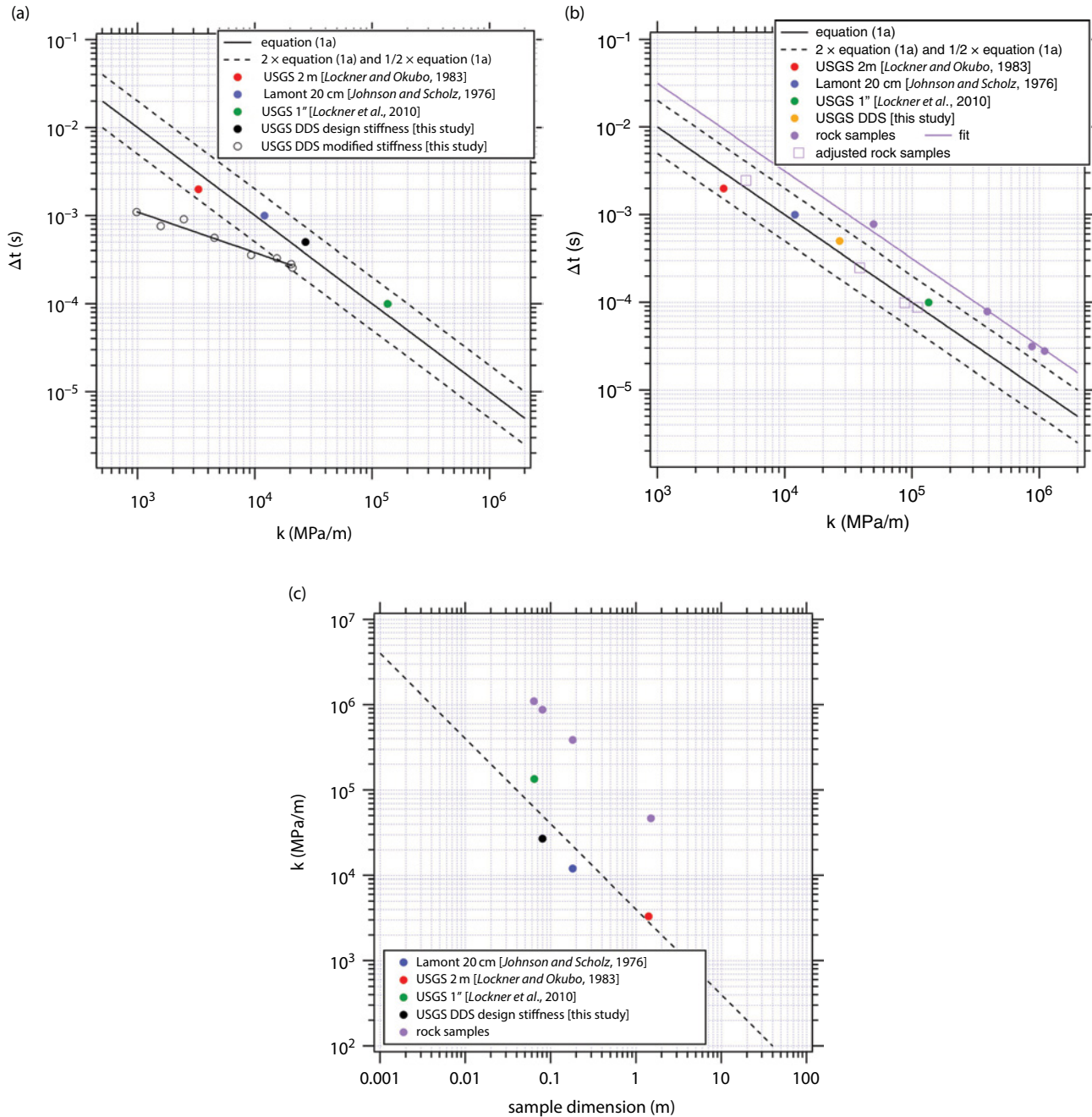


**Figure 8.6** Earthquake source properties from stick-slip. (a) Duration versus stiffness as shown in Figure 8.1a with the addition of the design stiffness and observed duration of stick-slip in the USGS double direct shear (DDS) machine (solid triangles), and the results from the same machine with its stiffness systematically reduced (open black circles). The solid line is the scale-independent prediction, equation (8.1a) with  $\mu/\beta=10\text{ MPa s/m}$ , and the two dashed lines are one half and two times equation (8.1a). (b) Duration versus stiffness as shown in part (a) for the four testing machines. X's are estimated durations assuming the rock samples of the four testing machines are the most compliant element in the system (see text). Dash-dotted line is a constrained fit to an inverse proportionality resulting  $k\Delta t=31\text{ MPa s/m}$ . The +'s squares result from reducing the stiffness ten times less than that of the rock samples (see text). (c) Stiffness versus sample dimension for the four testing machines. The dashed line is an inverse scaling relationship that suggests apparatus stiffness is approximately inversely proportional to sample size for these machines collectively. Shown for reference is the estimated stiffness of the rock samples, which is calculated from the sample dimension in Table 8.1 and an assumed modulus (see text for discussion).

Furthermore, while slip decreases with stiffness as it does for natural earthquakes, the dependences of duration and slip velocity on stiffness are inconsistent with results for earthquakes. Despite these complications, there may be some value in these measurements. In particular, the static stress drops in this study are in the range of 0.25 to 0.74 MPa, within the bounds, but in the lower range observed for natural earthquakes [Baltay *et al.*, 2010, 2011] probably owing to the low normal stress (2 MPa). The lack of a strong or systematic dependence of stress drop on stiffness is also consistent with the natural observations. Nevertheless, given the expected and observed normal stress dependence of stress drop [e.g., Lockner *et al.*, 2017], the resemblance with natural stress drops may be fortuitous. Similarly, the estimate of apparent stress in the appendix is consistent with earthquakes, but it is unclear whether this is a coincidence. In prior studies of rapid slip with a slider-block model [e.g., Beeler, 2001] the ratio of apparent stress to stress drop for stick-slip is fixed at about 0.25, which agrees well with the 0.22 as estimated in the appendix. These values are not unlike standard earthquake models [e.g., Brune, 1970; Singh and Ordaz, 1994] and are consistent with natural observations [Baltay *et al.*, 2011]. Unfortunately, the estimated average ratio of apparent stress to stress drop determined from the data, 0.22, is not well constrained by the observations, and it is unknown to what degree this measure of efficiency is influenced by the properties of the machine; slip during unconfined rupture in most test geometries is mechanically constrained to overshoot.

Despite these questions concerning relevance to earthquakes, in the next few paragraphs we develop a broader view of scaling of stick-slip by considering the procedures used in the experiments, the unaltered properties of all the testing machines shown in Figure 8.1, and the properties of the DDS apparatus. This analysis is qualitative in nature but is strongly supported by the empirical data, leading to a more optimistic perspective on the value of stick-slip to understanding the earthquake source and additional support for McGarr's [2012] hypothesis. Experiments conducted at the unaltered machine stiffness of the DDS apparatus 27 GPa/m (Table 8.1), result in a measured duration of  $\sim 0.0005$  s. These values plot well within bounds of the prior studies (Figure 8.6a), and the product of stiffness and duration is 13.5 MPa s/m, of the same order as in the other testing machines. So, while the duration and stiffness from the primary experiments plot well off trend from the results of prior studies (Figure 8.6a) and earthquakes (Figure 8.1a), this seems to result entirely from the testing procedure where the stiffness is reduced. A simple view, which we will expand upon momentarily, is that the relationships between stiffness and duration (Figure 8.5a), stress drop and loading velocity (Figure 8.5b), and slip

and slip velocity (Figure 8.5c) are "artificial" due to the stiffness being changed, independent of the scale of the fault. Implicit in this interpretation, which we will also expand upon momentarily, is that the scaling of earthquake source properties, such as between stress drop and slip speed, can only be inferred from stick-slip experiments in a single machine when the stiffness is constant at the design value and stress drop varies significantly (Figure 8.1b). Similarly, the relation between duration and stiffness can only be inferred from comparing values between machines (Figures 8.1a and 8.6b), where stiffness and scale are apparently interdependent in the same way as for earthquakes.

Throughout the remaining discussion, we use the adjectives *design* or *natural* to refer to the stiffness or stick-slip duration that results when these various rock testing apparatuses are used as intended by their designers and manufacturers. These adjectives should not be interpreted to imply that resulting stiffness or stick-slip duration was intended to produce realistic earthquake source properties. On the contrary, as described below, our conclusion is that realistic and scale-dependent earthquake source properties result during stick-slip largely as a consequence of using rock samples with the same elastic properties as the earth and from consistent but unintentional design practices that are themselves scale-independent.

McGarr's [2012] hypothesis requires both that the product  $k\Delta t$  is scale independent in experiments, as it is for earthquakes, and that the product is of the same order as for earthquakes. How these requirements are met in practice, apparently fortuitously [Johnson and Scholz, 1976], can be understood qualitatively by further examining constraints of the particular experimental geometries, noting the mechanical requirements for stick-slip, and by considering the intended purpose of the various testing machines. While a detailed mechanical analysis of the four individual machines is beyond the scope of the present study, the scale independent  $k\Delta t$  arises primarily from basic requirements of doing faulting tests at different scales. For example, even though there are four different machines and three different fault geometries (direct shear, double direct shear, and triaxial), collectively the rock sample masses, fault areas, and characteristic dimensions  $L$  (Table 8.1) conform to the requirements of  $k\Delta t$  being scale independent. That is, we assume the rock sample is the most compliant element in each of the four machines. Then, taking the loading stiffness to be  $E/L$ ,  $\rho = 2700 \text{ kg/m}^3$  and  $E = 70 \text{ GPa}$  results in the durations calculated from equation (8.2a) shown as X's in Figure 8.6b. The product of the sample stiffness and this duration is included in Table 8.1 as the "estimated sample  $k\Delta t$ ." A power law fit to these sample-inferred duration and stiffness produces a slope of  $-1.08$ , very close to the inverse proportionality. A constrained fit for

the inverse proportionality results in the product being 31 MPa s/m (dash-dotted line), only a factor of three larger than the ~10 MPa s/m, appropriate for earthquakes and the representative value for the testing machines. That stick-slip is not possible if the rock samples provide all of the system compliance is a rationale for why the testing machines that are capable of producing stick-slip have a smaller stiffness, larger duration, and smaller product than the samples they load. A comparison of the sample stiffness to the stiffness of the testing machines and how these stiffnesses scale with sample dimension is shown in Figure 8.6c.

In the case of the triaxial and DDS configurations, these machines were intended to be primarily used for stable frictional sliding, rather than stick-slip, and indeed their loading frames are quite stiff. For example, *Lockner et al.* [2017] find that about two thirds of the compliance of the triaxial is from the sample itself and one third from the apparatus (Figure 8.6c). Stick-slip can be accessed in these stiff machines in their design configuration by conducting experiments at high normal stress in triaxial [*Lockner et al.*, 2017] or in DDS experiments using faults with highly polished surfaces [*Dieterich, 1978*]. Similarly, though the Lamont and 2 meter biaxial machines were intended for rupture propagation and stick-slip, they are not highly compliant relative to the others once the differences in scale are accounted for. Although there is scatter in the scaling relation (Figure 8.6c), the dashed line indicates an inverse proportionality. Based on this plot we conclude that even though the intended purpose of these testing apparatuses was not for stick-slip in all cases, their stiffnesses scale approximately inversely with the size of the samples; furthermore, the scaling is in part just a requirement of conducting experiments on different-sized samples. This scaling can be rationalized by noting that all designs consist of similar components (platens, tie bars, pistons, hydraulics) of the same composition (steel, hydraulic oil). Likely, the relatively tight scaling is also influenced by design practice requirements for the relatively compliant machines to nonetheless have fairly high stiffness to reduce long period vibrations, and to minimize bending and stored elastic energy for performance and safety considerations.

Returning to the scaling of duration and stiffness estimated from the four samples (Figure 8.6b, X's), since the requirement for stick-slip is more compliance than the rock samples and the time constant goes as  $1/\sqrt{k}$ , a reduction in stiffness increases the time constant. The net effect is a smaller reduction in the  $k\Delta t$  than in the stiffness. So, for example, a 10x reduction from the stiffness of the rock samples produces an approximate 3x increase in duration and 3x reduction in the product (Figure 8.6b, +'s). While the shift from the sample stiffness and duration in this simple calculation is not an exact match for all four of the

machines, a 10x reduction in stiffness produces overall shifts of the duration and the product that are consistent with the collective observations.

## 8.5. LIMITATIONS, CONSTRAINTS ON LAB-INFERRED SOURCE PROPERTIES, AND CAUTION

Significant experimental limitations on the data from this study include the measurement problems associated with shear stress measured at the load cell (Figure 8.3b). This issue may be resolved by replacing the present load cell with an instrument with a higher resonance frequency. Direct measurement of on-fault shear resistance using strain gauges and also employing a near fault thermocouple that could be used to determine the average shear resistance should complete energy accounting during stick-slip and provide measurement redundancy. It would be ideal to measure radiated displacements directly and to determine radiated energy for comparison with calculations described in the appendix. Complications include small sample dimensions relative to the normal and shear loading column lengths, which lead to returning reflected waves from the piston-sample interface that are nearly instantaneous relative to the total duration of fault slip if the measurements are made on the rock samples. Nevertheless, the calibration approach described by *McLaskey et al.* [2015] may be suitable for this kind of accounting.

The experiments in this study were intentionally limited to a single normal stress and loading rate to focus on mechanical interactions between the fault and the testing machine. Experiments over a range of normal stresses are necessary to fully relate stick-slip results to natural seismogenic depths. The 2 MPa normal stress in the present tests correspond to a depth of a few hundred meters in the Earth, whereas, for example, the effective normal stress at the base of the seismogenic zone on the San Andreas may be roughly 100 times higher. Experiments with variations in loading rate and experiments at the same stressing rate are also needed for a more complete study of stick-slip source properties. The extrapolation to the Earth entails much lower stressing rates than in the present suite of experiments. The lowest stressing rate in our experiments is about 5.8 GPa/yr compared with tenths or hundredths of an MPa/year for natural M6 and larger earthquakes. Unfortunately, experimental difficulties arise in the unconfined double direct shear geometry at higher normal stress. To increase the normal stress significantly requires a larger testing machine or a different geometry. Similarly, since our double direct shear apparatus lacks confinement, such as in the triaxial experiments in Figure 8.1 [*Lockner et al.*, 2010, 2017], tests at elevated

temperature and pore pressure would allow more confident application to natural faulting.

Since reducing the machine stiffness in the DDS apparatus produces stick-slip source properties that scale differently from the natural counterparts (Figure 8.6a), the source properties stress drop, duration, slip, and slip speed from high-speed laboratory faulting and stick-slip are only directly relevant to natural earthquakes under limited conditions. The bounds depicted in Figures 8.6 and 8.7 are necessary requirements for earthquake-like source properties, namely, that the product of stiffness and duration, equivalently the quotient of static stress drop and sliding speed, lies between 5 and 20 MPa s/m. In reference to values well outside those bounds, as shown in Figure 8.7, these are offered here as examples of interesting experiments that may not be directly relevant to typical natural earthquakes. The very lowest stress drops

in the *Beeler et al.* [2012] study (Figure 8.7) lie to the left of the bounds and therefore are “slow” relative to earthquakes. As described in more detail in the original study, these tests are conducted at the lowest normal stresses on a fault with high fracture energy. The fracture energy reduces the slip speed, and these events would be faster and have shorter durations were slip not damped by this dissipation. These may be relatable to “low-frequency earthquakes” [Shelly et al., 2006], events that have both lower rupture propagation rates and slip speeds when compared with typical earthquakes with the same moment. Fracture energy is not accounted for in equations (8.1) or (8.2).

At the other extreme are the largest stress drops of the *Lockner et al.* [2010] study (black solid circles). These also plot to the left of the bound and are slower than earthquakes of equivalent stress drop, despite having inferred

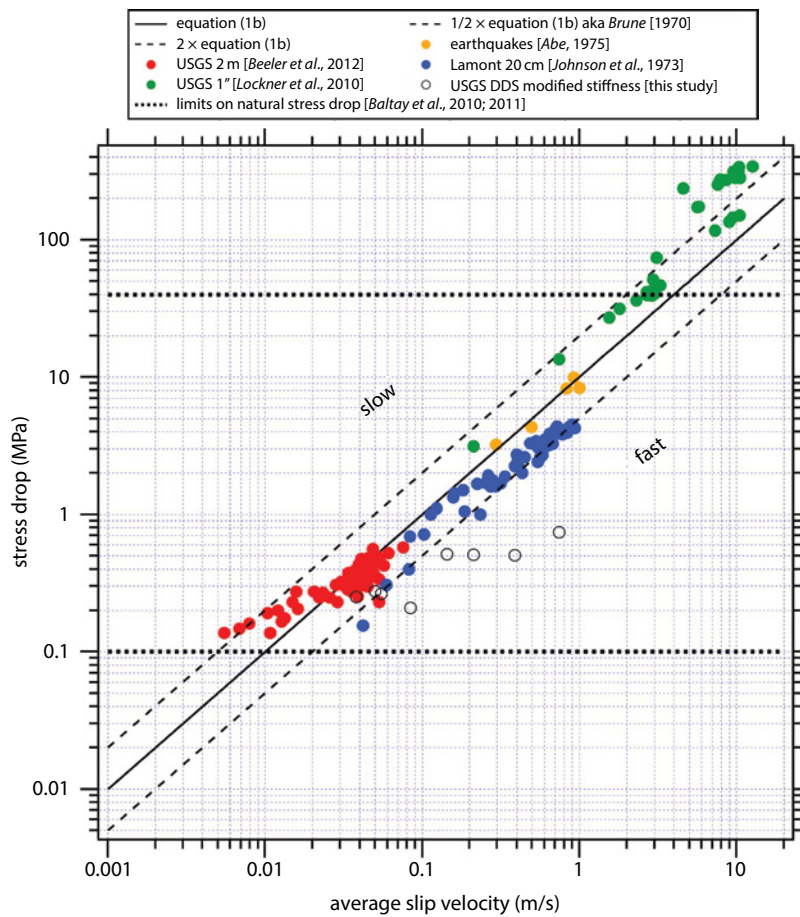


**Figure 8.7** Scaling of earthquake source properties from laboratory stick-slip. Static stress drop versus average slip velocity. Data for individual stick-slip events from this study (open circles) are shown along with the prior studies in three different testing machines [Johnson et al., 1973; Beeler et al., 2012; Lockner et al., 2017] and from five Japanese earthquakes [Abe, 1975]. The solid line is the scale-independent prediction, equation (1a) with the impedance  $\mu/\beta = 10 \text{ MPa s/m}$ , and the two dashed lines are one half and two times (1a). The horizontal dotted lines demarcate the range of typical natural stress drops (0.1 to 40 MPa) inferred from recent analysis using a *Brune* [1970] source model [Baltay et al., 2010; 2011].

slip speeds in excess of 4 m/s. The origin of the damping of slip for these events is not yet completely understood. These produce enough shear heat to melt the fault zone, at least in part, and it is possible that there is dissipation associated with the generation or subsequent freezing of the shear melt that reduces the sliding speed [e.g., *Koizumi et al.*, 2004]. Could this be shown definitively it may provide a signature frequency content of natural melt-generating earthquakes. However, another possibility is that the slow slip is due to contributions from the testing machine. These tests are at the highest confining pressures in the *Lockner et al.* [2010; 2017] study. The confining fluid is a silicone oil whose viscosity increases with pressure and may contribute to slowing the slip rate at high confining pressure. Further limits on the relevance of laboratory-inferred fault properties come from typical earthquake stress drops that are in the range of 0.1 to 40 MPa [*Baltay et al.*, 2010; 2011] (heavy dotted horizontal lines, Figure 8.7). These imply limits on average slip speed of 0.005 to 8 m/s. Both the upper limit on stress drop and slip speed are exceeded in the *Lockner et al.* [2010] experiments at the highest confining pressures. Explaining those differences and other implied differences between laboratory stress drops and earthquakes [e.g., *Di Toro et al.*, 2011] is beyond the scope of the present study but is an important remaining challenge for the experimental fault mechanics community.

## 8.6. SUMMARY AND CONCLUSIONS

Laboratory stick-slip in standard direct shear, triaxial, and double direct shear testing configurations have effectively scale-independent values of the ratio of static stress drop to average slip rate, between 5 and 20 MPa s/m, so long as the experiments are conducted on rock and at the design elastic properties of the testing machine. The ratio is essentially the same as found for natural earthquakes and, as in seismic source theory [e.g., *Brune*, 1970], is of the same order as the impedance, the ratio of the elastic modulus to the wave speed; the ratio is also equal to the product of the stiffness and the rise time. Collectively, these results confirm the hypothesis of *McGarr* [2012] that the product of stiffness and rise time for stick-slip is scale independent and the same as for earthquakes. The constant ratio arises because the square root of the ratio of the product of sample mass and stiffness to fault area of experimental samples is independent of scale, the apparatus stiffnesses vary inversely with sample size, and the stiffness of the testing machines is approximately ten times smaller than that of the rock samples. Expected and documented exceptions to this rule are cases where fault slip is damped by fault properties (or machine effects), producing events that have lower slip rates than their natural counterparts of equivalent stress drop, and

cases where the testing machine stiffness is reduced from the design values, resulting in larger slip rates than for natural earthquakes of the same stress drop.

## ACKNOWLEDGMENTS

Greg McLaskey of the USGS provided a review that significantly improved the manuscript. Monograph reviews by Nicolas Brantut and Chris Marone are gratefully acknowledged. Any use of trade, firm, or product names is for descriptive purposes only and does not imply endorsement by the U.S. Government.

## APPENDIX

### Estimating Radiated Energy During Stick-Slip

In our experiments radiated energy is not directly measured using high-frequency seismic instrumentation; nonetheless, it might be reliably estimated from slip velocity measurements under some circumstances. For fixed fault area the amount of energy available to be radiated as shear waves due to fault slip is

$$E_{nf} = \frac{A\zeta}{2} \int_0^{\Delta t} V^2 dt \quad (8.A1a)$$

[e.g., *Kanamori*, 2001], where  $\zeta$  is the impedance. For a fault in an elastic continuum,  $\zeta = \mu/\beta$ . As pointed out by *McGarr and Fletcher* [2001], for an earthquake, some of this available energy (8.A1a) remains in the near-field and goes into producing the static elastic distortions about the rupture. Laboratory experiments typically lack such a near-field reduction of equation (8.A1a) because spatially uniform slip on the fault nearly always results once rupture reaches the free surfaces at the fault ends, and there is no increase in near-field static strain energy. Therefore, arguably,  $E_r = E_{nf}$  and the radiated energy during stick-slip is given by (A1a). Accordingly, all that is needed to estimate radiated energy is the slip velocity. As the apparent stress relates to radiated energy as  $\tau_a = E_r / A\Delta\delta$ , then

$$\tau_a = \frac{\zeta}{2\Delta d} \int_0^{\Delta t} V^2 dt. \quad (8.A1b)$$

Equation (A1b) for apparent stress is consistent with continuum and slider block models that are radiation damped [*Rice*, 1993; *Beeler*, 2001]. However, for our stick-slip experiments the elastic impedance is constrained by the observations to be much less than  $\mu/\beta$ . For example, assuming constant slip rate at the average velocity, the apparent stress in (A1b) becomes  $\tau_a = \frac{\zeta \hat{V}}{2}$ ; taking the impedance to be 10 MPa s/m and the average

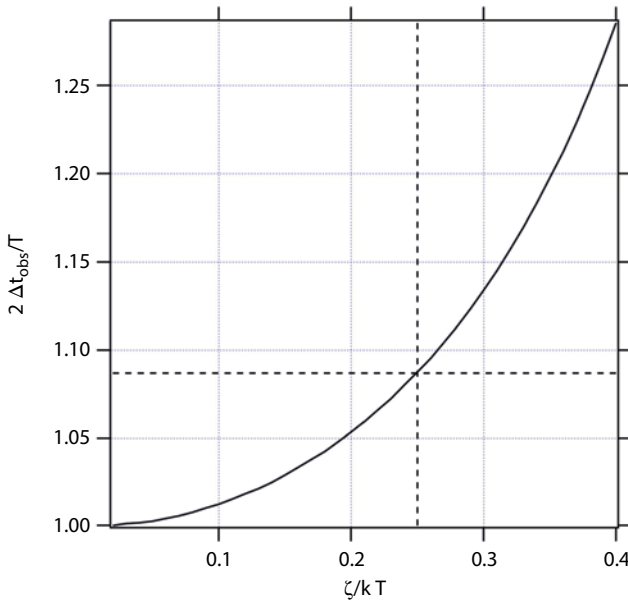


**Figure 8.A1** Relative increase in event duration with impedance in a slider block model.

slip rate from the lowest stiffness tests,  $\sim 0.75$  m/s, apparent stress would be  $3.75$  MPa, an order of magnitude larger than the stress drop and higher than the normal stress on the fault. This is a physically impossible value for apparent stress.

A more appropriate estimate for the impedance can be made using a slider block model that accounts for radiation loss [Beeler, 2001]. The idea is to attribute to radiation loss the difference between the observed event durations and those inferred using the undamped slider block model, equation (8.2a) (Figure 8.5a, Table 8.2). For a static-kinetic fault strength relation with dynamic stress drop  $\Delta\tau_d$  and a single degree of freedom spring-slider block model, the equation of motion is the balance of the mass times acceleration against the difference between the spring force and the frictional resisting stress, less the radiated energy:

$$\left(\frac{T}{2\pi}\right)^2 \frac{\partial^2 \delta}{\partial t^2} = \frac{\Delta\tau_d}{k} - \delta - \frac{\zeta}{2k} \frac{\partial \delta}{\partial t}. \quad (8.A2a)$$

$T$  is the undamped characteristic oscillation period, and the event duration in the absence of radiation is  $\Delta t = T/2$ .  $k$  is stiffness,  $\zeta$  is impedance, and  $\delta$  is slip on the fault. The third term on the right-hand side of (A2a) is the “radiation damping” term, used to approximate energy lost as propagating seismic waves, here assumed to be planar shear waves [Rice, 1993]. The observed event duration  $\Delta t_{obs}$  is larger than  $\Delta t$  when radiation losses are significant. That condition is met when the impedance is a significant fraction of the characteristic impedance  $kT$  of

the undamped spring slider. Averaging the slip velocity over an entire event produces a stress measure of the radiated energy, the apparent stress

$$\tau_a = \frac{\zeta \hat{V}}{2}. \quad (8.A2b)$$

To estimate radiated energy and apparent stress, equation (8.A2a) is solved numerically for slip, stress, and slip rate with time for a range of values for the impedance, representing possible amounts of radiation loss, for comparison with the experiments. Figure 8.A1 shows the ratio of observed duration normalized by the characteristic duration  $\Delta t_{obs}/0.5T$  resulting from a range of impedances from zero to 40%  $kT$ . To apply these simulations to the observations shown in Figure 8.5a, the experiments are treated collectively by interpreting radiation loss as the difference between the observed event durations and those inferred using the undamped slider block model, equation (8.1a) (Figure 8.5a, Table 2). That is, using the difference between the dashed lines in Figure 8.5a as a lengthening of event duration due to energy lost to radiation. On average the observed durations (Figure 8.5a, slider-block model fit line) are around 10% higher than expected (slider-block prediction line). The corresponding ratio of the predicted duration to the observed duration is  $\Delta t_{obs}/\Delta t = 1.09$ . To produce this relative increase requires a value of the impedance that is about 25% of product of the stiffness and the resonance time constant  $T$  as indicated by the dashed reference lines on Figure 8.A1. In terms of the observed event duration and average velocity, apparent stress for these experiments is

$$\tau_a = 0.22 \hat{V} k \Delta t_{obs}. \quad (8.A2c)$$

Resulting values from equation (8.A2c) using the tabled values of average velocity, stiffness, and duration (Table 8.2) range from 0.05 to 0.18 MPa. The estimated average radiation efficiency, the ratio of apparent stress to static stress drop [Savage and Wood, 1971], is 0.22. This ratio fixes the average slip overshoot,  $\xi = 0.5 - \tau_a/\Delta\tau_s$  [Savage and Wood, 1971], to be 0.28. These results compare favorably with estimates for earthquakes, stick-slip experiments, and prior slider-block models [McGarr, 2012, and references therein].

## REFERENCES

- Abe, K. (1975), Static and dynamic fault parameters of the Saitama earthquake of July 1, 1968, *Tectonophysics*, 27, 223–238.  
 Baltay, A., S. Ide, G. A. Prieto, and G. C. Beroza (2011), Variability in earthquake stress drop and apparent stress, *Geophys. Res. Lett.*, 38, L06303, doi:10.1029/2011GL046698.

- Baltay, A., G. Prieto, and G. C. Beroza (2010), Radiated seismic energy from coda measurements indicates no scaling in apparent stress with seismic moment, *J. Geophys. Res.*, **115**, B08314, doi:10.1029/2009JB006736.
- Beeler, N. M. (2001), Stress drop with constant, scale independent seismic efficiency and overshoot, *Geophys. Res. Lett.*, **28**, 3353–3356.
- Beeler, N. M., B. Kilgore, A. McGarr, J. Fletcher, J. Evans, and S. R. Baker (2012), Observed source parameters for dynamic rupture with non-uniform initial stress and relatively high fracture energy, *Journal of Structural Geology* (Spec. Iss.), **38**, p. 77–89.
- Brace, W. F., and J. D. Byerlee (1966), Stick-slip as a mechanism for earthquakes, *Science*, **153**, 990–992.
- Brune, J. N. (1970), Tectonic stress and the spectra of seismic shear waves from earthquakes, *J. Geophys. Res.*, **75**, 4997–5009.
- Byerlee, J. D., and W. F. Brace (1968), Stick slip, stable sliding, and earthquakes: Effect of rock type, pressure, strain rate and stiffness, *J. Geophys. Res.*, **73**, 6031–6037.
- Di Toro, G., R. Han, T. Hirose, N. De Paola, K. Mizoguchi, F. Ferri, M. Cocco, and T. Shimamoto (2011), Fault lubrication during earthquakes, *Nature*, **471**, 494–499.
- Dieterich, J. H. (1978), Time-dependent friction and the mechanics of stick-slip, *Pure Appl. Geophys.*, **116**, 790–806.
- Johnson, T., F. T. Wu, and C. H. Scholz (1973), Source parameters for stick-slip and for earthquakes, *Science*, **179**, 278.
- Johnson, T. L., and C. H. Scholz (1976), Dynamic properties of stick-slip friction of rock, *J. Geophys. Res.*, **81**(5), 881–888, doi:10.1029/JB081i005p00881.
- Kanamori, H. (2001), Energy budget of earthquakes and seismic efficiency, in *Earthquake thermodynamics and phase transformations in the Earth's interior*, Edited by R. Teisseyre and E. Majewski, pp 293–305, Academic Press, New York.
- Kilgore, B. D., Blanpied, M. L., and Dieterich, J. H. (1993), Velocity dependent friction of granite over a wide range of conditions, *Geophys. Res. Lett.*, **20**, 903–906.
- Kilgore, B., J. Lozos, N. M. Beeler, and D. Oglesby (2012), Laboratory observations of fault strength in response to changes in normal stress, *Journal of Applied Mechanics* (Jim Rice Spec. Iss.), JAM-11-1213.
- Koizumi, Y., K. Otsuki, A. Takeuchi, and H. Nagahama (2004), Frictional melting can terminate seismic slips, experimental results of stick-slips, *Geophys. Res. Lett.*, **31**, L21605.
- Linker, M. F., and J. H. Dieterich (1992), Effects of variable normal stress on rock friction: Observations and constitutive equations, *J. Geophys. Res.*, **97**, 4923–4940.
- Lockner, D. A., B. D. Kilgore, N. M. Beeler, and D. E. Moore (2017), The transition from frictional sliding to shear melting in laboratory experiments, in *Fault zone dynamic processes: Evolution of fault properties during seismic rupture*, Edited by M. Y. Thomas, T. M. Mitchell, and H. S. Bhat, this volume, AGU, Hoboken, NJ.
- Lockner, D. A., D. E. Moore, N. M. Beeler, and B. D. Kilgore (2010), Surface Melt Produced on Faults During Laboratory Stick-Slip Experiments, Abstract T23A-2245, presented at 2010 Fall Meeting, AGU, San Francisco, Calif., 13–17 Dec.
- Lockner, D. A., and P. G. Okubo (1983), Measurements of frictional heating in granite, *J. Geophys. Res.*, **88**, 4313–4320.
- McGarr, A. (1994), Some comparisons between mining-induced and laboratory earthquakes, *Pure Appl. Geophys.*, **142**, 467–489.
- McGarr, A. (1999), On relating apparent stress to the stress causing earthquake fault slip, *J. Geophys. Res.*, **104**, 3003–3011.
- McGarr, A. (2012), Relating stick-slip friction experiments to earthquake source parameters, *Geophys. Res. Lett.*, **39**, L05303, doi:10.1029/2011GL050327.
- McGarr, A., and J. B. Fletcher (2001), A method for mapping apparent stress and energy radiation applied to the 1994 Northridge Earthquake Fault Zone—Revisited, *Geophysical Research Letters*, **28**, 3529–3532, doi:10.1029/2001GL013094.
- McLaskey, G. C., B. D. Kilgore, D. A. Lockner, and N. M. Beeler (2015), A robust calibration technique for acoustic emission systems based on momentum transfer from a ball drop, *Bulletin of the Seismological Society of America*, **105**, 257–271, doi:10.1785/0120140170.
- Rice, J. R. (1993), Spatio-temporal complexity of slip on a fault, *J. Geophys. Res.*, **98**, 9885–9907.
- Rice, J. R., and S. T. Tse (1986), Dynamic motion of a single degree of freedom system following a rate and state dependent friction law, *J. Geophys. Res.*, **91**, 521–530.
- Savage, J. C., and M. D. Wood (1971), The relation between apparent stress and stress drop, *Bull. Seismol. Soc. Am.*, **61**, 1381–1388.
- Shelly, D. R., G. C. Beroza, S. Ide, and S. Nakamura (2006), Low frequency earthquakes in Shikoku, Japan, and their relationship to episodic tremor and slip, *Nature*, **442**, 188–191, doi:10.1038/nature04931.
- Shimamoto, T., J. Handin, and J. M. Logan (1980), Specimen-apparatus interaction during stick-slip in a triaxial compression machine: A decoupled tow-degree of freedom model, *Tectonophysics*, **67**, 175–205.
- Singh, S. K., and M. Ordaz (1994), Seismic energy release in Mexican subduction zone earthquakes, *Bull. Seismol. Soc. Am.*, **84**, 1533–1550.
- Wald, D. J., T. H. Heaton, and K. W. Hudnut (1996), The slip history of the 1994 Northridge, California, earthquake determined from strong motion, teleseismic, GPS, and leveling data, *Bull. Seismol. Soc. Am.*, **86**, S49–S70.
- Walsh, J. B. (1971), Stiffness in faulting and in friction experiments, *J. Geophys. Res.*, **76**, 8597–8598, doi:10.1029/JB076i035p08597.

# 9

## Dynamic Weakening and the Depth Dependence of Earthquake Faulting

Nicolas Brantut<sup>1</sup> and John D. Platt<sup>2</sup>

### ABSTRACT

Earthquake propagation is controlled by both the applied stresses and the dynamic frictional strength of fault rocks. Dynamic friction of rocks is characterized by strong weakening driven by shear heating and power dissipation. Here, we investigate the efficiency of two major weakening mechanisms, flash heating and thermal pressurization, as a function of depth across a range of representative geological settings. We first determine the relevant characteristic parameters for each mechanism. Flash heating is activated above a critical weakening velocity and controlled by two critical weakening times; thermal pressurization is controlled by a critical weakening strain at small slip and a critical weakening slip at large slip. We quantify how these parameters vary with pressure and temperature according to available published data, computing their values as a function of depth for a range of geological settings. We find that thermal pressurization is most efficient at shallow depths, with a peak efficiency at mid-crustal depths, while flash heating is most efficient in deeper parts of the faults. If driven by flash heating, earthquake ruptures appear to be able to propagate through the brittle-plastic transition. The arrest of ruptures at further depth is likely due to the decrease in the background driving stress.

### 9.1. INTRODUCTION

The Earth's seismicity is largely confined to the upper crust, typically above the 600 °C isotherm [McKenzie *et al.*, 2005], where rocks accommodate deformation by brittle failure. The maximum strength of the seismogenic crust is generally assumed to be the frictional resistance to sliding on an optimally oriented fault plane, which is well approximated by a frictional rupture envelope with a friction coefficient between 0.6 and 0.8 [e.g., Brace and Kohlstedt, 1980; Kohlstedt *et al.*, 1995]. However, this strength estimate is *local* and *static*: it is a measure of whether a faulted rock can slide or not. As such, it bears

no information about the *stability* of fault slip, which determines whether frictional deformation is steady and stable or whether earthquakes (i.e., unstable, fast, slip events) dominate the dynamics of faulting.

Determining when earthquake nucleation occurs requires additional knowledge about the details of the frictional constitutive law on the fault. In the framework of rate and state constitutive friction laws, a number of authors [e.g., Dieterich, 1978; Ruina, 1983] have demonstrated that the key parameter controlling the nucleation of earthquakes is the rate dependency of friction: steady-state velocity-strengthening faults slide stably while steady-state velocity-weakening faults are prone to dynamic instabilities. These theoretical considerations are supported by experimental and geological observations that show the depth distribution of seismicity in the crust and in subduction zones closely matches the depth dependence of the velocity-strengthening/weakening parameter of fault rocks, with shallow seismicity markedly decaying

<sup>1</sup>Rock and Ice Physics Laboratory and Seismological Laboratory, Department of Earth Sciences, University College London, London, UK

<sup>2</sup>Department of Terrestrial Magnetism, Carnegie Institution for Science, Washington, DC, USA

above the depth of the transition from velocity-weakening to velocity-strengthening friction [e.g., *Marone and Scholz*, 1988; *Scholz*, 1998]. Stability analyzes have shown that the earthquake nucleation size is much smaller (typically a few meters to tens of meters) than typical fault dimensions [e.g., *Rice and Ruina*, 1983; *Rice et al.*, 2001; *Rubin and Ampuero*, 2005; *Ampuero and Rubin*, 2008]. This raises the key following question: If an earthquake nucleates on a small portion of a fault, what controls its propagation and depth extent?

In contrast with local considerations of static strength, the problem of earthquake propagation is essentially a *non local* problem. Slip redistributes stress along the fault, with large stresses concentrated near the rupture tip, allowing slip to occur dynamically in regions where the initial background stress prior to the earthquake is significantly lower than the static brittle strength [e.g., *Rice*, 1996; *Lapusta and Rice*, 2003; *Rice*, 2006; *Noda et al.*, 2009]. The minimum background stress level above which earthquakes can propagate is controlled by how the fault dynamically weakens with increasing slip and slip rate. Therefore, the extent of seismic ruptures is controlled by a balance between the initial background stress distribution, which represents the stored elastic energy density, and the dynamic strength of the fault, which determines when and where energy is dissipated on the fault plane.

In the past decade, a number of experimental and theoretical studies have shown that fault rocks tend to weaken dramatically at high slip rates (typically above 0.1 m/s) [e.g., *Di Toro et al.*, 2011]. The weakening mechanisms vary between rock types and experimental conditions, but all are driven by the high dissipation rates associated with the onset of rapid slip. For dry rocks the dominant dynamic weakening mechanism in the earliest stages of slip is flash heating at asperity contacts [e.g., *Rice*, 1999, 2006; *Beeler et al.*, 2008; *Goldsby and Tullis*, 2011]. In this process, the macroscopic friction coefficient decreases at high slip rates because the local frictional heating at highly stressed asperity contacts is sufficient to melt or thermally decompose them. The slip displacement required to activate flash heating is comparable to the size of asperities, typically a few tens of micrometers, so flash heating commences as soon as dynamic rupture starts, provided that the slip rate exceeds a critical value. As we will show in section 9.2, even at moderate slip rates the increase in bulk temperature due to frictional heating tends to facilitate the activation of flash heating, so that this mechanism is likely to play a major role throughout dynamic ruptures.

Thermal pressurization is another dynamic weakening mechanism driven by thermal expansion of in-situ pore fluid [e.g., *Lachenbruch*, 1980; *Mase and Smith*, 1985, 1987; *Rice*, 2006], which leads to a decrease in effective stress and thus fault strength. Most estimates show that

thermal pressurization is expected to become significant for slips larger than a centimeter and potentially leads to a total loss of strength [e.g., *Noda and Shimamoto*, 2005; *Wibberley and Shimamoto*, 2005; *Rice*, 2006; *Rempel and Rice*, 2006]. Other weakening mechanisms may provide significant dynamic weakening at larger slips, including melting [e.g., *Hirose and Shimamoto*, 2005; *Di Toro et al.*, 2005], gel formation [*Goldsby and Tullis*, 2002; *Di Toro et al.*, 2004], or thermal decomposition [e.g., *Han et al.*, 2007; *Hirose and Bystricky*, 2007; *Brantut et al.*, 2008].

In order to understand what controls the maximum depth of earthquake propagation, we constrain the efficiency of flash heating and thermal pressurization as a function of depth in the crust. The term *efficiency* used here and throughout this chapter is defined as the rapidity with which the local fault strength decreases at the onset of slip. With increasing depth, changes in the ambient temperature, effective pressure, and physical properties of fault rocks (e.g., permeability, porosity) and pore fluid (thermal expansivity, compressibility) alter the efficiency of dynamic weakening significantly. In section 9.2, we review and further develop the physical models and key parameters governing weakening by flash heating and thermal pressurization. In section 9.3 we present and discuss the parameter values used as inputs for the two weakening models, as well as our selection of geotherms and rock types for three seismogenic environments: a continental strike-slip fault, an oceanic transform fault, and a subduction megathrust. The resulting profiles of the key weakening parameters, described in section 9.4, indicate that flash heating becomes increasingly efficient with depth, while thermal pressurization is most efficient at mid-crustal depths. Our results show that despite the high efficiency of flash heating at great depth, the relatively low background stress allowed by long-term creep mechanisms tends inevitably to stop earthquake propagation through the lower crust.

## 9.2. THERMALLY ACTIVATED WEAKENING MECHANISMS

In this section we summarize the theoretical background used to quantify the efficiency of thermal pressurization and flash heating. We study each mechanism in isolation, aiming to find a limited set of characteristic parameters that controls the rapidity and efficiency of weakening. In what follows, we emphasize the natural variables characterizing each model (e.g., slip, time, or strain) and the sensitivity to the exact slip rate history of the fault. Because we eventually aim to characterize the potency for rupture propagation, one key parameter to compute for each mechanism, context, and depth is the shear fracture energy  $G$ . Fracture energy is only well defined for a purely slip-dependent friction law with a constant residual

strength beyond a threshold slip [Palmer and Rice, 1973], a situation unlikely to occur during seismic slip. To avoid this issue, we use here the generalization given by Rice [2006], who defines  $G$  for an event with slip  $\delta$  as

$$G(\delta) = \int_0^\delta [\tau(\delta') - \tau(\delta)] d\delta', \quad (9.1)$$

where  $\tau$  is the shear stress on the fault and  $\delta$  is slip. Equation (9.1) is only valid for a monotonically decreasing shear strength  $\tau(\delta)$ , which will be the case throughout this paper. Complex rupture histories, including self-healing ruptures, would typically involve restrengthening near the rupture's tail, in which case a more general formula for  $G$  ought to be used [see, for instance, Garagash, 2012].

### 9.2.1. Flash Heating

Flash heating, adapted for rocks by Rice [1999, 2006] from a similar concept established in metal friction [Archard, 1958/1959], is based on the idea that the *local* temperature rise of a highly stressed frictional asperity far exceeds the average bulk temperature rise. The high temperatures at these microscale asperities during rapid slip trigger weakening mechanisms such as melting or thermal decomposition at the contact scale that lead to significant drops in the macroscopic friction coefficient. The analysis of flash heating presented in this section summarizes previous theoretical results obtained by Rice [1999], Rice [2006], Rempel [2006], Beeler *et al.* [2008], Proctor *et al.* [2014] and Platt *et al.* [2014a], and we refer the reader to these studies for further details of the analysis.

To begin, we use the slip rate  $V$  and a typical asperity contact size  $D$  to estimate the contact lifetime

$$t_{\text{con}} = \frac{D}{V}. \quad (9.2)$$

For typical seismic slip rates of the order of  $1 \text{ ms}^{-1}$  and contact sizes of a few tens of microns,  $t_{\text{con}}$  is just a few tens of microseconds, allowing us to assume that the slip rate and bulk fault temperature  $T$  do not change during the lifetime of a single contact. Assuming that all sliding occurs on a plane, we use a Green's function to solve for the temperature evolution of the contact,

$$T_{\text{con}} = T + \frac{\tau_c V}{\rho c} \sqrt{\frac{1}{\pi \alpha_{\text{th}}}}, \quad (9.3)$$

where  $T$  is the fault bulk temperature,  $\tau_c$  is the shear stress supported by the contact,  $t$  is the time since the contact came into existence,  $\rho c$  is the effective heat capacity per unit reference volume, and  $\alpha_{\text{th}}$  is the thermal

diffusivity. Next we assume that weakening occurs if the contact temperature exceeds a weakening temperature  $T_w$ , which corresponds to a threshold temperature for either melting or thermal breakdown of the contact. Equation (9.3) shows that the contact temperature reaching  $T_w$  is equivalent to the contact lifetime exceeding a critical weakening timescale

$$t_{\text{cw}} = \pi \alpha_{\text{th}} \left( \frac{\rho c (T_w - T)}{\tau_c V} \right)^2. \quad (9.4)$$

Thus, flash heating occurs if  $t_{\text{con}} > t_{\text{cw}}$ , which is equivalent to the slip rate exceeding a critical weakening slip rate

$$V_w(T) = \frac{\pi \alpha_{\text{th}}}{D} \left( \frac{\rho c (T_w - T)}{\tau_c V} \right)^2. \quad (9.5)$$

Next we predict the dependence of the macroscopic friction coefficient on slip rate when flash heating is active by calculating the time the contact spends in the weakened and unweakened states. We assume that in the unweakened state the macroscopic friction coefficient is  $f_0$  and model weakening by lowering this value to a weakened friction coefficient  $f_w$ . As shown in Rice [2006] and Beeler *et al.* [2008], the macroscopic friction is equal to

$$f = f_0 \frac{t_{\text{cw}}}{t_{\text{con}}} + f_w \left( 1 - \frac{t_{\text{cw}}}{t_{\text{con}}} \right), \quad (9.6)$$

which rearranges to give

$$f = (f_0 - f_w) \frac{V_w(T)}{V} + f_w. \quad (9.7)$$

The assumption that weakening can be modeled by instantaneously dropping the contact strength to a weakened value is crude, though Rempel and Weaver [2008] and Chen and Rempel [2014] developed a better model accounting for the thin melt layer that forms at a contact. However, Goldsby and Tullis [2011] found good agreement with equation (9.7) in experiments on a range of materials, suggesting that this formula provides a good first-order estimate of the weakening from flash heating.

In the previous steps we assumed that the contact scale slip rate is equal to the macroscopic slip rate. While this assumption is valid for sliding of bare surfaces, it is not a good approximation for distributed deformation in a gouge. Rempel [2006] and Beeler *et al.* [2008] modeled flash heating in a gouge by assuming that the total slip rate is shared between an array of contacts. For an array of contacts, weakening occurs when the *local* slip rate at each contact reaches the nominal weakening slip rate  $V_w$ ,

which implies that the effective weakening velocity for slip across gouge is, on average,

$$V_{w,\text{gouge}}(T) = V_w(T) \times N_c, \quad (9.8)$$

where  $N_c$  is the number of contacts mobilized across the gouge and is typically around 10 to 20 (see Rice [2006], section 1.1).

While flash heating is naturally expressed in terms of a critical weakening slip rate and previous experiments have mostly focused on the slip rate dependence, Platt *et al.* [2014a] recently argued that temperature effects dominate flash heating at seismogenic depths. The critical weakening slip rate decreases as the fault temperature rises, leading to potentially significant weakening, as demonstrated experimentally in Proctor *et al.* [2014]. To quantify the temperature weakening effects, we model the evolution of fault bulk temperature during seismic slip. Initially the thermal boundary layer adjacent to the deforming gouge is much smaller than the gouge thickness and therefore the early stages of slip occur under mostly adiabatic conditions. By contrast, for large slips (or a thin gouge layer) the thermal boundary layer becomes much wider than the shear zone width, and the behavior is expected to be well approximated by a model in which slip occurs on a mathematical plane. In the remainder of this section we develop these two end-member solutions and determine the associated characteristic weakening parameters.

To model flash heating under macroscopically adiabatic conditions, we follow the model of Platt *et al.* [2014a]. Conservation of energy leads to an equation for the bulk temperature  $T$ :

$$\frac{\partial T}{\partial t} = \frac{\tau V}{\rho c W}, \quad (9.9)$$

Where  $\tau$  is the macroscopic shear strength of the gouge layer and  $W$  is the thickness of the deforming gouge. Setting the shear strength equal to the product of the ambient effective stress ( $\sigma_n - p_0$ ) and the velocity-dependent friction coefficient, we obtain

$$\frac{\partial T}{\partial t} = \frac{f_0(\sigma_n - p_0)}{\rho c} \frac{\pi \alpha_{th}}{DW/N_c} \left( \frac{\rho c(T_w - T)}{\tau_c} \right)^2, \quad (9.10)$$

where we have assumed that  $f_w = 0$  and that the slip rate is greater than the initial value of  $V_w$ . Note that because the friction coefficient for flash heating is proportional to  $1/V$ , the rate of frictional heating, and thus the evolution of  $V_w$  is independent of slip rate. However, the friction coefficient is controlled by the ratio  $V_w/V$  so

the shear strength evolution of flash heating is sensitive to the exact slip rate history of the fault.

We solve equation (9.10) to find the bulk temperature evolution

$$T(t) = T_0 + (T_w - T_0) \frac{t}{t + t_w^A}, \quad (9.11)$$

which is controlled by the critical weakening timescale for adiabatic conditions

$$t_w^A = \frac{(W/N_c)D\tau_c^2}{f_0(\sigma_n - p_0)\pi\alpha_{th}\rho c(T_w - T_0)}. \quad (9.12)$$

Inserting equation (9.11) for the temperature evolution in the gouge into the constitutive relation (7) (with the critical velocity  $V_{w,\text{gouge}}$ ), we observe that the shear stress evolution is controlled by the weakening time  $t_w^A$ . Using the shear stress evolution  $\tau(t) = f(t) \times (\sigma_n - p_0)$ , we find that the fracture energy for flash heating under adiabatic conditions is

$$G(t) = W\rho c(T_w - T_0) \frac{t}{t_w^A + t} \left( 1 - \frac{t_w^A}{t_w^A + t} \right), \quad (9.13)$$

which tends to

$$G_{FH}^A = W\rho c(T_w - T_0) \quad (9.14)$$

for  $t \gg t_w^A$ . The fracture energy is simply the energy required to heat the gouge from the ambient temperature  $T_0$  up to the weakening temperature  $T_w$ .

At large slips, where the shear zone width is much smaller than the thickness of the thermal boundary layer adjacent to the deforming zone, we can model deformation as slip on a mathematical plane. For this limit, the bulk temperature evolution in the deforming zone is solved for using a Green's function to find [Carslaw and Jaeger, 1959]

$$T(t) = T_0 + \int_0^t \frac{\tau(s)V(s)}{\rho c} \frac{1}{\sqrt{4\pi\alpha_{th}(t-s)}} ds. \quad (9.15)$$

Using the velocity-dependent expression for strength given in equation (9.7) (where as before we neglect the contribution of  $f_w$ ), we nondimensionalize equation (9.15) to find

$$\tilde{T}(\tilde{t}) = \int_0^{\tilde{t}} \frac{(1 - \tilde{T})^2}{\sqrt{4\pi(\tilde{t} - \tilde{s})}} d\tilde{s}, \quad (9.16)$$

where dimensionless variables are denoted with tildes and we use the scalings  $T = T_a + (T_w - T_a)\tilde{T}$  and  $t = t_w^{SP}\tilde{t}$ , defining the weakening timescale as

$$t_w^{SP} = \frac{\alpha_{th}}{V_{w,gouge}} \left( \frac{\rho c (T_w - T_0)}{f_0 (\sigma_n - p_0)} \right)^2. \quad (9.17)$$

Equation (9.16) shows that the temperature evolution is of the form

$$T(t) = T_0 + (T_w - T_0) F\left(\frac{t}{t_w^{SP}}\right), \quad (9.18)$$

where  $F(\cdot)$  is a nondimensional, monotonically growing function with  $F(0) = 0$  and  $\lim_{t \rightarrow \infty} F(t) = 1$ . An asymptotic analysis of equation (9.16), checked against numerical solutions, shows that

$$T(t) \approx T_0 + (T_w - T_0) \left( 1 - \sqrt{2} \left( \pi t / t_w^{SP} \right)^{-1/4} \right) \quad (9.19)$$

for  $t \gg t_w^{SP}$ . The temperature evolution, and therefore the strength evolution, is controlled by a single characteristic weakening timescale  $t_w^{SP}$  given by equation (9.17). Note that as in the solution for adiabatic conditions given in equation (9.11), the temperature evolution in the slip-on-a-plane limit is independent of the exact slip rate history of the fault because the friction coefficient is proportional to  $1/V$ . Thus, the evolution of  $V_w$  is independent of the exact slip rate history of the fault, though the strength evolution of the fault is still sensitive to the slip rate history because the friction coefficient is equal to  $V_w/V$ .

For deformation at constant slip rate, the weakening timescale given in equation (9.17) directly translates into a slip weakening distance. For the slip-on-a-plane limit we calculate the fracture energy

$$G_{FH}^{SP} = \frac{\tau_c^2 D}{N_c \pi f_0 (\sigma_n - p_0)} \times F'\left(\frac{t}{t_w^{SP}}\right), \quad (9.20)$$

where  $F'(\cdot)$  is again a nondimensional, monotonically growing function, but not bounded.  $F'$  cannot be determined in closed form, and we use a numerical solution to calculate  $F'$ , avoiding further approximations. Nevertheless, based on the asymptotic form (19) for temperature, we can determine the following asymptotic scaling of fracture energy for  $t \gg t_w^{SP}$ :

$$G_{FH}^{SP}(t) \approx \frac{\tau_c^2 D}{N_c \pi f_0 (\sigma_n - p_0)} \left( 2 \sqrt{\frac{t}{\pi t_w^{SP}}} \right), \quad (9.21)$$

which shows that the leading term at large time is proportional to  $\sqrt{t}$ .

### 9.2.2. Thermal Pressurization of Pore Fluid

Our analysis for thermal pressurization closely follows previous work by Lachenbruch [1980], Mase and Smith [1985], Mase and Smith [1987], Rice [2006], and Rempel and Rice [2006]. Here we summarize the main results and governing equations, and refer the reader to the aforementioned literature for the details of the model and solutions. We consider a one-dimensional model of a gouge layer with thickness  $W$  sheared between two undeforming half-spaces with a slip rate  $V$ .

Conservation of energy leads to an equation for  $T$  that balances frictional heating and thermal diffusion,

$$\frac{\partial T}{\partial t} = \frac{\tau \dot{\gamma}}{\rho c} + \alpha_{th} \frac{\partial^2 T}{\partial y^2}, \quad (9.22)$$

where  $\tau$  is the shear stress in the gouge layer and  $\dot{\gamma}$  is the strain rate. Following previous work, we have assumed here that all of the frictional work is converted into heat and that the gouge properties are constant in space and time. In addition, we have neglected small heat fluxes associated with pore fluid flow, which Mase and Smith [1985] and Mase and Smith [1987] showed is a good assumption for typical fault rock permeabilities.

In a fluid saturated material, the increase in temperature induced by shear heating leads to an increase in pore pressure due to the difference between the thermal expansivities of the fluid and of the rock. Conservation of pore fluid mass leads to an equation for the pore pressure  $p$  that balances thermal pressurization and hydraulic diffusion,

$$\frac{\partial p}{\partial t} = \Lambda \frac{\partial T}{\partial t} + \alpha_{hy} \frac{\partial^2 p}{\partial y^2}, \quad (9.23)$$

where  $\Lambda$  is the ratio of pore pressure rise to temperature rise for undrained conditions and  $\alpha_{hy}$  is the hydraulic diffusivity. As before, we have assumed that the gouge properties are constant in space and time. The parameter  $\Lambda$  controls the efficiency of the thermal pressurization process and is defined as

$$\Lambda = \frac{\lambda_f - \lambda_n}{\beta_f + \beta_n}, \quad (9.24)$$

where  $\lambda_f$  and  $\lambda_n$  are the thermal expansion coefficients of the fluid and of the pore space, and  $\beta_f$  and  $\beta_n$  are the compressibilities of the fluid and of the pore space, respectively. The hydraulic diffusivity is expressed as

$$\alpha_{hy} = \frac{k_f}{n(\beta_n + \beta_f)\eta}, \quad (9.25)$$

where  $k_f$  is the permeability of the rock,  $n$  is the porosity, and  $\eta$  is the viscosity of the saturating fluid.

The governing equations for temperature and pore pressure are linked to the fault strength  $\tau_{\text{fault}}$  through the Terzaghi effective stress, which combines with the friction coefficient  $f$  to give

$$\tau_{\text{fault}} = f(\sigma_n - p_0). \quad (9.26)$$

For simplicity and throughout the remainder of this chapter we assume a constant friction coefficient. This simplification allows us to investigate thermal pressurization independently from flash heating.

To close the model, we need an equation to describe how strain is distributed across the deforming gouge. Previously published models typically choose a fixed spatial distribution of strain rate, the amplitude of which can vary in time [e.g., *Andrews*, 2002; *Rempel and Rice*, 2006; *Noda et al.*, 2009]. In the spirit of making elementary estimates, we choose a simple model with uniform shear in the deforming zone,

$$\dot{\gamma} = \frac{V}{W} \quad \text{when } |y| < W/2. \quad (9.27)$$

The assumption of a constant deforming zone thickness is likely a great simplification. *Rice et al.* [2014] and *Platt et al.* [2014b] showed that thermal pressurization drives significant strain localization, as first suggested in *Rice* [2006]. However, *Platt et al.* [2014b] showed that while strain localization greatly influences the details of shear strength evolution at large slip, the early stages of slip, for which undrained and adiabatic conditions best apply, remain controlled by the initial imposed thickness  $W$ . Therefore, the first-order model based on equation (27) still provides excellent estimates for the efficiency of weakening by thermal pressurization under adiabatic, undrained conditions.

Two well-studied limits exist for thermal pressurization, controlled by the ratio between the thickness of the deforming gouge and the thickness of the diffusive boundary layer that forms adjacent to it. During the early stages of slip, the effects of hydrothermal diffusion are negligible and deformation occurs under effectively undrained and adiabatic conditions. At large slips the diffusive boundary layer is much greater than the deforming zone thickness, allowing deformation to be modeled as slip on a mathematical plane. *Rempel and Rice* [2006] showed that for intermediate slips the shear strength smoothly transitions from the undrained and adiabatic limit to the slip-on-a-plane limit, and thus these two limits can be used to estimate the efficiency of thermal pressurization.

First we analyze the small-slip limit, where thermal pressurization occurs under undrained and adiabatic

conditions. *Lachenbruch* [1980] solved for the shear strength evolution in this limit to find

$$\tau_{\text{fault}} = f(\sigma_n - p_0) \exp\left(-\frac{f\Lambda}{\rho c} \frac{\delta}{W}\right), \quad (9.28)$$

where  $p_0$  is the ambient pore pressure before the onset of rapid slip and  $\delta$  is the total slip accommodated across the gouge layer, defined as

$$\delta(t) = \int_0^t V(s) ds. \quad (9.29)$$

Equation (9.28) shows that thermal pressurization under undrained and adiabatic conditions is controlled by a critical weakening strain

$$\gamma_c = \frac{\rho c}{f\Lambda}, \quad (9.30)$$

and is insensitive to details of the slip rate history. For sustained slip at high velocity, equation (9.28) predicts a total loss of strength. The existence of a critical strain indicates that the slip required to produce a given amount of weakening scales linearly with the deforming zone thickness, making thermal pressurization most effective when straining is highly localized. The temperature evolution for an undrained adiabatic deformation is given by [Lachenbruch, 1980]

$$T = T_0 + \frac{\sigma_n - p_0}{\Lambda} \left(1 - \exp\left[-\frac{f\Lambda}{\rho c} \frac{\delta}{W}\right]\right), \quad (9.31)$$

where  $T_0$  is the ambient temperature before the onset of rapid slip. The total strength drop associated with thermal pressurization leads to a finite maximum temperature rise:

$$\Delta T_{\max}^{\text{UA}} = \frac{\sigma_n - p_0}{\Lambda}. \quad (9.32)$$

Finally, we estimate the fracture energy  $G$  by inserting the shear strength given in equation (9.28) into equation (9.1). For deformation under undrained and adiabatic conditions we find that  $G$  tends to

$$G_{\text{TP}}^{\text{UA}} = W \frac{\rho c (\sigma_n - p_0)}{\Lambda}. \quad (9.33)$$

for  $\delta \gg \gamma_c \times W$ . The fracture energy for undrained and adiabatic conditions can be understood physically by noting that  $G_{\text{TP}}^{\text{UA}} = f(\sigma_n - p_0)\delta_c$ .

Next we analyze the large-slip limit, where deformation can be modeled as slip on a mathematical plane. Assuming a constant slip rate, *Rice* [2006] solved for this limit accounting for hydraulic and thermal diffusion, extending previous work of *Mase and Smith* [1985, 1987] that accounted for thermal or hydraulic diffusion alone, to find the shear strength evolution

$$\tau_{\text{fault}} = f(\sigma_n - p_0) \exp\left(\frac{\delta}{L^*}\right) \operatorname{erfc}\left(\sqrt{\frac{\delta}{L^*}}\right), \quad (9.34)$$

where  $L^*$  is a critical weakening slip defined as

$$L^* = \frac{4\alpha}{V} \left( \frac{\rho c}{f \Lambda} \right)^2 \quad (9.35)$$

and  $\alpha = (\sqrt{\alpha_{\text{th}}} + \sqrt{\alpha_{\text{hy}}})^2$  is a lumped hydrothermal diffusivity. Similarly to deformation under undrained and adiabatic conditions, thermal pressurization in the slip-on-a-plane limit leads to a total strength drop, though this is now controlled by the critical weakening slip  $L^*$ . Analytic solutions do not exist for arbitrary nonconstant slip rate histories, but we expect the shear strength evolution to depend sensitively on the slip rate history. The solutions of *Garagash* [2012] and *Viesca and Garagash* [2015] for self-healing slip pulses driven by thermal pressurization show that if the slip rate is initially high and subsequently drops, as expected during dynamic rupture propagation, hydrothermal diffusion can dominate the evolution of temperature and pore pressure, leading to rapid restrengthening. Nevertheless, equation (9.34) provides a useful end-member estimate for weakening by thermal pressurization at large slip. *Rice* [2006] also provides a closed-form solution for the maximum temperature increase on the sliding surface,

$$\Delta T_{\text{max}}^{\text{SP}} = \left( 1 + \sqrt{\frac{\alpha_{\text{hy}}}{\alpha_{\text{th}}}} \right) \frac{\sigma_n - p_0}{\Lambda}. \quad (9.36)$$

As for deformation under undrained and adiabatic conditions, the total strength drop associated with thermal pressurization leads to a finite temperature rise. Finally, to estimate the fracture energy we use the asymptotic expression from *Rice* [2006],

$$G_{\text{FH}}^{\text{SP}}(\delta) \approx f(\sigma_n - p_0) \sqrt{(\delta L^*)/\pi}, \quad (9.37)$$

which is valid when  $\delta \gg L^*$ . In contrast with thermal pressurization operating under undrained and adiabatic conditions, the fracture energy in the slip on plane limit is unbounded at large slip. Equation (9.37) shows that the

fracture energy is proportional to the initial shear strength  $f(\sigma_n - p_0)$  multiplied by a length found by taking the geometric mean of the characteristic weakening slip  $L^*$  and the total slip  $\delta$ .

### 9.3. PARAMETER VALUES AND GEODYNAMIC SETTINGS

As observed above, the efficiency of flash heating and thermal pressurization depends on a number of parameters that vary with rock type, stress, pore pressure, and temperature. In this section we describe how we estimate these parameters and present a selection of ambient temperature and stress profiles for continental, oceanic, and subduction faults.

Not all parameters have the same impact on the final results. Therefore, we use relatively precise values and include temperature and pressure dependencies only for those that provide key controls on the weakening processes. For flash heating, we account for variation of both mechanical (asperity yield strength) and thermal parameters (heat capacity and diffusivity). For thermal pressurization, we account for variations in all the parameters entering into the thermal pressurization factor  $\Lambda$  and the hydraulic diffusivity  $\alpha_{\text{hy}}$ .

Unfortunately, several important parameters are only loosely constrained (for example, the weakening temperature  $T_w$  and the pore pressure distribution at depth), and we therefore choose representative estimates rather than arbitrary specific values.

#### 9.3.1. Flash Heating: Yield Strength and Thermal Properties

Because flash heating is largely controlled by asperity-scale thermal and mechanical parameters, we use parameters associated with individual minerals rather than bulk ones. Here, we use thermal and strength data for two major rock-forming minerals, quartz and olivine, which will serve as representative minerals for the continental and oceanic (both in place and subducted) crust, respectively. Note that our model for the evolution of fault temperature involves thermal parameters related to the bulk; for simplicity, we assume that the bulk properties take the same values as the asperity-scale properties.

Thermal conductivity ( $k_T$ ) and heat capacity ( $\rho c$ ) data as a function of temperature for both quartz and olivine are taken from *Clauser and Huenges* [1995], and the data are interpolated with cubic splines to produce smoothly varying functions. For quartz, *Clauser and Huenges* [1995] provide data for two crystallographic orientations, and we use the arithmetic average of these data at each temperature.

The stress at asperity contacts is given by

$$\tau_c \approx f \times \sigma_A, \quad (9.38)$$

where  $f$  is a microscopic friction coefficient and  $\sigma_A$  the asperity yield stress. We use  $f = 0.6$  and  $\sigma_A$  values derived from hardness measurements as a function of temperature taken from *Evans and Goetze* [1979] (for olivine) and *Evans* [1984] (for quartz). For each mineral, the yield strength data are fitted with a second order polynomial to produce regular functions of temperature. The yield strength  $\sigma_A$  typically ranges from 2 to 5 GPa in olivine and from 7 to 13 GPa in quartz, between room temperature and 750 °C.

The weakening temperature  $T_w$  corresponds to the threshold temperature above which an asperity loses its strength. It is generally associated with the melting temperature or thermal decomposition temperature, which varies from mineral to mineral [e.g., *Rempel and Weaver*, 2008]. However, the precise mechanisms responsible for strength loss are not clear and do not necessarily correspond to conventional melting: minerals like quartz can be amorphized and form a gel [*Goldsby and Tullis*, 2002], and large concentrated strains can influence the melting temperature. Due to the large uncertainties, we follow here the approach of *Goldsby and Tullis* [2011] and assume a constant  $T_w = 1000^\circ\text{C}$  as an approximate weakening temperature.

A key parameter in the flash heating model is the diameter of microscale asperities  $D$ . In experimental studies, this parameter is often used as a fitting parameter with typical values of a few to tens of microns, but so far it has not been measured directly. Here we estimate how  $D$  depends on temperature and stress by modeling how the highly stressed contacts yield. In this approach we assume that the number of contacts remains the same with increasing stress, and that only the surface area of the contact changes. Following the method used by *Boettcher et al.* [2007] and *Hirth and Beeler* [2015], we compute  $D$  from the ratio of the real to nominal area of contact between the two rock surfaces, which is given by the ratio of the applied effective normal stress to the asperity yield strength (see *Scholz* [2002]):

$$\frac{A_R}{A} = \frac{\sigma_n - p_0}{\sigma_A}, \quad (9.39)$$

where  $A_R$  and  $A$  are the real and nominal area of contact per asperity, respectively. Inserting  $A_R = \pi D^2 / 4$  into equation (9.39) yields

$$D = D_0 \sqrt{\frac{\sigma_n - p_0}{\sigma_A}}, \quad (9.40)$$

where  $D_0 = \sqrt{4A/\pi}$  is a prefactor with dimension of length. Experimental results for flash heating between bare rock surfaces [*Goldsby and Tullis*, 2011; *Passelègue et al.*, 2014] indicate  $D$  values of the order of 10 μm at normal stresses of a few MPa at room temperature, which yields  $D_0$  values of the order of 200 μm.

### 9.3.2. Thermal Pressurization: Thermal and Hydraulic Properties

The efficiency of thermal pressurization depends on the hydraulic and thermal properties of the fault rock, as well as thermodynamic properties of the pore fluid. Here we are interested in essentially three different fault zone lithologies: one representative of a fault hosted in the igneous continental crust (e.g., granite), one for a mature, gouge-bearing crustal fault, and one for faults hosted in the oceanic crust (the same lithology is used for both in place and subducted oceanic crust). In all these cases we assume that the pore fluid is pure water and neglect any compositional effects on water properties.

Estimating the thermo-poro-elastic parameters  $\lambda_n$  and  $\beta_n$  used to compute the thermal pressurization factor  $\Lambda$  (equation (9.24)) requires some assumptions about the fault stresses (see discussion in *Rice* [2006], Appendix A). We follow here the hypothesis that the fault walls behave elastically, for which *Rice* [2006] gives the following expressions for the pore space compressibility and thermal expansivity:

$$\beta_n = \frac{(\beta_d - \beta_s)(\beta_d + r\beta_s)}{n(1+r)\beta_d} - \beta_s, \quad \lambda_n = \lambda_s \left( 1 - \frac{r}{(1+r)} \frac{\beta_d - \beta_s}{n\beta_d} \right), \quad (9.41)$$

where  $\beta_d$  is the drained compressibility of the rock,  $\beta_s$  and  $\lambda_s$  are the compressibility and thermal expansivity of the solid skeleton, respectively, and  $\lambda_s$  is a function of the drained Poisson's ratio of the rock. Following *Rice* [2006] we choose  $r = 1$ , which corresponds to a drained Poisson's ratio of 0.20. The estimates given in equations (9.41) are not valid for very large pore pressure and temperature rises (i.e., for large slip), since they lead to unsustainable differential stresses on the fault walls [*Rice*, 2006, Appendix A2]. Here, we are interested in stages of seismic slip where the pore pressure has not yet reached elevated values close to  $\sigma_n$ , and it is therefore reasonable to assume that the deformation around the fault core remains elastic.

For the case of faults hosted in igneous rocks, we choose compressibility values measured in sheared granitic gouge by *Zhang et al.* [1999]. The drained  $\beta_d$  was computed from the fault zone thickness vs. effective stress data, and is  $\beta_d = \beta_s + 1.1 \times 10^{-9} \exp(-(\sigma_n - p_0)/p_\beta)$  Pa<sup>-1</sup>, where  $p_\beta = 45.5$  MPa. We add the term  $\beta_s$  to ensure

that the drained compressibility of the rock does not fall below the compressibility of the solid grains, and thus  $\beta_n$  remains positive. The compressibility of solid grains is taken as that of a granitic composition and is  $\beta_s = 1.6 \times 10^{-11} \text{ Pa}^{-1}$ , as in Rice [2006]. For gouge, we use the drained compressibility measured by Wibberley and Shimamoto [2003] and reported by Rice [2006] as  $\beta_d = \beta_s + 1.39 \times 10^{-10} \exp(-(\sigma_n - p_0)/p_\beta) \text{ Pa}^{-1}$ , where  $p_\beta = 144.7 \text{ MPa}$ . The compressibility of the solid is generally much lower than the compressibility of the fluid  $\beta_f$ , so that our regularization of  $\beta_d$  using the additional  $\beta_s$  term has no quantitative impact at high effective pressure but provides a natural lower limit on compressibility at low effective pressure.

For all cases, the thermal expansivity of the solid particles is taken as  $\lambda_s = 2.45 \times 10^{-5} \text{ }^\circ\text{C}^{-1}$ . The thermal expansivity of the pore space is in general smaller than that of the pore fluid, so that the variations in  $\lambda_s$  arising from the range of modeled lithologies and pressure and temperature conditions do not produce significant changes in the thermal pressurization factor  $\Lambda$ .

The properties of the pore fluid, assumed to be pure water, vary widely as a function of pressure and temperature. The two key parameters, thermal expansivity  $\lambda_f$  and compressibility  $\beta_f$ , decrease with increasing pressure and increasing temperature. We compute the pore fluid thermal expansivity, compressibility, and viscosity as a function of  $p$  and  $T$  using the formulation given by the International Association for the Properties of Water and Steam [Wagner and Prupf, 2002; Junglas, 2009].

The permeability of fault rocks generally depends on effective stress according to an exponential relation. For igneous rocks, we use the permeability values measured in sheared granitic rocks [Zhang *et al.*, 1999], which yield  $k_f = 10^{-19} \exp(-(\sigma_n - p)/p_k) \text{ m}^2$ , where  $p_k = 357.1 \text{ MPa}$ . For gouge, we use the permeability measured in the central gouge zone of the Median Tectonic Line (Japan), reported by Rice [2006] as  $k_f = 2.12 \times 10^{-19} \exp(-(\sigma_n - p)/p_k) \text{ m}^2$ , where  $p_k = 34.7 \text{ MPa}$ .

The porosity of the rock within the central slip zone is computed as a function of the effective normal stress. For all cases except the clay-rich gouge, we use a porosity of  $n = 0.05 \times [1 + \exp(-(\sigma_n - p)/p_n)]$  with  $p_n = 45.5 \text{ MPa}$ , estimated from the dilation vs. pressure data given by Zhang *et al.* [1999]. For the clay-rich gouge, we use an exponential fit to the values reported by Rice [2006], which yields  $n = 0.06 \times \exp(-(\sigma_n - p)/p_n)$  with  $p_n = 263.2 \text{ MPa}$ .

The thermal diffusivity plays a less prominent role in the thermal pressurization model than in the flash heating model. Therefore, for the thermal pressurization computations we chose an average, constant value of  $\alpha_{th} = 1 \text{ mm}^2 \text{ s}^{-1}$ . Similarly, the heat capacity is assumed constant and equal to  $\rho c = 2.7 \text{ MPa } ^\circ\text{C}^{-1}$  [see Vosse and Schellschmidt, 2003].

All the above properties vary during slip as the pore pressure and temperature rise. However, the models presented in section 9.2 are only valid for constant parameter values. Here, we want to retain the essential features of the model while accounting for the variations in properties with pressure and temperature. To achieve this goal, we compute *path-averaged* properties based on the approach proposed by Rice [2006]. First, for each scenario (ambient temperature, pressure, and rock type) we compute *nominal* properties using the conditions at the onset of seismic slip. Second, we use the nominal properties to predict the pore pressure and temperature path as a function of slip using either the adiabatic and undrained or the slip-on-plane scenario. Finally, we compute path averaged properties using slip as the weight function:

$$\langle X \rangle = \frac{1}{\delta} \int_0^\delta X[p(\delta'), T(\delta')] d\delta', \quad (9.42)$$

where  $\langle X \rangle$  is the path averaged value of  $X(p, T)$  and  $\delta$  is slip. The net slip over which equation (9.42) is computed is either set to  $\delta_c$  in the case of adiabatic, undrained computations or to  $L^*$  in the case of slip-on-a-plane computations. Thus, for each scenario we produce two values of  $\alpha_{hy}$  and  $\Lambda$ , one thought to best describe the early stages of weakening and another that describes the weakening at larger slips.

In all thermal pressurization computations, we choose a constant slip rate of  $V = 1 \text{ m s}^{-1}$ , which is commonly used as a typical seismic slip rate [e.g., Brune, 1970]. The relevant friction coefficient at this slip rate is potentially affected by the flash heating mechanism. Rice [2006] and Rempel and Rice [2006] assumed reduced values of friction, as low as 0.25, to approximate the nearly-instantaneous effect of flash heating. However, this approach may not be valid for deforming gouge where flash heating is less effective because the effective critical weakening velocity is multiplied by the number density of contacts in the gouge width (typically at least a factor of  $N_c = 10$ ). Therefore, we choose here a “Byerlee”-type friction coefficient of  $f = 0.6$ , allowing us to study thermal pressurization in isolation. This choice of a relatively high value of  $f$  implies that our results will be upper bounds for the efficiency of thermal pressurization (i.e., lower bounds for  $\gamma_c$  and  $L^*$ ).

### 9.3.3. Thermal and Effective Stress Profiles

We investigate the dynamic weakening behavior of faults within three major geodynamic settings: active continental crust (where we use either clay-bearing or crushed granite as fault gouge material), near-ridge oceanic crust (which hosts oceanic transform faults), and subduction zones. The key difference between these

settings is the local geotherm, and to a lesser extent the lithostatic and hydrostatic stress profile.

Geotherms in tectonically active regions of the continental crust are quite variable, especially in their deepest parts [Jaupart and Mareschal, 2007]. Here we focus on the shallow seismogenic crust (typically above the 600°C isotherm), where surface heat flow measurements, together with estimates of radiogenic heat production, provide a solid estimate of temperature profiles. We follow a standard model using an exponential decay of radiogenic heat production with depth over a characteristic distance  $h_r = 10$  km, so that the temperature profile is given by Turcotte and Schubert [2002]:

$$T_0(z) = T_{\text{surface}} + \frac{A_0 h_r^2}{k_{\text{crust}}} (1 - e^{-z/h_r}) + \frac{(q - A_0 h_r) z}{k_r}, \quad (9.43)$$

where we use a surface temperature  $T_{\text{surface}} = 13^\circ\text{C}$ , an average thermal conductivity of  $k_{\text{crust}} = 3 \text{ W}^\circ\text{C}^{-1} \text{ m}^{-1}$  [Chapman, 1986; Jaupart and Mareschal, 2007], a nominal rate of internal energy production of  $A_0 = 2 \mu \text{W m}^{-3}$  [Turcotte and Schubert, 2002], and a surface heat flux of  $q = 80 \text{ mW m}^{-2}$  (based on heat flow measurements near the San Andreas fault, from Lachenbruch and Sass [1980]). We use an average rock density of  $2800 \text{ kg m}^{-3}$  to compute the lithostatic stress profile. The ambient pore pressure is assumed hydrostatic, and we calculate the ambient pore pressure profile using a pore pressure gradient of  $9.8 \text{ MPa km}^{-1}$ . This pressure gradient is based on a constant fluid density: the assumption of a hydrostatic pore fluid pressure at depth is a relatively strong one, and a detailed model including water density variations appears unnecessary at this stage.

The thermal structure of the oceanic crust is much better constrained than that of the active continental crust. It is well approximated by a cooling plate model, which is a function of the age of the crust [e.g., Turcotte and Schubert, 2002]:  $T_0(z) = T_M \text{erf}\left(z/\left(2\sqrt{k_T t_{\text{crust}}/\rho c}\right)\right)$ , where  $T_M$  is the mantle temperature, set to  $T_M = 1350^\circ\text{C}$ ,  $z$  is the depth, and  $t_{\text{crust}}$  is the age of the crust. For our calculations we used a heat conductivity of  $k_T = 3.14 \text{ W}^\circ\text{C}^{-1} \text{ m}^{-1}$  [Parsons and Sclater, 1977], and a crustal age of 1.25 My, which corresponds to a relatively young oceanic crust hosting an oceanic transform fault. The normal stress and pore pressure profiles in the oceanic crust are computed using a rock density of  $3200 \text{ kg m}^{-3}$  and a pore pressure gradient of  $9.8 \text{ MPa km}^{-1}$ . In addition, we considered a water depth above the crust of 2 km, which offsets both the ambient normal stress and pore pressure values by 20 MPa.

Finally, for the thermal profile of the subduction settings we assume a linear gradient of  $6^\circ\text{C km}^{-1}$ , which corresponds to a relatively cold subduction (e.g., Tohoku

or Nankai; see Hacker *et al.* [2003]). The rock density used to compute the lithostatic stress is  $3200 \text{ kg m}^{-3}$ , and we assume a water depth above the crust of 10 km, which offsets the normal stress and pore pressure by 100 MPa. In subduction zones, dehydration reactions of hydrous phases at depth tend to promote elevated pore pressures along the subduction interface [e.g., Peacock *et al.*, 2011]. We therefore tested two ambient pore pressure profiles, one hydrostatic ( $9.8 \text{ MPa km}^{-1}$ ) and another with elevated (near lithostatic) pore pressures ( $27.6 \text{ MPa km}^{-1}$ ), which corresponds to a pore pressure-to-lithostatic pressure ratio of 0.9.

## 9.4. DEPTH- AND CONTEXT-DEPENDENT DYNAMIC WEAKENING PROFILES

In this section we combine the parameter choices justified in section 9.3 with the models developed in section 9.2 to predict how the efficiency of dynamic weakening varies within the seismogenic zone. To begin, we analyze flash heating and thermal pressurization individually, then compare these results to predict how the dominant weakening mechanisms changes with depth.

### 9.4.1. Flash Heating

The critical weakening velocity  $V_{w,\text{gouge}}$  and characteristic weakening times  $t_w^A$  and  $t_w^{\text{SP}}$  for flash heating are plotted as a function of depth in Figure 9.1. In all cases,  $V_{w,\text{gouge}}$  decreases with increasing depth. In the continental crust, based on quartz mineral data,  $V_{w,\text{gouge}}$  decreases from around  $1 \text{ ms}^{-1}$  in subsurface conditions down to less than  $0.1 \text{ ms}^{-1}$  at 20 km depth, near the 600°C isotherm. The critical weakening velocities computed from olivine data are higher than those computed from quartz data due to the lower asperity strength  $\tau_c$ , and typically are of a few  $\text{ms}^{-1}$  at the top of the oceanic crust and subduction zones, and decrease by a factor of around 5 at 6 km and 50 km depth, respectively. For near-lithostatic pore pressure gradients (dashed lines in Figure 9.1c),  $V_{w,\text{gouge}}$  is offset toward higher values because the lower effective stresses induce lower asperity contact sizes  $D$  (see equation [9.40]).

The characteristic weakening times  $t_w^A$  and  $t_w^{\text{SP}}$  tend to either decrease or remain constant with increasing depth. In the continental crust, both these times remain of the order of  $10^{-2}$  s:  $t_w^A$  is approximately constant throughout the profile, while  $t_w^{\text{SP}}$  first decreases from around  $5 \times 10^{-2}$  s to  $10^{-2}$  s in the top 10 km, and then remains nearly constant below. By contrast, in both oceanic and subduction environments the weakening times monotonically decrease with increasing depth. In our modeled oceanic transform fault,  $t_w^A$  and  $t_w^{\text{SP}}$  are both of the order of  $10^{-2}$  s near the top of the crust, and decrease down to  $t_w^A = 1.8 \times 10^{-3}$  s and  $t_w^{\text{SP}} = 3.6 \times 10^{-4}$  s at 6 km depth. Similarly, in the modeled

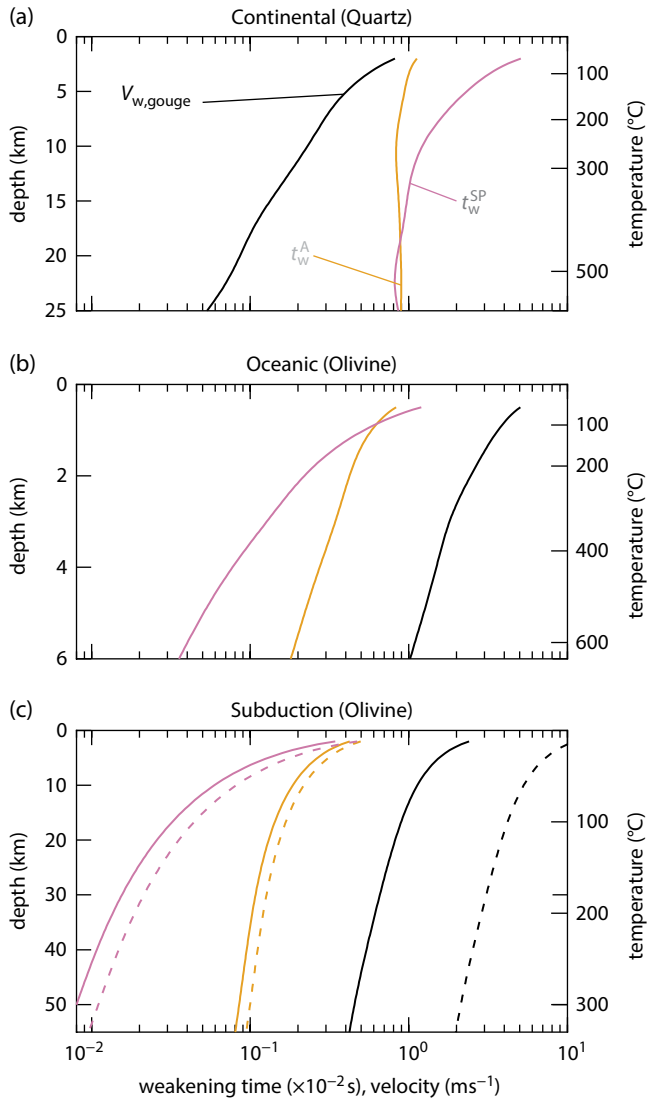


**Figure 9.1** Critical weakening velocity and weakening times for the flash heating mechanism, in continental (a), oceanic (b) and subduction (c) settings. The weakening time for adiabatic conditions  $t_w^A$  is computed using  $W = 100 \mu\text{m}$ . The solid and dashed lines in panel (c) correspond to hydrostatic and near-lithostatic pore pressure gradients, respectively. See electronic version for color representation.

subduction zone,  $t_w^A$  decreases from  $4.2 \times 10^{-3}$  s to  $8.0 \times 10^{-4}$  s between subsurface and 55 km depth, while  $t_w^{\text{SP}}$  drops from  $3.4 \times 10^{-3}$  s to  $7.0 \times 10^{-5}$  s over the same depth range. The change between hydrostatic and near-lithostatic pore pressure gradients does not affect the weakening times significantly, only by about 15% to 30%.

For comparison, we performed additional computations using a constant asperity size  $D = 10 \mu\text{m}$ , shown in Figure 9.2, which correspond to scenarios where the increase in real area of contact with effective normal stress is only due to an increase in the number of contacts.

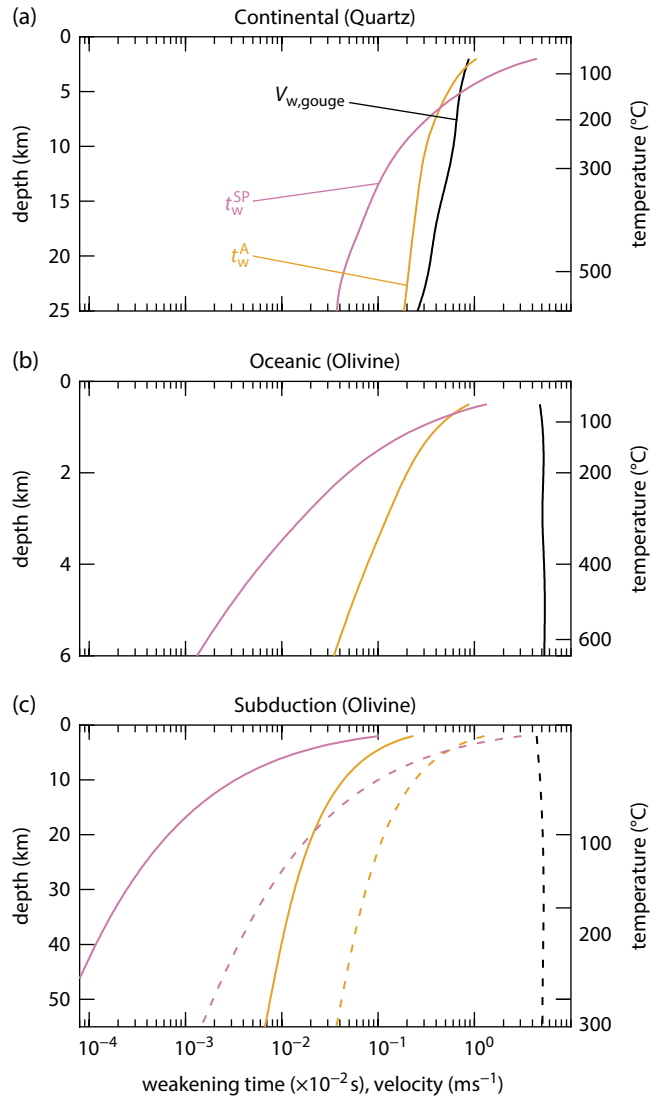


**Figure 9.2** Critical weakening velocity and weakening times for the flash heating mechanism assuming constant asperity diameter  $D = 10 \mu\text{m}$ , in continental (a), oceanic (b) and subduction (c) settings. The weakening time for adiabatic conditions  $t_w^A$  is computed using  $W = 100 \mu\text{m}$ . The solid and dashed lines in panel (c) correspond to hydrostatic and near-lithostatic pore pressure gradients, respectively. See electronic version for color representation.

These complementary tests show that the weakening velocity decreases only mildly or remains constant with increasing depth, while both weakening times decrease much more strongly compared to the case with variable  $D$ . These observations are consistent with the increase in contact size  $D$  with increasing depth, as computed from equation (9.40), and shown in Figure 9.3. If the increase in true contact area with increasing normal stress is accommodated by a combination of growing existing contacts and form new contacts, then the true depth dependence of flash heating likely lies between the two end-members shown in Figures 9.1 and 9.2.

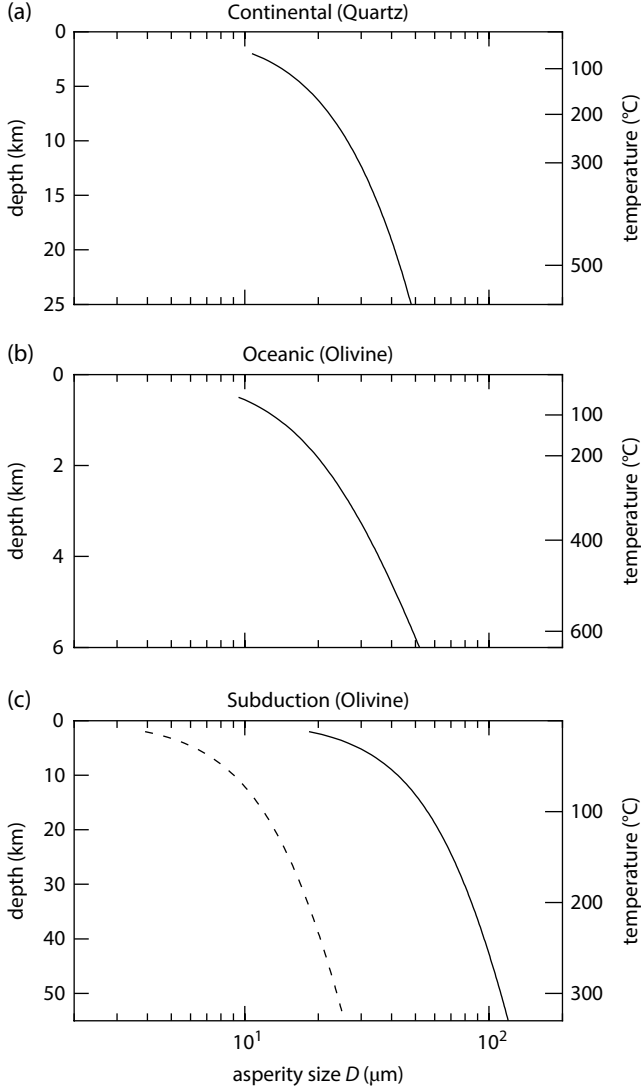


**Figure 9.3** Asperity contact size  $D$  as a function of depth in continental (a), oceanic (b) and subduction (c) settings., as computed from equation (9.40). Solid lines correspond to hydrostatic pore pressure gradients, and dashed line (in subplot [c]) corresponds to sublithostatic pore pressure gradients.

Overall, our results show that flash heating typically becomes more efficient with increasing depth, with lower critical weakening velocities and shorter weakening times. Temperature changes tend to reduce the weakening velocity and produce weakening in the first  $10^{-4}$  to  $10^{-1}$  s of slip. The decrease in  $V_{w,\text{gouge}}$  with depth is essentially due to the decrease in the difference between ambient and weakening temperatures ( $T_w - T_0$ ). However, the decrease in  $(T_w - T_0)$  with depth is somewhat compensated for by the concomitant decrease in yield stress  $\sigma_A$  and increase in heat diffusivity, so that the net change in  $V_w$  (and hence in  $V_{w,\text{gouge}}$ ) is rather moderate.

Our modeling results are qualitatively consistent with the experimental data of *Proctor et al.* [2014], which show

a more abrupt weakening with increasing normal stress. However, our results differ slightly from those of *Passelègue et al.* [2014], who showed a modest increase in  $V_w$  with increasing ambient temperature from room temperature to 300°C. A number of factors can explain this discrepancy, the major one being the sensitivity of the results to slight changes in  $\sigma_A$  and heat conductivity. In addition, the calculations of *Passelègue et al.* [2014] did not account for changes in asperity size, which tend to decrease the weakening velocity at increasing temperatures. Despite these uncertainties, we expect that the strong sensitivity of  $V_w$  to  $T_0$ , as shown in equation (9.5), overtakes other possibly counteracting effects at high temperatures.

#### 9.4.2. Thermal Pressurization

The efficiency of thermal pressurization relies heavily on the thermal pressurization factor  $\Lambda$ , which combines the thermo-poro-elastic properties of the fault rock and of the pore fluid. Depth profiles of  $\Lambda$  are shown in Figure 9.4. For each setting and rock type, two path-averaged values of  $\Lambda$  are given, one corresponding to the undrained, adiabatic limit (u.a.), and the other to the slip-on-a-plane limit (s.p.). In Figure 9.4, dashed parts of the curves indicate that the peak temperature (computed using equations [9.32] and [9.36]) during thermal pressurization exceeds 1100°C, which is taken as a representative bulk melting temperature.

For a fault hosted in the continental crust (Figure 9.4a),  $\Lambda$  is typically low near the surface: between 0.23 and 0.30 MPa °C<sup>-1</sup> in the granite gouge and between 0.44 and 0.58 MPa °C<sup>-1</sup> in the clay-rich gouge.  $\Lambda$  increases with increasing depth and reaches a maximum at depths between 8 and 13 km, below which it decreases again. In the undrained, adiabatic limit,  $\Lambda$  peaks at 0.81 MPa °C<sup>-1</sup> in the clay-rich gouge and at 0.97 MPa °C<sup>-1</sup> in the granite gouge. In the slip-on-a-plane limit, the peak in  $\Lambda$  is less marked (around 0.6 and 0.7 MPa °C<sup>-1</sup> for the granite and clay-rich gouge, respectively) and at shallower depths. The evolution of  $\Lambda$  with depth in our modeled oceanic crust is qualitatively similar to that in the continental crust (Figure 9.4b):  $\Lambda$  is relatively small near the surface (between 0.1 and 0.2 MPa °C<sup>-1</sup>), increases with depth up to a peak (around 0.5 MPa °C<sup>-1</sup> at depths between 2 and 4 km), and then decreases in deeper parts of the crust. In the subduction zone setting with hydrostatic pore pressure gradient (Figure 9.4c, black curves),  $\Lambda$  increases very markedly with depth and reaches values between 1.5 and 2.4 MPa °C<sup>-1</sup> at depths ranging from 20 to 35 km. By contrast, under near-lithostatic pore pressure conditions (gray curves), the increase in  $\Lambda$  is less pronounced, and both estimates (undrained adiabatic and slip on a plane) yield similar values reaching around 0.6 MPa °C<sup>-1</sup> at 50 km depth.

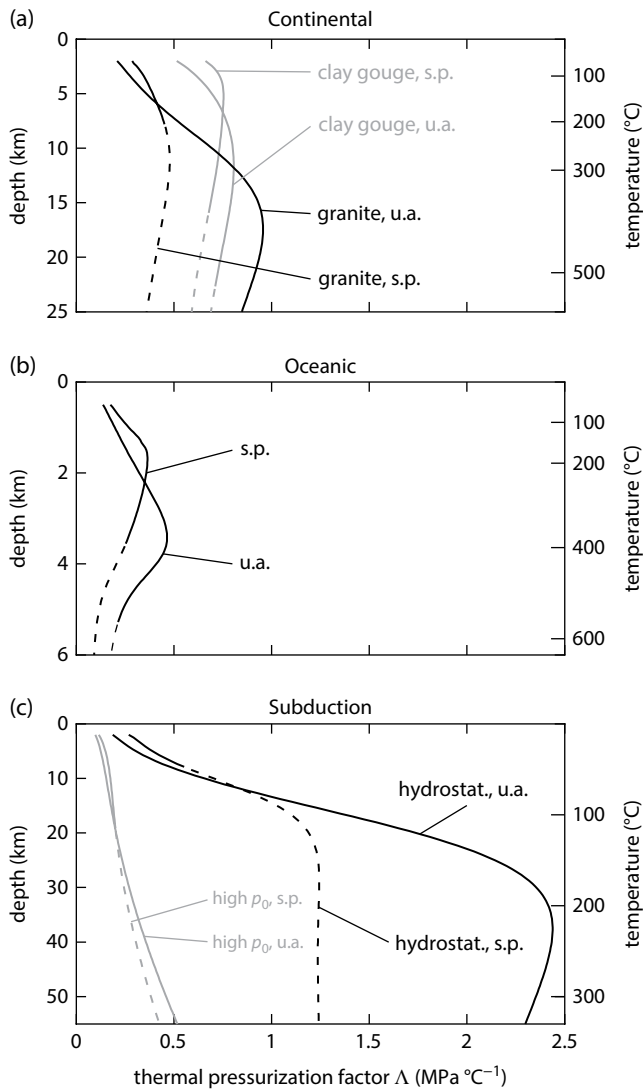


**Figure 9.4** Path-averaged value of the thermal pressurization factor  $\Lambda$  as a function of depth for continental (a), oceanic (b), and subduction (c) environments. For every case, two estimates are given: one for the slip-on-a-plane path (s.p.) and one for the undrained, adiabatic path (u.a.). Dashed sections of the curves corresponds to cases when the peak temperature during thermal pressurization is beyond 1100°C, which is chosen as the bulk melting point.

The evolution in  $\Lambda$  is essentially linked to the change in thermodynamic properties of water with pressure and temperature. This is illustrated in Figure 9.5, which compares  $\Lambda$  and the ratio  $\lambda_f/\beta_f$  (i.e., the thermal pressurization factor that would be obtained if the rock was incompressible). With increasing depth, both  $\lambda_f$  and  $\beta_f$  tend to increase, but  $\beta_f$  increases faster so that the ratio  $\lambda_f/\beta_f$  tends to decrease. In the shallow parts of the crust,  $\Lambda$  is significantly lower than  $\lambda_f/\beta_f$  because the pore space has a high compressibility, but the difference decreases

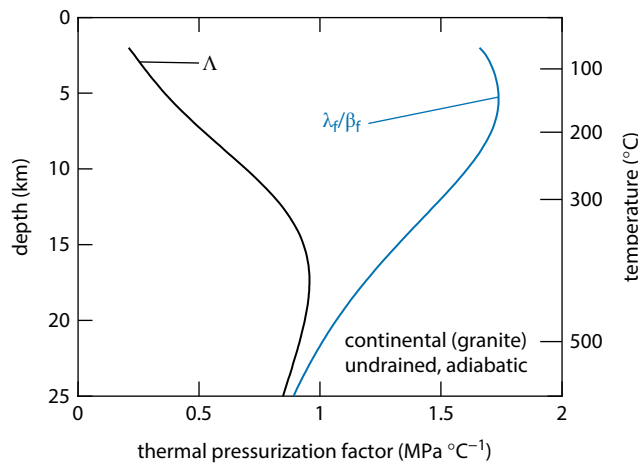


**Figure 9.5** Comparative evolution of the thermal pressurization factor  $\Lambda$  and the ratio  $\lambda_f/\beta_f$  with depth. This example corresponds to the continental geotherm, granite gouge properties, and values obtained from the undrained, adiabatic path. See electronic version for color representation.

with increasing depth owing to the pressure-dependency of the pore space compressibility. The peak in  $\Lambda$  occurs when the increase in  $\beta_f$  compensates the decrease in  $\beta_n$  with increasing depth.

The other key parameter controlling thermal pressurization is the hydraulic diffusivity  $\alpha_{hy}$ . Figure 9.6 summarizes the path-averaged diffusivity profiles for the continental, oceanic, and subduction contexts. For the clay-rich gouge material, the hydraulic diffusivity decreases markedly with increasing depth. In all other cases, the hydraulic diffusivity tends to remain constant (in the oceanic context) or increase with depth. Such an evolution is explained by comparing the pressure sensitivity of permeability to the pressure (and temperature) sensitivity of the storage capacity  $n(\beta_n + \beta_f)$ : the permeability of the clay-bearing gouge decreases strongly with effective pressure (small value of  $p_k$ ), whereas both the porosity and pore compressibility depend only moderately on pressure (relatively large values of  $p_\beta$  and  $p_n$ ). By contrast, the permeability of the granitic gouge (chosen in all other scenarios) exhibits a rather moderate pressure sensitivity (large  $p_k$ ), while both the porosity and compressibility decrease more strongly with pressure (small  $p_\beta$  and  $p_n$ ). In all cases, the decrease in fluid viscosity  $\eta_f$  with increasing temperature also contributes to increase the hydraulic diffusivity at depth.

Based on the path-averaged values of  $\Lambda$ ,  $\alpha_{hy}$ , and the remaining parameters, we compute estimates of the critical weakening strain  $\gamma_c$  and critical slip  $L^*$ . Figure 9.7 shows a series of profiles for the three representative settings. In all cases, the evolution in  $\gamma_c$  clearly mirrors the evolution in  $\Lambda$ , and exhibits a minimum at midcrustal depths. In the continental setting,  $\gamma_c$  ranges from 10 to 20

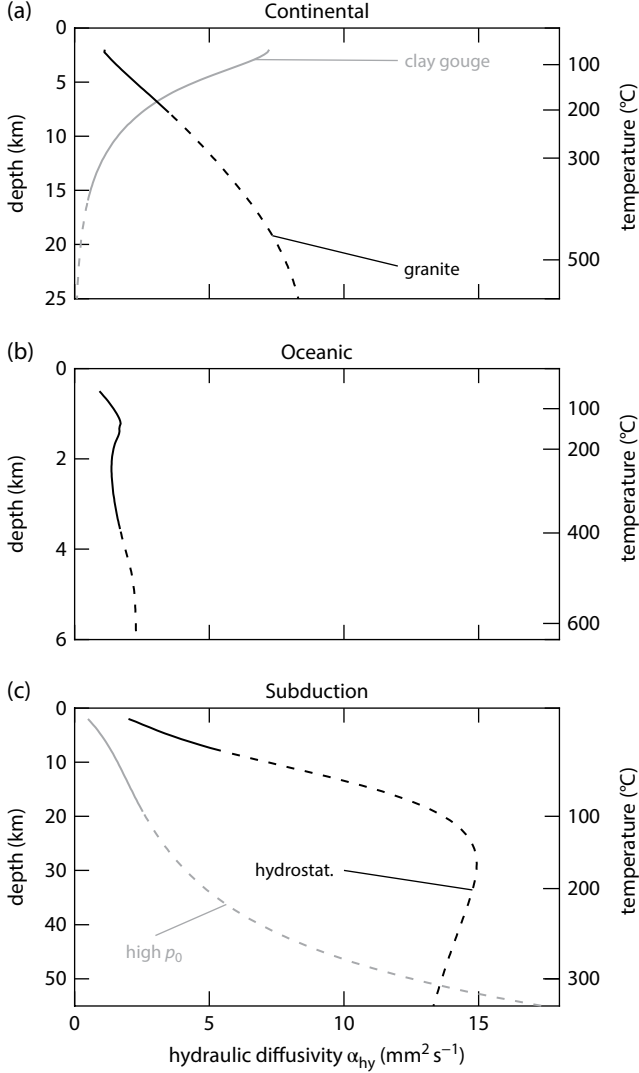


**Figure 9.6** Profiles of the path-averaged hydraulic diffusivity  $\alpha_{hy}$  in continental (a), oceanic (b), and subduction (c) settings. Dashed parts of each curve correspond to depths at which the peak temperature during thermal pressurization is above  $1100^\circ\text{C}$ .

near the surface and decreases to a minimum of around 5 at around 10 km depth. In the oceanic setting,  $\gamma_c$  follows a qualitatively similar evolution, with a shallow maximum around 30, and a midcrustal minimum of around 10. In the subduction setting,  $\gamma_c$  monotonically decreases from shallow to deep parts by a factor of 10 and 7 for hydrostatic and near-lithostatic pore pressure gradients, respectively. The depth profiles of  $L^*$  typically follow the profiles of  $\gamma_c$  at shallow depth, but  $L^*$  tends to remain small in deeper parts of the crust. The magnitude of  $L^*$  ranges between 0.5 and 15 mm, with the smallest values corresponding to the clay-rich gouge (which has a low hydraulic diffusivity).

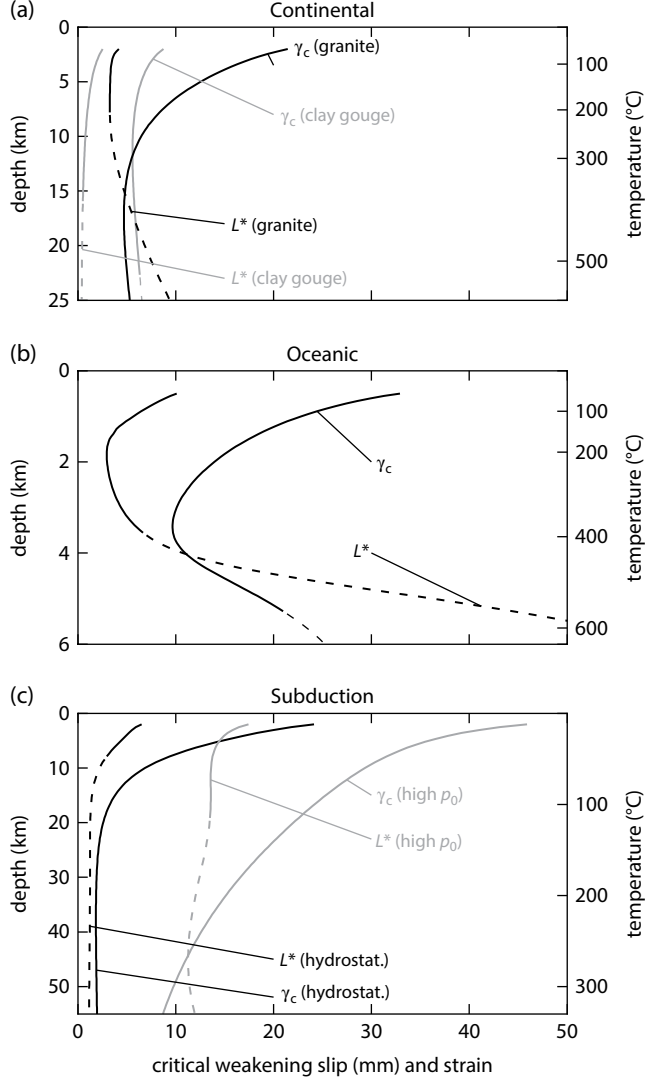


**Figure 9.7** Profiles of the critical weakening strain  $\gamma_c$  and slip  $L^*$  in continental (a), oceanic (b), and subduction (c) settings. Dashed parts of each curve correspond to depths at which the peak temperature during thermal pressurization is above  $1100^\circ\text{C}$ .

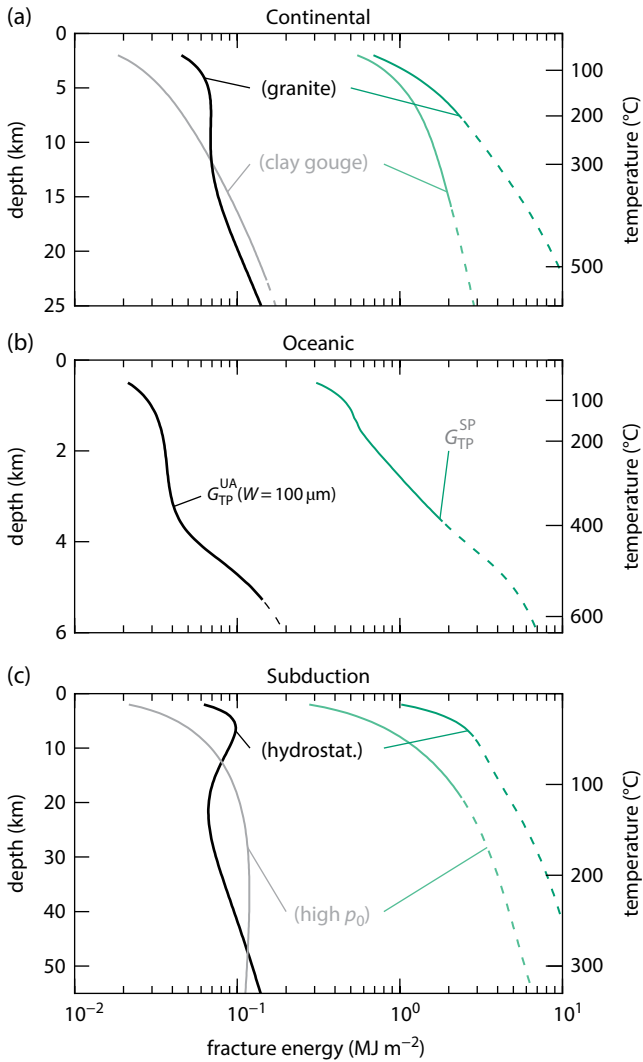
#### 9.4.3. Relation to Earthquake Dynamics

Overall, our computations of  $\gamma_c$  and  $L^*$  show that the efficiency of thermal pressurization increases with depth, reaching a peak at midcrustal depths. Flash heating is also more efficient with increasing depth, with decreasing critical weakening velocity and weakening times.

A more integrated estimate of the impact of thermal pressurization and flash heating on earthquake propagation is the fracture energy, which measures the energy required to advance the rupture front during an earthquake. As noted in section 9.2, some fracture energy estimates for flash heating and thermal pressurization

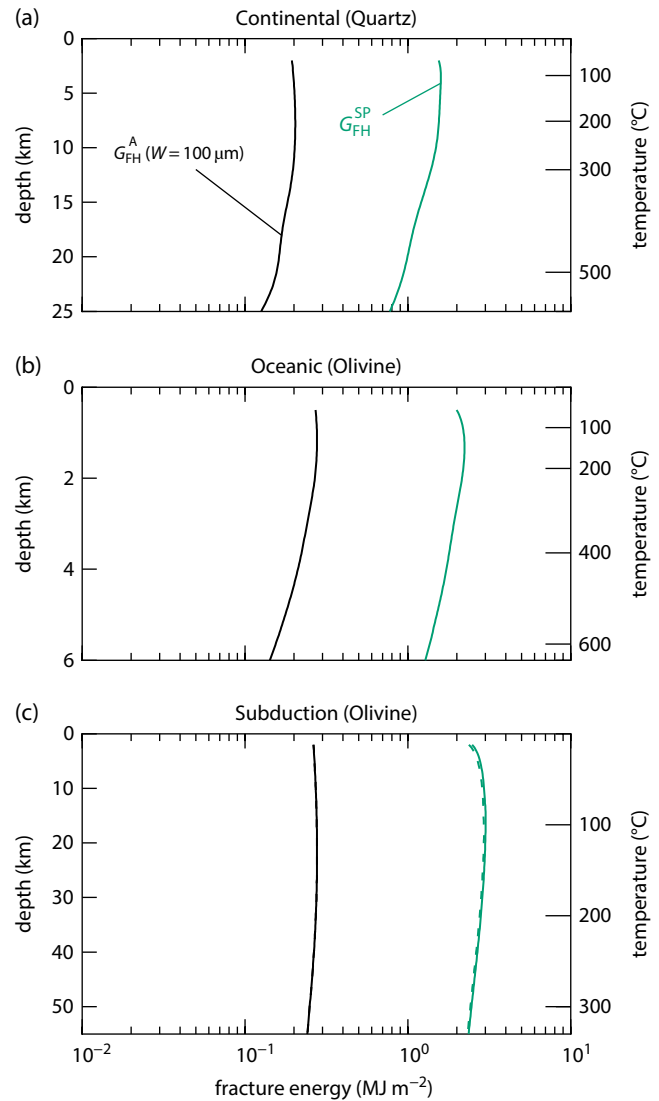
have an explicit dependence on total slip. For simplicity, we arbitrarily fix the slip at 1 m, which is representative of an Mw 6 earthquake. This allows us to easily compare the trends for fracture energy evolution vs. depth.

Figure 9.8 shows the profiles of  $G_{\text{TP}}^{\text{UA}}$  and  $G_{\text{TP}}^{\text{SP}}$ , computed using a total slip of  $\delta = 1 \text{ m}$ . For a shear zone width of  $W = 100 \mu\text{m}$ ,  $G_{\text{TP}}^{\text{UA}}$  typically increases from around  $2 \times 10^{-2}$  to  $2 \times 10^{-1} \text{ MJ m}^{-2}$  from shallow to deep parts of all our modeled settings. Remarkably, most profiles exhibit a minimum or at least a plateau at midcrustal depths, which reflects the existence of a peak in  $\Lambda$  at these depths. In the slip-on-a-plane limit, the computed fracture energy  $G_{\text{TP}}^{\text{SP}}$  also increases with increasing depth, with values ranging from around  $3 \times 10^{-1}$  to around  $5 \text{ MJ m}^{-2}$  in the deepest sections.



**Figure 9.8** Profiles of fracture energy from thermal pressurization in the undrained, adiabatic limit ( $G_{\text{TP}}^{\text{UA}}$ , black and grey curves, computed using  $W = 100 \mu\text{m}$ ) and slip-on-a-plane limit ( $G_{\text{TP}}^{\text{SP}}$ , green curves), computed at  $\delta = 1 \text{ m}$  slip, in continental (a), oceanic (b) and subduction (c) settings. See electronic version for color representation.

By contrast, the values of fracture energy computed from the flash heating mechanism, shown in Figure 9.9, generally remain constant or slightly decrease with increasing depth. Under adiabatic conditions, weakening by flash heating due to thermal effects corresponds to a fracture energy of the order of  $10^{-1} \text{ MJ m}^{-2}$ , with little variation (no more than a factor of 2) with depth in all our modeled settings. In the slip-on-a-plane limit, the fracture energy exhibits a similar trend, but at average values of the order of  $1 \text{ MJ m}^{-2}$ . The inferred range between 1 and  $10 \text{ MJ m}^{-2}$  is well within the observed



**Figure 9.9** Profiles of fracture energy from flash heating in the adiabatic limit ( $G_{\text{FH}}^{\text{A}}$ , black curves, computed using  $W = 100 \mu\text{m}$ ) and slip-on-a-plane limit ( $G_{\text{FH}}^{\text{SP}}$ , green curves), computed at  $\delta = 1 \text{ m}$  slip, in continental (a), oceanic (b) and subduction (c) settings. Solid lines correspond to hydrostatic pore pressure gradients, and dashed line (in subplot [c]) corresponds to sublithostatic pore pressure gradients. See electronic version for color representation.

range for earthquakes associated with a few meters of slip [Viesca and Garagash, 2015].

The comparison between fracture energies computed for weakening by thermal pressurization and flash heating in each limit (adiabatic/undrained or slip on a plane) shows that thermal pressurization tends to correspond to lower fracture energies at shallow depths, typically in the top 5 km, and is hence expected to be the dominant weakening process (at least for ruptures with slip of a few meters). In deeper parts of faults, flash heating becomes more efficient (essentially due to a decrease in the asperity yield stress and the proximity of the ambient temperature to the weakening temperature) and produces lower fracture energies than thermal pressurization. Furthermore, especially in the slip-on-a-plane limit, thermal pressurization tends to induce unreasonably large maximum temperature rises (beyond the bulk melting point; see dashed parts of curves in Figure 9.8). If the bulk melting temperature is reached, the model of thermal pressurization becomes invalid and different physical processes need to be accounted for. In some rock types, thermal decomposition might also occur, buffering the local temperature and providing another source of fluid pressure [e.g., Sulem and Famin, 2009; Brantut et al., 2010, 2011].

Figures 9.8 and 9.9 were obtained assuming a total slip distance of 1 m; however, for both mechanisms, flash heating and thermal pressurization, fracture energy tends to increase with slip. Figure 9.10 is a plot illustrating how fracture energy evolves across a wide range of slip distances, taken at depths of 3 km (left) and 10 km (right) in the case of continental crust. The curves for thermal

pressurization (in black) essentially reproduce the results from Rice [2006], showing an increase in  $G$  as  $\delta^{1/2}$  for large slip (in the slip-on-a-plane limit), and another scaling as  $\delta^2$  at small slip (in the adiabatic, undrained limit) [Viesca and Garagash, 2015]. Similarly, for flash heating, the adiabatic limit shows a scaling of  $G$  as  $t^2$ , which leads to  $G \propto \delta^2$  at constant slip rate. For longer time (or slip) scales, in the slip-on-a-plane limit, the fracture energy associated with flash heating shows a milder scaling, with a slip exponent approaching 1/2 (see equation [9.21]). Figure 9.10 clearly illustrates the overall decrease in  $G$  with depth for flash heating, over the whole computed range of total slip, together with the increase in  $G$  with depth for thermal pressurization. In addition to this general trend, some complexity appears at shallow depth, where the mechanism associated with the lowest fracture energy switches from flash heating at small slip to thermal pressurization at large slip. This highlights the limitation of our approach, which analyzes the two mechanisms separately, and clearly demonstrates the need for a coupled approach. An additional natural step is to also include realistic slip rate histories during rupture, as done for instance in Viesca and Garagash [2015].

Velocity-weakening mechanisms like flash heating tend to produce different rupture styles than slip-weakening mechanisms, with a propensity to develop self-healing as opposed to crack-like ruptures [e.g., Cochard and Madariaga, 1994; Zheng and Rice, 1998]. As demonstrated by Zheng and Rice [1998], in velocity-weakening faults there exists a critical background shear stress, denoted  $\tau_{\text{pulse}}$ , below which no crack-like ruptures can

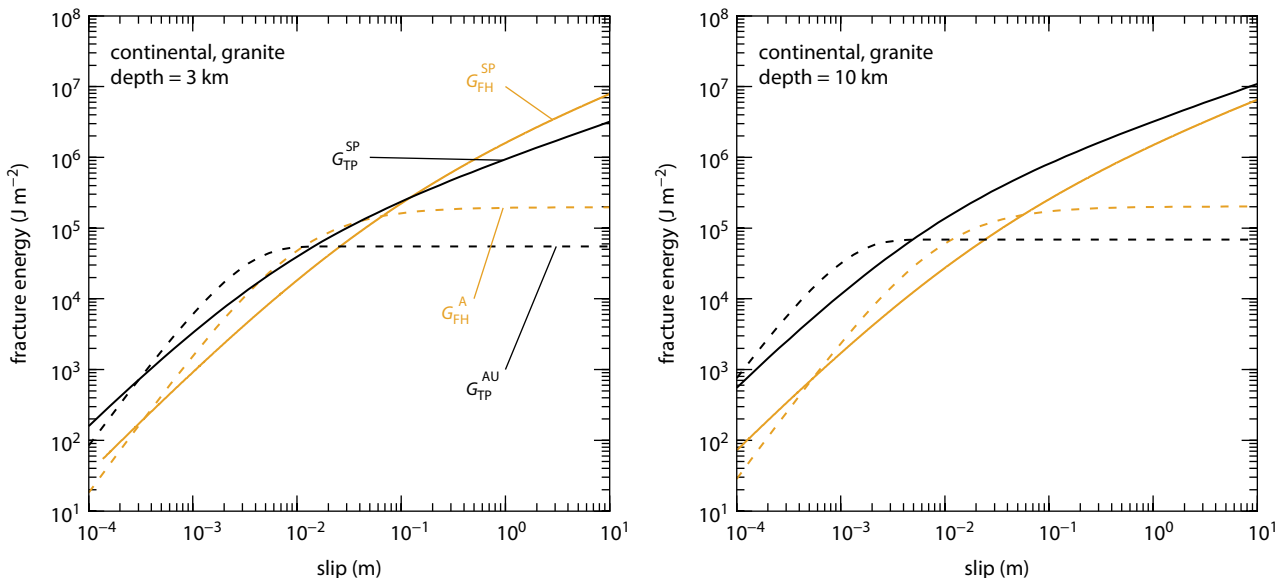


**Figure 9.10** Estimates of fracture energy for both thermal pressurization and flash heating, as a function of slip, illustrated in the case of the continental crust at 3 km (left) and 10 km (right) depth. For the adiabatic (undrained) limits, a shear zone width of  $W = 100 \mu\text{m}$  is chosen. In all cases a constant slip rate of  $V = 1 \text{ ms}^{-1}$  is imposed. See electronic version for color representation.

propagate and the only possible rupture mode is a self-healing slip pulse. For stresses significantly below the threshold  $\tau_{\text{pulse}}$ , propagating ruptures tend to behave as decaying slip pulses and naturally stop, while at larger stresses ruptures are expanding slip pulses and beyond  $\tau_{\text{pulse}}$  they become crack-like. Therefore,  $\tau_{\text{pulse}}$  is an instructive measure of the possible rupture styles and of the threshold stress below which ruptures will naturally arrest.

Following *Zheng and Rice* [1998],  $\tau_{\text{pulse}}$  is defined as the maximum background stress  $\tau_b$  satisfying  $\tau_b - (\mu/2c_s)V \leq \tau(V)$ , where  $\mu$  is the shear modulus of the material hosting the rupture,  $c_s$  is its shear wave speed,  $V$  is the slip rate, and  $\tau(V)$  is the dynamic strength. In the case of flash heating, assuming constant  $V_{w,\text{gouge}}$  (or  $V_w$  when modeling friction between bare rock surfaces),  $\tau_{\text{pulse}}$  can be computed using equation (9.7) as

$$\tau_{\text{pulse}} = \sqrt{2\mu f_0(\sigma_n - p_0)V_{w,\text{gouge}}/c_s}, \quad (9.44)$$

where we have neglected the contribution of  $f_w$ . Profiles of  $\tau_{\text{pulse}}$  as a function of depth are shown in Figure 9.11, where the static “Byerlee” frictional strength  $f_0(\sigma_n - p_0)$  is also plotted for comparison. The threshold  $\tau_{\text{pulse}}$  is typically of the order of a few tens of MPa throughout the depths investigated. By contrast, the static frictional strength increases linearly with depth according to the effective pressure gradient. In our computation for a continental crust using quartz properties (Figure 9.11a),  $\tau_{\text{pulse}}$  remains nearly constant at around 10 to 20 MPa, much smaller than the static strength, which implies that crack-like dynamic ruptures can easily propagate at stresses much below the local “Byerlee” strength. In our modeled oceanic setting (Figure 9.11b),  $\tau_{\text{pulse}}$  is initially larger than the static strength, down to a depth of around 3 km. Therefore, the shallow part of faults hosted in the oceanic crust is expected to only rupture in the self-healing pulse mode (or not rupture dynamically at all unless other weakening mechanisms are active). In the subduction setting with hydrostatic pore pressure gradient (Figure 9.11c, solid lines),  $\tau_{\text{pulse}}$  remains significantly smaller than  $f_0(\sigma_n - p_0)$  across most of the profile, reproducing a similar situation as in the continental crust. However, for near-lithostatic pore pressure profiles, the static strength is lower than  $\tau_{\text{pulse}}$  down to around 30 km depth, which implies that the top part of subduction zones are unlikely to generate crack-like ruptures if friction is controlled by flash heating in gouge.

Because other weakening mechanisms, such as thermal pressurization, are involved during earthquake propagation, the stress level  $\tau_{\text{pulse}}$  computed here based on flash heating only can be viewed as an upper bound of the actual stress separating pulse from cracks [*Noda et al.*, 2009]. Furthermore, our expression for  $\tau_{\text{pulse}}$  (equation [9.44]) is based on the assumption that the weakening velocity  $V_w$  is constant, i.e., neglecting the complex thermal effects out-

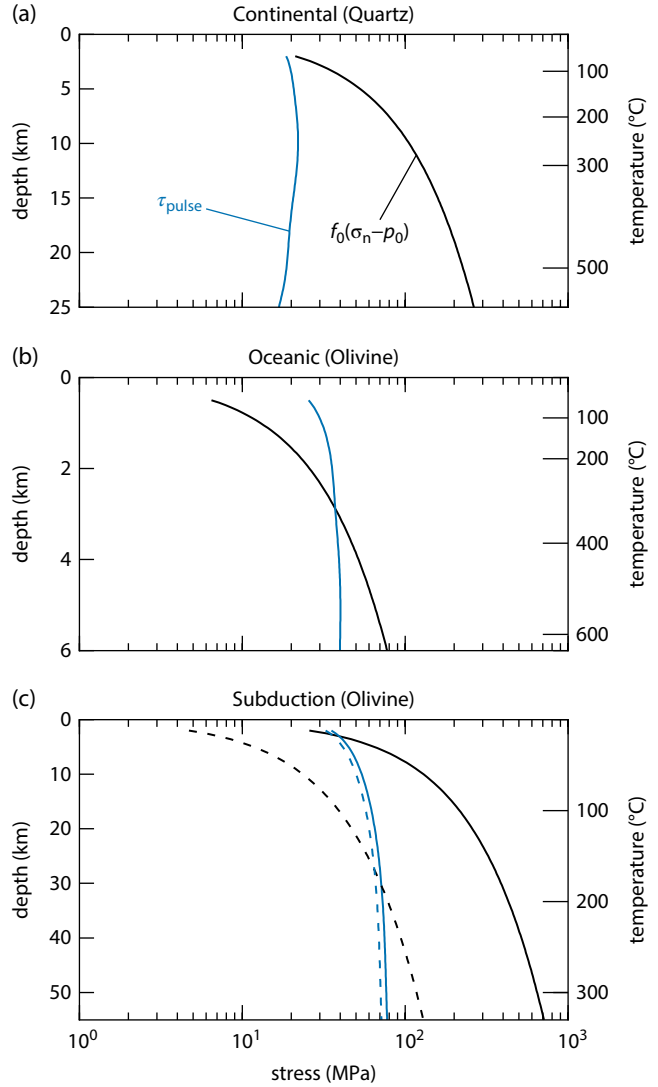


**Figure 9.11** Profiles of  $\tau_{\text{pulse}}$  (blue) and peak (static) frictional strength  $f_0(\sigma_n - p_0)$  (black) as a function of depth, in continental (a), oceanic (b) and subduction (c) settings. Solid lines correspond to hydrostatic pore pressure gradients, and dashed lines (in subplot [c]) correspond to sublithostatic pore pressure gradients. The threshold  $\tau_{\text{pulse}}$  separates a low-stress regime, in which only self-healing ruptures can propagate, and a high-stress regime, in which crack-like ruptures dominate. See electronic version for color representation.

lined in section 9.2. Hence, equation (9.44) is valid for flash heating provided that the bulk temperature rise (and thus slip) is small. For large slips leading to a significant temperature rise, the weakening velocity decreases and our value of  $\tau_{\text{pulse}}$  again provides an upper bound. Note, however, that the details of the rupture style (pulse vs. crack) in complex ruptures scenarios involving flash heating with thermal effects and thermal pressurization require fully dynamic rupture simulations, and predictions of rupture style based on a simple stress threshold might be very crude.

## 9.5. DISCUSSION

Our analysis demonstrates that thermal pressurization tends to be most efficient at midcrustal depths owing to the changes in the properties of water, while flash heating becomes more efficient with increasing depth due to the gradual reduction in the difference between ambient and weakening temperatures. The efficiency of flash heating is encapsulated by a combination of a critical slip rate  $V_{w,\text{gouge}}$  and critical times  $t_w^A$  and  $t_w^{\text{SP}}$ , while thermal pressurization is controlled by a critical strain  $\gamma_c$  at early times (independent from the slip rate) and a critical slip  $L^*$  (slip rate dependent) at larger slips. In this section, we discuss (i) limitations associated with the modeling approach, (ii) other potential weakening mechanisms that could be activated during seismic slip, and finally (iii) the implications of our results for the propagation of earthquakes down to the base of the seismogenic zone.

### 9.5.1. Limitations of the Approach

For simplicity we assumed a constant slip rate  $V = 1 \text{ ms}^{-1}$ , though we highlighted how our analysis would depend on the exact slip rate history of the fault. Here we reiterate the subtle differences between the slip rate dependence of flash heating and thermal pressurization. For flash heating, it follows from our assumption of  $f_w = 0$  that the temperature evolution, and thus the evolution of the weakening velocity, is independent of the slip rate history. The use of  $f_w = 0$ , although apparently arbitrary, appears to be quite natural in the absence of direct experimental measurements, and also considering that the strength of weakened asperities is unlikely to be simply frictional. Above the weakening velocity, the shear strength is controlled by the ratio of the weakening velocity to the slip rate, so the shear strength evolution is highly sensitive to the slip rate history. However, because the friction coefficient is proportional to  $1/V$ , the fracture energy is equal to the integral of the weakening velocity with respect to time. Thus, while the shear strength evolution for flash heating is sensitive to the slip rate history, the fracture energy is totally independent of the slip rate history of the fault and depends only on the slip duration. Obviously for slip rates below the weakening velocity, there is no dependence of shear strength on slip rate, though flash heating is likely triggered at larger slips if significant heat is produced during seismic slip because the weakening velocity depends strongly on the fault temperature.

In contrast with flash heating, the dependence on slip rate varies between the two limits for thermal pressurization. For deformation under undrained and adiabatic conditions, the shear strength evolution is insensitive to the details of the slip rate evolution and depends only on the total strain (i.e. slip) accommodated by the gouge

layer. This naturally leads to a fracture energy that is also independent of slip rate. Because thermal pressurization depends not only on generating high pore pressures but also on confining high pore pressures through inefficient hydrothermal diffusion into the surrounding material, the slip-on-a-plane limit is sensitive to the slip rate history. This can be clearly seen in the analytic solution for a constant slip rate, where the critical weakening slip  $L^*$  scales with  $1/V$ . In general, lowering the slip rate allows more efficient diffusion to occur for a given slip, and thus a higher shear strength and fracture energy. No analytic solutions exist for a variable slip rate, but the balance between the rates at which frictional heating generates pore pressures and hydrothermal diffusion relieves elevated pore pressures can be clearly seen in the solutions of Garagash [2012] for steady slip pulses driven by thermal pressurization. If the slip rate drops near the trailing edge of a rupture, then hydrothermal diffusion can dominate frictional heating, leading to rapid restrengthening. Of the four weakening scenarios considered in this chapter, thermal pressurization in the slip-on-a-plane limit displays the most varied range of behavior as the slip rate history changes.

Another major limitation of our model is the assumption of a constant shear zone width  $W$ . Flash heating and thermal pressurization both drive strain localization, so  $W$  is unlikely to remain constant during an earthquake [see Rice *et al.*, 2014; Platt *et al.*, 2014b, 2015]. Localization leads to more efficient weakening for both mechanisms. However, Platt *et al.* [2014b] showed that for thermal pressurization the onset of localization leads to a transition from the undrained and adiabatic limit to the slip-on-a-plane limit. Thus, our analysis with constant  $W$  likely still captures the essential elements of weakening. A detailed assessment of the effect of changes in  $W$  during rupture remains only accessible through detailed numerical computations.

Despite the important caveats regarding the evolution of slip rate and deforming zone thickness, our approach remains robust in terms of predicting the *relative* efficiency of flash heating and thermal pressurization with depth because the physics of these processes does not change. Flash heating will still become more efficient with depth as the background temperature approaches the weakening temperature, and the efficiency of thermal pressurization will be largely controlled by  $\Lambda$  and  $\alpha_{hy}$ .

Finally, we have neglected to model additional physics that may become important near the onset of bulk melting of the fault rock. Flash heating induces a weakening because the load-bearing asperities breakdown at high temperatures. However, when the background temperature reaches the melting point, the concept of load-bearing asperities is no longer valid, and the rock might even transiently strengthen at the onset of melting. Such transient restrengthening has been observed experimentally

[e.g., Hirose and Shimamoto, 2005]. In addition, if the melting temperature increases with pressure, then bulk melting may occur at temperatures below the asperity-scale melting temperature. No models currently exist for the transition from asperity-scale to bulk weakening, limiting our ability to properly quantify these processes.

### 9.5.2. Other Weakening/Strengthening Mechanisms

In this chapter we focus on flash heating and thermal pressurization, two well-studied processes thought to start immediately at the onset of sliding with strong quantitative support from high-velocity friction experiments [Goldsby and Tullis, 2011; Goldsby *et al.*, 2014; Proctor *et al.*, 2014]. However, a number of other weakening mechanisms have been proposed [see Niemeijer *et al.*, 2012]. Two efficient weakening mechanisms operating at relatively large slip are frictional melting [e.g., Hirose and Shimamoto, 2005; Nielsen *et al.*, 2008] and thermo-chemical pressurization [Sulem and Famin, 2009; Brantut *et al.*, 2010].

While the onset of melting may lead to transient restrengthening, melting leads to significant weakening once a continuous melt layer forms. The exact weakening depends on the melt viscosity, and thus the mineralogy of the fault, and the temperature dependence of the viscosity naturally leads to strain localization within the melt layer [Nielsen *et al.*, 2008, 2010].

Thermo-chemical pressurization corresponds to the release of fluids from devolatilization reactions such as decarbonation of carbonates [e.g., Han *et al.*, 2007] or dehydroxylation of clays [e.g., Brantut *et al.*, 2008]. Under typical crustal conditions, devolatilization reactions have a positive total volume change, and thus the released fluids are pressurized and further weaken the fault. Thermo-chemical pressurization is inherently linked to the presence of specific minerals (e.g., carbonates or clays) and is activated near threshold temperatures that correspond to each specific reaction, though the rate of weakening is typically dictated by the reaction kinetics.

Because both frictional heating and thermo-chemical pressurization are triggered once the fault temperature reaches a critical value, neither mechanism is expected to be active at the onset of slip and, depending on the efficiency of weakening provided by thermal pressurization, may never be triggered. The presence of a critical temperature means that both mechanisms are expected to provide relatively discrete weakening, in contrast with the more continuous weakening provided by flash heating and thermal pressurization.

Due to the sensitive dependence on the fault mineralogy and the uncertainty in peak temperature, we did not attempt to model thermo-chemical pressurization and frictional melting. In particular, addressing all of the possible variations in mineralogy far exceeds the scope of

this chapter. The reluctance to address a wide range of mineralogy is partly responsible for our assumption of a constant weakening temperature in our flash heating model (which could range between a few hundred degrees C for thermally unstable clays, up to more than 2000°C for the hardest oxides), though the poor constraints on the exact asperity-scale mechanisms that lead to weakening also played a role.

Despite not quantifying the weakening due to frictional melting and thermo-chemical pressurization, we speculate on the role they could play during dynamic rupture. Both mechanisms are most likely to be triggered near the base of the seismogenic zone where the temperature rises are largest. However, Platt *et al.* [2015] showed that thermo-chemical pressurization is controlled by the ratio of total pore pressure generated by the reaction and the ambient effective stress, so if the reaction-induced excess pressure is roughly constant with depth, then thermo-chemical pressurization will become less efficient with depth, at least if the effective normal stress increases with depth. In contrast, we expect frictional melting to become more efficient with depth because the dissipation rate increases, and thus a thicker melt layer can be formed. Conversely, while both mechanisms are likely rarely active at shallow depths, if triggered they could provide dramatic weakening.

Throughout this chapter we have considered only shear weakening mechanisms, but strength is not necessarily a decreasing function of slip. In particular, if dilatancy occurs, pore pressure can potentially decrease at the onset of slip, producing an initial strengthening accompanied by an excess heat production. A simple way to consider this problem, given by Rice [2006], is to assume that dilatancy occurs nearly instantaneously and has the effect of resetting the initial pore pressure. In the most extreme scenario, such as during the rupture of an intact rock, dilatancy could generate enough voids to desaturate the rock; in that case, only flash heating and potentially frictional melting could be considered as weakening mechanisms. In less extreme situations, Garagash and Rudnicki [2003] showed that strengthening by dilatancy can quickly be compensated for by thermal pressurization due to the excess heat generated; however, this excess heat could lead to premature melting. While the effect of dilatancy could potentially be dramatic, in the absence of a consistent published data set on dilatancy in overconsolidated materials during high-speed friction, modelling of such processes remains somewhat premature.

### 9.5.3. Implications for Earthquake Propagation at the Base of Seismogenic Zone

Our computations provide first-order estimates of the efficiency of thermal pressurization and flash heating mechanisms as a function of depth. For thermal pressurization, in

both our continental and oceanic crust models we observe a trend toward lower efficiency below midcrustal depths (around 10 km and 3 km depth for the continental and oceanic crust, respectively), which correspond approximately to the brittle-plastic transition in each case [e.g., Kohlstedt *et al.*, 1995]. Nevertheless, the decrease in efficiency (as illustrated, for instance, by the increase in fracture energy in Figure 9.8) below these depths is not strongly marked, and it is difficult to make the case for a threshold that would delineate the base of the seismogenic zone. Flash heating becomes generally increasingly efficient with increasing depth (see Figure 9.9), and again, no clear change exists that could set the base of the seismogenic zone. Therefore, constitutive dynamic rheology alone is insufficient to set the ultimate propagation depth of earthquakes.

In order to explain why earthquakes do not propagate through the whole lithosphere, we must appeal to additional mechanisms. One major process occurring at depth in the crust is creep of rocks, aided by the presence of water, which has two main effects: (i) it tends to heal and seal fault rocks, generating low-porosity cataclasites (typically below the 150°C isotherm [Sibson, 1986]) as opposed to the granulated, incohesive fault gouge that remains at shallow depths; (ii) it relaxes the long-term shear stress applied on faults.

The effect of healing and sealing of porosity is potentially dramatic for thermal pressurization, because it implies that earthquake slip is initially accompanied by dilatancy, which decreases the initial pore pressure [Rice, 2006] and makes thermal pressurization much less effective. In addition, porosity healing and sealing could also reduce the effective pressure coefficient [Hirth and Beeler, 2015], which both reduces the rapidity of thermal pressurization and prevents a total strength drop.

The stress relaxation due to creep tends to smooth stress heterogeneities and to lower the background shear stress. With increasing depth, creep relaxation becomes more efficient and the driving stresses decrease, implying that earthquake ruptures propagating downward would enter into regions of decreased background stress and naturally stop. This is illustrated in Figure 9.12, which shows upper limits on fault strength based on static friction (using  $f_0 = 0.6$ ) and creep flow laws for both our modeled continental and oceanic settings, as well as values of  $\tau_{\text{pulse}}$ . In the continental crust, below 15 km depth,  $\tau_{\text{pulse}}$  (for gouge) becomes larger than the creep strength, which implies that crack-like ruptures driven by flash heating cannot propagate, and that self-healing ruptures propagating downward will decay. For bare rock surfaces, the transition is at around 22 km depth.

To illustrate how the creep strength would compare with dynamically weakened friction, we also plot in Figure 9.12 tentative frictional strength using arbitrarily low friction

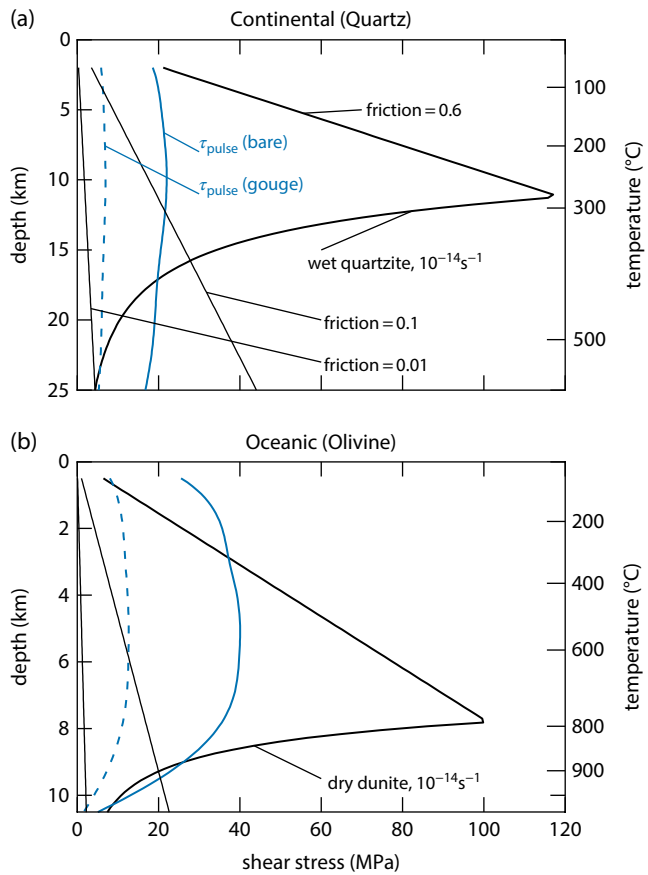


**Figure 9.12** Critical stress and strength levels in the continental (a) and oceanic (b) lithosphere. Thick black lines correspond to the upper limit for strength based on Byerlee's rule and flow law for wet quartzite [Hirth *et al.*, 2001] and dry dunite [Hirth and Kohlstedt, 2003] at  $10^{-14} \text{ s}^{-1}$  strain rate. Flow laws provide limits for differential stress, which was converted to resolved shear stress assuming that the fault is optimally oriented for frictional slip. Thin black lines are frictional strength assuming friction coefficients of 0.1 and 0.01, shown as potential lower limits for dynamic strength due to flash heating. Blue curves correspond to  $\tau_{\text{pulse}}$ , as computed for gouge (solid lines) or bare rock surfaces (dashed lines). See electronic version for color representation.

coefficients of 0.1 and 0.01 (which are used as representative estimates of the minimum friction level achieved during flash heating). Using a frictional strength with a friction coefficient of 0.1 to mimic the dynamic strength due to flash heating, we find that the creep strength, and therefore the maximum background shear stress on the fault, becomes lower than the dynamic strength below 15 km. For an even lower friction coefficient of 0.01, that crossover depth is 22 km. Because the creep strength decreases dramatically with increasing temperature, the crossover depth is only modestly sensitive to the specific value of the friction coefficient, which moderates the impact of having to choose arbitrary values. Below the

crossover depth, the potential stress drop decreases dramatically and dynamic ruptures will tend to stop. Taken together, these observations suggest that the maximum depth for earthquake propagation (driven by flash heating) is between 15 and 22 km. A similar construction is done for the oceanic lithosphere (Figure 9.12b), for which we find that the transition depth, both in terms of  $\tau_{\text{pulse}}$  and dynamic friction, is around 8 km. The temperature profile in our model is such that the 1000°C isotherm is crossed at around 11 km depth. Because we assumed  $T_w = 1000^\circ\text{C}$  in our flash heating calculations, weakening by flash heating below the 1000°C isotherm is not meaningful and the physics of high-velocity friction might be different (see section 9.5.1).

Overall, our calculations show that dynamic ruptures are efficiently stopped at depth due to a decrease in background stress, capped by the long-term creep strength of the fault rocks. Interestingly, we also note that rupture can propagate across the brittle-plastic transition, in regions where the upper limit given by friction or plastic flow is significantly higher than the dynamic strength, because of the high efficiency of dynamic weakening mechanisms, such as flash heating, at great depth. This is consistent with the fault zone model of Scholz [1988] and with the existence of fault rocks that exhibit mixtures of seismic (e.g., pseudotachylites) and creep (e.g., mylonites) features [e.g., Sibson, 1980].

In the case of subduction zones, the brittle-to-plastic transition occurs at greater depths than those of interest here. Hence, our results do not indicate any marked threshold for the maximum propagation depth. This is consistent with the continuous seismicity observed along subducting slabs. However, our results here are likely oversimplified because we did not account for the presence of weak minerals, like serpentines, that can produce low-stress zones [e.g., Hilairet *et al.*, 2007] and naturally prevent dynamic ruptures from propagating downward. Furthermore, prograde metamorphic reactions are also expected to generate complex lithological and stress/strength patterns, which is not captured by our simple approach. It is clear that the subduction zones should receive improved attention and refined modeling approaches to unravel their complexity and the associated seismic risk.

## 9.6. CONCLUSIONS

We have computed a series of characteristic parameters that describe how two major dynamic weakening mechanisms, thermal pressurization and flash heating, operate in a set of representative geological settings. Flash heating is initially controlled by a critical slip rate, but further weakening is induced by gradual increases in temperature due to shear heating. These thermal effects are controlled by critical times  $t_w^A$  (for adiabatic conditions, at small slip)

and  $t_w^{\text{SP}}$  (for slip-on-a-plane conditions, at large slip). The original formulation of flash heating was designed for bare rock surfaces; in gouge, flash heating is much less efficient (i.e., occurs at higher slip rates) and thermal effects likely dominate the weakening. Thermal pressurization is primarily controlled by the so-called thermal pressurization factor  $\Lambda$ , which quantifies the pore fluid pressure increase produced by a unit increase in fault zone temperature under undrained conditions, and strongly depends on the compressibility and thermal expansivity of the fluid. At small slip (under undrained, adiabatic conditions), the weakening due to thermal pressurization is controlled by a critical strain  $\gamma_c$ , while it is controlled by a critical slip  $L^*$  at large slip (in the slip-on-a-plane limit).

In all our computations, the critical weakening times  $t_w^A$  and  $t_w^{\text{SP}}$ , as well as the nominal critical weakening velocity  $V_w$ , tend to decrease with increasing depth, making flash heating the most efficient weakening mechanism near the base of the seismogenic zone. Due to the change in compressibility and thermal expansivity of water with increasing pressure and temperature at depth, the thermal pressurization factor  $\Lambda$  tends to peak at midcrustal depths (around 10 km and 3 km in the continental and oceanic crust, respectively), therefore making thermal pressurization the most efficient at these depths.

The maximum propagation depth of earthquake ruptures in both the continental and oceanic lithosphere is likely located significantly below the brittle-plastic transition and is mainly controlled by the lack of sufficient driving shear stresses due to efficient creep processes.

## ACKNOWLEDGMENTS

This work was supported by the UK Natural Environment Research Council through grant NE/K009656/1 to N.B. and by a Post-Doctoral Fellowship of the Carnegie Institution to J.D.P. The authors thank Jim Rice and Rob Viesca for fruitful discussions. Comments by two anonymous reviewers helped to clarify the manuscript. The Matlab codes used to generate the results of this paper are available at [https://github.com/nbrantut/Dynamic\\_Weakening\\_Depth](https://github.com/nbrantut/Dynamic_Weakening_Depth).

## REFERENCES

- Ampuero, J.-P., and A. M. Rubin (2008), Earthquake nucleation on rate and state faults: Aging and slip laws, *J. Geophys. Res.*, 113, B01302, doi:10.1029/2007JB005082.
- Andrews, D. J. (2002), A fault constitutive relation accounting for thermal pressurization of pore fluid, *J. Geophys. Res.*, 107(B12), 2363, doi:10.1029/2002JB001942.
- Archard, J. F. (1958/1959), The temperature of rubbing surfaces, *Wear*, 2, 438–455.

- Beeler, N. M., T. E. Tullis, and D. L. Goldsby (2008), Constitutive relationships and physical basis of fault strength due to flash heating, *J. Geophys. Res.*, 113, B01401, doi:10.1029/2007JB004988.
- Boettcher, M. S., G. Hirth, and B. Evans (2007), Olivine friction at the base of oceanic seismogenic zones, *J. Geophys. Res.*, 112, B01205, doi:10.1029/2006JB004301.
- Brace, W. F., and D. L. Kohlstedt (1980), Limits on lithospheric stress imposed by laboratory experiments, *J. Geophys. Res.*, 85(B11), 6248–6252.
- Brantut, N., R. Han, T. Shimamoto, N. Findling, and A. Schubnel (2011), Fast slip with inhibited temperature rise due to mineral dehydration: Evidence from experiments on gypsum, *Geology*, 39(1), 59–62.
- Brantut, N., A. Schubnel, J. Corvisier, and J. Sarout (2010), Thermochemical pressurization of faults during coseismic slip, *J. Geophys. Res.*, 115, B05314, doi:10.1029/2009JB006533.
- Brantut, N., A. Schubnel, J.-N. Rouzaud, F. Brunet, and T. Shimamoto (2008), High velocity frictional properties of a clay-bearing fault gouge and implications for earthquake mechanics, *J. Geophys. Res.*, 113, B10401, doi:10.1029/2007JB005551.
- Brune, J. N. (1970), Tectonic stress and the spectra of seismic shear waves from earthquakes, *J. Geophys. Res.*, 75(26), 4997–5009.
- Carslaw, H. S., and J. C. Jaeger (1959), *Conduction of heat in solids*, 2nd ed., Oxford University Press, New York.
- Chapman, D. S. (1986), Thermal gradients in the continental crust, in *The nature of the lower continental crust, Special Publications*, vol. 24, edited by J. B. Dawson, D. A. Carswell, J. Hall, and K. H. Wedepohl, pp. 63–70, Geological Society, London.
- Chen, J., and A. W. Rempel (2014), Progressive flash heating and the evolution of high-velocity rock friction, *J. Geophys. Res.*, 119(4), 3182–3200, doi:10.1002/2013JB010631.
- Clauser, C., and E. Huenges (1995), Thermal conductivity of rocks and minerals, in *Rock physics and phase relations: A handbook of physical constants*, edited by T. J. Ahrens, AGU Reference Shelf, American Geophysical Union, Washington, DC.
- Cochard, A., and R. Madariaga (1994), Dynamic faulting under rate-dependent friction, *Pure Appl. Geophys.*, 142(3/4), 419–445.
- Di Toro, G., D. Goldsby, and T. E. Tullis (2004), Friction falls towards zero in quartz rock as slip velocity approaches seismic rates, *Nature*, 427, 436–439.
- Di Toro, G., R. Han, T. Hirose, N. De Paola, S. N. K. Mizoguchi, F. Ferri, M. Cocco, and T. Shimamoto (2011), Fault lubrication during earthquakes, *Nature*, 471, 494–498.
- Di Toro, G., G. Pennacchioni, and G. Teza (2005), Can pseudotachylites be used to infer earthquake source parameters? An example of limitations in the study of exhumed faults, *Tectonophysics*, 402, 3–20.
- Dieterich, J. H. (1978), Time-dependent friction and mechanics of stick-slip, *Pure Appl. Geophys.*, 116, 790–806.
- Evans, B. (1984), The effect of temperature and impurity content on indentation hardness of quartz, *J. Geophys. Res.*, 89(B6), 4213–4222.
- Evans, B., and C. Goetze (1979), The temperature variation of hardness of olivine and its implication for polycrystalline yield stress, *J. Geophys. Res.*, 84(B10), 5505–5524.
- Garagash, D. I. (2012), Seismic and aseismic slip pulses driven by thermal pressurization of pore fluid, *J. Geophys. Res.*, 117, B04314, doi:10.1029/2011JB008889.
- Garagash, D. I., and J. W. Rudnicki (2003), Shear heating of a fluid-saturated slip-weakening dilatant fault zone: 1. Limiting regimes, *J. Geophys. Res.*, 108(B2), 2121, doi:10.1029/2001JB001653.
- Goldsby, D. L., and T. E. Tullis (2002), Low frictional strength of quartz rocks at subseismic slip rates, *Geophys. Res. Lett.*, 29(17), 1844, doi:10.1029/2002GL015240.
- Goldsby, D. L., and T. E. Tullis (2011), Flash heating leads to low frictional strength of crustal rocks at earthquake slip rates, *Science*, 334, 216–218.
- Goldsby, D. L., T. E. Tullis, K. Okazaki, J. D. Platt, and T. M. Mitchell (2014), Experimental studies of dynamic fault weakening due to thermal pore-fluid pressurization, abstract S11C-4357 presented at 2014 Fall Meeting, AGU, San Francisco, Calif., 15–19 December.
- Hacker, B. R., G. A. Abers, and S. M. Peacock (2003), Subduction factory: 1. Theoretical mineralogy, densities, seismic wave speeds, and  $\text{H}_2\text{O}$  content, *J. Geophys. Res.*, 108(B1), 2029, doi:10.1029/2001JB001127.
- Han, R., T. Shimamoto, T. Hirose, J. Ree, and J. Ando (2007), Ultra-low friction of carbonate faults caused by thermal decomposition, *Science*, 316 (5826), 878–881.
- Hilairet, N., B. Reynard, Y. Wang, I. Daniel, S. Merkel, N. Nishiyama, and S. Petitgirard (2007), High-pressure creep of serpentine, interseismic deformation, and initiation of subduction, *Science*, 318 (5858), 1910–1913.
- Hirose, T., and M. Bystricky (2007), Extreme dynamic weakening of faults during dehydration by coseismic shear heating, *Geophys. Res. Lett.*, 34, L14311, doi:10.1029/2007GL030049.
- Hirose, T., and T. Shimamoto (2005), Growth of molten zone as a mechanism of slip weakening of simulated faults in gabbro during frictional melting, *J. Geophys. Res.*, 110, B05202, doi:10.1029/2004JB003207.
- Hirth, G., and N. M. Beeler (2015), The role of fluid pressure on friction behavior at the base of the seismogenic zone, *Geology*, 43 (3), 223–226.
- Hirth, G., and D. L. Kohlstedt (2003), Rheology of the upper mantle and the mantle wedge: A view from the experimentalists, in *Inside the subduction factory, Geophys. Monogr. Ser.*, vol. 138, edited by J. Eiler, pp. 83–105, American Geophysical Union, Washington, DC.
- Hirth, G., C. Teyssier, and W. J. Dunlap (2001), An evaluation of quartzite flow laws based on comparisons between experimentally and naturally deformed rocks, *Geol. Rundsch.*, 90, 77–87.
- Jaupart, C., and J.-C. Mareschal (2007), Heat flow and thermal structure of the lithosphere, in *Treatise on Geophysics*, vol. 6, edited by G. Schubert, pp. 217–251, Elsevier, Oxford.
- Junglas, P. (2009), WATER95—A MATLAB implementation of the IAPWS-95 standard for use in thermodynamics lectures, *Int. J. Engng. Ed.*, 25(1), 3–18.

- Kohlstedt, D. L., B. Evans, and S. J. Mackwell (1995), Strength of the lithosphere: Constraints imposed by laboratory experiments, *J. Geophys. Res.*, 100(B9), 17,587–17,602.
- Lachenbruch, A. H. (1980), Frictional heating, fluid pressure, and the resistance to fault motion, *J. Geophys. Res.*, 85, 6097–6122.
- Lachenbruch, A. H., and J. H. Sass (1980), Heat flow and energetics of the San Andreas fault zone, *J. Geophys. Res.*, 85(B11), 6185–6223.
- Lapusta, N., and J. R. Rice (2003), Low-heat and low-stress fault operation in earthquake models of statically strong but dynamically weak faults, *Eos. Trans. AGU*, 84(46), Fall Meet. Suppl., Abstract S51B-02.
- Marone, C., and C. H. Scholz (1988), The depth of seismic faulting and the upper transition from stable to unstable slip regimes, *Geophys. Res. Lett.*, 15(6), 621–624.
- Mase, C. W., and L. Smith (1985), Pore-fluid pressures and frictional heating on a fault surface, *Pure Appl. Geophys.*, 122, 583–607.
- Mase, C. W., and L. Smith (1987), Effects of frictional heating on the thermal, hydrologic, and mechanical response of a fault, *J. Geophys. Res.*, 92 (B7), 6249–6272.
- McKenzie, D., J. Jackson, and K. Priestley (2005), Thermal structure of oceanic and continental lithosphere, *Earth Planet. Sci. Lett.*, 233, 337–349.
- Nielsen, S., G. Di Toro, T. Hirose, and T. Shimamoto (2008), Frictional melt and seismic slip, *J. Geophys. Res.*, 113, B01308, doi:10.1029/2007JB005122.
- Nielsen, S., P. Mosca, G. Giberti, G. Di Toro, T. Hirose, and T. Shimamoto (2010), On the transient behavior of frictional melt during seismic slip, *J. Geophys. Res.*, 115, B10301, doi:10.1029/2009JB007020.
- Niemeijer, A., G. Di Toro, W. A. Griffith, A. Bistacchi, S. A. F. Smith, and S. Nielsen (2012), Inferring earthquake physics and chemistry using an integrated field and laboratory approach, *J. Struct. Geol.*, 39, 2–36.
- Noda, H., E. M. Dunham, and J. R. Rice (2009), Earthquake ruptures with thermal weakening and the operation of major faults at low overall stress levels, *J. Geophys. Res.*, 114, B07302, doi:10.1029/2008JB006143.
- Noda, H., and T. Shimamoto (2005), Thermal pressurization and slip-weakening distance of a fault: An example of Hanaore fault, southwest Japan, *Bull. Seism. Soc. Am.*, 95(4), 1224–1233.
- Palmer, A. C., and J. R. Rice (1973), The growth of slip surfaces in the progressive failure of over-consolidated clay, *Proc. Roy. Soc. Lond. A.*, 332, 527–548.
- Parsons, B., and J. G. Sclater (1977), An analysis of the variation of ocean floor bathymetry and heat flow with age, *J. Geophys. Res.*, 82 (5), 803–827.
- Passelègue, F. X., D. L. Goldsby, and O. Fabbri (2014), The influence of ambient fault temperature on flash-heating phenomena, *Geophys. Res. Lett.*, 41, doi:10.1002/2013GL058374.
- Peacock, S. M., N. I. Christensen, M. G. Bostock, and P. Audet (2011), High pore pressures and porosity at 35 km depth in the Cascadia subduction zone, *Geology*, 39(5), 471–474, doi:10.1130/G31649.1.
- Platt, J. D., N. Brantut, and J. R. Rice (2015), Strain localization driven by thermal decomposition during seismic shear, *J. Geophys. Res.*, 120, doi:10.1002/2014JB011493.
- Platt, J. D., B. Proctor, T. M. Mitchell, G. Hirth, D. L. Goldsby, G. Di Toro, N. M. Beeler, and T. E. Tullis (2014a), The role of gouge and temperature on flash heating and its hysteresis, abstract S11C-4360 presented at 2014 Fall Meeting, AGU, San Francisco, Calif., 15–19 December.
- Platt, J. D., J. W. Rudnicki, and J. R. Rice (2014b), Stability and localization of rapid shear in fluid-saturated fault gouge: 2. Localized zone width and strength evolution, *J. Geophys. Res.*, 119, 4334–4359, doi:10.1002/2013JB010711.
- Proctor, B. P., T. M. Mitchell, G. Hirth, D. Goldsby, F. Zorzi, J. D. Platt, and G. Di Toro (2014), Dynamic weakening of serpentinite gouge and bare-surfaces at seismic slip rates, *J. Geophys. Res.*, 119, doi:10.1002/2014JB011057.
- Rempel, A., and J. R. Rice (2006), Thermal pressurization and onset of melting in fault zones, *J. Geophys. Res.*, 111, B09314, doi:10.1029/2005JB004006.
- Rempel, A. W. (2006), The effects of flash-weakening and damage on the evolution of fault strength and temperature, in *Earthquakes: Radiated energy and the physics of faulting*, *Geophys. Monogr. Ser.*, vol. 170, edited by R. Abercrombie, A. McGarr, G. Di Toro, and H. Kanamori, pp. 263–270, American Geophysical Union, Washington, DC.
- Rempel, A. W., and S. L. Weaver (2008), A model for flash weakening by asperity melting during high-speed earthquake slip, *J. Geophys. Res.*, 113, B11308, doi:10.1029/2008JB005649.
- Rice, J. R. (1996), Low-stress faulting: Strong but brittle faults with local stress concentrations, *Eos. Trans. AGU*, 77(46), Fall Meet. Suppl., F6811.
- Rice, J. R. (1999), Flash heating at asperity contacts and rate-depend friction, *Eos. Trans. AGU*, 80(46), Fall Meet. Suppl., F6811.
- Rice, J. R. (2006), Heating and weakening of faults during earthquake slip, *J. Geophys. Res.*, 111, B05311, doi:10.1029/2005JB004006.
- Rice, J. R., N. Lapusta, and K. Ranjith (2001), Rate and state dependent friction and the stability of sliding between elastically deformable solids, *J. Mech. Phys. Solids*, 49, 1865–1898.
- Rice, J. R., J. W. Rudnicki, and J. D. Platt (2014), Stability and localization of rapid shear in fluid-saturated fault gouge: 1. Linearized stability analysis, *J. Geophys. Res.*, 119, 4311–4333, doi:10.1002/2013JB01071.
- Rice, J. R., and A. L. Ruina (1983), Stability of steady frictional slipping, *J. Appl. Mech.*, 105, 343–349.
- Rubin, A. M., and J.-P. Ampuero (2005), Earthquake nucleation on (aging) rate and state faults, *J. Geophys. Res.*, 110, B11312, doi:10.1029/2005JB003686.
- Ruina, A. L. (1983), Slip instability and state variable friction laws, *J. Geophys. Res.*, 88, 10,359–10,370.
- Scholz, C. H. (1988), The critical slip distance for seismic faulting, *Nature*, 336, 761–763.
- Scholz, C. H. (1998), Earthquakes and friction laws, *Nature*, 391, 37–42.
- Scholz, C. H. (2002), *The mechanics of earthquake and faulting*, 2nd ed., Cambridge University Press, Cambridge, United Kingdom.
- Sibson, R. H. (1980), Transient discontinuities in ductile shear zones, *J. Struct. Geol.*, 2, 165–171.

- Sibson, R. H. (1986), Earthquakes and rock deformation in crustal fault zones, *Ann. Rev. Earth Planet. Sci.*, 14, 149–75.
- Sulem, J., and V. Famin (2009), Thermal decomposition of carbonates in fault zones: slip-weakening and temperature-limiting effects, *J. Geophys. Res.*, 114, B03309, doi:10.1029/2008JB005912.
- Turcotte, D. L., and G. Schubert (2002), *Geodynamics*, 2nd ed., Cambridge University Press, New York.
- Viesca, R. C., and D. I. Garagash (2015), Ubiquitous weakening of faults due to thermal pressurization, *Nat. Geosci.*, doi:10.1038/ngeo2554.
- Vosteen, H.-D., and R. Schellschmidt (2003), Influence of temperature on thermal conductivity, thermal capacity and thermal diffusivity for different types of rock, *Phys. Chem. Earth*, 28, 499–509.
- Wagner, W., and A. Prüß (2002), The IAPWS formulation 1995 for the thermodynamic properties of ordinary water substance for general and scientific use, *J. Phys. Chem. Ref. Data*, 43 (2), 387–535.
- Wibberley, C. A. J., and T. Shimamoto (2003), Internal structure and permeability of major-lip fault zones: the Median Tectonic Line in Mie Prefecture, southwest Japan, *J. Struct. Geol.*, 25, 59–78.
- Wibberley, C. A. J., and T. Shimamoto (2005), Earthquake slip weakening and asperities explained by thermal pressurization, *Nature*, 436(4), 689–692.
- Zhang, S., T. E. Tullis, and V. J. Scruggs (1999), Permeability anisotropy and pressure dependency of permeability in experimentally sheared gouge materials, *J. Struct. Geol.*, 21, 795–806.
- Zheng, G., and J. R. Rice (1998), Conditions under which velocity-weakening friction allows a self-healing versus a cracklike mode of rupture, *Bull. Seism. Soc. Am.*, 88(6), 1466–1483.

# **Part III**

# **Influence of Fault Properties on Coseismic Rupture**

# 10

## Scaling of Fault Roughness and Implications for Earthquake Mechanics

François Renard<sup>1,2,3</sup> and Thibault Candela<sup>4,5</sup>

### ABSTRACT

Fault slip surfaces and earthquake surface ruptures are not flat but show corrugations at all scales, also called roughness. These corrugations control the distribution of stress and strength on the fault plane and around. Here, we review the scaling properties of faults and earthquake slip roughness. Interestingly, both fault and earthquake datasets show power-law geometrical properties with similar scaling exponents, which indicate the existence of long-range spatial correlations. Several mechanisms are identified that control fault roughness, such as wear during slip and growth of a fault, by linking shear fracture segments. Scaling exponents are also found in numerical models where a rupture propagates into an elastic medium that contains mechanical heterogeneities: the roughness scaling emerges from the long-range elastic interactions and the pinning of the slip front by heterogeneities. Finally, several questions remain open on the effect of roughness on fault slip and could be the topic of future studies: (i) Is aseismic slip controlled by roughness? (ii) Is small scale-roughness (below millimeter scale) different from larger scale roughness and how does it record processes occurring during dynamic rupture and/or during fault healing? (iii) How do plastic and elastic processes interact to modify roughness and faulting?

### 10.1. INTRODUCTION

In the Earth's crust, part of the tectonic loading is dissipated through frictional processes occurring along localized shear zones and faults. In faults, both the damage in and around the fault zone and the frictional slip along well-defined surfaces participate in the dissipation of the tectonic strain energy. A question then arises on how the morphology of exhumed faults could be used to charac-

terize the mechanical processes occurring during stress buildup and strain release in the Earth's crust.

In the past century, the orientation and density of faults has been successfully used to inverse for stress tensor, assuming a Coulomb frictional relationship [Anderson, 1905; Angelier, 1979; Sibson, 2003]. In such approach, a fault is considered as a plane along which slip occurs when a frictional strength criteria is reached. However, observations of exhumed faults show that they display corrugations, i.e., roughness, at all scales [Power *et al.*, 1987; Saucier *et al.*, 1992; Lee and Bruhn, 1996; Renard *et al.*, 2006; Sagy *et al.*, 2007; Candela *et al.*, 2009, 2012; Bistacchi *et al.*, 2011; Renard *et al.*, 2013]. This roughness has formed through various mechanisms such as wear due to the drag of strong asperities along a fault surface [Bowden and Tabor, 1966; Power *et al.*, 1988], hierarchical linkage of segments as the fault expands laterally [Otsuki and Dilov, 2005], damage formation near the crack tip

<sup>1</sup>Université Grenoble Alpes, ISTerre, Grenoble, France

<sup>2</sup>CNRS, ISTerre, Grenoble, France

<sup>3</sup>PGP, Department of Geosciences, University of Oslo, Oslo, Norway

<sup>4</sup>Department of Earth and Planetary Sciences, University of California–Santa Cruz, Santa Cruz, California, USA

<sup>5</sup>TNO, Geological Survey of the Netherlands, Utrecht, Netherlands

[Sharon and Fineberg, 1996], brittle and plastic deformation occurring on the sliding interface during slow or seismic slip [Griffith et al., 2010; Davidesko et al., 2014; Tisato et al., 2012; Chen et al., 2013; Verberne et al., 2014; Siman-Tov et al., 2015].

Moreover, when an earthquake reaches the surface, the slip can be mapped in great details and shows as well nonlinear properties, with regions of large slip and regions with almost no slip; see *Rockwell and Klinger* [2013] for a representative example of rough surface coseismic slip during the Imperial Valley earthquake. In addition, the kinematic inversion of seismic slip during major earthquakes shows that the slip may be highly heterogeneous [Archuleta, 1984; Mai and Beroza, 2002], with patches of large slip, called asperities in the seismology community, and zones of negligible slip, called barriers. Asperities were proposed to correspond to strong patches along the fault, which are able to support higher shear stress than the surroundings and therefore slip more during an earthquake [Candela et al., 2011a, b]. The observation of such heterogeneities may have two interpretations. Either it is due to roughness of the fault surface and compositional spatial variations [Mai and Beroza, 2002], or due to dynamic effects during rupture propagation [Cochard and Madariaga, 1994]. For these two interpretations, a common consequence of the existence of fault roughness is that local stress concentrations in the fault will induce damage and energy dissipation not only on the fault plane but also in the volume around, as demonstrated in numerical models [Dieterich and Smith, 2010; Griffith et al., 2010]. As a consequence, fault roughness can influence both sliding characteristics and off-fault damage.

All these observations and models point to a description of a slip surface that is much more complex than a flat plane with homogeneous seismic slip. Both fault roughness and seismic slip are highly heterogeneous spatially, and the heterogeneities are present at all spatial scales investigated so far. It has been proposed that such geometrical complexity could explain the complexity of slip and slip velocities observed along faults [Manighetti et al., 2005; Candela et al., 2011a, b]. For example, *Bouchon et al.* [2010] proposed that supershear ruptures propagate when the geometry of the fault is very simple, almost planar. Using numerical simulations *Fournier and Morgan* [2012] proposed that fault roughness could explain the large variety of slip velocities, from aseismic creep to subshear ruptures, and the presence of large and small earthquakes on the same fault. At the gouge scale, the roughness of the interface controls the strength of the fault [Angheluta et al., 2011] and also how deformation localizes into the gouge [Rathbun et al., 2013]. In laboratory experiments, a transition between stick-slip behavior

and creep has been observed on a single slider, with a correlation with variations of roughness of the interface [Voisin et al., 2007]. Conversely, laboratory experiments show also that the dynamics of the rupture can be complex even on simple flat interfaces and produce roughness. For example, a transition from homogeneous sliding to the development of damage has been observed above a critical sliding velocity in PMMA polymer [Sharon and Fineberg, 1996; Fineberg et al., 1997].

In friction experiments where rock slabs were sheared at low sliding velocities, *Byerlee* [1978] proposed that the friction coefficient was more or less independent of the rock type and that the roughness of the slip surface (i) had an effect on friction at low normal stress and (ii) should not play a role in larger normal stresses relevant for crustal conditions. This concept has evolved since a series of experiments of shearing of rock material in a range of velocities from subseismic to seismic demonstrated the existence of a weakening effect when the sliding velocity reached a minimum value, with the drop of the friction coefficient from Byerlee-like values in the range 0.6–0.8 to smaller values in the range 0.1–0.3 [Di Toro et al., 2011; Tisato et al., 2012; Chen et al., 2013; Siman-Tov et al., 2015]. This is interpreted by thermally activated weakening mechanisms at the millimeter to micrometer scale on the sliding surface that decrease the shear resistance of the interface. As a consequence, the roughness of slip surfaces shows different geometric properties below this transition scale where weakening occurs, as measured in laboratory experiments [Tisato et al., 2012; Davidesko et al., 2014] and also control the shear resistance [Chen et al., 2013].

Because fault roughness has implications on both the frictional properties of the interface and also the complexity of the rupture, we review recent advances in this topic that have provided some answers to the following questions: (i) How can the out-of-plane fluctuations of faults surfaces be characterized using approaches coming from the statistical physics community? (ii) How are such corrugations formed? (iii) What are the consequences for stress distribution and slip distribution along such heterogeneous interfaces? We conclude that the answers to these three questions arise from the same mechanical phenomenon, the long-range elastic interactions of stress in a mechanically heterogeneous crust, when considering spatial scales above the millimeter. Such roughness below the millimeter scale is not considered in the present review.

In the following sections, we present the set of data used to characterize the long-range spatial correlations of fault roughness and spatial slip distribution, and the geometrical scaling laws derived from these data. These

**Table 10.1** Various Hurst exponents measured in faults and fractures. All of these exponents were measured from laboratory or field data, except  $H_{\tau}$ , which is inferred from a model and has been measured once in the field [Bouchon et al., 1998]. Note that  $H_R$  is measured in the direction of slip.

Type of Hurst Exponent	Notation	Characteristic Value
Fault roughness, parallel to the direction of slip	$H_{//}$	$0.6 \pm 0.1$
Fault roughness, perpendicular to slip	$H_{\perp}$	$0.8 \pm 0.1$
Surface rupture or seismic slip roughness	$H_R$	$0.6 \pm 0.1$
Stress field or stress drop roughness on a fault	$H_{\tau}$	$-0.4 \pm 0.1$
Rupture front roughness in lab. Experiments and numerical models	$H_s$	0.4 to 0.8
Width vs. thickness of lenses in fault zones	$H_w$	0.8
Length vs. thickness of lenses in fault zones	$H_L$	0.6

analyses show the existence of several scaling exponents summarized in Table 10.1. We also discuss the possible caveats during the analysis of these data, such as resolution of the data and noise in the acquisition system. Finally, we discuss how fault surface heterogeneities, i.e., strain, could be related to the state of stress in fault zones, using a mechanical model of elastic asperities squeeze, where asperity is defined here as a region of high stress. The main conclusion is that both fault surfaces and seismic slip show comparable spatial long-range correlations, and that therefore fault morphology has fossilized some information on the state of stress along major continental plate boundaries.

## 10.2. MEASURING THE ROUGHNESS OF FAULT SURFACES AND EARTHQUAKE RUPTURES

The measurement of fault surface topography, which we call roughness, was first developed in the field by building a mobile profilometer that allowed extracting one-dimensional profiles from a fault plane [Power et al., 1987]. Such data were complementary to laboratory measurements using mechanical or optical profilometers [Power et al., 1987; Schmittbuhl et al., 1995a]. A decade later, with the development of mobile LiDAR (Light Detection And Ranging) distance meter apparatuses and high-resolution laboratory profilometers or interferometers, two-dimensional roughness can be measured

accurately from scales of millimeters to scales of tens of meters [Renard et al., 2006; Sagy et al., 2007]. All these tools allow extracting the out-of-plane fluctuations of the topography of slip surfaces at various scales, which we call roughness (Figure 10.1).

### 10.2.1. Definition of Self-Affinity and Statistical Tools to Measure Fault Roughness

The roughness of fracture and fault surfaces was analyzed using the concept of fractals to search for scaling relationships [Mandelbrot et al., 1984; Power et al., 1987; Schmittbuhl et al., 1995a; Candela et al., 2009]. Fault geometry can be measured along one-dimensional profiles on the field [Power et al., 1987] or with two-dimensional profiling when fault surfaces are outcropping and LiDAR measurements can be performed or on hand samples [Renard et al., 2006; Sagy et al., 2007]. The spatial correlations of fault roughness, i.e., height profiles, is then characterized at all scales using several statistical physics approaches.

For each point  $x$  along the profile, the height  $h$  of the fault surface is measured and for each distance  $l = \Delta x$  along the profile, one can define the out-of-plane height:

$$\Delta h(x, l) = h(x + l) - h(x) \quad (10.1)$$

When this height is statistically translationally invariant, i.e., independent of  $x$  up to fluctuations, a distribution  $P(\Delta h)$  can be obtained for  $\Delta h$  considering all realizations of  $\Delta h(x, l)$  at all values of  $x$ . The profile  $h(x)$  is said to be self-affine with a Hurst exponent  $H$  if  $P(\Delta h)$  is scale invariant for all zoom factors  $\lambda$  under the geometrical transformation

$$\begin{cases} x \rightarrow \lambda x \\ h \rightarrow \lambda^H h \end{cases} \quad (10.2)$$

A common way to extract such feature is to obtain the statistical characteristics of the out-of-plane distance  $w = \Delta h$ . If the profile is self-affine with a power law exponent  $H$ , called the Hurst exponent, the characteristic distance  $w$  follows a scaling law of the type

$$w(l) = \alpha l^H, \quad (10.3)$$

where  $\alpha$  is a constant prefactor. If the Hurst exponent  $H$  is equal to 1.0, the interface is called self-similar and does not change its characteristic shape at different scales. If  $H$  is smaller than 1.0, the interface is called self-affine and becomes less rough on larger scales.

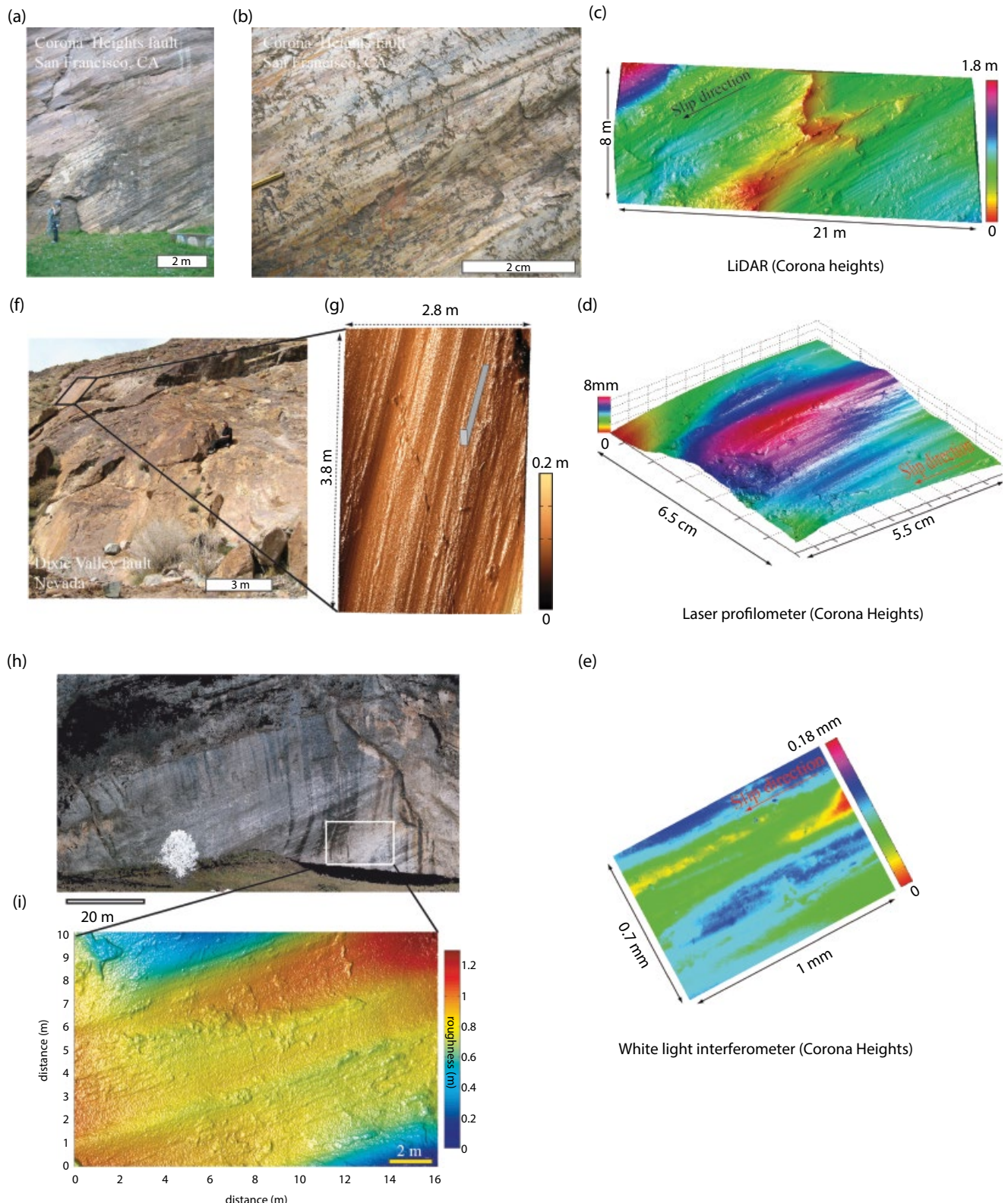


**Figure 10.1** Examples of corrugated fault surfaces and measurements of fault topography [Renard et al., 2006; Candela et al., 2012; Candela and Renard, 2012]. (a, b) Striated surface of the Corona Heights Fault (San Francisco, CA) in chert rocks at two different magnifications: meter scale (a) and centimeter scale (b). (c–e) Topography of the Corona Heights fault at three different resolutions: LiDAR with centimeter resolution (c), laboratory profilometer with 30 micrometer resolution (d), and white light interferometer with 0.5 micrometer spatial resolution (e). (f–g) Roughness of the Dixie Valley fault, Nevada. (h–i) LiDAR cloud of points and topography of the Vuache-Sillingy fault (French Alps) in a carbonate rock. See electronic version for color representation.

There are at least five classical ways (see reviews by *Barabási and Stanley* [1995] and *Meakin* [1998]) to extract the function  $w(l)$ , as described in the following.

(i) A root-mean-square average of profile width at scale  $l$ :

$$w(l) = \frac{1}{l} \left\langle \int_x^{x+l} dx' \left( h(x') - \frac{1}{l} \int_{x'}^{x+l} h(x'') dx'' \right)^2 \right\rangle^{1/2}, \quad (10.4)$$

where  $\langle \rangle$  refers to a spatial average over  $x$ , the starting points of the profiles.

(ii) It can also be the root-mean-square average at fixed distance lag  $l$ ,

$$w(l) = \left\langle (h(x+l) - h(x))^2 \right\rangle^{1/2} = C_2(l). \quad (10.5)$$

(iii) More generally, one can use structure functions [*Santucci et al.*, 2010] with higher order moments of the distribution of height-height differences  $P(\Delta h)$ , given by

$$w(l) = \left\langle |h(x+l) - h(x)|^N \right\rangle^{1/N} = C_N(l). \quad (10.6)$$

(iv) It can as well be estimated from the “min-max” estimator, or maximum difference between points lying up to an in-plane distance  $l$  from each other:

$$w(l) = \left\langle \text{Max}_{[x, x+l]}(h) - \text{Min}_{[x, x+l]}(h) \right\rangle. \quad (10.7)$$

(v) If a surface is self-affine with a Hurst exponent  $H$ , it also presents scaling laws for its Fourier power spectral density and average wavelet coefficient spectrum, as

$$P(k)^2 = \|\tilde{h}_k\|^2 \propto k^{(-1-2H)}, \quad (10.8)$$

where  $k$  is the wavenumber,  $\tilde{h}_k$  is the Fourier transform of the profile, and  $P(k)^2$  the modulus to the square of its Fourier power spectrum, and as

$$w(l) = \left\langle |w_a(x, l)| \right\rangle \propto l^{H+1/2}, \quad (10.9)$$

where  $w_a(x, l)$  is the wavelet transform of the profile [*Simonsen et al.*, 1998].

The fact that a profile follows a scaling law according to equation (10.4) for the root mean square, or for  $C_2(l)$ , or that its Fourier transform follows the scaling law equation (10.8), is often used as a weak definition of self-affinity. Figure 10.2 displays a 2D synthetic rough surface with a Hurst exponent equal to 0.6 and shows a 1D profile, with the same exponent, extracted in the center of the surface. The five statistical methods described above are

then used to show that the Hurst exponent can be recovered (Figure 10.2c–e). In the following, we choose to use only one statistical method, the Fourier transform, to analyze fault roughness. A thorough review of the five statistical methods above have shown that the Fourier transform is the method that is the least influenced by the noise of the measurement apparatus or by missing data when applied to fault roughness data [*Candela et al.*, 2009] or to fracture roughness data [*Schmittbuhl et al.*, 1995a].

### 10.2.2. Application of the Fourier Transform Method to Analyze Fault Roughness

In order to define the fault roughness for a range of scales, the Fourier spectrum of a fault patch is calculated using methods similar to the ones described by *Candela et al.* [2009, 2012]. From each fault patch (LiDAR or profilometer), several hundreds to thousands of profiles are extracted in the slip direction or perpendicular to it. The five steps in the procedure to compute the spectrum of each profile are as follows. First, a linear trend is removed from each profile by subtracting the best-fit line using the least squares method. Second, in order to ensure that there are no step functions at the end of the finite window, a 3% cosine taper is applied at the extremities of each rough profile. Third, the fast Fourier transform is calculated, and the power is the square of the amplitudes of the coefficients. Fourth, the power spectral density is calculated as the power spectrum normalized by the profile length. Finally, the representative mean Fourier spectrum of each fault patch is then computed by averaging the spectra of the profiles and restricting the results to the well-resolved wavenumbers. To extract the scaling exponent, the spectra is smoothed in the frequency space by averaging with logarithmic frequency binning for wavenumbers lower than those affected by the acquisition noise and higher than the Nyquist spatial frequency of the fault surface. The logarithmic binning provides a constant density of data points in the logarithmic representation and therefore avoids giving more weight to smaller scales in subsequent fitting procedures.

Care should be taken also when using this approach on natural data. Indeed, the range of scales over which a scaling relationship may exist varies depending on the tool used to measure roughness and on the dimensions of the fault that is measured. The roughness of a slip surface in carbonate rocks from the Cirque de Navacelle area, southern France, was measured using two techniques, a portable LiDAR and photogrammetry (Figure 10.3). The first technique uses a laser beam to measure the distance between the fault and the apparatus and provides height resolution close to 5cm. The second technique uses an optical camera and the fault surface is imaged at different angles of view before 3D reconstruction, the height resolution being close

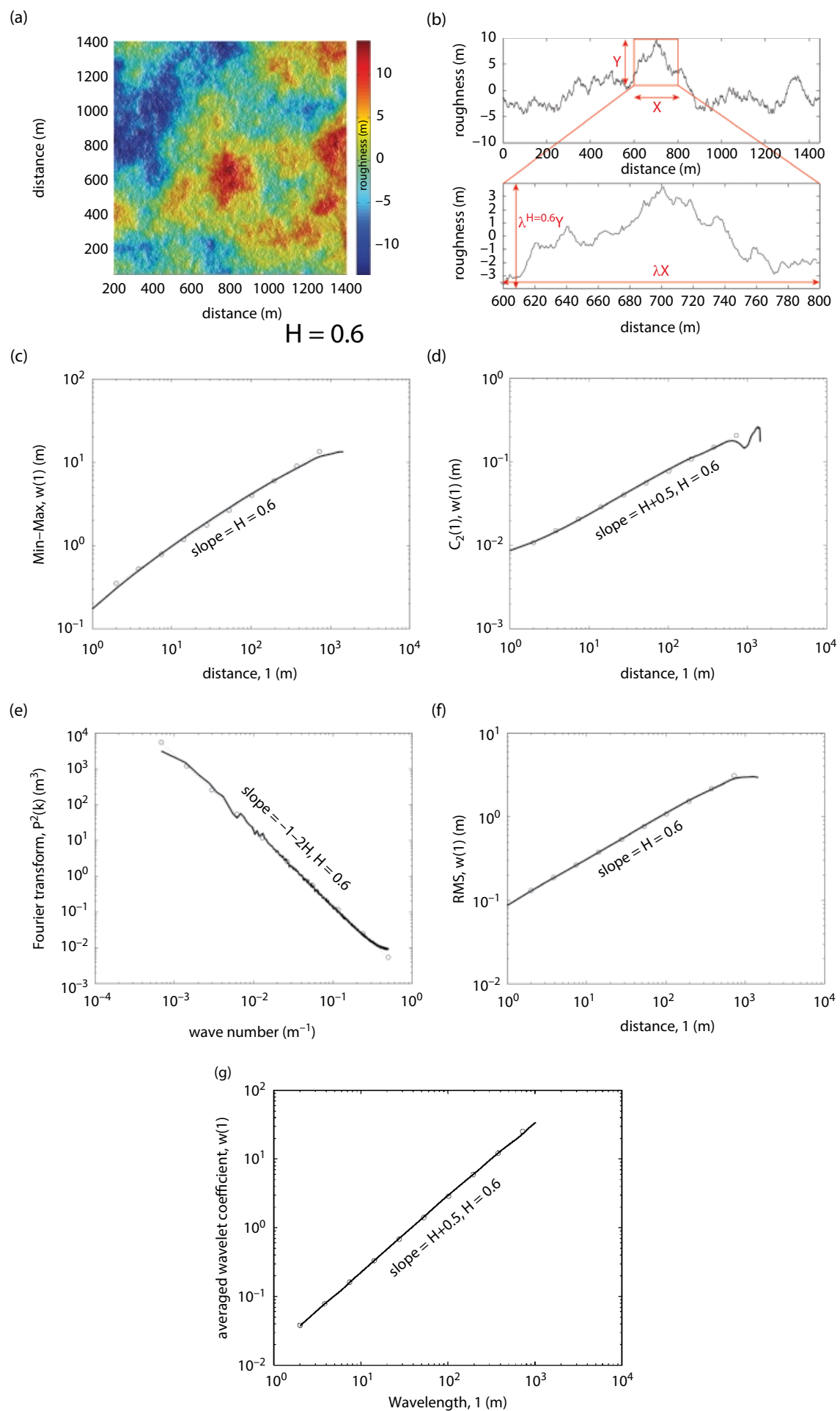


**Figure 10.2** (Continued)

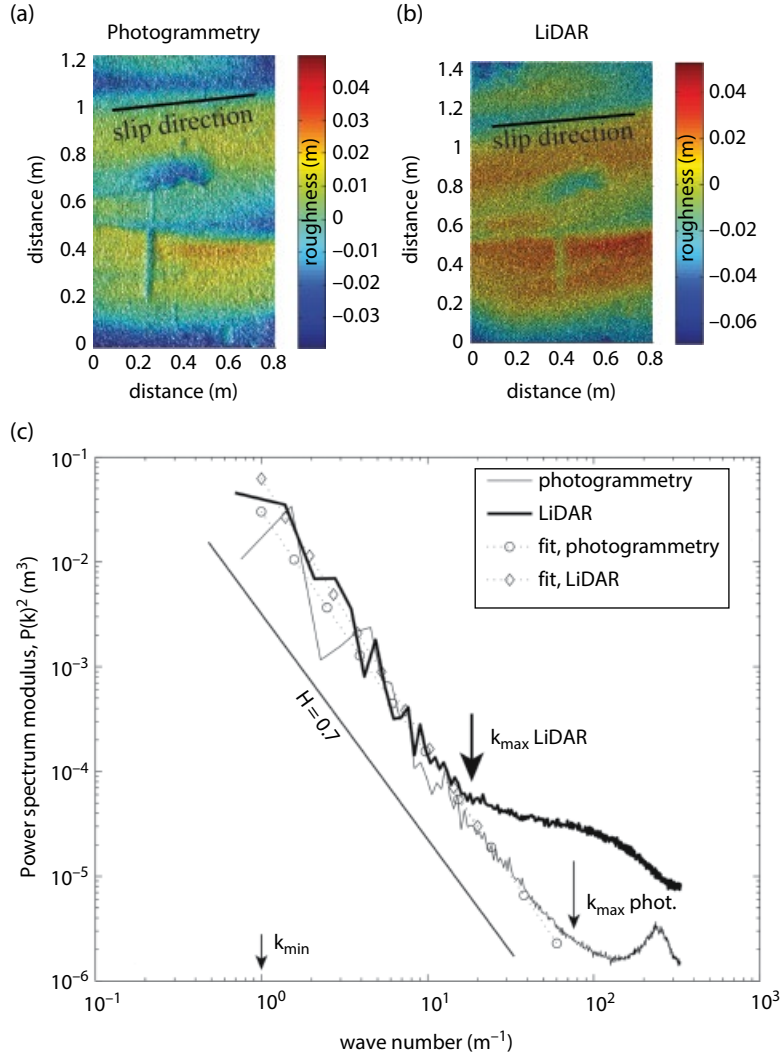


**Figure 10.3** Slip surface in carbonate rocks from the Cirque de Navacelle, southern France. (a) Fault roughness (i.e., height elevation) extracted with a photogrammetry technique. (b) Fault roughness extracted with a LiDAR apparatus. The slip direction on the fault is indicated with a line. (c) Fourier transform of vertical profiles of the two surfaces shown in (a) and (b). For both data, a scaling exponent emerges over a range of spatial wave numbers smaller than  $k_{\max}$ . The level of noise is different for both techniques, and  $k_{\max}$  is larger for the photogrammetry technique. For this case, the photogrammetry technique has a lower noise level and the data shows a power law over a larger range of scales. See electronic version for color representation.

to 0.8 cm when reconstructing the roughness. For both techniques, the fault surface can be extracted (Figure 10.3a–b), and the difference of noise is clearly visible in the height images, where the LiDAR data show fewer details and more noise in this case. When applying the Fourier transform on each data set, a scaling relationship emerges in a range of

wavenumbers [ $k_{\min}, k_{\max}$ ] between which a linear trend can be fitted in a log-log plot. The minimum wavenumber  $k_{\min}$  is related to the size of the surface divided by 2 and corresponds to the Nyquist frequency of the data. The maximum wavenumber  $k_{\max}$  is related to the noise in the data, mostly due to the spatial resolution of the acquisition

**Figure 10.2** (Continued) Statistical techniques to characterize a fractal geometry in fault roughness. (a) Synthetic 2D rough surface with a Hurst exponent equal to 0.6. (b) 1D profile extracted from the surface in (a) and definition of a self-similar property where a magnification by a factor  $\lambda$  in the x-direction requires a magnification by a factor  $\lambda^H$  in the y-direction to get a statistically similar profile.  $H$  is called the Hurst exponent. (c) Minimum-maximum correlation function (see equation [10.7]). (d) Height-height correlation function (see equation [10.5]). (e) Fourier transform (see equation [10.8]). (f) Root-mean-square function (see equation [10.4]). (g) Wavelet transform (see Equation 10.9). For all techniques (c–e), the fractal relationship emerges when a linear trend is observed in a log-log plot and the slope of the fit of this trend (dashed lines) is related to  $H$ .

system. Because there is more noise at small scales in the LiDAR data (Figure 10.3b), the range of spatial scales over which a linear trend can be defined in a log-log plot is smaller than for photogrammetry (Figure 10.3c). As a result, the Hurst exponent is found similar for both data set and close to 0.7, but the range of scales over which this scaling applies is larger for the photogrammetry data. As a conclusion, the range over which the power law behavior can be defined depends on the noise level and the spatial resolution of the technique used to measure the rough surface.

Another important effect is the presence of geometrical anisotropy on slip surface due to striations along the slip direction (Figure 10.1). As a consequence, the fractal geometry is dependent on the orientation of the 1D profiles extracted from the surface with respect to the slip direction. For example, the Vuache Fault in the French Alps, a strike-slip fault in limestone rocks, shows values of  $H$  in the range between 0.7, along the direction of slip, and 0.8, when considering a direction perpendicular to slip (Figure 10.4).

For most fault surfaces (see *Candela et al.* [2012] for a review of several tens of slip surfaces), the height profile  $h(x)$ , i.e., roughness, exhibits self-affine properties over

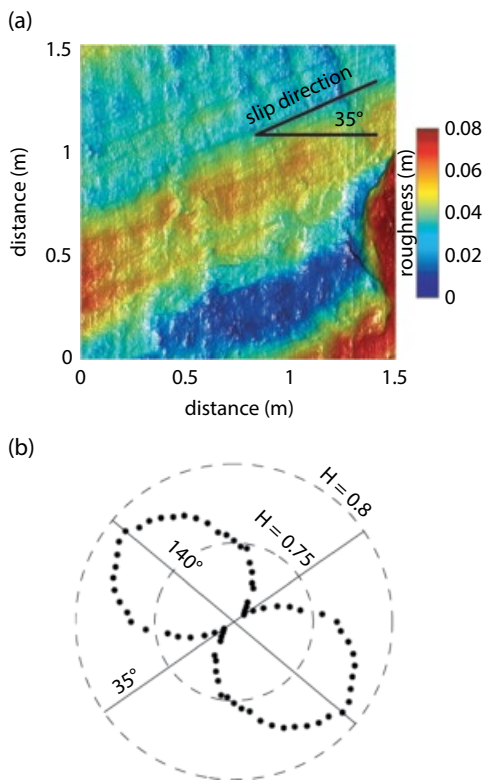


**Figure 10.4** (a) LiDAR measurement of the roughness (i.e., height elevation) of a fault surface in carbonate rocks, Vuache-Sillingy fault, French Alps. The slip direction is indicated and is at an angle of 35° with respect to the horizontal. (b) Variation of the Hurst exponent with respect to the direction on the fault. Along the slip direction,  $H$  is close to 0.7; perpendicular to it,  $H$  is close to 0.8. Modified from *Renard et al.* [2006]. See electronic version for color representation.

some scale range (a range of values of  $l$ ), i.e., it obeys a scaling law of the type  $w(l) = \alpha l^H$  (see equation [10.3]), where  $\alpha$  is a prefactor giving the amplitude of the roughness at a given spatial scale, and  $H$  is the power-law scaling exponent that describes the correlations between the different spatial scales. The first fault roughness measurements proposed that  $H$  was close to 1 [*Power et al.*, 1987], whereas more recent data have shown that  $H$  varies in the range 0.4–0.8 depending on the kind of fracture (mode I or slip surface) and the orientation with respect to slip. A detailed study of a large data set of fault surfaces indicates that  $H_{\parallel}$  is equal to 0.6 along the slip direction and  $H_{\perp}$  is equal to 0.8 perpendicular to it (Figure 10.5). This scaling relationship applies over nine orders of magnitude of spatial scales in the range  $5 \cdot 10^{-5}$ – $5 \cdot 10^4$  m [*Candela et al.*, 2012], and even eleven orders of magnitude when considering that the roughness of continent coastlines has recorded faulting processes during continental break-up [*Renard et al.*, 2013]. Here we have considered coastlines that (i) were formed by the opening of a continent and are called passive margins because these ones have registered only big fracturing events (ii) have spatial length scales above 50 km because length scales below are influenced by coastal erosion, rivers, deltas, and human activity [*Renard et al.*, 2013].

When considering the prefactor  $\alpha$  in equation (10.3), few studies were performed. With the current data available, it can be shown that this factor varies between different faults and for different patches within the same fault, and these variations show either a weak [*Brodsky et al.*, 2011] or no clear correlation [*Candela et al.*, 2012] with the total amount of slip on the fault. Nor could measurable correlation be found with the type of faulting (normal or strike-slip) or the type of rock [*Candela et al.*, 2012].

Another point is that all the 2D fault data analyzed to date come from exhumed faults and have recorded shallow slip conditions, usually from less than 5 kilometers depth. A question arises whether the observed roughness scaling is preserved at depth. In a study of faults exhumed from the seismogenic zone, *Bistacchi et al.* [2011] have extracted 1D profiles of slip surfaces and performed roughness analyses. They showed that, for these faults, a Hurst exponent in the range 0.6–0.8 could be measured over three to five orders of magnitude of length scales, and that the slip on these faults occurred at seismogenic depth. To our knowledge, this is the only example that shows that roughness scaling property observed at shallow depths could extend to mid-crustal conditions.

### 10.2.3. Application of the Fourier Transform Method to Analyze Slip Roughness

Other data that are available to characterize the heterogeneities of fault geometry are slip along a creeping fault

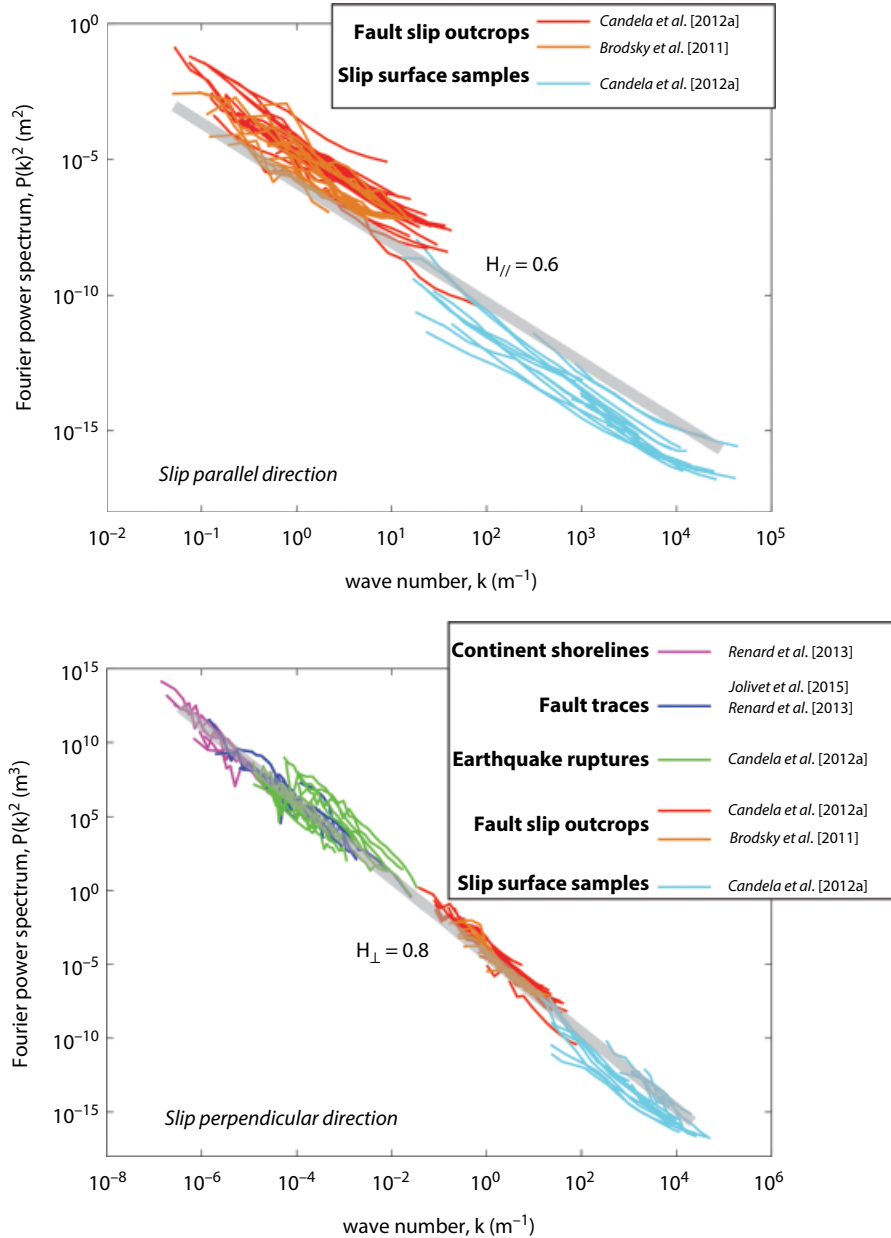


**Figure 10.5** Scaling of fault roughness over eleven orders of magnitude of length scales. Top: scaling along the direction of slip. Bottom: scaling perpendicularly to the direction of slip. The different colors indicate the various data sets: hand samples (light blue), outcrop fault slip surface (red, orange), fault traces (dark blue), earthquake ruptures (green), and continent shore lines (purple). Here, the square of the modulus of the Fourier transform for each data set is represented directly, without any correction of the prefactor that would have modified the vertical position of each curve. See electronic version for color representation.

or during an earthquake. These data come either from the inversion of seismological data and show how the slip extended at depth [Archuleta, 1984; Mai and Beroza, 2002] or from direct measurements of the amount of displacement at the surface [Rockwell and Klinger, 2013]. The spatiotemporal aseismic slip along creeping faults can come from InSAR measurements [Jolivet et al., 2015]. These data show that aseismic and seismic slip is hetero-

geneous. They also show the existence of long-range spatial correlations, as indicated by a power law relationship with a Hurst exponent with a value similar to that of fault roughness (Figure 10.6). A mechanical link between the long-range correlations of fault roughness and slip distribution is possible when considering a model of slip into an elastic medium with heterogeneities at all scales (see section 10.4).

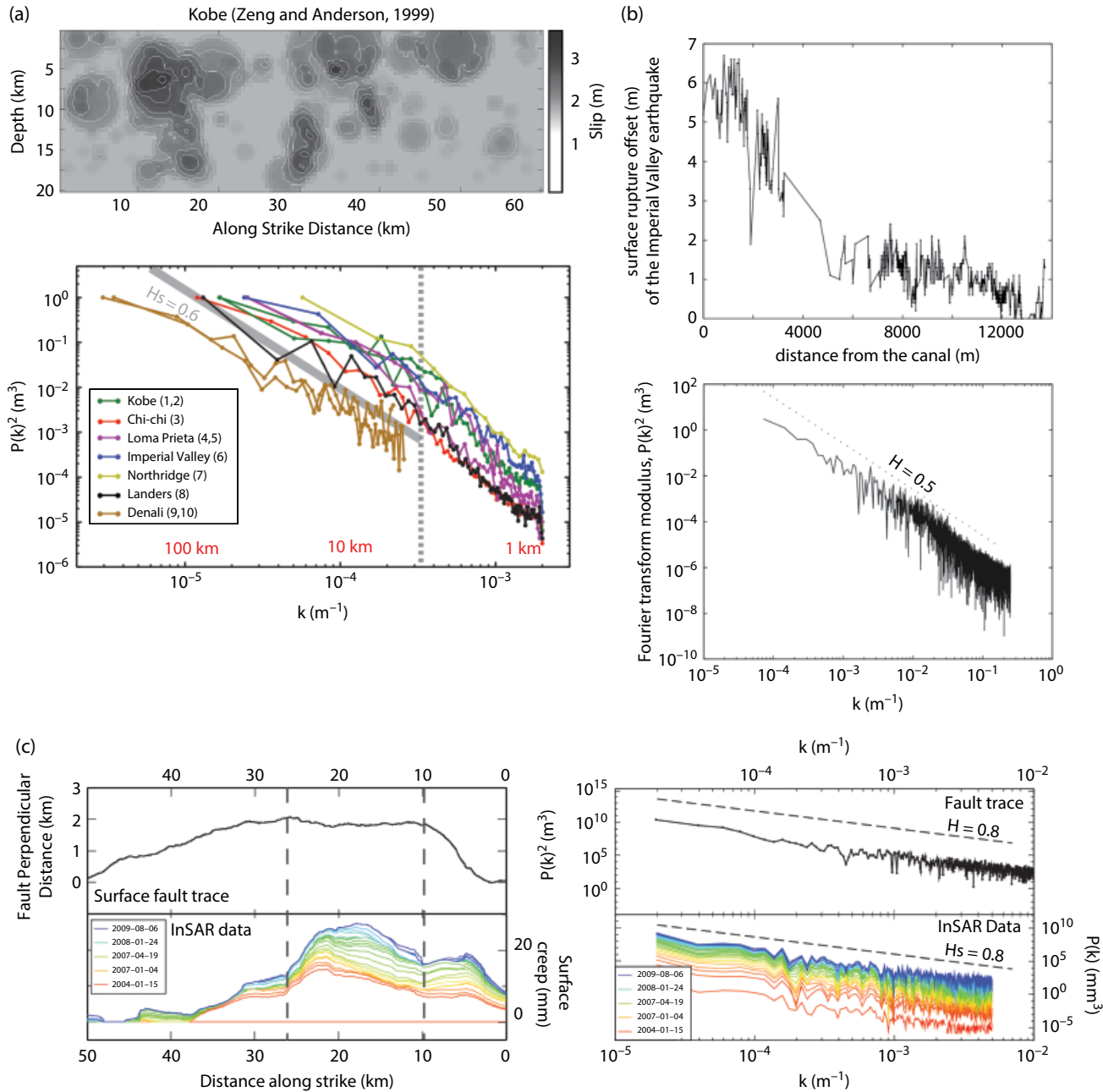


**Figure 10.6** Scaling of coseismic and aseismic spatial slip distribution. (a) Top: Spatial complexity of the seismological slip for the Kobe earthquake, 1995 [Zeng and Anderson, 2000]. (a) Bottom: Fourier transforms for seven seismological slip maps (modified from Candela et al. [2011a]) showing an identical scaling relationship with  $H_s$  equal to 0.6. The dashed line indicates the lower limit above which the power law fits were performed. (b) Top: Amount of coseismic slip at the surface after the Imperial Valley earthquake, measured using high resolution aerial images [Rockwell and Klinger, 2013]. The distance along the x-axis is taken from a canal, at the southern extremity of the surface rupture. (b) Bottom: Fourier transform of the coseismic slip distribution for the Imperial Valley earthquake, showing a scaling relationship with  $H_s$  equal to 0.5, close to 0.6 measured on average earthquake ruptures (Figure 10.5a). (c) Left: Fault surface roughness (up) and aseismic slip distribution (down) for the creeping section of the Haiyuan fault, China (modified from Jolivet et al. [2015]). (c) Right: The scaling of the surface roughness and creep distribution of the Haiyuan fault can be both characterized by an identical Hurst exponent equal to 0.8. See electronic version for color representation.

### 10.3. THE ORIGIN OF FAULT ROUGHNESS

The presence of a scaling relationship of fault roughness indicates that mechanical processes exist that create and destroy roughness. Two kinds of mechanisms can be separated: those that participate to create roughness during the formation of a fault and its lateral propagation, and those that modify the roughness during slip on an existing fault. First, we review studies from the physics community on the roughening of single fracture fronts due to long-range elastic interactions in material with local disorder. Then, three roughening processes specific to natural faults are reviewed, based on field observations and laboratory experiments: linkage of shear fracture (Figure 10.7a–d), wear and striation by asperities (Figure 10.7e–g) as the fault surface slips and extends laterally, and boudinage instability of a granular gouge layer [Sagy and Brodsky, 2009]. Other mechanisms, such as the creation of damage during coseismic slip (see chapter 4 by *Aben et al.* in the present volume and experiments by *Sharon and Fineberg* [1996]) and fracture healing [*Renard et al.*, 2012b] are not considered in the present review.

#### 10.3.1. Hurst Exponents and the Roughness of Fractured Materials

The value of the Hurst exponent in faults, in the range 0.6–0.8, has been observed in many studies of fracture roughness [Bouchaud *et al.*, 1990] and reviewed by Bouchaud [1997] and Bonamy and Bouchaud [2011]. Already in the work of Mandelbrot *et al.* [1984], the value of  $D=1.26$ , corresponding to  $H=2-D=0.74$  was proposed for fractures in metals, in the range of what is measured for faults [Candela *et al.*, 2012]. More recently, however, it was noticed that fracture surfaces are anisotropic and exhibit a significantly smaller Hurst exponent  $H_{\parallel}=0.6$  [Ponson *et al.*, 2006a; Renard *et al.*, 2006] if one considers profiles parallel to the direction of crack propagation. This is also what Candela *et al.* [2012] have observed in rocks (Figure 10.4).

Nevertheless, in some materials such as ceramics [Ponson *et al.*, 2006b] or homogeneous sandstone [Ponson *et al.*, 2007], the roughness exponent of mode I fractures is observed to be even smaller, with values  $H_{\parallel}=0.4$  in the direction of crack propagation, and  $H_{\perp}=0.5$  in the perpendicular direction. In this second case, it was shown that, at the scales of observation, these materials could be considered as perfectly linear elastic [Ponson *et al.*, 2006b], and a model was built using elasticity considerations that actually predicts these exponents [Bonamy and Bouchaud, 2011], based on the propagation of a fracture line into an elastic material where heterogeneities pin the moving fracture front, making it rough. Experimentally, it has

been confirmed that the presence of heterogeneities pin the fracture front. For example, a fracture into a porous limestone sample crosses statistically more pores (i.e., weak heterogeneities) than if the propagation were purely random [Renard *et al.*, 2009].

For the value  $H=0.8$ , there is no such mechanical model yet, but the interpretation is that the crack propagates through its own damage zone. Quite surprisingly, the measured roughness exponents are the same whether damage is due to plasticity, as in metallic alloys [Bouchaud, 1997], or to quasi-brittleness (see several references in Bonamy and Bouchaud [2011]). In all these cases, the crack front can no more be depicted as a single propagating line: it progresses also through the coalescence with the smaller cracks or cavities formed ahead. Furthermore, within the process zone, damage screens out long-range elastic interactions. In all the cases described above, the roughness finds its origin in a balance between more or less long-range mechanical (elastic) interactions along the crack front and the roughening effect of disorder [Schmittbuhl *et al.*, 1995b, Santucci *et al.*, 2010].

#### 10.3.2. Wear, Striation, and Polishing

Since the pioneering studies of Bowden and Tabor [1966], it is well known that during frictional sliding, a significant proportion of the shear resistance comes from the ploughing, grooving, or cracking of one surface by asperities on the other surface or in the gouge. Such processes both create and destroy roughness: they form grooves on the surface, and they also remove the asperities with the largest stress concentration by breaking them. As a result, some rock material moves to the gouge as slip progresses.

During slip, parts of the material are trapped along the interface and act as strong objects that damage the surface. Doing so, they create grooves, additional fracture damage, and deformation by plastically displacing the material on the side of the grooves (Figure 10.7e–g). Such wear of the sliding interface has two main properties. First, damage occurs in a volume that is several times larger than the size of the asperity, as witnessed by infrared measurements of plastic dissipation [Mair *et al.*, 2006; Renard *et al.*, 2012a] and numerical models [Griffith *et al.*, 2010]. Such damage occurs either by secondary fracture generation (Figure 10.7f) or plastic deformation of the material (Figure 10.7f, inset). Second, wear creates grooves that have a width proportional to the size of the asperities [Renard *et al.*, 2012a], and asperities can break during sliding [Mair and Abe, 2008]. As a result, if new asperities are not created, the interface roughness will evolve to a steady state as sliding proceeds. In this steady state, the amplitude of the roughness reaches a maximum (the parameter  $\alpha$  in equation [10.3] will attain a constant value

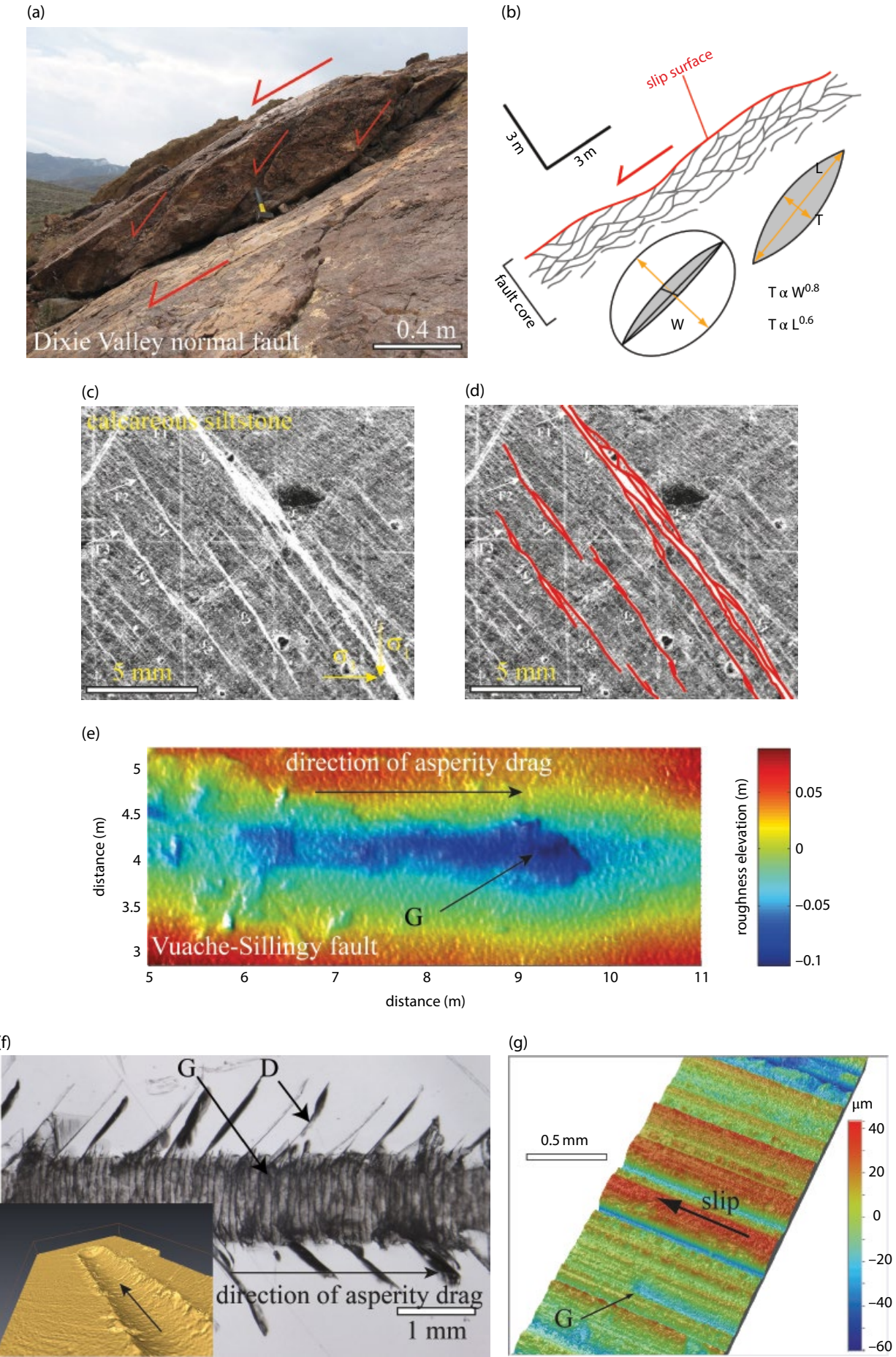


**Figure 10.7** (Continued)

with sliding), and the Hurst exponent must also reach some constant value, as observed experimentally for the roughening of salt surface by glass beads where  $H$  reaches a value of 0.5 after 1 m sliding [Renard *et al.*, 2012a]. This is a well-known effect used in engineering for polishing surfaces to a given grit. That wear processes bring new material in the fault and polish the interface with cumulated displacement, therefore reducing the amplitude of roughness with slip, has been proposed by Brodsky *et al.* [2011]. They concluded that the amplitude of roughness at a given scale (prefactor  $\alpha$  in equation [10.3]) decreased with cumulated slip with a quite low power law exponent, smaller than 0.1. Finally, the shear experiments of Davidesko *et al.* [2014] on rock slabs have shown that the sliding induces a reduction of the overall roughness amplitude, still preserving, however, a power law.

To summarize, mechanical wear can participate in roughening of the interface as sliding proceeds, but the roughness should reach a maximum value with slip, or even decrease, which is not observed in nature as the roughness scaling relationship in faults is maintained over a large number of orders of magnitude of length scales (Figure 10.5). However, we admit that to conclude that wear is not the main effect at the origin of fault roughness scaling, additional experimental data on a large variety of natural rocks should be acquired at different scales and amount of slip.

### 10.3.3. Fracture Linkage and Boudinage of Lenses

Field observations show that fault zones are rough because the fault zone is made of a series of lenses that correspond to the anastomosing process of the gouge and the protoliths along shear fractures [Faulkner *et al.*, 2003; Candela and Renard, 2012]. During its growth and lateral extension, a fault will also join other faults, as observed experimentally [Otsuki and Dilov, 2005]. The formation of lenses is due to the well-known effect

of stress screening when the stress fields of two propagating fractures located nearby interact each other's. Depending on material properties and the distance between fractures, the two fracture tips may kink and then join, leading to the formation of one such lens [Thomas and Pollard, 1993]. Because of the presence of a near-field stress at the fracture tip, the two fractures do not intersect perpendicularly but at an acute angle, which produces the typical elongated lens shape observed in the field.

By performing a detailed field study of the lenses of the Dixie Valley fault zone, Nevada, Candela and Renard [2012] have shown that such lenses exist at several scales. Moreover, their shapes, defined by three measurements ( $W$ : the fault in-plane lens width perpendicular to the fault slip direction,  $L$ : the fault in-plane extension along the slip direction, and  $T$ : the fault plane perpendicular thickness) also display scaling relationships (Figure 10.7b) such that  $T$  is proportional to  $L^{0.6}$  and  $W^{0.8}$ . Moreover, in the experiments of Otsuki and Dilov [2005], reproduced in Figure 10.7c–d, there is also a scaling relationship where the thickness of the lenses is proportional to  $L^{0.6}$ . The scaling exponents  $H_L = 0.6$  and  $H_W = 0.8$  observed for such lenses, in the field and in laboratory experiments, are the same as  $H_{\parallel}$  and  $H_{\perp}$  observed for the roughness of faults, providing a strong argument that fracture linkage is a key process to explain the scaling properties of fault roughness. Future studies would be necessary to develop a quantitative mechanical model that explains the scaling relationships observed for the shape of the lenses.

Once these lenses are created, they can deform internally, becoming damaged and producing a granular material. This is shown in the experiments of Otsuki and Dilov [2005], where microcracks form inside the lenses. As a consequence, this granular layer can evolve with sliding and form elongated bumps on the fault plane that can be interpreted as due to a boudinage instability [Sagy and Brodsky, 2009].

---

**Figure 10.7** (Continued) Origin of fault roughness by two main mechanisms: linkage of shear slip surface and mechanical wear. (a) Core of the Dixie Valley normal fault zone showing anastomosing slip surfaces. (b) Cartoon of (a) where the roughness of the main slip surface originates from the lenses at all scales produced by the linkage of slip surfaces [Candela and Renard, 2012]. The lenses have a thickness  $T$ , a width  $W$  (perpendicular to the slip direction), and a length  $L$  (parallel to the slip direction), with scaling relationships between  $T$ ,  $L$ , and  $W$ . (c–d) Laboratory experiment of fault nucleation and growth during triaxial deformation of a siltstone rock (modified from Otsuki and Dilov [2005]). The roughness of the fault is produced by the linkage of anastomosing shear fractures (underlined in red in d), producing the same lenses at those seen in (a–b). (e) Mechanical striation produced by the drag of a strong asperity that produced a groove (G) on the Vuache-Sillingy fault surface. (f) Mechanical striations produced on the surface of a single salt crystal by the drag of a single asperity that produced a groove (G) and additional fracture damage (D). The inset shows a 3D X-ray tomography view of the groove with lateral cracks and plastic deformation on the sides where the salt has been pushed like a snow plough. (g) Mechanical striations and grooves (G) produced by sliding sand paper on a single salt crystal. Modified from Renard *et al.* [2012a]. See electronic version for color representation.

### 10.3.4. Self-Affinity Controlled by the Scale-Dependent Strength of Rocks

*Brodsky et al.* [2015] have recently proposed that the scale-dependent strength of rock explains (i) that the overall roughness amplitude (prefactor  $\alpha$  in equation [10.3]) falls in a restricted range and (ii) the Hurst exponent is systematically smaller than 1. Their argument is based on the fact that the complete flattening of the fault surface requires a shear strain proportional to the roughness aspect ratio  $\delta/L$  with  $\delta$  the average asperity height at a given scale and the  $L$  the observation scale (see section 10.4.1 for more details). As the fault slips, wear processes smooth its surface and fracture linkage associated with boudinage roughen it. At every scale, the roughening process pushes the surface to the failure limit. Therefore, the fact that the rocks are weaker at large scales [*Jaeger and Cook*, 1976] might explain why only low roughness aspect ratios are maintained at large scales.

## 10.4. IMPLICATIONS FOR RUPTURE MECHANICS

Numerical models show that corrugations along a fault surface participate in stress transfer over some distance and in stress concentrations at the fault surface [*Dieterich and Smith*, 2010; *Griffith et al.*, 2010, *Angheluta et al.*, 2011, *Fournier and Morgan*, 2012], providing some heterogeneities in the stress distribution. In addition, kinematics inversions of earthquake slip are spatially highly heterogeneous [*Archuleta*, 1984, *Bouchon et al.*, 1998; *Mai and Beroza*, 2002], even if these data should be taken with caution because of potential smoothing or artefacts of the inversion technique [*Hansen*, 1998]. Direct measurements of the amount of displacement at the surface also show the seismic and aseismic slip (creep) complexity [*Rockwell and Klinger*, 2013; *Jolivet et al.*, 2015], with lateral slip variations. Figure 10.6 shows that long-range spatial correlations of two kinds of datasets, seismic slip and aseismic slip, are characterized by a power law relationship with a Hurst exponent with a value similar to that of fault geometrical roughness. Thus, a natural question is the link between the geometry of the fault surfaces and the spatial roughening of slip.

### 10.4.1. Geometrical Asperities and Stresses

Before discussing the mechanical link between the long-range correlations of fault roughness and those of slip, it is necessary to first understand what is happening in terms of stresses when two rough surfaces facing each other are sliding. Here, we approach this problem using a simple physical model where it is assumed that heterogeneities of roughness induce heterogeneities of stress for two surfaces in contact. At depth when submitted to a normal load, the

strain resulting from the complete elastic flattening of the geometrical asperities is proportional to the roughness aspect ratio  $\delta/L$  with  $\delta$  the average asperity height at a given scale and the  $L$  the observation scale. This relationship can be derived considering the asperities as spherical-Hertzian contacts (see Appendix 3 of *Johnson* [1985]). A proxy of the average asperity height is the standard deviation of the height distribution [*Williams*, 2005], and this last parameter is what we directly measure. One can then use Parseval's theorem, which states that the sum (i.e., the integral) of a square of a function is equal to the sum of the square of its Fourier transform, such that

$$\int_{-\infty}^{+\infty} |x(l)|^2 dl = \int_{-\infty}^{+\infty} |X(k)|^2 dk, \quad (10.10)$$

where  $x(l)$  is the roughness (i.e., elevation) along a profile with coordinate  $l$ , and  $X(k)$  is the Fourier transform of  $x(l)$ ,  $k$  being the wave number.

Following Parseval's theorem, the standard deviation of the height distribution at the scale  $L$  is an integral of the power estimates up to that scale, and thus,  $\delta \sim L^H$  [*Brodsky et al.*, 2011]. Finally, the roughness aspect ratio is  $\delta/L$ , and therefore the strain scales as  $L^{H-1}$ . In the elastic limit, normal stress  $\sigma$  is linearly related to strain. Consequently, normal stress under the contact asperities from full elastic squeeze of the geometrical asperities of the fault surfaces scales also as  $L^{H-1}$ . In fact, instead of Hertz's contact approximation, a more complex model considering sinusoidal surfaces [*Johnson*, 1985] or true elastic self-affine rough surfaces [*Hansen et al.*, 2000; *Batrouti et al.* 2002] will give the same scaling between normal stress and the observation scale. Since  $H$  is systematically less than 1 (Figure 10.5), the scaling  $\sigma \sim L^{H-1}$  predicts that normal stress along the fault should increase toward the smaller scales.

Assuming a homogeneous Coulomb-Byerlee threshold along the fault and that the fault is close to rupture, the shear stress  $\tau$  is linearly proportional to the normal stress through a friction coefficient, and also scales as  $\tau \sim L^{H-1}$ . In this approximation and following a conceptual rupture cascade model, *Candela et al.* [2011a] proposed that the stress drop should also follow the same scaling and that small earthquakes should rupture with a higher stress drop compared to large earthquakes. Currently, this conceptual model has been confirmed by only a few seismological observations [*Nadeau and Johnson*, 1998]. Most of the time, stress drop is thought to be scale invariant, but no clear physical model has been built yet for confirming this dogma. The wide dispersion of commonly accepted values of stress drop calls into question the assumption that earthquake source properties are scale invariant [*Scholz*, 2002].

### 10.4.2. Geometrical Asperities and Slip Distribution

Clearly the conceptual cascade rupture model of *Candela et al.* [2011a] oversimplified the complex friction problem. However, the proposed normal stress and by extension shear stress distribution under the contact asperities should hold, especially at large scales where elastic deformation dominates. Each asperity fails locally once this shear stress reaches the rock yield strength. The challenge is to resolve the friction that is controlled by the nontrivial interactions between each microfailure at asperity contacts.

In this framework, *Candela et al.* [2011b] proposed a link between slip and fault roughness using a quasi-static rupture model based on the study of *Perfettini et al.* [2001], where a slip line propagates in a quasi-static manner (i.e., dynamic effects are not considered) along an initially defined interface that cuts an elastic solid. The propagation of this line, which we call a slip

front, is perturbed by heterogeneities of frictional strength along the interface. On the basis of a local Coulomb-Byerlee friction criterion, the idea was to use the normal stress distribution, inferred from the full elastic squeeze of the geometrical asperities, as spatial heterogeneities in frictional strength for the model. It results as the slip propagates along a heterogeneous static pre-stress field that scales as  $L^{H-1}$ , that is,  $H_\tau = H - 1$  with  $H_\tau$  the Hurst exponent of the pre-stress spatial distribution and  $H$  the roughness exponent of the slip surface. In this model, the behavior of the system is controlled by the competition between two effects: the local fluctuations of the frictional strength and the effects of long-range elastic interactions. The first effect tends to pin the slip and slow down rupture propagation, whereas the second effect tends to propagate the rupture laterally.

The Fourier power spectrum of the modeled fronts exhibits a power-law behavior with a power exponent

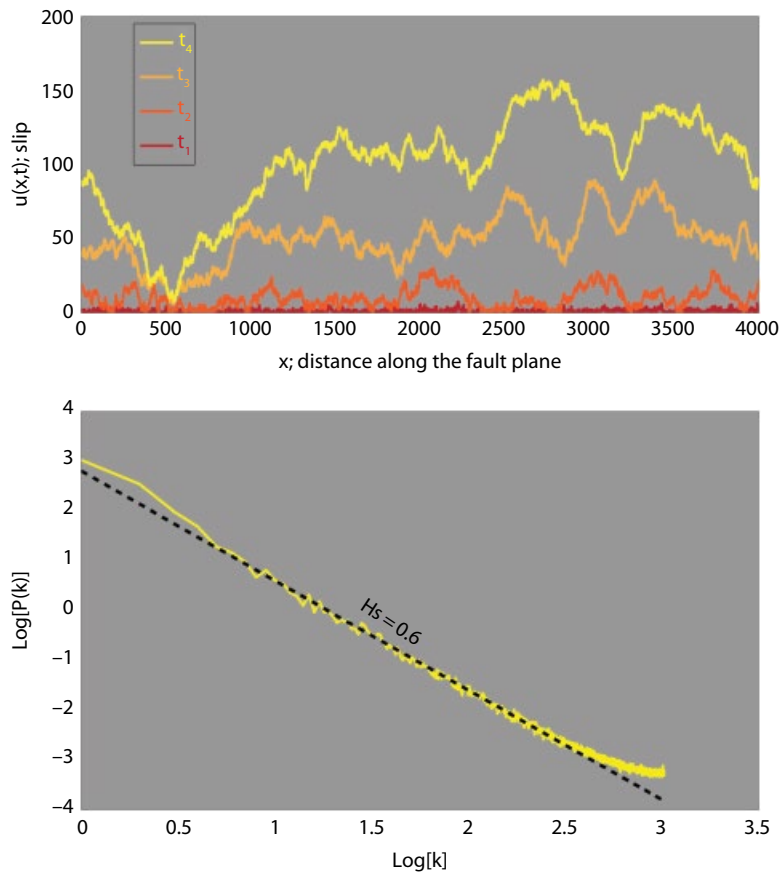


**Figure 10.8** Numerical modeling of the roughening of a 1D slip front (also called rupture front in the physics community). Top: Evolution at increasing time steps of slip distribution for a quasi-static slip model taking into account frictional (shear) strength correlations with a Hurst exponent  $H\tau = -0.4$ . Bottom: Power spectrum of slip distribution for the quasi-static rupture model averaged over 7322 model realizations, showing that it can be characterized by a Hurst exponent  $H_s = 0.6$ .

$\alpha = -2.2$ , which indicates a self-affine behavior with a Hurst exponent,  $H_s = 0.6$  (Figure 10.8). It is important to remind here that in this model, the frictional strength correlations were controlled by a Hurst exponent,  $H_t = -0.4$ . This particular pre-stress field distribution results from the squeeze of two self-affine rough fault surfaces characterized by a Hurst exponent of 0.6 as measured in the field for the slip direction (Figure 10.5). Therefore, the model prediction is that the 2D in-plane earthquake slip roughness should be spatially correlated with the out-of-plane topography roughness of the two facing fault planes hosting the rupture. For both in-plane slip and out-of-plane topography roughness, the Hurst exponents should be equal.

The quasi-static model of *Candela et al.* [2011b] is more adapted for creeping fault since inertia and wave effects are neglected. However, it seems to be in agreement with both seismic and aseismic events (see Figure 10.6). The spatial correlations of seismological slip maps and seismic and aseismic slip of surface rupture traces are all characterized by a power law relationship with a Hurst exponent similar to that of fault roughness. Clearly, it remains to incorporate the elastodynamic interactions between asperities in the model of *Candela et al.* [2011b], but the present results raise the question of the continuum between aseismic and seismic slip. Interestingly, *Jolivet et al.* [2015] observed that the size distribution of creep burst events, defined as local fluctuations in creep rates, follows a power-law behavior similar to the Gutenberg-Richter earthquake distribution. Slip on seismic and creeping faults may result from a common origin of a series of microevents controlled by the long-range elastic interactions within the heterogeneous Earth's crust. For creeping faults, microevents would correspond to silent creep burst events, and for seismic faults, microevents would correspond to brittle failure at asperity contacts.

## 10.5. CONCLUSION

In the past 10 years, geometrical measurements of fault topography and earthquake slip complexity have shown the existence of scaling properties: these data are rough and show long-range spatial correlations (Figure 10.9). The power law exponents of fault roughness, fault lense geometry, earthquake slip, and creep are similar (Table 10.1). Even if such similarity does not imply a causal link, mechanical models from the physics community allow proposing a link between these scaling properties. The elastic squeeze of geometrical rough asperities on a fault induce heterogeneities of the stress field. And

when seismic or aseismic ruptures propagate along such highly heterogeneously stressed interface, the slip front can be pinned and become rough, with the same scaling properties as the initial fault roughness. As a consequence, fault geometry shows a remarkable invariant property from the scales of 0.1 mm to the scale of several thousand kilometers that can be explained by the existence of long-range elastic interactions in the crust and the presence of heterogeneities. This geometry controls how stress is distributed on the fault plane and how it is transmitted in the volume around, participating in the general state of stress of the Earth's crust. It was also proposed recently that fault roughness scaling might be a fingerprint of the scale-dependence of the strength of rocks [*Brodsky et al.*, 2015].

There are, however, some open questions that will require more studies to confirm such a scenario.

- Among processes at the origin of roughness, both wear and segment linkage participate in roughness creation and destruction. How do these processes interact and which one dominates the fault roughness observed in nature?

- At small scales, not considered in the present review, recent studies have shown the importance of plasticity in reshaping the fault surface and the formation of nanoparticles. Does this imply that fault roughness is modified at small scales, below those considered in the present study? What are the implications for seismic and aseismic slip?

- Active faults display seismic and aseismic behaviors; some active faults also display supershear ruptures. Until now, no correlation was found between variations in  $H$  (power law exponent in equation [10.3]) and these various mechanical properties of fault. A possibility is that variations in the prefactor of fault roughness (factor  $\alpha$  in equation [10.3]) exist and should be looked for.

## ACKNOWLEDGMENTS

La Pihourdière (La Croix-du-Perche) and the Niels Bohr Institute (Copenhagen) are warmly thanked for hosting François Renard during the writing of this article. Nordea and Villum foundations are thanked for funding a visiting professorship grant to François Renard. D. Amitrano performed the analysis of Figure 10.3a. Data of the 2D fracture surfaces, faults, and earthquake slip used to produce the scaling relationship of Figure 10.5 are on open access and can be downloaded at <http://isterre.fr/recherche/equipes/mechanique-des-failles/observatoires-et-plateforme-de/article/fault-morphology-database>.

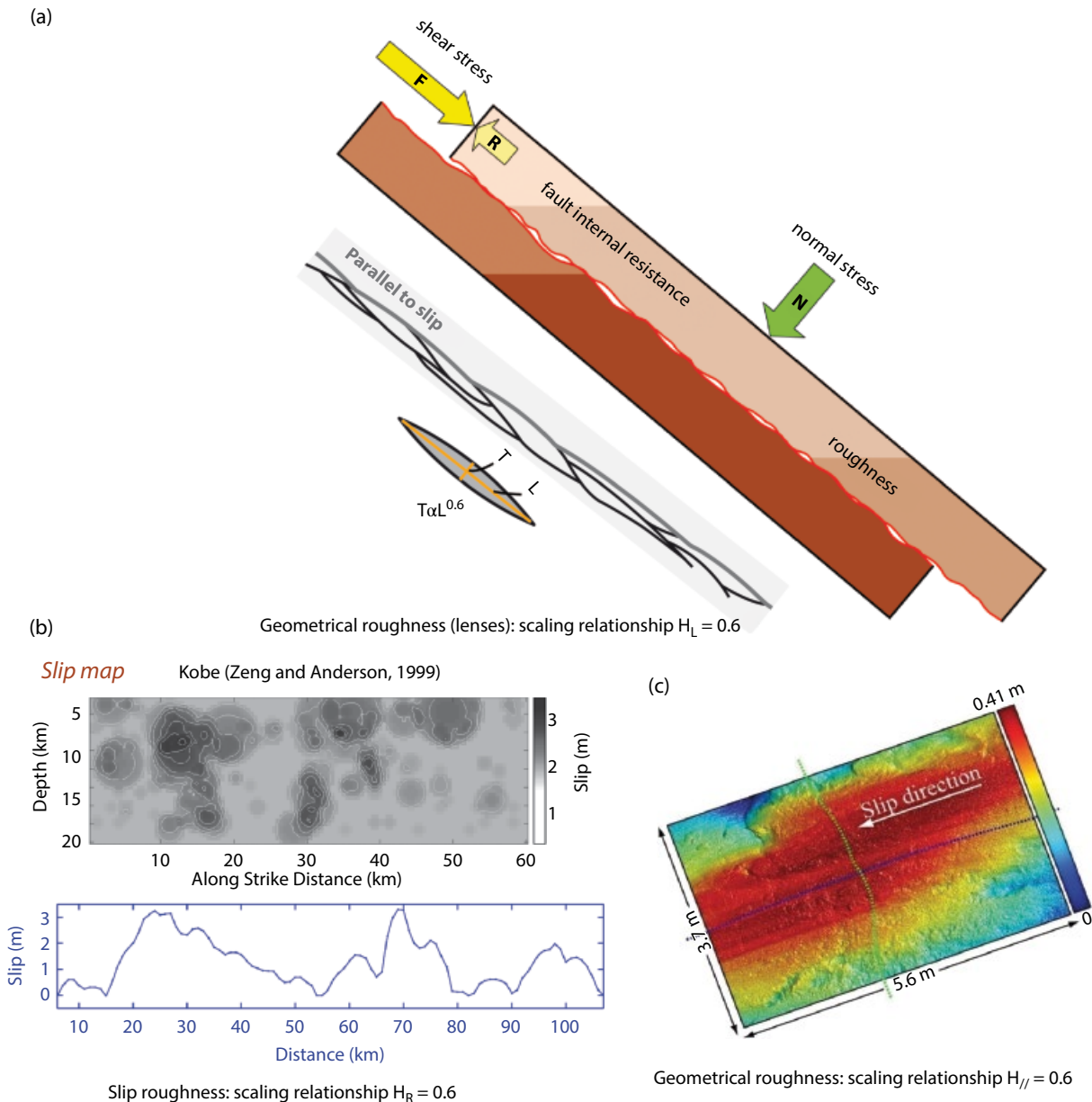


**Figure 10.9** Summary of the various scaling relationships observed for fault roughness and earthquake slip roughness in the direction of slip. Fault roughness participates to the heterogeneous distribution of stress by flattening geometrical asperities. The geometrical scaling of fault roughness is expressed both in the topography with  $H_{\parallel} = 0.6$  and the dimensions of individual lenses with  $H_L = 0.6$ . Finally, the roughness of seismic slip shows the same scaling property with  $H_R = 0.6$ . See electronic version for color representation.

## REFERENCES

- Anderson, E. M. (1905), The dynamics of faulting, *Transactions of the Edinburgh Geological Society*, 8, 387–402.  
 Angelier, J. (1979), Determination of the mean principal directions of stresses for a given fault population, *Tectonophysics*, 56(3), T17–T26.

- Angheluta, L., T. Candela, J. Mathiesen, and F. Renard (2011), Effect of surface morphology on the dissipation during shear and slip along a rock-rock interface that contains a visco-elastic core, *Pure and Applied Geophysics*, doi 10.1007/s00024-011-0272-8.  
 Archuleta, R. J. (1984), A faulting model for the 1979 Imperial Valley earthquake, *Journal of Geophysical Research: Solid Earth* (1978–2012), 89(B6), 4559–4585.

- Barabási, A. L., and H. E. Stanley (1995), *Fractal concepts in surface growth*, Cambridge University Press.
- Batrouni, G. G., A. Hansen, and J. Schmittbuhl (2002), Heterogeneous interfacial failure between two elastic blocks, *Physical Review E*, 65(3), 036126.
- Bistacchi, A., W. A. Griffith, S. A. Smith, G. Di Toro, R. Jones, and S. Nielsen (2011), Fault roughness at seismogenic depths from LIDAR and photogrammetric analysis, *Pure and Applied Geophysics*, 168(12), 2345–2363.
- Bonamy, D., and E. Bouchaud (2011), Failure of heterogeneous materials: A dynamic phase transition? *Physics Reports*, 498(1), 1–44.
- Bouchaud, E. (1997), Scaling properties of cracks, *Journal of Physics: Condensed Matter*, 9(21), 4319–4344.
- Bouchaud, E., G. Lapasset, and J. Planes (1990), Fractal dimension of fractured surfaces: A universal value? *Europhys. Lett.*, 13, 73–79.
- Bouchon, M., H. Karabulut, M.-P. Bouin, J. Schmittbuhl, M. Vallée, R. Archuleta, S. Das, F. Renard, and D. Marsan (2010), Faulting characteristics of supershear earthquakes, *Tectonophysics*, 493, 244–253, doi:10.1016/j.tecto.2010.06.011.
- Bouchon, M., H. Sekiguchi, K. Irikura, and T. Iwata (1998), Some characteristics of the stress field of the 1995 Hyogo-ken Nanbu (Kobe) earthquake, *Journal of Geophysical Research: Solid Earth*, 103(B10), 24271–24282.
- Bowden, F. P., and D. Tabor (1966), Friction, lubrication and wear: A survey of work during the last decade, *British Journal of Applied Physics*, 17(12), 1521.
- Brodsky, E. E., J. J. Gilchrist, A. Sagy, and C. Collettini (2011), Faults smooth gradually as a function of slip, *Earth and Planetary Science Letters*, 302(1), 185–193.
- Brodsky, E. E., J. D. Kirkpatrick, and T. Candela (2015), Constraints from fault roughness on the scale-dependent strength of rocks, *Geology*, G37206, doi:10.1130/G37206.1.
- Byerlee, J. (1978), Friction of rocks, *Pure and Applied Geophysics*, 116(4–5), 615–626.
- Candela, T., and F. Renard (2012), Segment linkage process at the origin of slip surface roughness: Evidence from the Dixie Valley fault, *Journal of Structural Geology*, 45, 87–100, doi:10.1016/j.jsg.2012.06.003.
- Candela, T., F. Renard, M. Bouchon, A. Brouste, D. Marsan, J. Schmittbuhl, and C. Voisin (2009), Characterization of fault roughness at various scales: Implications of three-dimensional high resolution topography measurements, *Pure and Applied Geophysics*, 166, 1817–1851, doi:10.1007/s00024-009-0521-2.
- Candela, T., F. Renard, M. Bouchon, J. Schmittbuhl, and E. E. Brodsky (2011a), Fault slip distribution and fault roughness, *Geophysical Journal International*, 187, 959–968, doi:10.1111/j.1365-246X.2011.05189.x.
- Candela, T., F. Renard, M. Bouchon, J. Schmittbuhl, and E. E. Brodsky (2011b), Stress drop during earthquakes: Effect of fault roughness scaling, *Bulletin of the Seismological Society of America*, 101, 2369–2387, doi:10.1785/0120100298.
- Candela, T., F. Renard, Y. Klinger, K. Mair, J. Schmittbuhl, and E. Brodsky (2012), Roughness of fault surfaces over nine decades of length scales, *Journal of Geophysical Research*, 117, B08409, doi:10.1029/2011JB009041.
- Chen, X., A. S. Madden, B. R. Bickmore, and Z. E. Reches (2013), Dynamic weakening by nanoscale smoothing during high-velocity fault slip, *Geology*, 41(7), 739–742.
- Cochard, A., and R. Madariaga (1994), Dynamic faulting under rate-dependent friction, *Pure and Applied Geophysics*, 142(3–4), 419–445.
- Davidesko, G., A. Sagy, and Y. H. Hatzor (2014), Evolution of slip surface roughness through shear, *Geophysical Research Letters*, 41(5), 1492–1498.
- Di Toro, G., R. Han, T. Hirose, N. De Paola, S. Nielsen, K. Mizoguchi, F. Ferri, M. Cocco, and T. Shimamoto (2011), Fault lubrication during earthquakes, *Nature*, 471(7339), 494–498.
- Dieterich, J. H., and D. E. Smith (2010), Nonplanar faults: Mechanics of slip and off-fault damage, in *Mechanics, structure and evolution of fault zones*, Birkhäuser Basel, pp. 1799–1815.
- Faulkner, D. R., A. C. Lewis, and E. H. Rutter (2003), On the internal structure and mechanics of large strike-slip fault zones: Field observations of the Carboneras fault in southeastern Spain, *Tectonophysics*, 367, 235–261.
- Fineberg, J., S. P. Gross, and E. Sharon (1997), Micro-branching as an instability in dynamic fracture, in *IUTAM Symposium on Nonlinear Analysis of Fracture* (pp. 177–189), Springer, Netherlands.
- Fournier, T., and J. K. Morgan (2012), Insights to slip behavior on rough faults using discrete element modeling, *Geophysical Research Letters*, 39, L12304, doi:10.1029/2012GL051899.
- Griffith, W. A., S. Nielsen, G. Di Toro, and S. A. Smith (2010), Rough faults, distributed weakening, and off-fault deformation, *Journal of Geophysical Research: Solid Earth*, 115, B08409, doi:10.1029/2009JB006925.
- Hansen, A., J. Schmittbuhl, G. G. Batrouni, and de F. A. Oliveira (2000), Normal stress distribution of rough surfaces in contact, *Geophysical Research Letters*, 27(22), 3639–3642.
- Hansen, P. C. (1998), *Rank-deficient and discrete ill-posed problems: Numerical aspects of linear inversion* (vol. 4), Siam.
- Jaeger, J. C., and N.G.W. Cook (1976), *Fundamentals of rock mechanics*, Chapman and Hall, London.
- Johnson, K. L. (1985), *Normal contact of elastic solids: Hertz theory*, *Contact Mechanics*, 84–106.
- Jolivet, R., T. Candela, C. Lasserre, F. Renard, Y. Klinger, and M.-P. Doin (2015), The burst-like behavior of aseismic slip on a rough fault: The creeping section of the Haiyuan fault, China, *Bulletin of the Seismological Society of America*, 105, 480–488.
- Lee, J. J., and R. L. Bruhn (1996), Structural anisotropy of normal fault surfaces, *Journal of Structural Geology*, 18(8), 1043–1059.
- Mai, P. M., and G. C. Beroza (2002), A spatial random field model to characterize complexity in earthquake slip, *Journal of Geophysical Research: Solid Earth*, 107, 2308, doi:10.1029/2001JB000588.
- Mair, K., and S. Abe (2008), 3D numerical simulations of fault gouge evolution during shear: Grain size reduction and strain localization, *Earth and Planetary Science Letters*, 274(1), 72–81.
- Mair, K., F. Renard, and O. Gundersen (2006), Thermal imaging on simulated faults during frictional sliding, *Geophysical Research Letters*, 33, L19301, doi:10.1029/2006GL027143.
- Mandelbrot, B. B., D. E. Passoja, and A. J. Paullay (1984), Fractal character of fracture surfaces of metals, *Nature*, 308, 721–722.
- Manighetti, I., M. Campillo, C. Sammis, P. M. Mai, G. King (2005), Evidence of self-similar, triangular slip distributions on earthquakes: Implications for earthquake and fault

- mechanics, *Journal of Geophysical Research*, B05302, doi:10.1029/2004JB003174.
- Meakin, P. (1998), *Fractals, scaling and growth far from equilibrium* (vol. 5), Cambridge University Press.
- Nadeau, R. M., and L. R. Johnson (1998), Seismological studies at Parkfield VI: Moment release rates and estimates of source parameters for small repeating earthquakes, *Bulletin of the Seismological Society of America*, 88(3), 790–814.
- Otsuki, K., and T. Dilov (2005), Evolution of hierarchical self-similar geometry of experimental fault zones: Implications for seismic nucleation and earthquake size, *Journal of Geophysical Research: Solid Earth*, 110, B03303, doi:10.1029/2004JB003359.
- Perfettini, H., J. Schmittbuhl, and J. Vilotte (2001), Slip correlations on a creeping fault, *Geophysical Research Letters*, 28, 2133–2136.
- Ponson, L., H. Auradou, M. Pessel, V. Lazarus, and J.-P. Hulin (2007), Failure mechanisms and surface roughness statistics of fractured Fontainebleau sandstone, *Physical Review E*, 76, 036108.
- Ponson, L., H. Auradou, P. Vie, and J.-P. Hulin (2006b), Low self-affine exponents of fractured glass ceramics surfaces, *Physical Review Letters*, 97, 125501.
- Ponson, L., D. Bonamy, and E. Bouchaud (2006a), Two-dimensional scaling properties of experimental fracture surfaces, *Physical Review Letters*, 96, 035506.
- Power, W. L., T. E. Tullis, S. R. Brown, G. N. Boitnott, and C. H. Scholz (1987), Roughness of natural fault surfaces, *Geophysical Research Letters*, 14(1), 29–32.
- Power, W. L., T. E. Tullis, and J. D. Weeks (1988), Roughness and wear during brittle faulting, *Journal of Geophysical Research: Solid Earth*, 93(B12), 15268–15278.
- Rathbun, A., F. Renard, and S. Abe (2013), Numerical investigation of the interplay between wall geometry and friction in fault gouge, *Journal of Geophysical Research*, 118, 878–896, doi:10.1002/jgrb.50106.
- Renard, F., S. Beauprêtre, C. Voisin, D. Zigone, T. Candela, D. K. Dysthe, and J.-P. Gratier (2012b), Strength evolution of a reactive frictional interface is controlled by the dynamics of contacts and chemical effects, *Earth and Planetary Science Letters*, 341–344, 20–34, doi: 10.1016/j.epsl.2012.04.048.
- Renard, F., D. Bernard, J. Desrues, and A. Ougier-Simonin (2009), 3D imaging of fracture propagation using synchrotron X-ray microtomography, *Earth and Planetary Science Letters*, 286, 285–291, doi 10.1016/j.epsl.2009.06.040.
- Renard, F., T. Candela, and E. Bouchaud (2013), Constant dimensionality of fault roughness from the scale of microfractures to the scale of continents, *Geophysical Research Letters*, doi:10.1029/2012GL054143.
- Renard, F., K. Mair, and O. Gundersen (2012a), Surface roughness evolution on experimentally simulated faults, *Journal of Structural Geology*, 45, 101–112, doi:10.1016/j.jsg.2012.03.009.
- Renard, F., C. Voisin, D. Marsan, and J. Schmittbuhl (2006), High resolution 3D laser scanner measurements of a strike-slip fault quantify its morphological anisotropy at all scales, *Geophysical Research Letters*, 33(4), L04305, doi:10.1029/2005GL025038.
- Rockwell, T. K., and Y. Klinger (2013), Surface rupture and slip distribution of the 1940 Imperial Valley earthquake, Imperial Fault, Southern California: Implications for rupture segmentation and dynamics, *Bulletin of the Seismological Society of America*, 103(2A), 629–640.
- Sagy, A., and E. E. Brodsky (2009), Geometric and rheological asperities in an exposed fault zone, *Journal of Geophysical Research: Solid Earth*, 114, B02301, doi:10.1029/2008JB005701.
- Sagy, A., E. E. Brodsky, and G. J. Axen (2007), Evolution of fault-surface roughness with slip, *Geology*, 35(3), 283–286.
- Santucci, S., M. Grob, R. Toussaint, J. Schmittbuhl, A. Hansen, and K. J. Måløy (2010), Fracture roughness scaling: A case study on planar cracks, *Europhysics Letters*, 92(4), 44001.
- Saucier, F., E. Humphreys, and R. Weldon (1992), Stress near geometrically complex strike-slip faults: Application to the San Andreas Fault at Cajon Pass, Southern California, *Journal of Geophysical Research: Solid Earth*, 97(B4), 5081–5094.
- Schmittbuhl, J., S. Roux, J. P. Vilotte, and K. J. Måløy (1995b), Interfacial crack pinning: Effect of nonlocal interactions, *Physical Review Letters*, 74(10), 1787.
- Schmittbuhl, J., J. P. Vilotte, and S. Roux (1995a), Reliability of self-affine measurements, *Physical Review E*, 51(1), 131.
- Scholz, C. H. (2002), *The mechanics of earthquakes and faulting* (2nd ed.), Cambridge University Press, Cambridge.
- Sharon, E., and J. Fineberg (1996), Microbranching instability and the dynamic fracture of brittle materials, *Physical Review B*, 54(10), 7128–7139.
- Sibson, R. H. (2003), Brittle-failure controls on maximum sustainable overpressure in different tectonic regimes, *AAPG Bulletin*, 87(6), 901–908.
- Siman-Tov, S., E. Aharonov, Y. Boneh, and Z. E. Reches (2015), Fault mirrors along carbonate faults: Formation and destruction during shear experiments, *Earth and Planetary Science Letters*, 430, 367–376.
- Simonsen, I., A. Hansen, and O. M. Nes (1998), Using wavelet transforms for Hurst exponent determination, *Phys. Rev. E*, 58, 2779–2787.
- Thomas, A. L., and D. D. Pollard (1993), The geometry of echelon fractures in rock: implications from laboratory and numerical experiments, *Journal of Structural Geology*, 15, 323–334.
- Tisato, N., G. Di Toro, N. De Rossi, M. Quaresimin, and T. Candela (2012), Experimental investigation of flash weakening in limestone, *Journal of Structural Geology*, 38, 183–199.
- Verberne, B. A., O. Plümper, D. A. Matthijs de Winter, C. J. Spiers (2014), Superplastic nanofibrous slip zones control seismogenic fault friction, *Science*, 346, 1342–1344.
- Voisin, C., F. Renard, and J.-R. Grasso (2007), Long term friction: From stick-slip to stable sliding, *Geophysical Research Letters*, 34, L13301, doi:10.1029/2007GL029715.
- Williams, J. (2005), *Engineering tribology*, Cambridge University Press, Cambridge.
- Zeng, Y., and J. Anderson (2000), Evaluation of numerical procedures for simulating near-fault long-period ground motions using Zeng method, *Report 2000/01 to the PEER Utilities Program*, available at <http://peer.berkeley.edu>.

# 11

## Fault Branching and Long-Term Earthquake Rupture Scenario for Strike-Slip Earthquakes

**Yann Klinger, Jin-Hyuck Choi, and Amaury Vallage**

### ABSTRACT

Careful examination of surface rupture for large continental strike-slip earthquakes reveals that for the majority of earthquakes, at least one major branch is involved in the rupture pattern. Often, branching might be either related to the location of the epicenter or located toward the end of the rupture, and possibly related to the stopping of the rupture. In this work, we examine three large continental earthquakes that show significant branches and for which ground surface rupture has been mapped in great details. In each case, rupture conditions are described, including dynamic parameters, past earthquakes history, and regional stress orientation, to see if the dynamic stress field would a priori favor branching. In one case, we show that it was not the first time that an earthquake was branching in a similar fashion. Long-term geomorphology hints at the existence of a strong asperity in the zone where the rupture branched off the main fault. There, no evidence of throughgoing rupture could be seen along the main fault, while the branch is well connected to the main fault. This set of observations suggests that for specific configurations, some rupture scenarios involving systematic branching are more likely than others.

### 11.1. INTRODUCTION

Surface ruptures associated with large continental earthquakes bring a wealth of information about rupture processes and fault structures [i.e., *Haeussler et al.*, 2004; *King et al.*, 2005; *Xu et al.*, 2006; *Wei et al.*, 2011; *Teran et al.*, 2015]. Until the late 80s, however, the potential of such information was not well recognized and details of surface ruptures during an earthquake were often poorly documented. Indeed, surface ruptures for large events are distributed over tens to hundreds of kilometers, depending on the magnitude of the event, making them difficult to be comprehended when one is limited only to field observation and/or to low-resolution aerial photos. In addition, earthquake source studies are mostly focused on teleseismic distances, which limits the frequency

domain addressed to be close to 1 Hz at most. Such frequency domain, 1 Hz and lower, corresponds to a resolution of a few kilometers at best, which is out of scale when compared to details of the rupture geometry seen during field survey. Less often, waveform inversion is carried out at higher frequency, allowing for a more detailed view of the seismic source at smaller scale [*Kim and Dreger*, 2008; *Ji et al.*, 2015].

Major improvements in remote sensing during the last two decades have opened new avenues to study details of surface rupture geometry and to build a corpus of homogeneous data to feed more and more efficient modeling tools. In 1992, the Mw 7.3 Landers earthquake was the first large earthquake for which the deformation field was imaged at once [*Massonnet et al.*, 1993]. In parallel, the Landers earthquake was also one of the first large events that were mapped at a very detailed scale over its entire length [*Sieh et al.*, 1993], thanks to excellent exposures and proximity of research centers. From the early 2000s,

---

*Institut de Physique du Globe de Paris, Université Sorbonne Paris Cité, Université Paris Diderot, Paris, France*

the availability of new submetric optical satellites and topography to civilian scientists increased the resolution by one order of magnitude. This has allowed scientists to investigate more thoroughly major continental ruptures around the world, without being constrained by the size of the rupture [i.e., *Klinger et al.*, 2005; *Li et al.*, 2005], including revisiting past large events [*Klinger et al.*, 2011; *Ren et al.*, 2016]. This improvement in image resolution and topography also helped with mapping active faults in general, contributing to a better knowledge of the surficial geometry of continental faults. Hence, over the last two decades scientists have been building data sets of surface rupture maps [*Wesnousky*, 2008; *Klinger*, 2010] with an increasing level of details, often down to a few meters or better, including revisiting past events and some of the old archived aerial photos. The number of events currently well documented is about 20 to 30, depending on the level of details needed.

The main outcome of this improvement in mapping ruptures has been to bring forward the fact that for continental earthquakes, at least, complexity of earthquake source and associated ground rupture is the general rule rather than the exception. Most of the recently documented earthquakes have proven to have complex ruptures to some extent, with significant fault segmentation and jogs, such as the 2001 Kunlun earthquake [*Klinger et al.*, 2005] or the 1999 Izmit-Duzce sequence [*Lettis et al.*, 2000], and several active branches such as the 2002 Denali earthquake [*Haeussler et al.*, 2004] or the 2010 El-Mayor earthquake [*Wei et al.*, 2011; *Oskin et al.*, 2012], to name only a few. In fact, complexity appears at all scales, from cracks at the metric scale, to kilometric-long branches [*Vallage et al.*, 2015]. Fault segmentation characterizing the complexity of the overall fault geometry on a larger scale (tens of kilometers) seems to be persistent over successive seismic cycles, although the details of geometry for individual fault segments could be modified during individual earthquakes [*Klinger*, 2010]. The relay zones that link segments, especially for strike-slip faults, have been regarded as playing a special role in initiation and arrest of earthquake ruptures [*Wesnousky*, 2006], related to the ill-configuration of local fault geometry that hinders efficient accommodation of the stress accumulated during the interseismic period [*King and Nabelek*, 1985]. Eventually, at the end of an earthquake rupture, the residual stress would be higher at jogs, compared to geometrically simpler fault segments, and more prone to initiate new ruptures [*Nielsen and Knopoff*, 1998; *Duan and Oglesby*, 2006].

Since the geometrical complexity appears to be an inherent characteristic of the fault structure, many studies have been conducted to explore the impact of the fault geometry on rupture dynamic processes. Indeed, geological observations remain difficult to include directly in rupture

models, as they often show a level of detail that is still beyond computational capabilities of state-of-the-art models. Hence, through simplified models, most often addressing the geometry in 2D, the effects of jogs, fault branching, or damage, in conjunction with local stress orientation and rupture speed, have been systematically explored [*Harris and Day*, 1993; 1999; *Poliakov et al.*, 2002; *Kame et al.*, 2003; *Thomas et al.*, 2017 (this volume)], as well as impact of fault geometry on evaluating various rupture scenario for specific fault systems [e.g., *Muller and Aydin*, 2004]. These seminal works show that earthquake rupture patterns and earthquake cycle can probably not be well understood if fault geometry is not properly taken into account [*Bhat et al.*, 2004; *Bhat et al.*, 2007; *Elliott et al.*, 2015].

Some of the geometrical asperities can be kilometric in size. More specifically, during several earthquakes it has been shown that the existence of large branches had affected the course of the rupture process significantly, in diverting the rupture propagation from what would be considered the long-term geological trace of the fault, as discussed further in coming sections of this chapter. These branches, however, because they are large-scale features well visible in the landscape, have to be long-lived features and could not be activated only during a single event. Hence, in the next sections we explore three pathological cases where large-scale branches were involved during large continental strike-slip ruptures. The three cases presented are the 1905 M8 Bolnay event, the 2002 Mw 7.9 Denali event, and the 2001 Mw 7.8 Kunlun event. For the Bolnay and the Kunlun earthquakes, new high-resolution maps of the surface rupture, focused on the location where branches are joining the main rupture, are presented. These maps are based on submetric satellite images, complemented with field observations. Special care has been taken when mapping to document secondary deformations that are likely relevant to the understanding of earthquake-rupture branching processes. Data for the Denali earthquake are solely derived from published literature. In the case of the Bolnay earthquake, although preservation of the landform is exceptional due to very limited erosion, it could not be excluded that some secondary cracks are not visible anymore, as images were acquired about a century after the event. In the case of the Kunlun event, images were acquired in the year following the event, and maps established from satellite imagery appear to be complete down to metric scale features, when compared with field observations [*Klinger et al.*, 2005]. In each case, we present the geometry of the rupture in detail and show how the rupture proceeded through the branching section. Eventually, in one case we present evidence suggesting that branching observed during the last event might have happened similarly during previous events. If this would be the case, then better

understanding of the condition leading to such persistent branching, as well as fault geometry, would allow the building of rupture scenarios with a more limited range of possible scenarios [Schwartz *et al.*, 2012; Mignan *et al.*, 2015].

## 11.2. CASE STUDIES

### 11.2.1. The 1905 M8 Bolnay Earthquake, Mongolia

In 1905, a series of earthquakes struck northwestern Mongolia with two  $M \sim 8$  earthquakes 14 days apart. The Tsetserleg M8 earthquake occurred on 9 July 1905 and the Bolnay M8+ event on 23 July 1905. This sequence is one of the largest continental earthquake sequences known. These earthquakes broke faults that relate to the northern most extent of the India-Eurasia collision [Tapponnier and Molnar, 1977]. Both earthquakes were dominated by strike-slip mechanisms. Several works have already addressed some details of the surface rupture, seismological aspects, or triggering issues for these two events [Khilko *et al.*, 1985; Baljinnyam *et al.*, 1993; Chéry *et al.*, 2001; Schlupp and Cisternas, 2007; Choi *et al.*, 2015; Rizza *et al.*, 2015] that will not be repeated here. Focus will be limited here to aspects more specifically related to branching during the rupture process of the second event, the Bolnay earthquake. No obvious branches were documented for the Tsetserleg event, although its surface rupture displays some degree of geometrical complexity, including significant changes of azimuth along the rupture path [Choi *et al.*, 2015].

The Bolnay rupture is formed by a main E-W rupture, about 385 km long, where strike-slip dominates the deformation style. The left-lateral surface slip averages 6 m with a maximum surface slip about 10.6 m, documented 200 km east of the epicenter. A major 80 km long branch, the Teregtiyn fault, is associated with the main rupture (Figure 11.1). This branch is itself divided into two sections 15 km long and 65 km long respectively. The Teregtiyn

fault strikes N140E, making an angle of 44° with the main rupture (Figure 11.1). Displacement along the Teregtiyn branch is mostly characterized by right-lateral strike-slip, kinematically consistent with the left-lateral motion along the main rupture, with some thrust component along the closest section to the main rupture. Horizontal slip is about 1 m to 3 m, and thrust motion reaches 1.3 m on average. For the sake of completeness, the Dungen fault should also be mentioned. It is oriented N-S, about 90° from the main rupture. This fault, located about 100 km eastward from the epicentral area, is about 35 km long. Ground surface ruptures are characterized by a series of right-lateral en-echelon cracks with no obvious primary fault plane. At this stage it is impossible to assess the existence of a fully connected fault plane even at depth. This part of the rupture is actually not connected to the main Bolnay rupture, and although it is classically associated with the rupture of the Bolnay earthquake [Schlupp and Cisternas, 2007], the timing of the rupture remains arguable, and it could be associated with the Tsetserleg event as well. In any case, this branch does not seem to have influenced the rupture pattern of the Bolnay earthquake significantly, and it will not be discussed further here.

The Bolnay event typifies events where the epicenter is located at the junction point between the main rupture and a major branch. Although uncertainty about epicentral location due to scarcity of records impedes more precision, seismic source inversion [Schlupp and Cisternas, 2007] suggests that the rupture might have actually started at the northern end of the Teregtiyn branch, triggering bilateral rupture along the main fault trace, from the junction point. During the same time, part of the rupture also propagated southward along the Teregtiyn fault. Both faults have a long-term imprint in the topography that denotes that they have been active for quite some time. Cumulative offsets along the Teregtiyn, however, are smaller with a maximum documented value of 16.5 m, which confirms that this fault

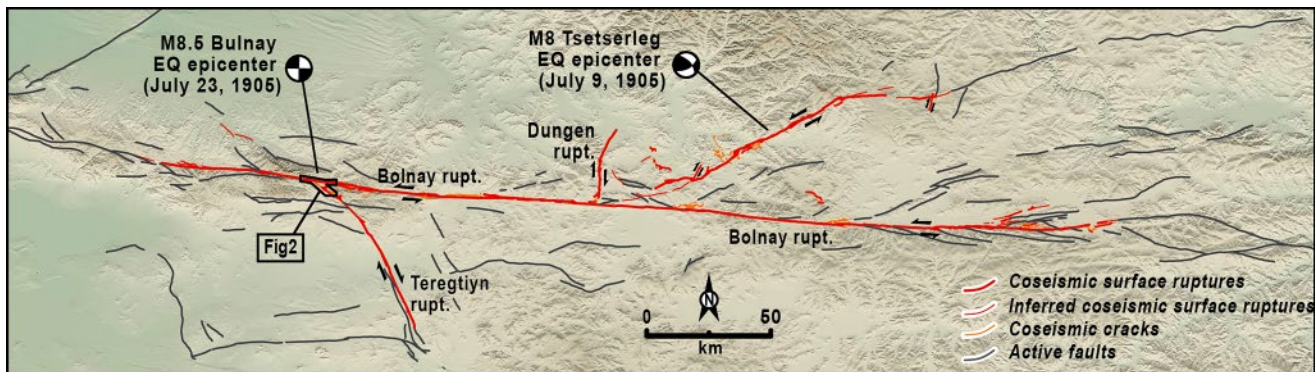


**Figure 11.1** General rupture map of the 1905 earthquake sequence in Mongolia, including both the Tsetserleg and the Bolnay earthquakes. The epicenter of the Bolnay rupture is located in the area where the Teregtiyn fault connects to the main Bolnay fault. See electronic version for color representation.

is a secondary structure, not necessarily activated every time the main Bolnay fault breaks. Mapping of the 1905 surface rupture reveals that the two faults do not join through a triple junction characterized by simple well-defined fault traces (Figure 11.2). Instead, the exact location of the junction is characterized by a maze of cracks mostly located in the inner corner between the two fault strands. Outside of this zone, damage is limited to a few cracks oriented according to the fabric of the local geology. Many cracks, including the structures bounding the area to the south, are mainly showing evidence of extension, in agreement with the local kinematic controlled by simultaneous

activation of the left-lateral Bolnay fault and the right-lateral Teregtyin segment. Indeed, the pattern of rupture illustrates that such junction could not be stable over long periods of time, and fault geometry at that location has to reconfigure itself during each event to accommodate negative volumetric change.

### 11.2.2. The 2002 Mw 7.9 Denali Earthquake, Alaska

On 3 November 2002, the Mw 7.9 Denali earthquake broke 340 km of the central part of the Denali fault (Figure 11.3) in Alaska, USA [Haeussler *et al.*, 2004].

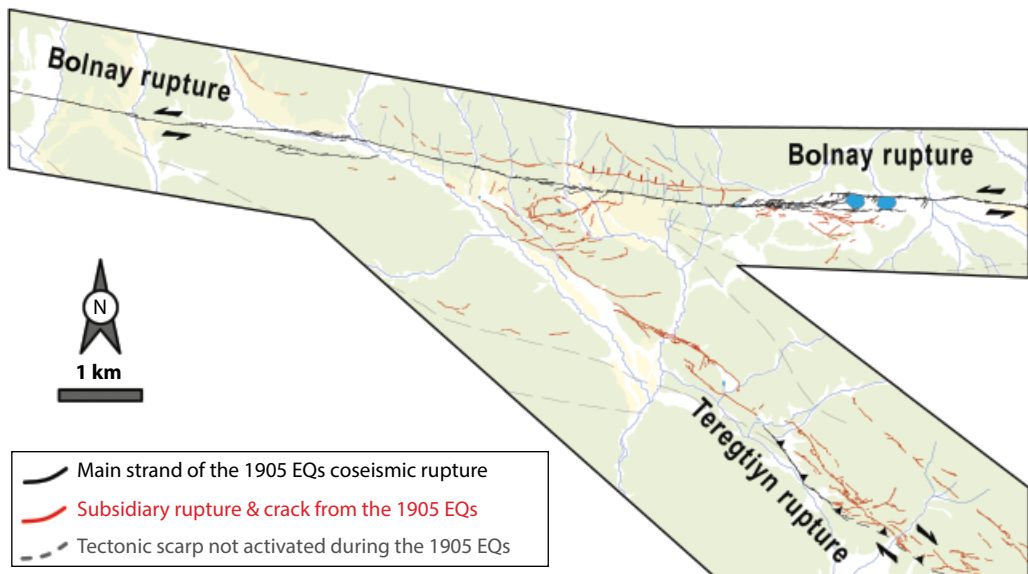


**Figure 11.2** Detail of the rupture pattern associated with the 1905 Bolnay earthquake, derived from satellite imagery analyses and field observations. The corner in-between the Bolnay rupture and the Teregtyin branch appears to be significantly shattered by randomly oriented cracks. See electronic version for color representation.

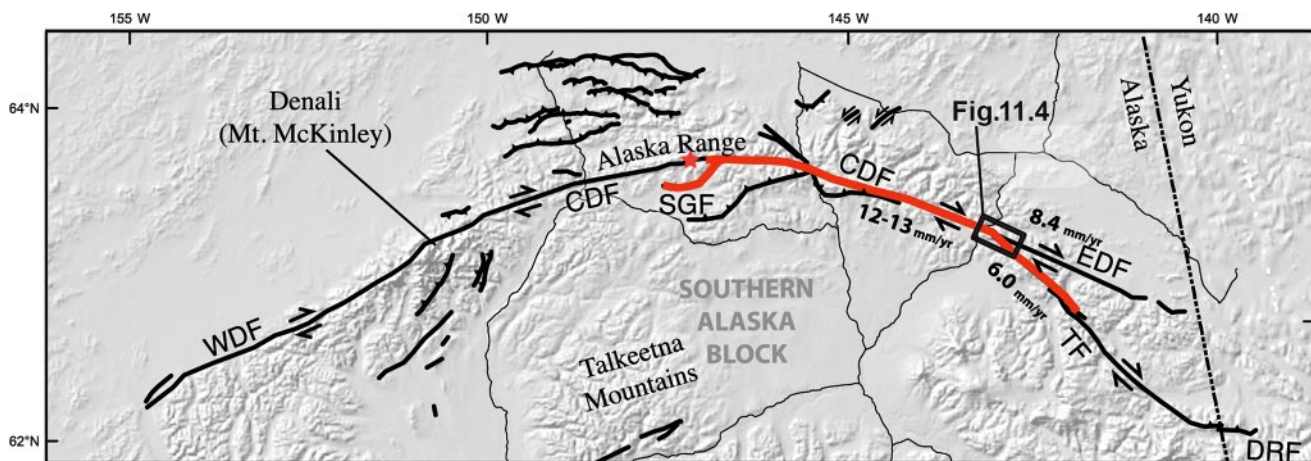


**Figure 11.3** General rupture map of the 2002 Denali rupture (in red) and of the Denali fault system. CDF = Central Denali fault, EDF = East Denali fault, WDF = West Denali fault, SGF = Susitna Glacier fault, TF = Totschunda fault. Adapted from Schwartz *et al.* [2012]. See electronic version for color representation.

This fault is part of the complex fault system that accommodates the collision between the Yakutat block and the North America block [Elliott et al., 2010] through a partitioned tectonic system [Vallage et al., 2014], where the Denali fault acts as a major right-lateral strike-slip fault. The long-term slip rate along the central part of the Denali fault is about  $12 \pm 3$  mm/yr [Matmon et al., 2006; Mériaux et al., 2009].

The rupture initiated along the Susitna Glacier fault segment, a thrust fault that was unrecognized before the 2002 earthquake [Haeussler et al., 2004]. After 48 km, this thrust fault connects to the central Denali fault, where the rupture developed as a pure strike-slip rupture for about 225 km, before branching onto the Totschunda fault, where it ruptured 66 km additional kilometers (Figure 11.4). On average, the horizontal motion was 4.5 m to 5 m with a reported maximum of 8.8 m [Haeussler et al., 2004]. The average right-lateral horizontal slip along the Totschunda segment is 1.7 m. Seismological records suggest that part of the rupture went super-shear in the central section, although it was only along a limited section that ended even before the rupture approached the junction between the proper Denali fault and the Totschunda fault branch [Dreger et al., 2004; Dunham and Archuleta, 2004].

The reason why the Denali rupture branched on the Totschunda fault has been widely discussed. Coming from the west along the Denali fault, at  $62.82^\circ\text{N}$ ,  $143.35^\circ\text{W}$  the Denali fault splits into two strands, the eastern Denali fault to the north and the Totschunda fault to the south. Each strand accommodates about half

of the total slip rate of the Denali fault [Matmon et al., 2006]. Although the full fault geometry is not yet well understood, the two strands get back together about 250 km farther south into a single Denali fault [Spotila and Berger, 2010]. Recent observations suggest that along the eastern Denali section, soon after the junction, the strike-slip component of the Denali fault becomes very small and that the fault is currently dominated by dip-slip motion [Marechal, 2015]. Most of the strike-slip component would then be accommodated along the Totschunda strand [Marechal et al., 2015]. In the field, however, the morphological trace of each segment can be followed to the exact junction point (Figure 11.4), suggesting that both segments have been active during the Late Quaternary. Schwartz et al. [2012], based on paleoseismological findings, argue that according to the timing of the last earthquake on each strand, it was more favorable for an earthquake rupture propagating eastward to continue along the Totschunda fault rather than along the eastern Denali fault; the accumulated slip-deficit since the last event on the east Denali fault would be somewhere between 0.62 m and 3.65 m, whereas the accumulated slip-deficit along the Totschunda fault would stand somewhere between 2.77 m and 5.29 m. Hence, for these authors, there was no need to invoke any additional processes to explain the branching of the Denali rupture. Conversely, several studies have considered more specifically the local stress conditions [Dreger et al., 2004] and the effect of dynamic propagation of the rupture during the Denali earthquake [Bhat et al., 2004] as the main causes for branching. In fact, the Totschunda branch is

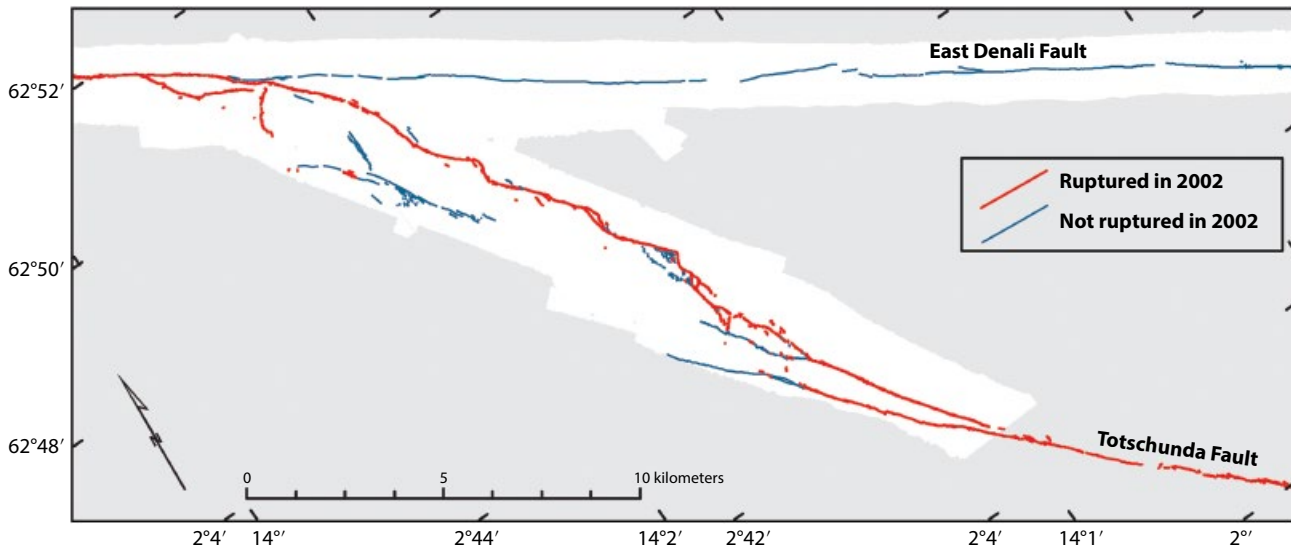


**Figure 11.4** Detail from Figure 11.3. Area where the Totschunda fault branches off from the Eastern Denali fault strand. The two fault systems appear to be well connected and the 2002 Denali rupture (in red) is very continuous across the junction. After Schwartz et al. [2012]. See electronic version for color representation.

located in the extensional quadrant of the central Denali fault and is naturally prone to rupture when dynamically loaded by a seismic rupture coming from west [Kame *et al.*, 2003], independently of the rupture speed. Hence, because the uncertainties on dating past earthquakes along the Denali fault and the Totschunda fault remain large, no definitive conclusion can be drawn from paleoseismic data alone. Also, it is difficult at this stage to ascertain that dynamic rupture effect is the only reason the rupture branched, it is clear that it could have only helped.

### 11.2.3. The 2001 Mw 7.8 Kunlun Earthquake, China

On 14 November 2001, the Kunlun earthquake, also coined the Kokoxili earthquake, broke 430 km of the Kunlun fault. The moment magnitude for this event, dominated by left-lateral strike-slip, is Mw 7.8. The Kunlun fault counts as one of the largest continental strike-slip faults to participate in the eastward extrusion of Tibet, in the context of the continental collision between the Indian plate and the Eurasian plate [Tappognier and Molnar, 1977]. The Kunlun fault is about 1500 km long, with a finite offset estimated to be about 150 km [Van Der Woerd *et al.*, 2000]. Slip rates at different time scales have been estimated along this fault; along the western section of the fault, which is of concern here, both geodetic and long-term geologic slip rates point to values about 10 mm/yr  $\pm$  2 mm/yr [Wang *et al.*, 2001; Van Der Woerd *et al.*, 2002; Li *et al.*, 2005]. The Kunlun fault is segmented at a different spatial scale; at a scale of hundreds of kilometers, the fault is characterized by sections with significant differences ( $>5^\circ$ ) in azimuth that translate into some dip-slip component, in addition to the dominant strike-slip motion. For example, the Xidatan section, located directly east of the Kunlun rupture, is characterized by a slight opening component in addition to the lateral motion to accommodate the  $\sim 10^\circ$  azimuth difference between the two successive fault sections. This first-order structuration of the fault is most probably related to the existence of an older suture

zone, associated with the progressive buildup of the Tibetan plateau [Tappognier *et al.*, 2001], that guided the early localization of the deformation during the more recent emplacement of the strike-slip fault. The fault appears also to be segmented at a smaller scale of 10 km to 20 km. Structural discontinuities, such as relay zones, bends, and joining side faults can be found along the 2001 earthquake surface rupture. These coincide with strong variation in the coseismic slip distribution and were interpreted as evidence of such segmentation [Klinger *et al.*, 2006; Klinger, 2010].

The Kunlun earthquake rupture was unilateral [Vallee *et al.*, 2008]. The rupture initiated in a small pull-apart basin and after going through an oblique normal fault section, it fully developed along the Kusai segment, over  $\sim 270$  km (Figure 11.5). Then the rupture branched southward on the so-called Kunlun Pass fault, where the rupture propagated for an extra 70 km before dying out, leaving the Xidatan segment, the long-term continuation of the Kunlun fault, unbroken. Along the eastern section of the Kunlun Pass fault, in addition to the strike-slip motion, a significant thrust component was observed with the fault dipping to the north [Klinger *et al.*, 2005]. Detailed measurements of the rupture velocity along the Kusai segment and the Kunlun Pass fault show that along a significant part of the Kusai segment the rupture went super-shear [Bouchon and Vallée, 2003; Vallee *et al.*, 2008]. Eventually, the rupture slowed down at the branching point that corresponds to a change of azimuth of about  $5^\circ$  southward along the rupture. The horizontal slip, after a progressive increase of up to  $\sim 6$  m when approaching the branching point location from the west, dropped abruptly to less than 2 m at the fault junction. Such asymmetric slip profile is often associated with fault asperities [Manighetti *et al.*, 2004; Klinger *et al.*, 2006], which would also be consistent with the brutal slow down of the rupture propagation.

The seismological history of the Xidatan section, the long-term continuation of the Kunlun fault east of the Kusai section, is not well established yet. The morphology

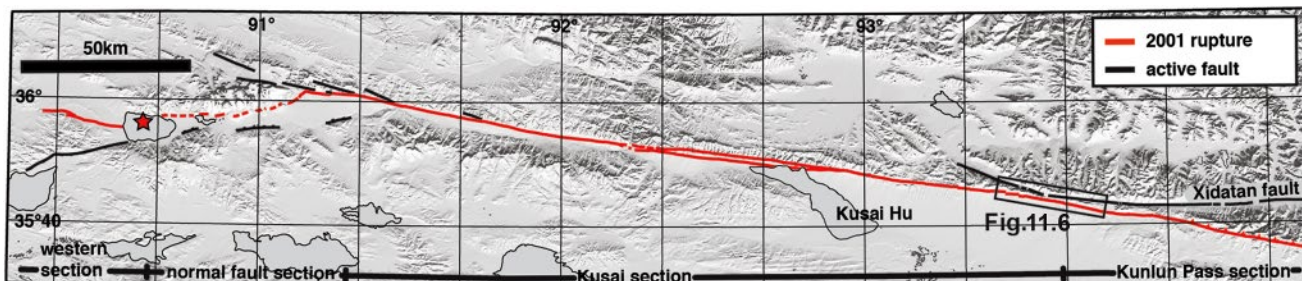


**Figure 11.5** Rupture map of the Mw 7.8 2001 Kunlun earthquake. The red star marks the epicenter location. The rupture went unilaterally and ended on the Kunlun Pass fault, leaving the Xidatan section unbroken. After Klinger *et al.* [2005]. See electronic version for color representation.

of the fault along this segment is rather smooth, and the few available dates from undeformed alluvial surfaces and paleoseismological trenches suggest that no earthquake has occurred along this segment during the last 280 years [Van Der Woerd *et al.*, 2002], although one earthquake probably occurred along the Xidatan section during the last 600 years [Lin *et al.*, 2006; Klinger *et al.*, 2015]. Along the Xidatan segment, as well as along the Kusai segment, few evidence for past earthquakes combined with measured coseismic deformation from the 2001 event and the slip-rate yield an average return time for a large event close to 500 years [Klinger *et al.*, 2015]. Hence, the Kunlun earthquake occurred at a time when one could expect that the adjacent segment was already partially tectonically loaded, although not necessarily yet on the verge of failure.

Detailed mapping of the surface rupture related to the 2001 earthquake at the branching location (Figures 11.6 and 11.7) reveals a complex pattern of rupture. Overall, the rupture appears continuous across the branching section. The rupture, however, which is rather linear along the Kusai section, becomes more segmented with several right-stepping jogs generating local small compressional features as it approaches the junction. Eventually, once the rupture has propagated through the junction and continues along the Kunlun Pass fault, the surface rupture pattern gets back to a simpler linear surface expression (Figure 11.6). At the junction location, the main rupture trace bounds to the south the area affected by cracks. No significant ground rupture can be observed directly south of the main surface rupture. Only a few extensional cracks are documented several kilometers south from the main rupture, which are associated with the super-shear rupture propagation [Bhat *et al.*, 2007] and are not directly related to the branching process. Conversely, the area, about 500 m wide and located

directly north of the main rupture trace, appears to be extensively affected (Figure 11.7) by a set of cracks that become more and more oblique to the main rupture trace as one moves eastward. The intensely damaged section is about 5.5 km long, starting from the place where the rupture begins to depart from the main Kusai section trace, right stepping toward the Kunlun Pass fault, to end where a well-established Kunlun Pass fault runs southward from the Xidatan section, about 1.2 km south of it. Actual sense of motion for individual cracks is not easy to determine, for each crack bears only a small amount of displacement. Most of the cracks, however, seem to accommodate at least a minor component of vertical deformation, while horizontal component is harder to recognize. The cracks are grossly parallel, aligned along a direction close to the local azimuth of the Xidatan section. The length of the cracks, which could also probably be called branches, varies from few meters to almost one kilometer for the longest. Such rupture pattern suggests that when the rupture arrived at the junction, probably at super-shear speed [Vallee *et al.*, 2008], the rupture attempted to breach toward the Xidatan segment. However, the triggering of the rupture along the western termination of the Xidatan section seems to have been hindered, probably by the presence of a strong asperity, while at the same time branching of the rupture along the Kunlun Pass fault was promoted by a low angle between the branch and the main fault, a close direction (<25°) of principal horizontal stress with the local fault azimuth, and a super-shear rupture [Kame *et al.*, 2003]. As the rupture fully developed along the Kunlun Pass fault, quickly the Xidatan section was in the shadow zone of the propagating rupture and could not rupture anymore. Hence, in the case of the Kunlun earthquake, both the specific geometry of the branch (low angle with the main fault) and the horizontal stress direction appear to have been key in promoting branching in

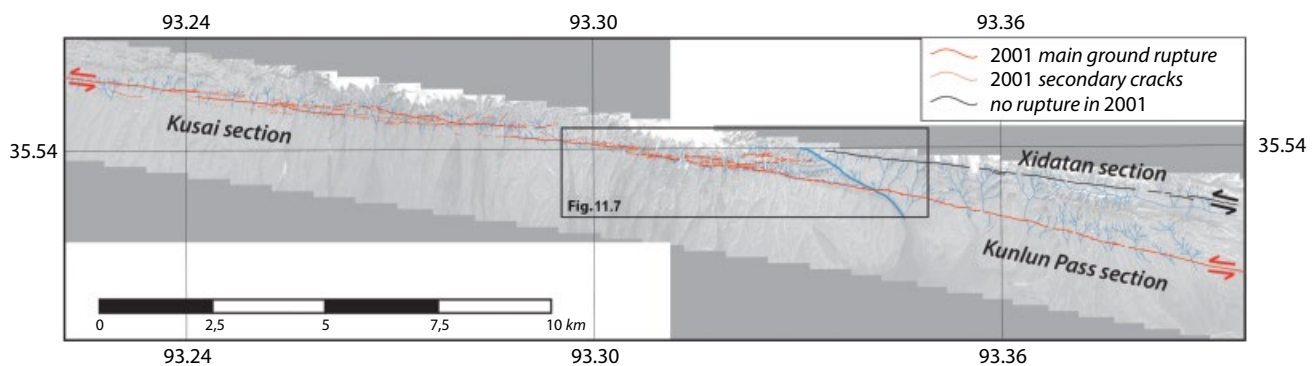


**Figure 11.6** Detail from Figure 11.5. Junction between the Kusai section, to the west, the Xidatan section, long-term continuation of the Kunlun fault, and the Kunlun Pass fault. The rupture progressively jumped southward as it was moving eastward. Long-term morphology suggests that the rupture was following the path already used by previous earthquakes. Metric-resolution satellite image in background gives some sense of topography. Almost all drainages, including the major drainage at the junction between Xidatan and Kusai sections, flow south. See electronic version for color representation.

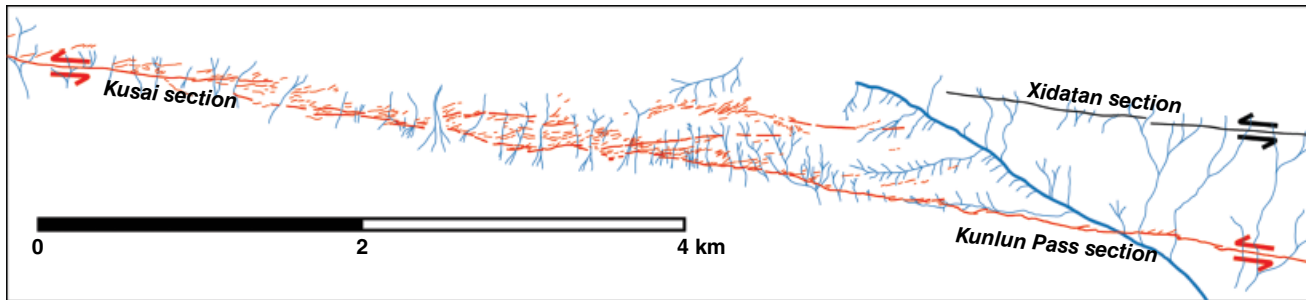


**Figure 11.7** Detail of the zone in Figure 11.6 where the rupture branched off on the Kunlun Pass fault, instead of rupturing the Xidatan section. Numerous cracks north of the main rupture trace attest that the rupture tried to connect to the Xidatan section. Interestingly, almost no cracks are visible south of the main rupture. See electronic version for color representation.

the compressional quadrant, when in most configurations it is easier to promote rupture in the extensional quadrant [Kame *et al.*, 2003]. In the case of the 2001 event, super-shear rupture velocity made this configuration even more favorable for such branching.

Interestingly, the Kunlun fault is characterized by distinctive morphology along most of its length, which attests to its long-term activity and makes it easily identifiable in the landscape [Li *et al.*, 2005; Klinger *et al.*, 2015]. Similarly, although cumulative offsets are smaller, the western end of the Kunlun Pass branch is also characterized by evidence for long-term activity and a significant imprint in the landscape. At the junction between the proper Kunlun fault and the Kunlun Pass fault, however, the morphology is more confused. Anywhere else, the Kunlun fault is usually characterized by some linear topographic features such as ridge, valley, or fault scarp aligned with the fault direction, that crosscut the general morphology associated with the Kunlun Range, grossly controlled by the regional north-south drainage direction. The location of the junction, instead, is characterized by some positive topography with no clear evidence for a throughgoing fault, and an oblique river channel flowing south across the range (Figures 11.6 and 11.7). The channel does not show any obvious evidence of long-term left-lateral offset, as should be expected if earthquake ruptures would regularly offset the channel. Eventually, it suggests that earthquake ruptures propagating eastward along the Kusai section might never fully break through this asperity to connect to the Xidatan section. Instead, due to geometry and stress condition, the rupture would just stop at the junction or might branch to the Kunlun Pass Fault. The effect would be even more enhanced when super-shear propagation occurs. The positive topography visible at the junction site would then be associated with compressional deformation related to the right stepping of the rupture, accommodated by a myriad of cracks in the jog area. Hence, such a scenario would imply that earthquakes rupturing the Xidatan segment would either initiate at the junction and propagate east-

ward, or if propagating from the east, they would systematically end at the junction. Because some deformation is accommodated at the pressure ridge, and because the Xidatan fault and the Kunlun Pass fault run almost parallel for some distance, allowing for a progressive transfer of deformation, no long-term slip deficit should be expected at the junction between the two faults. The exact nature of structural connection, including at depth, between the Kusai segment and the Xidatan segment might, however, be more complex than previously thought and would deserve further investigation.

### 11.3. DISCUSSION

In the last decade, significant efforts have been made to try to improve earthquake hazard assessment in the framework of national or international consortiums, such as the Uniform California Earthquake Rupture Forecast project [Field *et al.*, 2014] or the Global Earthquake Model project (<http://www.globalquakemodel.org/gem/>). The main emphasis, for aspects directly related to geology, is on compiling accurate fault maps and the most complete earthquake record, including paleoseismicity, for each fault system considered. The way to incorporate fault geometry and possibilities for a rupture to jump from one fault to the next one, or to trigger rupture on a secondary fault, are at the core of the most recent developments of such projects and are highly debated in the literature [Liu and Duan, 2015; Mignan *et al.*, 2015].

Fault branches are first-order features when it comes to characterizing fault geometry. Careful examination of earthquake ruptures during the last century, when acceptable quality rupture maps are available, shows that in the majority of strike-slip cases, a major branch is involved. In some cases the epicenter or the end of the rupture is co-located with the junction between the main fault and the branch, such as in the case of the Bolnay earthquake discussed earlier in this chapter, or the Mw 7.1 Hector Mine earthquake in 1999 [Jónsson *et al.*, 2002].

More interestingly, the rupture often branches off the main fault during propagation to end up in a cul-de-sac, where it dies out, stopping the earthquake. This is the case, for example, with the earthquakes of Denali or Kunlun, extensively discussed earlier in this chapter, but it has been documented for many other large earthquakes such as the Mw 7.9 1939 Erzincan earthquake along the North Anatolian fault, Turkey [Barka, 1996]; the Mw 7.2 Izmit/Mw 7.1 Duzce earthquake sequence in 1999, also along the North Anatolian fault [Rockwell *et al.*, 2002]; or the Mw 7.9 Manyi earthquake in Tibet [Peltzer *et al.*, 1999], to name only a few. In several cases, although the branch could be identified in the landform morphology even before the most recent earthquake took place, a well-developed connection between the main fault and the branch was not always easy to recognize, if existing at all. In fact, in the case of strike-slip motion, the location where a branch connects to the main fault is similar to a triple junction between three strike-slip faults and, as such, should not be expected to be stable through time [McKenzie and Morgan, 1969], possibly hindering development of a clear morphological signature. At short timescale, stress-shadowing effects during an individual rupture might also come into play to prevent concomitant rupturing and further connection of the three legs of the fault junction [Ando *et al.*, 2009].

Identification of such structures, understanding of their impact on rupture propagation, and incorporation of such knowledge in earthquake rupture scenario might, however, prove to be efficient in limiting the number of possible rupture scenarios to test while assessing seismic hazard for large regions. The example of the Kunlun rupture suggests that in that case, any rupture that would propagate eastward along the Kusai section might branch and die on the Kunlun Pass fault. Similarly, our observations suggest that rupture along the Xidatan section would either initiate or end at the junction but not go through this junction. Hence, such considerations limit the number of potential rupture scenarios along this part of the Kunlun fault, as well as the size of potential earthquakes. Similar factors have been taken into account in considering the following: various rupture scenarios along the Marmara Sea section of the North Anatolian fault [Oglesby *et al.*, 2008], possibilities of simultaneous ruptures of the southern section of the San Andreas fault and of the San Jacinto fault [Lozos *et al.*, 2012; Lozos, 2016], and rupture extent along the Altyn Tagh fault [Elliott *et al.*, 2015].

Eventually, it appears from case studies that fault branching is a major player in the propagation and arrest of, at the minimum, strike-slip ruptures. It is likely that branches would also be important during propagation of dip-slip ruptures [Templeton *et al.*, 2010; Melnick *et al.*, 2012; Xu *et al.*, 2015].

A significant effort in developing conceptual models and efficient modeling tools has been emerging in the last decades to account for such complex geometry. Taking advantage of the increase in computational capabilities, models including dynamic rupture propagation on multiple planar vertical fault planes embedded in a volume have been developed that give us some new insight into dynamic fault interaction, including fault branching [Oglesby *et al.*, 2008; Lozos, 2016]. Planar nonvertical faults have also been modeled to look at geometry effects for dip-slip faults, such as the thrust fault that caused the Mw 7.7 Chi-Chi earthquake in Taiwan in 1999 [Oglesby and Day, 2001]. Recent work explored possibilities of models including nonplanar faults [Duru and Dunham, 2016], which show the impact of fault roughness on wave propagation and deformation patterns [Bruhat *et al.*, 2016].

Eventually, these different approaches will converge to provide the community with some tools able to incorporate field data with a level of detail similar to what is presented in this chapter. Based on real case studies, we might then be able to better understand what actually controls rupture branching and to focus only on the most likely rupture schemes when running earthquake scenario for an entire fault system.

## ACKNOWLEDGMENTS

This work was partly funded by ANR Geosmech contract ANR-12-BS06-0016 and by a grant from the city of Paris. We thank the editor, M. Thomas, and two anonymous reviewers for insightful comments and suggestions that significantly improved this manuscript.

## REFERENCES

- Ando, R., B. E. Shaw, and C. H. Scholz (2009), Quantifying natural fault geometry: Statistics of splay fault angles, *Bulletin of the Seismological Society of America*, 99(1), 389–395, doi:10.1785/0120080942.
- Baljinnyam, I., *et al.* (1993), Ruptures of major earthquakes and active deformation in Mongolia and its surroundings, *Geological Society of America Memoir 181*, 62 pp., The Geological Society of America, Boulder.
- Barka, A. (1996), Slip distribution along the North Anatolian fault associated with the large earthquakes of the period 1939–1967, *Bull. Seism. Soc. Am.*, 86(5), 1238–1254.
- Bhat, H. S., R. Dmowska, G. C. P. King, Y. Klinger, and J. R. Rice (2007), Off-fault damage patterns due to supershear ruptures with application to the 2001 M-w 8.1 Kokoxili (Kunlun) Tibet earthquake, *Journal of Geophysical Research: Solid Earth*, 112, B06301, doi:10.1029/2006JB004425.
- Bhat, H., R. Dmowska, J. Rice, and N. Kame (2004), Dynamic slip transfer from the Denali to Totschunda faults, Alaska: Testing theory for fault branching, *Bulletin of the Seismological Society of America*, 94(6B), S202–S213.

- Bouchon, M., and M. Vallée (2003), Observation of long supershear rupture during the  $M_s=8.1$  Kunlunshan earthquake, *Science*, 301(5634), 824–826.
- Bruhat, L., Z. Fang, and E. M. Dunham (2016), Rupture complexity and the supershear transition on rough faults, *Journal of Geophysical Research: Solid Earth*, 121, doi:10.1002/2015JB012512.
- Chéry, J., S. Carretier, and J.-F. Ritz (2001), Postseismic stress transfer explains time clustering of large earthquakes in Mongolia, *Earth and Planetary Science Letters*, 194(1), 277–286.
- Choi, J.-H., et al. (2015), High-resolution surface-rupture map and slip distribution for the 1905 M8 Tsetserleg-Bulnay, Mongolia, earthquake sequence, paper presented at AGU Fall meeting, San Francisco CA, USA, 14–18 December.
- Dreger, D. S., D. D. Oglesby, R. Harris, N. Ratchkovski, and R. Hansen (2004), Kinematic and dynamic rupture models of the November 3, 2002 Mw7.9 Denali, Alaska, earthquake, *Geophysical Research Letters*, 31(4).
- Duan, B., and D. D. Oglesby (2006), Heterogeneous fault stresses from previous earthquakes and the effect on dynamics of parallel strike-slip faults, *Journal of Geophysical Research*, 111, B05309, doi:10.1029/2005JB004138.
- Dunham, E. M., and R. J. Archuleta (2004), Evidence for a supershear transient during the 2002 Denali fault earthquake, *Bulletin of the Seismological Society of America*, 94(6B), S256–S268.
- Duru, K., and E. M. Dunham (2016), Dynamic earthquake rupture simulations on nonplanar faults embedded in 3D geometrically complex, heterogeneous elastic solids, *Journal of Computational Physics*, 305, 185–207.
- Elliott, A. J., M. E. Oskin, J. Liu-Zeng, and Y. Shao (2015), Rupture termination at restraining bends: The last great earthquake on the Altyn Tagh Fault, *Geophysical Research Letters*, 42(7), 2164–2170.
- Elliott, J. L., C. F. Larsen, J. T. Freymueller, and R. J. Motyka (2010), Tectonic block motion and glacial isostatic adjustment in southeast Alaska and adjacent Canada constrained by GPS measurements, *Journal of Geophysical Research: Solid Earth* (1978–2012), 115(B9).
- Field, E. H., R. J. Arrowsmith, G. P. Biasi, P. Bird, T. E. Dawson, K. R. Felzer, D. D. Jackson, K. M. Johnson, T. H. Jordan, and C. Madden (2014), Uniform California Earthquake Rupture Forecast, Version 3 (UCERF3): The time-independent model, *Bulletin of the Seismological Society of America*, 104(3), 1122–1180.
- Haeussler, P. J., et al. (2004), Surface rupture and slip distribution of the Denali and Totschunda faults in the 3 November 2002 M 7.9 earthquake, Alaska, *Bulletin of the Seismological Society of America*, 94(6), S23–S52.
- Harris, R., and S. Day (1993), Dynamics of fault interaction: Parallel strike-slip faults, *J. Geophys. Res.*, 98(B3), 4461–4472.
- Harris, R., and S. Day (1999), Dynamic 3D simulations of earthquakes on en echelon faults, *Geophys. Res. Lett.*, 26(14), 2089–2092.
- Ji, C., R. J. Archuleta, and C. Twardzik (2015), Rupture history of 2014 Mw 6.0 South Napa earthquake inferred from near-fault strong motion data and its impact to the practice of ground strong motion prediction, *Geophysical Research Letters*, 42(7), 2149–2156.
- Jónsson, S., H. Zebker, P. Segall, and F. Amelung (2002), Fault slip distribution of the 1999 Mw 7.1 Hector Mine, California, earthquake, estimated from satellite radar and GPS measurements, *Bulletin of the Seismological Society of America*, 92(4), 1377–1389.
- Kame, N., J. R. Rice, and R. Dmowska (2003), Effects of pre-stress state and rupture velocity on dynamic fault branching, *J. Geophys. Res.*, 108(B5), 2265, doi:10.1029/2002JB002189.
- Khilko, S., R. Kurushin, V. Kotchetkov, L. Misharina, V. Melnikova, N. Gileva, S. Lastochkin, I. Baljinnyam, and D. Monhoo (1985), Earthquakes and the base of the seismogenic zoning of Mongolia, *Joint Soviet-Mongolian Research Geological Scientific Expedition*, 41, 225.
- Kim, A., and D. S. Dreger (2008), Rupture process of the 2004 Parkfield earthquake from near-fault seismic waveform and geodetic records, *Journal of Geophysical Research: Solid Earth*, 113(B7).
- King, G., Y. Klinger, D. Bowman, and P. Tapponnier (2005), Slip partitioned surface breaks for the 2001 Kokoxili earthquake, China (Mw 7.8), *Bull. Seis. Soc. Am.*, 95(2), 731–738.
- King, G. C., and J. Nabelek (1985), The role of fault bends in faults in the initiation and termination of earthquake rupture, *Science*, 283, 984–987.
- Klinger, Y. (2010), Relation between continental strike-slip earthquake segmentation and thickness of the crust, *J. Geophys. Res.*, 115, doi:10.1029/2009JB006550.
- Klinger, Y., M. Etchebe, P. Tapponnier, and C. Narreteau (2011), Characteristic slip for five great earthquakes along the Fuyun fault in China, *Nature Geoscience*, 4(6), 389–392, doi:10.1038/ngeo1158.
- Klinger, Y., R. Michel, and G. C. P. King (2006), Evidence for an earthquake barrier model from Mw similar to 7.8 Kokoxili (Tibet) earthquake slip-distribution, *Earth and Planetary Science Letters*, 242(3-4), 354–364.
- Klinger, Y., X. Xu, G. Chen, J. Van Der Woerd, J. Liu-Zeng, and J. M. Nocquet (2015), Fault segmentation and earthquake history of the Kunlun fault, China, paper presented at AGU Fall meeting, San Francisco CA, USA, 14–18 December.
- Klinger, Y., X. W. Xu, P. Tapponnier, J. Van der Woerd, C. Lasserre, and G. King (2005), High-resolution satellite imagery mapping of the surface rupture and slip distribution of the MW 7.8, 14 November 2001 Kokoxili Earthquake, Kunlun Fault, northern Tibet, China, *Bull. Seis. Soc. Am.*, 95(5), 1970–1987.
- Lettis, W., J. Bachhuber, A. Barka, R. Witter, and C. Brankman (Eds.) (2000), Surface fault rupture and segmentation during the Kocaeli earthquake, Istanbul Technical University, Istanbul.
- Li, H. B., J. Van der Woerd, P. Tapponnier, Y. Klinger, X. X. Qi, J. S. Yang, and Y. T. Zhu (2005), Slip rate on the Kunlun fault at Hongshui Gou, and recurrence time of great events comparable to the 14/11/2001, Mw similar to 7.9 Kokoxili earthquake, *Earth and Planetary Science Letters*, 237(1-2), 285–299.
- Lin, A. M., J. M. Guo, K. Kano, and Y. Awata (2006), Average slip rate and recurrence interval of large-magnitude earthquakes on the western segment of the strike-slip Kunlun

- fault, northern Tibet, *Bulletin of the Seismological Society of America*, 96, 1597–1611, doi:10.1785/0120050051.
- Liu, Z., and B. Duan (2015), Coseismic Slip Gradient and Rupture Jumps on Parallel Strike-Slip Faults, *Bulletin of the Seismological Society of America*.
- Lozos, J. C. (2016), A case for historic joint rupture of the San Andreas and San Jacinto faults, *Science Advances*, 2(3), e1500621.
- Lozos, J. C., D. D. Oglesby, J. N. Brune, and K. B. Olsen (2012), Small intermediate fault segments can either aid or hinder rupture propagation at stepovers, *Geophysical Research Letters*, 39(18).
- Manighetti, I., G. C. P. King, and C. G. Sammis (2004), The role of off-fault damage in the evolution of normal faults, *Earth and Planetary Science Letters*, 217, 399–408.
- Marechal, A. (2015), Tectonique active de la zone de collision Yakutat–Nord Amérique: Apport du GPS et de la géomorphologie à l'étude de la partition de la déformation, Université Montpellier.
- Marechal, A., S. Mazzotti, J. L. Elliot, J. T. Freymueller, and M. Schmidt (2015), Indentor-corner tectonics in the Yakutat-St. Elias collision constrained by GPS, *Journal of Geophysical Research: Solid Earth*, 120(5), 3897–3908.
- Massonnet, D., M. Rossi, C. Carmona, F. Adragna, G. Peltzer, K. Feigl, and T. Rabaute (1993), The displacement field of the Landers earthquake mapped by radar interferometry, *Nature*, 364(6433), 138–141.
- Matmon, A., D. Schwartz, P. J. Haeussler, R. Finkel, J. Lienkaemper, H. Stenner, and T. Dawson (2006), Denali fault slip rates and Holocene–late Pleistocene kinematics of central Alaska, *Geology*, 34(8), 645–648.
- McKenzie, D., and W. J. Morgan (1969), Evolution of triple junctions, *Nature*, 224, 125–133.
- Melnick, D., M. Moreno, M. Motagh, M. Cisternas, and R. L. Wesson (2012), Splay fault slip during the Mw 8.8 2010 Maule Chile earthquake, *Geology*, 40(3), 251–254.
- Mériaux, A. S., K. Sieh, R. C. Finkel, C. M. Rubin, M. H. Taylor, A. J. Meltzner, and F. J. Ryerson (2009), Kinematic behavior of southern Alaska constrained by westward decreasing postglacial slip rates on the Denali Fault, Alaska, *Journal of Geophysical Research: Solid Earth* (1978–2012), 114(B3).
- Mignan, A., L. Danciu, and D. Giardini (2015), Reassessment of the maximum fault rupture length of strike-slip earthquakes and inference on Mmax in the Anatolian Peninsula, Turkey, *Seismological Research Letters*, 86(3), 890–900.
- Muller, J. R., and A. Aydin (2004), Rupture progression along discontinuous oblique fault sets: Implications for the Karadere rupture segment of the 1999 Izmit earthquake, and future rupture in the Sea of Marmara, *Tectonophysics*, 391(1), 283–302.
- Nielsen, S., and L. Knopoff (1998), The equivalent strength of geometrical barriers to earthquakes, *Journal of Geophysical Research*, 103(B5), 9953–9965.
- Oglesby, D., M. Mai, K. Atakan, and S. Pucci (2008), Dynamic models of earthquakes on the North Anatolian fault zone under the Sea of Marmara: Effect of hypocenter location, *Geophys. Res. Lett.*, 35, doi:10.1029/2008GL035037.
- Oglesby, D. D., and S. M. Day (2001), The effect of fault geometry on the 1999 Chi-Chi (Taiwan) earthquake, *Geophysical Research Letters*, 28(9), 1831–1834.
- Oskin, M. E., et al. (2012), Near-field deformation from the El Mayor–Cucapah earthquake revealed by differential LIDAR, *Science*, 335(6069), 702–705, doi:10.1126/science.1213778.
- Peltzer, G., F. Crampe, and G. King (1999), Evidence of non-linear elasticity of the crust from the Mw7.6 Mani (Tibet) earthquake, *Science*, 286(8 October 1999), 272–276.
- Poliakov, A. N., R. Dmowska, and J. R. Rice (2002), Dynamic shear rupture interactions with fault bends and off-axis secondary faulting, *Journal of Geophysical Research*, 107(B11), 6–18, doi:10.1029/2001JB000572.
- Ren, Z., Z. Zhang, T. Chen, S. Yan, J. Yin, P. Zhang, W. Zheng, H. Zhang, and C. Li (2016), Clustering of offsets on the Haiyuan fault and their relationship to paleoearthquakes, *Geological Society of America Bulletin*, 128(1-2), 3–18.
- Rizza, M., J. F. Ritz, C. Prentice, R. Vassallo, R. Braucher, C. Larroque, A. Arzhannikova, S. Arzhannikov, S. Mahan, and M. Massault (2015), Earthquake geology of the Bulnay Fault (Mongolia), *Bulletin of the Seismological Society of America*, 105(1), 72–93.
- Rockwell, T., S. Lindvall, T. Dawson, R. Langridge, W. Letts, and Y. Klinger (2002), Lateral offsets on surveyed cultural features resulting from the 1999 Izmit and Duzce earthquakes, Turkey, *Bulletin Seismological Society America*, 92, 79–94.
- Schlupp, A., and A. Cisternas (2007), Source history of the 1905 great Mongolian earthquakes (Tsetserleg, Bolnay), *Geophysical Journal International*, 169(3), 1115–1131.
- Schwartz, D. P., H. Haessler, G. G. Seitz, and T. E. Dawson (2012), Why the 2002 Denali fault rupture propagated onto the Totschunda fault: Implication for fault branching and seismic hazards, *Journal of Geophysical Research: Solid Earth*, 117, B11304, doi:10.1029/2011JB008918.
- Sieh, K., et al. (1993), Near-field investigations of the Landers earthquake sequence, April to July 1992, *Science*, 260(5105), 171–176.
- Spotila, J. A., and A. L. Berger (2010), Exhumation at orogenic indentor corners under long-term glacial conditions: Example of the St. Elias orogen, southern Alaska, *Tectonophysics*, 490(3-4), 241–256.
- Tapponnier, P., and P. Molnar (1977), Active faulting and tectonics in China, *Journal of Geophysical Research*, 82, 2905–2930.
- Tapponnier, P., X. Zhiqin, F. Roger, B. Meyer, N. Arnaud, G. Wittlinger, and Y. Jingsui (2001), Oblique stepwise rise and growth of the Tibet plateau, *Science*, 294, 1671–1677.
- Templeton, E. L., H. Bhat, R. Dmowska, and J. Rice (2010), Dynamic rupture through branched fault configuration at Yucca Mountain and resulting ground motions, *Bul. Seis. Soc. Am.*, 100(4), 1485–1497.
- Teran, O. J., J. M. Fletcher, M. E. Oskin, T. K. Rockwell, K. W. Hudnut, R. M. Spelz, S. O. Akciz, A. P. Hernandez-Flores, and A. E. Morelan (2015), Geologic and structural controls on rupture zone fabric: A field-based study of the 2010 Mw 7.2 El Mayor–Cucapah earthquake surface rupture, *Geosphere*, 11(3), 899–920.
- Thomas, M., H. S. Bhat, and Y. Klinger (2017), Effect of brittle off-fault damage on earthquake rupture dynamics, in *Fault zone dynamic processes: Evolution of fault properties during seismic rupture*, edited by M. Y. Thomas, T. M. Mitchell, and H. S. Bhat, AGU/Wiley.

- Vallage, A., M. H. Devès, Y. Klinger, G. C. P. King, and N. A. Ruppert (2014), Localized slip and distributed deformation in oblique settings: The example of the Denali fault system, Alaska, *Geophysical Journal International*, 197(3), 1284–1298.
- Vallage, A., Y. Klinger, R. Grandin, H. S. Bhat, and M. Pierrot-Deseilligny (2015), Inelastic surface deformation during the 2013 Mw7.7 Balochistan, Pakistan, earthquake, *Geology*, 43(12), 1079–1082, doi:10.1130/G37290.1.
- Vallee, M., M. Landès, N. M. Shapiro, and Y. Klinger (2008), The 14 November 2001 Kokoxili (Tibet) earthquake: High-frequency seismic radiation originating from the transition between sub-Rayleigh and supershear rupture velocity regimes, *Journal of Geophysical Research*, 113, B07305, doi:10.1029/2007JB005520.
- Van Der Woerd, J., F. J. Ryerson, P. Tapponnier, A. S. Meriaux, Y. Gaudemer, B. Meyer, R. Finkel, M. Caffee, G. Zhao, and Z. Xu (2000), Uniform slip-rate along the Kunlun fault: Implication for seismic behaviour and large-scale tectonics, *Geophys. Res. Lett.*, 27, 2353–2356.
- Van Der Woerd, J., P. Tapponnier, F. J. Ryerson, A. S. Meriaux, B. Meyer, Y. Gaudemer, R. C. Finkel, M. W. Caffee, G. G. Zhao, and Z. Q. Xu (2002), Uniform postglacial slip-rate along the central 600 km of the Kunlun Fault (Tibet), from Al-26, Be-10, and C-14 dating of riser offsets, and climatic origin of the regional morphology, *Geophysical Journal International*, 148(3), 356–388.
- Wang, Q., et al. (2001), Present-day crustal deformation in China constrained by global positioning system measurements, *Science*, 294, 574–577.
- Wei, S., et al. (2011), Surficial simplicity of the 2010 El Mayor-Cucapah earthquake of Baja California in Mexico, *Nature Geoscience*, 4, 615–618, doi:10.1038/Ngeo1213.
- Wesnousky, S. (2006), Predicting the endpoints of earthquake ruptures, *Nature*, 444(7117), 358–360.
- Wesnousky, S. (2008), Displacement and geometrical characteristics of earthquake surface ruptures: Issues and implications for seismic-hazard analysis and the process of earthquake rupture, *Bull. Seis. Soc. Am.*, 98(4), 1609–1632, doi:10.1785/0120070111.
- Xu, S., E. Fukuyama, Y. Ben-Zion, and J.-P. Ampuero (2015), Dynamic rupture activation of backthrust fault branching, *Tectonophysics*, 644, 161–183.
- Xu, X. W., G. H. Yu, Y. Klinger, P. Tapponnier, and J. Van der Woerd (2006), Reevaluation of surface rupture parameters and faulting segmentation of the 2001 Kunlunshan earthquake (M(w)7.8), northern Tibetan Plateau, China, *J. Geophys. Res.*, 111(B5), B05316, doi:10.1029/2004JB003488.

# 12

## Influence of Fault Strength on Precursory Processes During Laboratory Earthquakes

François. X. Passelègue<sup>1,2</sup>, Soumaya Latour<sup>1</sup>, Alexandre Schubnel<sup>1</sup>, Stefan Nielsen<sup>3</sup>, Harsha S. Bhat<sup>4</sup>, and Raúl Madariaga<sup>1</sup>

### ABSTRACT

Recent seismological observations have highlighted increasing foreshock activity preceding the failure of large earthquakes. Foreshock sequences seem to be the signature of a precursory slip during the nucleation of earthquakes, as observed both prior the Tohoku-Oki Mw 9.0 and the recent Iquique 2014 Mw 8.1 earthquakes. Advances in laboratory experiments allow researchers to reproduce seismic ruptures and to study the earthquake nucleation phase. Here, we track the occurrence of precursory activity prior to stick-slip instabilities in crustal rocks. An exponential acceleration of the precursory slip is systematically observed. This exponential growth implies that (i) the nucleation phase has a characteristic time, (ii) the amount of precursory slip scales with the fracture energy of the fault, and (iii) the moment released seismically by foreshocks also increases exponentially with increasing fault strength. In summary, under upper crustal conditions, the intensity of precursory processes scales with the fracture energy of the largest asperity, which is eventually going to rupture. The larger the fracture energy of the main asperity, the larger the amount of precursory slip and the larger the amount of precursory slip released seismically.

### 12.1. INTRODUCTION

Recent seismological observations have highlighted increasing foreshock activity preceding the failure of large earthquakes [Jones and Molnar, 1976; Abercrombie and Mori, 1996; Bouchon *et al.*, 2011; Kato *et al.*, 2012; Bouchon *et al.*, 2013; Ruiz *et al.*, 2014]. Foreshock sequences seem to be the signature of a precursory slip during the nucleation of earthquakes, as observed prior to both the Tohoku-Oki Mw 9.0 [Kato *et al.*, 2012] and the recent Iquique 2014 Mw 8.1 earthquakes [Ruiz *et al.*, 2014; Kato and Nakagawa, 2014]. However, foreshocks sequences are not systematic [Bouchon *et al.*, 2013], and

the reason why they occur remains poorly understood. Earthquakes are generated because fault strength drops with increasing slip and slip-rate. Using either slip-weakening [Ida, 1972; Campillo and Ionescu, 1997; Uenishi and Rice, 2003] or rate- and state-dependent friction laws [Dieterich, 1979; Ruina, 1983], theoretical and numerical models show that dynamic rupture is preceded by a nucleation phase during which the rupture grows and accelerates on a localized portion of the fault [Ida, 1972; Campillo and Ionescu, 1997; Uenishi and Rice, 2003; Dieterich, 1979; Ruina, 1983]. This behavior has already been observed during laboratory experiments under low normal stress conditions [Ohnaka, 2003; Nielsen *et al.*, 2010; McLaskey and Kilgore, 2013; Latour *et al.*, 2013] and under upper crustal conditions, with the observations of premonitory slip and foreshocks sequence [Thompson *et al.*, 2009; Goebel *et al.*, 2013; McLaskey and Lockner, 2014; Kwiatek *et al.*, 2014]. These results suggest that if a similar nucleation stage exists along natural faults, the

<sup>1</sup>Laboratoire de Géologie, CNRS, École Normale Supérieure, Paris, France

<sup>2</sup>University of Manchester, Manchester, UK

<sup>3</sup>Durham University, Durham, UK

<sup>4</sup>Institut de Physique du Globe de Paris, Paris, France

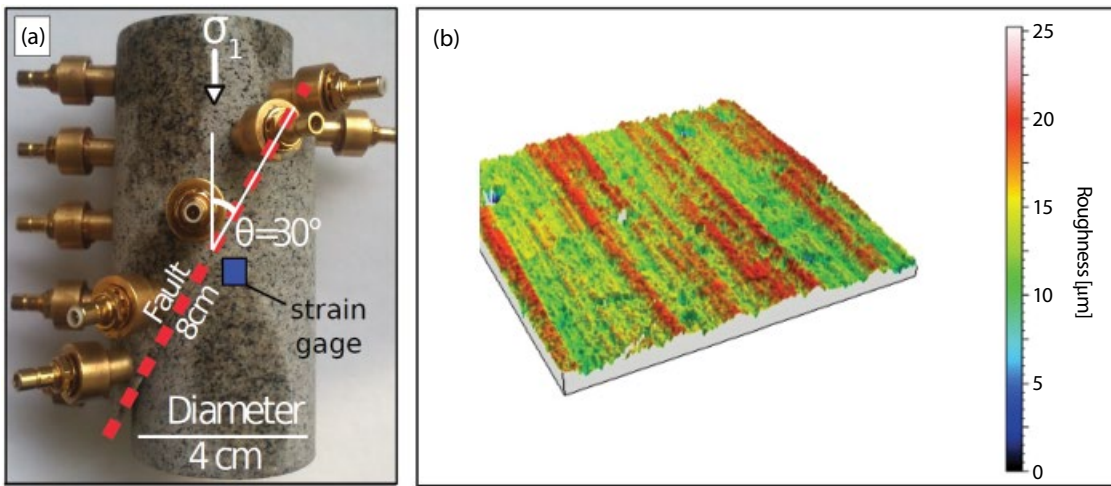


**Figure 12.1** Experimental setup. (a) The fault system is simulated using a saw cut Westerly granite sample. The fault is inclined at an angle  $\Theta = 30^\circ$  to  $\sigma_1$ . Blue square refers to the location of the strain gauges used to estimate the friction coefficient at the onset of instability and the dynamic stress change. (b) Measurement of the initial roughness of the fault surface. See electronic version for color representation.

deformation processes prior the dynamic rupture could be detectable by the records of foreshocks or slow slip events. While it remains difficult to unravel the physical processes using seismological or geodesic observations, laboratory experiments allow the measurement of rupture processes occurring under controlled conditions. Therefore, they can give us good insight into the physical processes leading or not to foreshock activity. Experiments conducted under a broad range of stresses, fault geometries, and rheologies could allow us to understand the physical meaning of these deformation processes observed in nature before earthquakes.

In this chapter, we present results from experiments performed on saw cut Westerly granite samples (Figure 12.1a) submitted to triaxial loading, at conditions representative of the upper crust under various confining pressures (10 to 100 MPa), and covering the range of pressure investigated using biaxial experiments [Ohnaka, 2003; Nielsen *et al.*, 2010; McLaskey and Kilgore, 2013; Latour *et al.*, 2013] and triaxial experiments [Thompson *et al.*, 2009; Goebel *et al.*, 2013; McLaskey and Lockner, 2014; Kwiatek *et al.*, 2014]. The confining pressure is a free parameter in this study, allowing us to understand the influence of the stress acting on the fault and the nucleation processes of laboratory earthquakes.

## 12.2. EXPERIMENTAL SETUP

### 12.2.1. The Triaxial Loading Cell

The apparatus used here is a triaxial oil-medium loading cell ( $\sigma_1 > \sigma_2 = \sigma_3$ ) built by Sanchez Technologies. The apparatus can support a confining pressure of 100 MPa

and up to 600 MPa in differential stress (for 40 mm sample diameter). The confining pressure ( $\sigma_2 = \sigma_3$ ) and the axial stress ( $\sigma_1$ ) are servo-controlled independently. Experiments are conducted by imposing a constant strain rate, ranging from  $10^{-5}/\text{s}$  to  $10^{-4}/\text{s}$ . Fault displacement was measured externally by capacitive displacement gap sensors.

### 12.2.2. Sample Preparation

A sample consists in a cylinder of granite presenting a diameter of 40 mm and a length of 88 mm. The basal areas are ground first with a surface grinder to assure maximal perpendicularity to the long axis of the sample. Then the cylinder is cut at an angle of 30 degrees to create a weak fault interface (Figure 12.1a) so that the experimental fault is elliptical, 40 mm in width and 80 mm in length along strike (Figure 12.1a). The fault surface is polished with a surface grinder and then roughened with 240# grit paper to insure constant roughness conditions at the beginning of each experiment. The roughness characterized using laser interferometry is approximately of  $\pm 12.5 \mu\text{m}$  (Figure 12.1b). Once assembled, the sample is insulated from the confining oil medium by a neoprene jacket 125 mm long and of 50 mm wall thickness. To record acoustic emissions during experiments, the jacket is perforated by 16 holes of 7 mm diameter. The position of each hole is measured accurately to obtain relative sensor locations. Piezoelectric sensors are glued on the rock surface using cyanocrylate adhesive. The sealing between the jacket and the sensors is provided by two layers of flexible and nonbrittle adhesive (Loctite 9455 Hysol). Sixteen P sensors are used in this study (Figure 12.1a).

### 12.2.2.1. Strain Gauges

In order to remove the deformation of the apparatus (i.e., of the column), external data are compared with the axial deformation measured on the sample using strain gauges. Up to four pairs of strain gauges were used during each experiments. Each pair of strain gauges is composed of two resistances ( $\Omega = 120$  ohms) measuring respectively the axial and the radial strain, corresponding to  $\varepsilon_1$  and  $\varepsilon_2$  in the selected referential. Stresses, axial displacement, and strains are recorded continuously at a sampling rate of 10 to 1000 Hz. The measurement of the dynamic stress-strain change is not possible with these devices since the duration of the rupture propagation is too short ( $<20\mu\text{s}$ ) [Passelègue *et al.*, 2013]. However, strain gauge data give us good estimates of the sample elastic constants. During the inelastic parts, they can thus be used as a “low-frequency and near-field” stress gauge, enabling us to infer near-field friction, for instance. Using the axial strain gauge measure, the external measurement of the axial displacement can be corrected for the stiffness of the apparatus using the relation

$$\varepsilon_{ax}^{FS} = \varepsilon_{ax}^{sample} + \frac{\Delta\sigma}{E_{ap}}, \quad (12.1)$$

where  $\varepsilon_{ax}^{FS}$  is the average axial strain measured on gap sensors,  $\varepsilon_{ax}^{sample}$  is the real axial strain of the sample,  $\Delta\sigma$  is the differential stress, and  $E_{ap}$  is the rigidity of the apparatus. The rigidity of the apparatus is estimated by comparing the axial strain (using strain gauges) during the elastic part of the experiment with the external measurement of the axial displacement using gap sensors. In addition, using linear elastic theory, strain measurements can

provide a good estimate of the local static stress changes during experiments. However, as said before, the full capture of the dynamic stress change requires a higher sampling rate.

### 12.2.3. High-Frequency Stress Measurement

In addition to classical strain gauges, up to four complete Wheatstone bridge strain gauges (referred to as dynamic stress gauge hereafter) were glued directly on the rock sample close to the fault plane (Figure 12.1a, strain gauge). Each dynamic stress gauge is composed of four resistors ( $\Omega = 350$  ohms) measuring together the differential strain  $\varepsilon_1 - \varepsilon_3$ . The signal is relayed to a custom-designed high-frequency amplifier and then recorded, along with the acoustics, on a 16-channel USB oscilloscope at 10 MHz sampling rate. The dynamic stress gauges are calibrated during the elastic loading before each mainshock, assuming a constant Young modulus (64 GPa) of the rock. The amplified (calibrated) signal thus measures at a high sampling rate the dynamic evolution of the differential stress (i.e.,  $\sigma_1 - \sigma_3$ ) during dynamic rupture propagation [Passelègue *et al.*, 2016; Brantut *et al.*, 2016]. Measurements of the dynamic stress evolution at high sampling rate have been conducted during experiments WGsc16 and WGsc17 only (Table 12.1).

### 12.2.3.1. Passive Record of Acoustic Emissions (AEs)

The piezo-ceramic sensors used consist of a PZT crystal (PI ceramic PI255, 5 mm in diameter and 0.5 mm in thickness) encapsulated within a brass casing. All the piezoelectric crystals are polarized in the same way and record preferentially compressional waves. Different ways of recording are used independently or coupled (Figure 12.2). First, the unamplified signal is relayed to

**Table 12.1** List of stick-slip experiments presented in this study.

Experiments	$P_c$ (MPa)	Final Axial Shortening (mm)	Peak Shear Stress at First Event (MPa)	Dynamic Strain Gauge	Continuous AE Recording	Number of STE
WGsc3	10	4	8.58	—	—	129
WGsc4	30	2.3	21.5	—	—	42
WGsc5	50	8.4	98.9	—	—	18
WGsc6	50	6.6	82.1	—	—	10
WGsc7	40	5.5	62.1	—	—	4
WGsc9	40	7.3	59.8	—	yes	15
WGsc16a	10	—	12.6	yes	—	3
WGsc16b	30	—	33	yes	—	5
WGsc16c	50	—	47.3	yes	—	13
WGsc16d	100	—	154.5	yes	yes	5
WGsc17a	10	—	8.9	yes	—	1
WGsc17b	20	—	18.6	yes	—	13
WGsc17c	40	—	43.1	yes	—	10
WGsc17d	70	—	72.6	yes	yes	9

Note: AE = acoustic emission; STE = stick-slip events.

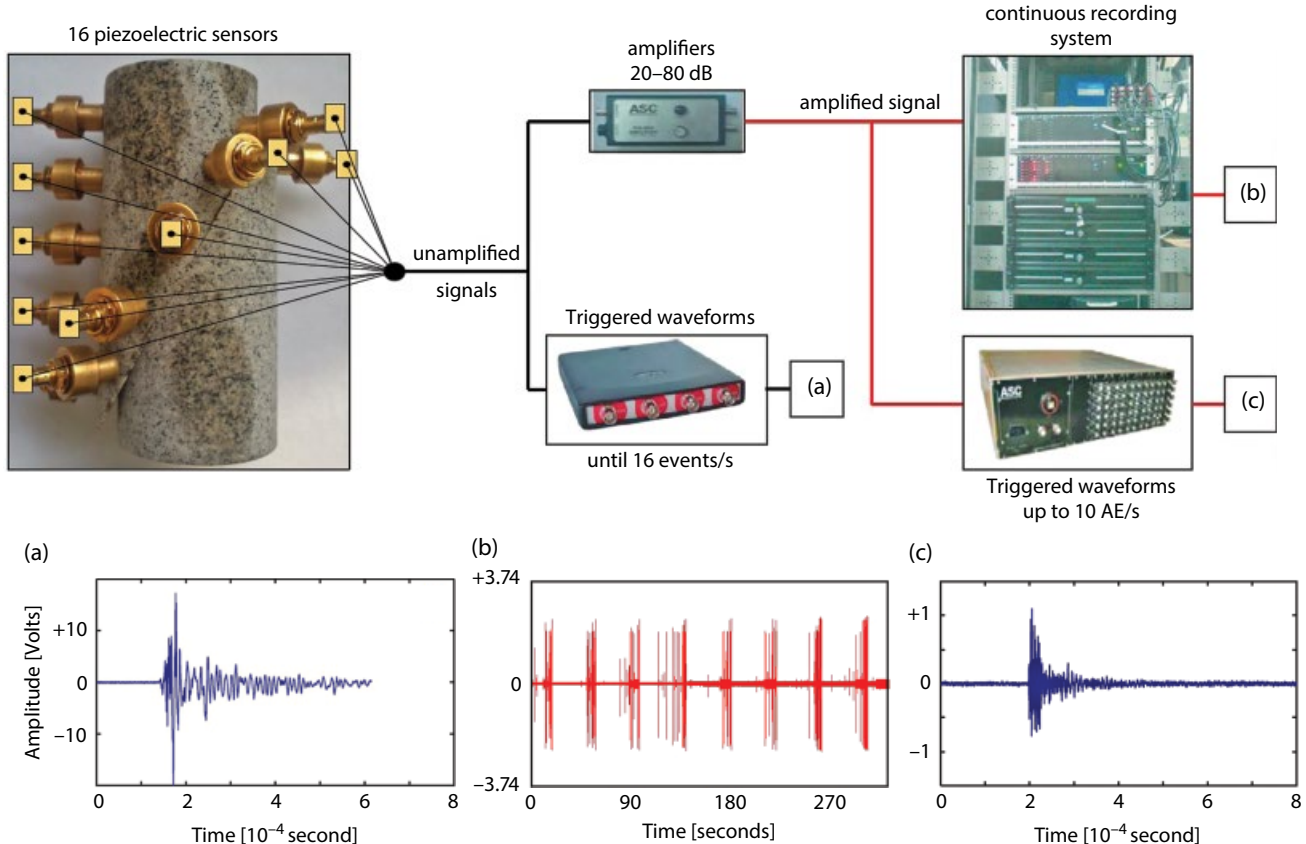


**Figure 12.2** Schematic diagram of the AE recording system. Most of the signals are recorded twice, using a digital 16-channel USB oscilloscopes (triggered data) and a 16-channel continuous recorder (continuous data). Foreshock signals are amplified at 45 dB prior to recording, allowing the detection of small events.

a 16-channel digital oscilloscope at a sampling rate of 10 MHz (Figure 12.2a and d). Recording is triggered, on a single arbitrary channel, by the macroscopic dynamic rupture (i.e., rupture of the entire fault) during the experiments [Schubnel *et al.*, 2011; Passelègue *et al.*, 2013].

Using a second system, signals are amplified at 45 dB via 16 preamplifiers. The amplified signals are then relayed to a trigger logic box and, if verifying a given pattern (i.e., a threshold amplitude on a given number of channels in a given time window), are relayed to and recorded by a second 16-channel oscilloscope at 10 MHz sampling rate. In this case, the amplified signals allow the recording of small events before or after the macroscopic events (Figure 12.2b and e). In addition, some stick-slip experiments have been conducted using continuous recording of the acoustic waveforms during the entire experiment at 4 MHz sampling rate (Figure 12.2c and f). The complete waveforms are then analyzed and harvested into single AE again when the signals verify a given pattern. This system is used to record the complete AE waveforms catalogs during experiments while the “triggered data system” (Figure 12.2b and e) is limited to 10 AEs/second.

In total, a catalog of more than 200 Stick-slip Events (STE or mainshock) was obtained. Using a continuous AE monitoring, approximately 900 foreshocks were recorded and located for 30 STE or mainshocks, which were preceded by a foreshock sequence. The stress conditions were imposed to mimic those of the upper crust. Normal stress acting on the fault ranged from 15 to 110 MPa. Shear stress and normal stresses on the fault are estimated using the measurements of  $\sigma_1$  and  $\sigma_3$ , assuming Mohr circle relationships.

## 12.3. EXPERIMENTAL RESULTS

### 12.3.1. Mechanical and Acoustic Results

The configuration used in this study is such that when the axial stress is increased, both the normal ( $\sigma_n$ ) and the tangential stress ( $\tau$ ) acting on the fault increase. When the state of stress reaches a critical value corresponding to the peak of stress of the fault  $\tau_c$ , instabilities occur, leading to a macroscopic friction drop ( $\tau/\sigma_n$ ) (Figure 12.3).

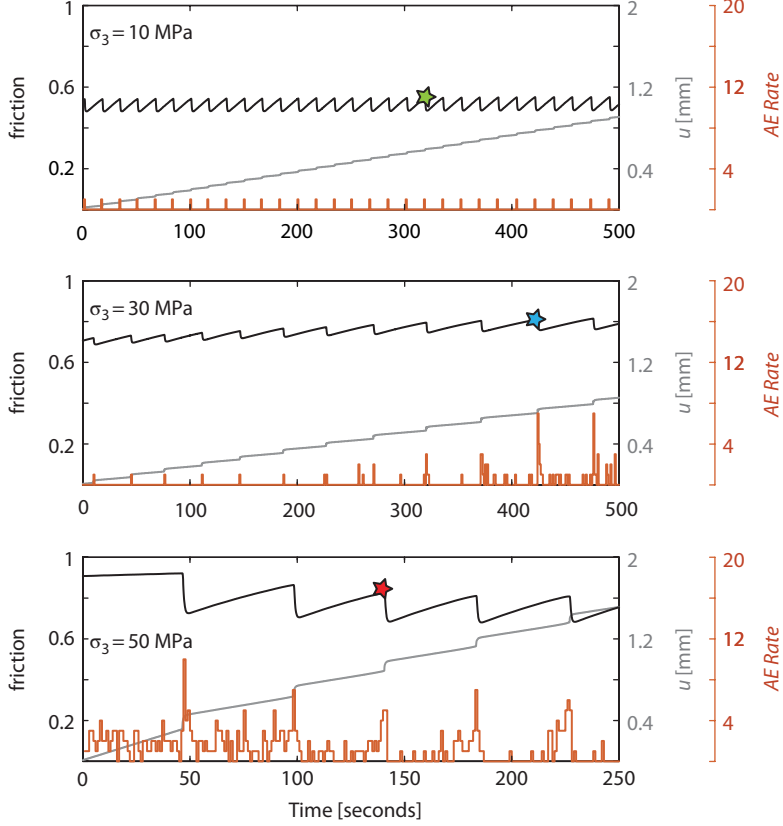


**Figure 12.3** Evolution of resolved friction coefficient, displacement, and acoustic emissions rate during stick-slip sequences conducted at 10, 30, and 50 MPa confining pressure. Black, grey, and red solid lines correspond respectively to the friction coefficient, the axial displacement, and the AE-rate (AE/s). Colored stars refer to individual main shocks presented in Figure 12.4. See electronic version for color representation.

Three STE sequences at 10, 30, and 50 MPa of confining pressure are displayed in Figures 12.3a, b, and c, respectively. Experimental results highlight that (i) the static friction coefficient, (ii) the stress drop, and consequently, (iii) the moment magnitude (and total seismic slip) and the rupture speed of the mainshock systematically increase with increasing the confining pressure, i.e., the critical shear stress  $\tau_c$  at the onset of rupture [Passelègue *et al.*, 2013]. Increasing confining pressure also leads to an increase of the acoustic activity. At low confining pressure ( $\sigma_3 = 10$  MPa), a single acoustic emission is recorded per stick-slip cycle, and this AE corresponds to the mainshock. However, increasing the confining pressure ( $\sigma_3 = 30$  or 50 MPa) leads to an increase of the acoustic activity during stick-slip cycle. The peak of activity is systematically observed in the second preceding the mainshock (Figure 12.3b, c).

The relationship between the frictional behavior of the fault interface and the acoustic activity is presented in Figure 12.4, for three individual events of each STE sequence presented in Figure 12.3. For low values of  $\tau_c$  (<40 MPa), no foreshocks are recorded, although slip acceleration along the fault is observed (Figure 12.4a).

This result suggests that most of the precursory slip is aseismic or that AEs amplitudes are below the threshold of the acoustic monitoring system. In addition, slip strengthening behavior is observed on the fault (i.e., friction increases continuously with fault slip) up to the occurrence of the main shock.

For higher values of  $\tau_c$  (>40 MPa), we systematically record foreshocks (Figure 12.4b, c). Contrary to the behavior observed for low values of  $\tau_c$  (<40 MPa), friction measurement ( $\tau_c / \sigma_n$ ) departs significantly from linearity in the few seconds preceding the mainshock, indicating a local stress release, which coincides both with the occurrence of foreshocks and fault slip acceleration (Figure 12.4b, c). The acceleration in acoustic emission activity corresponds with that of the onset of slip-weakening behavior.

To further investigate the characteristic of foreshock sequences, the acoustic energy released by AEs was estimated similarly to Zang *et al.* [1998] following

$$E_a = \sqrt{\frac{1}{k} \sum (A_i)^2}, \quad (12.2)$$

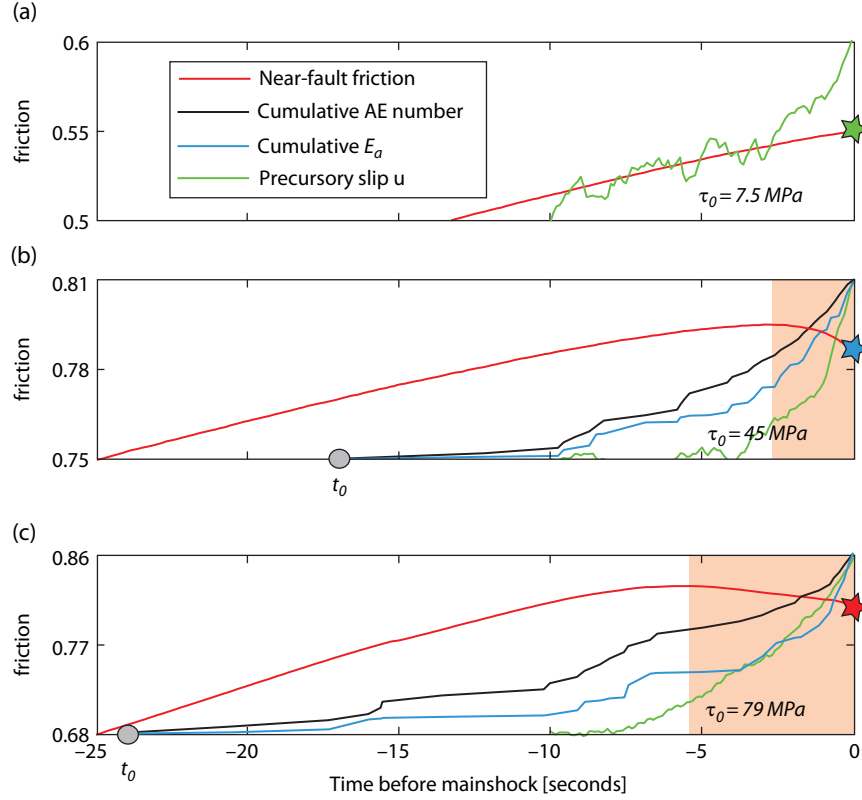


**Figure 12.4** Friction and foreshock dynamics at the onset of stick-slip instability. (a, b) Evolution of friction during three isolated stick-slip events under different critical shear stress conditions (colored stars refer to the STE presented in Figure 12.3). The friction is estimated using strain gauges located 3 mm away from the fault plane (Figure 12.1b). The number of AEs, the cumulative acoustic energy ( $E_a$ ), and the precursory slip are normalized by their final values and vary from 0 to 1. The signal-to-noise ratio increases with increasing final values of precursory slip (as the critical shear stress increases). Final values of precursory slip are respectively 1.3, 3.2, and 9.5  $\mu\text{m}$  for a, b, and c. Background orange area presents the fraction of time under slip weakening regime. Note that this fraction of time increases with  $\tau_c$ . See electronic version for color representation.

where  $A_i$  is the maximum amplitude of the AE “ $i$ ” and  $k$  is the number of sensors used for the amplitude calculation. An abrupt acceleration in the cumulative acoustic energy occurs in the few seconds preceding the main-shock. Since the cumulative acoustic energy increases faster than the cumulative AE number, this indicates that the average moment of AEs is getting larger, or in other terms, that the  $b$ -value of the Gutenberg-Richter law is decreasing prior to failure, as already observed by several experimental studies [Sammonds *et al.*, 1992; Goebel *et al.*, 2012, 2013; Kwiatek *et al.*, 2014]. In summary, increasing the critical shear stress  $\tau_c$  in our experiments leads to an increase of (i) the number of foreshocks, (ii) the amount of precursory slip, and (iii) the precursory cumulative acoustic energy release (Figure 12.4). These observations suggest that  $\tau_c$  controls the intensity of the precursory activity.

### 12.3.2. Location of Acoustic Emissions

P-wave arrival recorded on each sensor was automatically picked using a simple RMS function (the accuracy of autopicking is on the order of  $0.1 \mu\text{s}$ ). Next, to locate AEs, we calculate the theoretical travel times between a possible nucleation point ( $X, Y, Z$ ) next to the fault plane and each piezoelectric sensor location in the array. We assume a 3D geometry, with a fault thickness of 1 cm, which corresponds to the size of the largest crack observed on the postmortem samples. At a given station  $k$ , theoretical P-wave travel times from nucleation point ( $X, Y, Z$ ) can be calculated following

$$t = \frac{\sqrt{(X - X_k)^2 + (Y - Y_k)^2 + (Z - Z_k)^2}}{C_p}, \quad (12.3)$$

where  $C_p$  is the compressional wave velocity. For each AE event, time residuals  $\Delta t$ , between observed arrival times  $t^{exp}$  and theoretical ones  $t_k$ , are calculated for different possible initiation times ( $t_0$ ) following

$$\Delta t = \sqrt{\frac{\sum_0^k |t_k^{exp} - t_k - t_0|}{n}}, \quad (12.4)$$

where  $n$  is the number of experimental arrival times used.

The sum of the residual time is then minimized using a least-square function. The minimization outputs the nucleation point of the event and its time of initiation. The average value of the residual time for all AEs located is about  $0.1\text{ }\mu\text{s}$ , corresponding to a location accuracy of  $0.5\text{ mm}$  assuming  $C_p = 5800\text{ m/s}$ . This method allows us to remove AEs nucleating far away from the fault. Note, however, that more than 95% of the foreshocks are located within the considered fault thickness.

The distribution of foreshock hypocenters and magnitudes as a function of time along the fault for representative foreshock sequences is presented in Figure 12.5. Initially, most of the foreshocks have low magnitudes and are located

at the periphery of the fault surface (Figure 12.5a–c). The average magnitude of foreshocks gradually increases with time, while the hypocenters migrate toward the inner section of the fault plane (Figure 12.5). The strongest foreshock generally occurs just prior to the mainshock (Figure 12.5). In Figure 12.5a, we can also note the presence of clusters, and in particular, the fact that the same foreshock source (or asperity) may be able to break twice within a small time window, sometimes with over one order magnitude difference in moment release.

### 12.3.3. Dynamic Stress Drop During Mainshocks

The raw data representing the differential stress evolution during a mainshock observed at  $50\text{ MPa}$  confining pressure (middle range of pressure explored in this study) is displayed in Figure 12.6a. The stress is stable until the passage of the rupture front. Then, a strong and abrupt decrease of the stress is observed down to a minimum value. The difference between the peak stress and the minimal value corresponds to the dynamic stress change and can be used to estimate the dynamic shear stress drop by considering a 2D geometry. After the drop, frame oscillations are observed

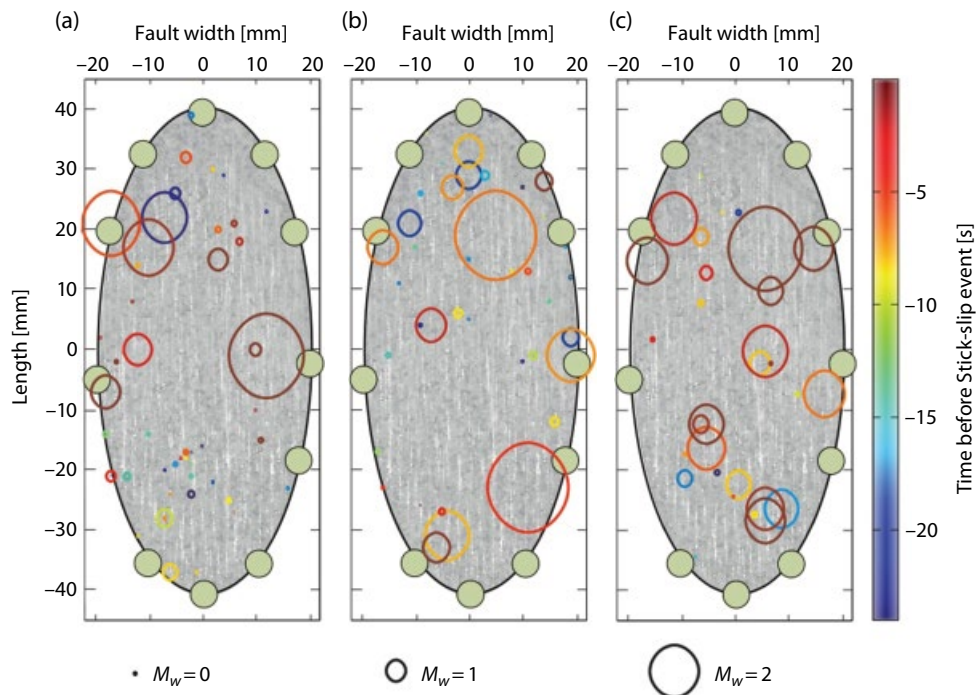


**Figure 12.5** Location of foreshock epicenters prior to main shocks. (a–c) Results of the location of foreshocks along the fault plane prior to three main shocks induced at  $50\text{ MPa}$  confining pressure. The colored bar corresponds to the initiation time of each foreshock relative to the main shock. Note that one part of the fault (central part) remains devoid of acoustic activity. The background image presents the fault surface striation after the experiment. The marker size corresponds to the relative magnitude of each foreshock. Gray circles around the fault correspond to sensor locations. See electronic version for color representation.

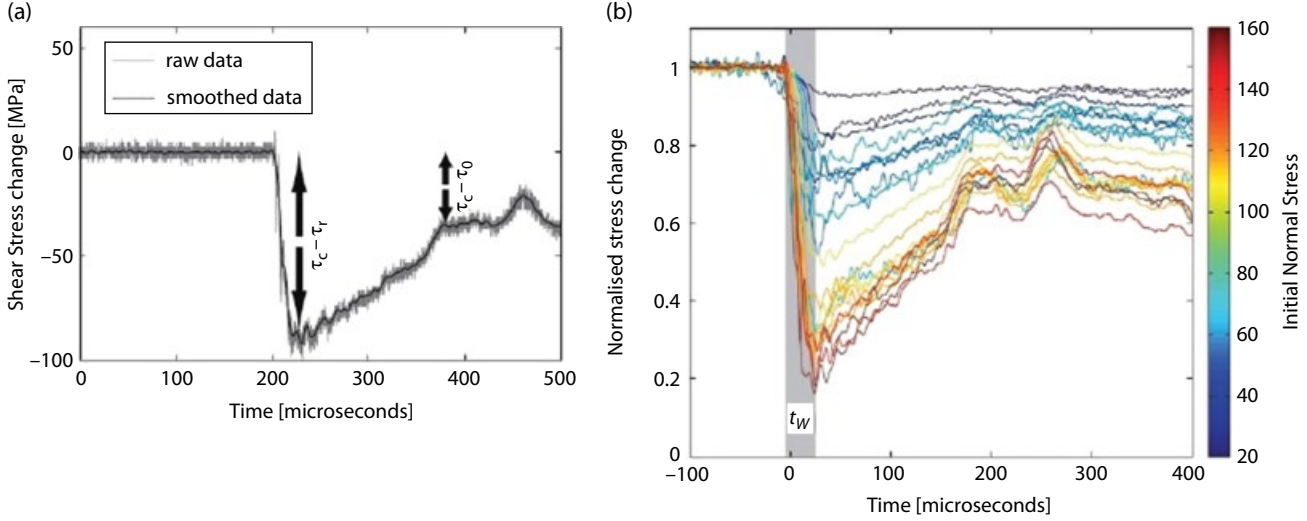


**Figure 12.6** High-frequency stress measurements. (a) Evolution of the stress during stick-slip instability at 130 MPa in normal stress. Grey solid line corresponds to raw data. The data have been smoothed using low-pass filter at 200 KHz in order to remove noise (black solid line). A strong dynamic stress drop is first observed. The final stress difference corresponds to the static stress drop. (b) Relative dynamic stress change curves recorded for 20 main shocks. All curves are normalized by the critical shear stress ( $\tau_c$ ) measured at the onset of rupture. Both dynamic and static stress drops increase with the initial state of stress. The weakening time  $t_w$  tends to decrease with stress. Stress oscillations after the dynamic stress drop are probably due to resonances of the apparatus frame. See electronic version for color representation.

due to the rapid release of stress, which generally occurs in a few microseconds (i.e., the weakening time  $t_w \approx 20 \mu s$ ). The amplitude of the oscillations decreases with time until the stress reaches a stable value (Figure 12.6a), which corresponds to the final stress after instability [Beeler *et al.*, 2012]. The difference between the initial shear stress and the final stress value is consistent with the static stress drop recorded using low sampling rate measurements. All the data presented below have been smoothed using a low-pass filter at 200 KHz in order to remove the high-frequency content related to electrical noise and wave propagation. The influence of the stress acting on the fault on the dynamic strength drop is presented in Figure 12.6b. For low values of critical shear stress ( $\tau_c < 20$  MPa), only a fraction of the stress ( $0.1 \tau_c$ ), i.e., of the elastic strain, is released during macroscopic rupture. However, increasing the normal stress acting on the fault leads to an increase of the fraction of the shear stress released during the macroscopic rupture, which can go up to  $0.8 \tau_c$ .

#### 12.4. EXPONENTIAL INCREASE OF THE PRECURSORY ACTIVITY

Precursory slip was systematically observed even at low shear stress (Figure 12.7a). The evolution of the precursory slip evolves exponentially with time following

$$u(t) = e^{\frac{t}{t_c}}, \quad (12.5)$$

where  $t_c$  is a characteristic time for the nucleation phase, previously defined during laboratory experiments [Latour *et al.*, 2013]. Note that  $t_c$  differs from the time to failure. It corresponds to the characteristic time of the exponential, i.e., the tangent at  $t=0$ . The time to failure corresponds to the time for the exponential slip to grow up to a critical value after which dramatic slip weakening occurs and the rupture becomes dynamic. In these new experiments, this parameter is between 2 and 4 seconds and is independent of  $\tau_c$  (Figure 12.7b). These values of  $t_c$  were determined from the maximum slip rate measured just prior to main shocks following  $\dot{u} = u_c/t_c$ . Both values of  $u_c$  and  $\dot{u}$  increase, with  $\tau_c$  leading to a same order of magnitude of  $t_c$ . This parameter was also found to be independent of the stress in a previous experimental study [Latour *et al.*, 2013]. Predicted by several theoretical and experimental studies [Ohnaka, 2003; Ida, 1972; Campillo and Ionescu, 1997; Uenishi and Rice, 2003], this is clear experimental evidence of systematic exponential precursory slip growth, independent of the state of stress and of the friction of the fault interface (here,  $0.4 < f < 0.9$ ). However, the inferred value of  $t_c$  is three orders of magnitude larger in this study than in the study of Latour *et al.* [2013], which suggests that this parameter might be a function of the fault geometry and the frictional properties of the fault interface.

The characteristic time  $t_c$  of nucleation can be approximated by Latour *et al.* [2013],

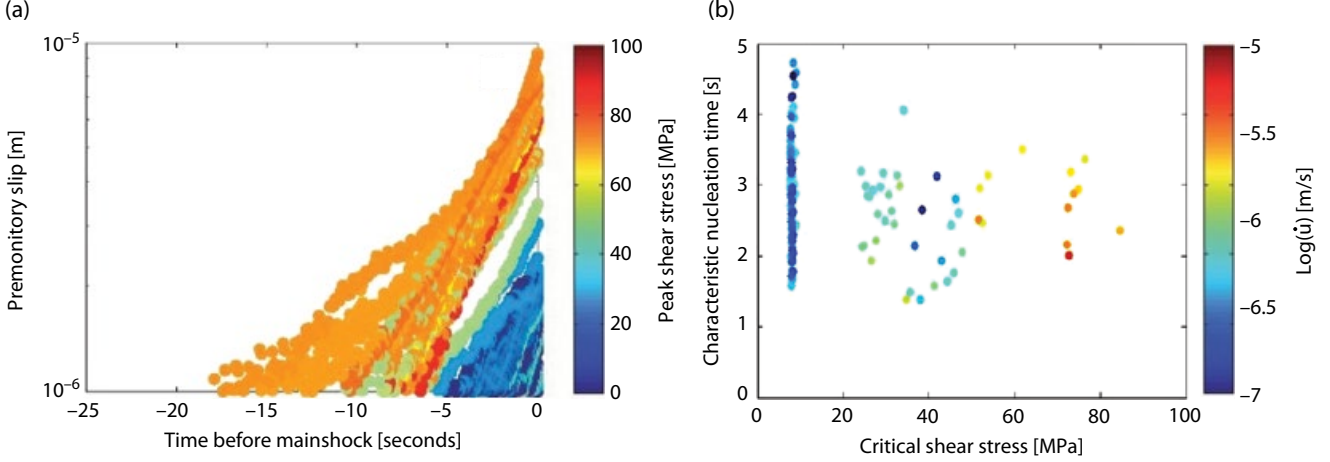


**Figure 12.7** Characteristic of the precursory slip. (a) Precursory slip evolution curves of all main shocks. The slip is corrected from elastic effects. The colored bar represents the critical shear stress at the onset of each main shock. Displacement is plotted in logarithmic scale, demonstrating an exponential acceleration of slip prior to the dynamic slip instability. The final value  $u_c$  of precursory slip increases with  $\tau_c$ . (b) Characteristic nucleation time of each main shock as a function of the critical initial shear stress. The colored bar presents the maximal sliding velocity reached during the nucleation. While the characteristic time is independent of stress ( $t_c \approx 3$ ), the peak sliding velocity increases with stress. See electronic version for color representation.

$$t_c = \frac{k\mu}{p_0} \frac{D_c}{f_s - f_d}, \quad (12.6)$$

where  $k$  is the ratio between the sliding velocity and the rupture velocity,  $p_0$  is a characteristic power density leading to the weakening of the fault surface [Di Toro *et al.*, 2011],  $D_c$  is the critical weakening distance,  $\mu$  is the shear modulus of the granite, and  $(f_s - f_d)$  is the friction drop. Using the average values measured directly here for one of the events with the longest foreshock sequence ( $(f_s - f_d) \approx 0.02$  during the nucleation phase, Figure 12.4;  $D_c \approx u_c \approx 10 \mu\text{m}$ , Figure 12.6a;  $t_c \approx 3$  s, Figure 12.6b), a typical ratio of sliding velocity versus rupture velocity of  $3.10^{-4}$  [Latour *et al.*, 2013] and of the shear modulus of Westerly granite (34GPa) yields a critical power density  $p_0$  value of  $\approx 1700 \pm 150 \text{ W/m}^2$ , which is compatible with a recent experimental compilation of critical power densities [Di Toro *et al.*, 2011]. However, there does not seem to be a systematic relationship between  $t_c$  and  $\tau_c$  (Figure 12.7b). This equation can be written (with  $D_c \approx u_c$ ) as  $f_s - f_d = \frac{k\mu u_c}{p_0 t_c}$ , assuming further that  $k$  and  $p_0$  are independent on  $\tau_c$  [Latour *et al.*, 2013; Di Toro *et al.*, 2011]. Given that  $t_c$  presents same order of magnitude values, the friction drop ( $f_s - f_d$ ) increases with  $\tau_c$  in the same way as  $u_c$ .

In addition, normalizing the cumulative acoustic energy  $E(t)$  with the final cumulative acoustic energy  $E_a$  and time with the duration  $t_0$  of each foreshock sequences, we can show that, when foreshocks are

recorded, the precursory acoustic energy also increases exponentially (Figure 12.8):

$$\frac{E(t)}{E_1} = e^{\alpha \frac{(t-t_0)}{t_0}}, \quad (12.7)$$

where  $\alpha$  is a scaling constant (the best fit has been determined using  $\alpha = 3.47$ ). This observation demonstrates that the rupture of initially small asperities are followed by the rupture of larger and larger ones, and so on up to the rupture of the main asperity (Figures 12.5c and 12.8).

## 12.5. INFLUENCE OF STRESS ON THE PRECURSORY ACTIVITY

The critical slip  $u_c$  required to trigger the mainshock increases with critical shear stress (Figure 12.7a), which suggests that, for the main asperity,  $D_c$  increases with  $\tau_c$ . To further investigate the influence of  $\tau_c$  on the fault mechanical properties, we now estimate the effective fracture energy  $G = D_c \sigma_n \frac{f_s - f_d}{2}$  of main shocks using the dynamic stress drop records (Figure 12.6). The effective fracture energy ( $\text{J/m}^2$ ) is a known proxy for the strength of the fault [Wong, 1982, 1986; Ohnaka, 2003]. Assuming a constant rupture velocity (i.e., a constant sliding velocity) and a purely slip weakening behavior, the critical slip distance  $D_c$  can be estimated using the equation [Ida, 1972; Palmer and Rice, 1973; Rice, 1979]

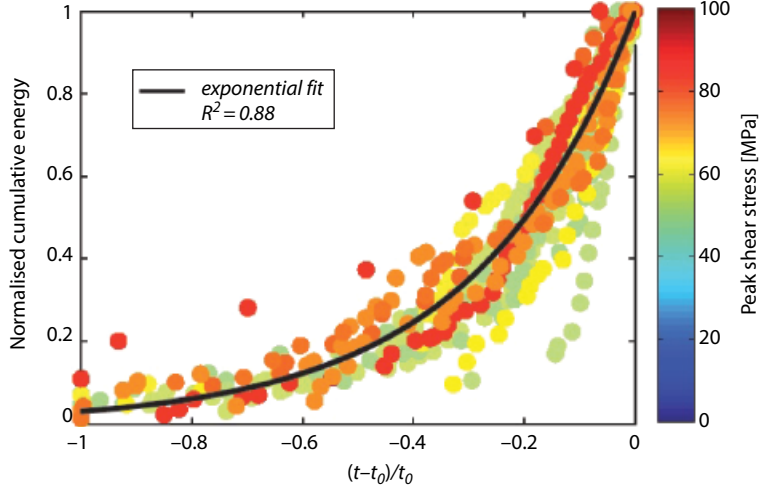


**Figure 12.8** Normalized cumulative acoustic energy released as a function of normalized time for 20 stick-slip cycles. Foreshock sequences collapse to an exponential law (black solid line) with  $\alpha \approx 3.5$ . See electronic version for color representation.

$$D_c = \frac{16(1-\nu)}{9\pi} \frac{V_r t_w \sigma_n (f_s - f_d)}{\mu}, \quad (12.8)$$

where  $\mu$  is the shear modulus of the granite estimated using strain measurements ( $\mu = 34 \text{ GPa}$ ).

The value of the rupture velocity  $V_r$  at a given point of the fault can be estimated during main shock using the dominant arrival recorded on the near-field sensor records as shown in Schubnel *et al.* [2011] and Passelègue *et al.* [2013]. For simplicity, we approximate the shape of the rupture front by a circular shape at sub-Rayleigh velocity and by an elliptical shape at supershear velocity, where the ratio of the two axes corresponds to the ratio of the velocities in the in-plane direction. Thereafter, the value of the rupture velocity at a given point of the fault can be estimated during the event using

$$V_{r(X,Y)} = \frac{1}{\sqrt{\frac{\cos^2 \alpha}{C_s^2} + \frac{\sin^2 \alpha}{V_H^2}}}, \quad (12.9)$$

where  $V_H$  is the rupture velocity along strike and  $\alpha$  is the angle between the coordinates of the given point  $(X, Y)$  and the mode-III direction (Figure 12.6a). Both sub-Rayleigh and supershear ruptures are observed during experiments [Schubnel *et al.*, 2011; Passelègue *et al.*, 2013].

Using this estimation of the rupture velocity, the values of the dynamic stress drop, and the values of the weakening time  $t_w$  (Figure 12.6), the values of  $D_c$  and  $G$  were estimated for each mainshock. The values of  $D_c$  obtained using equation (12.8) can be considered overestimates because our measurements of the stress change are not

performed directly on the fault plane [Svetlizky and Fineberg, 2014]. However, using this simple relation,  $D_c$  remains always smaller than the final displacement, suggesting that this calculation provides good estimates. Both  $D_c$  and  $G$  increase with  $\tau_c$ . This result agrees with previous experimental studies [Wong, 1986; Kato *et al.*, 2003].

A strong correlation between  $G$  and the intensity of the precursory activity is observed. At low critical shear stress ( $\tau_c < 20 \text{ MPa}$ ), where no foreshocks are observed,  $G$  falls between 1 and  $10 \text{ J/m}^2$ , i.e., close to values for the rupture of single minerals [Fredrich and Wong, 1986]. However, a power four dependence of  $G$  with critical shear stress is observed, and  $G$  reaches values close to  $10^4 \text{ J/m}^2$  for the highest value of stress attained during macroscopic rupture (Figure 12.9). In agreement with previous experimental studies [Wong, 1982, 1986; Ohnaka, 2003], this demonstrates that the strength of the fault increases with the stress acting on the fault plane. This is expected from nucleation length theory [Ida, 1972; Campillo and Ionescu, 1997; Uenishi and Rice, 2003] (Figure 12.9), because the transition between stable slip and dynamic rupture theoretically depends on both normal stress and the fracture energy. Indeed, for a linear slip weakening friction law [Ida, 1972; Campillo and Ionescu, 1997; Uenishi and Rice, 2003], the critical nucleation length can be defined as

$$L_c = 2\beta \frac{\mu G}{\left(\tau_c \left(1 - \frac{f_d}{f_s}\right)\right)^2}, \quad (12.10)$$

where  $\beta$  is a nondimensional shape factor coefficient ( $\approx 1.158$ ) [Campillo and Ionescu, 1997]. Asperities of size

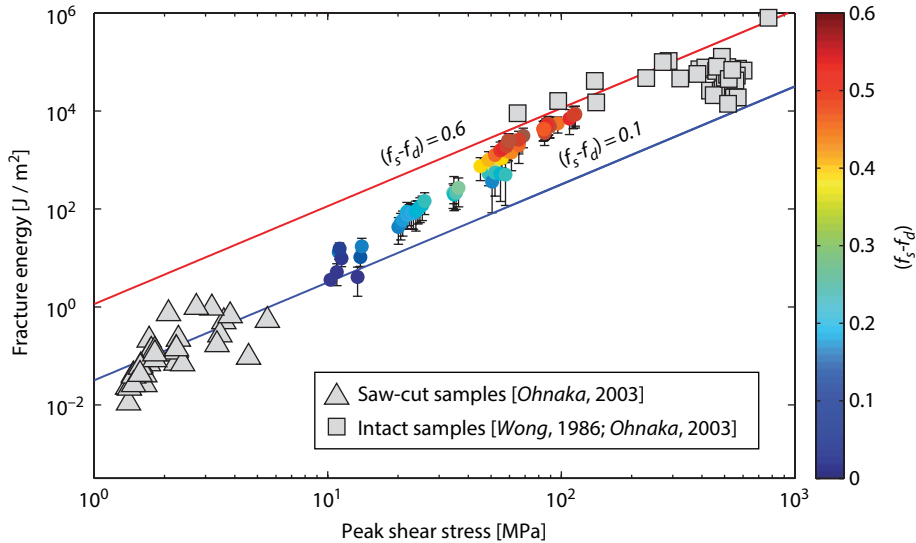


**Figure 12.9** Influence of the state of stress on fault strength. Comparison of peak shear stress dependence of fracture energy ( $G$ ) computed for our experiments with previous experimental results on saw-cut samples [Ohnaka, 2003a] and on intact rocks [Wong, 1982; Ohnaka, 2003a]. The fracture energy is calculated using dynamic stress drop measurements. The colored bar corresponds to the value of the dynamic friction drop. In the background, fracture energy  $G$  (solid lines) as a function of critical shear stress  $\tau_c$  at the transition from stable to dynamic rupture for two values of friction drop (0.6 and 0.1 for red and blue solid lines, respectively).  $G$  is calculated following equation (12.4), assuming that  $\tau_p = \tau_c$  and considering  $L$  equal to the fault length ( $L_f = 0.08\text{m}$ ). See electronic version for color representation.

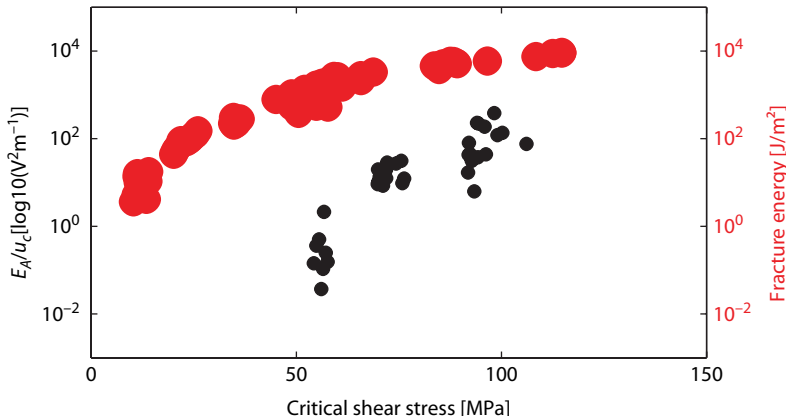


**Figure 12.10** Ratio between the acoustic energy and the total precursory moment release measured on the fault ( $M_p = \hat{A}\mu u_c S$ ) as a function of critical shear stress (black circles). In the background, large red circles present values of fracture energy  $G$  of main shocks as a function of  $\tau_c$  (Figure 12.9). Foreshocks are observed when the fracture energy of the main shocks becomes large behind the fracture energy for small minerals. The larger the fracture energy of the main shock, the larger the intensity of the foreshock sequence.

$L$  can slip seismically only if  $L > L_c(\tau_c, G)$ , otherwise, the slip remains aseismic. Assuming  $L_c = L_f$ , a power exponent 2 is expected from equation (12.4). In our experiments, a power four dependence of  $G$  with respect to  $\tau_c$  is observed because the friction drop also increases linearly with  $\tau_c$  [Passelègue, 2014; Passelègue *et al.*, 2016].

The precursory acoustic energy release rate  $\kappa$  ( $\text{V}^2/\text{m}$ ), i.e., the amount of acoustic energy released by foreshocks

( $E_{a'} V^2$ ) per amount of precursory slip  $u_c$  (m), increases with  $\tau_c$  (Figure 12.10). At low stress, the lack of foreshocks may be due to a technical limit (AE threshold sensibility). However, at higher stresses, the precursory acoustic energy release rate  $\kappa$  increases with increasing critical shear stress, i.e., with increasing fault strength. In other words, the ratio between seismic and aseismic premonitory slip increases with  $\tau_c$  and  $G$ .

## 12.6. CONCLUSIONS AND IMPLICATIONS FOR NATURAL EARTHQUAKES

Our experimental results demonstrate that premonitory slip is systematically observed during the nucleation stage of mainshocks. This result agrees with previous experimental studies conducted at low stress conditions [Ohnaka, 2003; McLaskey and Kilgore, 2013; Latour *et al.*, 2013] and under upper crustal stress conditions [McLaskey and Lockner, 2014]. We demonstrate that this premonitory slip evolves exponentially up to the dynamic rupture of the entire experimental fault. In addition, this premonitory slip can be (i) mostly aseismic at low stress conditions or (ii) signaled by a sequence of foreshocks, which also evolves exponentially, at higher stress conditions. This observation can be explained by the coupling of two phenomena: (1) at low stress conditions, the fracture energy of the entire fault is comparable to the fracture energy of minerals. In these conditions, the rupture of small asperities could release enough energy to propagate the rupture through the entire fault. On the contrary, under high stress conditions, small asperities can fail seismically without rupturing the entire fault because of the large fracture energy required to propagate the rupture of the entire fault; (2) As expected by equation (12.10), the increase of stress acting along the fault decreases the nucleation length. For small asperities, assuming that the fracture energy scales with the size of the rupture [Abercrombie and Rice, 2005], increasing the stress acting on the fault could promote the dynamic failure of small asperities, which would slip aseismically at low stress conditions.

As observed in nature [Kato *et al.*, 2012; Bouchon *et al.*, 2013; Ruiz *et al.*, 2014], foreshock sequences are the signature of a precursory slip during the nucleation of laboratory earthquakes. While no foreshocks are detected at low stress conditions ( $\tau_c < 20 \text{ MPa}$ ), the trigger of the premonitory slip triggers a foreshock sequence at larger stress conditions. In these conditions, the foreshock activity also evolves exponentially up to the rupture of the mainshock. These experimental results are in agreement with natural observations along the interplate interface [Bouchon *et al.*, 2013] and with the cascade model proposed by Ellsworth *et al.* [2004] and Beroza and Ellsworth [1996].

As stated previously, the occurrence of foreshock sequences is related to high stress conditions in the laboratory and to the increase of the fracture energy of the experimental fault. Along natural faults, an accurate estimate of the absolute stress is difficult. However, it has been noted that the foreshock activity that preceded the 2011 Tohoku Mw 9.0 earthquake was confined under a certain depth [Ide and Aochi, 2013]. The same observation has been reported during the Iquique earthquake [Ruiz *et al.*, 2014]. This might be explained by the fact

that at shallow depth the relatively small asperities that may cause foreshocks will not fail dynamically [Ide and Aochi, 2013; Noda and Lapusta, 2013], because the critical nucleation length  $L_c$  is larger than small size asperity.

Of course, many other parameters could play an important role in the premonitory phase of crustal earthquakes. For example, high pore fluid pressures may reduce fault strength, increase the nucleation size, and prevent the occurrence of foreshocks. In addition, at the bottom of the seismogenic layer, intracrystalline plasticity and ductile deformation processes are active [Brace and Kohlstedt, 1980] so that again, the nucleation size could be large enough to prevent small asperities from being seismic. Fault geometry will also have a strong influence on the occurrence of foreshocks. Indeed, both the distribution of the sizes of asperities and the way that their effective frictional properties scale up plays an important role in the occurrence of foreshocks. Finally, premonitory slip or stable slip seems to be the necessary condition to observe foreshock sequence. Fault complexity decreases with cumulative slip and fault maturity [Stirling *et al.*, 1996]. Plate boundary faults should be less segmented than intraplate ones and thus promote the occurrence of fore-shock sequence induced by stable slip around seismic asperities [Bouchon *et al.*, 2013; Kato *et al.*, 2012; Ruiz *et al.*, 2014].

## ACKNOWLEDGMENTS

We acknowledge the technical help of Yves Pinquier (ENS) during the course of the experiments. Mai-Linh Doan (UJF) and Gérard Gary (Ecole Polytechnique) provided the technical drawings for the high-frequency strain gauge amplifier. We thank A. Niemeijer and an anonymous reviewer who helped enhance the quality of the paper, and also three anonymous reviewers who revised an earlier version of the work. This work was partially supported via the ANR program ANR-12-JS06-0003 DELF.

## REFERENCES

- Abercrombie, R. E., and J. Mori (1996), Occurrence patterns of foreshocks to large earthquakes in the western United States, *Nature*, 381(6580), 303–307.
- Abercrombie, R. E., and J. R. Rice (2005), Can observations of earthquake scaling constrain slip weakening? *Geophysical Journal International*, 162(2), 406–424.
- Beeler, N., B. Kilgore, A. McGarr, J. Fletcher, J. Evans, and S. R. Baker (2012), Observed source parameters for dynamic rupture with non-uniform initial stress and relatively high fracture energy, *Journal of Structural Geology*, 38(0), 77–89, doi:<https://doi.org/10.1016/j.jsg.2011.11.013>.
- Beroza, G. C., and W. L. Ellsworth (1996), Properties of the seismic nucleation phase, *Tectonophysics*, 261(1), 209–227.

- Bouchon, M., V. Durand, D. Marsan, H. Karabulut, and J. Schmittbuhl (2013), The long precursory phase of most large interplate earthquakes, *Nature Geoscience*, 6(4), 299–302.
- Bouchon, M., H. Karabulut, M. Aktar, S. Özalaybey, J. Schmittbuhl, and M.-P. Bouin (2011), Extended nucleation of the 1999 Mw 7.6 Izmit earthquake, *Science*, 331(6019), 877–880.
- Brace, W., and D. Kohlstedt (1980), Limits on lithospheric stress imposed by laboratory experiments, *Journal of Geophysical Research: Solid Earth* (1978–2012), 85(B11), 6248–6252.
- Brantut, N., F. X. Passelègue, D. Deldicque, J.-N. Rouzaud, and A. Schubnel (2016), Dynamic weakening and amorphization in serpentinite during laboratory earthquakes, *Geology*, 44(8), 607–610.
- Campillo, M., and I. R. Ionescu (1997), Initiation of antiplane shear instability under slip dependent friction, *Journal of Geophysical Research: Solid Earth* (1978–2012), 102(B9), 20,363–20,371.
- Di Toro, G., R. Han, T. Hirose, N. De Paola, S. Nielsen, K. Mizoguchi, F. Ferri, M. Cocco, and T. Shimamoto (2011), Fault lubrication during earthquakes, *Nature*, 471(7339), 494–498.
- Dieterich, J. H. (1979), Modeling of rock friction: 1. Experimental results and constitutive equations, *Journal of Geophysical Research: Solid Earth* (1978–2012), 84(B5), 2161–2168.
- Ellsworth, W. L., M. Celebi, J. R. Evans, E. G. Jensen, R. Kayen, M. C. Metz, D. J. Nyman, J. W. Roddick, P. Spudich, and C. D. Stephens (2004), Near-field ground motion of the 2002 Denali fault, Alaska, earthquake recorded at pump station 10, *Earthquake Spectra*, 20(3), 597–615, doi:10.1193/1.1778172.
- Fredrich, J. T., and T.-F. Wong (1986), Micromechanics of thermally induced cracking in three crustal rocks, *Journal of Geophysical Research: Solid Earth* (1978–2012), 91(B12), 12,743–12,764.
- Goebel, T., T. Becker, D. Schorlemmer, S. Stanchits, C. Sammis, E. Rybacki, and G. Dresen (2012), Identifying fault heterogeneity through mapping spatial anomalies in acoustic emission statistics, *Journal of Geophysical Research: Solid Earth* (1978–2012), 117(B3).
- Goebel, T., D. Schorlemmer, T. Becker, G. Dresen, and C. Sammis (2013), Acoustic emissions document stress changes over many seismic cycles in stick-slip experiments, *Geophysical Research Letters*, 40(10), 2049–2054.
- Ida, Y. (1972), Cohesive force across the tip of a longitudinal-shear crack and griffith's specific surface energy, *Journal of Geophysical Research*, 77(20), 3796–3805.
- Ide, S., and H. Aochi (2013), Historical seismicity and dynamic rupture process of the 2011 Tohoku-Oki earthquake, *Tectonophysics*, 600, 1–13.
- Jones, L., and P. Molnar (1976), Frequency of foreshocks, *Nature*, 262(5570).
- Kato, A., and S. Nakagawa (2014), Multiple slow-slip events during a foreshock sequence of the 2014 Iquique, Chile Mw 8.1 earthquake, *Geophysical Research Letters*, 41(15), doi:10.1002/2014GL061138.
- Kato, A., K. Obara, T. Igarashi, H. Tsuruoka, S. Nakagawa, and N. Hirata (2012), Propagation of slow slip leading up to the 2011 Mw 9.0 Tohoku-Oki earthquake, *Science*, 335(6069), 705–708.
- Kato, A., M. Ohnaka, and H. Mochizuki (2003), Constitutive properties for the shear failure of intact granite in seismogenic environments, *J. Geophys. Res.*, 108(B1).
- Kwiatek, G., T. H. W. Goebel, and G. Dresen (2014), Seismic moment tensor and b value variations over successive seismic cycles in laboratory stick-slip experiments, *Geophys. Res. Lett.*, 41(16), 5838–5846.
- Latour, S., A. Schubnel, S. Nielsen, R. Madariaga, and S. Vinciguerra (2013), Characterization of nucleation during laboratory earthquakes, *Geophysical Research Letters*, 40(19), 5064–5069.
- McLaskey, G. C., and B. D. Kilgore (2013), Foreshocks during the nucleation of stick-slip instability, *Journal of Geophysical Research: Solid Earth*, 118(6), 2982–2997.
- McLaskey, G. C., and D. A. Lockner (2014), Preslip and cascade processes initiate laboratory stick-slip, *Journal of Geophysical Research: Solid Earth*.
- Nielsen, S., J. Taddeucci, and S. Vinciguerra (2010), Experimental observation of stick-slip instability fronts, *Geophysical Journal International*, 180(2), 697–702, doi:10.1111/j.1365-246X.2009.04444.x.
- Noda, H., and N. Lapusta (2013), Stable creeping fault segments can become destructive as a result of dynamic weakening, *Nature*, 493(7433), 518–521.
- Ohnaka, M. (2003), A constitutive scaling law and a unified comprehension for frictional slip failure, shear fracture of intact rock, and earthquake rupture, *J. Geophys. Res.*, 108(B2), 2080.
- Palmer, A. C., and J. R. Rice (1973), The growth of slip surfaces in the progressive failure of over-consolidated clay, *Proceedings of the Royal Society of London. A. Mathematical and Physical Sciences*, 332(1591), 527–548, doi:10.1098/rspa.1973.0040.
- Passelègue, F. X. (2014), Experimental study of the seismic rupture, Ph.D. thesis, École Normale Supérieure de Paris.
- Passelègue, F., A. Schubnel, S. Nielsen, H. S. Bhat, D. Deldicque, R. Madariaga, et al. (2016), Dynamic rupture processes inferred from laboratory microearthquakes, *Journal of Geophysical Research: Solid Earth*, doi:10.1002/2015JB012694.
- Passelègue, F. X., A. Schubnel, S. Nielsen, H. S. Bhat, and R. Madariaga (2013), From sub-rayleigh to supershear ruptures during stick-slip experiments on crustal rocks, *Science*, 340(6137), 1208–1211.
- Rice, J. (1979), *The mechanics of earthquake rupture*, Division of Engineering, Brown University.
- Ruina, A. (1983), Slip instability and state variable friction laws, *Journal of Geophysical Research: Solid Earth* (1978–2012), 88(B12), 10,359–10,370.
- Ruiz, S., M. Metois, A. Fuenzalida, J. Ruiz, F. Leyton, R. Grandin, C. Vigny, R. Madariaga, and J. Campos (2014), Intense foreshocks and a slow slip event preceded the 2014 Iquique Mw 8.1 earthquake, *Science*, 345(6201), 1165–1169.
- Sammonds, P., P. Meredith, and I. Main (1992), Role of pore fluids in the generation of seismic precursors to shear fracture, *Nature*, 359(6392), 228–230.

- Schubnel, A., S. Nielsen, J. Taddeucci, S. Vinciguerra, and S. Rao (2011), Photo-acoustic study of subshear and supershear ruptures in the laboratory, *Earth and Planetary Science Letters*, 308, 424–432, doi:10.1016/j.epsl.2011.06.013.
- Stirling, M. W., S. G. Wesnousky, and K. Shimazaki (1996), Fault trace complexity, cumulative slip, and the shape of the magnitude-frequency distribution for strike-slip faults: A global survey, *Geophysical Journal International*, 124(3), 833–868.
- Svetlizky, I., and J. Fineberg (2014), Classical shear cracks drive the onset of dry frictional motion, *Nature*, 509, 205–208.
- Thompson, B. D., R. P. Young, and D. A. Lockner (2009), Premonitory acoustic emissions and stick-slip in natural and smooth-faulted westerly granite, *J. Geophys. Res.*, 114, B02205.
- Uenishi, K., and J. R. Rice (2003), Universal nucleation length for slip-weakening rupture instability under nonuniform fault loading, *Journal of Geophysical Research: Solid Earth* (1978–2012), 108(B1).
- Wong, T.-f. (1982), Shear fracture energy of Westerly granite from post-failure behavior, *Journal of Geophysical Research: Solid Earth* (1978–2012), 87(B2), 990–1000.
- Wong, T.-F. (1986), On the normal stress dependence of the shear fracture energy, *Earthquake Source Mechanics*, pp. 1–11.
- Zang, A., F. C. Wagner, S. Stanchits, G. Dresen, R. Andresen, and M. A. Haidekker (1998), Source analysis of acoustic emissions in aue granite cores under symmetric and asymmetric compressive loads, *Geophysical Journal International*, 135(3), 1113–1130.

# 13

## Upper Limit on Damage Zone Thickness Controlled by Seismogenic Depth

Jean Paul Ampuero and Xiaolin Mao

### ABSTRACT

The thickness of fault damage zones, a characteristic length of the cross-fault distribution of secondary fractures, significantly affects fault stress, earthquake rupture, ground motions, and crustal fluid transport. Field observations indicate that damage zone thickness scales with accumulated fault displacement at short displacements but saturates at a few hundred meters for displacements larger than a few kilometers. To explain this transition of scaling behavior, we conduct 3D numerical simulations of dynamic rupture with off-fault inelastic deformation on long strike-slip faults. We find that the distribution of coseismic inelastic strain is controlled by the transition from crack-like to pulse-like rupture propagation associated with saturation of the seismogenic depth. The yielding zone reaches its maximum thickness when the rupture becomes a stable pulse-like rupture. Considering fracture mechanics theory, we show that seismogenic depth controls the upper bound of damage zone thickness on mature faults by limiting the efficiency of stress concentration near earthquake rupture fronts. We obtain a quantitative relation between limiting damage zone thickness, background stress, dynamic fault strength, off-fault yield strength, and seismogenic depth, which agrees with first-order field observations. Our results help link dynamic rupture processes with field observations and contribute to a fundamental understanding of damage zone properties.

### 13.1. INTRODUCTION

A typical fault zone architecture comprises a highly deformed core surrounded by a damage zone composed of rocks with higher fracture density and lower elastic moduli than the host rocks. In most mature faults, damage zones are 100 to 400 m wide and have between 20% and 60% wave velocity reductions relative to their host rock [e.g., *Huang and Ampuero, 2011*, and references therein]. Studying the formation of damage zones provides insight into the mechanical, hydraulic, and seismic behavior of faults. Fault zone damage is in part inherited from the early process of fracture coalescence and strain localization that led to the formation of the fault, and in

part results from damage during earthquakes [*Mitchell and Faulkner, 2009*]. Damage zone thickness, defined as a characteristic scale of the cross-fault distribution of fracture density, varies from a few centimeters on small faults to a few hundred meters on large mature faults. Field observations indicate that damage zone thickness scales linearly with accumulated fault displacement, which is one measure of fault maturity, but saturates at a few hundred meters for fault displacements larger than a few kilometers [*Mitchell and Faulkner, 2009, 2012; Savage and Brodsky, 2011*]. Explaining this transition of scaling behavior is the main goal of the present work.

Understanding what controls damage zone thickness is important because this parameter can have significant effects on earthquake rupture, seismic wave radiation, state of stress, and hydromechanical properties of the crust. The transition from damage zone to host rock is

---

*Seismological Laboratory, California Institute of Technology, Pasadena, California, USA*

often sharp, marked by a change of decay rate of fracture density as a function of distance to the fault core [Johri *et al.*, 2014b]. Earthquakes happening inside damage zones can thus generate reflected waves and head waves, which can enhance ground motion near the fault [Spudich and Olsen, 2001] but also interact with earthquake ruptures and modulate rupture properties such as rupture speed, slip rate, and rise time [Huang *et al.*, 2014; Pelties *et al.*, 2014]. In particular, seismological evidence of rupture speeds enhanced by fault zone effects was recently presented by Huang *et al.* [2015] and Perrin *et al.* [2016b]. Damage zones may also alter the stress field surrounding faults, leading to mean stress increase and stress rotations, thereby allowing high pore fluid pressure weakening of unfavorably oriented faults [Faulkner *et al.*, 2006]. The effect of reduced elastic moduli in damage zones and their systematic changes along strike induced by fault growth help explain patterns of long-term fault displacement and earthquake slip distributions [Cappa *et al.*, 2014; Perrin *et al.*, 2016b]. Damage zone thickness is also an important factor affecting the fluid transport and storage properties of the crust and reservoirs [Johri *et al.*, 2014b].

Off-fault inelastic deformation is observed all along the rupture trace of large earthquakes [e.g., Milliner *et al.*, 2015], demonstrating the importance of damage generated coseismically in the vicinity of propagating rupture fronts. Off-fault yielding during dynamic rupture propagation has been previously studied through analytical approaches [Poljakov *et al.*, 2002; Rice *et al.*, 2005] and numerical simulations with off-fault plasticity [e.g., Andrews, 1976a, 2005; Gabriel *et al.*, 2013] or continuum damage [Xu *et al.*, 2014]. Plastic strain is often discussed as a proxy for damage [e.g., Xu *et al.*, 2012a, b] and can be mapped into fracture density for comparison with field observations [Johri *et al.*, 2014a]. The thickness of the off-fault yielding zone generated by a single self-similar rupture (crack-like or pulse-like) increases linearly with distance from the hypocenter [Andrews, 2005; Gabriel *et al.*, 2013]. In contrast, the yielding zone thickness generated by steady-state pulse-like ruptures remains constant [Ben-Zion and Shi, 2005; Ben-Zion and Ampuero, 2009; Xu *et al.*, 2012a, b]. The accumulated effect of multiple slip events can be considered a superposition of the coseismic plastic strain fields of each individual slip event [Johri *et al.*, 2014a]. Most previous numerical studies of coseismic damage are based on 2D models or on 3D models of relatively short ruptures [Ma and Andrews, 2010] and are unable to consider the influence of the aspect ratio of a rupture, i.e., the ratio of its along-strike length to along-dip width. A notable exception is the 3D simulations of long ruptures by Shi and Day [2013], which yielded an eventually stable thickness of the off-fault plastic zone. As proposed by Day [1982] on the basis of

an asymptotic analysis of stress concentration near a 3D rupture front, the inelastic deformation induced by a rupture with high aspect ratio is controlled by width rather than length.

In this study, we use 3D numerical simulations of dynamic rupture on strike-slip faults with large aspect ratios to study first-order aspects of the off-fault yielding pattern in long faults. In particular, we assess the role of seismogenic depth in limiting fault zone thickness. The ingredients of our model, described in section 13.2, are intentionally minimalist: material properties surrounding the fault are uniform, a linear slip-weakening friction law is assumed on the fault. In section 13.3, comparing results of simulations with different seismogenic depths, we find that the distribution of inelastic strain is controlled by the transition from crack-like to pulse-like rupture propagation associated with saturation of the seismogenic depth. The yielding zone reaches its maximum thickness when the rupture becomes a stable pulse-like rupture. In section 13.4 we develop quantitative insight, from the perspective of fracture mechanics, on how the transition to pulse-like rupture in long faults explains the saturation of damage zone thickness with accumulated fault displacement. In particular, we show that seismogenic depth controls the upper limit of damage zone thickness on mature faults. In section 13.5 we discuss how our results help link dynamic rupture models with field observations and contribute to a fundamental understanding of damage zone properties.

## 13.2. MODEL DESCRIPTION

The geometry of our numerical model is shown in Figure 13.1a. The fault is long enough (along strike) for dynamic rupture to reach an approximately steady state after it reaches the surface and bottom boundaries of the fault (Figures 13.2 and 13.3a). The simulation domain is large enough to avoid boundary effects. We aim to demonstrate the influence of seismogenic depth ( $W$ ) on rupture propagation and inelastic response near advancing rupture fronts. Therefore, we consider a single, vertical, and planar strike-slip fault embedded in a uniform material with P-wave velocity of 6 km/s, S-wave velocity of 3.464 km/s, and density of 2670 kg/m<sup>3</sup>.

The initial stress field is depth dependent, and fluid pressure is hydrostatic and time independent. The directions of principal stresses are shown in Figure 13.1a and the initial effective normal stress and shear stress on the fault in Figures 13.1b and c, respectively, for the case with  $W=15$  km. To avoid a sudden arrest of rupture at depth, the deviatoric components of stress are linearly tapered to zero from 12 km to 15 km depth and the normal stress increases up to the same value as the effective intermediate principal stress.

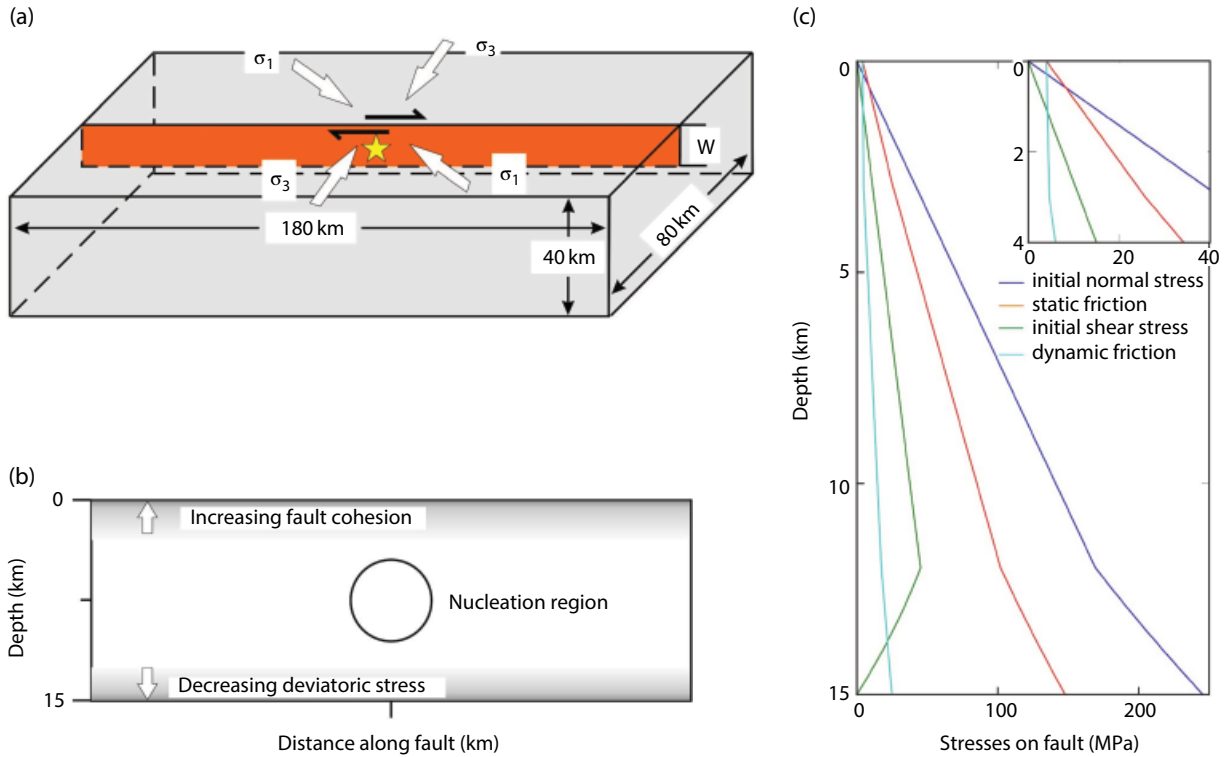


**Figure 13.1** Model setup. (a) Model geometry and background stresses.  $\sigma_1$  and  $\sigma_3$  are maximum and minimum principal initial stresses, respectively. The angle between  $\sigma_1$  and the fault strike is  $30.96^\circ$  and the intermediate principal stress is vertical. The seismogenic zone depth is denoted by  $W$ . (b) Fault plane view showing the nucleation zone (circle), a shallow zone of increased cohesion and a deep zone of tapered stresses. (c) Initial stresses and frictional strength on the fault as a function of depth.

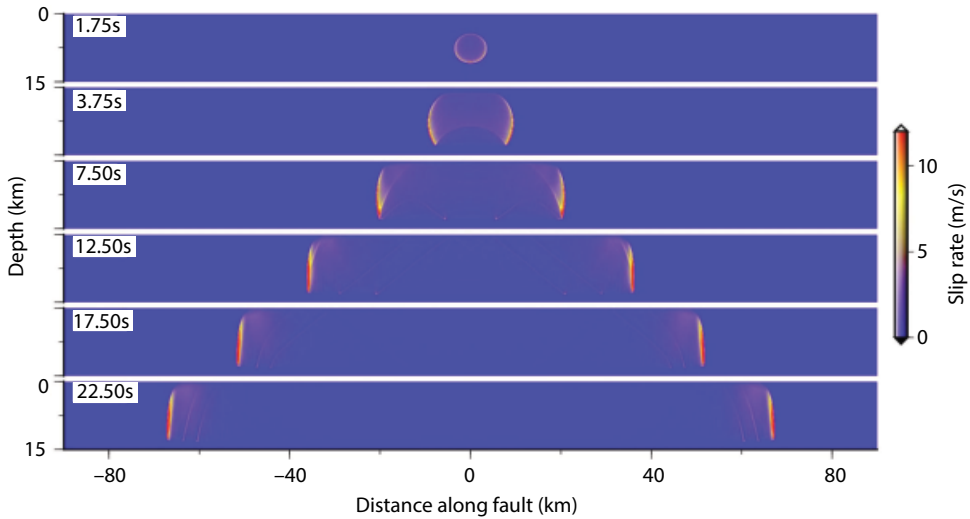


**Figure 13.2** Development of a steady pulse-like rupture on a long fault. Distribution of horizontal slip rate at six different times (indicated by labels on the top left of each panel) in a dynamic rupture simulation with seismogenic depth  $W = 15$  km. See electronic version for color representation.

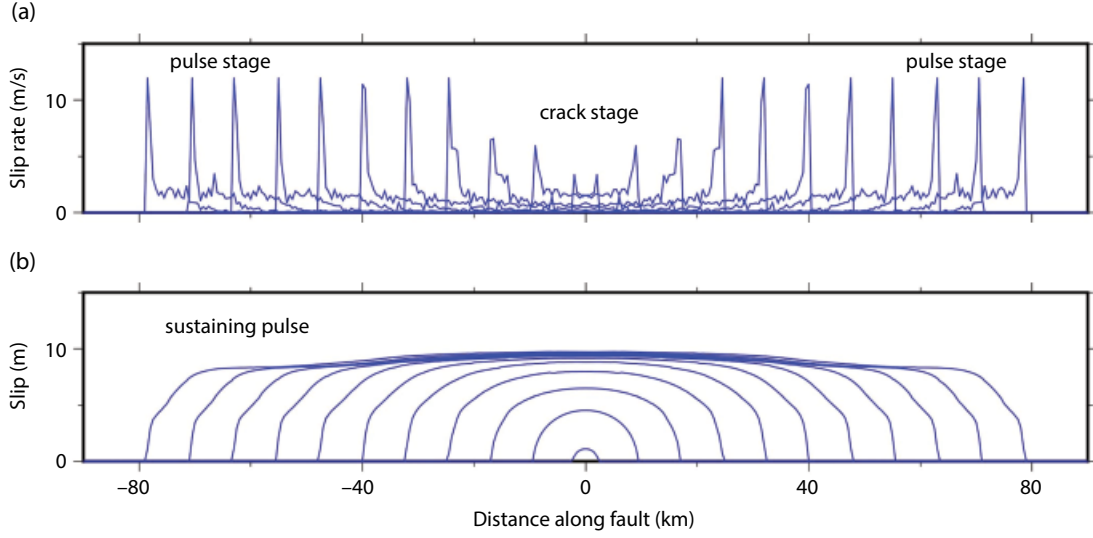


**Figure 13.3** Slip rate (a) and slip (b) profiles every 2.5 s from 1.25 s to 26.25 s at 7.5 km depth for the rupture model with  $W = 15$  km.

A linear slip-weakening friction law [Andrews, 1976a] is employed in which the friction coefficient  $\mu$  is a function of cumulative slip  $D$ :

$$\mu(D) = \mu_s - (\mu_s - \mu_d) \min(D/D_c, 1), \quad (13.1)$$

where  $\mu_d$  is the dynamic friction coefficient,  $\mu_s$  is the static friction coefficient, and  $D_c$  is the critical slip-weakening distance. Here, we assume  $\mu_s = 0.6$ ,  $\mu_d = 0.1$  (representative of thermally weakened faults), and  $D_c = 0.3$  m (representative of seismological estimates for large earthquakes). The fault strength  $\tau$  includes a cohesion  $C_o$  (different from off-fault plastic cohesion  $C$ , which will be discussed later):

$$\tau = C_o + \mu(\sigma_n - P_f), \quad (13.2)$$

where  $\sigma_n$  is normal stress on the fault and  $P_f$  is fluid pressure. To avoid an excessively intense surface break of the rupture,  $C_o$  is set to 0.4 MPa at depths larger than 3 km and linearly increases to 4 MPa from 3 km depth to the surface (Figure 13.1b, c). The relative strength  $S$  parameter [Andrews, 1976b; Das and Aki, 1977], defined by

$$S = \frac{\tau_s - \tau_0}{\tau_0 - \tau_d}, \quad (13.3)$$

where  $\tau_0$  is initial shear stress,  $\tau_s = \mu_s \sigma_0$  is static strength,  $\tau_d = \mu_d \sigma_0$  is dynamic strength, and  $\sigma_0$  is initial normal stress, is set to 2 on most of the fault (Figure 13.1c).

Rupture initiation is achieved by forcing the fault to rupture within a circular zone surrounding the hypocenter (Figure 13.1b). We linearly reduce the friction coefficient from its static value at specified time  $T$  to its dynamic value within a time period  $t_o = 0.5$  s.  $T$  is set to be infinity outside the nucleation zone, and inside the nucleation zone

$$T = \frac{r}{0.7V_s} + \frac{0.081r_{crit}}{0.7V_s} \left( \frac{1}{1 - \left( \frac{r}{r_{crit}} \right)^2} - 1 \right), \quad (13.4)$$

where  $r$  is the distance from the hypocenter,  $r_{crit}$  is the radius of the nucleation zone (set to 3 km here), and  $V_s$  is shear wave velocity. This procedure forces the rupture to expand at a variable speed, about  $0.7V_s$  near the hypocenter and decreasing to zero at  $r_{crit}$ . Spontaneous rupture gradually overtakes the ever-slowing forced rupture.

The Drucker-Prager yield criterion [Drucker and Prager, 1952] is adopted in our study as the off-fault yielding criterion, by which the yield stress  $Y(\sigma)$  depends on the mean normal stress:

$$Y(\sigma) = -(\sigma_{kk}/3 + P_f) \sin\varphi + C \cos\varphi, \quad (13.5)$$

where  $\sigma$  is the stress tensor,  $\varphi$  is the internal frictional angle, and  $C$  is the plastic cohesion. The maximum shear stress is

$$\tau_{max} = \sqrt{\frac{1}{2} S_{ij} S_{ij}}, \quad (13.6)$$

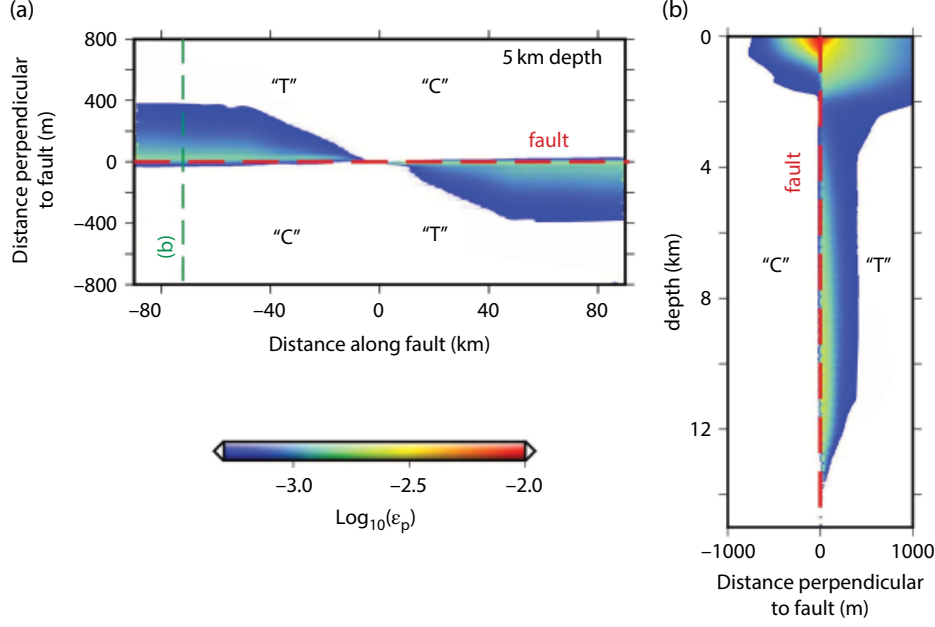


**Figure 13.4** Distribution of plastic strain ( $\varepsilon_p$ ) for the model with  $W = 15$  km: (a) horizontal distribution at 5 km depth and (b) vertical distribution along the cross-section shown by a dashed line in (a). The label C indicates a compressional region, and T a tensional region. See electronic version for color representation.

where  $s$  is the deviatoric part of the stress tensor

$$s_{ij} = \sigma_{ij} - \frac{1}{3}\sigma_{kk}\delta_{ij}. \quad (13.7)$$

A Drucker-Prager yield function is defined as

$$F(\sigma) = \tau_{\max} - Y(\sigma), \quad (13.8)$$

with yielding starting when  $F(\sigma) = 0$ . After yielding starts, the Duvaut-Lions-type viscoplasticity [e.g., Duan and Day, 2008] is used to calculate the accumulation of plastic strain  $\varepsilon_p$  through

$$\dot{\varepsilon}_{ij} = \frac{1}{2\mu T_v} F(\sigma) \frac{s_{ij}}{\tau_{\max}}, \quad (13.9)$$

where  $\mu$  is shear modulus and  $T_v$  is the viscoplastic relaxation time scale. Viscosity is included here as an artificial means to mitigate mesh-dependency due to extreme strain localization [Templeton and Rice, 2008]. A scalar quantity is defined to describe the magnitude of plastic strain (Figures 13.4 and 13.5) as

$$\varepsilon_0^p = \sqrt{2\varepsilon_{ij}^p \varepsilon_{ij}^p}. \quad (13.10)$$

In this study  $\varphi = \arctan(0.6)$ ,  $C = 1.36$  MPa, and  $T_v = 0.03$  s.

The 3D dynamic rupture problem coupled to wave propagation and plastic deformation is solved numerically with SPECFEM3D, a code based on the spectral

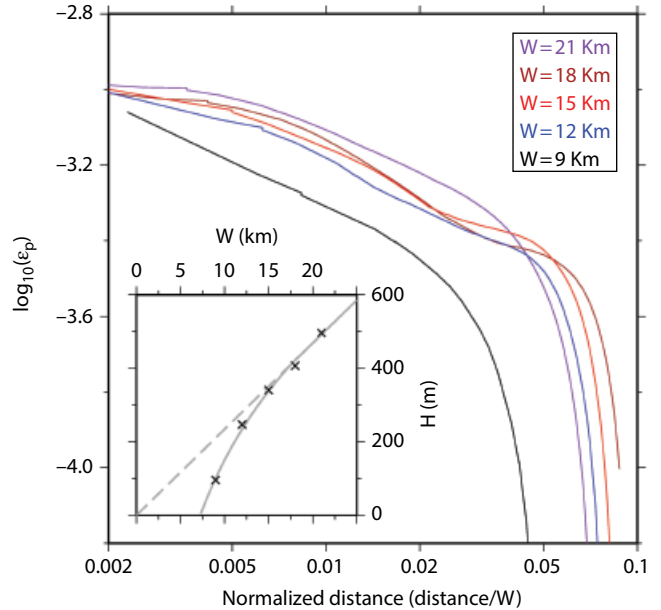


**Figure 13.5** Plastic strain ( $\varepsilon_p$ ) as a function of distance from the fault plane for models with different seismogenic depths ( $W$ ) ranging from 9 to 21 km. Profiles are located at 5 km depth and 70 km horizontal distance from the hypocenter. The inset shows with crosses the damage zone thickness ( $H$ ), defined here as the distance at which  $\varepsilon_p = 10^{-3.3}$ , as a function of  $W$  for all simulations. The solid gray curve is our interpretation of the nonlinear trend in the simulation data. The dashed gray line is an asymptotic linear relation between  $H$  and  $W$  at large  $W$  motivated by our theoretical analysis. See electronic version for color representation.

element method [Kaneko *et al.*, 2008; Galvez *et al.*, 2014]. The implementation of viscoplasticity in SPECFEM3D was verified by comparison to other numerical methods in a community benchmark problem [Harris *et al.*, 2011].

### 13.3. SIMULATION RESULTS

#### 13.3.1. Crack- to Pulse-Like Rupture Transition Controlled by Fault Geometry

Seismic observations and dynamic rupture models indicate that rise time, the duration of earthquake slip at a given point on a fault, can be either comparable to or much shorter than the overall earthquake duration. The former case defines crack-like ruptures [Madariaga, 1976], while the latter case corresponds to pulse-like ruptures [Heaton, 1990]. Proposed mechanisms of local slip arrest leading to pulse-like ruptures include self-healing due to velocity-dependent friction [e.g., Perrin *et al.*, 1995; Beeler and Tullis, 1996] and stopping phases (healing fronts) generated by spatial changes of initial stress or strength on the fault [e.g., Beroza and Mikumo, 1996]. A particular case of the latter mechanism, first described by Day [1982], is the generation of stopping phases at the deep limit of the seismogenic zone, which acts as a rupture barrier.

On mature strike-slip faults, the fault length is usually much larger than the fault width, as in the model setup described in Figure 13.1a. Our first example of dynamic rupture simulation with off-fault plasticity is on a long fault with  $W=15\text{ km}$ . We show resulting snapshots of slip rate in Figure 13.2 and slip rate and slip profiles at 7.5 km depth in Figures 13.3a and b, respectively. The rupture first grows as a self-similar crack-like rupture: the rupture front expands in all directions from the hypocenter, the peak slip rate increases with rupture propagation distance, and slip occurs simultaneously within the whole ruptured region. When the rupture front reaches the bottom boundary of the seismogenic zone, a stopping front is generated and propagates back into the ruptured area. When the healing front reaches the surface, the rupture splits into two pulses (i.e., a pair of rupture fronts followed closely by healing fronts) that propagate in separate directions along the fault strike. The pulses eventually reach a steady state, characterized by stable slip, rupture speed, and peak slip velocity. Notably, the steady pulse width (i.e., the along-strike length of the region of active slip at a given time) is comparable to the seismogenic width  $W$  (Figure 13.3a).

#### 13.3.2. Plastic Strain Distribution

Figure 13.4 shows horizontal and vertical plastic strain distributions of our model with  $W=15\text{ km}$ . Similar to Johri *et al.* [2014a], we observe that plastic strain decays

as a function of distance from the fault core as a power-law at short distance, and drops more abruptly, exponentially at larger distance (Figure 13.5). In this simulation and in those presented in the next section, the change of plastic strain decay behavior occurs near  $\varepsilon_p = 10^{-3.3}$ . Hence, to facilitate the comparison between all our simulations, we define the thickness of the damage zone,  $H$ , as the distance at which  $\varepsilon_p = 10^{-3.3}$ . In the presence of dilatancy (volumetric and deviatoric plastic strains are proportional) and assuming the average fracture aperture is spatially uniform, fracture density is proportional to  $\varepsilon_p$  [Johri *et al.*, 2014a]. This relation connects rupture models with plasticity to field studies, in which the definition of damage zone thickness is based on fracture density. Field data on fracture density vs. distance has been interpreted either as power laws [e.g., Savage and Brodsky, 2011] or as exponential [Mitchell and Faulkner, 2009], but to our knowledge a transition between these two decay behaviors has not been reported. The field data shown in Figure 7a of Savage and Brodsky [2011] is a rare example reminiscent of such transition. Nevertheless, based on the theoretical arguments developed in section 13.4, we expect the scaling properties discussed in this work to hold also for other definitions of  $H$ .

In Figure 13.4a, along the fault, the thickness of the damage zone first grows with increasing rupture distance, as found in 2D models [e.g., Gabriel *et al.*, 2013; Xu *et al.*, 2012b]. However,  $H$  saturates at distances over  $\sim 50\text{ km}$ , where the rupture becomes a stable pulse. This saturation was also noted in 3D simulations by Shi and Day [2013]. In the deep region, damage is limited to the extensional quadrants. In Figure 13.4b, the vertical plastic strain pattern shows a “flower-like” structure with a narrow damage zone of nearly constant thickness in the deeper region and a wide damage zone of increasing thickness near the surface. Similar flower-like patterns of plastic strain were observed in previous 3D simulations [Ma and Andrews, 2010]. In the shallower region, the inelastic strain is induced by seismic waves ahead of the rupture front and is distributed in both extensional and compressional regions. The constant  $H$  in the deeper region in our model is explained in section 13.5 as a result of a linear depth-distribution of both initial stress and strength.

#### 13.3.3. Damage Zone Thickness Comparison for Different Seismogenic Depths

We now examine the effect of the seismogenic depth  $W$  on the damage zone thickness  $H$  at mid-seismogenic depth. We conduct four additional simulations in which all settings are the same as in the previous one except the seismogenic depth, which is taken as  $W=9, 12, 18$ , and  $21\text{ km}$ , respectively. The width of the stress tapering zone near the fault bottom and the width of the zone of increased fault cohesion near the surface are set proportional to  $W$ .

In Figure 13.6 we compare the plastic strain distributions resulting from the three simulations with  $W \leq 15$  km. The plastic strain patterns are similar for the three models. In particular, they all eventually reach a steady damage zone geometry at sufficient distance from the hypocenter. However, the off-fault extent of their plastic zones is different; it increases as a function of  $W$ . Figure 13.5 compares fault-normal profiles of plastic strain at 5 km depth and at a horizontal distance of 70 km from the hypocenter, a distance at which the damage zone has already reached a steady thickness,  $H_{max}$ , in all five simulations. In this figure, distance is normalized by  $W$  and the inset shows how our measure of damage zone thickness  $H$  (the distance from the fault at which plastic strain is  $\varepsilon_p = 10^{-3.3}$ ) depends on  $W$ . The steady damage zone thicknesses in our five models vary from  $\sim 100$  to  $\sim 500$  meters, a range of values that agrees well with the largest values obtained from field observations [Savage and Brodsky, 2011]. The approximate collapse in Figure 13.5 of the normalized plastic strain profiles corresponding to the four models with  $W \geq 12$  km indicates that  $H_{max}$  is approximately proportional to  $W$  if

$W$  is large enough. The dark gray line in the inset of Figure 13.5 is a hypothesized asymptotic linear  $H_{max} - W$  scaling. The model with the smallest  $W$  (9 km) has an  $H_{max}$  significantly overpredicted by the linear  $H_{max} - W$  scaling (Figure 13.5 inset). These key results of our simulations are put on a theoretical basis in the next section.

### 13.4. THEORETICAL ESTIMATE OF DAMAGE ZONE THICKNESS

On the basis of fracture mechanics arguments, Ben-Zion and Ampuero [2009] and Xu *et al.* [2012b] developed theoretical relations between the thickness of dynamically generated damage zones, initial stresses, material strength, and rupture speed. Xu *et al.* [2012b] found that this approach predicts well the yielding zone thickness obtained in 2D dynamic crack-like rupture simulations with off-fault plasticity. A fracture mechanics analysis of damage zones formed by quasi-static fault growth was developed by Scholz *et al.* [1993]. These models predict a self-similar scaling in which  $H$  is proportional to fault or rupture

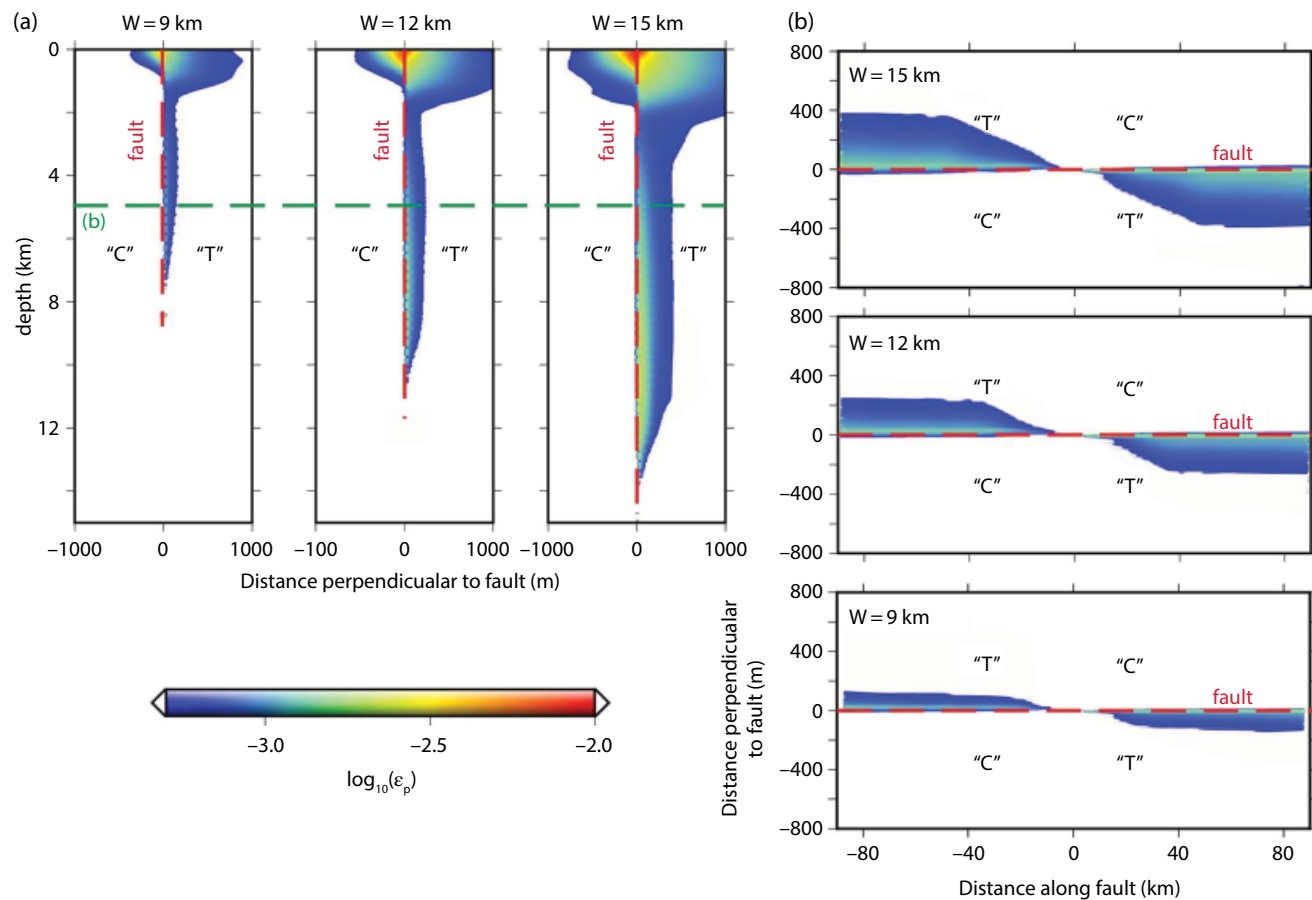


**Figure 13.6** Comparison of the plastic strain distributions among different models with  $W = 9$ , 12, and 15 km, respectively, (a) along a vertical cross-section at 70 km horizontal distance from the hypocenter and (b) on a horizontal cross-section at 5 km depth. See electronic version for color representation.

length  $L$ , without saturation. Here, we apply the dynamic fracture mechanics approach to pulse-like ruptures in 3D, which allows us to assess the effect of seismogenic width.

An estimate of the thickness of the damage zone generated by a dynamic rupture is the distance at which the stress concentration near the rupture tip exceeds the yield strength of the material (e.g., equation 14a of *Ben-Zion and Ampuero* [2009]):

$$H \approx \left( \frac{K}{\tau_s - \tau_0} \right)^2, \quad (13.11)$$

where  $K$  is the dynamic stress intensity factor. The yield strength  $\tau_s$  involved in this equation pertains to the off-fault material and can be higher than the yield strength of the fault. This estimate assumes that the on-fault slip-weakening zone near the rupture front is much smaller than the rupture dimensions, which is the case in our simulations, and significantly smaller than  $H$ , which is better satisfied at large  $W$  as discussed at the end of this section. The squared stress intensity factor  $K^2$  scales with a characteristic length of the rupture. For small earthquakes, represented as circular ruptures, the characteristic length is the rupture radius, and equation (13.11) predicts self-similar scaling between  $H$  and rupture length  $L$ . For larger earthquakes with elongated rupture area  $L \gg W$ , the characteristic length that controls  $K$  is the shortest one [e.g., *Eshelby*, 1957]; hence,  $H$  scales with rupture width  $W$ . For pulse-like ruptures, the characteristic length is the along-strike width of the pulse. As illustrated in section 13.3.1, large earthquake ruptures that saturate the seismogenic depth are inevitably pulse-like, and their pulse width scales with seismogenic depth  $W$ . This break in self-similarity leads to a linear relation between  $H$  and  $W$ , as found in our simulations with large  $W$  (inset of Figure 13.5).

In more detail, following *Xu et al.* [2012b] but considering pulse-like ruptures and ignoring some factors of order one,

$$H \approx \left( k(v_r) \frac{\tau_0 - \tau_d}{\tau_s - \tau_d} \right)^2 W, \quad (13.12)$$

where  $k$  is a decreasing dimensionless function of rupture speed  $v_r$ . In particular,  $k$  and  $K$  are larger at the stopping ends of a rupture, especially if arrest occurs in a fault region with large fracture energy rather than low initial stress. Moreover, pulse width can be smaller than in our simulations if the pulse-like behavior is controlled by self-healing due to dynamic weakening mechanisms [*Heaton*, 1990] instead of a geometric effect of the finite

seismogenic depth. Hence, an upper bound on coseismic damage zone thickness is

$$H_{max} \approx \left( \frac{\tau_0 - \tau_d}{\tau_s - \tau_d} \right)^2 W. \quad (13.13)$$

This linear  $H_{max} - W$  relation is consistent with our simulation results at large  $W$  (Figure 13.5 inset, dashed gray line). Equations (13.12) and (13.13) should be understood as containing a multiplicative factor of order 1 that accommodates different definitions of  $H$  and encapsulates geometric effects ignored in our derivation. For instance, free surface effects can contribute a factor 2, resulting from the effective doubling of  $W$  by a mirror-image rupture.

The departure from a linear  $H_{max} - W$  scaling at low  $W$  in our simulations (Figure 13.5 inset) is attributed here to a blunting effect of the on-fault slip-weakening zone. The derivation of Equation (13.13) assumes that  $H_{max}$  is significantly larger than the slip-weakening zone size  $\ell_c$ . Using equation 24 of *Gabriel et al.* [2013], we find that the ratio  $H_{max}/\ell_c$  is proportional to a function of rupture speed and, more importantly, to the nondimensional number  $\kappa$  introduced by *Madariaga and Olsen* [2000] to represent the ratio between available elastic energy and fracture energy:

$$\kappa = W(\tau_0 - \sigma_0 \mu_d)^2 / G \sigma_0 (\mu_s - \mu_d) D_c, \quad (13.14)$$

where  $G$  is shear modulus. Because the initial stresses  $\tau_0$  and  $\sigma_0$  increase linearly with depth in our models,  $\kappa$  is proportional to  $W^2$ , and decreasing  $W$  rapidly decreases  $\kappa$ . We thus consider that the model with  $W=9$  km has approached an unusual regime associated with low values of  $H_{max}/\ell_c$ , in which the smoothening effect of the slip-weakening zone reduces significantly the off-fault stresses and hence the damage zone thickness. This is simply an artifact of the large value of critical slip-weakening distance ( $D_c$ ) and low value of initial stress ratio  $\tau_0/\sigma_0$ , adopted here to limit the computational cost of the simulations. We expect that simulations with smaller  $\kappa$  should give a nearly linear  $H_{max} - W$  relation down to smaller values of  $W$ . Moreover, regardless of the value of  $\kappa$ , equation (13.13) provides a useful upper bound on  $H_{max}$ .

### 13.5. DISCUSSION AND CONCLUSIONS

Our 3D dynamic rupture simulations and fracture mechanics arguments indicate that damage zone thickness is ultimately bounded in long faults by the limiting effect of seismogenic depth on the efficiency of stress concentration near a rupture front. In particular, equation (13.13) provides a quantitative prediction of the relation

between limiting damage zone thickness, state of stress, dynamic fault strength, off-fault yield strength, and seismogenic depth, which we can compare to field observations.

Average stress drops ( $\tau_0 - \tau_d$ ) of large earthquakes are typically on the order of a few MPa, an order of magnitude smaller than estimates of strength drop ( $\tau_s - \tau_d = \sigma_0(\mu_s - \mu_d)$ ) based on typical values of effective confining stress  $\sigma_0$  at seismogenic depth and of static and dynamic friction coefficients. Hence, the predicted  $H_{max}$  is about two orders of magnitude smaller than  $W$ , that is, a few 100 m. This order-of-magnitude estimate is consistent with field observations of damage zone thickness on large-displacement faults [Savage and Brodsky, 2011; Mitchell and Faulkner, 2009, 2012].

The saturation of  $H$  as a function of fault displacement (long-term cumulative slip) in the data compiled by Savage and Brodsky [2011] occurs at displacements of a few km or less. Considering that displacement to fault length ratios typically range from 0.1 to 0.01 on faults with displacement shorter than a few km [Kim and Sanderson, 2005], the saturation of  $H$  starts at fault lengths ranging from a few 10 km to a few 100 km. This range encompasses the typical values of seismogenic depth, which is consistent with our model. In particular, in the data of strike-slip faults compiled by Kim and Sanderson [2005], a displacement of a few km corresponds to a length of a few 10 km, which quantitatively supports our interpretation of the role of seismogenic depth in limiting damage zone thickness.

The constant thickness of deep damage zones found in our simulations can be rationalized from a theoretical basis. Our model assumed linearly increasing initial shear stress and material strength, such that the ratio  $(\tau_0 - \tau_d)/(\tau_s - \tau_d)$  is independent of depth. Equation (13.13) predicts a constant  $H$  in this situation. This estimate is not appropriate near the surface, where dynamic free surface effects and cohesion play important roles. Damage zone properties at seismogenic depth are difficult to resolve by seismological techniques. Current field data compilations [e.g., Savage and Brodsky, 2011] include observations on exhumed faults that capture fault zone structures from a range of depths, including shallow and deep ones, which may contribute to the data scatter. In this study, we have focused on a scaling feature (saturation of  $H$ ) that is apparent in the field data despite its significant scatter.

Our theoretical argument further suggests that the ratio  $H_{max}/W$  is a relative measure of the stress  $\tau_0$  at which an active fault operates in the long term. In particular, equation (13.13) predicts that a critically stressed fault, in which the average shear stress is close to yield ( $\tau_0 \approx \tau_s$ ), would have a thicker damage zone than a fault operating

at subcritical stress. According to this model, the small value of  $H_{max}/W$  in natural faults is additional evidence that long mature faults operate at stresses significantly lower than the crustal yield strength.

The simulations presented here are intentionally based on simplifying assumptions regarding fault friction, fault geometry, state of stress, and material heterogeneities. An important next step in the development of earthquake models is to study the evolution of fault zone damage through multiple earthquake cycles on long faults, including not only the accumulation of plastic strain but also the reduction in elastic moduli around the fault [Kaneko et al., 2011; Xu et al., 2014]. If the evolution of a fault towards increasing maturity is accompanied by a tendency to operate at lower stress [Fang and Dunham, 2013], our theoretical results suggest the hypothesis that further damage may localize on thinner zones, which could be tested in simulations of long-term damage evolution. Such a simulation framework could also provide insight on how fault growth leaves systematic changes of damage zone properties along strike that may control the distribution of earthquake slip and rupture speed [Cappa et al., 2014; Perrin et al., 2016b].

An additional argument allows us to conclude that short-term damage processes are essential in the evolution of fault zone structure. While the present work emphasizes damage occurring over coseismic time scales, a similar saturation of damage zone thickness is predicted for slower, quasi-static damage processes because the static stress intensity factor  $K$  is also limited by the depth extent of fault slip (seismic or aseismic). However, if damage were dominated by time scales longer than deep afterslip and longer than the relaxation time of the asthenosphere, the relevant model would be a throughgoing crack in a thin elastic slab (the lithosphere, decoupled from the asthenosphere). The long-term  $K$  would no longer be limited by  $W$ , as shown by Lehner et al. [1981], and the damage zone thickness would not saturate.

These different predictions of scaling behavior also help us identify aspects of fault zone evolution that may be controlled by long-term damage processes. At a larger scale than the damage zones considered here, faults develop an “outer damage zone” [Perrin et al., 2016b] that encompasses a network of secondary faults. The younger fault branches often organize near the tips of the main fault into splay fault fans, whose width scales with fault length without saturation [Perrin et al., 2016a]. This observation is consistent with a model in which the evolution of outer damage zones is controlled by fault growth and branching processes operating over time scales longer than the viscous relaxation time of the asthenosphere.

## ACKNOWLEDGMENTS

This work was supported by the Southern California Earthquake Center (Contribution No. 7202. SCEC is funded by NSF Cooperative Agreement EAR-1033462 and USGS Cooperative Agreement G12AC20038) and by the National Science Foundation (CAREER award EAR-1151926). We thank Yoshihiro Kaneko for sharing his version of the SPECFEM3D code modified for the SCEC TPV27 benchmark, and Steve Day and an anonymous reviewer for their stimulating comments.

## REFERENCES

- Andrews, D. J. (1976a), Rupture propagation with finite stress in antiplane strain, *J. Geophys. Res.*, 81(20), 3575–3582.
- Andrews, D. J. (1976b), Rupture velocity of plane strain shear cracks, *J. Geophys. Res.*, 81(32), 5679–5687, doi:10.1029/JB081i032p05679.
- Andrews, D. J. (2005), Rupture dynamics with energy loss outside the slip zone, *J. Geophys. Res.*, 110, B01307, doi:10.1029/2004JB003191.
- Beeler, N. M., and T. E. Tullis (1996), Self-healing slip pulses in dynamic rupture models due to velocity-dependent strength, *Bull. Seismol. Soc. Am.*, 86(4), 1130–1148.
- Ben-Zion, Y., and J.-P. Ampuero (2009), Seismic radiation from regions sustaining material damage, *Geophys. J. Int.*, 178(3), 1351–1356, doi:10.1111/j.1365-246X.2009.04285.x.
- Ben-Zion, Y., and Z. Shi (2005), Dynamic rupture on a material interface with spontaneous generation of plastic strain in the bulk, *Earth Planet. Sci. Lett.*, 236, 486–496, doi:10.1016/j.epsl.2005.03.025.
- Beroza, G. C., and T. Mikumo (1996), Short slip duration in dynamic rupture in the presence of heterogeneous fault properties, *J. Geophys. Res.*, 101(B10), 22,449–22,460, doi:10.1029/96JB02291.
- Cappa, F., C. Perrin, I. Manighetti, and E. Delor (2014), Off-fault long-term damage: A condition to account for generic, triangular earthquake slip profiles, *Geochem. Geophys. Geosys.*, 15, 1476–1493, doi:10.1002/2013GC005182.
- Das, S., and K. Aki (1977), A numerical study of two-dimensional spontaneous rupture propagation, *Geophys. J. R. Astron. Soc.*, 50(3), 643–668, doi:10.1111/j.1365-246X.1977.tb01339.x.
- Day, S. M. (1982), Three-dimensional finite difference simulation of fault dynamics: Rectangular faults with fixed rupture velocity, *Bull. Seismol. Soc. Am.*, 72(3), 705–727.
- Drucker, D. C., and W. Prager (1952), Soil mechanics and plastic analysis or limit design, *Q. Appl. Math.*, 10, 157–165.
- Duan, B., and S. M. Day (2008), Inelastic strain distribution and seismic radiation from rupture of a fault kink, *J. Geophys. Res.*, 113, B12311, doi:10.1029/2008JB005847.
- Eshelby, J. D. (1957), The determination of the elastic field of an elliptical inclusion, and related problems, *Proc. R. Soc. London*, 241, 376–396.
- Fang, Z., and E. M. Dunham (2013), Additional shear resistance from fault roughness and stress levels on geometrically complex faults, *J. Geophys. Res.*, 118(7), 3642–3654, doi:10.1002/jgrb.50262.
- Faulkner, D. R., T. M. Mitchell, D. Healy, and M. J. Heap (2006), Slip on “weak” faults by the rotation of regional stress in the fracture damage zone, *Nature*, 444, 922–925, doi:10.1038/nature05353.
- Gabriel, A. A., J. P. Ampuero, L. A. Dalguer, and P. M. Mai (2013), Source properties of dynamic rupture pulses with off-fault plasticity, *J. Geophys. Res.*, 118(8), 4117–4126, doi:10.1002/jgrb.50213.
- Galvez, P., J. P. Ampuero, L. A. Dalguer, S. N. Somalia, and T. F. Nissen-Meyer (2014), Dynamic earthquake rupture modelled with an unstructured 3-D spectral element method applied to the 2011 M9 Tohoku earthquake, *Geophys. J. Int.*, 198(2), 1222–1240, doi:10.1093/gji/ggu203.
- Harris, R. A., et al. (2011), Verifying a computational method for predicting extreme ground motion, *Seis. Res. Lett.*, 82(5), 638–644, doi:10.1785/gssrl.82.5.638.
- Heaton, T. H. (1990), Evidence for and implications of self-healing pulses of slip in earthquake rupture, *Phys. Earth Planet. Inter.*, 64(1), 1–20.
- Huang, Y., and J. P. Ampuero (2011), Pulse-like ruptures induced by low-velocity fault zones, *J. Geophys. Res.*, 116, B12307, doi:10.1029/2011JB008684.
- Huang, Y., J. P. Ampuero, and D. V. Helmberger (2014), Earthquake ruptures modulated by waves in damaged fault zones, *J. Geophys. Res. Solid Earth*, 119, 3133–3154, doi:10.1002/2013JB010724.
- Huang, Y., J. P. Ampuero, and D. V. Helmberger (2015), The potential for supershear earthquakes in damaged fault zones: Theory and observations, *Earth Planet. Sci. Lett.*, 433, 109–115, doi:10.1016/j.epsl.2015.10.046.
- Johri, M., E. M. Dunham, M. D. Zoback, and Z. Fang (2014a), Predicting fault damage zones by modeling dynamic rupture propagation and comparison with field observations, *J. Geophys. Res. Solid Earth*, 119, 1251–1272, doi:10.1002/2013JB010335.
- Johri, M., M. D. Zoback, and P. Hennings (2014b), A scaling law to characterize fault-damage zones at reservoir depths, *AAPG Bull.*, 98(10), 2057–2079.
- Kaneko, Y., N. Lapusta, and J. P. Ampuero (2008), Spectral-element modeling of spontaneous earthquake rupture on rate and state faults: Effect of velocity-strengthening friction at shallow depths, *J. Geophys. Res.*, 113(B9), B09317, doi:10.1029/2007JB005553.
- Kaneko, Y., J. P. Ampuero, and N. Lapusta (2011), Spectral-element simulations of long-term fault slip: Effect of low-rigidity layers on earthquake-cycle dynamics, *J. Geophys. Res.*, 116, B10313, doi:10.1029/2011JB008395.
- Kim, Y. S., and D. J. Sanderson (2005), The relationship between displacement and length of faults: A review, *Earth-Science Reviews*, 68(3), 317–334. <http://dx.doi.org/10.1016/j.earscirev.2004.06.003>.
- Lehner, F. K., V. C. Li, and J. R. Rice (1981), Stress diffusion along rupturing plate boundaries, *J. Geophys. Res.*, 86(B7), 6155–6169, doi:10.1029/JB086iB07p06155.
- Ma, S., and D. J. Andrews (2010), Inelastic off-fault response and three-dimensional dynamics of earthquake rupture on a strike-slip fault, *J. Geophys. Res.*, 115, B04304, doi:10.1029/2009JB006382.

- Madariaga, R. (1976), Dynamics of an expanding circular fault, *Bull. Seismol. Soc. Am.*, 66(3), 639–666.
- Madariaga, R., and K. B. Olsen (2000), Criticality of rupture dynamics in 3-D, *Pure Appl. Geophys.*, 157(11-12), 1981–2001.
- Milliner, C. W., J. F. Dolan, J. Hollingsworth, S. Leprince, F. Ayoub, and C. Sammis (2015), Quantifying near-field and off-fault deformation patterns of the 1992 Mw 7.3 Landers earthquake, *Geochem. Geophys. Geosyst.*, 16(5), 1577–1598, doi:10.1002/2014GC005693.
- Mitchell, T. M., and D. R. Faulkner (2009), The nature and origin of off-fault damage surrounding strike-slip fault zones with a wide range of displacements: A field study from the Atacama fault system, northern Chile, *J. Struct. Geol.*, 31, 802–816, doi:10.1016/j.jsg.2009.05.002.
- Mitchell, T. M., and D. R. Faulkner (2012), Towards quantifying the matrix permeability of fault damage zones in low porosity rocks, *Earth Planet. Sci. Lett.*, 339–340, 24–31.
- Perrin, C., I. Manighetti, and Y. Gaudemer (2016a), Off-fault tip splay networks: A genetic and generic property of faults indicative of their long-term propagation, *C. R. Geosci.*, 348, 52–60, doi:10.1016/j.crte.2015.05.002.
- Perrin, C., I. Manighetti, J. P. Ampuero, F. Cappa, and Y. Gaudemer (2016b), Location of largest earthquake slip and fast rupture controlled by along-strike change in fault structural maturity due to fault growth, *J. Geophys. Res.*, 121(5), 3666–3685, doi:10.1002/2015JB012671.
- Perrin, G., J. R. Rice, and G. Zheng (1995), Self-healing slip pulse on a frictional surface, *J. Mech. Phys. Solids*, 43(9), 1461–1495.
- Pelties, C., Y. Huang, and J. P. Ampuero (2014), Pulse-like rupture induced by three-dimensional fault zone flower structures, *Pure Appl. Geophys.*, 172(5), 1229–1241, doi:10.1007/s00024-014-0881-0.
- Poliakov, A. N., R. Dmowska, and J. R. Rice (2002), Dynamic shear rupture interactions with fault bends and off-axis secondary faulting, *J. Geophys. Res.*, 107(B11), ESE-6.
- Rice, J. R., C. G. Sammis, and R. Parsons (2005), Off-fault secondary failure induced by a dynamic slip pulse, *Bull. Seismol. Soc. Am.*, 95(1), 109–134.
- Savage, H. M., and E. E. Brodsky (2011), Collateral damage: Evolution with displacement of fracture distribution and secondary fault strands in fault damage zones, *J. Geophys. Res.*, 116, B03405, doi:10.1029/2010JB007665.
- Scholz, C. H., N. H. Dawers, J. Z. Yu, M. H. Anders, and P. A. Cowie (1993), Fault growth and fault scaling laws: Preliminary results, *J. Geophys. Res.*, 98(B12), 21951–21961.
- Shi, Z., and S. M. Day (2013), Rupture dynamics and ground motion from 3-D rough-fault simulations, *J. Geophys. Res.*, 118, 1122–1141, doi:10.1002/jgrb.50094.
- Spudich, P., and K. Olsen (2001), Fault zone amplified waves as a possible seismic hazard along the Calaveras fault in central California, *Geophys. Res. Lett.*, 28(13), 2533–2536, doi:10.1029/2000GL011902.
- Templeton, E. L., and J. R. Rice (2008), Off-fault plasticity and earthquake rupture dynamics: 1. Dry materials or neglect of fluid pressure changes, *J. Geophys. Res.*, 113(B9), B09306, doi:10.1029/2007JB005529.
- Xu, S., Y. Ben-Zion, and J. P. Ampuero (2012a), Properties of inelastic yielding zones generated by in-plane dynamic ruptures: I. Model description and basic results, *Geophys. J. Int.*, 191(3), 1325–1342, doi:10.1111/j.1365-246X.2012.05679.x.
- Xu, S., Y. Ben-Zion, and J. P. Ampuero (2012b), Properties of inelastic yielding zones generated by in-plane dynamic ruptures: II. Detailed parameter-space study, *Geophys. J. Int.*, 191(3), 1343–1360, doi:10.1111/j.1365-246X.2012.05685.x.
- Xu, S., Y. Ben-Zion, J. P. Ampuero, and V. Lyakhovsky (2014), Dynamic ruptures on a frictional interface with off-fault brittle damage: Feedback mechanisms and effects on slip and near-fault motion, *Pure Appl. Geophys.*, 172(5), 1243–1267, doi:10.1007/s00024-014-0923-7.

# 14

## Effect of Brittle Off-Fault Damage on Earthquake Rupture Dynamics

Marion Y. Thomas<sup>1,2</sup>, Harsha S. Bhat<sup>1,3</sup>, and Yann Klinger<sup>1</sup>

### ABSTRACT

In the shallow brittle crust, following earthquake ruptures, geophysical observations show a dramatic drop of seismic wave speeds in the shallow off-fault medium. Seismic ruptures generate, or reactivate, damage around faults that alter the constitutive response of the surrounding medium, which in turn modifies the earthquake itself, the seismic radiation, and the near-fault ground motion. This numerical study aims to assess the interplay between earthquake ruptures and dynamically evolving off-fault medium and to underline the damage-related features pertinent to interpret geophysical observations. We present a micromechanics-based constitutive model that account for dynamic evolution of elastic moduli at high-strain rates. We consider 2D inplane models, with a 1D right lateral fault featuring slip-weakening friction law. We demonstrate that the response of the damaged elastic solid is different in the compressional and tensional quadrant. We observe that dynamic damage induces a reduction in elastic moduli and produces slip rate oscillations that result in high-frequency content in the radiated ground motion, consistent with strong motion records. We underline the importance of incorporating off-fault medium history in earthquake rupture processes. We find that dynamic damage generation is sensitive to material contrast and that it introduces an additional asymmetry beyond that of a bimaterial fault, in agreement with experimental studies.

### 14.1. INTRODUCTION

Deformation of natural fault zones in the brittle crust ( $\sim$ 0 to 40 km depth) is conventionally perceived of as two planes, sliding one against the other, loaded by constant slip at greater depth, and whose behavior is controlled by the frictional properties of the interface [Scholz, 1998]. Depending on these properties, when the frictional

resistance is overcome, the accumulated stress is released by stable sliding or by unstable dynamic events. As a consequence, in recent years, numerous studies have been carried out to determine these properties for various settings [e.g., Byerlee, 1978; Scholz, 1998; King and Marone, 2012; den Hartog *et al.*, 2012]. However, if the behavior of fault zones is intrinsically linked to the properties of the fault interface, it also depends on those of the surrounding medium [e.g., Andrews, 2005]. Fault not only consist of a fine-grained narrow fault core where slip occurs, but it is also surrounded by pervasively fractured rocks, within a complex 3D geometry.

Sibson's [1977] contribution is largely recognized as the first attempt to give a coherent description of an active fault zone. Scholz [2002] further proposed a slightly

<sup>1</sup>Institut de Physique du Globe de Paris, Université Sorbonne Paris Cité, Université Paris Diderot, Paris, France

<sup>2</sup>Department of Earth Sciences, University of Oxford, Oxford, UK

<sup>3</sup>Laboratoire de Géologie, Ecole Normale supérieure, CNRS-UMR 8538, PSL Research University, Paris, France

different fault rock classification, which is widely used nowadays. Following the enticing review by *Biegel and Sammis* [2004], one can use the Punchbowl fault zone as a representative model of “mature” strike-slip faults that have recorded large displacement. Fault zone may be then idealized as an intricate structure consisting of a fault core, surrounded by a damage zone. Based on the revised description of the Punchbowl fault structure by *Chester et al.* [1993], the fault core comprises an inner layer of ultracataclasite bounded by an outer layer of foliated cataclasite. The extremely fine-grained core material is then surrounded by a damage zone that includes layers of gouge and breccia bordered by fractured rocks. The last two layers are included in the damage zone because they lacked extensive shearing [*Chester et al.*, 1993; *Biegel and Sammis*, 2004]. Evidently, there are significant variations from one fault zone to another, but they share in common a highly fine-grained fault core (often extremely narrow band), where most of the displacement has occurred, surrounded by a damaged wall rock. However, the gouge and breccia layer is missing along various faults [*Biegel and Sammis*, 2004].

Systematic micro- and macrostructural field studies have recently been performed on damage zones [*Shipton and Cowie*, 2001; *Faulkner et al.*, 2006; *Dor et al.*, 2006; *Mitchell and Faulkner*, 2009; *Faulkner et al.*, 2011; *Savage and Brodsky*, 2011] as a key component to understand the energy balance of earthquakes [e.g., *Rice*, 2002; *Kanamori*, 2006]. The width of the damage zone is determined by measuring the decay in crack intensity away from the fault core, until it falls to the background level of the host rock [e.g., *Chester and Logan*, 1986; *Biegel and Sammis*, 2004; *Faulkner et al.*, 2011]. The fractured rocks usually have a spatial scale of the order of meters to kilometers; however, this is difficult to define and particularly time consuming. Hence, there are few field surveys focused on the structure of the damage zone. Among them, several studies in low-porosity rocks (crystalline, sedimentary rocks) have highlighted an exponential decay of crack density away from the fault [*Vermilye and Scholz*, 1998; *Wilson et al.*, 2003; *Mitchell and Faulkner*, 2009; *Faulkner et al.*, 2006, 2011], or alternatively, that the decay could be fit using a power law [*Savage and Brodsky*, 2011]. As underlined by *Faulkner et al.* [2011], the trend is less clear for faults developed in higher porosity rocks [*Shipton and Cowie*, 2001]. Possible mechanisms responsible for the development of off-fault damage could include the fault geometry, the linking of structures, the quasi-static stress field, the process zone associated with fault growth, and the coseismic fracture damage [*Vermilye and Scholz*, 1998; *Rice et al.*, 2005; *Childs et al.*, 2009; *Faulkner et al.*, 2011; *Vallage et al.*, 2015]. In their study of the Bolívar fault in northern Chile, *Faulkner et al.* [2011]

discussed several processes that could explain the development of the observed scaling inside the fault zone and concluded that the spatial extent of damage might be better explained by the damage zone growth with increasing displacement, due to geometric irregularities, or by coseismic damage.

Fault zone structure is of key importance in the mechanics of faulting. In fact, several studies have underlined the importance of the fault zone fabric in controlling the slip behavior of fault zones [*Collettini et al.*, 2009; *Niemeijer et al.*, 2010; *Thomas et al.*, 2014a; *Audet and Burgmann*, 2014; *Klinger et al.*, 2016]. For example, *Audet and Burgmann* [2014] recently highlighted a direct relation between the properties of the overlying forearc crust in subduction zones and the average recurrence time of slow earthquakes. Along the Longitudinal Valley fault in Taiwan, a structural analysis and a kinematic study have demonstrated that the damaged forearc formation favors aseismic creep, whereas the locked segments of the fault are in contact with intact rocks, or the protolith [*Thomas et al.*, 2014b, a]. Fault zone structure is equally important during seismic slip. The complexity of the fault zone system impacts the rheological properties of the fault core and the surrounding medium, both of which influence the seismogenic behavior of the fault. The changes in elastic stiffness of the bulk control the amount of elastic strain energy that can be stored during tectonic loading and released during earthquakes and can induce a stress rotations (due to contrasting elastic moduli with the host rock), allowing faults to slip under less-optimal far-field stress conditions [*Faulkner et al.*, 2006]. During seismic faulting, the stress concentration at the tip of the rupture generates, or reactivates, damage (fractures) around faults that modifies the microstructure and the constitutive response of the surrounding medium [e.g., *Rice et al.*, 2005]. Seismic ruptures can trigger a significant coseismic drop in velocity (reduction in elastic stiffness of up to 40%), on spatial scales of hundreds of meters normal to the fault and a few kilometers along depth, followed by a time-dependent recovery over a couple of years [*Hiramatsu et al.*, 2005; *Li et al.*, 2006; *Brenguier et al.*, 2008; *Cochran et al.*, 2009; *Froment et al.*, 2014]. In turn, the coseismic change in elastic moduli influences the rupture itself, which has a direct effect on the size of the earthquake, the radiated waves field, and near-fault ground motion [*Walsh*, 1965a, b; *Faulkner et al.*, 2006; *Bhat et al.*, 2012]. Therefore, recognizing the evolution of damage during earthquakes is critical to understanding the nucleation, propagation, and arrest of earthquakes. This numerical study in particular aims to explore intricate feedbacks between the spontaneous off-fault damage generation and the dynamic rupture propagation.

Numerous studies in the last couple of decades have explored the effect of off-fault plasticity on seismic

rupture, using either analytical approaches [Rice *et al.*, 2005; Ngo *et al.*, 2012] or numerical simulations (see following references). Some models have explored the effect of damage on the properties of the dynamic rupture (mode, speed, and directivity) and final slip by prescribing a low-velocity zone around the fault [e.g., Kaneko and Fialko, 2011; Cappa *et al.*, 2014; Huang *et al.*, 2014]. Another set of models uses a Mohr-Coulomb [e.g., Andrews and Harris, 2005; Ben-Zion and Shi, 2005; Hok *et al.*, 2010; Gabriel *et al.*, 2013] or Drucker-Prager [e.g., Templeton and Rice, 2008; Ma, 2008; Dunham *et al.*, 2011] yield criterion to investigate dynamic rupture propagation with spontaneous dynamic formation of off-fault damage. In their studies, Yamashita [2000] and Daguier *et al.* [2003] model the generation of off-fault damage as the formation of tensile cracks, using a stress- and fracture-energy-based criterion, respectively. If these types of study provide a good insight on the effect of damage structure on seismic rupture, they do not account for dynamic changes of elastic moduli in the medium and therefore do not completely model the feedbacks between the off-fault damage and the seismic rupture. Determining the constitutive behavior of the surrounding medium requires developing models based on the mechanics of cracks and how they respond to the applied loading. It requires using an energy-based approach to develop the new constitutive law [e.g., Lyakhovsky *et al.*, 1997a; Finzi *et al.*, 2009; Suzuki, 2012; Xu *et al.*, 2014; Lyakhovsky and Ben-Zion, 2014]. In particular, these models need to include a physical crack growth law to model the evolution of damage. Ideally, this law should incorporate the loading rate crack-tip velocities dependency of fracture toughness [Chen *et al.*, 2009; Dai *et al.*, 2010, 2011; Wang *et al.*, 2010, 2011; Zhang and Zhao, 2013], which is particularly important to model earthquake-related processes. The latter constitutes the essential difference between the model presented in this chapter and the models aforementioned.

The development of the constitutive model is presented in section 14.2, followed by a description of the numerical method and the parameters we used for this chapter. In the third section we consider three different scenarios to explore the interplay between earthquake rupture and off-fault damage, how it affects both the hosting medium and the rupture propagation, and what the damage-related features are that can be pertinent to interpret geophysical observations. Our findings are summarized in section 14.5.

## 14.2. CONSTITUTIVE MODEL

This numerical study aims to explore the effect of spontaneous off-fault damage generation on dynamic rupture propagation. This section provides the description of the constitutive model used to account for the dynamic

**Table 14.1** Parameters of the damage constitutive model.

Parameter	Symbol	Equation
Angle to $\sigma_1$ for microcracks	$\Phi$	eq. 12
Projection of $a$ to $\sigma_1$	$\alpha$	$\cos\Phi$
Damage variable	$D$	eq. 13
Initial damage variable	$D_0$	eq. 11
Stress intensity factor	$K_I$	eq. 21, 27
Dynamic stress intensity factor	$K_I^d$	Bhat [2012], eq. 43
Dynamic initiation toughness	$K_{IC}^D$	Bhat [2012], eq. 45
Dynamic fracture toughness	$K_{IC}^d$	Bhat [2012], eq. 46
Instantaneous wing-crack speed	$v \equiv dl/dt$	Bhat [2012], eq. 50
Stress	$\sigma_{ij}$ or $\sigma$	eq. 32, 35, 41
Stress invariant	$\sigma, \tau$	Bhat [2012], eq. 11
Strain	$\epsilon_{ij}$ or $\epsilon$	eq. 6, 15
Strain invariant	$\epsilon, \gamma$	eq. 30

evolution of elastic properties in the surrounding medium, related to dynamic off-fault damage. The different parameters and constants used for the constitutive model are summarized in Table 14.1.

### 14.2.1. Energy-Based Approach: General Considerations

The micromechanical method used in this study followed an energy-based approach to determine the constitutive strain-stress relationship of a damaged solid, as defined by Rice [1971], Hill and Rice [1973] and Rice [1975]. In other words, to account for fracture damage, we create an energetically equivalent solid. This formalism, thermodynamically argued, was developed to model the inelastic behavior at macroscopic scale that arises from specific structural rearrangements at microscale, such as twinning in crystals, grain-boundary-sliding, phase transformation, or microcrack development. This approach relates inelastic deformation of a given solid to a sequence of constrained equilibrium states, characterized by the values of strain  $\epsilon$ , temperature  $T$ , and internal variables  $\xi$  (such as damaged state). Then the relation between these properties and macroscopic stress are determined by fixing the internal variables at their current values for each imaginary equilibrium state, for which elastic constitutive law can therefore be applied. In practice, internal variables will have a time-dependent evolution, determined by the local conditions, but the kinetic aspect of it is taken care of separately (see section 14.2.7). Hence, the formalism of equilibrium thermodynamics can be adopted and using the properties of thermodynamic potentials, local

structural rearrangement can be related to corresponding changes in the macroscopic stress and strain state [Rice, 1971].

Let  $\boldsymbol{\epsilon}$  denote the strain tensor for an arbitrary equilibrium state and let  $\boldsymbol{\sigma}$  be the corresponding stress tensor such that  $\boldsymbol{\sigma}d\boldsymbol{\epsilon}$  is the work per unit volume for any virtual deformation  $d\boldsymbol{\epsilon}$ . The variable  $\xi$  denotes the current “inelastic” state of the material. Following the thermodynamic principles, we can therefore write:

$$\boldsymbol{\sigma} = \boldsymbol{\sigma}(\boldsymbol{\epsilon}, T, \xi). \quad (14.1)$$

The basic assumption is that work potential

$$W^H = W^H(\boldsymbol{\epsilon}, T, \xi) \quad (14.2)$$

exists at each  $\xi$  within the associated  $\boldsymbol{\epsilon}$  domain. Then for any strain variation  $\delta\boldsymbol{\epsilon}$  at fixed  $\xi$ , i.e., for which we obtain purely elastic deformation, we can write:

$$\boldsymbol{\sigma}\delta\boldsymbol{\epsilon} = \delta W^H(\boldsymbol{\epsilon}, T, \xi), \quad (14.3)$$

and therefore, we can determine the stress tensor as follows:

$$\boldsymbol{\sigma} = \frac{\partial W^H(\boldsymbol{\epsilon}, T, \xi)}{\partial \boldsymbol{\epsilon}}. \quad (14.4)$$

Within the elastic domain for any given  $\xi$ ,  $W^H$  actually corresponds to Helmholtz free energy [Rice, 1971]. The complementary potential is the Gibbs free energy, so that

$$W^G = W^G(\boldsymbol{\sigma}, T, \xi) = \boldsymbol{\sigma} : \boldsymbol{\epsilon} - W^H \quad (14.5)$$

and

$$\boldsymbol{\epsilon} = \frac{\partial W^G(\boldsymbol{\sigma}, T, \xi)}{\partial \boldsymbol{\sigma}}. \quad (14.6)$$

Variations in state at fixed  $\xi$ , noted  $\delta\boldsymbol{\epsilon}$ ,  $\delta\Psi$ , etc., should be reversible (path independent). More general variations that involve a change  $d\xi$  are defined by  $d\boldsymbol{\epsilon}$ ,  $d\Psi$ , etc. In particular, let  $d\Psi^i$  denote the change in the free energy function when the solid undergoes deformation that takes it from state  $\xi$  to state  $\xi + d\xi$  at constant  $\boldsymbol{\sigma}$  and  $T$ :

$$dW^{G_i} = W^G(\boldsymbol{\sigma}, T, \xi + d\xi) - W^G(\boldsymbol{\sigma}, T, \xi) \quad (14.7)$$

Therefore, the inelastic strain associated with  $d\xi$ , by differentiating equation (14.7), is given by

$$d^i\boldsymbol{\epsilon}_{ij} = \frac{\partial}{\partial \sigma_{ij}}(dW^{G_i}). \quad (14.8)$$

Thus, inelastic variations in the potentials are themselves potentials for inelastic variations in stress and strain [Rice, 1971]. As for the full strain increment, we can write that

$$d\boldsymbol{\epsilon}_{ij} = M_{ijkl}d\sigma_{kl} + \alpha_{ij}dT + d^i\boldsymbol{\epsilon}_{ij}, \quad (14.9)$$

the first term corresponding to the purely elastic strain and the second to the thermoelastic effect, with the compliance tensor  $M$  given by

$$M_{ijkl} = \frac{\partial^2 W^G(\boldsymbol{\sigma}, T, \xi)}{\partial \sigma_{ij} \partial \sigma_{kl}}. \quad (14.10)$$

Hence, following this framework, we can develop a damage-constitutive model that accounts for inelastic deformation. The following section (14.2.2) defines the internal variable ( $\xi$ ) used in our micromechanical model to describe the inelastic state, and then using the energy-based approach, we develop a constitutive strain-stress relationship (section 14.2.5).

#### 14.2.2. Inelastic Deformation in the Brittle Crust Is Largely Controlled by the Presence of Preexisting Fractures

Inelastic deformation in the brittle crust occurs by nucleation, growth, and/or sliding on preexisting “fractures” at different scales. Fractures includes faults and joints but also smaller scale cracks and flaws such as mineral twins or defects in the crystal structure, grain boundaries, and pores. Frictional sliding occurs under compressive stress on preexisting fractures when the shear stress overcomes the frictional resistance acting on the fracture interface. Tensile cracking, on the other hand, can have different origins. Under regional tensile loading, the stress concentration allows the local stresses at the crack tips to exceed the rock strength, leading to crack propagation. Tensile cracking can also occur by hydraulic cracking: locally, the pore pressure increase can lead to tensile stresses at the crack tips, even under compressive loading. Finally, frictional sliding on fractures under compression creates a tensile force (as the faces slide in opposing direction) that opens wing cracks at the tip of the shear fractures. The wing cracks nucleate and grow in  $\sigma_1$  direction (most compressive) and open in  $\sigma_3$  direction (least compressive).

Flaws described above (e.g., fractures, microcracks, faults, mineral defects, grain boundaries, pores), are found in all natural rocks. Therefore, for the purpose of this study, and following Ashby and Sammis [1990], and Deshpande and Evans [2008], we represent the medium surrounding faults as an isotropic elastic solid that contains preexisting monosized flaws, here represented

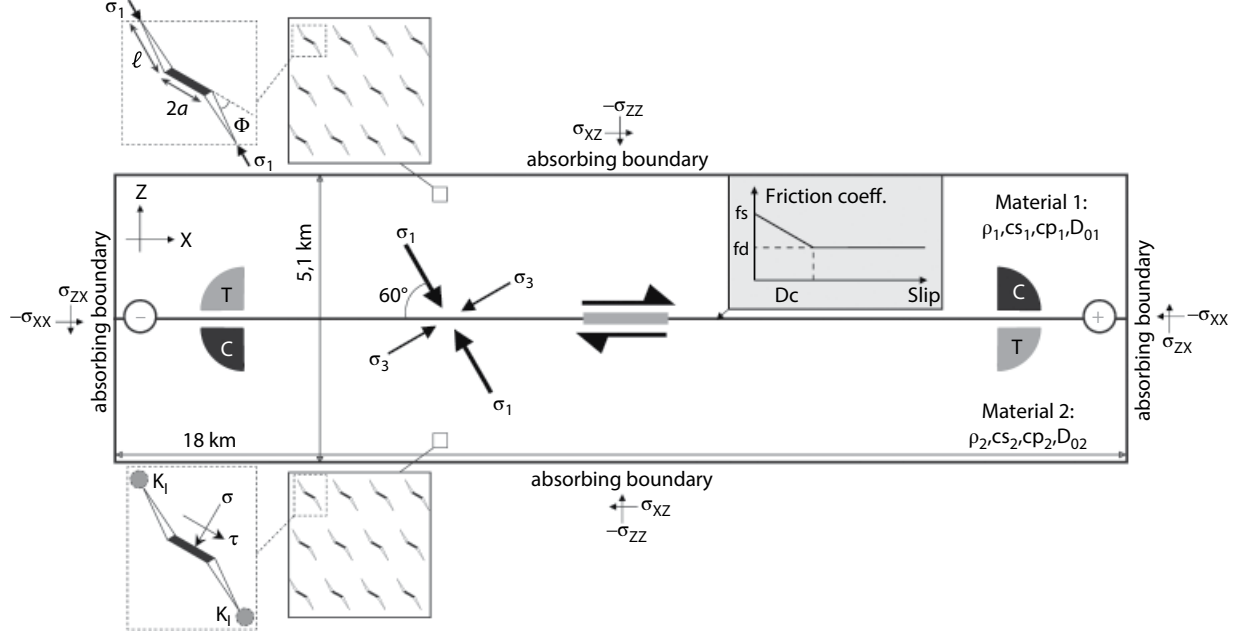


**Figure 14.1** Schematics and parameters for simulations of dynamic ruptures in a 2D inplane model. We consider a right-lateral planar fault (black line in the middle), embedded in a brittle off-fault medium with a damage-constitutive law. Material properties are defined by the density ( $\rho$ ), the S- and P-waves speed ( $c_s$  and  $c_p$ ), and the initial damage density ( $D_0$ ). In some simulations, we assume a material contrast across the fault. In that case, material 1 is always the softer material, and material 2 the stiffer. Slip-weakening friction (gray box) acts on the 18 km long fault,  $C$  and  $T$  denoting the compressional and the tensional quadrants, respectively. Also shown are the “+” and “-” directions defined by the material contrast across the fault. The “+” direction is defined as the direction of motion of the more compliant material (M2 in our case). The medium is loaded by uniform background stresses with the maximum compressive stress  $\sigma_1$  making an angle of  $60^\circ$  with the fault plane. The thick gray line corresponds to the nucleation-prone patch where the initial shear stress is set up to be just above the fault strength.

by penny-shaped cracks of radius  $a$  (Figure 14.1). They are assumed to have a volume density  $N_v$  (prescribed) that remains fixed during the loading (i.e., no nucleation of new cracks). The density of these initial flaws per unit volume is characterized by a scalar  $D_0$  defined as

$$D_0 = \frac{4\pi}{3} N_v (\alpha a)^3, \quad (14.11)$$

where  $\alpha a$  is the projection of the crack radius parallel to the direction of  $\sigma_1$ . We only take into account the cracks that are optimally oriented from a Coulomb friction perspective for a given stress state, i.e., the cracks are aligned at the same angle  $\Phi$  to the largest (most negative) remote compressive stress,  $\sigma_1$  (see Bhat *et al.* [2011] for a justification):

$$\Phi = \frac{1}{2} \tan^{-1}(1/f), \quad (14.12)$$

where  $f$  is the coefficient of friction.

Under suitable conditions, inelastic deformation occurs in the model by either opening the preexisting cracks or by propagation of cracks. For simplicity, we account for opening and propagation of cracks due to regional tensile loading and frictional sliding (compressive loading), but we do not include hydrofracturing in the model. Cracks grow in the form of tensile wing cracks that nucleate at the tips of the penny-shaped flaws. Wings cracks, each of length  $l$ , grow parallel to the  $\sigma_1$  axis (Figure 14.1), and the current damage state is then defined by the scalar  $D$  (fraction of volume occupied by micro-cracks):

$$D = \frac{4\pi}{3} N_v (\alpha a + l)^3. \quad (14.13)$$

$D$  approaching 1 corresponds to the coalescence stage that leads to the macroscopic fracture of the solid. Henceforth, the internal variable  $D$ , which describes the current damage state of our solid, denotes the inelastic state of the material (replacing  $\xi$  in section 14.2.1).

### 14.2.3. Gibbs Free Energy of a Damage Solid

In this chapter, we use the aforementioned energy-based framework (section 14.2.1) to determine the strain-stress relationship of a damaged solid by defining the constitutive relationship in terms of Gibbs free energy  $W^G$ . Henceforth, we assume isothermal conditions, and the Gibbs free energy density of a damaged solid, for a given stress state  $\sigma$  and damage state  $D$ , can be written as the sum of (i) the free energy  $W^{G_e}(\sigma)$  of a solid, without flaws, deforming purely elastically and (ii) the free energy  $W^{G_i}(\sigma, D)$  corresponding to the contribution of microcracks :

$$W^G(\sigma, D) = W^{G_e}(\sigma) + W^{G_i}(\sigma, D). \quad (14.14)$$

Consequently, the associated elastic and inelastic strains,  $\varepsilon_{ij}^e$  and  $\varepsilon_{ij}^i$ , respectively, can be expressed as:

$$\varepsilon_{ij} = \varepsilon_{ij}^e + \varepsilon_{ij}^i = \frac{\partial W^{G_e}(\sigma)}{\partial \sigma_{ij}} + \frac{\partial W^{G_i}(\sigma, D)}{\partial \sigma_{ij}}. \quad (14.15)$$

Properties of the linear elastic material are described by its shear modulus  $\mu$ , Poisson's ratio  $v$ , and mass density  $\rho$ . The elastic strain energy density is given by

$$W^{G_e}(\sigma) = \frac{1}{4\mu} \left[ 2\tau^2 + \frac{3(1-2v)}{(1+v)} \sigma^2 \right]. \quad (14.16)$$

Then, since all cracks in our model have the same orientation, the Gibbs function associated with inelastic deformation at constant  $\sigma$  can be written in terms of the Gibbs free energy per crack  $\Delta W^G(\sigma, D)$  times the number of cracks per unit volume ( $N_v$ ):

$$W^{G_i}(\sigma, D) = N_v \Delta W^G(\sigma, D). \quad (14.17)$$

The Gibbs free energy per crack depends on the fracture energy release rate  $G$  (crack growth) and the surface energy  $\gamma_s$  (to create a surface):

$$\Delta W^{G_i}(\sigma, D) = N_v \Delta W^G(\sigma, D), \quad (14.18)$$

where  $ds$  describes the position along the microcrack and  $\Gamma$  corresponds to the locus of all crack fronts. Based on fracture mechanics, for an isotropic elastic solid, the energy release rate  $G$  can be related to the stress intensity factors at the tip of the crack by

$$G(\sigma, D) = \frac{1-v^2}{E} \left[ K_I^2(\sigma, D) + K_{II}^2(\sigma, D) + \frac{K_{III}^2(\sigma, D)}{(1-v)} \right], \quad (14.19)$$

where  $E$  is the Young's modulus. However, under dynamic loading rates, the wing cracks quickly quit mode II and mode III to become purely tensile. As a consequence, their contributions are neglected in this model. We also neglect the work done by the starter flaws. The total Gibbs free energy of the damaged solid can thus be approximated as

$$W^G(\sigma, D) = W^{G_e}(\sigma) + N_v \int_{\Gamma} \left[ \frac{1-v^2}{E} K_I^2(\sigma, D) - 2\gamma_s \right] ds. \quad (14.20)$$

The evaluation of the Gibbs free energy, and thus the mechanical constitutive description of the modeled brittle material, is hence based on the evaluation of the stress intensity factor  $K_I$  at the tip of the microcracks inside the solid (see section 14.2.4).

### 14.2.4. Evaluating the Stress Intensity Factors at the Tip of the Crack

To account for the energy "lost" in the medium due to inelastic deformation in the brittle crust, we therefore need to compute the stress intensity factor  $K_I$ . Once the loading is sufficiently large to induce inelastic deformation, it does so by opening preexisting cracks or by propagation of cracks. Based on structural observations (see section 14.2.2), we defined three regimes, depending on the overall stress-state: one for tensile loading and two for compressive loading. Under Regime I (compressive loading), stresses are not high enough to allow sliding or opening of the microcracks. Hence, the solid is assumed to behave like an isotropic linear elastic solid, and therefore  $W^{G_i}(\sigma, D)$  is assumed to be zero. Still for compressive loading, Regime II is reached when the shear stress  $\tau$  overcomes the frictional resistance  $f(-\sigma)$  acting on microcracks. Then, as previously described, inelastic deformation is accounted for by growing tensile wing cracks at the tip of the penny-shaped cracks. Finally, our model also accounts for the overall remote tensile loading (Regime III). In that particular case, both penny-shaped cracks and wing cracks open due to normal tensile stress.

Under Regime II (compressive loading), the mode I stress intensity factor  $K_I^{R-II}$  for a unit volume containing  $N_v$  cracks of size  $(l + \alpha a)$  can be expressed as

$$K_I^{R-II}(\sigma, D) = \sqrt{\pi a_0} [A(D)\sigma + B(D)\tau], \quad (14.21)$$

where  $\sigma$  and  $\tau$  correspond to the first invariant of the stress tensor and the second invariant of the deviatoric stress tensor, respectively (equation [14.11] in Bhat *et al.* [2012]). The parameters  $A$  and  $B$  both depend on the damage variable, with

$$A(D) = fc_1(D) + c_3(D)[fc_2(D) + 1] \quad (14.22)$$

$$B(D) = c_1(D) + c_2(D)c_3(D) \quad (14.23)$$

and

$$c_1(D) = \frac{\sqrt{1-\alpha^2}}{\pi\alpha^{3/2} \left[ \left( D/D_0 \right)^{1/3} - 1 + \beta/\alpha \right]^{3/2}} \quad (14.24)$$

$$c_2(D) = \left( \frac{\sqrt{1-\alpha^2}}{\alpha} \right) \left( \frac{D_0^{2/3}}{1-D^{2/3}} \right) \quad (14.25)$$

$$c_3(D) = \frac{2\sqrt{\alpha}}{\pi} \left[ \left( D/D_0 \right)^{1/3} - 1 \right]^{1/2} \quad (14.26)$$

Regime III prevails under tensile loading, and the stress intensity factor  $K_I^{R-III}$  is a quadratic function of the stress invariants:

$$K_I^{R-III}(\sigma, D) = \sqrt{\pi a_0} [C^2(D)\sigma^2 + O^2(D)\tau^2]^{1/2} \quad (14.27)$$

with

$$C(D) = A + \Omega\sqrt{\alpha[D/D_0]^{1/3}} \quad (14.28)$$

$$O(D) = \sqrt{\frac{B^2 C^2}{C^2 - A^2}}. \quad (14.29)$$

#### 14.2.5. Determining the Constitutive Stress-Strain Relationship

Following the energy-based approach described in sections 14.2.1 and 14.2.3, we can define the constitutive stress-strain relationship for a damage solid. The Gibbs free energy function  $W^G(\sigma, D)$  is determined by computing the stress intensity factors  $K_I$  as described in section 14.2.4, depending on the regime. Then, following equations (14.6) and (14.10),  $W^G$  is differentiated once with respect to stress to obtain the strain-stress relationship, and twice with respect to stress to get the compliance tensor. The Gibbs free energy can also be expressed in terms of the conjugate strains invariants:

$$\varepsilon = \varepsilon_{kk} \quad \text{and} \quad \gamma = \sqrt{2e_{ij}e_{ij}} \quad \text{with} \quad e_{ij} = \varepsilon_{ij} - \frac{\varepsilon}{3}\delta_{ij}, \quad (14.30)$$

which gives the Helmotz free energy,  $W^H$  (see equation [14.5]). Differentiating twice  $W^H(\varepsilon, D)$  with respect to strain will then give the stiffness tensor  $C_{ijkl}$ .

##### 14.2.5.1. Constitutive Relationship for Regime I

Under Regime I, there is no sliding or opening of the microcracks. Therefore, the Gibbs free energy is given by

$$W^G(\sigma, D) = W^{G_e}(\sigma) = \frac{1}{4\mu} \left[ 2\tau^2 + \frac{3(1-2\nu)}{(1+\nu)} \sigma^2 \right], \quad (14.31)$$

and the strain-stress relationship follows linear elasticity:

$$\sigma_{ij} = 2\mu \left[ \varepsilon_{ij} + \frac{\nu}{1-2\nu} \varepsilon \delta_{ij} \right] = 2\mu\varepsilon_{ij} + \lambda\varepsilon\delta_{ij}, \quad (14.32)$$

where  $\lambda$  is the Lamé's first parameter.

##### 14.2.5.2. Constitutive Relationship for Regime II

For Regime II and III, following equation (14.20), the Gibbs free energy can be written as the sum of the elastic contribution,  $W^{G_e}(\sigma)$ , and the inelastic contribution due to the presence of microcracks,  $W^{G_c}(\sigma, D)$  (see equation [14.20]). Following Deshpande and Evans [2008] and Bhat et al. [2012], we assume that the constants  $A$  and  $B$  of  $K_I^{R-II}$  and  $C$  and  $O$  of  $K_I^{R-III}$  are only a function of the ratio  $l/a$  (and not  $l$  and  $a$  separately), and therefore we can treat them as constants. We thus find that the Gibbs free function for Regime II can be approximated by

$$W^G(\sigma, D) = W^{G_e}(\sigma) = \frac{1}{4\mu} [A_l\sigma + B_l\tau]^2, \quad (14.33)$$

where

$$A_l = A \sqrt{\frac{\pi D_0(1-\nu)}{\alpha^3}} \quad \text{and} \quad B_l = B \sqrt{\frac{\pi D_0(1-\nu)}{\alpha^3}}; \quad (14.34)$$

If we state the above expression in terms of conjugate strains ( $\varepsilon$  and  $\gamma$ ), we obtain the Helmotz free energy that can be differentiated once with respect to strain to obtain the stress-strain relation:

$$\begin{aligned} \sigma_{ij} = & \frac{\mu}{\Gamma} \left\{ \left( \frac{3(1-2\nu)}{(1+\nu)} + A_l^2 - \frac{A_l B_l \varepsilon}{\gamma} \right) \varepsilon_{ij} \right. \\ & \left. + \left( \frac{3\nu}{(1+\nu)} + \frac{B_l^2}{2} - \frac{A_l^2}{3} + \frac{A_l B_l \varepsilon}{3\gamma} \right) \varepsilon \delta_{ij} - \left( \frac{A_l B_l}{2} \right) \gamma \delta_{ij} \right\} \end{aligned} \quad (14.35)$$

$$\text{with } \Gamma = \left[ \frac{3(1-2\nu)}{2(1+\nu)} + \frac{3(1-2\nu)}{4(1+\nu)} + \frac{A_l^2}{2} \right]. \quad (14.36)$$

Based on equation (14.35), we can define the equivalent Lamé parameters  $\mu^*$  and  $\lambda^*$ :

$$\mu^* = \frac{\mu}{2\Gamma} \left( \frac{3(1-2\nu)}{(1+\nu)} + A_1^2 \right) \text{ and } \lambda^* = \frac{\mu}{\Gamma} \left( \frac{3\nu}{(1+\nu)} + \frac{B_1^2}{2} - \frac{A_1^2}{3} \right), \quad (14.37)$$

and therefore approximate the change in waves speed occurring in the medium:

$$c_p^* = \sqrt{\frac{\lambda^* + 2\mu^*}{\rho}} \text{ and } c_s^* = \sqrt{\frac{\mu^*}{\rho}}. \quad (14.38)$$

#### 14.2.5.3. Constitutive Relationship for Regime III

Under Regime III, the Gibbs free energy is given by

$$W^G(\sigma, D) = W^{G_e} + \frac{1}{4\mu} [C_1^2 \sigma^2 + O_1^2 \tau^2], \quad (14.39)$$

where

$$C_1 = C \sqrt{\frac{\pi D_0 (1-\nu)}{\alpha^3}} \text{ and } O_1 = O \sqrt{\frac{\pi D_0 (1-\nu)}{\alpha^3}}, \quad (14.40)$$

If we state the above expression in terms of conjugate strains, and differentiating the obtained Helmotz free energy  $W^H$  with respect to strain, we can derive the the constitutive relationship

$$\sigma_{ij} = \mu \left\{ \left( \frac{4}{2+O_1^2} \right) \varepsilon_{ij} + \left( \frac{2}{\frac{3(1-2\nu)}{(1+\nu)} + C_1^2} - \frac{4}{3[O_1^2 + 2]} \right) \varepsilon \delta_{ij} \right\}. \quad (14.41)$$

Following the same logic as for Regime II, we can define the equivalent Lamé parameters  $\mu^*$  and  $\lambda^*$ :

$$\mu^* = \mu \left( \frac{4}{2+O_1^2} \right) \text{ and } \lambda^* = \mu \left( \frac{2}{\frac{3(1-2\nu)}{(1+\nu)} + C_1^2} - \frac{4}{3[O_1^2 + 2]} \right), \quad (14.42)$$

and therefore compute the change in wave speed occurring in the medium.

#### 14.2.6. Criteria for Regime Transition

Criteria to determine the regimes to be applied in the model are defined based on the stress intensity factor  $K_I$ . In Regime I the stresses are not sufficient to allow inelastic

deformation (sliding or opening of the microcracks). This implies  $K_I \leq 0$  at the tip of the cracks ( $K_I^{RI}$  or  $K_I^{RIII}$ , since  $C$  and  $O$  are related to  $A$  and  $B$ ). Therefore, based on equation (14.21), the criteria for Regime I is

$$A\sigma + B\tau \leq 0. \quad (14.43)$$

For the two regimes (II and III) undergoing inelastic deformation,  $K_I$  is positive and the transition between regimes is obtained by ensuring the continuity of conjugate plastic strains  $\varepsilon^i$  and  $\gamma^i$ . Following equation (14.8), the conjugate plastic strains are derived as  $\varepsilon^i = \partial W^{G_i}/\partial \sigma$  and  $\gamma^i = \partial W^{G_i}/\partial \tau$ . The first invariant of the plastic strain tensor corresponds to the opening of the microcracks, whereas the second invariant is related to the frictional sliding of the penny-shaped cracks. Under compressive loading, tensile deformation only occurs by opening of the wing cracks, whereas under Regime III, both penny-shaped cracks and wing cracks open due to normal tensile stress. As a consequence,  $\varepsilon^i$  is smaller for compressive loading (Regime II) than for tensile loading (Regime III). Therefore, we are in Regime II when

$$A\sigma + B\tau > 0 \text{ and } (A^2 - C^2)\sigma + AB\tau > 0 \quad (14.44)$$

and Regime III is reached for

$$A\sigma + B\tau > 0 \text{ and } (A^2 - C^2)\sigma + AB\tau < 0. \quad (14.45)$$

#### 14.2.7. Dynamic Crack Growth Law

In the previous sections, we have developed the constitutive laws that prescribe the response of a damaged solid to a remote tensile or compressive loading. The energy-based approach used in this model requires computing of the Gibbs free energy,  $W^G(\sigma, D)$ , which depends on the stress tensor and the microcrack density  $D$  per unit volume (section 14.2.3). Therefore, we need to define the state of cracks in the medium, or how they respond to remote loading, since as cracks grow, the state parameter  $D$  also increases (equation [14.13]), which in turn affects the constitutive response of the material (section 14.2.5). To complete the constitutive model, we thus define a state evolution law for the parameter  $D$ . Differentiating equation (14.13) with respect to time leads to

$$\frac{dD}{dt} = \left( \frac{3D^{2/3}D_0^{1/3}}{\alpha a} \right) \frac{dl}{dt}, \quad (14.46)$$

where  $dl/dt = v$  corresponds to the instantaneous wing-crack tip speed. We adopt the crack growth law developed by *Bhat et al.* [2012] that accounts for loading rate dependent fracture initiation toughness,  $K_{IC}^D$  [*Wang et al.*,

2010, 2011; *Zhang and Zhao*, 2013], and propagation toughness,  $K_I^d$  [Chen et al., 2009; Dai et al., 2010, 2011; Zhou and Aydin, 2010; Gao et al., 2015].

### 14.3. NUMERICAL METHOD AND MODEL DESCRIPTION

#### 14.3.1. Numerical Method

This study aims to evaluate the influence of the dynamic evolution of damage in the surrounding medium on seismic ruptures. Therefore, the constitutive damage model described above has been implemented in the 2D spectral element code SEM2DPACK [Ampuero, 2002, available at <http://web.gps.caltech.edu/~ampuero/software.html>]. Reactivation of damage depends on the state of stress in the medium, which in turn is influenced by the dynamic evolution of damage density (see section 14.2.5). Hence, to realize the micromechanics-based model, in the context of dynamic rupture, we developed a constitutive update scheme that takes into account this intricate feedback, using a Runge-Kutta-Fehlberg (RKF) method to integrate equation (14.46). Between each time step during the simulations, for a given a strain field ( $\epsilon$ ), we solve for the new damage density field  $D$  using an RKF update. Then, given this new value of the state parameter, we solve for the stress field ( $\sigma$ ) using the damage constitutive law (section 14.2.5).

#### 14.3.2. Model Setup

In our simulations, we consider a 2D inplane model with a 1D right lateral fault embedded in a brittle off-fault medium that allows for dynamic evolution of elastic

moduli (Figure 14.1). To simplify the problem, we assume plane strain conditions. In our simulations, the medium is loaded by uniform background stresses. The maximum compressive stress  $\sigma_1$  and the minimum compressive stress  $\sigma_3$  are in the  $x-z$  plane, whereas the intermediate principal stress  $\sigma_2$  coincides with  $\sigma_{yy}$ . The fault plane makes a 60° angle with  $\sigma_1$ , and we assume a uniform normal stress ( $\sigma_0 = \sigma_{zz}^0$ ) and shear stress ( $\tau_0 = \sigma_{xz}^0$ ) distribution on the fault, except for the nucleation-prone patch (thick gray line in Figure 14.1), for which we assign a value slightly above the nominal static strength (section 14.3.3). Finally, to warrant any interference with the propagating dynamic rupture, we set the domain (5.1×18 km) large enough and we apply absorbing boundary conditions on the edge of the computation domain. Reference values for the different parameters are summarized in Table 14.2.

#### 14.3.3. Friction Law and Nucleation Procedure

Rupture propagation along the fault plane is governed by a slip-weakening friction law [e.g. *Palmer and Rice*, 1973]. Slip occurs when the on-fault shear stress reaches the shear strength  $\tau = f(-\sigma^*)$  (see section 14.3.4 for a definition of  $\sigma^*$ ). The friction coefficient  $f$  depends on the cumulated slip ( $\delta$ ) and drops from a static ( $f_s$ ) to a dynamic ( $f_d$ ) value over a characteristic distance  $\delta_c$ :

$$f = \begin{cases} f_s - (f_s - f_d)\delta/\delta_c & \text{if } \delta \leq \delta_c \\ f_d & \text{if } \delta > \delta_c \end{cases}. \quad (14.47)$$

In our models, we set the static friction coefficient at 0.6, which corresponds to a value measured in laboratory

**Table 14.2** Input parameters for our simulations.

Parameter	Symbol	Value	
Normal stress on the fault (MPa)	$\sigma_0$	60.7	
Shear stress on the fault (MPa)	$\tau_0$	19.9 or 36.4	
Static friction coefficient	$f_s$	0.6	
Dynamic friction coefficient	$f_d$	0.1	
Characteristic slip (m)	$\delta_c$	1	
<i>Prakash and Clifton</i> [1993] time (s)	$t^*$	$40 \times 10^{-3}$	
Poisson's ratio	$\nu$	0.276	
Branching speed (km.s <sup>-1</sup> )	$v_m$	1.58	
Quasi-static fracture toughness	$K_{Ic}^{ss}$	$1.2 \times 10^6$	
<i>Ashby and Sammis</i> [1990] factor	$\beta$	0.1	
Crack factor	$\Omega$	2.0	
Parameter for Material	Symbol	Granite (m1, m2)	Gabbro (m2)
Penny-shaped cracks radius (m)	$a_0$	60 or ~ 0	60
Volume density of cracks ( $\times 10^{-7}$ #/m <sup>3</sup> )	$N_v$	1.68 or 3.36	1.68
Density	$\rho$	$2.7 \times 10^3$	$3 \times 10^3$
S-wave speed (m.s <sup>-1</sup> )	$c_s$	$3.12 \times 10^3$	$3.25 \times 10^3$
P-wave speed (m.s <sup>-1</sup> )	$c_p$	$5.6 \times 10^3$	$5.84 \times 10^3$

experiments for a large range of rocks [Byerlee, 1978]. Then, following high strain-rate experiments at range covering earthquake slip rate, we assign a value of 0.1 for the dynamic friction coefficient [Wibberley *et al.*, 2008].

To promote dynamic rupture, we create a nucleation-prone patch in the middle of the fault (see blue line in Figure 14.1), for which  $\tau_0$  is defined to be just above the fault strength ( $\sim 0.03\%$  greater). Following Kame *et al.* [2003], the minimum nucleation size  $L_c$  determined by the energy balanced for a slip weakening law is

$$L_c = \frac{16}{3\pi} \frac{\mu G}{(\tau^0 - \tau_d)^2} = \frac{64}{9\pi^2} \left( \frac{\tau_s - \tau_d}{\tau^0 - \tau_d} \right)^2, \quad (14.48)$$

where

$$\tau_s = f_s(-\sigma_{zz}) \quad \text{and} \quad \tau_d = f_d(-\sigma_{zz}). \quad (14.49)$$

Here  $\mu$  is the shear modulus,  $G$  is the fracture energy of the medium, and  $R_0 = (3\pi/4)[\mu G/(\tau_d - \tau^0)^2]$  is the length of the static sleep weakening zone as defined by Palmer and Rice [1973]. For our simulations and choice of parameters we set the size of the nucleation patch to be 1.5 km.

#### 14.3.4. Regularization for Bimaterial Effect

Andrews and Ben-Zion [1997] and Cochard and Rice [2000] have shown that the problem of slip on bimaterial fault is ill posed. Yet in our simulations, evolution of off-fault damage during the rupture leads to dynamic changes of elastic moduli, which creates a damage-related material contrast across the fault. Moreover, the effect of off-fault damage on dynamic rupture has been explored for both homogeneous and dissimilar material. To provide a regularization to the ill-posed problem in such scenarios, a characteristic time or slip scale of normal stress response has been proposed [Cochard and Rice, 2000; Ranjith and Rice, 2001]. Following Rubin and Ampuero [2007], we adopt a simplified form of the Prakash and Clifton [1993] law, where the fault strength is assumed to be proportional to a modified normal stress  $\sigma^*$ , which evolves toward a residual value over a time scale  $t^*$  in response to abrupt change of the actual fault normal stress:

$$\dot{\sigma}^* = \frac{1}{t^*} (\sigma - \sigma^*). \quad (14.50)$$

Ideally,  $t^*$  should be much larger than the time step during the simulation ( $\Delta t$ ) yet much smaller than the time to undergo slip weakening,  $T$ . Here we use  $t^* = 4\Delta x/c_s \approx 40 \times 10^{-3}$  s.

Another possibility to reduce numerical oscillations is to add an artificial Kelvin-Voigt visco-elastic layer around

the fault [e.g., Brietzke and Ben-Zion, 2006; Xu *et al.*, 2012, 2014]. However, this may also remove true small scale features and modify the response of the off-fault medium by absorbing energy. Therefore, we did not damp the high-frequency numerical noise with such method to avoid tampering the physical response in our models.

#### 14.3.5. Resolution

To properly solve the problem at hand, we need to define a grid spacing  $\Delta x$  that is small enough to resolve the smallest physical length scale. The spatial discretization  $\Delta x$  (distance between two neighbor nodes) is taken so that there are multiple cells to resolve the process zone  $\Lambda$  for a slip-weakening law, the shortest wavelength  $\lambda_{min}$ , and the nucleation stage.

Following Day *et al.* [2005], if we assume that the process zone  $\Lambda$  is small enough to use a small-scale yielding limit of fracture mechanics [Rice, 1968] (stress field around  $\Lambda$  dominated by the singular part of the crack front) and if we assume the crack propagation to be steady, for a slip-weakening law  $\Lambda$  can be expressed as

$$\Lambda = \Lambda_0 \varphi^{-1}(v_r) \quad (14.51)$$

$$\text{with } \Lambda_0 = \frac{9\pi}{32(1-v)} \frac{\delta_c \rho c_s^2}{(f_d - f_s)\sigma_{zz}}, \quad (14.52)$$

where  $\Lambda_0$  is the static value of the process zone ( $v_r = 0$ ) for a mode II rupture and  $\varphi^{-1}$  is a monotonic function of the rupture speed (see Day *et al.* [2005] for details) for details). Consequently, values for the process zone go from  $\Lambda_0$  to 0, when  $v_r$  reaches the limiting speed, which corresponds to the Rayleigh wave speed  $c_R$  for a mode-II rupture in homogeneous solid, and the shear-wave speed for mode III (see Rubin and Ampuero [2007] for an estimate of the  $\Lambda$  when there is a material contrast across the fault).  $\Lambda_0$  is therefore a convenient upper bound for the process zone size, and numerical simulation should resolve with more than one spatial element. In our models, to ensure a good resolution for the dynamic phenomena, the domain is discretized into square  $600 \times 170$  elements with three Gauss-Lobatto-Legendre nodes (Ngl) nonuniformly distributed per element edge. This provides an element size  $h$  of 30 m, and a  $\Delta x$  of  $\sim 3$  m. The grid spacing  $\Delta x$  is much smaller than the element size  $h$  ( $\approx Ngl^2$  times smaller) since in SEM code, each element is subdivided onto a nonregular grid of  $Ngl \times Ngl$  nodes. Consequently, the process zone is resolved with  $\sim 35$  spatial elements, or  $\sim 316$  nodes. This also satisfies a Bhat *et al.* [2012] criterion that requires  $h/a < 1$  to properly account for off-fault damage evolution.

Finally, the time step  $\Delta t$  during the simulations is determined from the Courant-Friedrichs-Lowy (CFL) stability criterion:

$$CFL = c_p \Delta t / \Delta x, \quad (14.53)$$

where  $c_p$  is the P-wave speed. For stability, the CFL is taken to be 0.55 in all simulations.

## 14.4. RESULTS

An important result of this chapter is that we model not only what is happening on the fault plane but also the constitutive response of the surrounding medium to the dynamic rupture. In the following section we explore the dynamics of earthquake rupture and the associated generation of new damage, how it affects both the hosting medium and the rupture propagation, and what are the damage-related features that can be pertinent to interpret geophysical observations. To investigate the intricate feedbacks between off-fault damage generation and earthquake rupture propagation, we start the study with a simple

case, a 2D right-lateral fault inside a homogeneous medium (Granite), where damage is only occurring on one side. Then we increase complexity by first keeping a homogeneous elastic medium but with different initial damage on both sides. The last example presented in this study explores the combined effect of a bimaterial fault (Granite/Gabbro) and a damage evolution law. Reference values for the different parameters are summarized in Table 14.2.

### 14.4.1. Effect of Damage on Dynamic Rupture for a Single Material

To provide an element of comparison, we first discuss the results for a dynamic rupture in a homogeneous solid (typical Granite, see Table 14.2 for properties) with damage evolution only on the top side of the fault (material 1 in Figure 14.2a). The initial flaw size ( $a$ , radius of penny-shaped cracks) was assumed to be 60 m for material 1, which scales with secondary fractures that usually surround main faults extending over several tens of kilometers. The volume density of cracks,  $N_v$ , was set to be  $1.68 \times 10^{-7}$ , which gives an initial damage density value,  $D_0$ , of 0.1. To prevent

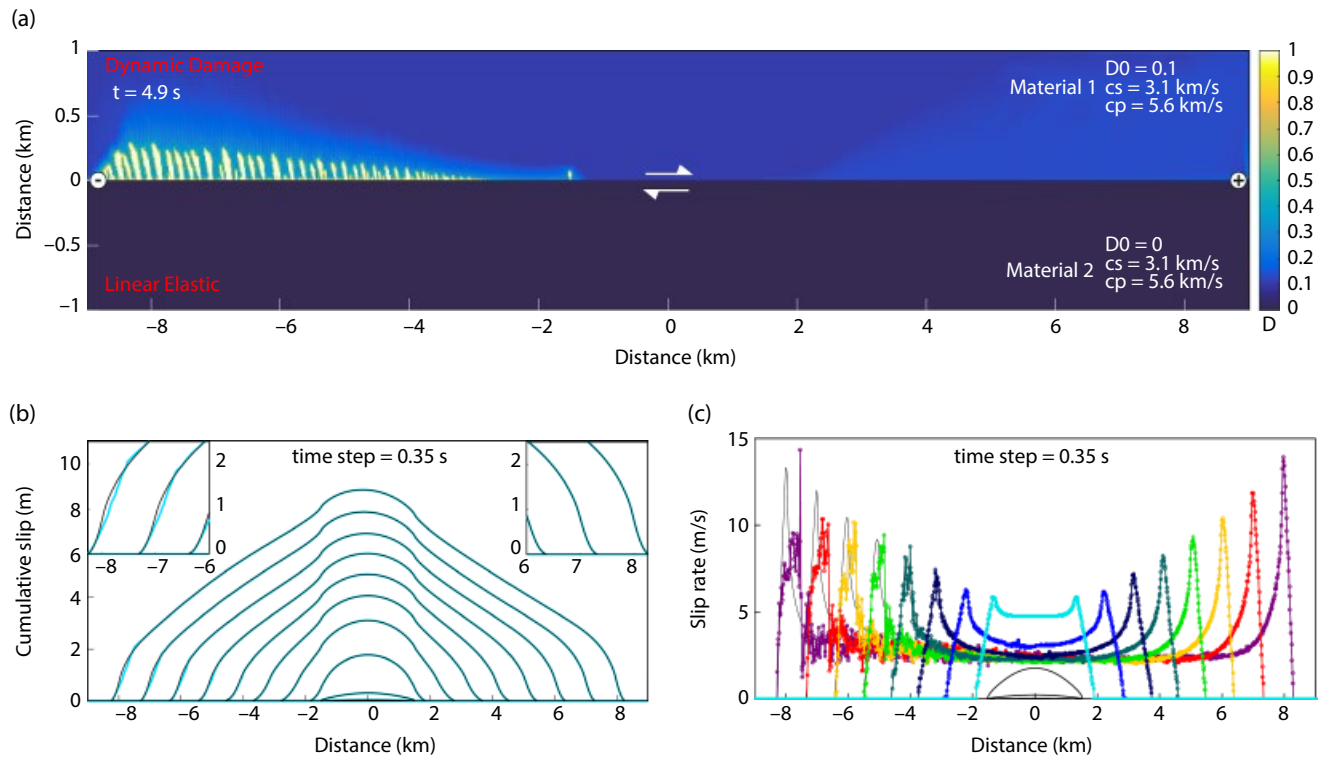


**Figure 14.2** Simulation of a dynamic rupture on a right-lateral fault embedded in a homogeneous medium (Granite). We impose a material contrast across the fault by changing the size of the initial microcracks (60 m and 0), which leads to damage evolution on only the top side of the fault. (a) Evolution of the state parameter  $D$  (density of microcracks in the medium) at  $t = 4.9$  s. Also shown are the “+” and “-” directions as defined in Figure 14.1). Dynamic damage essentially occurs in the tensile quadrant. Cumulative slip (b) and slip rate (c) on the fault are displayed with a time increment of 0.35 s. Colored curves correspond to the dynamic simulation with the damage evolution law; thin black curves depict a simulation with the same parametrization only for a pure elastic medium. See electronic version for color representation.

damage from occurring on the bottom side of the fault, we simply assigned a very small initial flaw size for material 2 ( $a = 6 \times 10^{-8}$  m). Keeping  $N_v$  constant, this returns a value of  $D_0 \approx 0$ . As a consequence, the medium on the bottom side of the fault is behaving in a purely elastic manner.

#### 14.4.1.1. Damage Density and Dynamic Changes of Wave Speeds

Figure 14.2a shows a snapshot (at  $t = 4.9$  s) of the state parameter  $D$  (density of microcracks in the medium),

for a bilateral rupture propagating along the interface between the damaged (above in the graph) and the undamaged material (below). This corresponds to the final stage, at the end of the numerical simulation, chosen to avoid boundary effects. Time evolution of damage with respect to slip rate on the fault is also represented in Figure 14.3. For a right-lateral fault, the rupture tip propagating to the left puts material 1 in tension while the rupture tip on the right induces compression in the medium (T- and C-directions, respectively, in Figure 14.1).

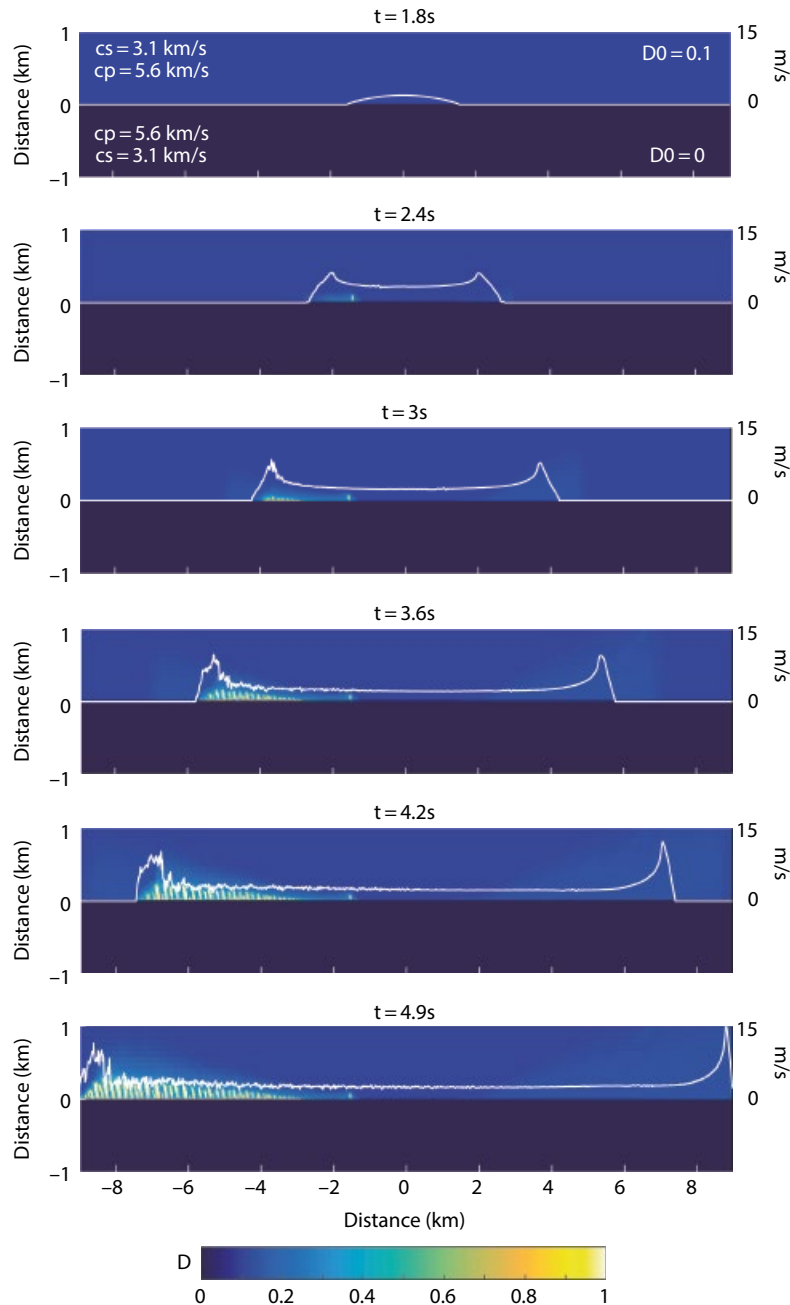


**Figure 14.3** Temporal evolution of the damage parameter  $D$  for a dynamic rupture on a right-lateral fault embedded in a homogeneous medium (Granite) with damage evolution only on the top side of the fault (see also Figure 14.2). Corresponding slip rate (white) is superimposed on the snapshots. See electronic version for color representation.

As illustrated by the parameter  $D$ , the response of the damaged elastic solid is different in the compressional and tensional quadrants, with more damage in the tensile lobe. Thus, the rupture traveling on the compressional side activates and/or interacts little with the off-fault damage; whereas on the extensional side, the rupture tip induces a reduction in elastic moduli (Figure 14.4), which differs from a classic bimaterial rupture since the generation of damage induces a dynamic evolution of the elastic properties (or a “dynamic” bimaterial effect). Based on equations (14.37), (14.38), and (14.42), we record a maximum change of 32.7% for S-wave and 28.0% for P-wave. Those results are consistent with geophysical observations of temporal changes in seismic velocity along a natural fault following earthquake ruptures [Hiramatsu *et al.*, 2005; Li *et al.*, 2006; Brenguier *et al.*, 2008; Cochran *et al.*, 2009; Froment *et al.*, 2014]. At the maximum, the width of the newly created damage zone reaches 900 m and corresponds to the location where the higher slip rate has been recorded (Figure 14.2c). However, the extent of the highly damaged zone ( $D \geq 0.5$ ) does not exceed 300 m.

In all our models, we also note the formation of localized damage zones, which is a direct consequence of the constitutive law. This localization of high damage density could be related to the occurrence of branched faults along mature faults. On average, they form a  $60^\circ$  angle with the main fault plane. However, at this stage, caution must prevail and these results should be taken more qualitatively here. Capturing localization accurately in numerical simulations is impossible for constitutive laws that do not have an internal length scale. There are few ways to address this problem, and we are in the process of exploring these remediations. We therefore do not make any conclusions about spacing between branched faults or the width of these localized damage zones.

#### 14.4.1.2. Cumulative Slip, Slip Rate, and Rupture Speed on the Fault

Figures 14.2b and 14.2c display the cumulative slip and slip rate on the fault, respectively, with a time increment of 0.35 s. We compare the model (colored lines) with a right-lateral rupture occurring in a pure elastic medium

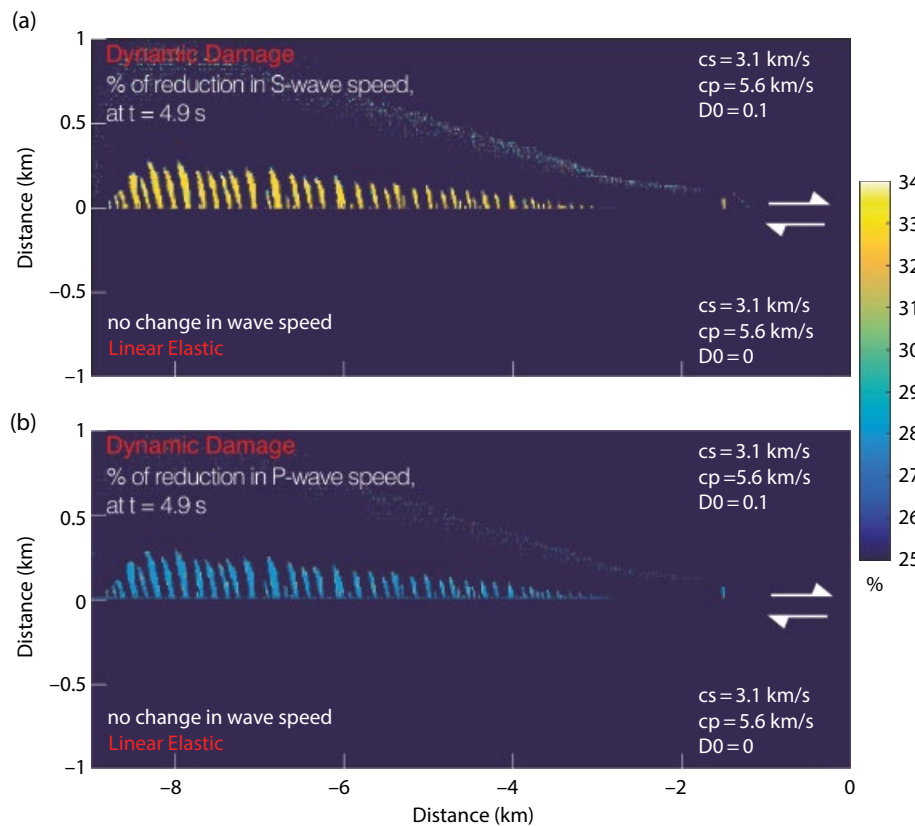


**Figure 14.4** Reduction (in %) of S-wave (a) and P-wave (b) speeds in the medium at  $t = 4.9$  s, in relation to off-fault damage for a dynamic rupture occurring in a homogeneous medium (Granite) with damage evolution only on the top side of the fault (Figure 14.2). Since evolution of damage essentially occurs on the upper tensile quadrant (Figure 14.2a), we only show that part. Formulas to compute the new  $c_p$  and  $c_s$  values, based on the regime, are described in equations (14.37), (14.38), and (14.42). For this particular simulation we record a maximum change of 32.7% for S-wave speed and 28.0% for P-wave speed. See electronic version for color representation.

(thin black curves). In terms of cumulative slip, we observe little differences with the pure elastic model. In both cases, we record a crack-like rupture and we only observe a small decrease in total slip at the rupture tip, where the widest damage zone was developed (between  $-8.5$  and  $-6$  km, left zoom in Figure 14.2b).

On the other hand, evolution of slip rate along the fault plane strongly differs from a classic elastic model. Figure 14.2c shows that the rupture is bilateral but is asymmetric, with more complexity in the negative direction, which results in high-frequency content in the radiated ground motion (see section 14.4.3). The development of slip rate oscillations is likely related to the development of a low-velocity zone (LVZ), with up to 32.7% drop in wave-speed (Figure 14.4). In fact, we observe that the oscillations occur at some distance behind the rupture front and that they are developed only with the emergence of a damage zone around the fault, in relation to the rupture propagation (Figure 14.3). We also notice that oscillations increase in amplitude as the LVZ becomes larger. As shown by the spacing between symbols on Figure 14.2c, which corresponds to the value at each node, the oscillations of slip rate are well resolved numerically. The development of a material contrast (LVZ) can produce internal wave reflections, which in turn gives rise to an additional feedback mechanism between the evolving off-fault medium and the dynamic rupture [e.g., Huang *et al.*, 2014]. Similar trapped waves were recognized by Li *et al.* [1994] during the 1992 Landers earthquake. From this study, authors estimated a fault zone width of  $\sim 180$  m, and a strong decrease of fault zone shear velocity ( $\sim 30\%$ ), as observed in our simulations (see in particular results for a bimaterial fault, section 14.4.2.2). However, in regard to the complex pattern of the LVZ, it is hard to evaluate the relative importance of the different parameters on the complicated feedbacks we can observe (e.g., velocity contrast, width, and relative distance between branches, etc.).

Finally, in our simulations with damage evolution we observe little modulation of the rupture front, compared to the elastic case. This is because the dynamic rupture, which propagates at subshear velocity on average ( $\sim 2.7$  Km.s $^{-1}$ ), interacts with an intact material (Figure 14.3). However, some modulation can be observed, and sometimes the rupture can even reach supershear velocity locally. This is probably related to a process where the radiated waves interact with the LVZ behind the rupture front and further interfere with the rupture front itself.

#### 14.4.2. Evolution of Damage for Dissimilar Materials

For the two following scenarios we chose to increase the complexity by introducing a material contrast across the fault, as usually observed for natural cases. First, we

simply keep the same material (Granite) on both sides but assign a different initial damage density (see section 14.4.2.1 and Table 14.2 for details). This could be interpreted as being the cumulative result of dynamic events, propagating dominantly in one direction, which would create a damage contrast across the fault. In the second scenario, we assign different elastic properties on both sides but keep the damage density constant (see section 14.4.2.2 and Table 14.2 for details). For both scenarios, we set the initial microcrack size at 60 m.

##### 14.4.2.1. Variation in Initial Damage Density

For this particular simulation (Figure 14.5a), the elastic properties correspond to those of a typical Granite (Table 14.2), but we change the damage density across the fault:  $D_0 = 0.2$  on the top part of the fault (material 1) and  $D_0 = 0.1$  for the bottom part (material 2). For an initial microcrack size of 60 m, this leads to a volume density of cracks  $N_v$  of  $3.36 \times 10^{-7}$  (#/m $^3$ ) and  $1.68 \times 10^{-7}$  (#/m $^3$ ), respectively.

Figure 14.5a shows a snapshot of the state parameter  $D$  at  $t = 4.9$  s, which corresponds to the end of the numerical simulation. Time evolution of damage with respect to slip rate on the fault is also represented in Figure 14.6a. The small initial difference in damage density actively impacts the final result since we observe more dynamic damage generation in the softer material ( $D_0 = 0.2$ ). On the left tensile quadrant, the highly damaged zone ( $D \geq 0.5$ ) extends up to 600 m, whereas in the right tensile lobe, it does not exceed 300 m. We also notice a more “gradual” decay in damage density for material 1. Concurrently, we observe a stronger reduction in elastic properties for the more compliant material (maximum change of 34.4% for S-wave and 28.2% for P-wave) than for the material with less initial damage (maximum change of 32.7% for S-wave and 28.0% for P-wave).

Figures 14.5b and 14.5c display the cumulative slip and slip rate on the fault, respectively, with a time increment of 0.35 s. In accordance with previous observations (section 14.4.1.2), the cumulative slip in the negative direction is slightly smaller than in the positive direction, where less damage is recorded. We also notice slip rate oscillations in both directions. However, they occur earlier in the negative direction, in relation to the development of an LVZ that arises closer to the nucleation prone patch on that part of the fault. Finally, this simulation displays little modulation in the rupture speed, with no significant difference between the two rupture fronts. Again, this is likely related to the fact that the subshear rupture propagates inside an intact material, in both directions.

This simple scenario underlines the importance of incorporating not only the fault history but also the off-fault medium history in dynamic modeling of earthquakes: damage can accumulate over time and influence

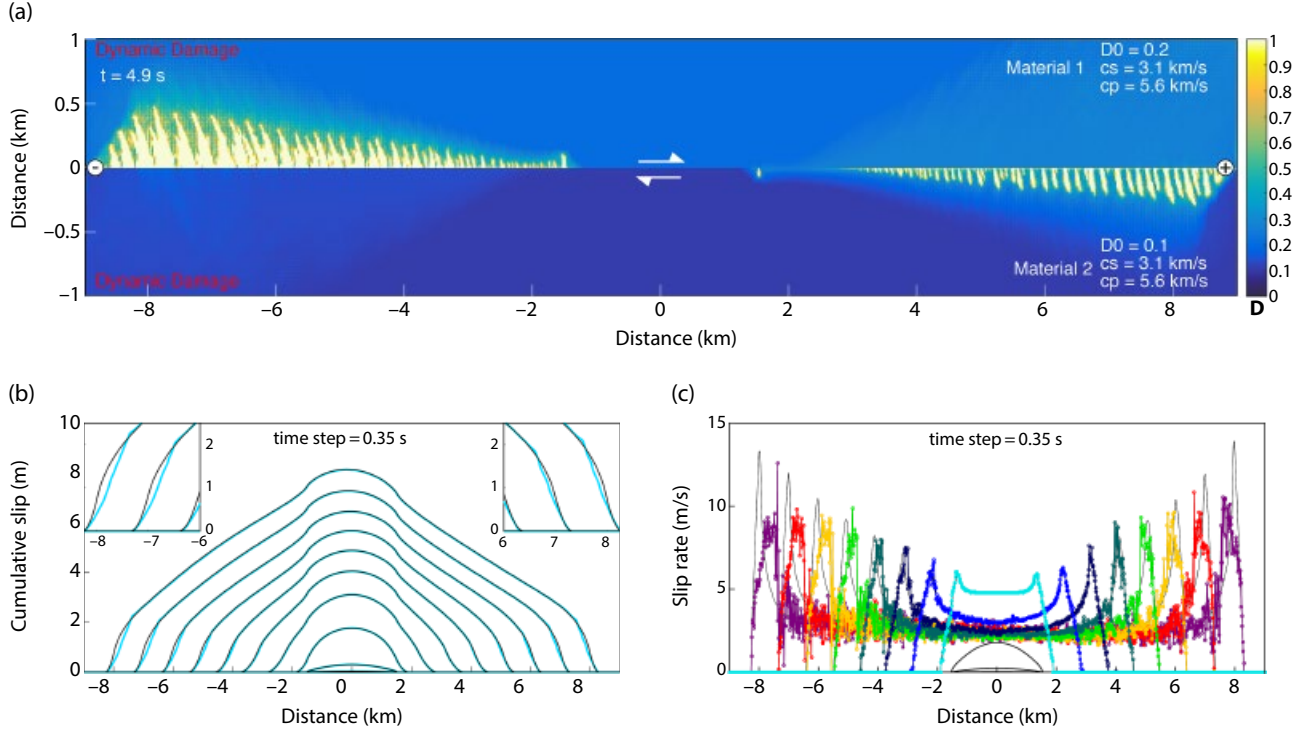


**Figure 14.5** Simulation of a dynamic rupture on a right-lateral fault embedded in a homogeneous medium (Granite). We impose a material contrast across the fault by changing the initial damage density:  $D_0 = 0.2$  on the top side of the fault, and  $D_0 = 0.1$  on the bottom. (a) Evolution of the state parameter  $D$  (density of microcracks in the medium) at  $t = 4.9$  s. The damage zone is more prominent when  $D_0$  is higher. Also shown are the “+” and “-” directions as defined in Figure 14.1). Cumulative slip (b) and slip rate (c) on the fault are displayed with a time increment of 0.35 s. Colored curves correspond to the dynamic simulation with the damage evolution law; thin black curves depict a simulation with the same parametrization only for a pure elastic medium. See electronic version for color representation.

the following rupture [Cappa *et al.*, 2014; Huang *et al.*, 2014]. However, one should be very cautious in developing such a model since other mechanisms can kick off during the interseismic period and heal, at least partly, newly created damage. Indeed, geophysical observations suggest that the damage effect is transient, with gradual (sometimes incomplete) recovery of the elastic properties [e.g., Brenguier *et al.*, 2008; Froment *et al.*, 2014]. This evolution is likely related to healing processes that affect microcracks, fractures, and faults through precipitation of soluble materials or clay mineralization [Mitchell and Faulkner, 2008].

#### 14.4.2.2. Bimaterial Fault

The third scenario explores the combined effects of a damage evolution law and a bimaterial rupture. We keep the top part of the fault (material 1) as Granite, whereas the bottom part's properties (material 2) are typical values for Gabbro (cf Table 14.2). In both cases, we assign an initial damage density of  $D_0 = 0.1$ . For an initial microcrack size of 60 m, this leads to a volume density of cracks,  $N_v$ , of  $3.36 \times 10^{-7}$  (#/m<sup>3</sup>).

For a simulation in a homogeneous medium (same elastic properties, same  $D_0$ ) the dynamic rupture propagates as a bilateral, symmetric crack and produces the same damage pattern on both sides (not shown here). However, adding a material contrast across the fault (but same  $D_0$  on both sides) creates an asymmetry in the damage pattern (Figures 14.7a and 14.6b) and the fault rupture dynamics (Figure 14.7b, c). For a bimaterial rupture, we observe more dynamic damage generation in the softer material. For the tensile quadrant in Granite, the highly damaged zone ( $D \geq 0.5$ ) extends up to 250 m, whereas in the right tensile lobe (Gabbro), it does not exceed 160 m. Concurrently, we observe a stronger reduction in elastic properties for the more compliant material (maximum change of 35.5% for S-wave and 31.0% for P-wave) than for the stiffer material (maximum change of 32.6% for S-wave and 27.9% for P-wave).

Moreover, if we compare with the homogeneous case (difference between upper parts in Figures 14.2a and 14.7a), there is overall less damage for a bimaterial rupture. Ruptures propagating along bimaterial interface generate dynamic changes of the normal stress along the fault.

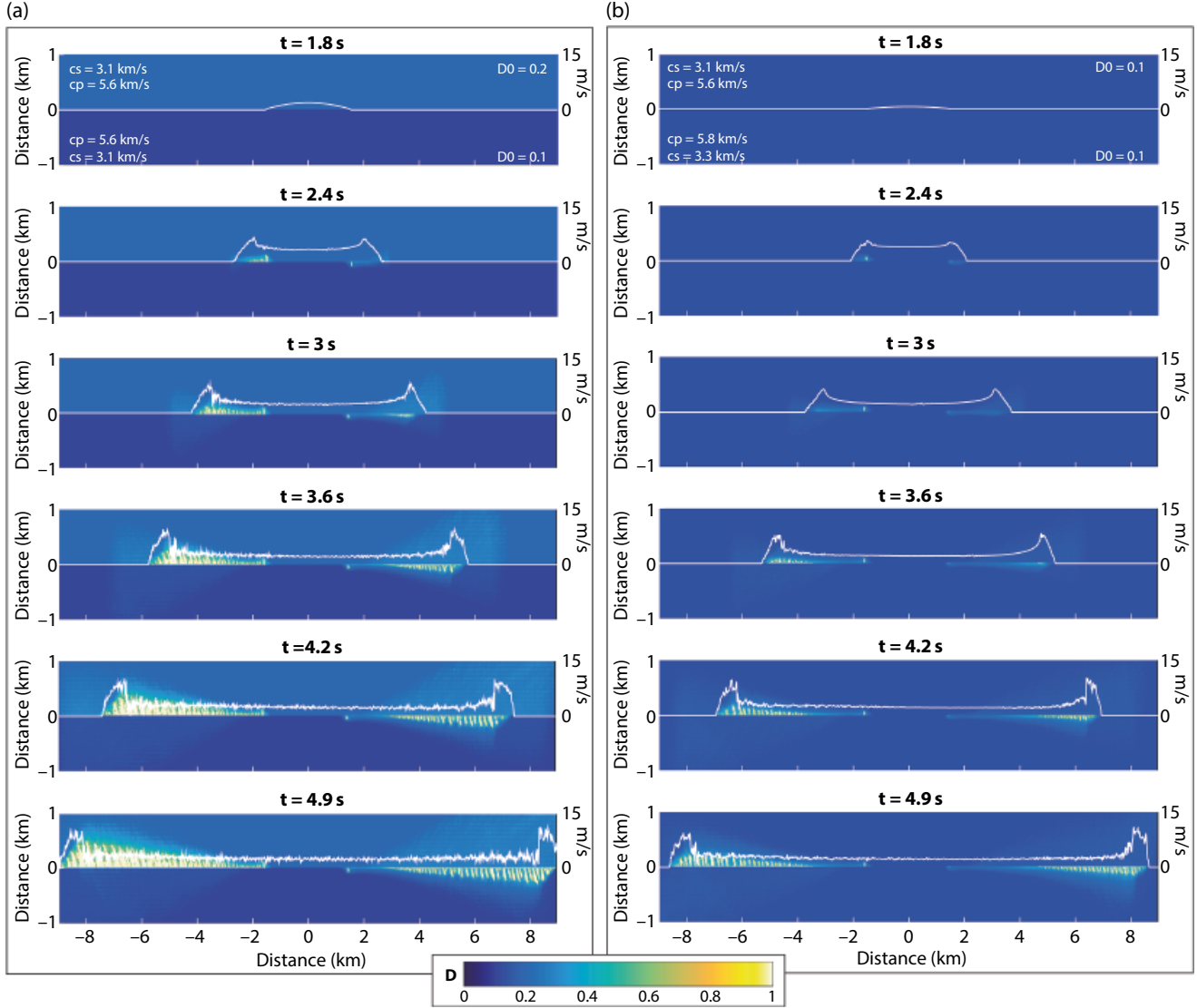


**Figure 14.6** Temporal evolution of the damage parameter  $D$  for (a) a dynamic rupture on a right-lateral fault embedded in a homogeneous medium (Granite) with a material contrast across the fault by changing the initial damage density (see also Figure 14.5) and (b) a dynamic rupture on a bimaterial fault with the initial damage density of  $D_0 = 0.1$  on both sides. Corresponding slip rate (white) is superimposed on the snapshots. See electronic version for color representation.

For subshear ruptures, this bimaterial effect instigates a normal stress change behind the rupture tip, with a tensile stress perturbation in the positive direction and a dynamic compression in the opposite direction [e.g., Rice, 2002; Shi and Ben-Zion, 2006; Langer *et al.*, 2013]. The effect is also sensitive to the degree of material contrast and to the details of static and dynamic friction on the fault plane. In turn, the change in normal stress influences the generation of damage. The compressive perturbation in the negative direction likely explains why the off-fault medium is less damaged when the fault is a bimaterial interface.

Figures 14.7b and 14.7c display the cumulative slip and slip rate on the fault, respectively, with a time increment

of 0.35 s. The first subfigure shows a correlation between the size of the LVZ and the importance of cumulative slip reduction, in comparison to the elastic case, like we observed before. In Figure 14.7c, as expected, the material contrast leads to a reduction in slip rate, compared to the homogeneous case (Figure 14.2c). We also notice that the size of the damage zone correlates with the occurrence of slip rate oscillations. They are more important and occurred earlier in the negative direction, in relation to the development of an LVZ that arises closer to the nucleation-prone patch on that part of the fault. As for the previous simulations, there is also very little modulation in the rupture speed, with no significant difference

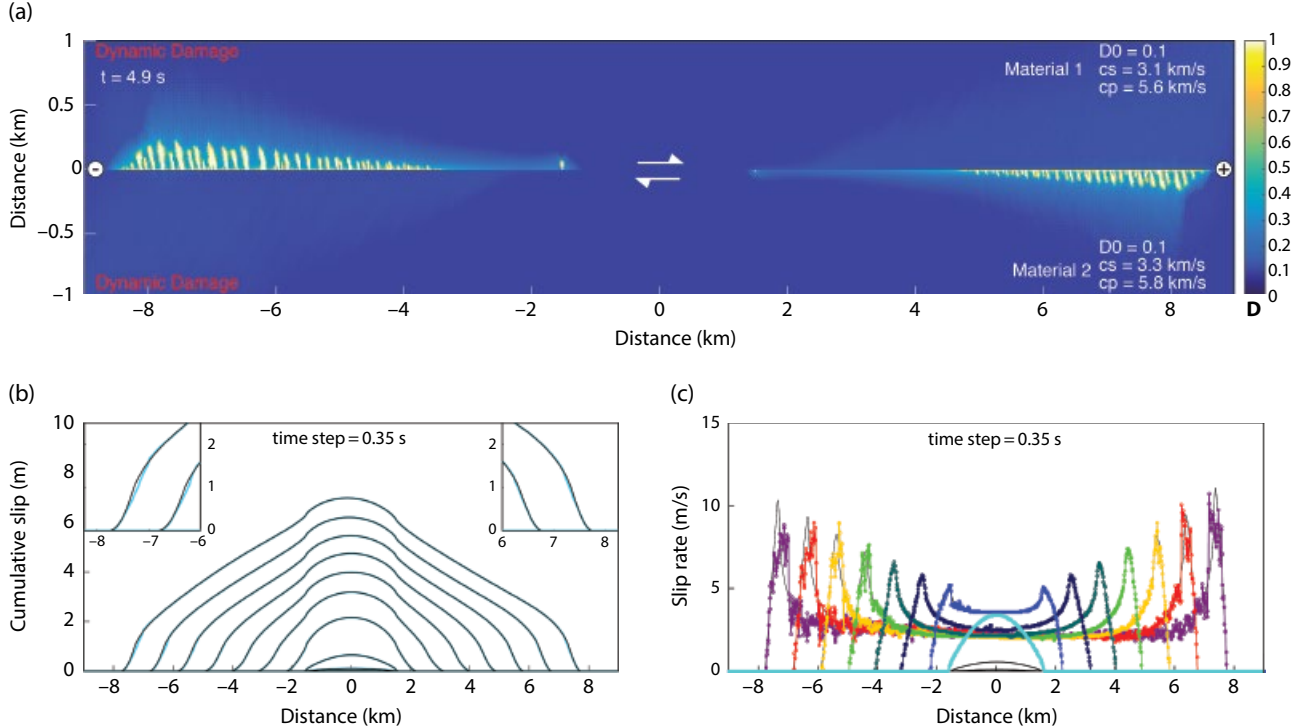


**Figure 14.7** Simulation of a dynamic rupture on a bimaterial fault. We impose a material contrast across the fault by changing the elastic properties: Granite on the top side of the fault, and Gabbro on the bottom. In both cases, we assign an initial damage density of  $D_0 = 0.1$ . (a) Evolution of the state parameter  $D$  (density of microcracks in the medium) at  $t = 4.9$  s. The damage zone is more prominent for the softer material. Also shown are the “+” and “-” directions as defined in Figure 14.1. Cumulative slip (b) and slip rate (c) on the fault are displayed with a time increment of 0.35 s. Colored curves correspond to the dynamic simulation with the damage evolution law; thin black curves depict a simulation for a bimaterial fault embedded in a pure elastic medium. See electronic version for color representation.

between the two rupture fronts (rupture propagates inside an intact material, in both directions).

In the different simulations we run, we also explore the case where we have a material and a damage density contrast across the fault (Granite &  $D_0 = 0.2$  for material 1 and Gabbro &  $D_0 = 0.2$  for material 2). For that particular scenario (not shown here), we basically observe the combined effects described in this section and the section above. The material on the top part of the fault is even more compliant, and we observe a strong difference in damage pattern on both sides of the fault. We also notice that overall less damage is occurring than for the homogeneous case (section 14.4.2.1). The broken symmetry in this simulation is the combined result of contrast in elastic properties and the dynamic inelastic asymmetry. The latter depends on whether the tensile or compressive stress concentration lobe is on the side of the fault with a low or high initial damage density. This is coherent with experimental studies that found that fracture damage introduces an additional asymmetry beyond that due to the associated elastic contrast [Bhat *et al.*, 2010; Biegel *et al.*, 2010]. Based on these simulations, one should

expect to see a cumulative effect on the off-fault medium that would produce an asymmetric damage pattern across the fault, which has been observed by Dor *et al.* [2006].

#### 14.4.3. Effects of Damage on Near-Fault Ground Motion

This last section explores the effects of off-fault damage generation on strong ground motion in the near-source region. Figure 14.8 displays synthetic seismograms of fault-parallel and fault-normal velocities for a dynamic rupture on a right-lateral fault embedded in a homogeneous medium (Granite) with different initial damage on both sides of the fault (cf section 4.2.1 and Figure 14.5). For comparison, we also plot the velocities for an elastic medium without damage evolution (colored curves). Seismograms are located on the extensional side and sample the two newly created damaged zones and the medium that has not undergone any reduction in wave speed. As expected for a sub-Rayleigh rupture, the fault-normal component dominates over the fault-parallel component in both cases. Then, if we compare the different

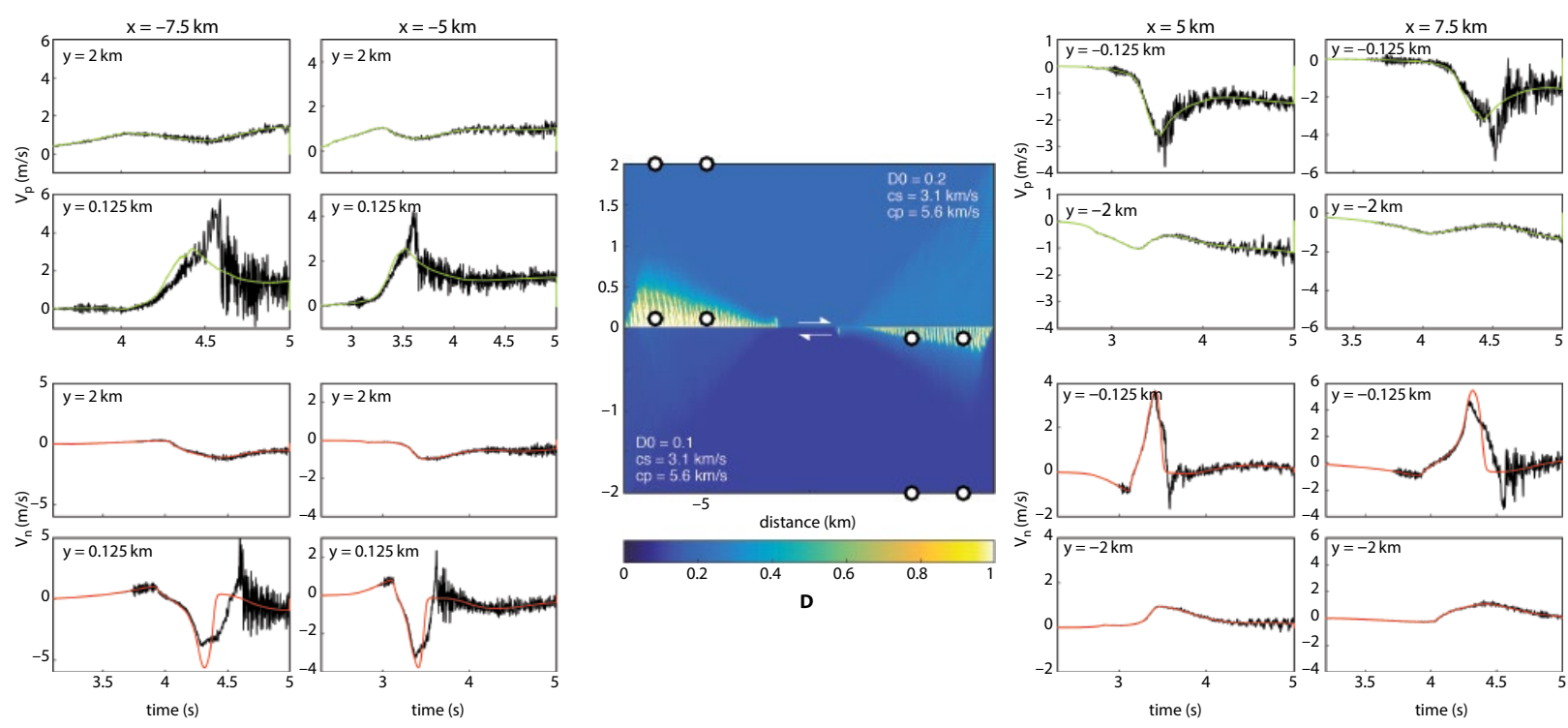


**Figure 14.8** Synthetic seismograms of fault-parallel velocity,  $v_p$  (eight upper quadrants with green curves), and fault-normal velocity,  $v_n$  (eight lower quadrants with red curves). Seismograms are selected so that they sample the damaged and undamaged zones (see the white dots in the middle for location). Black curves correspond to the dynamic simulation with homogeneous elastic properties but different initial damage (section 14.4.2.1 and Figure 14.5). Colored curves correspond to a simulation with the same parametrization but within a pure elastic medium. See electronic version for color representation.

seismograms, we observe at first that the four receivers near the fault, inside the LVZs, record long-lived signal oscillations higher in amplitude than the receivers farther away from the fault. We also notice that this phenomenon is even more emphasized for the two receivers located in the softer material, which has undergone a stronger reduction in elastic properties (section 14.4.2.1). Thereafter, if we compare the simulations with a damage evolution's law and those without, we can see that the velocity profiles are superimposed at first, but then there is a strong mismatch in particle velocity behind the rupture front. This is due to the fact that the rupture front propagates at first in an undamaged material. The oscillations and changes in particle velocity we further observe are related to the off-fault reduction in elastic properties due to dynamic damage and the potential reflections of seismic waves in LVZs. As a consequence, the seismograms located farther away from the fault are less likely to be affected by these oscillations than the receivers inside the LVZs, which record more intense ground shaking. Seismic waves are in fact affected by the damage zone at first, but then propagate away in a homogeneous medium.

Figure 14.9 shows the Fourier velocity spectra of the synthetic seismograms displayed in Figure 14.8. For comparison, we also compute the Fourier amplitude spectra (FAS) for a dynamic rupture in an elastic medium without damage evolution (colored curves). If we compare the two models, we can see that incorporating off-fault damage evolution changes the high-frequency content of the seismograms. We observe that between 5 and 100 Hz, Fourier velocity spectra has a higher slope than the elastic case. This contrast is essentially observed for the fault-normal component and to a smaller extent for the fault-parallel component. The difference between the two models is also more pronounced for the receivers that sample the damaged zones than for the ones farther away from the fault. The complexity we observe in slip rate (section 14.4.1.2), together with the change in elastic properties, is responsible for the high-frequency content in the velocity spectra. The additional high-frequency content is most likely due to the localized nature of damage. Since these localized zones are effectively cracks accelerating at a significant fraction of the shear wave speed, they should contribute to the high-frequency content. This is consistent with the near-fault strong motion records of real earthquakes [Housner, 1947; Wald and Heaton, 1994; Semmane et al., 2005; Dunham et al., 2011] and laboratory experiment observations. Indeed, in his PhD thesis, Passelègue [2015] relates the high-frequency radiation recorded during laboratory earthquakes to the amount of damage that was produced. However, in natural cases, damage is not likely the only source

contribution to high-frequency content. *Dunham et al.* [2011] has, for example, demonstrated that fault roughness induces accelerations and decelerations of the dynamic rupture, together with slip heterogeneities, which also result in ground acceleration spectra that are flat at high frequency. With the model we developed, we can explore in future work these combined effects on the radiated ground motion.

#### 14.4.4. Resolution Test

We appraised the robustness of the results discussed in previous sections by comparing simulations with the same parametrization but for different grid resolutions (Figure 14.10). We compare simulations for a dynamic rupture on a right-lateral fault embedded in a homogeneous medium (Granite) with damage evolution only on the top side of the fault for two different mesh sizes: 30 m (as in section 14.4.1) and 15 m. Figure 14.10 displays synthetic seismograms of fault-normal velocity and the corresponding FAS. Although we observe differences in the location and amplitude of the small oscillations (as a result of localization of damage), overall, the velocity profiles are fairly well captured (Figure 14.10a–d). Accordingly, the Fourier analyses performed on these seismograms show very similar profiles with the same slope for the two different resolutions (Figure 14.10e–h), supporting further the robustness of the features described in section 14.4. Notably, we observe a similar high-frequency content we relate to dynamic damage generation (section 14.4.3), for the two different resolutions. At this stage, we offer once again a note of caution that our results have to be taken more qualitatively here. As previously underlined in section 14.4.1.1, our constitutive law does not have an internal length scale, which affects the exact localization of damage branches.

### 14.5. DISCUSSION AND CONCLUSION

In this chapter, we have provided the description of a micromechanical model that accounts for the dynamic evolution of elastic properties in the surrounding medium, related to dynamic off-fault damage. We have numerically investigated the role of spontaneous off-fault damage generation on earthquake rupture processes and underlined damage-related features that can be pertinent to interpret geophysical observations.

The main difference with models allowing for plastic deformation is that the developed constitutive law accounts for dynamic changes of elastic properties in the off-fault medium. These changes of elastic moduli, related to damage generation, have been observed along natural faults during earthquakes and in laboratory experiments

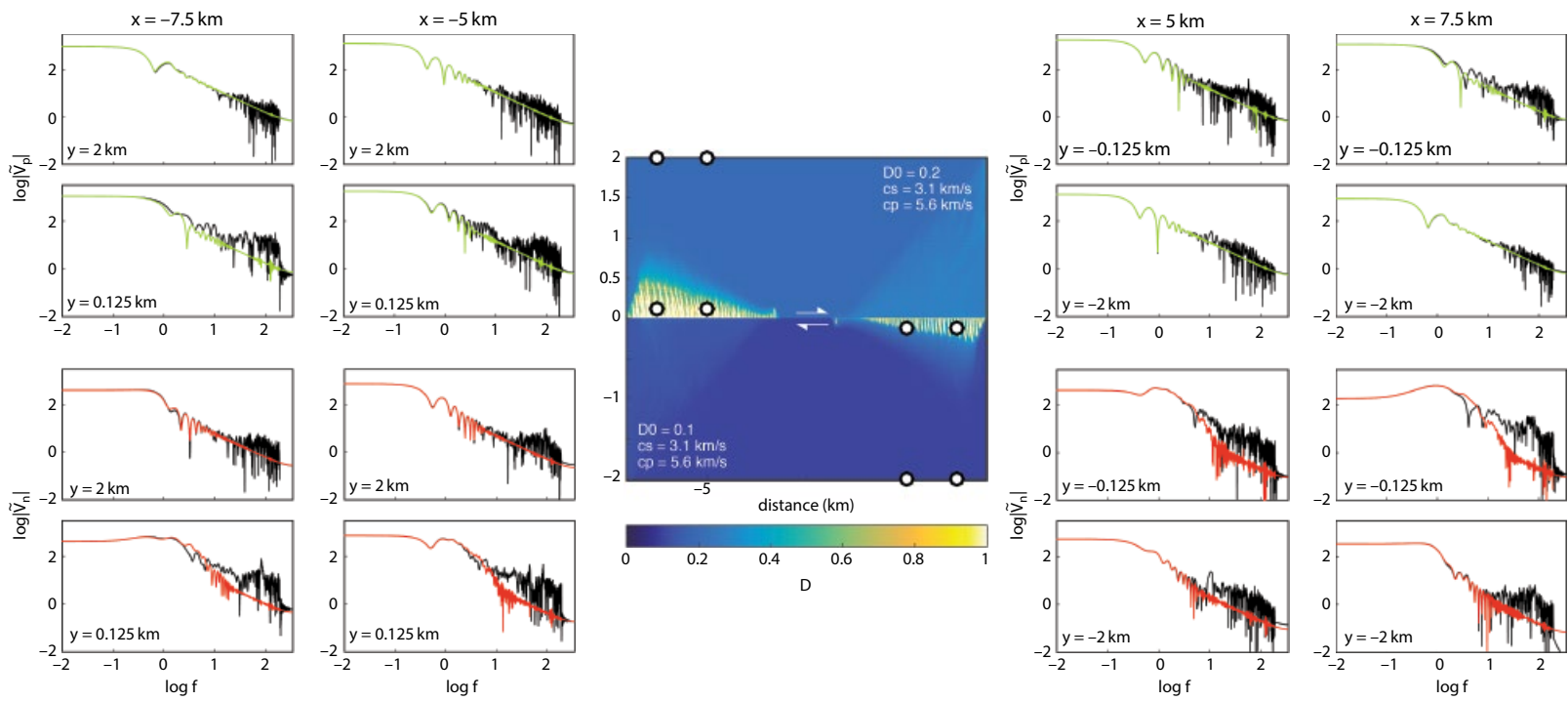


**Figure 14.9** Fourier amplitude spectra (FAS) of fault-parallel velocity,  $v_p$  (eight upper quadrants with green curves), and fault-normal velocity,  $v_n$  (eight lower quadrants with red curves), corresponding to the seismograms in Figure 14.8. Black curves correspond to the dynamic simulation with homogenous elastic properties but different initial damage (section 4.2.1 and Figure 14.5). Colored curves correspond to a simulation with the same parametrization but within a pure elastic medium. Seismograms are selected in order to sample both the damaged and undamaged zones (see the white dots in the middle for location). See electronic version for color representation.

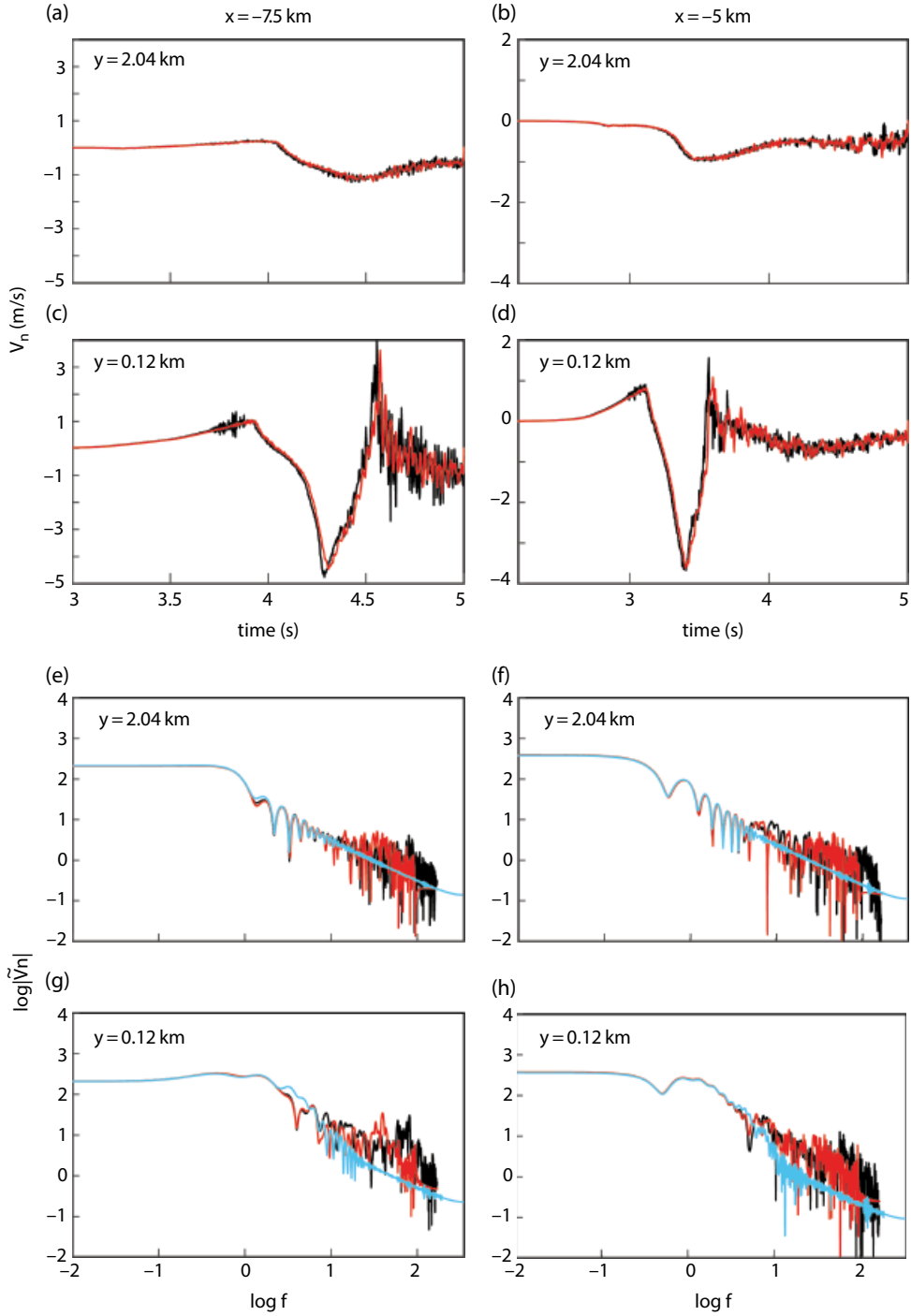


**Figure 14.10** Numerical tests on the resolutions of our model with two different mesh sizes. We compare four synthetic seismograms of fault-normal velocity (a–d) and their corresponding FAS (e–h) for a dynamic rupture on a right-lateral fault embedded in a homogeneous medium (Granite) with damage evolution only on the top side of the fault (section 14.4.1 and Figure 14.2). Black and red curves correspond to the dynamic simulations with a 15 m and 30 m mesh size, respectively. For the FAS (e–h), the light blue curves correspond to a simulation with a 30 m mesh size, with the same parametrization but within a pure elastic medium. See *electronic version* for color representation.

[e.g., Faulkner *et al.*, 2006; Brenguier *et al.*, 2008; Cochran *et al.*, 2009; Froment *et al.*, 2014]. Dynamic changes of elastic properties during earthquakes generate intricate feedbacks between the off-fault damage generation and the dynamic rupture itself that cannot be modeled with plasticity. Moreover, in comparison with preexisting damage models [e.g., Lyakhovsky *et al.*, 1997b; Xu *et al.*, 2014], our constitutive law accounts for the fracture toughness's dependency on loading rate and crack-tip velocities [Chen *et al.*, 2009; Dai *et al.*, 2010, 2011; Wang *et al.*, 2010, 2011; Zhang and Zhao, 2013], which is essential to model properly the microphysics of damage evolution related to earthquake rupture.

We demonstrated that the response of the damage elastic solid is different in the compressional and tensional quadrants with more damage in the tensile lobe (section 14.4.1). This creates an asymmetric pattern across the fault that is expected to increase over time if the fault ruptures in a self-similar fashion. In turn, dynamic damage influences the slip rate on the fault with the development of slip rate oscillations that result in high-frequency content in the radiated ground motion.

Numerical simulation described in section 14.4.2.1 has underlined the importance of incorporating not only the fault history but also the off-fault medium history in dynamic modeling of earthquakes. A small difference in initial damage actively impacts the final pattern, with more dynamic damage generation in the softer material (greater density of initial microcracks). A significant but very challenging step further would be to develop a numerical model of the full fault slip history that accounts for the evolution of elastic properties of the surrounding medium, due to dynamic damage and healing of microcracks in the postseismic period.

In this chapter we have also explored the combined effects of having a damage evolution law and a static bimaterial fault. Detailed investigation has shown that dynamic damage generation is sensitive to material contrast and that the fracture damage introduces an additional asymmetry beyond that due to the associated elastic contrast. The asymmetry produced by the interaction between the rupture front and the off-fault damage can be opposite to that produced by velocity contrast and therefore cannot be modeled with a simple reduction in elastic stiffness. These numerical simulations are in complete agreement with previous experimental studies of mode-II ruptures on an interface that combines a bulk elastic mismatch with a contrast in off-fault damage [Bhat *et al.*, 2010; Biegel *et al.*, 2010].

In the last results section we explored the effects of off-fault damage on strong ground motion in the near-source region. The high-frequency content we observe in the velocity records is related to dynamic damage generation

that induces a reduction in elastic moduli and produces slip-rate oscillations on the fault. It is compatible with strong motion records of real earthquakes and laboratory experiment observations [Housner, 1947; Wald and Heaton, 1994; Semmane *et al.*, 2005; Dunham *et al.*, 2011; Passelègue, 2015]. These results are essential for seismic risk mitigation; however, we investigated only one possible source of high-frequency ground motion. As previously underlined by Dunham *et al.* [2011], fault-roughness, scattering in a nonhomogeneous medium, and local site conditions would also play a role in high-frequency generation during an earthquake.

Our primary results leave open the question of dimensionality. Obviously, wave propagation should differ between a 2D and a 3D model, and therefore this would potentially affect both the damage generation and the ground motion. However, we don't expect too much difference between 2D and 3D when it comes to rupture propagation, since most of the dynamic damage occurs behind the rupture tip. Moreover, damage is sensitive to the background stress, and one should expect to see a depth dependency in the generation of damaged rocks that would affect dynamic ruptures over several seismic cycles. There is a clear need to extend further this kind of model in 3D.

Finally, geophysical observations suggest that off-fault damage is a transient effect, since we observe a gradual recovery of the elastic properties [e.g., Froment *et al.*, 2014]. This evolution is likely related to healing processes that affect microcracks, fractures, and faults through precipitation of soluble materials or clay mineralization [Mitchell and Faulkner, 2008]. While laboratory experiments are in favor of a relatively quick (hours to months) healing of damage [e.g., Morrow *et al.*, 2001], field observations suggest that this damage effect can persist for several years and, in some cases, for thousands of years [e.g., Cochran *et al.*, 2009]. This means that damage does not simply cumulate over time; rather, it is a complex competition between the intensity of the coseismic rupture, the efficiency of healing processes, and time recurrence between earthquakes. When it comes to model fault slip evolution over several seismic cycles, this phenomenon should be taken into account.

## ACKNOWLEDGMENTS

This study was supported by the Agence National de la Recherche (ANR) GeoSMEC contract ANR-12-BS060016. We thank the two anonymous reviewers for insightful detailed comments that helped us improve the manuscript. We also thank J.-P. Ampuero for providing the SEM2DPACK code and for his useful comments on how to add the new constitutive model to the SEM code.

## REFERENCES

- Ampuero, J. P. (2002), Etude physique et numérique de la nucléation des séismes, Ph.D. thesis, Université Paris VII.
- Andrews, D. J. (2005), Rupture dynamics with energy loss outside the slip zone, *Journal of Geophysical Research: Solid Earth*, 110(B1), 307.
- Andrews, D. J., and Y. Ben-Zion (1997), Wrinkle-like slip pulse on a fault between different materials, *Journal of Geophysical Research: Solid Earth*, 102(B1), 553–571.
- Andrews, D. J., and R. A. Harris (2005), The wrinkle-like slip pulse is not important in earthquake dynamics, *Geophysical Research Letters*, 32(23), L23,303.
- Ashby, M. F., and C. G. Sammis (1990), The damage mechanics of brittle solids in compression, *Pure and Applied Geophysics*, 133(3), 489–521.
- Audet, P., and R. Burgmann (2014), Possible control of subduction zone slow-earthquake periodicity by silica enrichment, *Nature*, 510(7505), 389–392.
- Ben-Zion, Y., and Z. Q. Shi (2005), Dynamic rupture on a material interface with spontaneous generation of plastic strain in the bulk, *Earth and Planetary Science Letters*, 236(1-2), 486–496, doi:10.1016/j.epsl.2005.03.025.
- Bhat, H., R. Biegel, A. Rosakis, and C. Sammis (2010), The effect of asymmetric damage on dynamic shear rupture propagation II: With mismatch in bulk elasticity, *Tectonophysics*, 493(3-4), 263–271.
- Bhat, H. S., A. J. Rosakis, and C. G. Sammis (2012), A micro-mechanics based constitutive model for brittle failure at high strain rates, *Journal of Applied Mechanics: Transactions of the ASME*, 79(3), 031,016.
- Bhat, H. S., C. G. Sammis, and A. J. Rosakis (2011), The micro-mechanics of Westerley granite at large compressive loads, *Pure and Applied Geophysics*, 168(12), 2181–2198.
- Biegel, R., H. Bhat, C. Sammis, and A. Rosakis (2010), The effect of asymmetric damage on dynamic shear rupture propagation I: No mismatch in bulk elasticity, *Tectonophysics*, 493(3-4), 254–262.
- Biegel, R. L., and C. G. Sammis (2004), Relating fault mechanics to fault zone structure, in *Advances in geophysics*, vol. 47, pp. 65–111, Elsevier.
- Brenguier, F., M. Campillo, C. Hadzioannou, N. M. Shapiro, R. M. Nadeau, and E. Larose (2008), Postseismic relaxation along the San Andreas fault at Parkfield from continuous seismological observations, *Science*, 321(5895), 1478–1481.
- Bretzke, G. B., and Y. Ben-Zion (2006), Examining tendencies of in-plane rupture to migrate to material interfaces, *Geophysical Journal International*, 167(2), 807–819, doi:10.1111/j.1365-246X.2006.03137.x.
- Byerlee, J. (1978), Friction of rocks, *Pure and Applied Geophysics*, 116(4-5), 615–626.
- Cappa, F., C. Perrin, I. Manighetti, and E. Delor (2014), Off-fault long-term damage: A condition to account for generic, triangular earthquake slip profiles, *Geochem. Geophys. Geosyst.*, 15(4), 1476–1493.
- Chen, R., K. Xia, F. Dai, F. Lu, and S. Luo (2009), Determination of dynamic fracture parameters using a semi-circular bend technique in split Hopkinson pressure bar testing, *Engineering Fracture Mechanics*, 76(9), 1268–1276.
- Chester, F. M., J. P. Evans, and R. L. Biegel (1993), Internal structure and weakening mechanisms of the San Andreas fault, *Journal of Geophysical Research: Solid Earth*, 98(B1), 771–786.
- Chester, F. M., and J. M. Logan (1986), Implications for mechanical properties of brittle faults from observations of the Punchbowl fault zone, California, *Pure and Applied Geophysics*, 124(1), 79–106, doi:10.1007/BF00875720.
- Childs, C., T. Manzocchi, J. J. Walsh, C. G. Bonson, A. Nicol, and M. P. Schpfer (2009), A geometric model of fault zone and fault rock thickness variations, *Journal of Structural Geology*, 31(2), 117–127.
- Cochard, A., and J. R. Rice (2000), Fault rupture between dissimilar materials: Ill-posedness, regularization, and slip-pulse response, *Journal of Geophysical Research: Solid Earth*, 105(B11), 25,891–25,907.
- Cochran, E. S., Y. G. Li, P. M. Shearer, S. Barbot, Y. Fialko, and J. E. Vidale (2009), Seismic and geodetic evidence for extensive, long-lived fault damage zones, *Geology*, 37(4), 315–318.
- Collettini, C., C. Viti, S. A. F. Smith, and R. E. Holdsworth (2009), Development of interconnected talc networks and weakening of continental low-angle normal faults, *Geology*, 37(6), 567–570.
- Dai, F., R. Chen, M. Iqbal, and K. Xia (2010), Dynamic cracked chevron notched Brazilian disc method for measuring rock fracture parameters, *International Journal of Rock Mechanics and Mining Sciences*, 47(4), 606–613.
- Dai, F., K. Xia, H. Zheng, and Y. Wang (2011), Determination of dynamic rock mode-I fracture parameters using cracked chevron notched semi-circular bend specimen, *Engineering Fracture Mechanics*, 78(15), 2633–2644.
- Dalguer, L. A., K. Irikura, and J. D. Riera (2003), Simulation of tensile crack generation by three-dimensional dynamic shear rupture propagation during an earthquake, *J. Geophys. Res.*, 108(B3).
- Day, S. M., L. A. Dalguer, N. Lapusta, and Y. Liu (2005), Comparison of finite difference and boundary integral solutions to three-dimensional spontaneous rupture, *Journal of Geophysical Research: Solid Earth*, 110(B12), B12,307, doi:10.1029/2005JB003813.
- den Hartog, S. A. M., C. J. Peach, D. A. M. de Winter, C. J. Spiers, and T. Shimamoto (2012), Frictional properties of megathrust fault gouges at low sliding velocities: New data on effects of normal stress and temperature, *Journal of Structural Geology*, 38, 156–171.
- Deshpande, V. S., and A. G. Evans (2008), Inelastic deformation and energy dissipation in ceramics: A mechanism-based constitutive model, *Journal of the Mechanics and Physics of Solids*, 56(10), 3077–3100.
- Dor, O., T. K. Rockwell, and Y. Ben-Zion (2006), Geological observations of damage asymmetry in the structure of the San Jacinto, San Andreas and Punchbowl faults in Southern California: A possible indicator for preferred rupture propagation direction, *Pure and Applied Geophysics*, 163(2), 301–349, doi:10.1007/s00024-005-0023-9.

- Dunham, E. M., D. Belanger, L. Cong, and J. E. Kozdon (2011), Earthquake ruptures with strongly rate-weakening friction and off-fault plasticity, part 2: Nonplanar faults, *Bulletin of the Seismological Society of America*, 101(5), 2308–2322.
- Faulkner, D. R., T. M. Mitchell, D. Healy, and M. J. Heap (2006), Slip on “weak” faults by the rotation of regional stress in the fracture damage zone, *Nature*, 444(7121), 922–925.
- Faulkner, D. R., T. M. Mitchell, E. Jensen, and J. Cembrano (2011), Scaling of fault damage zones with displacement and the implications for fault growth processes, *J. Geophys. Res.*, 116(B5).
- Finzi, Y., E. H. Hearn, Y. Ben-Zion, and V. Lyakhovsky (2009), Structural properties and deformation patterns of evolving strike-slip faults: Numerical simulations incorporating damage rheology, *Pure and Applied Geophysics*, 166(10), 1537–1573, doi:10.1007/s00024-009-0522-1.
- Froment, B., J. J. McGuire, R. D. van der Hilst, P. Gouédard, E. C. Roland, H. Zhang, and J. A. Collins (2014), Imaging along-strike variations in mechanical properties of the Gofar Transform fault, East Pacific Rise, *Journal of Geophysical Research: Solid Earth*, 119(9), 7175–7194.
- Gabriel, A. A., J. P. Ampuero, L. A. Dalguer, and P. M. Mai (2013), Source properties of dynamic rupture pulses with off-fault plasticity, *Journal of Geophysical Research: Solid Earth*, 118(8), 4117–4126, doi:10.1002/jgrb.50213.
- Gao, G., W. Yao, K. Xia, and Z. Li (2015), Investigation of the rate dependence of fracture propagation in rocks using digital image correlation (DIC) method, *Engineering Fracture Mechanics*, 138, 146–155, doi:10.1016/j.engfracmech.2015.02.021.
- Hill, R., and J. R. Rice (1973), Elastic potentials and structure of inelastic constitutive laws, *Siam Journal on Applied Mathematics*, 25(3), 448–461.
- Hiramatsu, Y., H. Honma, A. Saiga, M. Furumoto, and T. Ooida (2005), Seismological evidence on characteristic time of crack healing in the shallow crust, *Geophys. Res. Lett.*, 32(9).
- Hok, S., M. Campillo, F. Cotton, P. Favreau, and I. Ionescu (2010), Off-fault plasticity favors the arrest of dynamic ruptures on strength heterogeneity: Two-dimensional cases, *Geophysical Research Letters*, 37, L02,306, doi:10.1029/2009GL041888.
- Housner, G. W. (1947), Characteristics of strong-motion earthquakes, *Bulletin of the Seismological Society of America*, 37(1), 19–31.
- Huang, Y., J.-P. Ampuero, and D. V. Helmberger (2014), Earthquake ruptures modulated by waves in damaged fault zones, *J. Geophys. Res. Solid Earth*, 119(4), 3133–3154.
- Kame, N., J. R. Rice, and R. Dmowska (2003), Effects of pre-stress state and rupture velocity on dynamic fault branching, *J. Geophys. Res.*, 108(B5).
- Kanamori, H. (2006), Lessons from the 2004 Sumatra-Andaman earthquake, pp. 1927–1945, Royal Society.
- Kaneko, Y., and Y. Fialko (2011), Shallow slip deficit due to large strike-slip earthquakes in dynamic rupture simulations with elasto-plastic off-fault response, *Geophysical Journal International*, 186(3), 1389–1403.
- King, D. S. H., and C. Marone (2012), Frictional properties of olivine at high temperature with applications to the strength and dynamics of the oceanic lithosphere, *Journal of Geophysical Research: Solid Earth*, 117, B12,203, doi:10.1029/2012JB009511.
- Klinger, Y., J.-H. Choi, and A. Vallage (2017), Fault branching and long-term earthquake rupture scenario for strike-slip earthquakes, in *Fault Zone Dynamic Processes: Evolution of Fault Properties During Seismic Rupture*, edited by M. Thomas, H. S. Bhat, and T. Mitchell, this volume, AGU/Wiley.
- Langer, S., D. Weatherley, L. Olsen-Kettle, and Y. Finzi (2013), Stress heterogeneities in earthquake rupture experiments with material contrasts, *Journal of the Mechanics and Physics of Solids*, 61(3), 742–761.
- Li, Y.-G., K. Aki, D. Adams, A. Hasemi, and W. H. K. Lee (1994), Seismic guided waves trapped in the fault zone of the Landers, California, earthquake of 1992, *J. Geophys. Res.*, 99(B6), 11,705–11,722.
- Li, Y.-G., P. Chen, E. S. Cochran, J. E. Vidale, and T. Burdette (2006), Seismic evidence for rock damage and healing on the San Andreas fault associated with the 2004 m 6.0 Parkfield earthquake, *Bulletin of the Seismological Society of America*, 96(4B), S349–S363, doi:10.1785/0120050803.
- Lyakhovsky, V., and Y. Ben-Zion (2014), A continuum damage-breakage faulting model and solid-granular transitions, *Pure and Applied Geophysics*, 171(11), 3099–3123, doi:10.1007/s00024-014-0845-4.
- Lyakhovsky, V., Y. Ben-Zion, and A. Agnon (1997a), Distributed damage, faulting, and friction, *Journal of Geophysical Research: Solid Earth*, 102(B12), 27,635–27,649.
- Lyakhovsky, V., Z. Reches, R. Weinberger, and T. E. Scott (1997b), Non-linear elastic behaviour of damaged rocks, *Geophysical Journal International*, 130(1), 157–166.
- Ma, S. (2008), A physical model for widespread near-surface and fault zone damage induced by earthquakes, *Geochem. Geophys. Geosyst.*, 9(11).
- Mitchell, T. M., and D. R. Faulkner (2008), Experimental measurements of permeability evolution during triaxial compression of initially intact crystalline rocks and implications for fluid flow in fault zones, *Journal of Geophysical Research: Solid Earth*, 113(B11), 412.
- Mitchell, T. M., and D. R. Faulkner (2009), The nature and origin of off-fault damage surrounding strike-slip fault zones with a wide range of displacements: A field study from the Atacama fault system, Northern Chile, *Journal of Structural Geology*, 31(8), 802–816.
- Morrow, C. A., D. E. Moore, and D. A. Lockner (2001), Permeability reduction in granite under hydrothermal conditions, *J. Geophys. Res.*, 106(B12), 30,551–30,560.
- Ngo, D., Y. Huang, A. Rosakis, W. A. Griffith, and D. Pollard (2012), Off-fault tensile cracks: A link between geological fault observations, lab experiments, and dynamic rupture models, *J. Geophys. Res.*, 117(B1).
- Niemeijer, A., C. Marone, and D. Elsworth (2010), Fabric induced weakness of tectonic faults, *Geophysical Research Letters*, 37, L03,304.

- Palmer, A. C., and J. R. Rice (1973), The growth of slip surfaces in the progressive failure of over-consolidated clay, *Proceedings of the Royal Society of London A: Mathematical, Physical and Engineering Sciences*, 332(1591), 527–548, doi:10.1098/rspa.1973.0040.
- Passelègue, F. (2015), Experimental study of the seismic rupture., Ph.D. thesis, Laboratoire de Géologie de l'École Normale Supérieure, advisors: Ral Madariaga and Alexandre Schubnel.
- Prakash, V., and R. Clifton (1993), Time resolved dynamic friction measurements in pressure shear, *Experimental Techniques in the Dynamics of Deformable Solids*, 165, 33–48.
- Ranjith, K., and J. Rice (2001), Slip dynamics at an interface between dissimilar materials, *Journal of the Mechanics and Physics of Solids*, 49(2), 341–361.
- Rice, J. R. (1968), A path independent integral and the approximate analysis of strain concentration by notches and cracks, *Journal of Applied Mechanics*, 35(2), 379–386, doi:10.1115/1.3601206.
- Rice, J. R. (1971), Inelastic constitutive relations for solids: An internal-variable theory and its application to metal plasticity, *Journal of the Mechanics and Physics of Solids*, 19(6), 433–455, doi:10.1016/0022-5096(71)90010-X.
- Rice, J. R. (1975), Continuum mechanics and thermodynamics of plasticity in relation to microscale deformation mechanisms, in *Constitutive equations in plasticity*, edited by A. Argon, chap. 2, MIT Press, Cambridge, Mass.
- Rice, J. R. (2002), New perspectives on crack and fault dynamics, *Mechanics for a New Millennium: Proceedings of the 20th International Congress of Theoretical and Applied Mechanics Chicago, Illinois, USA 27 August–2 September 2000*, pp. 1–24, Springer, Netherlands, Dordrecht.
- Rice, J. R., C. G. Sammis, and R. Parsons (2005), Off-fault secondary failure induced by a dynamic slip pulse, *Bulletin of the Seismological Society of America*, 95(1), 109–134, doi:10.1785/0120030166.
- Rubin, A. M., and J.-P. Ampuero (2007), Aftershock asymmetry on a bimaterial interface, *J. Geophys. Res.*, 112(B5).
- Savage, H. M., and E. E. Brodsky (2011), Collateral damage: Evolution with displacement of fracture distribution and secondary fault strands in fault damage zones, *J. Geophys. Res.*, 116, B03405, doi:10.1029/2010JB007665.
- Scholz (2002), *The mechanics of earthquakes and faulting*, Cambridge University Press.
- Scholz, C. H. (1998), Earthquakes and friction laws, *Nature*, 391, 37–42.
- Semmane, F., F. Cotton, and M. Campillo (2005), The 2000 Tottori earthquake: A shallow earthquake with no surface rupture and slip properties controlled by depth, *J. Geophys. Res.*, 110(B3).
- Shi, Z., and Y. Ben-Zion (2006), Dynamic rupture on a bimaterial interface governed by slip-weakening friction, *Geophysical Journal International*, 165(2), 469–484.
- Shipton, Z., and P. Cowie (2001), Damage zone and slip-surface evolution over  $\mu\text{m}$  to km scales in high-porosity Navajo sandstone, Utah, *Journal of Structural Geology*, 23(12), 1825–1844.
- Sibson, R. H. (1977), Fault rocks and fault mechanisms, *Journal of the Geological Society of London*, 133(3), 191–213, doi:10.1144/gsjgs.133.3.0191.
- Suzuki, T. (2012), Understanding of dynamic earthquake slip behavior using damage as a tensor variable: Microcrack distribution, orientation, and mode and secondary faulting, *J. Geophys. Res.*, 117(B5).
- Templeton, E. L., and J. R. Rice (2008), Off-fault plasticity and earthquake rupture dynamics: 1. dry materials or neglect of fluid pressure changes, *J. Geophys. Res.*, 113(B9).
- Thomas, M. Y., J.-P. Avouac, J.-P. Gratier, and J.-C. Lee (2014a), Lithological control on the deformation mechanism and the mode of fault slip on the Longitudinal Valley fault, *Taiwan, Tectonophysics*, 632, 48–63.
- Thomas, M. Y., J.-P. Avouac, J. Champenois, J.-C. Lee, and L.-C. Kuo (2014b), Spatiotemporal evolution of seismic and aseismic slip on the Longitudinal Valley fault, *Taiwan, Journal of Geophysical Research: Solid Earth*, 119, 5114–5139.
- Vallage, A., Y. Klinger, R. Grandin, H. S. Bhat, and M. Pierrot-Deseilligny (2015), Inelastic surface deformation during the 2013 Mw 7.7 Balochistan, Pakistan, earthquake, *Geology*, 43(12), 1079–1082.
- Vermilye, J. M., and C. H. Scholz (1998), The process zone: A microstructural view of fault growth, *Journal of Geophysical Research: Solid Earth*, 103(B6), 12,223–12,237.
- Wald, D. J., and T. H. Heaton (1994), Spatial and temporal distribution of slip for the 1992 Landers, California, earthquake, *Bulletin of the Seismological Society of America*, 84(3), 668–691.
- Walsh, J. B. (1965a), The effect of cracks in rocks on Poisson's ratio, *J. Geophys. Res.*, 70(20), 5249–5257.
- Walsh, J. B. (1965b), The effect of cracks on the compressibility of rock, *J. Geophys. Res.*, 70(2), 381–389.
- Wang, L., S. Hainzl, M. Sinan Zeren, and Y. Ben-Zion (2010), Postseismic deformation induced by brittle rock damage of aftershocks, *Journal of Geophysical Research*, 115(B10), 422.
- Wang, Q., F. Feng, M. Ni, and X. Gou (2011), Measurement of mode I and mode II rock dynamic fracture toughness with cracked straight through flattened Brazilian disc impacted by split Hopkinson pressure bar, *Engineering Fracture Mechanics*, 78(12), 2455–2469.
- Wibberley, C. A., G. Yielding, and G. Di Toro (2008), Recent advances in the understanding of fault zone internal structure: A review, *Geological Society, London, Special Publications*, 299(1), 5–33.
- Wilson, J. E., J. S. Chester, and F. M. Chester (2003), Microfracture analysis of fault growth and wear processes, Punchbowl fault, San Andreas system, California, *Journal of Structural Geology*, 25(11), 1855–1873.
- Xu, S., Y. Ben-Zion, and J.-P. Ampuero (2012), Properties of inelastic yielding zones generated by in-plane dynamic ruptures II. Detailed parameter-space study, *Geophysical Journal International*, 191(3), 1343–1360, doi:10.1111/j.1365-246X.2012.05685.x.
- Xu, S., Y. Ben-Zion, J.-P. Ampuero, and V. Lyakhovsky (2014), Dynamic ruptures on a frictional interface with off-fault brittle damage: Feedback mechanisms and effects on slip and

- near-fault motion, *Pure and Applied Geophysics*, 172(5), 1243–1267, doi:10.1007/s00024-014-0923-7.
- Yamashita, T. (2000), Generation of microcracks by dynamic shear rupture and its effects on rupture growth and elastic wave radiation, *Geophysical Journal International*, 143(2), 395–406.
- Zhang, Q., and J. Zhao (2013), Effect of loading rate on fracture toughness and failure micromechanisms in marble, *Engineering Fracture Mechanics*, 102, 288–309.
- Zhou, X., and A. Aydin (2010), Mechanics of pressure solution seam growth and evolution, *Journal of Geophysical Research*, 115(B12), 207.